The Use of Laboratory Erosion Tests for the Prediction of Wear in Pneumatic Conveyor Bends

by

Anthony John Burnett

Vol II

Thesis submitted in partial fulfilment of the
requirements for the award of the degree of
Doctor of Philosophy
under the conditions of the award of
higher degrees of
The University of Greenwich

The University of Greenwich
Woolwich, London, UK

June 1996

VOLUME 2

The Use of Laboratory Erosion Tests for the Prediction of Wear in Pneumatic Conveyor Bends

Anthony J. Burnett

Abstract

This thesis describes a programme of work which has been undertaken with the objective of investigating means of using a laboratory erosion tester to predict the life of a bend in a pneumatic conveyor.

Providing a link between a laboratory erosion tester and erosion tests on a pneumatic conveyor would lead to the development of an inexpensive way of predicting the life of a pipe bend operating under any given set of conveying conditions.

An extensive literature review was carried out. From this it was concluded that very little work of an experimental corroborative nature had been carried out to substantiate whether erosion test results from a laboratory tester could be used to predict the live of a pneumatic conveyor bend.

Two test facilities were constructed to carry out tests under accurately controlled conditions. The first of these was a laboratory 'rotating disc accelerator' erosion tester, and the second an industrially scaled pneumatic conveying test facility.

Both test facilities yielded results that followed previously reported trends but also illustrated some trends that have been unreported in earlier work. It was found that the 'rotating disc accelerator' simulated erosion with minimal interference from inter-particulate collisions. For the pneumatic conveyor test bend used it was found that puncture of the bend wall occurred in the region where secondary particle impacts occurred, rather than in the region of primary impacts as reported in earlier work. Explanations for both these observations are given.

An optically based construction for a cylindrical mirror was used to predict the location of the puncture point in the bend, and the intensification of particle impacts in the region of the pipe bend due to the geometry of the bend. When this was combined with an empirical erosion model derived from results obtained from the rotating disc accelerator, an accurate estimate of the life of the bend could be made. Further development of this model is discussed.

An extensive series of recommendations for further work to address some of the findings discovered during this work are given.

Acknowledgements

Numerous people have helped and supported me throughout this project, and it would be extremely remiss of me not to thank them.

Firstly, I would like to thank both Professor Alan Reed and Dr. Mike Bradley of The Wolfson Centre for Bulk Solids Handling Technology, The University of Greenwich for initiating the project and fulfilling the roles of supervisors, mentors and, when the going got tough, motivators, so well throughout the duration of this project. Dr. Mike Bradley deserves special distinction for being so thorough during the proof reading of the final document, as well as for instigating some stimulating discussions concerning the analysis of the results obtained from the test work carried out during this project.

I gratefully acknowledge the assistance of Mr. Roger Barnes and Dr. Steve Woodhead, (both of The Wolfson Centre for Bulk Solids Handling Technology), who provided much needed assistance in my struggle to overcome difficulties with the electrical installations in both of the test rigs. Without their input I would not have got as far as I have. Dr. Mayur Patel (The University of Greenwich) and Dr. Tim Selves (now Trebor Bassett Ltd. formerly The University of Greenwich) are thanked for giving me assistance in numerical modelling and instrumentation, respectively.

Professor Sunil De Silva, Mr. G.J. Liaklev of Department of Powder Science Technology, Telemark Technological Research and Development Centre, Porsgrunn, Norway and Mr. P.T. Moore of Loughborough University of Technology, UK deserve a special word of mention for embracing the concept of collaborative erosion test rig comparison work so enthusiastically, and carrying out the work so efficiently.

The assistance of the technical staff of The Wolfson Centre for Bulk Solids Handling Technology, The University of Greenwich, in particular; Messrs Mike Holman, John O'Connor and Tony Kelly is gratefully acknowledged. Both of the test rigs used in this project would not have existed without the application of their skills to the rig construction. The assistance of the innovative outlook of Mr. Andrew Pittman in the design of critical parts of the test equipment also deserves mention, and my thanks.

Financial support from the Science and Engineering Research Council (now EPSRC) and the donation of test materials from PoliHi Solidur Ltd and Morgan Matroc Ltd. is gratefully acknowledged.

I would like to thank my family and friends. They all deserve my thanks for putting up with my mildly obsessive and anti-social behaviour at times, I sincerely hope that I can make amends. I know they have wondered why I undertook this project, but despite this they have never failed to provide me with encouragement and unconditional support.

Finally, I would like to dedicate this work to both of my grandfathers. Firstly, Dr. Jack Burnett, a man for whom the pursuit of knowledge was a passion and a hobby and, secondly, Charles Ward, a craftsman and engineer. I know they would have derived much pleasure as well as satisfaction from the completion of this work.

Author's Note

All of the work in this thesis is the sole and original work of the author, except where stated otherwise by acknowledgement or reference.

Table of Contents

Abstract i
Acknowledgements ii
Author's Note iv
Table of Contents v

VOLUME 1

Chapter 1: Introduction 1
1.1 Introduction 1
1.2 Project Objectives 3
1.3 Project Preview 4

Chapter 2: A Review of the Technology Applied to the Prediction of Erosion in Pneumatic Conveyors to Date 6
2.1 Introduction 6
2.2 A Discussion Concerning the Inter-relation of System Properties which Affect Erosion in Pneumatic Conveyors 6
  2.2.1 A Description of Two Phase Flows and Their Effect on Erosion 7
  2.2.2 The Geometry of the Surfaces Suffering Erosion in Pneumatic Conveyors 11
  2.2.3 Pipe Wall and Particle Material Properties Which Affect Erosion 17
2.3 Erosion Studies Previously Carried Out on Pneumatic Conveyor Bends, and the Models that have been Derived for the Prediction of their Lives 19
  2.3.1 Brauer H. and Kriegel E. 1964-1970 19
  2.3.2 Mason J.S., Smith B.V., *et al.* 1972-1973 and Yeung W.S., 1979 19
  2.3.3 Bikbaev F.A., Maksimenko M.Z., Krasnov V.I. *et al.* 1972-1973 20
  2.3.4 Mills D., Mason J.S., Tong K.N. and Agarwal V.K. 1975-1986 20
  2.3.5 Shimoda K. and Yukawa T., 1983 21
  2.3.6 Hoadley D. and Johnson T.D. 1985-1987 21
  2.3.7 Flemmer R.L.C., Flemmer C.L. *et al.*, 1988 21
  2.3.8 Sato S., Shimizu A., Yagi Y., Yoshida H. and Yokomine T. 1993-1994 22
2.4 Investigation of Erosion Using Bench Sized Erosion Testing Devices 22
  2.4.1 Introduction to the Requirement and Use of Small Scale Erosion Testing Devices 22
  2.4.2 Rotating Disc Accelerator Erosion Tester 23
  2.4.3 Gas Blast Erosion Tester 23
  2.4.4 Gas Gun Impact Testers 26
  2.4.5 The Whirling Arm Test Rig 26
  2.4.6 Free Fall Rig 26

2.4.7 Submerged Rotating Arm Rig 26

2.5 A Detailed Review of the Test Work Carried Out on Laboratory Erosion Testers and Its Comparison with Pneumatic Conveyor Tests 27

2.5.1 Shimoda K. and Yukawa T., 1983 [S4] 27

2.5.2 Mills S., *et al.*, 1987 [M7] 28

2.5.3 Hoadley D. and Johnson T.D., *et al.* 1987 [H8,J1,H9,J2] 29

2.5.4 Sato S. and Shimizu A., *et al.* 1993-1994 [S5,S6] 30

2.6 Conclusions Made as a Consequence of this Literature Review 31

Chapter 3: The Structure of the Experimental Investigation 33

3.1 Introduction 33

3.2 Choice of Variables to be Investigated 33

3.3 The Choice of the Laboratory Erosion Tester 35

3.3.1 The Effect that the Choice of Test Variables had on the Design and Use of the 'Rotating Disc Accelerator' Erosion Tester 38

3.4 The Pneumatic Conveyor Test Facility 39

3.4.1 The Effect that the Choice of Test Variables had on the Design and Use of the Pneumatic Conveyor Test Facility 39

3.5 The Structure of the Complete Test Programme 41

Chapter 4: A Description of the Work Carried Out on the 'Rotating Disc Accelerator' Erosion Tester 43

4.1 Introduction 43

4.2 Design and Construction of the Rotating Disc Accelerator Erosion Tester 43

4.2.1 Design of the Rotating Disc Accelerator Erosion Tester 43

4.2.1.1 Design Features that were Considered for the Construction of the Rotating Disc Accelerator Erosion Tester 43

4.2.1.2 A Brief Description of the Rotating Disc Accelerator Erosion Tester 43

4.2.2 Selection of the Materials Used in the Test Programme 46

4.2.3 Development of a Model of the Rig Operation 46

4.2.3.1 Introduction 46

4.2.3.2 Calculation of the Particle Velocity at Exit from the Rotating Disc 48

4.2.3.3 Calculation of the Impingement Angles of the Particles on the Target Surfaces 49

4.2.3.4 Calculation of the Mass of Abrasive Particles Striking the Target Surface 49

4.2.3.5 Calculation of the Particle Jet Dispersion and Its Effects on the Particle Dynamics at the Target Surface 49

4.2.4 Calibration of the Test Facility 51

4.2.4.1 Introduction to the Calibration Methods 51

4.2.4.2 Calibration of the Vibratory Feeder 51
4.2.4.3 Calibration Tests to Confirm the Accuracy of the Particle Velocity Vector on Exit from the Rotating Disc 52
4.2.4.4 Calibration Tests for Assessing the Dispersion of the Particle Jet at the Target Surface 52
4.2.4.5 Summary of the Calibration Work 54
4.2.5 Test Method Employed for the Rotating Disc Accelerator Erosion Tester 54
4.2.6 Comparisons Between the Rotating Disc Accelerator and Another Form of Erosion Tester 55
4.2.6.1 The Reasons for Carrying out Comparative Tests 55
4.2.6.2 Details Regarding the Design of the Erosion Testers Used in this Work 55
4.2.6.3 Details of the Comparative Test Programme 56
4.2.6.4 Comparative Test Programme Results 56
4.2.6.5 Conclusions Drawn from this Comparative Test Programme 57
4.3 The Detailed Analysis of the Erosion Resistance of a Structural Mild Steel 58
4.3.1 Reasons for Carrying Out this Test Programme 58
4.3.2 Details of the Mild Steel Test Programme 59
4.3.2.1 Test Conditions in the Rotating Disc Accelerator Erosion Tester 59
4.3.2.2 Test Materials 59
4.3.2.3 Notes on the Test Method Used 60
4.3.3 Results of the Mild Steel Test Programme 60
4.3.4 An Empirical Numerical Model for the Erosion of Mild Steel 63
4.3.4.1 Development of the Numerical Model 63
4.3.4.2 Conclusions 69
4.3.5 The Use of the Semi-Empirical Finnie / Bitter Model for the Prediction of Solid Particle Impact Erosion Damage 71
4.3.5.1 Introduction 71
4.3.5.2 A Description of the Finnie / Bitter Erosion Model 71
4.3.5.3 A Discussion Concerning the Empirical Constants Found for the Fitting of the Finnie / Bitter Erosion Model to the Experimental Test Results with Steel 72
4.3.6 A Discussion on the Position of the Apex of the Curve of Erosion Damage Versus Impingement Angle 73
4.3.6.1 Introduction 73
4.3.6.2 A Discussion of Whether Erosion at an Impingement Angle of 0° Has Any Real Significance 73
4.3.6.3 What are the Physical Reasons for the Peak in the Erosion Damage Curve Occurring at Impingement Angles Closer to 0°? 75
4.3.6.4 Conclusions Regarding the Position of the Apex in the Curve of the Erosion Damage versus Angle of Impingement 86

4.4 Conclusions Drawn from the Experience of Using the 'Rotating Disc Accelerator' Erosion Tester 87

Chapter 5: A Description of the Work Associated with the Pneumatic Conveying Test Facility 89
5.1 Introduction 89
5.2 Design and Construction of the Pneumatic Conveying Test Facility 89
5.2.1 Design Features that were Considered for the Construction of the Pneumatic Conveying Test Facility 89
5.2.1.1 A Brief Description of the Pneumatic Conveying Test Facility 90
5.2.2 Specification of the Materials Used During the Tests 92
5.2.3 Calibration of the Instrumentation Used on the Pneumatic Conveyor Test Facility 93
5.2.4 Test Method Employed During Conveying Tests 94
5.2.4.1 Method of Carrying Out Conveying Characteristic and Bend Penetration Measurements 94
5.2.4.2 Method of Carrying out Particle Distribution Assessment Using the Laser Obscuration Technique 95
5.2.5 Test Conditions 95
5.3 Test Results 96
5.3.1 Results Obtained for the General Conveying Conditions 96
5.3.2 Results Obtained for the Bend Wall Penetration 97
5.3.3 Results Obtained from the Laser Obscuration Tests for Particle Distribution 101
5.3.4 Conclusions and Discussions Regarding the Results of this Test Work 107
5.3.4.1 A Discussion Regarding the Reasons Why an Asymmetrical Particle Distribution in the Pipe Bore Occurs 107
5.3.4.2 The Effects of the Skewed Particle Concentration Distribution on the Bend Wall Penetration 110
5.3.4.3 A Description of a Possible History of Erosive Penetration in a Pneumatic Conveyor Bend 114
5.4 Prediction of the Location of the Puncture Point in a Bend Using a Model Based Upon the Curve of Aberration for a Cylindrical Mirror 116
5.4.1 A Brief Description of the Method of Generating the Curve of Aberration for a Cylindrical Mirror 116
5.4.2 Predicting the Point of Bend Wall Puncture 118
5.4.3 Results of the Analysis Based Upon the Curve of Aberration for a Cylindrical Mirror 118
5.5 Conclusions and Discussion Regarding the Pneumatic Conveying Test Work and the Analysis of the Results Obtained From It 120

Chapter 6: Predicting the Erosion of the Pneumatic Conveyor Test Bend 122
6.1 Introduction 122
6.2 Prediction Using Previously Derived Models for the Erosion of Pneumatic Conveyor Bends 122
6.2.1 Use of the Bikbaev Model 123
6.2.2 Use of the Mills and Mason Type Bend Erosion Models 124
6.3 Predicting the Erosion Damage Seen in the Region of Primary Impact by Combining Particle Trajectory and Erosion Models 125
6.3.1 Use of the Yeung Trajectory Model and its Combination with Erosion Models 126
6.3.2 Observations Related to the Predictive Capability of the Combined Trajectory and Erosion Models 126
6.3.3 Conclusions Relating to these Predictions 131
6.4 The Combined Model Based Upon the Curve of Aberration for a Cylindrical Mirror and the Power Law Erosion Model 131
6.4.1 Construction of the Model Based Upon the Curve of Aberration for a Cylindrical Mirror and the Power Law Erosion Model 131
6.4.2 Observations on the Use of this Model 132
6.4.3 Conclusions Related to the Use of the Model Based Upon the Curve of Aberration for a Cylindrical Mirror and the Power Law Erosion Model 135
6.5 Conclusions Relating to the Accuracy of the Pneumatic Conveyor Bend Wear Models Used in this Work 135
6.5.1 Comments Relating to Models Proposed by Other Authors 136
6.5.2 Comments Relating to Combined Erosion / Trajectory Models 137
6.5.3 Comments Related to the Model Based Upon the Curve of Aberration for a Cylindrical Mirror and the Power Law Erosion Model 138

Chapter 7: Structure and Development of the Conveyor Bend Erosion Model Based Upon the Curve of Aberration for a Cylindrical Mirror 139
7.1 Introduction 139
7.2 A Description of the Basic Technique that was Adopted 139
7.3 The Model of the Curve of Aberration for a Cylindrical Mirror 140
7.3.1 Construction and Use of the Curve of Aberration of a Cylindrical Mirror to Find the Location of the Puncture Point in the Bend 141
7.3.1.1 Construction of the Curve of Aberration for a Cylindrical Mirror 141
7.3.1.2 Finding the Location of the Point of Bend Wall Puncture 141
7.3.2 Linking the Curve of Aberration for a Cylindrical Mirror to the Power Law Erosion Model 143
7.3.3 Determining a Particle Impact Intensification Factor from the Model Based Upon the Curve of Aberration 143

7.4 Further Development of the Model for Predicting the Life of a Long Radius Pneumatic Conveyor Bend Using the Curve of Aberration Model 146
7.4.1 The Addition of Further Coefficients 146
7.4.2 Further Work 148
7.5 Conclusions 148

Chapter 8: Conclusions and Further Work 149
8.1 Introduction 149
8.2 Results of the Work Carried Out to Meet the Subsidiary Goals Detailed in Chapter 1 149
8.2.1 Results of the Literature Review 149
8.2.2 Planning and Building the Test Rigs 150
8.2.3 Comparing the Rotating Disc Accelerator Erosion Tester to the Gas Blast Erosion Tester 150
8.2.4 Results from Using the Rotating Disc Accelerator Erosion Tester 151
8.2.5 Findings from the Industrial Scale Pneumatic Conveying Test Facility 152
8.2.6 Prediction of the Bend Life from the Laboratory Erosion Tester Results 153
8.3 Has the Work Carried Out Achieved the Goal Originally Set for this Project? 154
8.4 Further Work 154

REFERENCES **R1-R13**

VOLUME 2

APPENDICES

Appendix 2A: A Review of the Mechanisms of Erosive Wear for Various Materials 2A.1 - 2A.24
Appendix 2B: Advantages and Disadvantages of Using Various Forms of Laboratory Erosion Testers 2B.1 - 2B.3

Appendix 3A: Materials Specification for the Main Test Programme 3A.1 - 3A.4

Appendix 4A: The Design and Development of the Rotating Disc Accelerator Erosion Tester 4A.1 - 4A.19
Appendix 4B: Modelling the Particle Dynamics Within the Rotating Disc Accelerator Erosion Tester 4B.1 - 4B.26
Appendix 4C: Calibration of the Rotating Disc Accelerator Erosion Rig 4C.1 - 4C.6
Appendix 4D: The Method of Carrying Out Tests on the Rotating Disc Accelerator Erosion Rig 4D.1 - 4D.2

Appendix 4E: Comparisons Between the 'Rotating Disc Accelerator' Erosion Tester and the 'Gas Blast' Erosion Tester 4E.1 - 4E.16
Appendix 4F: Mild Steel Test Programme Results 4F.1 - 4F.12
Appendix 4G: Modelling the Mild Steel Erosion Performance Using the Combined Finnie / Bitter Model 4G.1 - 4G.14

Appendix 5A: The Design and Development of the Pneumatic Conveying Test Facility 5A.1 - 5A.18
Appendix 5B: Calibration of the Instrumentation Used on the Pneumatic Conveyor Test Facility 5B.1 - 5B.7
Appendix 5C: Method of Carrying Out Tests on the Pneumatic Conveyor Test Facility 5C.1 - 5C.4
Appendix 5D: Data Collected During the Main Pneumatic Conveying Trials 5D.1 - 5D.5
Appendix 5E: Data Manipulation for the Particle Distribution Assessment Results 5E.1 - 5E.23
Appendix 5F: Modelling the Particle Trajectories Within the Test Bend 5F.1 - 5F.22
Appendix 5G: Predicting the Bend Puncture Location Using an Optical Analogy 5G.1 - 5G.8

Appendix 6A: The Bikbaev Model [B8] for Predicting Wear in Pneumatic Conveyor Bends 6A.1 - 6A.4
Appendix 6B: The Combined Yeung Trajectory and Erosion Model for Predicting Penetration in the Region of Primary Impacts 6B.1 - 6B.18
Appendix 6C: Bend Puncture Predicted Using the Model Based Upon the Curve of Aberration for a Cylindrical Mirror 6C.1 - 6C.15

PUBLICATIONS

APPENDICES

Appendix 2A: A Review of the Mechanisms of Erosive Wear for Various Materials

2A.1 Introduction

The purpose of this appendix is to describe the mechanisms of erosion for various groups of materials. To this end this appendix is divided into five sections:-

a) A general discussion of the effects of variables associated with the eroding particles.
b) A review of the mechanisms of erosion of metallic materials.
c) A discussion concerning the mechanisms of erosion of ceramic materials.
d) A review of the mechanisms of the erosion of polymeric materials.
e) Comments relating to the mechanisms of erosion of elastomeric materials.

Not included in this work is a discussion regarding the erosive wear of coated substrates. The erosion resistance of coated materials is more often than not determined by the strength of the bond between the coating and the substrate rather than the materials themselves. Resistance to erosion of types of materials that can be used to form coatings and substrates will be discussed in the sections describing the erosion resistance of the individual material groups mentioned above a) through to e).

2A.2 Properties of the Particles Striking the Material Surface and their Effect on Erosion

There are several properties of the particles that will significantly effect erosion damage in general terms. These are as follows:-

1/ Dynamics of the particle at impact, i.e. translational and rotational velocity components, intensity of particle impacts, and the orientation of the particle at impact if it has an irregular shape.
2/ Geometrical properties of the particles, i.e. their shape and size.
3/ Mechanical properties of the particles in relation to those of the target material.

2A.2.1 Effects of the Particle Dynamics at Impact

The importance of the particle velocity at impact was quickly realised early on in the study of erosive wear of materials. However, the possible influence of the particle velocity on the mechanisms of erosive wear, was not fully appreciated until Hutchings [H3], illustrated, using a basic quasi-static

Hertzian contact model, the effect of particle velocity on the strain rate of deformation during impact. This theoretical work was experimentally confirmed by Buttle and Scruby [B3]. In general terms it was deduced that as the particle velocity increases the strain rate of deformation would also increase. From research on metallic materials being deformed at high strain rates [C2], (of the order of 10^6 s^{-1} being suggested as being common in erosion processes), a rapid increase in yield strength is indicated (see Figure 2A.1). As the strain rate increases the rate of change of flow stress increases rapidly leading to a situation where flow stress is directly proportional to strain rate. This behaviour is consistent with a viscous flow model of deformation [H5]. It is certain that all materials will have properties that will vary to a greater or lesser extent with rate of strain of deformation. Strain rate dependency in ceramic materials is most evident and was recognised very soon during research into erosion resistance of these materials [R4].

Rotation of particles at contact will dictate the motion of the particle surface relative to the eroding surface. This may, in conjunction with the shape of the particle, dictate the mechanism of erosion damage that occurs. A coefficient of dynamic friction will have an effect during particle / material contact in instances where particle rotation is significant [R2]. Difficulties in measuring particle rotation have led to theoretical models, that have not been experimentally substantiated, being used to give an indication of the likely effects of particle rotation on erosion [F7,B5]. The importance of particle rotation on the mechanisms of erosive wear that occur will become apparent in the following sections of this appendix.

It is evident from reviewing previous literature, that the mechanisms of material removal in some instances depend on several particle impacts occurring in close proximity to each other. This implies that the frequency of particle impact per unit surface area of the eroding surface is important in determining the bulk erosive wear rate. Description of the necessity of multiple neighbouring impacts is given in the following sections of this appendix.

2A.2.2 The Effect of Geometric Particle Properties

There are two geometric particle properties that have a significant effect on the mechanisms of erosive wear of materials. These are the particle shape and size. The effect of these two properties are to some degree interconnected.

It has been theoretically shown by Hutchings [H3] that the strain rate of material deformation increases with a reduction in particle size (see Figure 2A.1), and therefore the amount of erosion

Figure 2A.1 Strain rate versus particle impact velocity for various particle radii after Hutchings [H3].

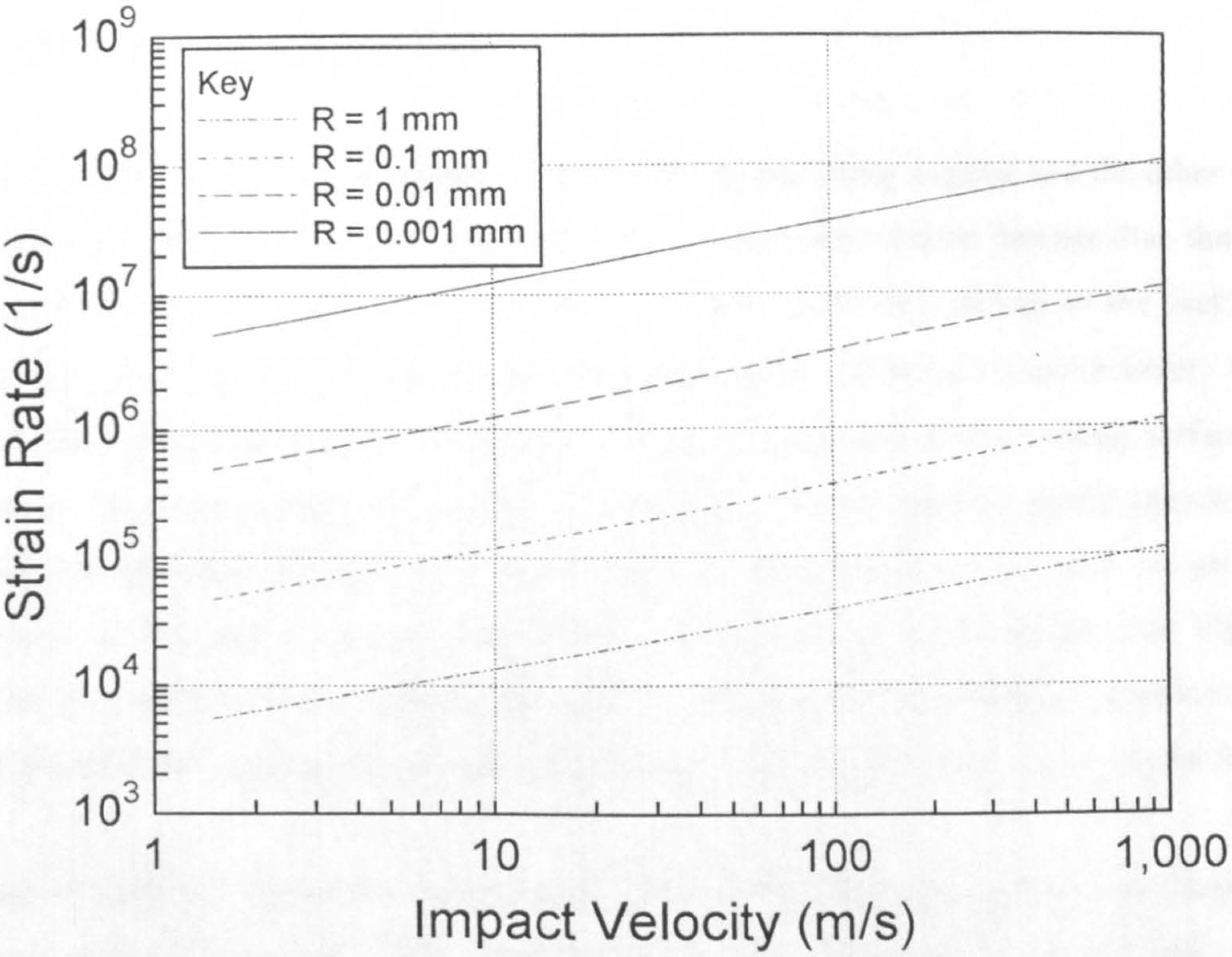

Figure 2A.2 The effect of particle shape on the erosion damage and penetration of the material surface.

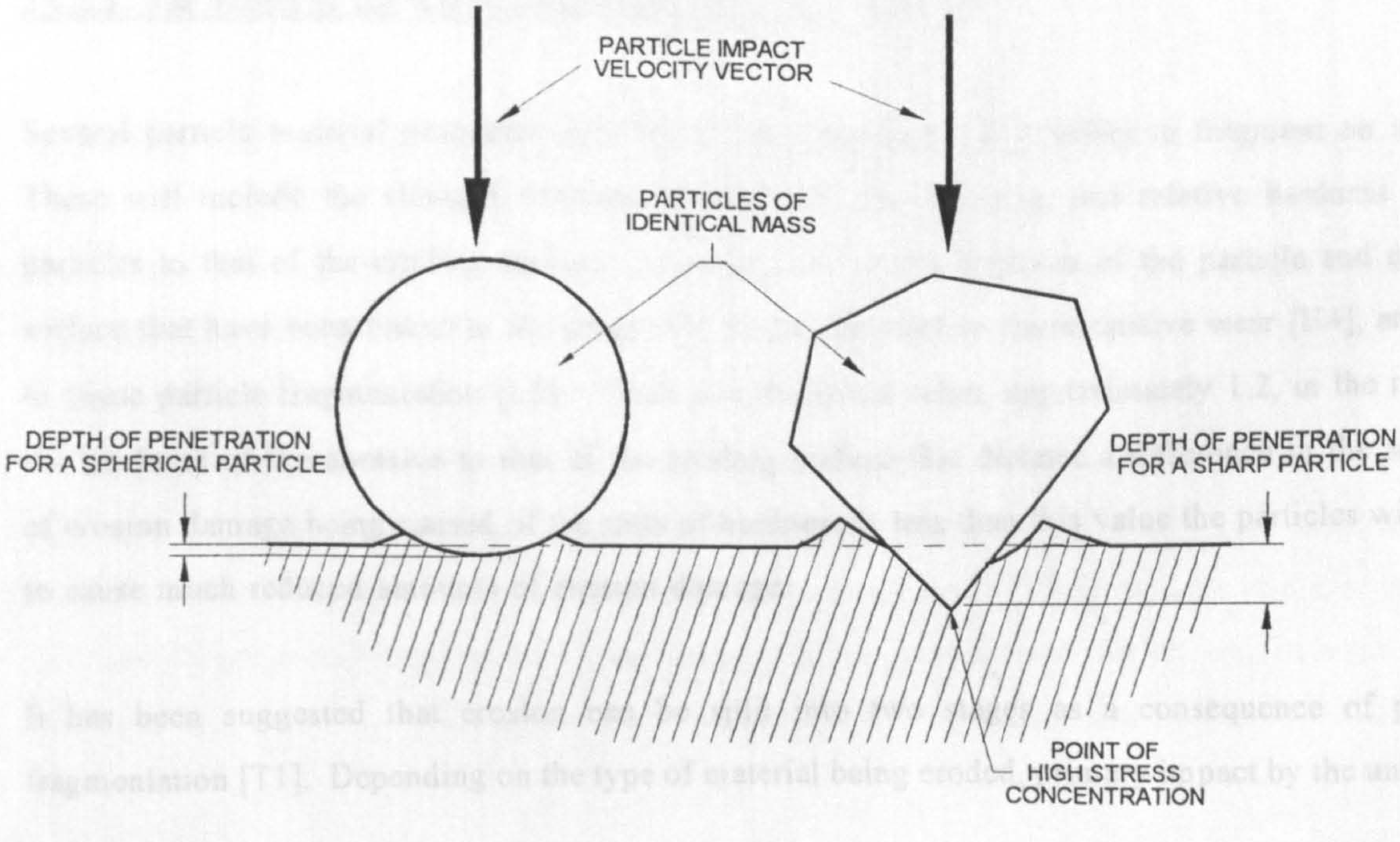

damage caused by small particles reduces. This is because, in the case of ductile metals, the flow stress increases with an increase in strain rate [H5]. For ceramic materials, since the strain rate dependency of the behaviour of these materials is strong, changes in mechanism of wear have been noticed with changes in strain rate [R4].

If two particles of the same mean diameter are considered, one being angular and the other spherical, it has been shown that the angular particle will tend to cause more erosion damage than the spherical particle [L5,L1,C3,S13]. Under identical impact velocity conditions, owing to the fact that both particles have a similar mean diameter, their kinetic energies will be of a similar order. However, it is likely that an angular particle will have a smaller contact area with the eroding surface because of its shape. The concentration of force per unit contact area in the case of angular particles striking a surface will therefore be greater. Penetration into the material surface will be greater as a consequence of this and more extensive damage will occur for ductile metals (see Figure 2A.2 above). In the case of ceramic materials, angular particles have been observed to cause more damage due to a change in the mechanism of wear (this will be discussed in section 2A.4.1 of this Appendix).

The shape of particles will tend to have another effect on erosion damage that is also dependent on the particle rotation at impact. The direction of rotation of a particle at impact will dictate the manner in which asperities, (on an angular particle), contact the eroding surface. This has been suggested as having an effect on the mechanism of erosion, and will be discussed in later sections of this appendix.

2A.2.3 The Effect of the Mechanical Properties of the Particles

Several particle material properties will dictate the propensity of particles to fragment on impact. These will include the strength, fracture toughness of the particles, and relative hardness of the particles to that of the eroding surface. It is the ratio of the hardness of the particle and eroding surface that have been linked to the propensity of the particles to cause erosive wear [H4], and also to cause particle fragmentation [L5]. There is a threshold value, approximately 1.2, in the ratio of the hardness of the abrasive to that of the eroding surface that dictates a difference in the severity of erosion damage being caused; if the ratio of hardness is less than this value the particles will tend to cause much reduced amounts of erosion damage.

It has been suggested that erosion can be split into two stages as a consequence of particle fragmentation [T1]. Depending on the type of material being eroded, primary impact by the unbroken particle will cause damage in the various ways described in the following sections of this Appendix. However, breakage of the particle may occur in this impact. It is suggested that the fragments of the broken particle will tend to wash over the areas of the surface neighbouring the primary impact site. In ductile materials this will tend to cause removal of weakly attached material features from the sites of previous primary impacts in this area. Another effect of particle fragmentation is the possibility of particle fragments becoming embedded in the eroding surface and affecting the erosion damage process. For ceramic composite materials, the smaller fragments will better be able to attack any binders than the original complete particle [V2]. It has also been suggested that particulate materials significantly softer than the ceramic material they are striking can cause damage by causing plastic deformation [V2].

2A.3 Erosion Mechanisms for Metallic Materials

Study of the erosion of metallic substances has formed the bulk of the work concerned with erosion mechanisms. This being due to the fact that metals remain the most commonly used materials in engineering applications.

The work carried out can be broadly divided into three groups:-

a) work to assess the erosive damage caused by individual particle impacts,

b) studies concerned with erosion damage mechanisms that occur during multiple particle impact, and

c) thermodynamic effects during erosion of ductile metals.

Each of these groups will be discussed in turn.

2A.3.1 Observations of the Mechanisms of Erosive Wear Caused by Single Particle Impacts

The major contributor to the understanding of erosive wear by carrying out single particle impact tests was Hutchings [H13,H14,H15].

Single spherical particle impact tests at a wide range of angles of impingement were carried out using a gas gun type tester. In general raised lips of highly strained (strain of 25 m/m) material were observed surrounding the impact craters. The temperatures generated during the impacts were not sufficient to cause recrystallization of the material in the impact crater for all conditions, i.e. they were less than ~700°C. This temperature is considerably more than that measured by Uetz and

Gommel in 1966. These authors measured the temperature generated during the impact of a 1mm diameter particle at 60 m/s against a steel surface as being a maximum of 380°C [U1]. However, the difference between the values measured or discussed above could be due to the difference in the particle velocities used in the experiments. Work carried out by Hutchings was undertaken at velocities greater than 100 m/s, whilst the maximum velocity used by Uetz *et al.* was 60 m/s. These differences in particle velocity will lead to changes in the strain rate, which will, in turn, affect the temperature as well as cause a considerable difference in the amounts of plastic deformation of the target surfaces. (A more detailed discussion of the effects of heat generation and its effects on erosion damage is given in section 2A.3.3). However, the flow stress of steel is significantly affected by temperatures less than the maximum value suggested by Hutchings. Hutchings concluded that thermal softening contributed to lip formation and that as a consequence, localised thermoplastic shear was important in solid particle impact erosion [H13]. In erosion tests of pre-work hardened target materials, it was concluded that the presence of a work hardened surface layer caused by the erosion caused the deformation of the material to be concentrated in the surface layers. This led to the formation of a more fragile lip than if the surface was in its annealed state. Also the presence of a work hardened layer reduced the volume of material deformed by the impact [H15].

In further single particle impact tests, this time using non-spherical particles, (cylinders and cubes), three major types of particle damage mechanism were observed. These mechanisms depended on the shape of the particle and its orientation at impact, its direction of rotation at impact and the angle of impingement. The mechanisms were described as 'ploughing', 'type I cutting' and 'type II cutting' (see Figure 2A.3) [H14].

i) Rounded particles tended to cause ploughed impact craters where the material from the crater was displaced to either side and in front of the particle. Subsequent impacts in sites close to this impact site are necessary to remove the weaker crater lips.

ii) In the case of 'type I cutting', the particle rotation causes the particle to roll into the eroding surface, this raises lips around the impact site which have to be struck by subsequent particle impacts for them to be removed. If the particles are angular, the lips formed tend to be larger than those formed by the ploughing mechanism owing to the greater penetration caused by the irregular particle shape used.

iii) Finally, in the case of 'type II cutting', (for angular particles), the particle rolls away from the eroding surface causing an asperity on the particle surface to cut out a chip of material. This

Figure 2A.3 Mechanisms of single particle impact damage according to Hutchings [H14].

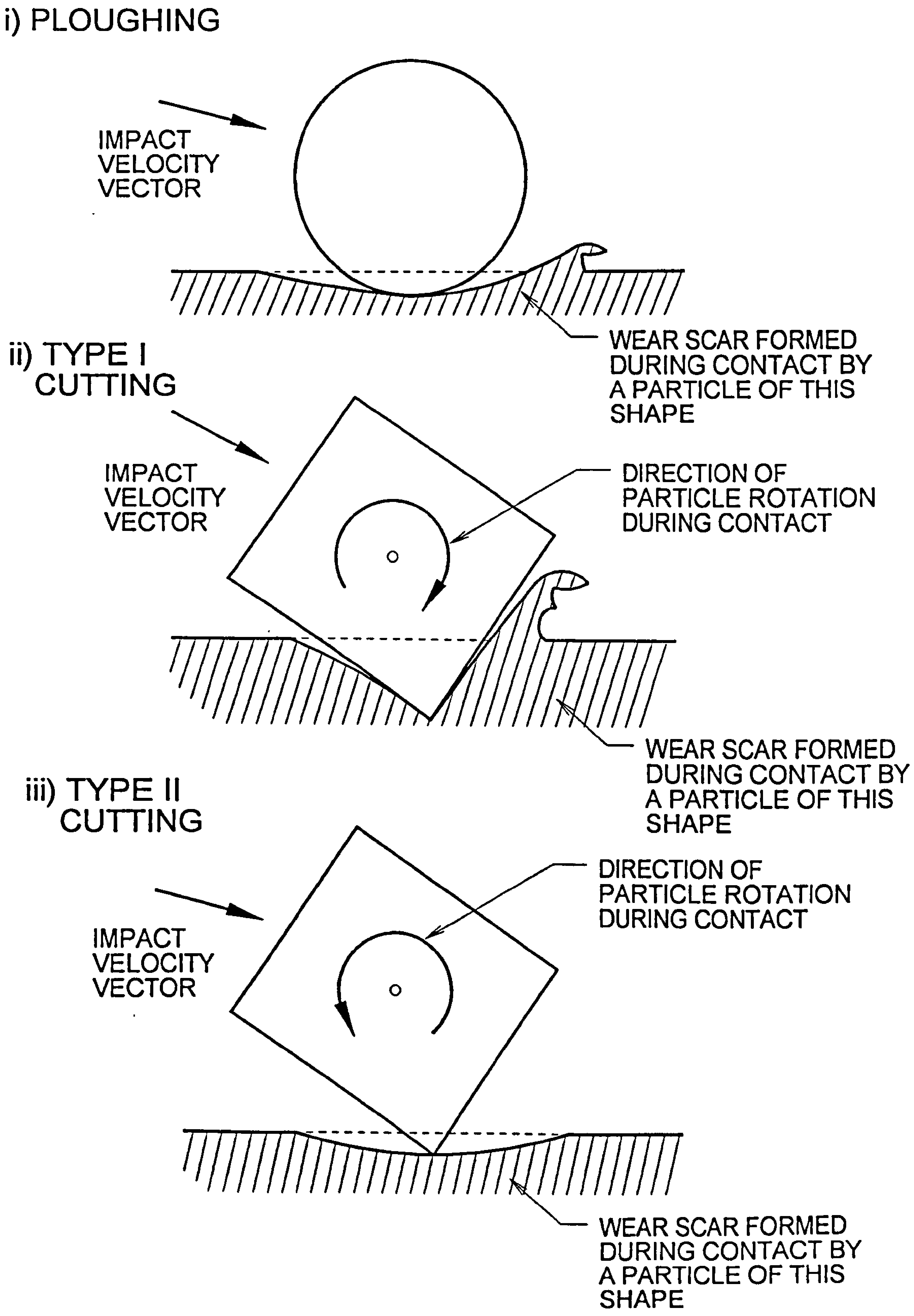

is the only mechanism of wear where by a single particle can remove material in a single impact, however, it only occurs within a narrow range of particle impact orientations and with specific particle geometries.

Throughout all of these single particle tests, except in the rare situations where 'type II cutting' occurred, negligible amounts of surface material removal occurred. It was therefore concluded that the mechanisms of wear were dependent on multiple impacts occurring. It was also realised that multiple impacts would tend to work harden the surface being eroded before material removal occurred [H15].

2A.3.2 Observations of the Mechanisms of Erosive Wear Caused by Multiple Impacts

Early work on erosive wear caused by multiple particle impacts clearly showed a distinctive trend in the amount of erosion damage caused with respect to angle of impingement [W3]. Subsequent work by Finnie offered cutting wear (at oblique impact angles) as a suggested mechanism, and a model of this form of wear was proposed [F5]. However, this model failed to account for material loss at normal impact angles. Bitter [B11,B12] later offered deformation wear to attempt to address this deficiency.

With the advent of scanning electron microscope (SEM) technology detailed investigations of the mechanisms of wear could be undertaken in detail for the first time. In one of the first attempts at the analysis of erosive wear by capturing wear fragments, Ruff [R7] discovered using SEM techniques, that the majority of wear fragments produced during erosion by multiple particle impact took the form of 'platelets' rather than cut fragments. Further work was required before the reasons for these fragments being formed became apparent.

Owing to the fact that several particle impacts were observed to be required to ensure material removal, Hutchings proposed a model that was based upon low cycle fatigue and critical strain values [H16]. This work accounted for the incubation phase of erosion that was commonly observed in multiple particle erosion studies, where a certain number of particle impacts had to occur before steady state erosion was established. This indicated that the surface must be subject to modification in some way before steady state erosion was established.

Work by Bellman and Levy suggested a likely mechanism of material removal by multiple particle impacts [B16]. They concluded that the lip formation mechanisms proposed by Hutchings occurred for all angles of impingement with irregularly shaped particles. It was concluded that the repeated deformation of work hardened crater lips caused them to ultimately crack at their joint with the bulk material; this led to their removal from the eroding surface (see Figure 2A.4). Salik and Buckley indicated that a sub-surface work hardened layer covered with a layer of softer material could be observed during the erosion of a ductile material by multiple particle impacts [S13]. Further detailed work by Cousens and Hutchings [C8] described a mechanism of backward extrusion of soft non-work hardened material through fissures formed in a work hardened surface layer. The soft material was subsequently beaten into 'platelets' by the hammering action of the striking particles compressing this soft material against the work hardened surface layer (see Figure 2A.5). Material removal by cracking at their points of attachment to the eroding surface was observed. This work confirmed the ideas proposed by both Bellman and Salik. Yet further evidence of this form of mechanism of material removal has been given by Levy [L5,L6] and Hammarsten [H17].

Efforts to measure the variation of the hardness with depth from the surface of eroded steel targets was carried out by Koller *et al.* [K12] and Trilok *et al.* [T8]. The work of Trilok resulted in the observation that steels of austenitic structure, when eroded, form a work hardened surface layer, however, it was noticed that steels of a martensitic nature tended to form a sub-surface work hardened layer similar to that reported by both Bellman and Salik [B16,S13]. Presence of the sub-surface work hardened layer in the martensitic steel was felt to be due to the fact that this material was found to have a low work-hardening coefficient. Consequently, tempering in the surface layer was suggested to have occurred as a consequence of the high strain rate, high temperature plastic deformation of the material surface during particle impact. However, Koller [K12] found that it was essential to support the eroded surface by a significant amount of plating before micro-Vickers hardness tests were taken. It is not certain that Trilok ensured that this was done, and therefore, his results might be in error.

Collection of erosion debris carried out by Hammarsten *et al.* [H17] indicated that there were three main types of fragments produced during the erosion of mild steel by irregularly shaped particles of sand. These were, cut fragments (formed approximately 15% of the time at 30° impingement angle), platelet like flakes and extruded 'tufts' of ruptured material (both formed in approximately equal proportions). Both the tufts and platelet type flakes were suggested to have occurred via the mechanisms proposed above. The major differences between the two non-cutting wear fragments were that the tufts in many instances were observed to have been formed of recrystallised material indicating significant temperature rises during their removal; while in the case of flakes or platelets the fragments were found to shown indications of severe deformation, and therefore work hardened embrittlement, but no effects due to recrystallisation. This behaviour was ascribed to the manner in

Figure 2A.4 Schematic illustrating the platelet formation mechanism

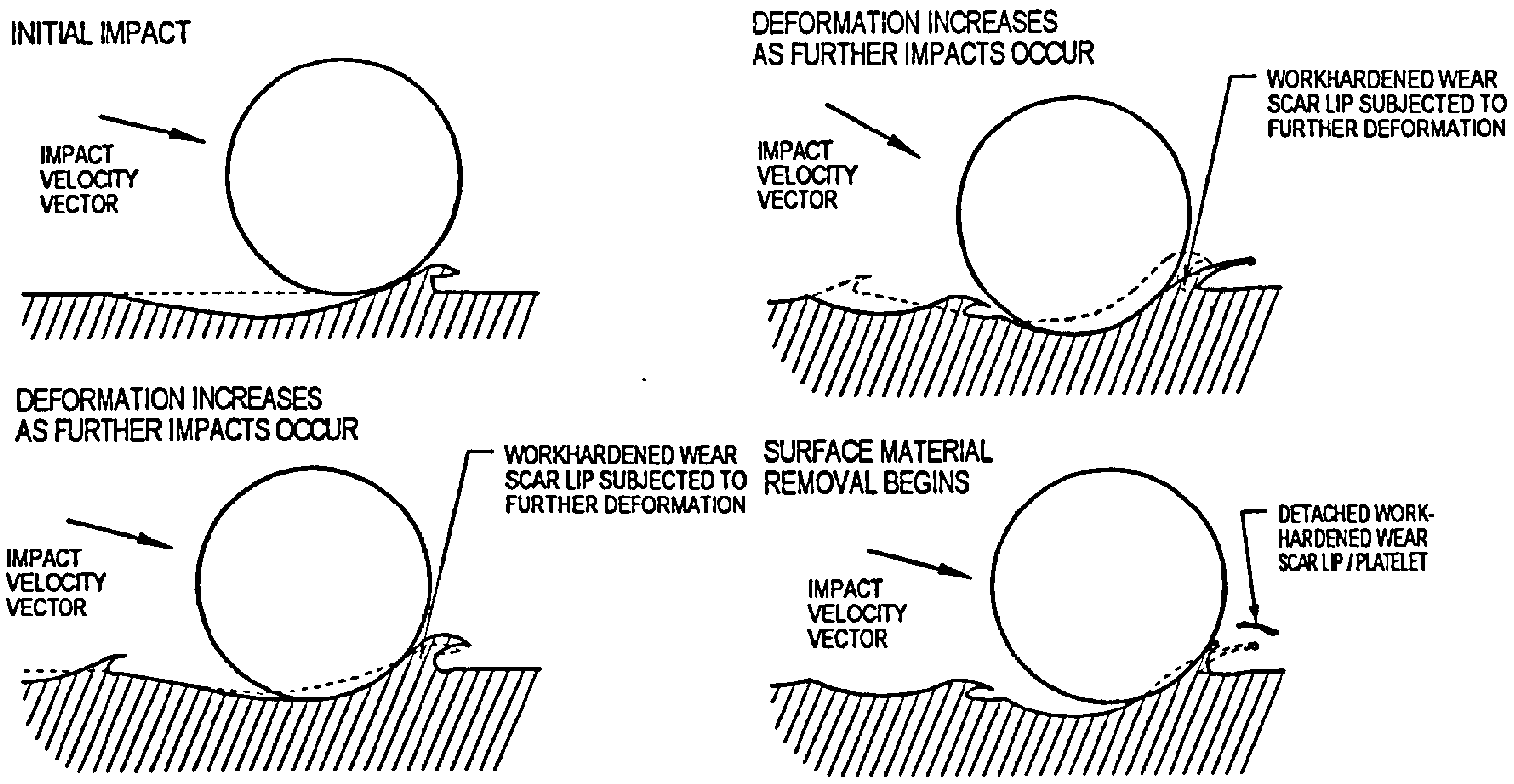

Figure 2A.5 The formation of subsurface layers in the erosion of a ductile metal.

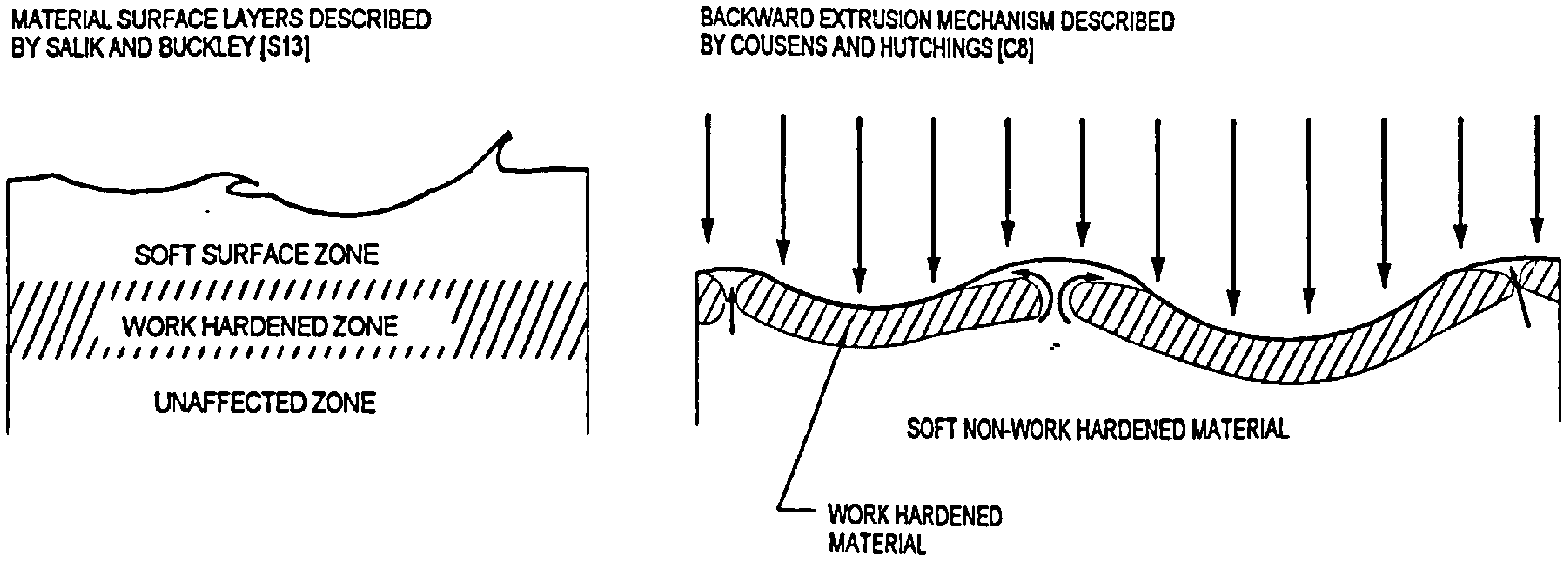

Figure 2A.6 Illustration of the different way tufts and flakes or platelets are formed; according to Hammersten *et al.* [H17].

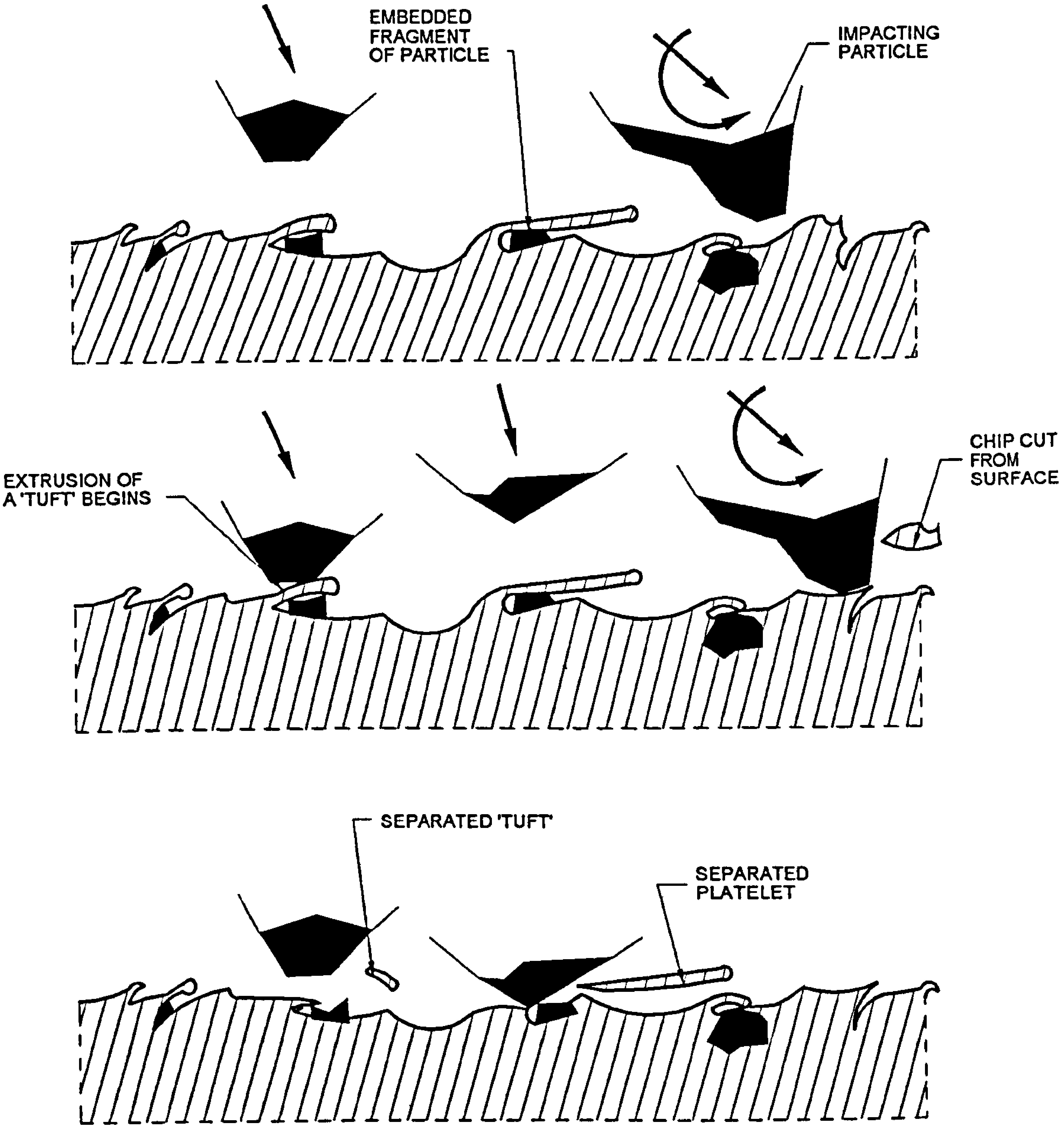

which the particle contacted the future fragment of surface material during the removal process, this behaviour is illustrated in Figure 2A.6 above.

2A.3.3 Thermodynamic Effects During the Erosion of Ductile Metals

As has been mentioned above in sections 2A.3.1 and 2A.3.2, thermodynamic behaviour of the materials during the particle surface contact may have a significant effect on the erosion mechanisms taking place. Several researchers have in the past reported that evidence of surface melting or thermal recrystallisation / softening had been observed as a result of the erosion process [H17,R4,H7,S13,B16,H6,S16, etc]. However, reports of high temperatures generated during erosion are limited to the work of Neilson and Gilchrist, who indicated that temperatures of 170°C were reached during the erosion of hardened steel samples by 297μm and 500μm diameter particles striking at 290 m/s [N2]. Hutchings [H6], has observed that deformation seen in the region of a particle impact crater was localised. This was attributed to thermal effects, (because of the high strain rates that occur, and the near adiabatic conditions that predominate because of the short duration of the particle impact event, high temperatures are generated). This results in a large change in the yield stress of the metal.

Two of the most detailed micro-scale mechanistic studies of erosion have shown evidence of surface melting. Each of these will be covered in turn.

1. Bellman and Levy [B16] showed a micrograph of a captured particle after erosion. Aluminium, (the target material in this case), was found to be fused to the surface of a particle that had caused erosion damage. It was suggested that adiabatic conditions should occur in the particle because of its size and poor thermal conductivity (in this case silicon carbide), while the target acts as a heat sink and consequently melting of the target surface does not occur.

2. Hammarsten *et al.* [H17] observed that some fragments of surface material that had been worn away, (most notably tufts, see above in section 2A.3.2), illustrated microstructural features consistent with recrystallisation. These researchers suggested that it was possible for a particle to have a significant heating effect on a previously formed crater lip alone. Therefore, owing to the small volume of surface material in the lip being affected, the temperature rises are expected to be large.

Efforts to theoretically model the temperatures generated in multiple particle impact erosion have been undertaken by Hutchings and Levy [H7]. This work was further expanded upon by Doyle and Ball [D2]. However, the results of this research have indicated that it is not possible for successive particle impacts to raise the temperature of the bulk of an eroding ductile target sample unless a very high frequency of impacts occurs. Using a different approach from that suggested by Hutchings and Levy, Doyle and Ball have suggested that the temperature generated as a result of the plastic deformation of the material directly in contact with the particle during an impact could be high enough to cause a change in microstructure for martensitic steel alloys. Levy [L6] and Sundararajan [S16] have also indicated that this is probable.

2A.3.4 Conclusions Relating to the Erosion of Ductile Metals

The erosive wear of ductile metallic materials occurs as a consequence of two types of mechanism. These are cutting in a micro-machining mechanism (a single particle impact results in material removal), or more commonly by repeated severe deformation of the target surfaces leading to an accumulation of strain and cracking as a consequence of work-hardening embrittlement (multiple particle impacts required to remove material). In either case large scale plastic deformation occurs at high strain rates and consequently high temperatures are generated. These two facts will tend to alter the behaviour of the metal from that commonly observed during normal engineering property tests carried out at room temperature.

2A.4 Erosion Mechanisms for Ceramic Materials

The erosion of ceramic materials has only been studied in detail from the late 1970's. Difficulties occur in the understanding of the erosion of ceramics as a consequence of the diverse types of available ceramics; two of the major groups of ceramics that are available are, a) glass ceramics (such as cast igneous rock materials), and b) bonded sintered ceramics. However, there are many others including a large range of composite materials, i.e. those materials that are composed from a wide range of distinctly different types of material. Composite materials consist of a matrix of very hard particles that are bound together by a softer material. Ceramic linings for pneumatic conveyor pipelines are most commonly sintered alumina or cast igneous rock derived ceramics. For this reason this section of this appendix will tend to avoid discussion concerning the more advanced and expensive ceramic materials that are available.

This section will be divided into three sections. The first of these will be concerned with the general mechanisms of the erosion of brittle materials, while the second will consider the erosion of glass ceramics, and finally, the third will consider the erosion of sintered ceramics.

2A.4.1 The Mechanisms of the Erosive Wear of Brittle Materials

Brittle materials erode as a consequence of a combination of the intersection of cracks caused by multiple particle impacts [S8], and plastic deformation [R4,H19]; in solid particle impact erosion of ceramic materials plastic deformation occurs in by far the majority of cases, albeit in the very local region of the particle / target contact area. However, it is the formation of cracks that lead to the loss of material from an eroding ceramic surface. There are three major types of cracks that can be formed during particle impact. These are:-

a) the formation of Hertzian conical cracks [H3,T9],

b) the formation of median vent cracks [E3,H18], and

c) the formation of lateral vent cracks [E3,H18,R4].

Figure 2A.7 illustrates the formation of these cracks. The formation of a crack of any of these types depends greatly on the shape of the particle, its size and the velocity at which it strikes the target surface. A review of the studies that have been carried out concerning the thresholds at which damage mechanisms change in the erosion of ceramic materials has recently been given by Hutchings [H20].

2A.4.1.1 Hertzian Crack Formation

Cracks of this type are conical in shape and spread into the bulk of the eroding target material from the point of impact of the particle. However, cracks of this type are usually formed by the impact of soft round particles, and are caused as a consequence of the response of the eroding target surface to the propagation of elastic and plastic shock waves [E3].

It has been reported in the past that there is a threshold velocity below which Hertzian cracks will not form. Ruff and Weiderhorn stated that it required an impact velocity of 30 m/s for a 800μm tungsten carbide sphere to begin the formation of this form of crack in glass [R4].

The formation of cracks of this type by a single particle impact do not normally lead to material removal on their own [H19]. Multiple impacts are normally required to cause material removal.

2A.7 Types of cracks formed in the erosion of brittle materials [H18]

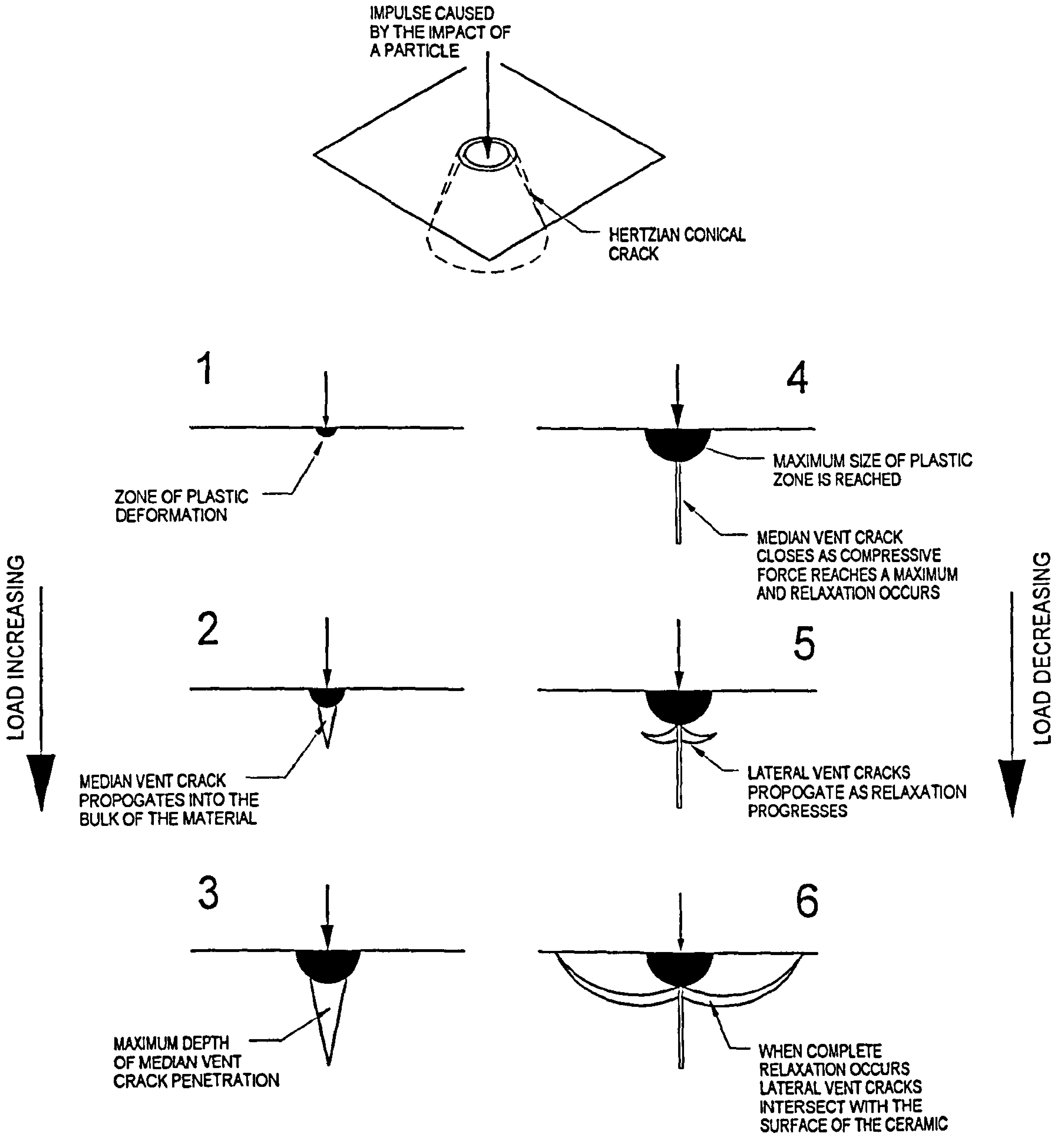

2A.4.1.2 Median Vent Crack Formation

Median vent cracks are formed during the impact phase of the particle impact, i.e. before the particle comes to rest and begins to rebound. They are formed as a response to the propagation of the elastic and plastic shock waves in the material [E3], and the very high intensities of radial stress caused in the material in contact with the particle, (once the target material has deformed beyond its plastic limit) [H18]. Generally, the higher the impact velocity, and the more angular the shape of the particle the greater the extent of any median vent crack. Cracks of this type do not extend further into the bulk of the target material with relaxation of the stresses when the particle begins to rebound, but they close up at this stage during the particle / surface interaction [H18].

As with the formation of Hertzian conical cracks, material is not normally removed by the presence of such cracks in the target material as a consequence of a single impact.

2A.4.1.3 Formation of Lateral Vent Cracks

Lateral vent cracks are formed during the rebound phase of a particle impact. Their formation is caused by the relaxation of residual elastic stresses in the deformed material surrounding the region of contact. The cracks intersect with the material surface when all the residual elastic stresses have relaxed [E3,H18,R4]. Formation of this type of crack can lead to immediate removal of material from the eroding surface. Particle shape has an effect on whether this type of crack is formed or not; since with sharp particles the magnitude of the elastic stresses in the eroding surface is greater than those that occur with a rounded particle.

2A.4.1.4 The Role of Plastic Deformation, Temperature and Strain Rate in the Erosion of Ceramic Materials

As has been stated above, in the majority of cases ceramics do suffer some amount of plastic deformation of the target material surface that is directly in contact with the particle during impact [H18].

In work carried out by Hockey *et al* [H19], it was discovered that high densities of dislocations were found beneath particle impact indentations. Cracks were found to penetrate into the bulk of the ceramic material only to be arrested in regions free from dislocations. It has been suggested by Doyle and Ball [D2] that the change in the density of dislocations occurs as a consequence of the generation of high temperatures during each particle impact; these high temperatures cause a significant reduction in the yield stress of the material subjected to heating; this increases the dislocation activity, and results in an increase in the amount of plastic deformation observed.

According to these researchers, the temperatures that could in theory occur in the erosion of alumina by silicon carbide particles striking at 40 m/s, was a maximum of 5694°C. This extremely high temperature was derived from a theoretical analysis that assumed adiabatic conditions to occur. However, such high temperatures may be possible since both Hockey *et al.* [H19], (soda-lime silicate glass eroded by 150μm diameter SiC particles at 15° impact angle and 54 m/s impact velocity), and Vaughan and Ball [V2], (alumina eroded by 100μm diameter SiC at 90° impact angle and 40 m/s), have discovered evidence of melting of the material directly in contact with the impacting particle. Further work [R4,V2] on the erosion of ceramic targets at elevated temperatures have indicated that the increase in dislocation activity is a viable mechanism by which plastic flow can affect the erosion of ceramics. However, despite the increase in the amount of plastic deformation caused by high temperatures being generated in the eroding ceramic surface, the predominant mechanism by which material is removed from a surface is always by cracking and chip formation [H19].

Ruff and Weiderhorn [R4] stated the following:-

> 'The role of plastic deformation, relative to fracture, is enhanced by reducing the impact load during erosion by reducing either the impact velocity, particle size or angle of impingement.'

They concluded by saying that strain rate effects on the erosion of ceramic materials were much more important than any possible temperature rise.

2A.4.2 The Erosion of Glass Ceramics

Cast ceramic materials such as cast basalt have been used extensively in pneumatic conveying pipelines. This is because it is possible to cast this material into complex shapes, such as bifurcations in conveying pipelines. This ease of manufacture, in conjunction with the fact that this type of material has been found to resist erosion well when in use in pulverised fuel conveying pipelines in use in the power generation industry, have led to wide use of this material in pneumatic conveyors suffering from erosive wear. Several synthetic glass ceramics have also been seen on the market recently; these are made in many instances from the waste products obtained from blast furnaces.

In a recent study of the erosion performance of Silceram, a synthetic glass ceramic, carried out by Sparks *et al.* [S17] it was reported that three different wear regimes could be identified. The regime of wear that occurred was dependent on the shape of the particle and the severity of impact. This conclusion indicates that the assertions of Ruff and Weiderhorn presented above [R4] regarding the importance of strain rate in the erosion of ceramics could be applied to this type of material. It was found that the predominant mechanism by which material was removed from the ceramic surface was that of lateral fracture and flake formation as described in section 2A.4.1.3. Cracking of this type was found to occur only for impacts by angular particles, or rounded particles above an impact velocity of 50 m/s; removal of surface material occurred with each impact because of this mechanism. For impacts of rounded particles below 50 m/s, erosion occurred by fine scale fracture and plastic flow in the impact site. Sparks [S17] called this mode of wear 'plastic fatigue wear'. A third mechanism of wear, that of 'elastic fatigue wear' was observed by Sparks during erosion by glass ballotini at an impingement angle normal to the eroding surface. This third mechanism consisted of fine scale fracture with minimal plastic deformation. Many particle impacts were required to cause erosion by the second and third mechanisms of wear described by Sparks [S17].

Aghajanian *et al.* [A3], following tests carried out on the erosion of cast basalt stated that 'the effects of the microstructure of such a material are very large and cannot be described by models which take account only of bulk properties be these microstructure sensitive or not'. This statement implies that the porous nature of cast ceramics significantly affects their erosion resistance. Little progress has been made in the modelling of the erosion of cast ceramics since this work.

2A.4.3 The Erosion of Bonded or Sintered Ceramics

In the influential work of Vaughn and Ball [V2] the erosion behaviour of bonded and sintered ceramics was extensively surveyed. It was discovered that in general terms the smaller the crystallites used to form the ceramic material the lower the erosion rate.

Much was found to depend on the relative size of the crystallites to the particles striking the target surface. If the density of particles is high in the volume of surface material being affected, the material acts in a the manner described in section 2A.4.1 above, and can be generally said to resist erosion well. Conversely, when the density of crystallites is low, the impacting particles can either affect the material used to bond the crystallites together (which is usually soft in comparison to that of the crystallites), or in the worst case affect an individual crystallite. Figure A2.8 illustrates these two scenarios.

Obviously, the probability of either of these two modes of erosive wear occurring depends on the relative quantities of binding material and hard crystallites contained in the ceramic. If the amount of binding material is low, inter-crystallite cracking becomes an important mechanism of erosive

Figure 2A.8 The effect of crystallite density on the erosion of bonded ceramics [H18].

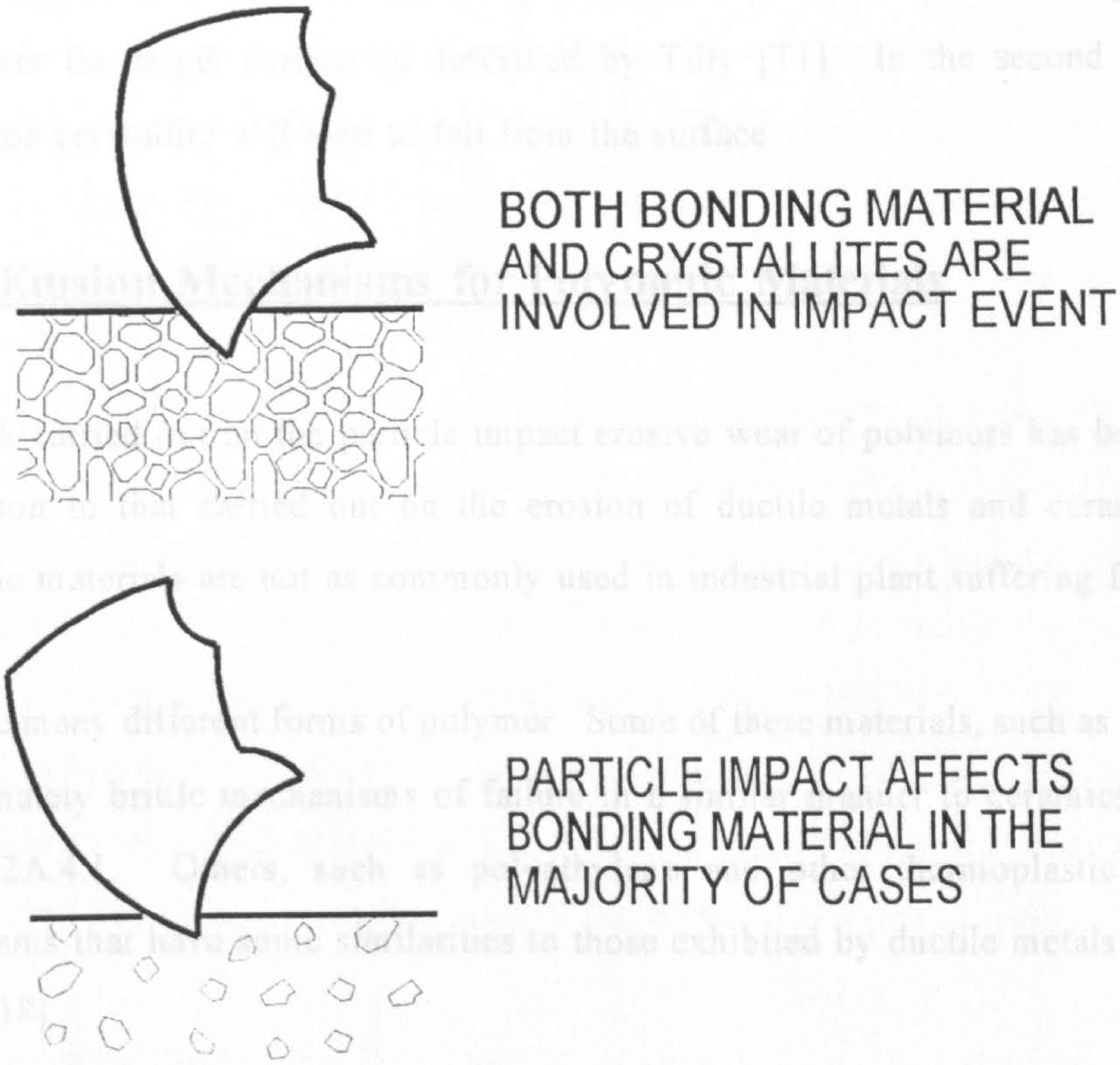

wear. This behaviour was reported by Vaughn and Ball [V2]. When the volume of material affected by the particle impact has a low density of crystallites two further mechanisms of material removal can occur. The first of these is that the energy of the particle striking the target is absorbed by an individual crystallite; if this occurs the impacting particle will either push the crystallite into the softer binding material, which, in turn will be extruded from around the crystallite, or the crystallite will fracture. In the first of these two cases the extruded binding material will be more exposed and more likely to be removed from the surface by subsequent particle impacts or fragments of particles that 'wash' over the target surface as described by Tilly [T1]. In the second case the pieces of the fragmented crystallite will tend to fall from the surface.

2A.5 Erosion Mechanisms for Polymeric Materials

The work carried out on the particle impact erosive wear of polymers has been limited in extent in comparison to that carried out on the erosion of ductile metals and ceramics. This is because polymeric materials are not as commonly used in industrial plant suffering from erosive wear.

There are many different forms of polymer. Some of these materials, such as perspex, tend to exhibit predominately brittle mechanisms of failure in a similar manner to ceramics as described above in section 2A.4.1. Others, such as polyethylene and other thermoplastic polymers, wear with mechanisms that have some similarities to those exhibited by ductile metals as described in section 2A.3 [H18].

Detailed investigation of the mechanisms of wear of polymers by single solid particle impacts have mainly been carried out at Cambridge, UK. Walley *et al.* [W5] carried out single spherical particle impact tests (normally using 4 mm diameter spheres at a variety of impact velocities) on polypropylene and identified five main types of wear scars. These were as follows:-

a) Smooth scars, where no detectable microscopic surface modification occurred. This type of scar occurred across the full range of angles of impingement from 0° to 90°, however they occurred more frequently at low angles of impingement.

b) Wear scars with lips form the second category of scar described by Walley *et al.*. These wear scars were similar to those described for ductile metals in section 2A.3.1 with the exception that, in the by far the majority of cases, the crater lips were much more firmly attached than those that have been observed in scars in metals [W5]. This form of wear scar was found to occur for polypropylene at almost all angles of impingement. However, at low angles a different form of wear scar, called a banded wear scar, tended to occur in preference to the scar with lips. Evidence of rapid relaxation of the plastically deformed material was observed to occur.

c) At low angles of impingement and above a specific particle velocity threshold, banded wear scars were seen. These wear scars featured the formation of transverse cracks and bands. On closer examination fine fibres of plastic were observed to be stretched across the cracks. The formation of the fibres was deduced to be a consequence of high temperatures being generated during the impact of a particle and the contraction of highly sheared material under the action of surface forces. Cracks were orientated in the banded surface to follow the direction of pre-existing flaws in the surface of the material that were caused by polishing prior to the tests.

d) During high velocity impacts at angles of impingement from about 30° up to 90° what were termed as penetration wear scars were observed by Walley *et al.* [W5]. This form of wear scar was deemed to occur when the particle penetrated into the target surface to a depth greater than the particle diameter. Normally in such situations the particle was expelled from the damaged surface by the relaxing elastic stress field.

e) The last form of wear scar observed by Walley *et al.* [W5] was that of embedment where the particle remained embedded in the target surface. This form of wear scar was formed only when the impact velocities were of the order of 250 m/s or more.

During the work carried out by Walley *et al.* it was found that there were three ways in which material removal from a surface could occur as a consequence of a single particle impact. These were a) the drawing out of filaments of material that were attached to the particle, b) the adhesion of thin films of surface material to the particles, and c) the combined fracture, cutting and extrusion of blocks of polymer caused at low angles of impingement [W5]. The last of these mechanisms occurred when the particles were angular whilst the previous two mechanisms occurred when the particle was more rounded [W1]. In this work it was also discovered that visco-elastic relaxation and thermal material properties may have a significant part to play in the erosion of this material.

These wear scar types have also been observed to occur, (by Walley *et al.* [W1,W6]), in the behaviour of polyethylene and polyetheretherketone as well.

Multi-particle impact tests on polyethylene, carried out by Walley *et al.* [W1] using a gas blast type erosion tester, indicated that a large number of particle impacts were required to remove the lips formed in low impingement angle impacts. This was because it was stated that the lips were attached strongly in polymers when compared to lips formed in metals. Because of the strong attachment of material formed into lips, mass loss at normal impact was not observed for polyethylene.

Walley [W1] also indicated that as a consequence of the thermal properties of polymers thermal reinforcement, i.e. an increase in the temperature of the surface of the polymer subjected to erosion because of successive impacts, could occur if the particle mass flux at impact became too great. However, the work by Doyle and Ball [D2] using the model for thermal reinforcement proposed by Hutchings and Levy [H7] indicate that because of the mechanical properties of polyethylene the temperatures generated during particle impact of this material results in the generation of a temperature of only 23°C occurring during each impact. This result may have been confirmed since results of the measurement of the temperature generated during plastic deformation caused by a single particle impact obtained by Swallowe *et al.* [S19] indicate that temperatures much less than 200°C are likely in the deformation of polyethylene. Despite this, any increase of the temperature of the surface of the polymer would lead to changes in the mechanisms of erosion taking place because the material will become softer. However, it is unlikely that melting of the surface material will occur.

2A.6 Mechanisms of the Erosion of Elastomers

Again, work on the mechanisms of the erosion of natural and synthetic rubbers, (called elastomers from now on), has been limited in extent when compared to the volume of work carried out on ceramics and ductile metals.

However, it has been concluded that at particle impact velocities similar to those that would occur in pneumatic conveying, the basic mechanism of erosion for elastomeric materials is by the formation of fine fatigue cracks caused by the tensile surface forces caused during particle impacts [L7,A7]. Intersection between the cracks lead to surface material falling out of the surface.

At velocities higher than 50 m/s, the amount of erosion of unfilled natural rubbers caused by the impact of 130μm diameter silica sand was found by Arnold and Hutchings, to increase quite dramatically [A7]. This was because it was found that the particles were beginning to embed themselves in the eroding surface. This caused the mechanism of erosion to change.

It has been found that an elastomer that resists abrasive wear well will tend not to resist erosive wear with the converse being true [M15,A7]. This implies that compliant elastomers will resist erosive wear well with hard rubbers suffering large amounts of wear under similar conditions. However, the cause of material removal in both erosive and abrasive wear is the same. In both abrasive and erosive wear it is the degree of stress induced in the surface of the elastomer during the wearing process that dictates the amount of damage caused.

In work involved in carrying out erosion tests on elastomers in the presence of a silicone based lubricant a dramatic reduction in erosion rate was found to occur [A7]. This was concluded to indicate that the erosion of elastomers depended on the dynamic friction between the particle and the surface caused during the particle impact and the tensile surface generated as a consequence of this interaction.

Work concerning the impact friction of polymeric materials carried out by Ratner and Styller [R2] found that the impact friction coefficient of elastomers decreased with an increase in the angle of attack. As a consequence of this behaviour it is to be expected that the tensile forces generated in the surface of the elastomer at low angles of impingement will be greater than those that occur at higher angles of impingement. This is a logical reason why it has been observed that there is a peak in the curve of erosion damage when plotted against angle of impingement for elastomeric materials at low angles of impingement [A8].

Researchers have attempted to determine what material properties have the greatest effect on the erosion resistance of elastomers [A7,L7]. Until 1990 no specific trend in the variation of erosion resistance with material properties was observed with the possible exception of material resilience measured using a steel ball bounce test. However, Li [L7] in a series of detailed tests on polyurethane elastomers which had the same impact resilience, found that a trend of increase in erosion resistance occurred with increases in hardness, tensile modulus and tensile strength.

2A.7 Conclusions

This appendix is intended to convey an overview of the state of knowledge regarding the effect of materials and particle properties on the mechanisms of erosion that occur with various materials. Readers are directed to the various references that are referred to in this Appendix for further information. The complex behaviour of the response of a material to the impact of small particles at high speed mean that there is still considerable scope for improving the understanding of the erosion of materials of various types. Attention must still be given to establishing the inter-relationship between the degree of deformation, strain rate and temperature rise generated during the impact of a single particle and the effect that these variables have on erosion damage. Obviously, the continuing development of materials for specialised use in aggressive environments will necessitate further investigation of the erosive resistance of these new materials.

Appendix 2B: Advantages and Disadvantages of Using Various Forms of Laboratory Erosion Testers

2B.1 Introduction

This appendix contains information related to the advantages and disadvantages of using various forms of laboratory erosion tester to simulate erosive conditions seen in pneumatic conveying applications. This information is presented in tabular form.

2B.2 Perceived Advantages and Disadvantages of Using Various Laboratory Erosion Tester

Type of Erosion Tester	Advantages	Disadvantages
Rotating Disc Accelerator Erosion Tester (Further information concerning the use this tester is contained in Chapter 4 sections 4.1, 4.25 & 4.3.6.3.3, Appendices 4A, 4B & 4D, & [B13,G1,K6,K9,S5,S6, S8]).	- ten targets can be tested simultaneously (problems due to experimental error are minimised). - velocity determination is simple. - reasonable range of particle concentration simulation at impact. - gas / particle interaction is miminal. - steady state erosion conditions are easily assessed due to the test method that was adopted. - comparative erosion results are easily obtained from this tester.	- difficulty in assessing the mass of abrasive that strikes each target. - test duration is long due to the necessity of finding the erosion versus time history of each target. - erosion does not take place as a continuous process because of the method of dispensing and accelerating the abrasive particles.
Gas Blast Erosion Tester (Further information concerning the use this tester is contained in Chapter 4 sections, 4.22, 4.25 & 4.3.6.3.4, and [B13,A4,D3,N3,S11]).	- short test duration. - simple results analysis. - continuous erosion process.	- difficulty in assessing when steady state erosion conditions occur (prior experience is often required). - difficulty in assessing particle velocity. - high probability of adverse gas / particle interactions occurring, especially with small particles.

Type of Erosion Tester	Advantages	Disadvantages
Gas Gun Impact Tester (Further information concerning the use of this form of tester can be obtained from [S7,W1]).	- good control over the particle impact velocity is possible. - accurate tests at different angles of impact are possible. - measurement of detailed mechanistic effects for material removal is possible.	- erosion is normally caused by multiple impacts in close proximity to each other; this rig cannot simulate this behaviour. - to promote material removal by an individual impact, higher impact velocities than those occurring in pneumatic conveyor applications need to be used. - particles of fixed regular shape are required.
Whirling Arm Test Rig (Further information concerning the use of this form of tester can be obtained from [G2]).	- particle impact velocity and angles are well controlled provided the erosion process takes place in an evacuated chamber. - a reasonable range of particle concentrations at impact can be obtained. - two targets can be used simultaneously, therefore comparative erosion results are easily obtained . - very high particle impact velocities can be achieved.	- if the chamber in which erosion takes place is not evacuated, problems with unwanted gas / particle interactions may occur. - problems occur in assessing the mass of abrasive that strikes each target. - the erosion process is not continuous.
Submerged Rotating Arm Erosion Tester (Further information concerning the use of this form of tester can be obtained from [H10,C4,C5]).	- comparative erosion results are easily obtained from this type of tester. - the erosion process is continuous.	- particle velocity is very difficult to measure. - particle concentration upon impingement is not controllable. - degradation of the abrasive material may affect the erosion that does occur. - the erosion process is dependent on the fluid in which the particles are suspended. - interparticulate or particle/fluid interactions may have a significant effect on the erosion process. - difficulty in assessing when steady state erosion conditions occur (prior experience is often required).

Type of Erosion Tester	Advantages	Disadvantages
Free Fall Rig	- a reasonable range of particle concentrations at impact can be achieved. - simple results analysis. - the erosion process is continuous.	- assessment of the particle impact velocity can be difficult unless tests are carried out in an evacuated chamber. - a very limited range of particle impact velocities are possible. - gas / particle interaction can cause problems unless tests are undertaken in an evacuated chamber. - difficulty in assessing when steady state erosion conditions occur (prior experience is often required).

Appendix 3A: Materials Specification for the Main Test Programme

3A.1 Introduction

This appendix contains detailed information relating to the materials that were used for the majority of the test work described in this thesis. Details of the particulate abrasive and the steel used in the construction of the pneumatic conveyor test bend are described in the following sections. The steel used for samples in the bulk of the rotating disc accelerator erosion test work was to the same specification as that used in the pneumatic conveyor bend.

3A.2 The Specification of the Abrasive Material

Throughout the entire duration of this project a single form of abrasive medium was used. This was a relatively fine olivine sand, marketed under the name 'Renova Fine' by Hepworth Minerals and Chemicals Ltd., Staffordshire, UK. Olivine sand was selected since it is a freely available mineral product which shares many properties and the main abrasive constituent in common with many mineral contaminants seen in industrial products which consist principally of silica. This material was also selected since it contains amorphous, not crystalline, silica and therefore any airborne dust produced during handling will be much less likely to cause silicosis than that produced from an ordinary silica sand. Olivine sand consists mainly of $(Mg,Fe)_2SiO_4$ with the remainder being made up from traces of metallic oxides. It was irregularly shaped and chemically inert under ambient conditions. The mean particle diameter was 324μm. The range of the size distribution showed that 10% of the sample was below 213μm and 90% was below 455μm in diameter (a full size analysis is given in Figure 3A.1). The particle density was measured, using a Beckman air comparison pycnometer, to be 3280 kg/m^3. Particle hardness was measured, using a micro-Vickers hardness tester, to be equivalent to 6.5-7 on the Moh scale. It was found that an indication of the sphericity could be obtained by comparing photographs of the olivine sand particles with outlines shown in the Rittenhouse sphericity scale [R1]. A photograph illustrating the range of shapes that can be expected for this material are shown in Figure 3A.2. The sphericity index, obtained by this means, was approximately 0.75.

3A.3 A Description of the Structural Mild Steel Used As the Main Test Material

The mild steel that was selected for the test programme was cut from pipe of the type that is used in the construction of pneumatic conveyor pipe work. The steel was made according to BS4360 Grade 43C / BS EN10210 Parts 1 & 2. The steel had the following constituents:- Carbon 0.21% (±0.03%), Silicon 0.5% (+0.05%-0%), Manganese 1.3% (±0.1%), Phosphorus 0.05% (±0.01%) and Sulphur 0.05% (±0.01%). This steel was supplied in the hot rolled condition but included the effects of rolling into tube form and resistance welding along the seam. The samples from the pipe segment were cut to 25 mm square and machined to give one flat surface. They were then cleaned using 240 grit abrasive paper to give a uniform surface finish. Samples were not taken from areas next to the welded seam. The samples were orientated so that the grain structure was aligned with the direction of particle motion as would be the case in the actual pipes. Chemical etching and microscopic examination of the microstructure of the steel showed that it consisted of large ferrite grains within which could be seen evidence of sub-boundaries. On the sub-boundaries, plate-like cementite was formed and there was a small quantity of pearlite clusters contained within the bulk of the material (see Figure 3A.3). The hardness of the steel was measured to be 122 N/mm^2 on the surface of the target and 126 N/mm^2 in the bulk of the target (these results were found on Vicker's equipment) (≈45 on the Rockwell A Scale).

Figure 3A.1 Malvern Size Analysis Results for the Olivine Sand Abrasive

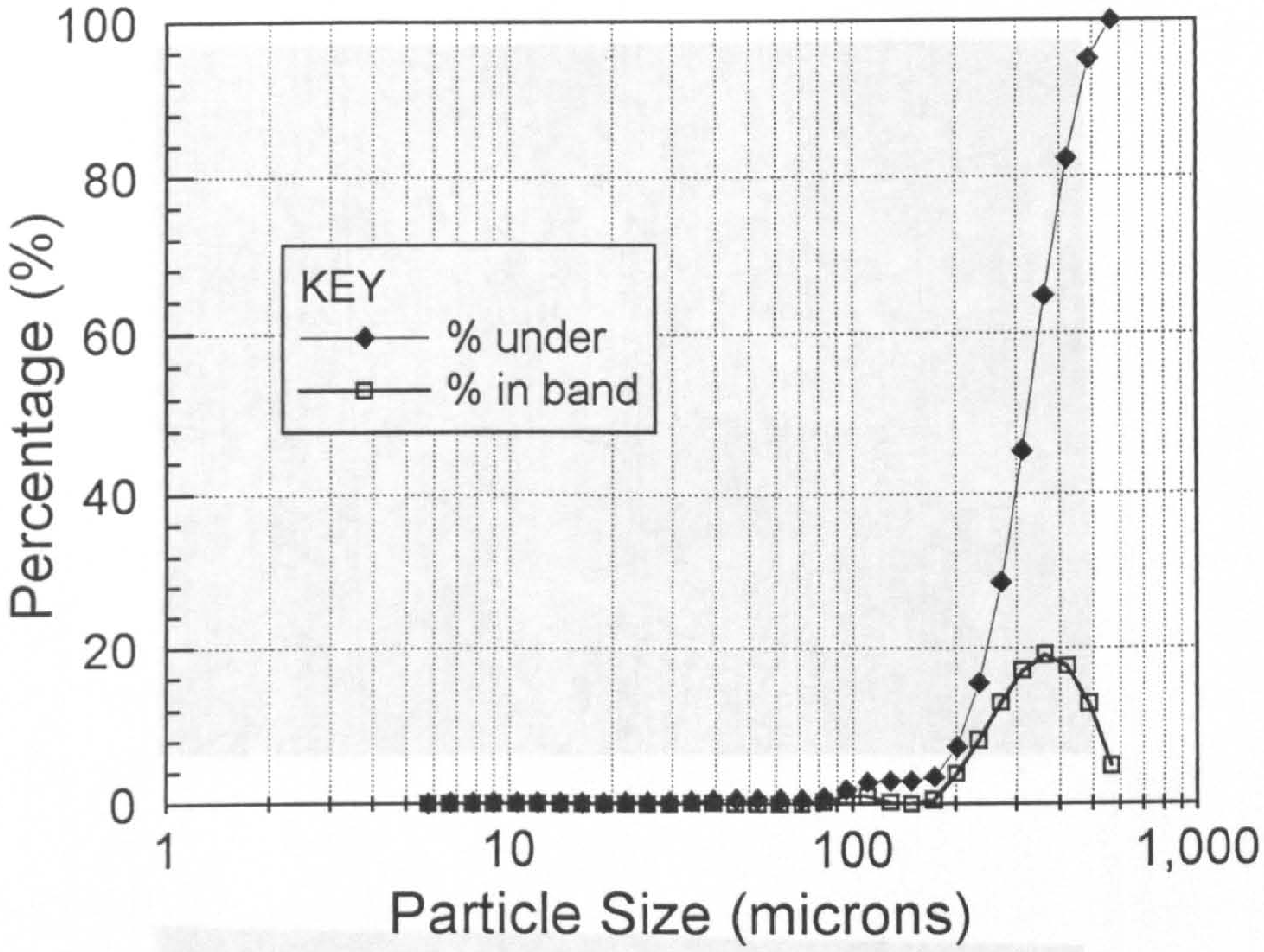

Figure 3A.2 Photograph of Abrasive Particles Indicating their Shape

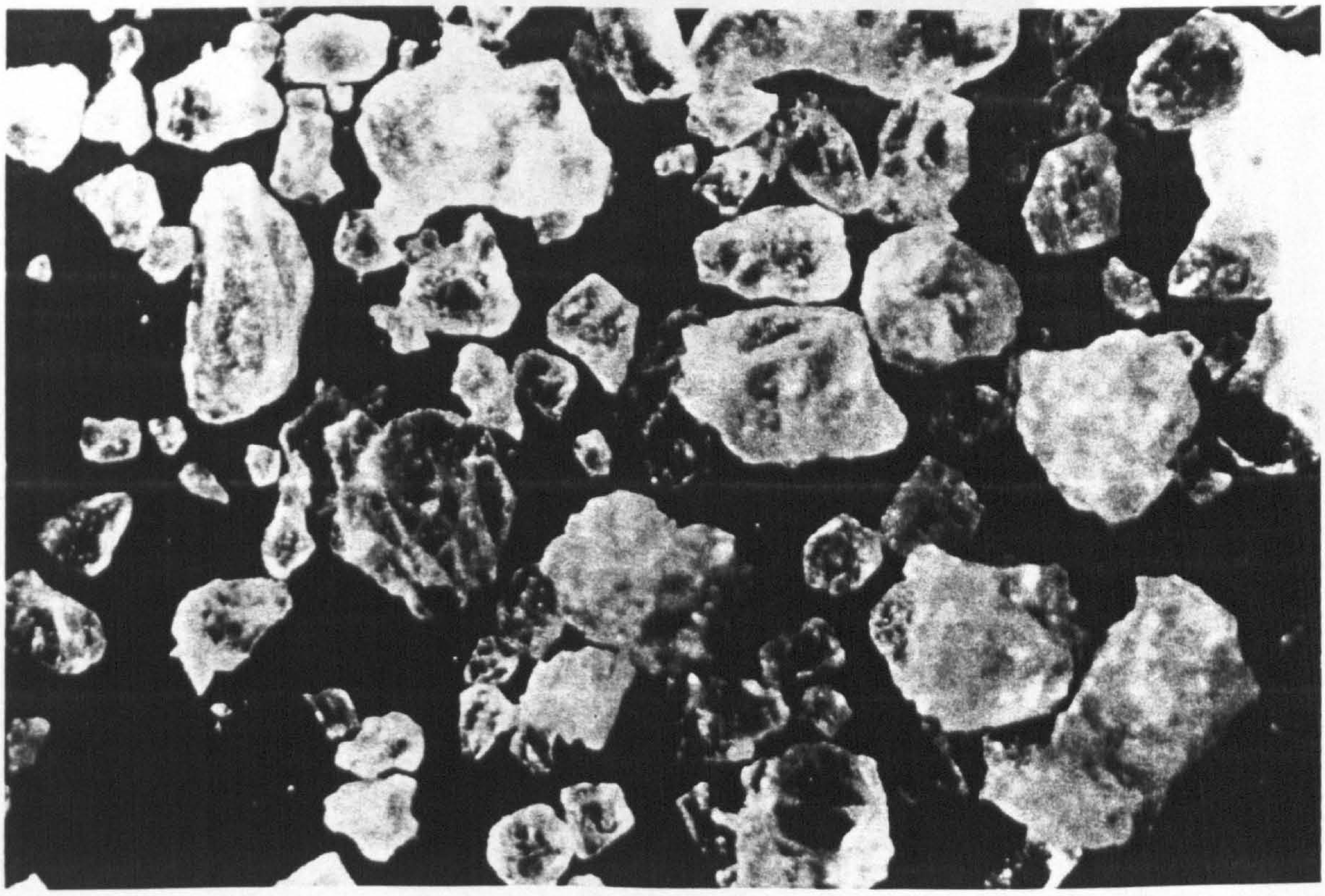

Figure 3A.3 SEM Photomicrographs of the Mild Steel (at 350x magnification).

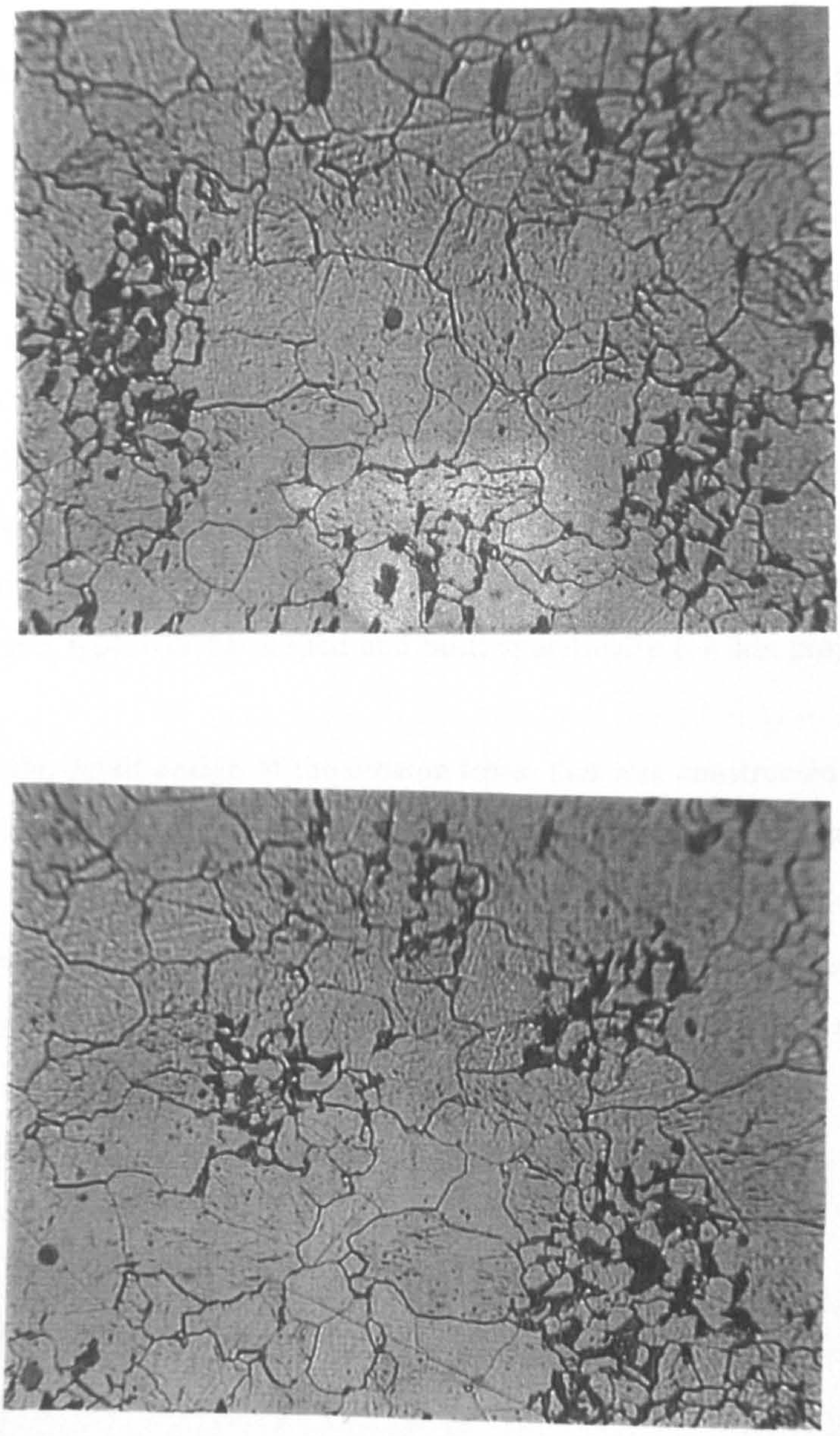

Appendix 4A: The Design and Development of the Rotating Disc Accelerator Erosion Tester

4A.1 Introduction to the Rotating Disc Accelerator Erosion Tester

The literature review findings described in Chapter 2 enabled a thorough survey to be made of the designs of various forms of erosion tester that had been used in the past. The advantages and disadvantages of all of the various erosion tester designs available are highlighted in Appendix 2B of this thesis. It was decided that the most effective form of tester that could be used was the rotating disc accelerator form. This form of test apparatus is the subject of the Soviet standard GOST 23.201-78 [G1], and it was subsequently discovered that erosion testers of this form have been used successfully in the countries that used to form the Soviet Union [K6], Sweden [S8] and Japan [S5]. A test facility of this type was developed and built specifically for this project.

A key element in the detail design of the erosion tester that was constructed for this project was that it should be able to simulate the conditions prevalent in the use of pneumatic conveyors.

The design concept that was used as the basis for the erosion tester constructed for this project was that developed by Söderberg *et al.* [S8]. However, the purposes to which the erosion tester was to be put dictated that changes would have to be made to this original design. The overall rig has been divided into the following systems for the purposes of this description:

- Erosion testing centre.
- Abrasive storage system.
- Fresh abrasive feed system.
- Spent abrasive handling system.
- Dust extraction system.
- Control system.

A brief description of the overall rig will be given before each of these systems is discussed.

4A.2 Overview of the Entire Rotating Disc Accelerator Erosion Test Facility

Figure 4A.1 shows a schematic view of the entire test facility indicating the inter-relationship between the relevant systems. Figure 4A.2 shows the test facility in its entirety upon completion.

On the left hand side and centre of the erosion test facility was the fresh abrasive storage hopper and handling system. This system was responsible for ensuring the safe containment and provision of fresh abrasive material to the erosion centre. The erosion centre contained all the necessary items to control the feed of the abrasive into the particle acceleration mechanism, and for the abrasive to be projected against the targets. Once the abrasive had passed through the erosion centre, it fell into a small hopper which captured the used abrasive. This small hopper was part of the spent abrasive disposal system, which passed the used abrasive into the spent abrasive storage hopper on the right hand side.

The dust extraction system was responsible for extracting dust from the main dust generation sources i.e. the erosion centre and the combined ends of the airslides. This system ensured that the environment surrounding the test facility contained minimal amounts of escaped olivine sand dust.

The control system permitted control of the test facility to be exercised from a central control point. The operation of the all of the other systems were managed by the control system.

The most important system was the erosion centre. All the other systems simply served to ensure that abrasive was fed into and removed from this system in the correct sequences.

4A.3 The Erosion Testing Centre

The erosion centre consisted of several major parts. These were the particle acceleration mechanism; the abrasive feeding device; and the target holding devices. Each of these will be discussed in turn. Figure 4A.3 illustrates the relative arrangement of these items with respect to each other.

The particle acceleration mechanism consisted of a balanced disc whose velocity of rotation could be set at any speed between 0 and 6000 rpm. This range of rotational velocities was achieved by using an inverter controlled 2.2 kW AC motor driving the particle acceleration disc through a 2:1 step up belt drive. This range of rotational velocities generated particle velocities between 0 and 90 m/s. The rotating disc had a very low inertia and it was possible to select a rotational velocity using a potentiometer set point alone, via control options available on the inverter drive system. Acceleration disc speed was displayed on the control panel by a counter. The count that was displayed was obtained from a vaned disc attached to the main acceleration disc spindle which passed through a hall effect transducer. The acceleration disc was 0.12 m in radius and was constructed from heat treated

Figure 4A.1 Schematic View of the Entire Test Facility

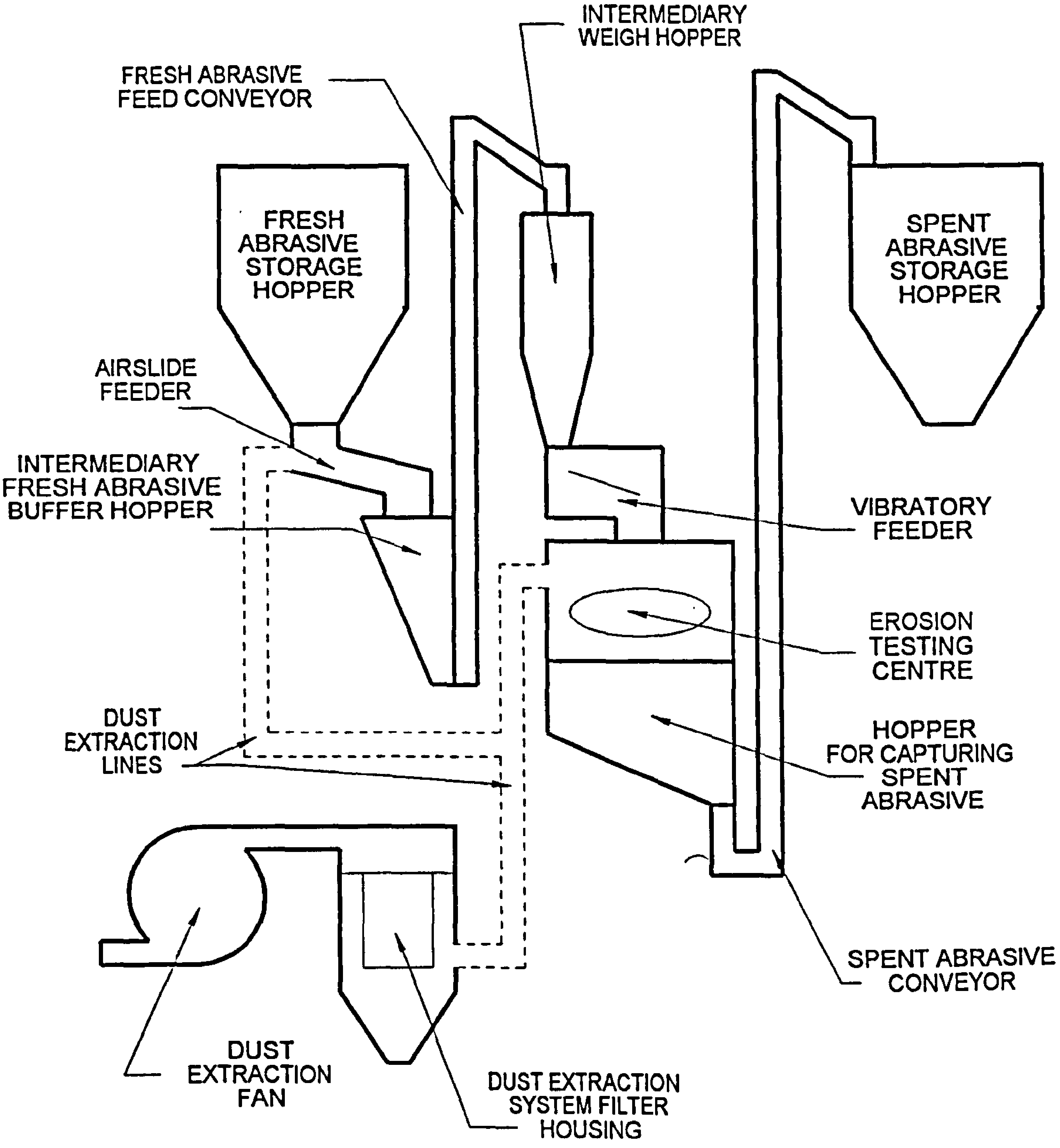

Figure 4A.2 Photograph of the Entire Test Facility Upon Completion

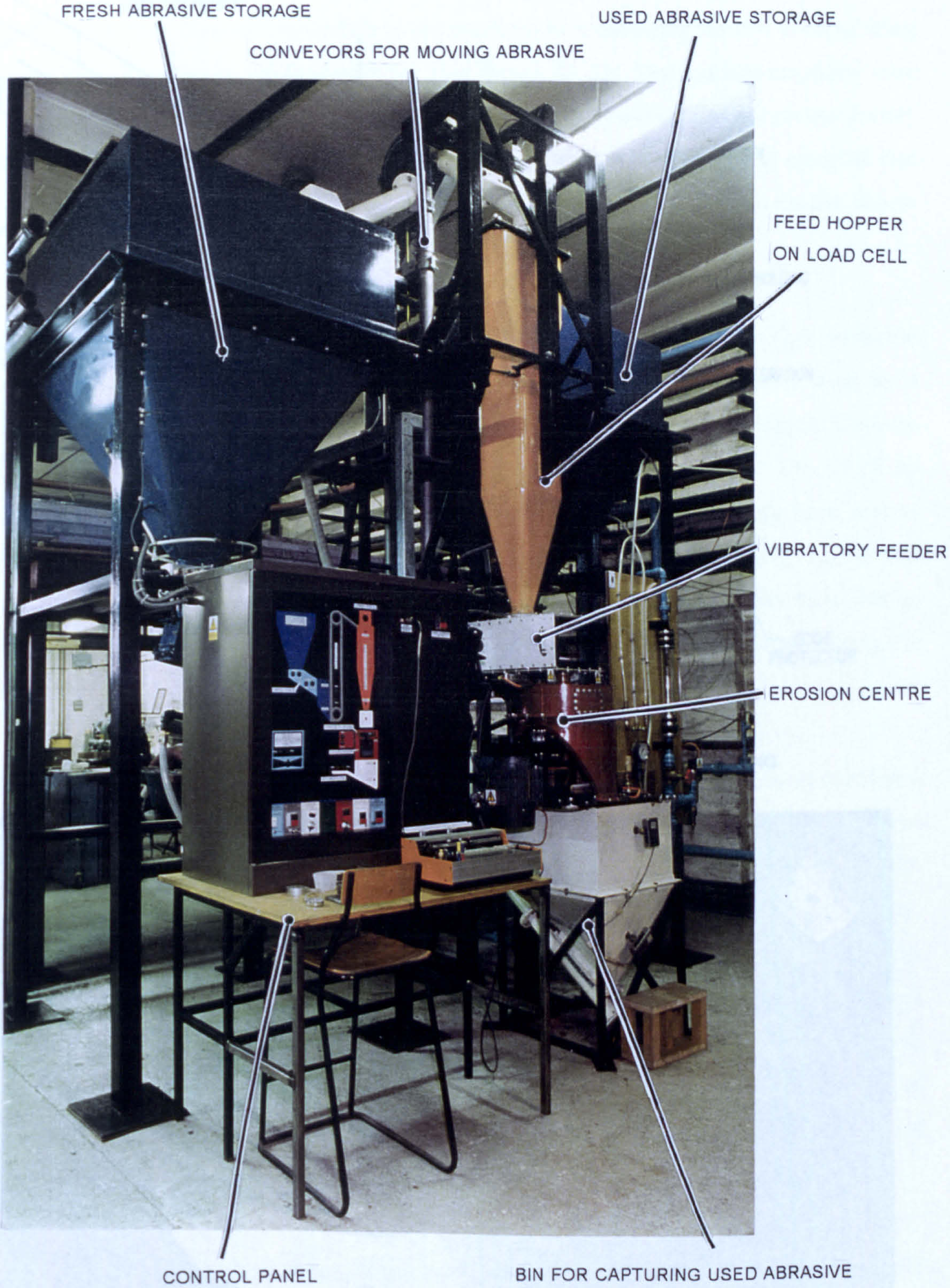

Figure 4A.3 Details of the Rotating Disc Accelerator Mechanism

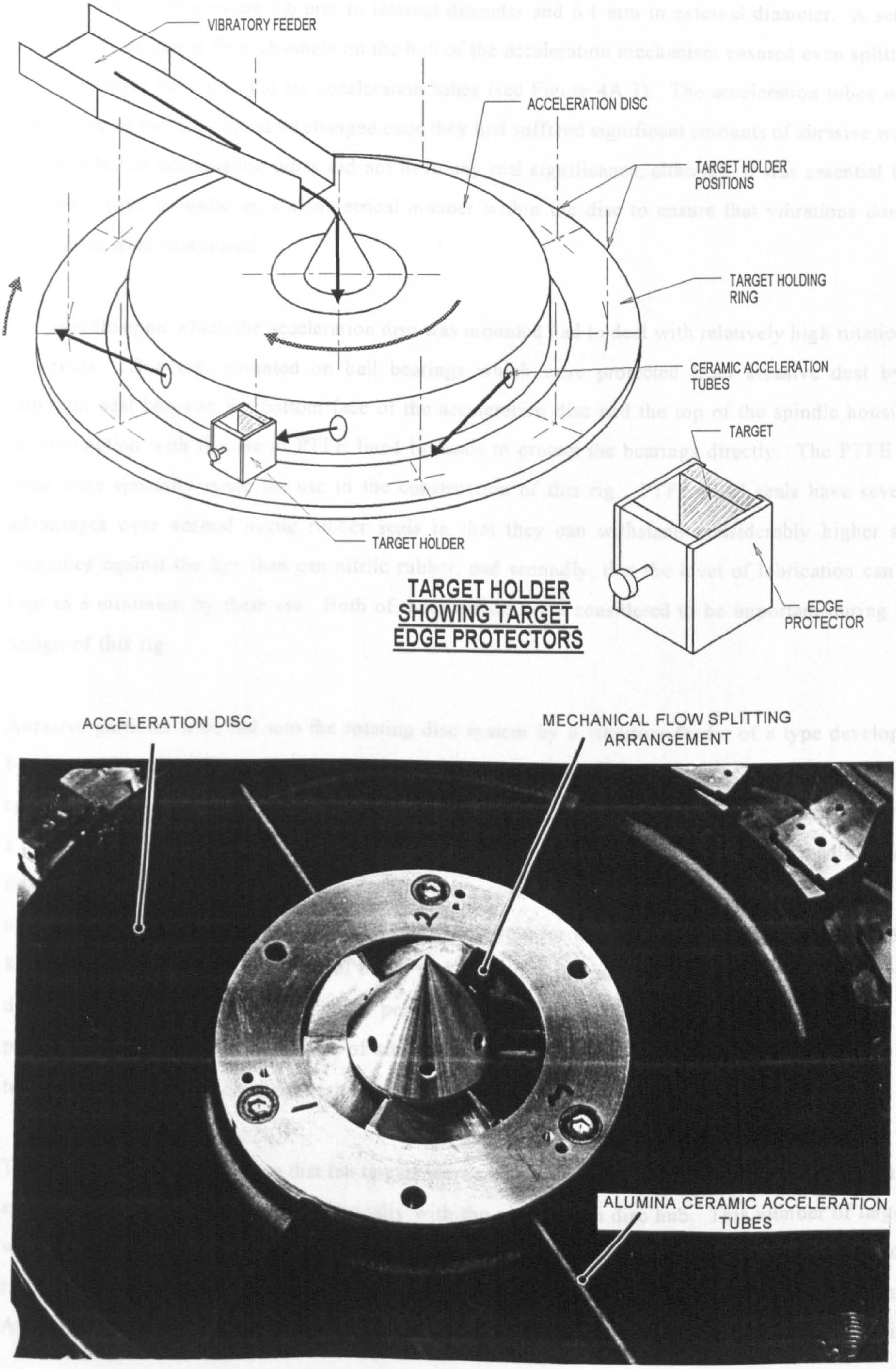

and hard anodised aluminium alloy. It contained six radial channels made from high quality alumina ceramic tubes. These were 2.6 mm in internal diameter and 6.1 mm in external diameter. A series of specially designed flow channels on the hub of the acceleration mechanism ensured even splitting of the abrasive flow into the six acceleration tubes (see Figure 4A.3). The acceleration tubes were removable so that they could be changed once they had suffered significant amounts of abrasive wear. The number of acceleration tubes did not have any real significance, although, it was essential that the tubes were mounted in a symmetrical manner within the disc to ensure that vibrations due to imbalance were minimised.

The spindle upon which the acceleration disc was mounted had to deal with relatively high rotational velocities. This was mounted on ball bearings which were protected from abrasive dust by a labyrinth seal between the bottom face of the acceleration disc and the top of the spindle housing, in conjunction with the use of PTFE lined lip seals to protect the bearings directly. The PTFE lip seals were specially made for use in the construction of this rig. PTFE lined seals have several advantages over normal nitrile rubber seals in that they can withstand considerably higher slip velocities against the lips than can nitrile rubber, and secondly, that the level of lubrication can be kept to a minimum by their use. Both of these effects were considered to be important during the design of this rig.

Abrasive particles were fed into the rotating disc system by a vibratory feeder of a type developed by Barnes [B15]. This feeder consisted of a lightweight tray, supported by flexible sheet type springs, which sat beneath a feeding hopper (see Figure 4A.4). The small hopper was designed with a baffle inside it so that the abrasive material contained in the hopper did not directly load the tray; this kept the force necessary to move the tray more constant. The tray movement was achieved by using an electromagnetic drive system. The motive force for the electromagnets was provided by a 80 V DC power supply and a control board that generated the pulsed electrical signal necessary to drive the electromagnets. This feeder permitted the selection of a given constant feed rate of particles. This was achieved by use of amplitude feedback control to ensure that the amplitude of tray vibration was kept constant despite variations in the load on the feeder tray.

The test rig was constructed so that ten targets were utilised per test. Ten target holders were equally spaced around a ring running concentrically with the acceleration disc hub. This number of targets was chosen, because this was the maximum number of targets that could be employed without restrictions in the movement of one target holder occurring because of the close proximity of another. Also, with the spacing the targets achieved in this arrangement, minimal interference in the erosion

Figure 4A.4 Diagram of Details of the Vibratory Feeder System

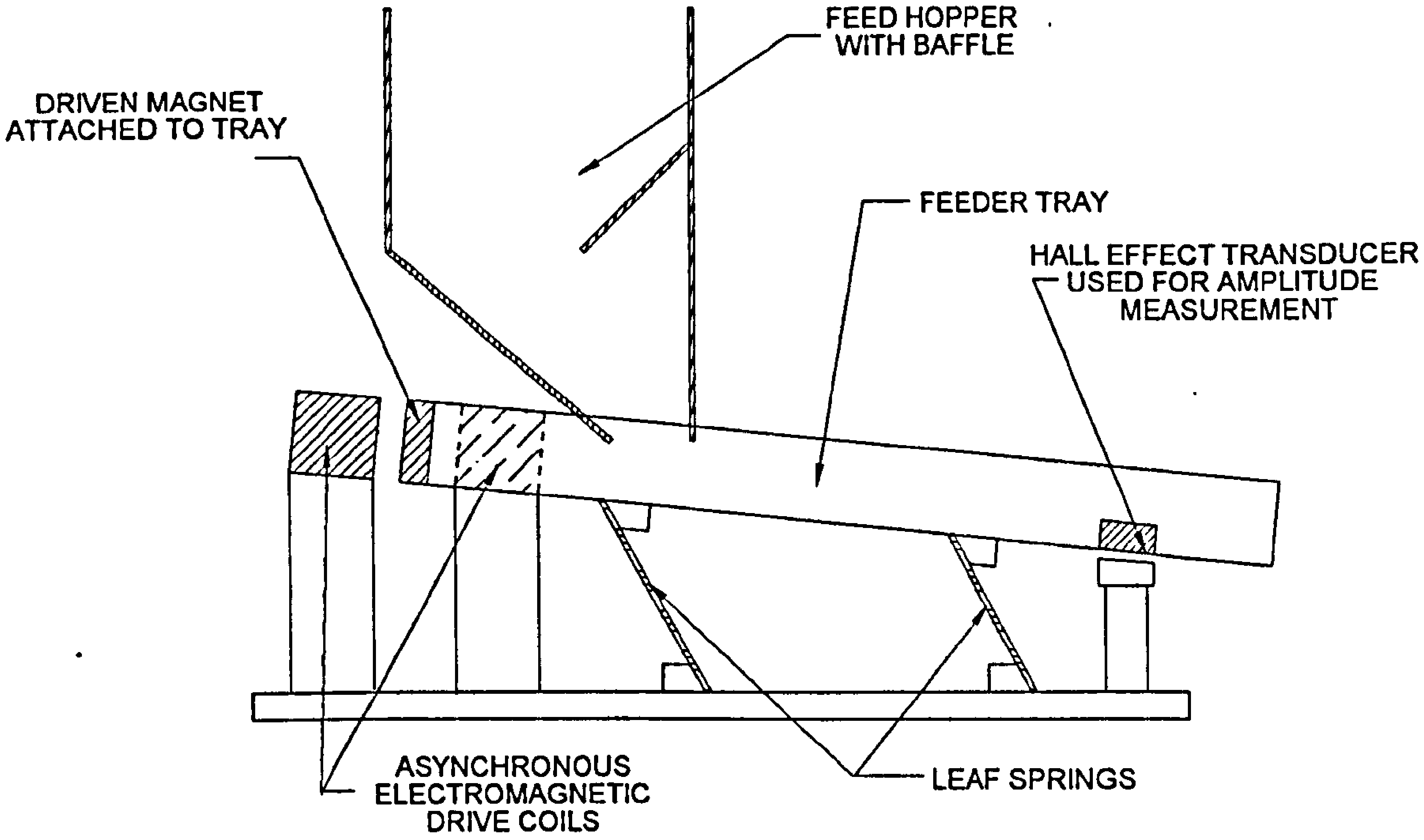

of one target by particles rebounding from another was found to occur. The rotational motion of target holder ring was maintained at 10 rpm by a 100 W 24 V DC geared motor connected to the target holder ring hub by a 1:2 belt drive system. The rotation of the target holder ring was used to minimise any effect of bias in the way in which the rotating disc dispensed abrasive particles. Each target holder could be angled independently to the particle flow in 5° increments for angles of orientation from 5° to 90° to the trajectory of the particles. The targets were mounted with their surfaces vertical. The major difference in the design of this test facility over that of Söderberg *et al.* [S8] was that protection was given to both the leading and trailing edges of the target. This prevented erosion taking place at unwanted angles of impingement. The targets themselves were fastened into position by pushing them up against the projecting lips (as shown in Figure 4A.3) of the edge protectors. In this way the edges of the targets were enveloped by the edge protectors.

The whole erosion testing centre was encased in a 10mm thick steel shell which was designed to prevent flying debris from escaping if the structural integrity of the acceleration disc failed during a test. It was also designed to resist the erosion damage caused by the abrasive that missed striking the targets by incorporating a replaceable sacrificial ring mounted on the internal surface of the steel shell. The spent abrasive was swept out beyond the radius of the target holder ring by an arm attached to this ring, whereupon it fell down an annular gap formed in the casing surrounding the hub of the rotating components. The spent abrasive was collected in a small bin, from which it was conveyed away to more permanent larger capacity storage.

Access to the erosion testing centre was by a panel in the top of the casing for the erosion centre (see Figure 4A.5). An interlock was installed so that if this panel was missing, the inverter drive system would not start. Once the accelerating disc was in motion and rotating at a velocity above 400 rpm the actuation of two small solenoid bolts occurred to ensure that access to the centre was denied until the velocity had fallen below this limit. This panel was secured in place by four small screws that were fastened down whenever the lid was replaced after removal.

Obviously, during erosion testing the formation of dust is unavoidable. To prevent contamination of the surrounding environment by fine dust, a take off to the dust extraction system was fitted to the top of the spent abrasive capturing hopper which formed part of this self contained system. Air inlet positions for the extraction system were on the side of the vibratory feeder housing. The dust extraction system was manually started before a test began.

Figure 4A.5 Photograph of the Rotating Disc Accelerator Housing Including Safety Interlock Details

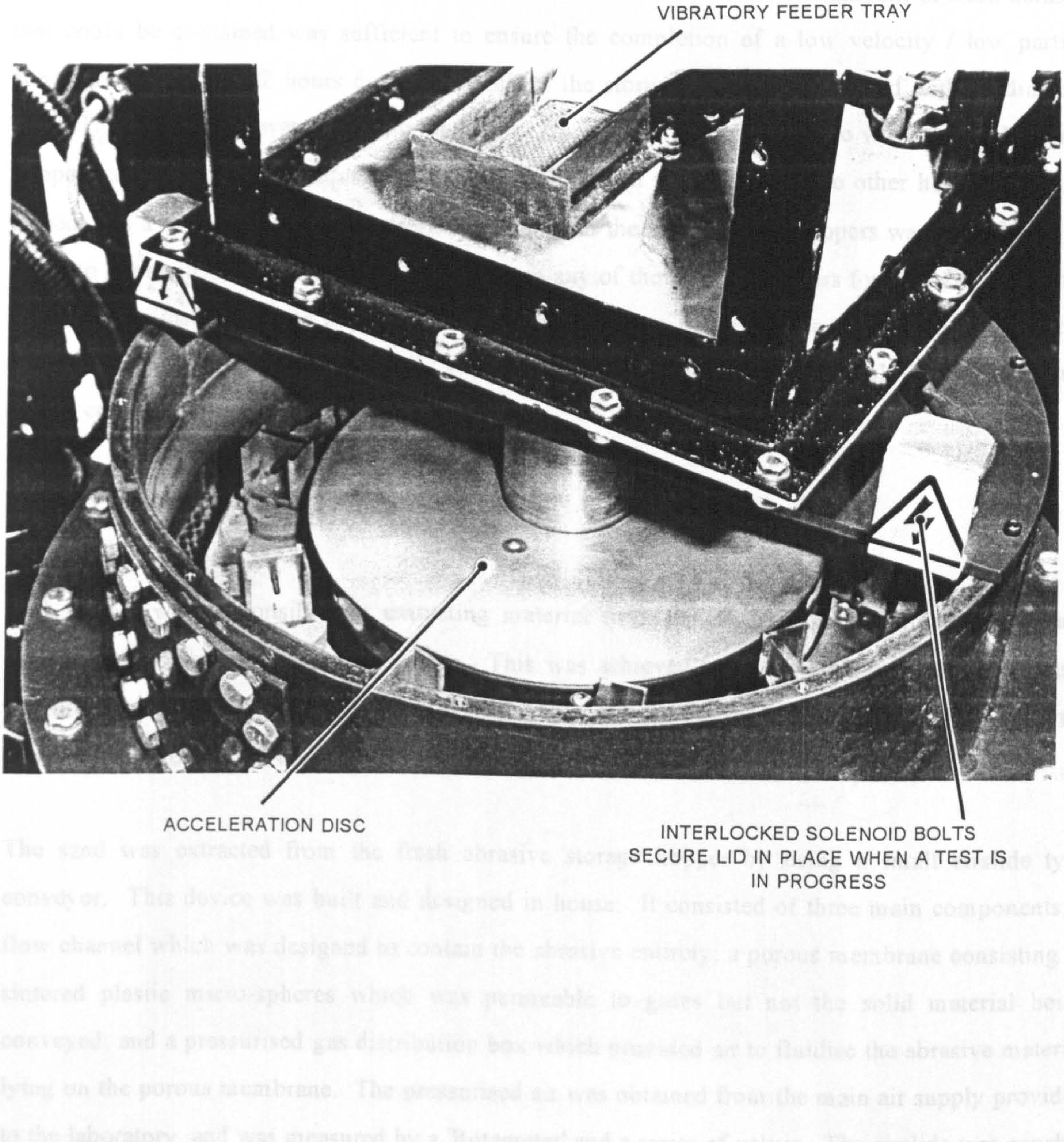

4A.4 The Abrasive Storage System

The abrasive particle storage facility consisted of two storage bins of 3 m^3 capacity. One of these was used to store fresh abrasive whilst the other stored used abrasive. The amount of fresh abrasive that could be contained was sufficient to ensure the completion of a low velocity / low particle concentration test of 42 hours duration. Both of the storage hoppers were fitted with 6" diameter butterfly valves which were manually operated. During normal operation, the valve on the left hand hopper used to store fresh abrasive material was left open whilst that on the other hopper was kept closed. As a consequence of this, fresh abrasive from the main storage hoppers was available at all times to maintain the correct levels of abrasive in any of the feeding hoppers for the system. Figure 4A.2 above illustrates these hoppers. Both of these storage hoppers were discharged onto airslide conveyors. This design was essentially symmetrical so that the purpose to which the hoppers could be put could be reversed if necessary.

4A.5 The Fresh Abrasive Feed System

This system was responsible for extracting material from the fresh abrasive storage hopper and delivering it to the erosion testing centre. This was achieved by using a series of conveyors and intermediate storage hoppers. This was necessary because the limited headroom available within the laboratory prevented the feed hopper from being mounted directly above the erosion centre.

The sand was extracted from the fresh abrasive storage hopper by using a small airslide type conveyor. This device was built and designed in house. It consisted of three main components; a flow channel which was designed to contain the abrasive entirely; a porous membrane consisting of sintered plastic micro-spheres which was permeable to gases but not the solid material being conveyed; and a pressurised gas distribution box which provided air to fluidise the abrasive material lying on the porous membrane. The pressurised air was obtained from the main air supply provided to the laboratory, and was measured by a 'Rotameter' and a series of valves. The airslide was capable of conveying at a rate of up to approximately 3 m^3 of abrasive per minute (see Figure 4A.6).

The material extracted from the fresh abrasive storage hopper was delivered by the airslide conveyor to an intermediate storage hopper. This hopper fed the abrasive material into another conveyor which lifted the material to the next hopper in the sequence. This was a rope and disc type conveyor made by Entecon Ltd. It had a 3" bore conveying tube and conveyed at the rate of approximately 150 kg

Figure 4A.6 Photograph of one of the Airslide Conveyors

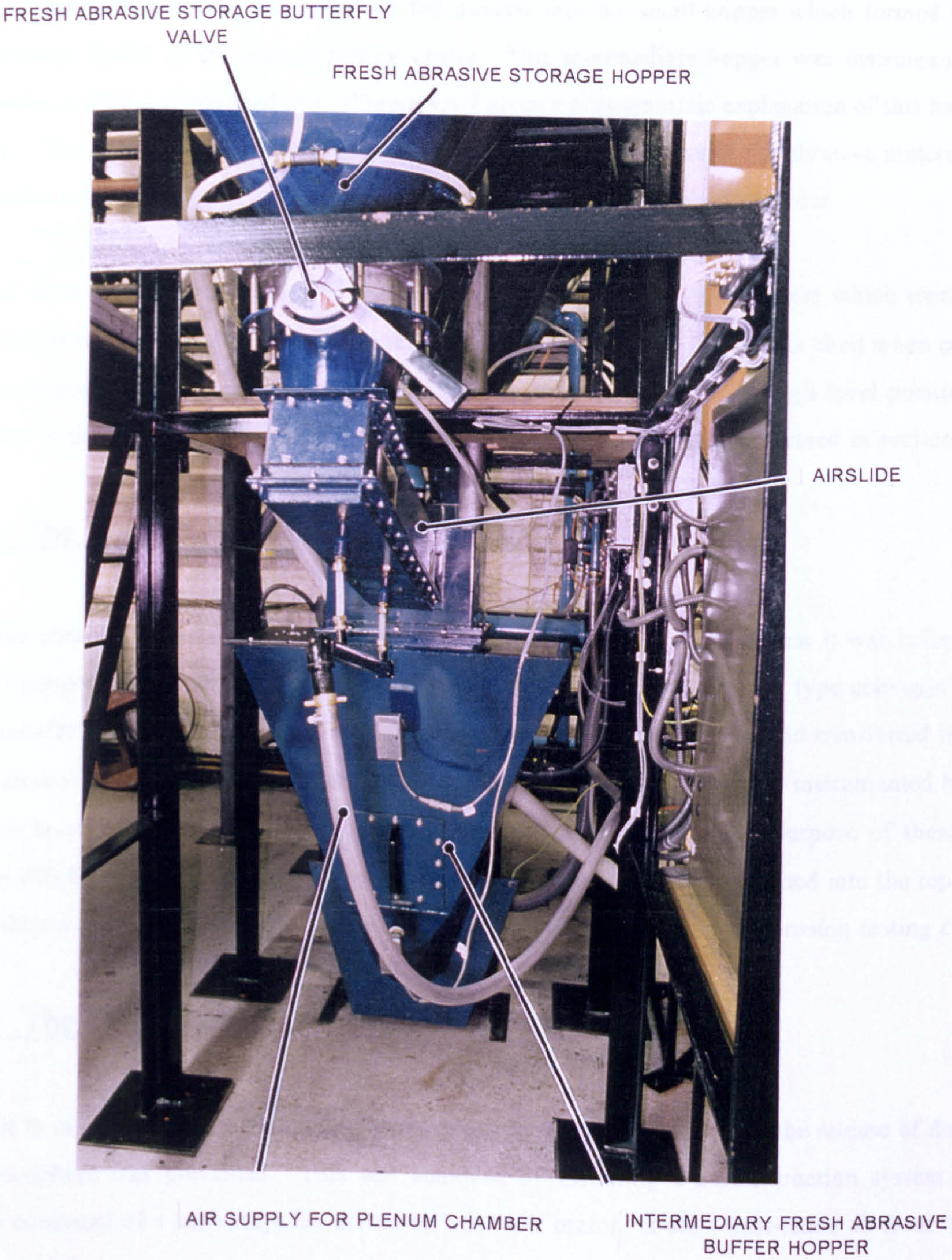

of olivine sand per minute. The destination of the abrasive material conveyed by this device was another intermediate storage hopper which fed directly into the small hopper which formed part of the vibratory feeder of the erosion testing centre. This intermediate hopper was instrumented by suspending it from a single load cell. (Figure 4A.7 gives a diagrammatic explanation of this handling system). The output of the load cell was used to confirm the feed rate of the abrasive material into the erosion testing centre. The load cell output was connected to a chart recorder.

Both of these intermediate storage hoppers were instrumented with level sensors which worked on the principle of changing capacitance between an insulated probe and the hopper shell when covered and uncovered. The hoppers were fitted with two sensors each, one in the high level position and the other in the low level position. The purpose of these sensors will be discussed in section 4A.8.

4A.6 The Spent Abrasive Disposal System

Once the abrasive material had passed through the erosion testing centre system it was collected in a small hopper. This hopper fed via a sliding gate valve into a ribbon screw type conveyor of the type manufactured by Spiroflow Ltd. This conveyor took the used abrasive and transferred it to the spent abrasive storage hopper. The hopper used to catch the used abrasive was instrumented by high and low level level sensors of the capacitive type described above. The purpose of these level sensors will be described later in section 4A.8. A dust extraction point was fitted into the top of the spent abrasive capturing hopper to allow the extraction of the dust from the erosion testing centre.

4A.7 The Dust Extraction System

In order to maintain ambient air quality levels it was necessary to ensure that the release of dust into the atmosphere was prevented. This was achieved by installing a dust extraction system. This system consisted of a multistage fan driven by a 2.2 kW motor. It drew dust-laden air from the end of the airslide conveyors and the erosion testing centre through a cartridge filter system. The cartridge filter had a 2 m^2 area and the filtration velocity through the filter was designed to be 0.5 m/s. The filter was housed in a small hopper so that the disentrained dust particles could be contained. The filter was cleaned by reverse jet air pulsing. The air required for this was taken from the main laboratory air supply at 6 bar and released into the filter housing via a solenoid valve from a pressure vessel whose volume was 35 litres of air at ambient conditions (see Figure 4A.8).

Figure 4A.7 Schematic View of the Fresh Abrasive Handling System

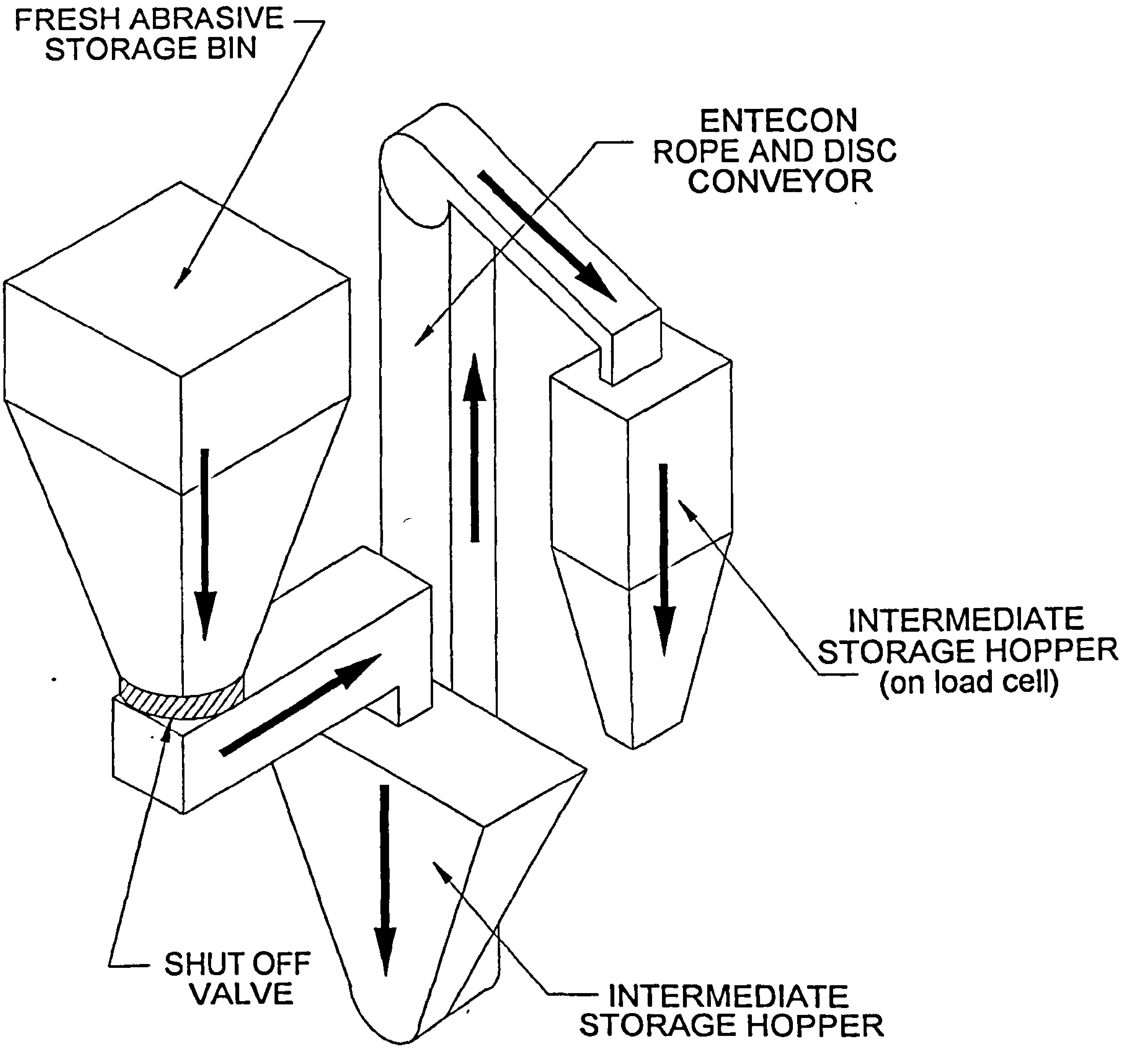

Figure 4A.8 Photograph of the Dust Extraction System

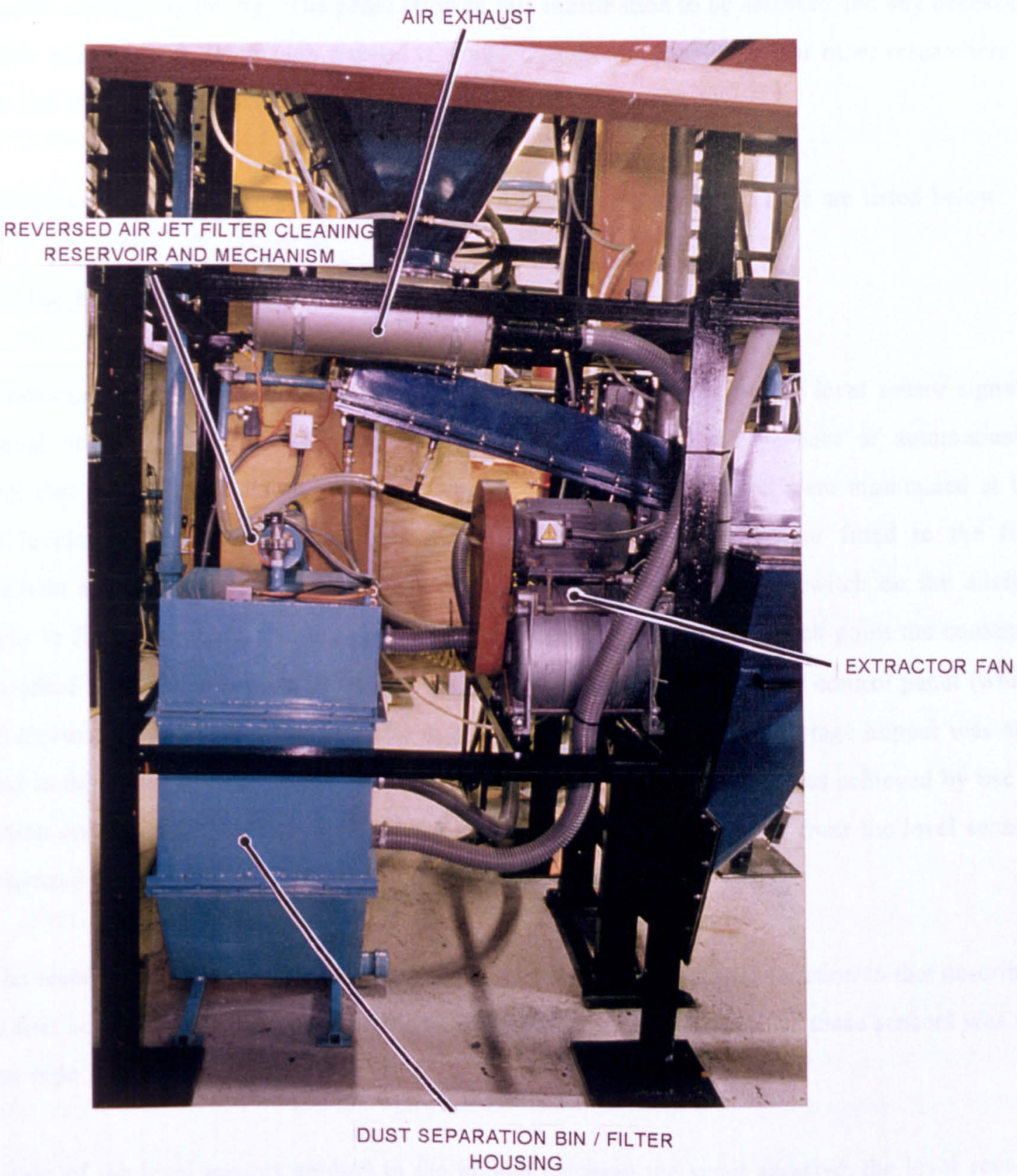

4A.8 The Control System

Provision of a combined mimic / control panel was felt to be important during the design of this test facility. Therefore the rig was fitted with a central control panel that mimicked the status of all of the systems comprising the rig. The panel allowed this information to be assessed and any necessary corrective action taken. With such a panel it would become relatively easy for other researchers to learn to use the equipment with the minimum of difficulty or instruction.

There were several elements involved in the control of this test facility. These are listed below:

4A.8.1 The Level Sensors Fitted to Various Hoppers

Either automatic, (i.e. filling of the hopper using conveyors controlled by the level sensor signals) or manual operation could be selected. The level sensors served the purpose of automatically ensuring that the materials stored in the hoppers to which they were fitted were maintained at the correct levels. When switched into automatic mode, the low level sensor fitted to the first intermediate storage hopper in the fresh abrasive feed system was used to switch on the airslide conveyor to fill the hopper up to the position of the high level sensor, at which point the conveyor was switched off. The operation of the airslide conveyor was controlled at the control panel (which will be discussed later in this section). The airslide that fed from the other storage hopper was also operated in this manner. The selection of which airslide was to be operated was achieved by use of a selection switch on the control panel. At all times indication of the signal from the level sensors were repeated on the mimic panel.

With the second intermediate storage hopper the level sensors had a similar function to that described for the first hopper of this kind. However, the conveyor that was activated by these sensors was the Entecon rope and disc conveyor.

In the case of the level sensors applied to the hopper catching the spent abrasive, the level sensors were to ensure that the transfer of used abrasive into more permanent storage was activated when required. Again the level sensor control of the level of material in the hopper could be implemented by switching the system into automatic control or, alternatively, manual control could be selected. If the automatic option was chosen the high level sensor, when tripped, would switch on the Spiroflow conveyor, emptying the contents of the hopper into the spent abrasive storage hopper.

The Spiroflow conveyor was switched off when level of abrasive in the bin dropped below the position of the low level sensor.

The status of each of the level sensors was mimicked on the control panel by the illumination of LEDs. The on / off status of each of the conveyors on the rig was also indicated on the control panel by LEDs.

All the hardware necessary to carry out these control functions were contained within the control panel case. The logic of these control functions was achieved by the extensive use of relays.

4A.8.2 Control of the Vibratory Feeder

The vibratory feeder controls were situated on the control panel. They consisted of a potentiometer which was used to select an amplitude setting for the vibration of the tray. This dictated the feed rate of material through the feeder. The calibration of the potentiometer to the actual mass feed rate of the feeder is discussed in Appendix 4C. Accompanying the amplitude selection potentiometer was the on / off switch for the feeder. This switch also incorporated the activation of the tray amplitude feedback loop, which used a hall effect transducer, or just allowed open loop control of the feeder. The feedback loop was activated when erosion tests were in progress. Its function was to prevent the level of the material within the feed hoppers above the vibratory feeder from affecting the throughput of the feeder as the test progressed. The on / off status of the vibratory feeder was shown on the control panel by LEDs.

4A.8.3 Control of the Dust Extraction System

Control of the dust extraction system was by two simple on / off switches. One operated the fan on the dust extraction system and the other was a push button switch which operated the reverse air jet filter cleaning by opening the solenoid valve provided for this purpose. There was an alarm signal generated for the dust control system. This was generated by sensing when a voltage was applied to the motor driving the fan and combining this with a signal generated from a pressure switch mounted on the dust extraction system casing. These two signals had their voltages regulated. They were then passed to a tri-colour LED on the control panel which indicated whether the dust extraction system was operating correctly or not. The use of such an LED enabled the source of any instrumentation faults to be traced.

4A.8.4 Control of the Erosion Testing Centre

The rotational velocity of the acceleration disc within the erosion testing centre was also controlled from the control panel. A potentiometer which operated directly on the inverter drive providing power to the motor was used to select the rotational velocity of the disc, and therefore the particle velocity. A count of the actual rpm of the disc was obtained from a vaned disc passing through a hall effect transducer. The vaned disc was attached to the bottom of the main spindle for the acceleration disc. The count acquired from this hall effect transducer was checked against a fixed frequency clock time pulse which was used to estimate when the velocity of the disc had exceeded 400 rpm. Once this set point was exceeded, the solenoid bolts on the access panel of the erosion testing centre casing were actuated so that the panel was effectively bolted in place. If the panel was missing an interrupt to the power supply operating the inverter drive occurred. This ensured that the inverter drive could not be made to work if this panel was missing. LEDs on the front of the control panel indicated whether the inverter drive was in operation and whether the panel was locked or not.

The simple on / off control of the motor that drove the target holder ring at 10 rpm was also controlled separately on the control panel. This was achieved by the use of a simple on / off toggle switch. LED indication of the status of this motor was also made on the control panel by using the status of the current being passed through the motor as an indication of its correct operation.

4A.8.5 Control of the Airslide Air Pressure

Since the airslides were operated from an air supply derived from a 6 bar pressurised air main in the laboratory, which was further reduced to below 1 bar by a regulator, it was necessary to ensure that the pressure did not exceed 1 bar. The reason this limit was imposed was that the 'Rotameter' that was used to control the air mass flow rate supplied to the airslides had a maximum pressure rating of 1 bar gauge due to its glass construction. Ensuring that this limit was complied with was achieved by two devices. The first of these was a simple mechanical pressure relief valve; however, valves of this type are not always reliable so a backup to this was included. This consisted of a pressure switch which was used to activate a 2" bore solenoid valve to shut the main air supply line to the rig if the air pressure rose above this limit. These limiting conditions were applied automatically and therefore did not appear on the front of the control panel.

4A.8.6 The Control / Mimic Panel

The control / mimic panel housed all of the switches and indicators necessary to ensure the correct operation of the test facility as a whole. Behind the panel all of the electrical hardware necessary to accomplish this operation was placed. This included all of the necessary PCB's, power supplies and relay logic required by the test facility.

The front panel of the control panel took the form of a colour coded schematic view of the test facility where all of the major components of the rig were displayed on the panel in sequential order with the appropriate mimic signal systems (see Figure 4A.9).

Also incorporated into the front of the control panel was a socket for the connection of the lead for the output of the load cell. The load cell weighed the contents of the second intermediate storage hopper in the fresh abrasive feed system. This lead was connected to a chart recorder to enable a continuous reading of the change in mass of the intermediate hopper with time to be obtained.

Figure 4A.9 Photograph of the Control / Mimic Panel

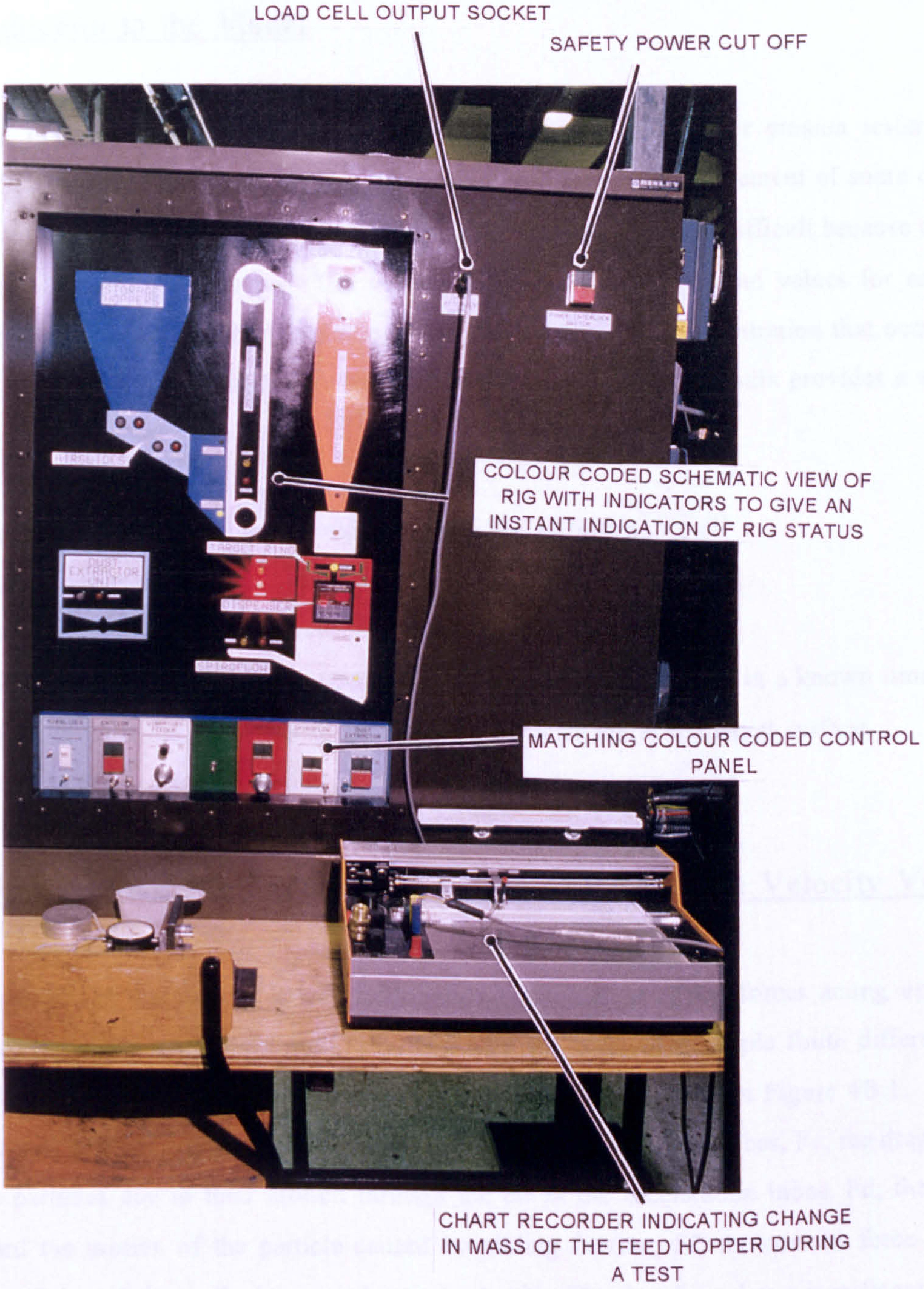

Appendix 4B: Modelling the Particle Dynamics Within the Rotating Disc Accelerator Erosion Tester

4B.1 Introduction to the Model

The modelling of the particle dynamics within the rotating disc accelerator erosion tester is a prerequisite of carrying out successful erosion tests using this device. Measurement of some of the variables that are important to the study of erosion by solid particle impact is difficult because of the design features of testers of this type. The variables that are difficult to find values for are the magnitude and direction of the particle velocity vector, and the particle concentration that occurs at the target surface. The model described in the following sections of this appendix provides a means of obtaining values for these variables.

This appendix is divided into five main sections. They are as follows:-

i) Evaluating the magnitude and direction of the particle velocity vector.
ii) Finding the angles of impingement that occur on the target surface.
iii) Calculating the mass of abrasive particles striking each target surface in a known time.
iv) Discovering what the behaviour of the abrasive particles are at the target surface.
v) A listing of the completed model.

4B.2 Evaluating the Magnitude and Direction of the Particle Velocity Vector

The model derived for this test work was based upon a summation of the forces acting upon an individual particle within the acceleration tube, and took the form of a simple finite differencing model. A schematic of the forces acting on an individual particle is given in Figure 4B.1. These forces include the centripetal force caused by the rotation of the acceleration tubes, Fc; the drag force acting on the particles due to their motion through the air in the acceleration tubes, Fd; the force acting to retard the motion of the particle caused by sliding friction, Ff; the coriolis force acting between the particle and the wall of the acceleration tube, N. This last force has a significant effect on the force of sliding friction.

Figure 4B.1. Schematic of the forces acting on a particle within the acceleration mechanism of the rotating disc accelerator.

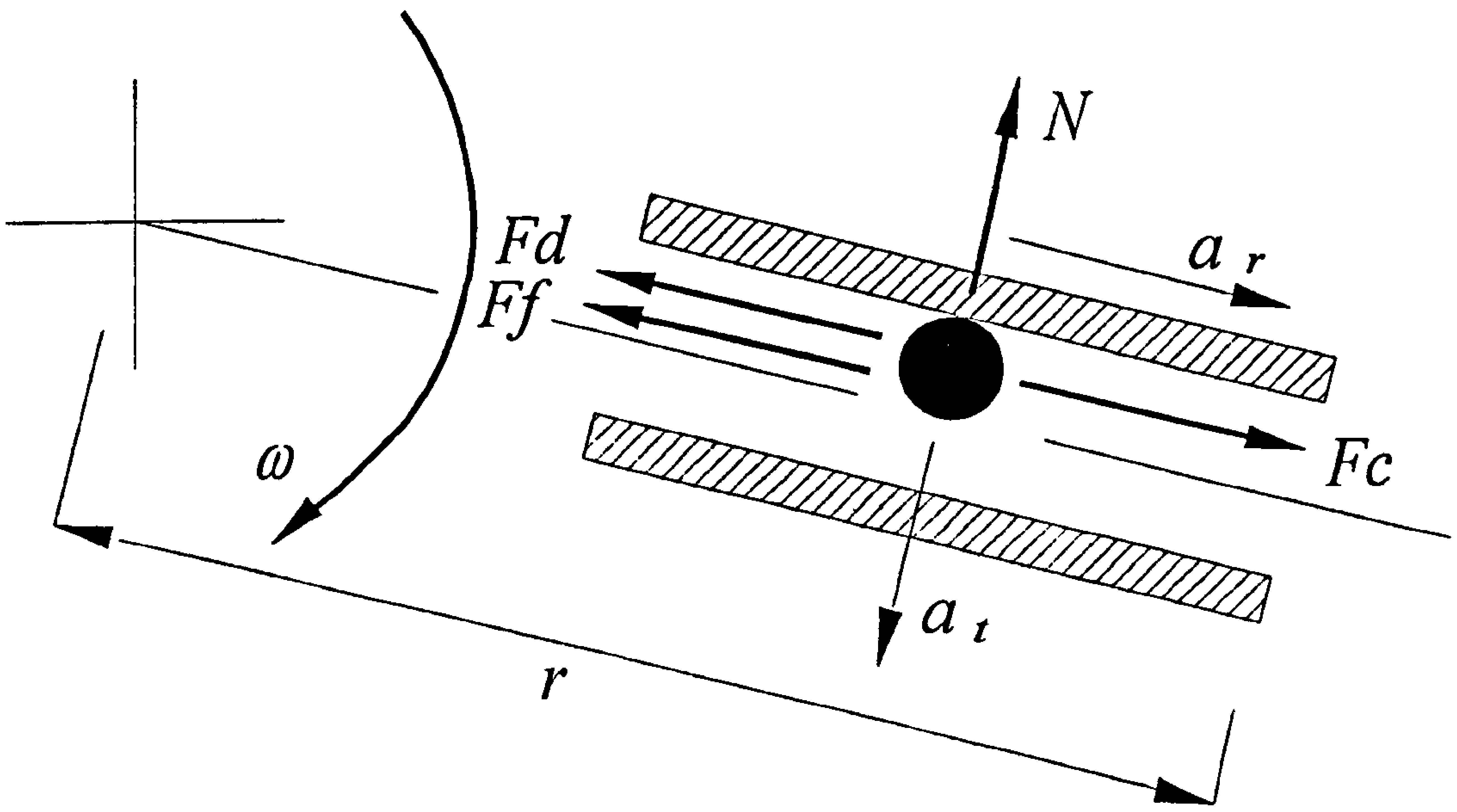
SCHEMATIC ILLUSTRATING THE FORCES ACTING ON A PARTICLE

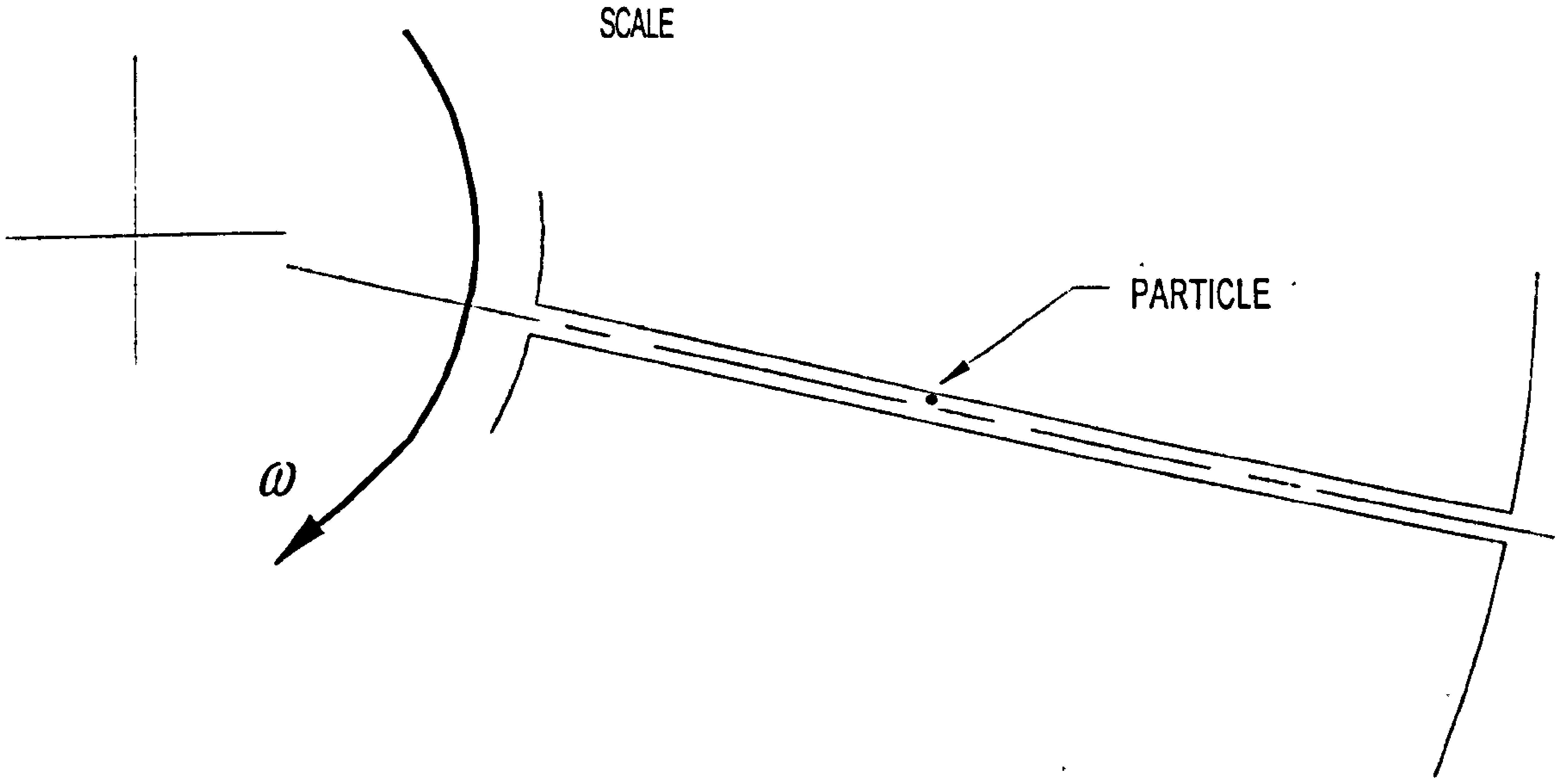
OUTLINE OF TUBE ARRANGEMENT TO SCALE

Several simplifications were made to the modelling process. These were as follows:-

- It was envisaged that the motion of the particle would induce movement in the gas surrounding it in the acceleration tubes. Since the force causing the motion of gas was the drag force between the particle and the gas, a value for the particle shape was required. To simplify the problem the particle was assumed to be a homogenous sphere. This was justifiable since the forces due to particle drag through the air were small in comparison to the other forces acting on the particle. Consequently, the inaccuracies introduced by taking the particles to be spheres when they are actually somewhat angular were minimal.
- Detailed work using the model has indicated that due to the particle concentrations which were simulated in this rig, the particles were a significant distance apart when they reached the end of the acceleration tubes. Therefore, the effects of interparticulate collisions between the particles travelling along the tubes could be discounted.
- A coefficient of friction was required to model the interaction between the particle and the wall of the acceleration tube. In the erosion tester used at The Wolfson Centre the acceleration tubes were made from fused alumina ceramic and the abrasive particles had a consistency similar to glass fragments. The particle size was also small. Considering the hardness of the materials involved and the small force pushing the particles into the surface of the tubes (this being the coriolis component of the acceleration multiplied by the particle mass) it was felt that the friction coefficient could be taken to be constant. To further support this assertion it was felt that the contact area between the particle and the tube surface would not change significantly due to material deformation. The value of the coefficient of friction selected was 0.2 [M14] which corresponds to the unlubricated coefficient of dynamic friction of glass on glass. It was felt that this value would not be too dissimilar from that expected for olivine sand particles sliding against alumina ceramic under very low normal loads.
- The abrasive material used in this test programme was not mono-sized. It was expected that particles of different sizes would tend to cause a range of particle velocities to occur. A decision was made to use the mean particle size to represent the velocity of the abrasive stream. By using various values of particle diameter in the model, it was confirmed that for a variety of particle sizes within the expected range for the chosen abrasive, that the effect on the particle velocity of a change in particle size was minimal.

In running the finite differencing model two conditions had to be satisfied before the velocity of the particle had converged to the final value. These were that the value of the radial position of the particle was greater than the actual radius of the rotating disc and that the pressure drop of the air within the tube was the same as the pressure rise caused by the motion of the particles. The reason for the second condition being applied was that whilst the particles are accelerated along the acceleration tubes one of the forces retarding their motion is that of the drag with the air in the tubes. Since the air acts to retard the particle motion owing to Newtons third law the air must move along the tubes. Only when the air pressure rise caused by the motion of the particles in the tubes is balanced with the pressure drop due to flow friction can the forces acting on both the particles and the air in the tubes be said to be in equilibrium. These requirements led to the model containing two loops.

The pressure loss within the acceleration tubes was calculated by using the Darcy equation for pressure drop in a pipe.

$$P_{loss} = \left(\frac{4\ ff\ L_t}{2\ R_t}\right)\left(\frac{\rho_a\ C_a^2}{2}\right) \quad \text{— Darcy eq}^n \quad \text{where}$$

$$\frac{1}{\sqrt{ff}} = 2.0\ \log\left(\frac{\varepsilon\ 2.0}{R_t\ 3.7} + \frac{2.52}{Re_t\ \sqrt{ff}}\right) \quad \text{— Colebrook - White eq}^n$$

$$\text{where} \quad Re_t = \left|\frac{C_a\ 2\ R_t}{\nu}\right|.$$

(4B.1)

where ff is the Moody friction factor which was solved using a form of the Colebrook-White equation [F6]; ε is the value of the pipe wall surface roughness; R_t is the radius of the acceleration tube bore; Re_t is the value of the Reynolds number for the air flowing in the acceleration tubes; C_a is the value of the air velocity in the acceleration tubes; ν is the value of the kinematic viscosity of the air; ρ_a is the density of the air and L_t is the length of the accelerating tubes.

The equations used to describe the particle motion within an acceleration tube were as follows:-

a) The tangential velocity component, V_t was given by the expression:-

$$V_t = \omega\ r_i \qquad \textbf{(4B.2)}$$

where ω is the rotational velocity of the acceleration disc in radians per second and r_i is the previously calculated value of the radial distance travelled by the particle.

b) The force component normal to the axis of the acceleration tube, N was given by:-

$$N = M_p\ A_t \qquad \textbf{(4B.3)}$$

where M_p is the mass of the particle and A_t is the previously calculated value of the tangential acceleration component.

c) The relative velocity between the particle and the air, C_{rel} was calculated by:-

$$C_{rel} = V_r - C_a \tag{4B.4}$$

where V_r is the previously calculated value of the radial velocity component of the particle and C_a is the value of the air velocity in the acceleration tubes.

d) The Reynolds number for the flow of air over the particle, Re_p was calculated as follows:-

$$Re_p = \left| \frac{C_{rel}\ 2\ R_p}{v} \right| \tag{4B.5}$$

where R_p is the radius of the particle.

e) The drag coefficient for the particle, C_d, was found using the following expression which was derived from empirical curve fitting to the curve of values of drag coefficient for a sphere plotted against Reynold's number (Schiller and Nauman, 1933 [C1,M12]):-

$$C_{d_i} = \frac{24}{Re_{pi}^{0.646}} \qquad C_{d_i} \geq 0.5 \text{ for all values.} \tag{4B.6}$$

f) The drag force acting on the particle because of the presence of the air, F_{drag}, had a value as follows:-

$$F_{drag} = C_d\ A_p \left(\frac{\rho_a\ (C_{rel_i})^2}{2} \right) \tag{4B.7}$$

where A_p is the projected area of the particle on a plane normal to the relative velocity between the air and the particle.

g) The force balance in the radial direction, F_{rd}, consisted of three terms. The first term on the right hand side of this expression is the centripetal force acting on the particle; the second is the retarding sliding friction force and the third term is the drag force acting between the particles and the air (see Figure 4B.1). F_{rd} was calculated using the following expression:-

$$F_{rd} = M_p\ r_i\ \omega^2 - \mu\ N_i - F_{drag_i} \tag{4B.8}$$

where μ is the value of the sliding coefficient of friction.

h) The value of the radial acceleration component, A_r was found using Newtons second law to be:-

$$A_{r_i} = \frac{F_{rd_i}}{M_p} \qquad \textbf{(4B.9)}$$

i) The new value of the radial velocity of the particle, V_r was found using the following expression:-

$$V_{r_{i+1}} = V_{r_i} + A_{r_i}\,\Delta t \qquad \textbf{(4B.10)}$$

where Δt is the fixed time increment used in the finite differencing time stepping routine.

j) The increment in the radial position of the particle in the last time step, ΔR was calculated as follows:-

$$\Delta R = V_{r_i}\,\Delta t \qquad \textbf{(4B.11)}$$

k) The value of the radial distance of the particle from the centre of the accelerating disc, r, was updated using:-

$$r_{i+1} = r_i + \Delta R_i \qquad \textbf{(4B.12)}$$

This expression was valid until the radial position of the particle exceeded the radius of the accelerating disc.

l) The increment in the tangential velocity due to the particle travelling a distance of ΔR, ΔV_t was calculated using the following expression:-

$$\Delta V_{t_i} = \Delta R_i\,\omega \qquad \textbf{(4B.13)}$$

m) The new value of the tangential component of acceleration (Coriolis acceleration component), A_t was found using the standard equation for the Coriolis component of acceleration:-

$$A_{t_i} = 2\,\omega\,V_{t_i} \qquad \textbf{(4B.14)}$$

n) The value of the force applied to the air in the small volume of the acceleration tube through which the particles passed during the last increment of time being considered, F_{ae}, was calculated using:-

$$F_{ae_{i+1}} = F_{drag_i}\,N_p \qquad \textbf{(4B.15)}$$

where N_p is the number of particles moving through the acceleration tube per time step of the finite differencing routine. The value of N_p is calculated from the mass flow rate of the abrasive material being passed through the acceleration disc by the vibratory feeder.

o) A cumulative total of the force applied to the air within the acceleration tubes during each time increment via the particle drag force, F_a, was calculated using the following expression:-

$$F_{a_{t+1}} = F_{a_t} + F_{ae_t} \tag{4B.16}$$

This equation was formed on the basis of the particles always travelling faster than the air, since the particle motion effectively drags the air through the acceleration tubes. It could be argued that at the entrance to the acceleration tubes the air velocity is greater than the particle velocity. However, within very few time increments this position is changed. The error induced in the model by this assertion was therefore felt to be minimal, and considering the number of other possible sources of error in the model, it was discounted.

These equations were solved in turn for increments of time until the radial position of the particle exceeded the radius of the acceleration disc. The other convergence criterion, that of the balance in pressure loss in the acceleration tube compared to the pressure rise caused by the particle motion, was met by manually adjusting the value of the air velocity in the tubes. Once both of these convergence criteria had been satisfied the iterative calculations were stopped and the actual exit velocity vector was calculated. A value of the rotational velocity of the disc was taken at the beginning of the model. Since the disc radius was a fixed value the tangential component of velocity of the disc, and consequently of a particle as it exits the disc, was easily calculated. The model calculated the corresponding value of the radial particle velocity. Using the vector triangle of velocity, the resultant velocity vector can be calculated as follows:-

$$\begin{gathered} V_{res} = \sqrt{\left(V_{r_{final}}\right)^2 + \left(V_{t_{final}}\right)^2} \\ \kappa = \arctan\left(\frac{V_{r_{final}}}{V_{t_{final}}}\right) \end{gathered} \tag{4B.17}$$

where κ is the angle between the velocity vector and the tangent to the acceleration disc at the acceleration tube nozzle (see Figure 4B.2).

4B.3 Finding the Angles of Impingement that Occur on the Target Surface

Owing to the finite width of the targets, the angle of impingement with which the particles struck the target surface varied with position across the target face. The reasons for this were purely geometrical. Since the full spectrum of impingement angles, in 5° increments, was needed for the test work contained within this thesis, the calculations required were performed for impingement

Figure 4B.2 Schematic view of the particle velocity vector at exit from the acceleration disc.

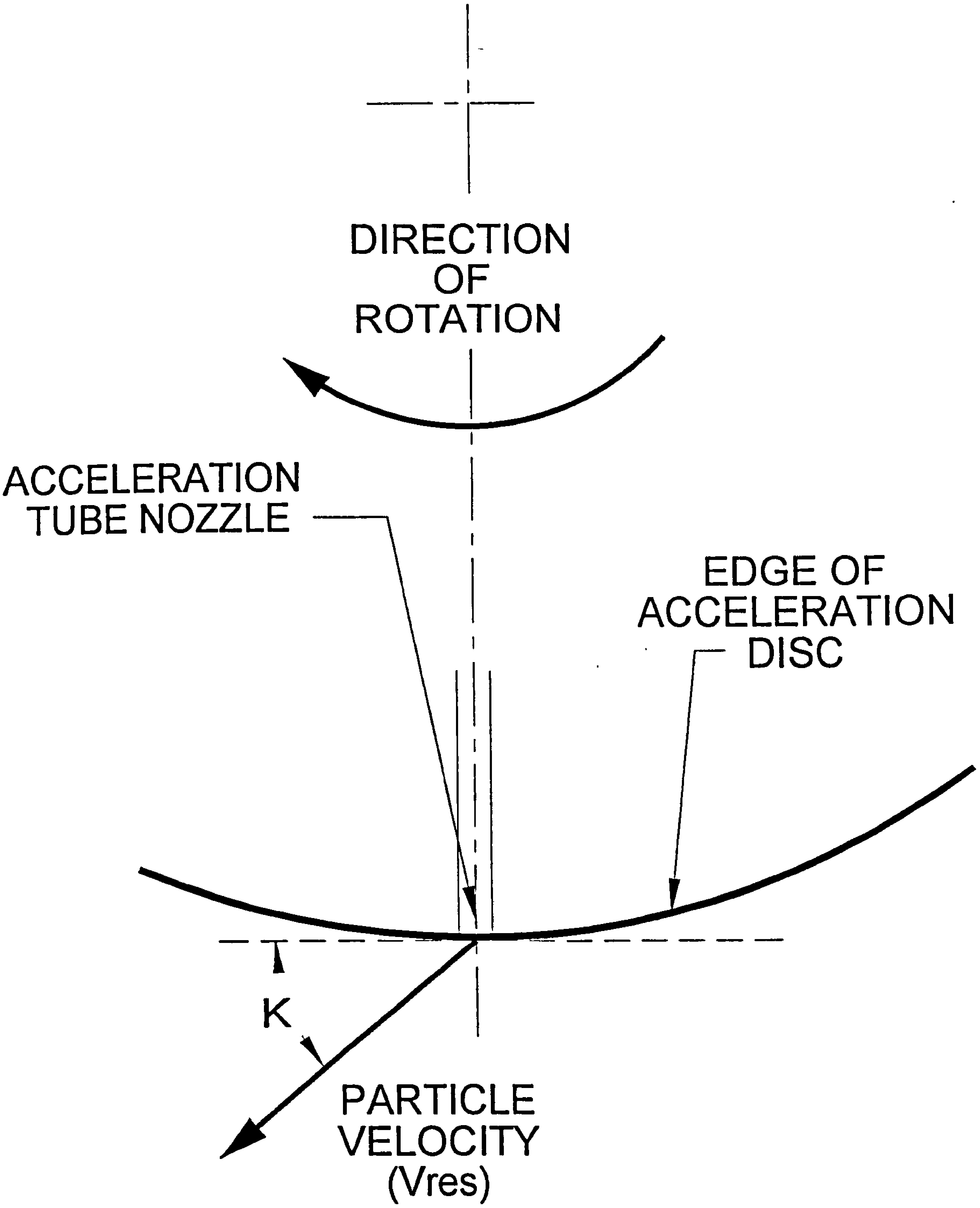

angles between 5° and 90°. Figure 4B.3 illustrates the geometry of the impacts at the centre of rotation of a target and its edges. From this geometrical consideration of a similar system, the following equations were derived by Söderberg *et al.* [S8]. These equations were also used in this model.

The impact angle of the abrasive particles at the target centre (see Figure 4B.3) was obtained by applying the sine rule to the triangle OCP_2 to find the angle β, which was then subtracted from the angle α, the target holder orientation angle, to give the impact angle, γ. The equation which gave the impact angle at the target centre was therefore:-

$$\gamma = \alpha - \arcsin\left[\frac{L_t \sin\left(\frac{\pi}{2} + \kappa\right)}{L_t + x_d}\right]. \qquad \textbf{(4B.18)}$$

where x_d is the distance between the periphery of the rotating disc and the centre of the targets. The impact angle that occurs at the edges of the targets was more difficult to determine. This was because the edges of the targets were protected during tests using holder side plates which hook around the front edges of the target (see Figure 4.1 Chapter 4). The edge of the target labelled B in Figure 4B.3 above was therefore shielded to a certain extent. The equation that was used to derive the distance x_b needed to be modified to account for this fact, before the true impact angle at this edge could be calculated. Owing to the construction of the target holders the side protectors extended 1 mm in front of the target surface. The length of the target which was shielded was therefore found using (see Figure 4B.4):-

$$bb = a - \left|\frac{0.001}{\tan(\gamma)}\right| \qquad \textbf{(4B.19)}$$

Hence the distances x_b and x_a could be written as follows:-

$$\begin{aligned} x_b &= L_t + \sqrt{\left[\,(L_t + x_d)^2 + (bb)^2\,\right] + 2\,bb\,(L_t + x_d)\cos(\alpha)} \\ x_a &= L_t + \sqrt{\left[\,(L_t + x_d)^2 + (a)^2\,\right] - 2\,a\,(L_t + x_d)\cos(\alpha)} \end{aligned} \qquad \textbf{(4B.20)}$$

where a is half the target face width (see Figure 4B.3). The angle β was then found using the values for x_a and x_b for the two target edges A and B.

4B.3 Geometry of particle impacts on the target surface.

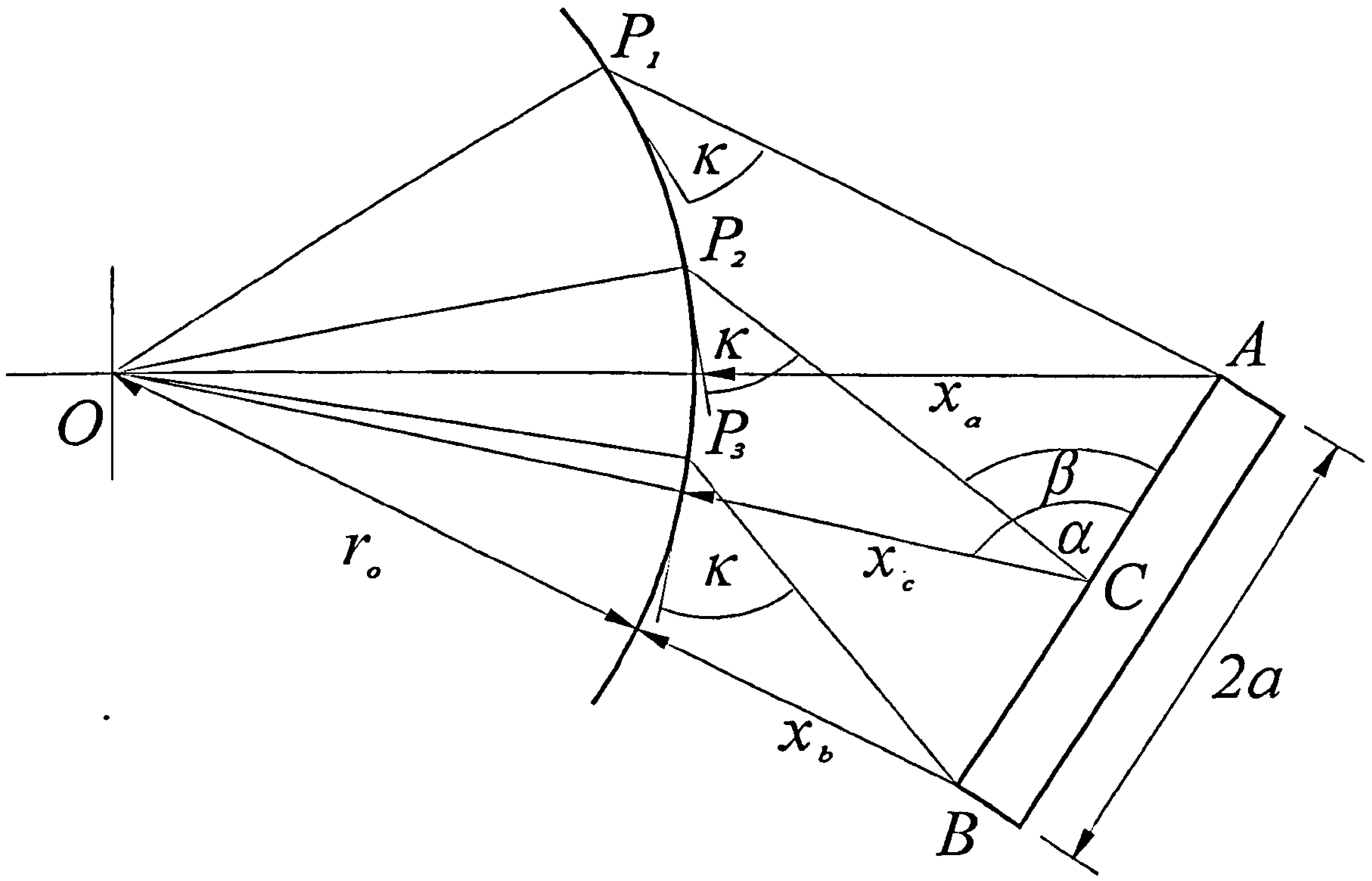

4B.4 Shielding of the target from particle impacts by the edge protector.

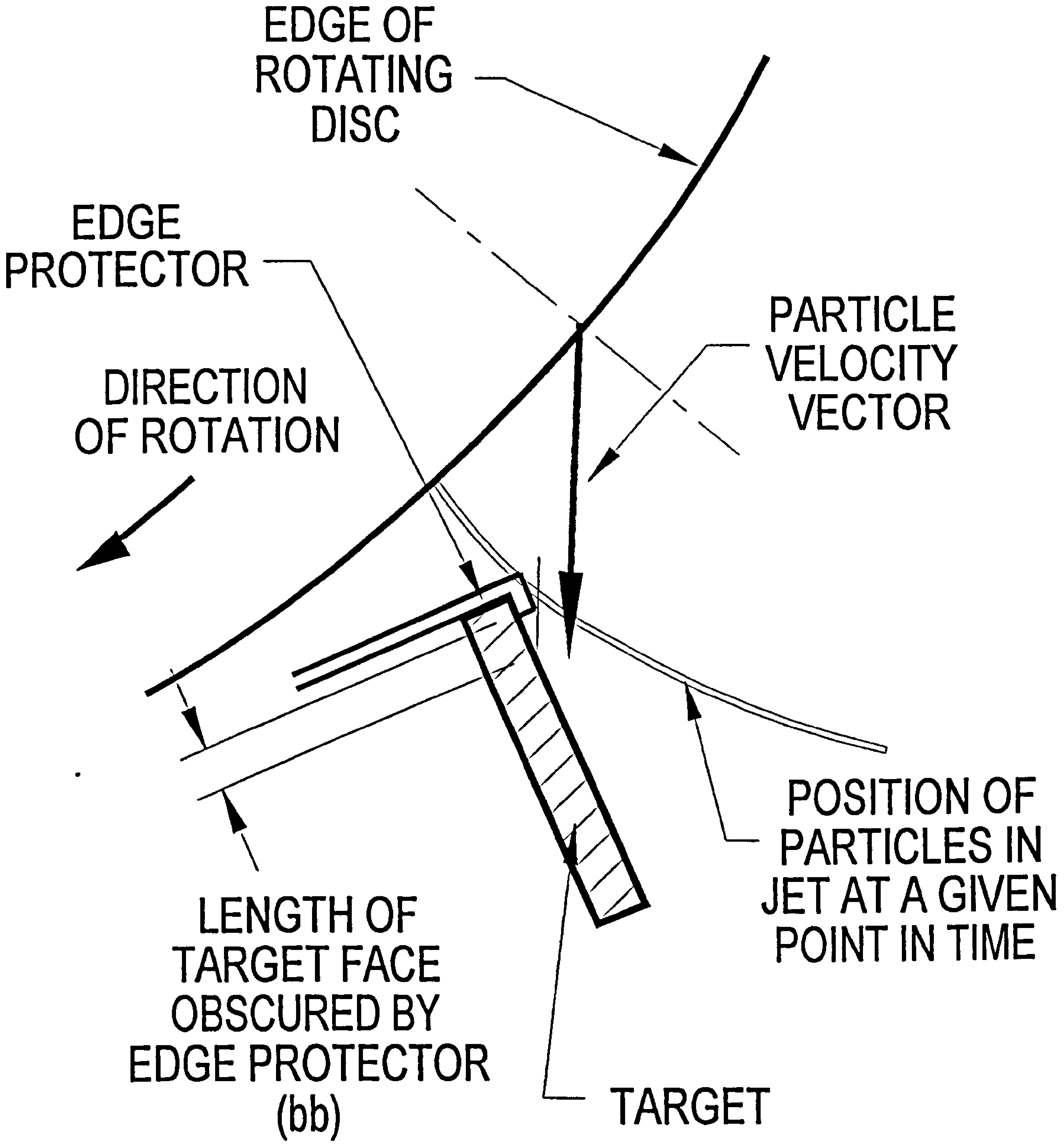

$$\beta_a = \arcsin\left[\frac{L_t \sin\left(\frac{\pi}{2} + \kappa\right)}{L_t + x_a}\right]$$

$$\beta_b = \arcsin\left[\frac{L_t \sin\left(\frac{\pi}{2} + \kappa\right)}{L_t + x_b}\right] \qquad \textbf{(4B.21)}$$

The angles of impingement at the edges of the target surface could be calculated using the following equations:-

$$\gamma_a = \alpha - \arcsin\left(\frac{a}{L_t + x_d}\right)\sin(\alpha) - \beta_a$$

$$\gamma_b = \alpha - \arcsin\left(\frac{bb}{L_t + x_d}\right)\sin(\alpha) - \beta_b. \qquad \textbf{(4B.22)}$$

4B.4 Calculating the Mass of Abrasive Particles Striking Each Target Surface

The mass of abrasive particles that strikes the target surface depends on the flow rate of the material into the erosion tester. To account for this in the model, the calibration results obtained for the vibratory feeder (as shown in section 4.1.4.2. Chapter 4) were included in the model. The model was used to calculate a value for the potentiometer set point from this data, to give the particle concentration required.

The mass of abrasive that struck the target surfaces varied according to the orientation of the target surface to the flow of particles. The geometry of the system indicates that the variation of the impact angle across the face of the target divided by 360° was equivalent to the proportion of a full circle around the disc occupied by the target. The mass flow rate of the abrasive particles into the erosion tester was used to produce a figure for the mass flow rate per acceleration tube per revolution. The mass of abrasive striking each target per minute was calculated as follows:-

$$M'_{target} = \frac{\Delta\gamma}{360}\,\frac{M_{fr}}{T_{num}\,\omega}\,2\,\pi\,N_r \qquad \text{where} \qquad \Delta\gamma = \left|\gamma_a - \gamma_b\right|.$$

(4B.23)

where M_{fr} is the total abrasive mass flow rate being fed into the erosion tester; T_{num} is the number of acceleration tubes in the rotating disc and N_r is the rotational speed of the disc in rpm.

4B.5 Calculating the Intensity of Abrasive Particle Impacts on the Target Surface

The importance of the intensity of impacts in the region of an eroding surface to the amount of damage inflicted has been highlighted by several researchers [K9,B13,K8,S11,A2,A5]. Numerous methods have been proposed to account for these effects. Some of these methods are incorporated into the numerical model described in this appendix.

McClusky [M10] showed the likely dispersion of particle jets being injected into gas flows by carrying out particle image velocimetry measurement of the emerging abrasive jet. Extrapolation from data presented in the work by McClusky for the divergence of a plume of particles emitted into a flowing air stream from a nozzle, by carrying out elementary curve fitting, has yielded the following equation (see Figure 4B.5):

$$R_j = \left(3.92.10^{-3}\ V_{res} + 0.075 \right) x_d + r \tag{4B.24}$$

Where R_j is the radius of the jet in m, V_{res} is the average particle velocity in m/s, x_d is the distance from the nozzle to the target in m, and r is the radius of the acceleration tube bore in m. This equation was utilised as an estimate since the test data on which it was derived was found as part of some tests carried out at 12.5 m/s and a particle concentration of only 4 kg/m^3. The data for jet dispersion at 25 and 35 m/s with the accompanying suggested particle concentrations was not available at the time of testing. However, the use of this equation enabled an estimate of the jet dispersion to be undertaken to an accuracy of ±15% on average as can be seen from the results shown in Appendix 4C, which describes the calibration of the rig. This was considered to be good enough for the purposes of this work.

This equation was then used in the calculation of the spread of the jet of particles at each of the edges of the target. Combining the calculation of the actual length of the target suffering erosive damage (i.e. the target face length (2a - see Figure 4B.3) less the shielded length) with the spread of the particle jet at the target edges was used to give the area of the target being eroded. Once the area undergoing erosion was calculated it was possible to calculate a mean value of the particle mass flux with time on the target surface using the following equation:-

$$M_{flux} = \frac{M'_{target}}{A_{eroded}} \tag{4B.25}$$

Figure 4B.5 Graph showing the extrapolation from data presented by McClusky [M10] for particle jet divergence.

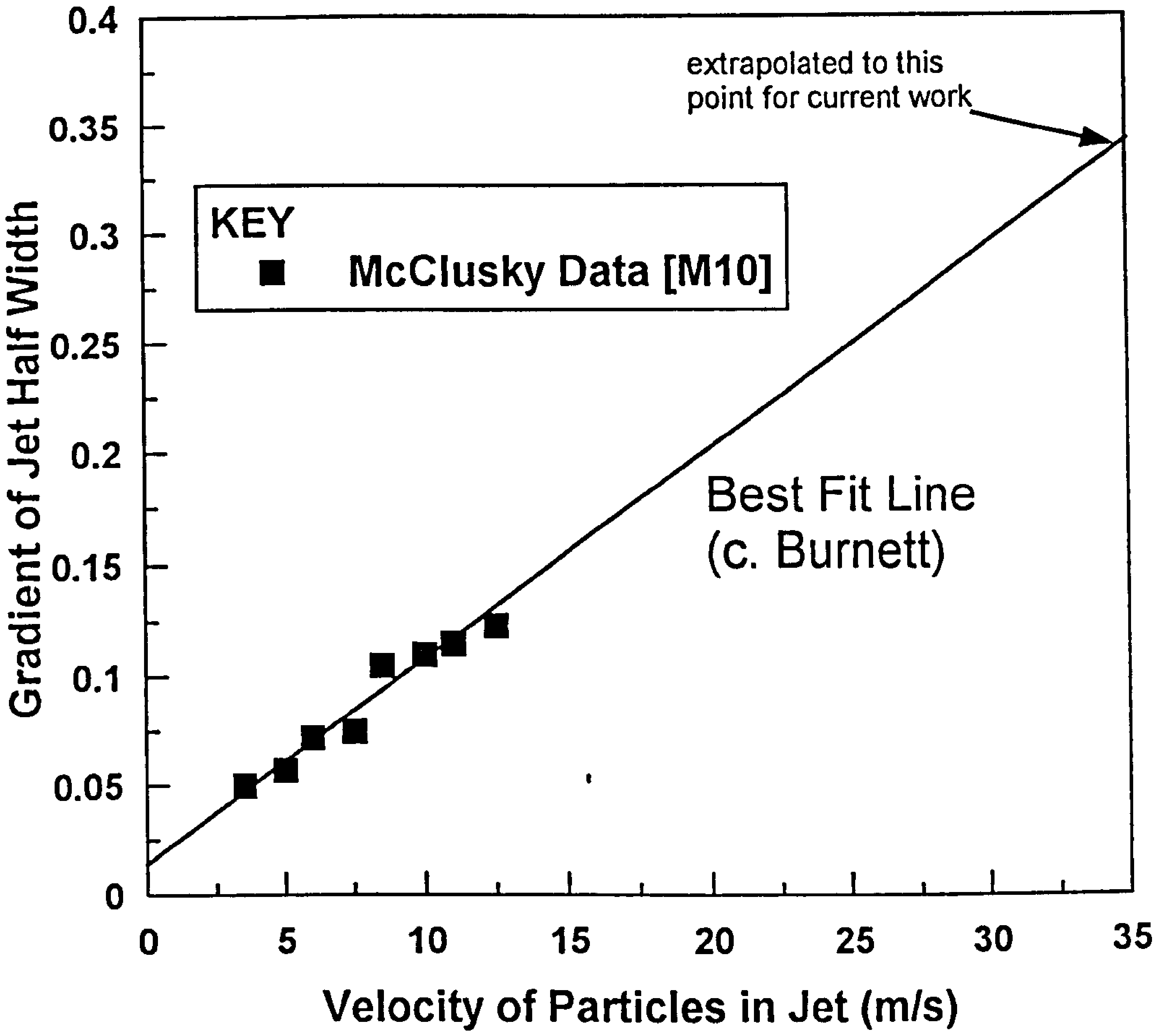

where M_{flux} is the particle mass flux; M'_{target} is the mass of abrasive striking the target surface per unit time and A_{eroded} is the actual area suffering erosion damage. It is important to note that this is the particle mass flux based upon the area of the target which is not necessarily normal to the flow of the particles. It is extremely important to appreciate that this is different from the usual definition of a particle mass flux which is calculated normal to the flow.

Further to this value of the particle mass flux, an instantaneous particle mass flux can also be calculated as suggested by Kleis *et al.* [K9]. These calculations are based on finding the mass of abrasive striking the target surface per traverse of an acceleration tube nozzle, the area of the target affected by erosion damage, and the period of time over which this event takes place. The mass of abrasive striking the target surface per cycle, M_{cycle} is found by using:-

$$M_{cycle} = \frac{M'_{target}}{N_r \, T_{num}} \tag{4B.26}$$

The length of the perimeter of the circle, where the circumference is placed on the target pivot points, occupied by the target face, ls is calculated as follows:-

$$ls = \frac{\Delta\gamma}{360} \, 2.0 \, \pi \, (x_d + L_t) \tag{4B.27}$$

The time taken for the acceleration tube nozzle to pass over the target, T_{cycle} is given by the following expression:-

$$T_{cycle} = \frac{ls}{\omega \, L_t} \tag{4B.28}$$

The instantaneous mass flux, M_{fi} can then be found:-

$$M_{fi} = \frac{M_{cycle}}{A_{eroded} \, T_{cycle}} \tag{4B.29}$$

The mean particle mass flux with time was manipulated to give an indication of the actual physical spread of the particles in the region of the eroding area of the target. This was carried out to give a more easily understood idea of the physical spacing of the particles as they strike the target area than that presented for any figure for the particle mass flux. This method was originally proposed by Shipway *et al.* [S11], and relies upon taking the spread of particles to be homogenous in order to simplify the calculations required. Non-dimensional spacing of the particle, i.e. particle spacing expressed in terms of particle diameters, was simply found by reducing an expression for the mean particle mass flux with time to a non-dimensional value by using existing fixed variables. The expression used to achieve this was as follows:-

$$L_{bp} = \left(\frac{M_p \, V_{res}}{M_{flux}} \right)^{\frac{1}{3}} \frac{1}{R_p} \qquad \textbf{(4B.30)}$$

The equations 4B.1 to 4B.30 are incorporated into a numerical model coded in MathCad syntax. Section 4B.6 of this appendix contains a listing of this programme.

4B.6 MathCad Listing of the Model

The example of the MathCad listing shown in this section, contains all of the input data necessary, to carry out the calculations necessary for a situation where the desired particle velocity is 25 m/s and the suspension density is 4 kg/m^3. The listing begins on the following page.

Finite Differencing Modelling of the Particle Dynamics in the 'Rotating Disc Accelerator' Erosion Tester

The purpose of this programme is to simulate the conditions of particle velocity, concentration & particle / wall material orientation that occur in a rotating disc accelerator type erosion tester. The variables just mentioned will be the primary output given by this programme.

Definition of the Major Input Variables:-

$V_{air} := 25.3 \cdot \frac{m}{sec}$ $N_r := 1605$ (N is in rpm). $C_a := 4.87 \cdot \frac{m}{sec}$ (This variable needs to be manually adjusted to ensure that convergence to a solution occurs).

$\rho_{ph} := 4.0 \cdot \frac{kg}{m^3}$ $R_p := 161.9 \cdot 10^{-6} \cdot m$ $\rho_s := 3287.2 \cdot \frac{kg}{m^3}$

Definition of the Fixed Variables:-

$\mu := 0.2$ $\Delta t := 0.0001 \cdot sec$ $x_d := 0.0225 \cdot m$ $\nu := 0.000015 \cdot \frac{m^2}{sec}$ $f := 0.1$

NB; aa & ab denote the distance from the pivot of each target to the targets edges.

$aa := 0.006 \cdot m$ $ab := 0.017 \cdot m$ $d_{pipe} := 0.0547 \cdot m$ $\rho_a := 1.19 \cdot \frac{kg}{m^3}$

$L_t := 0.1205 \cdot m$ $T_{num} := 6.0$ $R_t := 0.0013 \cdot m$

$\Delta g := 3.91484 \cdot 10^{-3} \cdot V_{air} \cdot \frac{sec}{m} + 0.075$ $R_i := \Delta g \cdot x_d + R_t$ $R_i = 0.0052 \cdot m$

NB. Delta g was derived empirically from data presented by McClusky [M10]

Calculations follow:-

The area of the pneumatic conveyor pipe system cross-section to be simulated is:

$A_{pipe} := \frac{\pi \cdot d_{pipe}^{\,2}}{4}$ $A_{pipe} = 0.00235 \cdot m^2$

The rotational frequency of the spinning disc is determined in rad/sec:-

$\omega := \frac{N_r \cdot 2.0 \cdot \pi}{60.0} \cdot sec^{-1}$ $\omega = 168.0752 \cdot sec^{-1}$

The area of the dispensing tubes in the disc is determined:-

$A_b := \pi \cdot R_t^{\,2}$ $A_b = 5.3093 \cdot 10^{-6} \cdot m^2$

The calculation of the solids mass flow rate is carried out:-

$M_{fr} := \rho_{ph} \cdot \left(R_i \cdot 0.6\right)^2 \cdot \pi \cdot T_{num} \cdot V_{air}$ $M_{fr} = 0.018684 \cdot kg \cdot sec^{-1}$

NOTE: Alteration made to account for the effects of the particle velocity distribution within the jet.

$M_{frhr} := M_{fr}$ $M_{frhr} = 67.2613 \cdot \frac{kg}{hr}$

Reading in the Vibratory Feeder Calibration Information:

$D := READPRN(data)$

$x := D^{<0>}$ $y2 := D^{<2>} \cdot \frac{kg}{sec}$ $y4 := D^{<4>} \cdot \frac{kg}{sec}$

$y1 := D^{<1>} \cdot \frac{kg}{sec}$ $y3 := D^{<3>} \cdot \frac{kg}{sec}$ $y5 := D^{<5>} \cdot \frac{kg}{sec}$

The data file is read in and split into its constituent vectors. These are then manipulated to produce the required graphical information for setting of the vibratory feeder.

$$D = \begin{bmatrix} 2 & 0.0013 & 0.0012 & 0.0011 & 0.0012 & 0.0013 \\ 3 & 0.0067 & 0.0066 & 0.0066 & 0.0066 & 0.0068 \\ 4 & 0.0173 & 0.0167 & 0.0171 & 0.0168 & 0.0171 \\ 5 & 0.0249 & 0.0253 & 0.0248 & 0.025 & 0.0256 \\ 6 & 0.0369 & 0.0367 & 0.0361 & 0.036 & 0.0361 \\ 7 & 0.0517 & 0.0519 & 0.0514 & 0.0515 & 0.0517 \\ 8 & 0.07 & 0.0697 & 0.0711 & 0.0692 & 0.0705 \\ 9 & 0.0897 & 0.0901 & 0.0891 & 0.0898 & 0.0895 \\ 10 & 0.1066 & 0.1061 & 0.105 & 0.1063 & 0.1058 \end{bmatrix}$$

A vector of the average values of the mass flow rate data is created.

$k := 0, 1 .. (\mathrm{rows}(D) - 1)$ $\qquad y_a := \dfrac{y1 + y2 + y3 + y4 + y5}{(\mathrm{cols}(D) - 1)}$

Creating a matrix of the values of the mass flow rates so that sorting of the maximum and minimum values at each setting of the control panel dial can be achieved.

$A_a := \mathrm{augment}(\mathrm{augment}(\mathrm{augment}(\mathrm{augment}(y1, y2), y3), y4), y5)$ $\qquad A_{at} := A_a^{T}$

This matrix is split into its component groups of mass flow rate readings;

$E1 := A_{at}^{<0>}$ $\quad E2 := A_{at}^{<1>}$ $\quad E3 := A_{at}^{<2>}$ $\quad E4 := A_{at}^{<3>}$ $\quad E5 := A_{at}^{<4>}$

$E6 := A_{at}^{<5>}$ $\quad E7 := A_{at}^{<6>}$ $\quad E8 := A_{at}^{<7>}$ $\quad E9 := A_{at}^{<8>}$

The maximum and minimum values of each grouping of mass flow rate readings are determined;

$$A_{max} := \begin{bmatrix} \max(E1) \\ \max(E2) \\ \max(E3) \\ \max(E4) \\ \max(E5) \\ \max(E6) \\ \max(E7) \\ \max(E8) \\ \max(E9) \end{bmatrix} \qquad A_{min} := \begin{bmatrix} \min(E1) \\ \min(E2) \\ \min(E3) \\ \min(E4) \\ \min(E5) \\ \min(E6) \\ \min(E7) \\ \min(E8) \\ \min(E9) \end{bmatrix}$$

NB The x values are dial readings and the y_a values are values of the average mass flow rate for the required suspension density.

Graph of the Average Mass Flow Rate of Abrasive Verses Potentiometer Setting.

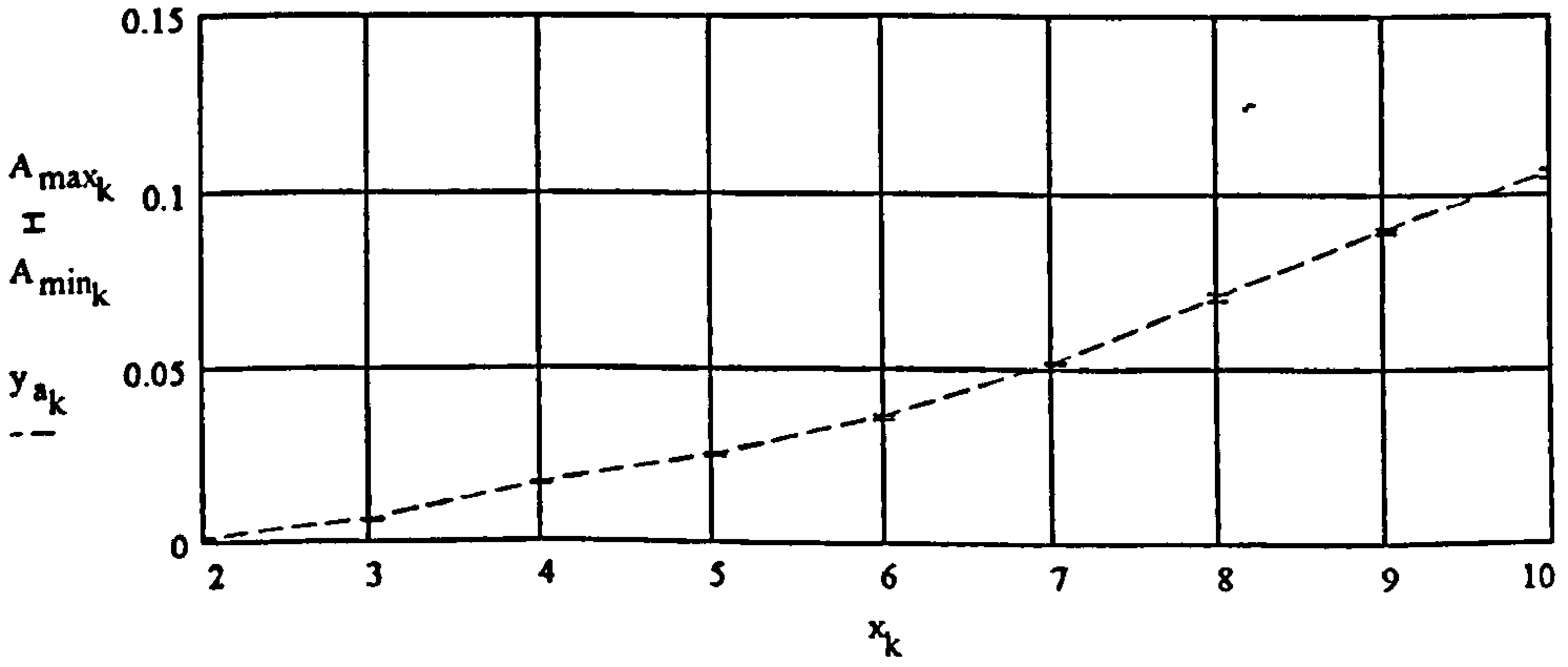

Interpolation can now be carried out to provide Erosion Rig Set Point Values:

The MathCad linear interpolation function is now used to determine the set point required on the control panel dial for the vibratory feeder;

$xx_k := y_{a_k}$ $\quad vy_k := x_k$ $\quad Vib_{sp} := \mathrm{linterp}(xx, vy, M_{fr})$ $\quad Vib_{sp} = 4.2074$

$Vib_{sp} = 4.21$ corresponds to a mass flow rate of $M_{fr} = 0.0187 \cdot kg \cdot sec^{-1}$

which will simulate approximately (check load cell output) a suspension density of $\rho_{ph} = 4 \cdot kg \cdot m^{-3}$

This mass flow rate correponds to an hourly mass flow rate of $M_{fr} = 67.3 \cdot \frac{kg}{hr}$

RETURNING TO THE CALCULATIONS NECESSARY FOR THE FINITE DIFFERENCING MODEL:-

The frontal area of the particle is determined as follows since the particle is assumed to be a sphere:-

$A_p := \pi \cdot R_p^{\,2}$ $\qquad A_p = 8.2346 \cdot 10^{-8} \cdot m^2$

The volume of the particle is calculated based upon the assumption that the particle is taken to be a perfect sphere:-

$Vol_p := \frac{4}{3} \cdot \pi \cdot R_p^{\,3}$ $\qquad Vol_p = 1.7776 \cdot 10^{-11} \cdot m^3$

The mass of each particle is as follows:-

$M_p := Vol_p \cdot \rho_s$ $\qquad M_p = 5.8433 \cdot 10^{-8} \cdot kg$

The number of particles that are worked with in each iterative calculation is a constant as determined below:-

$N_p := \frac{M_{fr} \cdot \Delta t}{M_p}$ $\qquad N_p = 31.9748$

The Reyñold's number for the tube is now calculated along with the friction factor so that the pressure drop in the tube due to the air flow can be determined:-

Given

$$\frac{1}{\sqrt{f}} = -2.0 \cdot \log\left(\frac{\varepsilon \cdot 2 \cdot R_t^{\,-1}}{3.7} + \frac{2.51}{Re_t \cdot \sqrt{f}}\right)$$

NB This is the Colebrook-White Formula,see Fox, pp198 [F6].

$FricFac(Re_t, R_t, \varepsilon) := \mathrm{Find}(f)$

$\varepsilon := 0.000061 \cdot m$ $\quad R_t := 0.0013 \cdot m$ $\quad \nu = 1.5 \cdot 10^{-5} \cdot m^2 \cdot sec^{-1}$

$Re_t := \left|\frac{C_a \cdot 2 \cdot R_t}{\nu}\right|$ $\qquad Re_t = 844.1333$

$ff := FricFac(Re_t, R_t, \varepsilon)$ $\qquad ff = 0.1161$

The value of the friction factor just determined is used to calculate the pressure loss in the tube:-

$P_{loss} := \left(\frac{4 \cdot ff \cdot L_t}{2 \cdot R_t}\right) \cdot \left(\frac{\rho_a \cdot C_a^{\,2}}{2}\right)$ $\qquad P_{loss} = 303.7448 \cdot kg \cdot m^{-1} \cdot sec^{-2}$

The initial conditions for the iterative calculations and the counting subscript for the iterative calculations are now defined. (NB MathCad requires the equations to be solved to be entered in column matrix/vector format).

$i := 0 .. 300$

$$\begin{bmatrix} V_{t_0} \\ N_0 \\ C_{rel_0} \\ Re_{p_0} \\ C_{d_0} \\ Fdrag_0 \\ F_{rd_0} \\ A_{r_0} \\ V_{r_0} \\ \Delta R_0 \\ r_0 \\ \Delta V_{t_0} \\ A_{t_0} \\ F_{ae_0} \\ F_{a_0} \end{bmatrix} := \begin{bmatrix} 0 \cdot \frac{m}{sec} \\ 0 \cdot \left(\frac{kg \cdot m}{sec^2} \right) \\ 1.0 \cdot \frac{m}{sec} \\ 10 \\ 1 \\ 0 \cdot newton \\ 0 \cdot newton \\ 0 \cdot \frac{m}{sec^2} \\ 1.1 \cdot \frac{m}{sec} \\ 0 \cdot m \\ 0.01 \cdot m \\ 0 \cdot \frac{m}{sec} \\ 0 \cdot \frac{m}{sec^2} \\ 0 \cdot newton \\ 0 \cdot newton \end{bmatrix}$$

V_t is the vector of the tangential velocity components.

N is the vector of the normal force components.

C_{rel} is the vector of the relative velocities between the particle and air.

R_{ep} is the vector of particle Reynold's numbers.

C_d is the vector of the particle drag coefficients.

Fdrag is the vector of the drag force components.

F_{rd} is the vector of the summed drag forces on the particles

A_r is the vector of the radial accelerations on the particles.

V_r is a vector of the radial velocity components of the particles.

DeltaR is a vector of the increment in the particles radial position.

r is the new radial distance achieved.

DeltaV_t is the increment in the tangential velocity achieved.

A_t is the new value of the tangential acceleration.

F_{ae} is the value of the increment in the particle effect on the air.

F_a is a vector of the incremental effect of the particles on the air motion.

$$\begin{bmatrix} V_{t_{(i+1)}} \\ N_{(i+1)} \\ C_{rel_{(i+1)}} \\ Re_{p_{(i+1)}} \\ C_{d_{(i+1)}} \\ Fdrag_{(i+1)} \\ F_{rd_{(i+1)}} \\ A_{r_{(i+1)}} \\ V_{r_{(i+1)}} \\ \Delta R_{(i+1)} \\ r_{(i+1)} \\ \Delta V_{t_{(i+1)}} \\ A_{t_{(i+1)}} \\ F_{ae_{(i+1)}} \\ F_{a_{(i+1)}} \end{bmatrix} := \begin{bmatrix} r_i \cdot \omega \\ M_p \cdot A_{t_i} \\ V_{r_i} - C_a \\ \left| \dfrac{C_{rel_i} \cdot 2 \cdot R_p}{v} \right| \\ \mathrm{if}\left[\left(C_{d_i} > 0.5 \right), \left[\dfrac{24}{\left(Re_{p_i} \right)^{0.646}} \right], 0.5 \right] \\ \mathrm{if}\left[\left(C_{rel_i} < 0 \cdot \dfrac{m}{sec} \right), \left[\dfrac{C_{d_i} \cdot A_p \cdot \rho_a \cdot \left(C_{rel_i} \right)^2}{2} \right] \cdot (-1), \left[\dfrac{C_{d_i} \cdot A_p \cdot \rho_a \cdot \left(C_{rel_i} \right)^2}{2} \right] \right] \\ M_p \cdot r_i \cdot \omega^2 - \mu \cdot N_i - Fdrag_i \\ \dfrac{F_{rd_i}}{M_p} \\ V_{r_i} + A_{r_i} \cdot \Delta t \\ V_{r_i} \cdot \Delta t \\ \mathrm{until}\left(L_t - r_i, r_i + \Delta R_i \right) \\ \Delta R_i \cdot \omega \\ 2 \cdot \omega \cdot V_{t_i} \\ Fdrag_i \cdot N_p \\ F_{a_i} + F_{ae_i} \end{bmatrix}$$

$N2 := \mathrm{last}(r) - 1$ $N2 = 198$

The values of the velocities of the particles and the force driving the air due to the particle motion are extracted from t data above. This is accomplished by determining when the value of r_i exceeds L_t.

$j := 0 .. N2$

$F_{a_{N2}} = 0.0016 \cdot kg \cdot m \cdot sec^{-2}$ $V_{r_{N2}} = 15.4478 \cdot m \cdot sec^{-1}$ $V_{t_{N2}} = 19.7514 \cdot m \cdot sec^{-1}$

The pressure rise in the dispensing tubes due to the air drag effects accelerating the air can be calculated as follows:-

$P_{rise} := \dfrac{F_{a_{N2}}}{A_b}$ $P_{rise} = 302.0035 \cdot \dfrac{newton}{m^2}$

in comparison to the pressure loss of...

$P_{loss} = 303.7448 \cdot \dfrac{newton}{m^2}$

$trial := P_{rise} - P_{loss}$ $trial = -1.7413 \cdot kg \cdot m^{-1} \cdot sec^{-2}$

The above calculations are iteratively calculated until a value of C_a is selected where $P_{loss} = P_{rise}$. To calculate the particle velocity and its angle of exit from the disc the following values need to be found:-

$$V_{res} = \sqrt{\left[\left(V_{r_{N2}}\right)^2 + \left[\left(V_{t_{N2}}\right)^2\right]\right]} \qquad \kappa := \operatorname{atan}\left(\frac{V_{r_{N2}}}{V_{t_{N2}}}\right)$$

$$V_{res} = 25.075 \cdot m \cdot sec^{-1} \qquad \kappa = 38.0294 \cdot deg$$

The angle of particle impingement on each of the targets in the target ring will now be calculated. Calculations will performed for each five degree increment of target position for the impingement angle at the centre of each target. This will be followed by a calculation of the maximum variation of the impingement angle across the face of each target. Alpha is the target holder angle and eta the angle of particle impingement.

$$n := 0..72 \qquad \alpha_n := \mathrm{if}\left[n \geq 36, \frac{\pi}{36}\cdot(n-36), -\frac{\pi}{36}\cdot(36-n)\right]$$

$$\alpha_{d_n} := \frac{\alpha_n \cdot 180}{\pi} \qquad vy_n := \alpha_{d_n} \qquad \gamma_n := \alpha_n - \operatorname{asin}\left(\frac{L_t \cdot \sin\left(\frac{\pi}{2} + \kappa\right)}{L_t + x_d}\right)$$

$$\gamma_{d_n} := \frac{\gamma_n \cdot 180}{\pi} \qquad vx_n := \gamma_{d_n} \qquad \operatorname{asin}\left(\frac{L_t \cdot \sin\left(\frac{\pi}{2} + \kappa\right)}{L_t + x_d}\right) = 41.587 \cdot deg$$

The values of the eta angle which give the required alpha angles shown below, are in the order such that the first value gives the 90 deg impact angle and the last the 0 deg impact angle. The positive values of alpha so interpolated indicate that the target holder has been rotated in a clockwise direction beyond the position where the target face is in line with a line drawn radially from the centre of the dispensing discs. Those values of alpha so interpolated as to be negative are anti-clockwise of this position.

linterp(vx,vy,-90) = -48.413
linterp(vx,vy,-75) = -33.413
linterp(vx,vy,-60) = -18.413
linterp(vx,vy,-55) = -13.413
linterp(vx,vy,-45) = -3.413
linterp(vx,vy,-35) = 6.587
linterp(vx,vy,-25) = 16.587
linterp(vx,vy,-15) = 26.587
linterp(vx,vy,0) = 41.587

The axes of the above system are switched so that interpolation for given values of alpha can be used to yield actual impact vector angles.

$$k := 1..19 \qquad \alpha k_k := 5 \cdot k - 55 \qquad wx_n := \alpha_{d_n} \qquad wy_n := \gamma_{d_n}$$

$$\gamma\_def_k := \operatorname{linterp}\left(wx, wy, \alpha k_k\right)$$

Graph of the Variance in Impingement Angle with Target Angle.

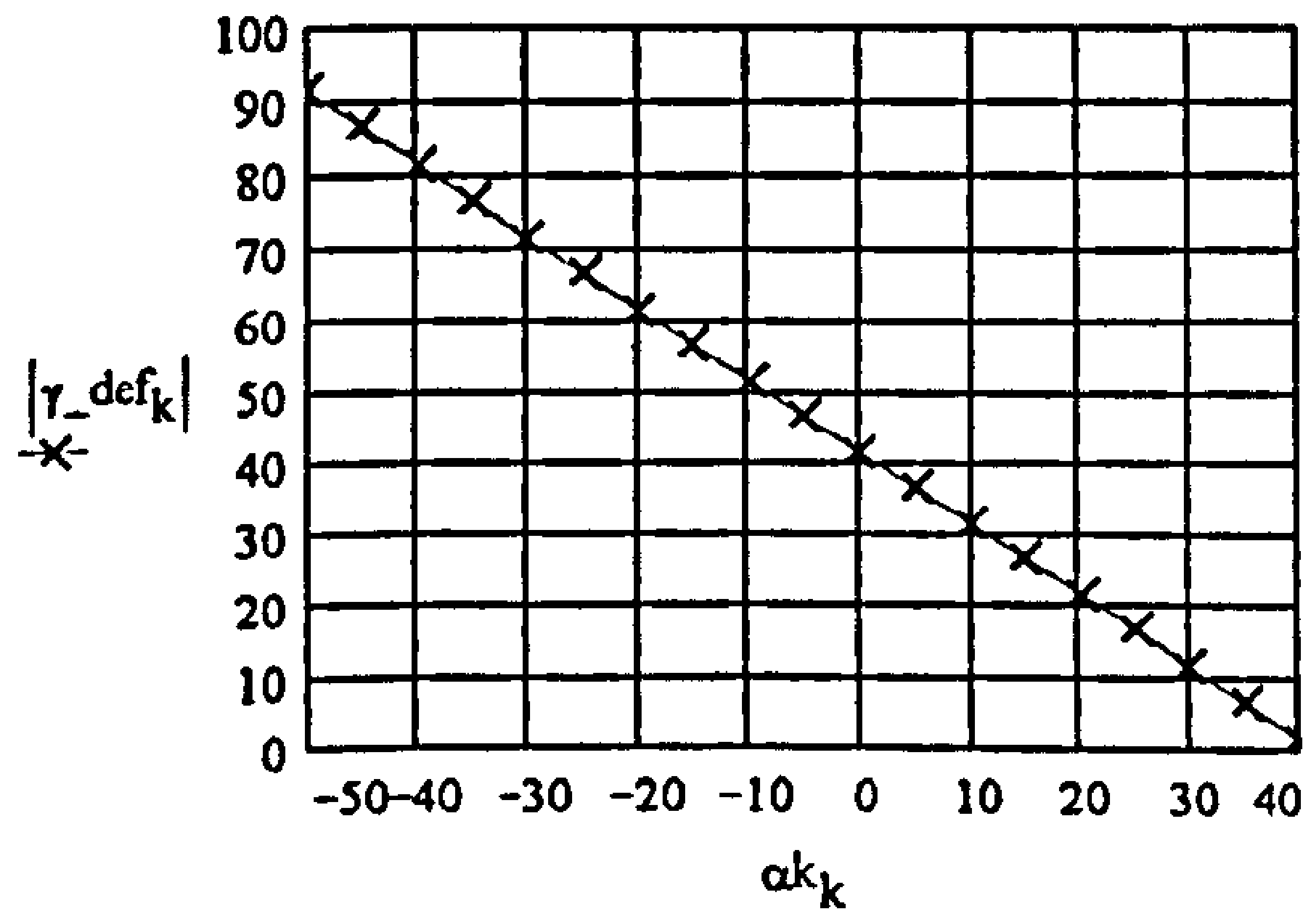

$$\alpha_{act_0} := \left|\operatorname{linterp}(wx, wy, -45)\right|$$

$$\alpha_{act_1} := \left|\operatorname{linterp}(wx, wy, -35)\right|$$

$$\alpha_{act_2} := \left|\operatorname{linterp}(wx, wy, -25)\right|$$

$$\alpha_{act_3} := \left|\operatorname{linterp}(wx, wy, -15)\right|$$

$$\alpha_{act_4} := \left|\operatorname{linterp}(wx, wy, -5)\right|$$

$$\alpha_{act_5} := \left|\operatorname{linterp}(wx, wy, 5)\right|$$

$$\alpha_{act_6} := \left|\operatorname{linterp}(wx, wy, 15)\right| \qquad \alpha_{act_7} := \left|\operatorname{linterp}(wx, wy, 25)\right| \qquad \alpha_{act_8} := \left|\operatorname{linterp}(wx, wy, 30)\right|$$

$$l := 0, 1..8$$

Calculation of the reduction in the target face width dimensions owing to the projection of the target edge protectors (NB Eta_def is in terms of degrees and needs to be converted to radians):-

$$\gamma\_def_{r_k} := \frac{\gamma\_def_k \cdot \pi}{180} \qquad aa\_sub_k := \left| \frac{0.001}{\tan\left(\gamma\_def_{r_k}\right)} \right| \cdot m \qquad a_k := aa - aa\_sub_k \qquad \alpha k_{r_k} := \frac{\alpha k_k \cdot \pi}{180}$$

Calculation of the distance from the edge of the disc to the edge of the targets (NB b is closest to the dispensing disc):

$$x_{a_k} := -L_t + \sqrt{\left[\left(L_t + x_d\right)^2 + (ab)^2\right] + 2 \cdot ab \cdot \left(L_t + x_d\right) \cdot \cos\left(\alpha k_{r_k}\right)}$$

$$x_{b_k} := -L_t + \sqrt{\left[\left(L_t + x_d\right)^2 + \left(a_k\right)^2\right] - 2 \cdot a_k \cdot \left(L_t + x_d\right) \cdot \cos\left(\alpha k_{r_k}\right)}$$

Calculation of the particle trajectory to the target face angle variation is found at the target edges:-

$$\beta_{a_k} := \operatorname{asin}\left(\frac{L_t \cdot \sin\left(\frac{\pi}{2} + \kappa\right)}{L_t + x_{a_k}}\right) \qquad \beta_{b_k} := \operatorname{asin}\left(\frac{L_t \cdot \sin\left(\frac{\pi}{2} + \kappa\right)}{L_t + x_{b_k}}\right)$$

The variation in impingement angle is as follows:-

$$\gamma_{a_k} := \left(\alpha k_{r_k} - \operatorname{asin}\left(\frac{a_k}{L_t + x_{a_k}}\right) \cdot \sin\left(\alpha k_{r_k}\right)\right) - \beta_{a_k} \qquad \gamma_{b_k} := \left(\alpha k_{r_k} + \operatorname{asin}\left(\frac{ab}{L_t + x_{b_k}}\right) \cdot \sin\left(\alpha k_{r_k}\right)\right) - \beta_{b_k}$$

$$\gamma_{ad_k} := \frac{\gamma_{a_k} \cdot 180}{\pi} \qquad \gamma_{bd_k} := \frac{\gamma_{b_k} \cdot 180}{\pi}$$

Graph of the Variation of the Impingement Angles at the Edges & Centre of the Targets at the Given Orientations.

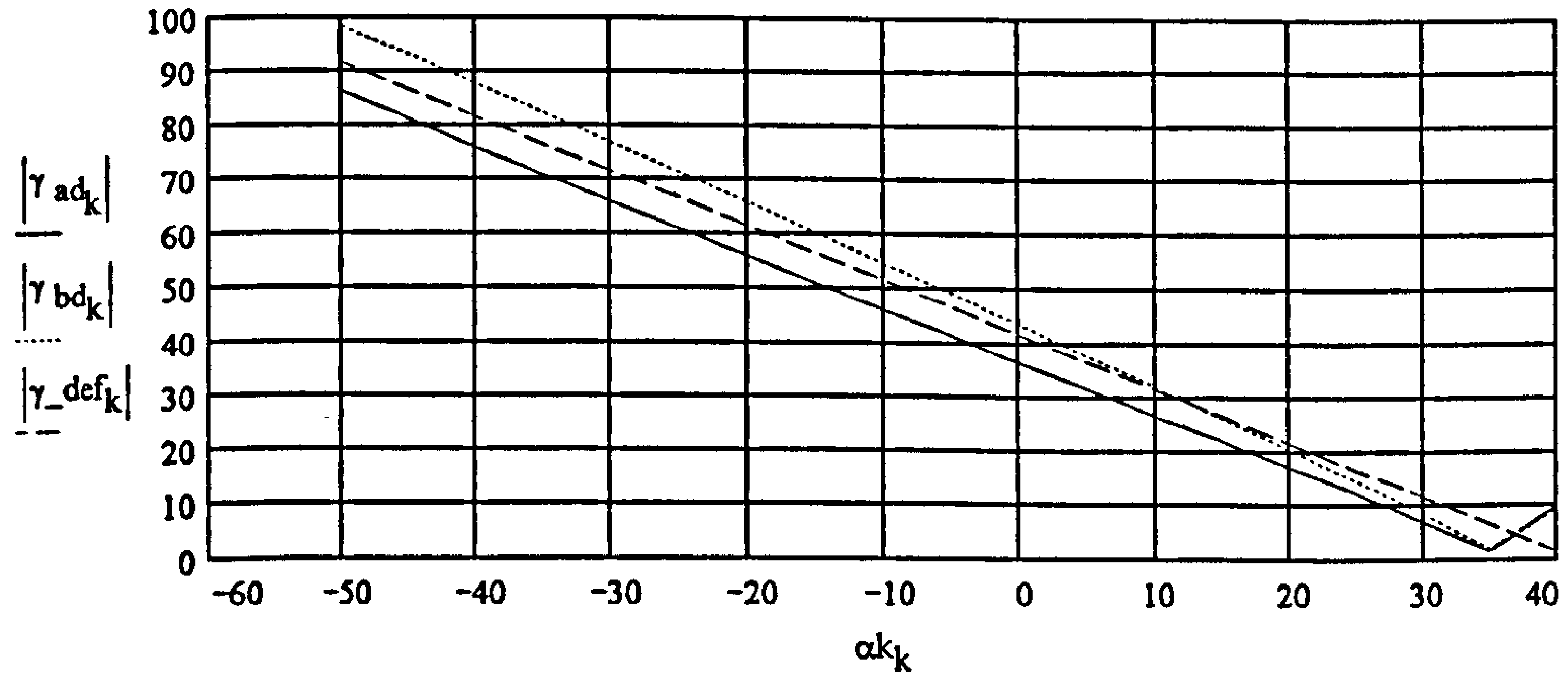

The following calculations determine the amount of abrasive material that strikes each target given the particular orientation of the target to the tangent of the target ring:-

$$\Delta\gamma_k := \left|\gamma_{a_k} - \gamma_{b_k}\right| \qquad \Delta\gamma_{d_k} := \frac{\Delta\gamma_k \cdot 180}{\pi}$$

The variation of impact angle across the face of the target is required for further information. The information so obtained will used to produce error bars on the graphs for the erosion damage verses angle of impact. The 'a' designated angles are for the target edges closest to the disc.

$$\gamma d_{a_0} := \left|\gamma_{ad_2}\right| \qquad \gamma d_{a_1} := \left|\gamma_{ad_4}\right| \qquad \gamma d_{a_2} := \left|\gamma_{ad_6}\right| \qquad \gamma d_{a_3} := \left|\gamma_{ad_8}\right| \qquad \gamma d_{a_4} := \left|\gamma_{ad_{10}}\right|$$

$$\gamma d_{a_5} := \left|\gamma_{ad_{12}}\right| \qquad \gamma d_{a_6} := \left|\gamma_{ad_{14}}\right| \qquad \gamma d_{a_7} := \left|\gamma_{ad_{16}}\right| \qquad \gamma d_{a_8} := \left|\gamma_{ad_{17}}\right|$$

The 'b' designated angles are for the target edges furthest from the disc.

$\gamma d_{b_0} := \left|\gamma bd_2\right|$ $\gamma d_{b_1} := \left|\gamma bd_4\right|$ $\gamma d_{b_2} := \left|\gamma bd_6\right|$ $\gamma d_{b_3} := \left|\gamma bd_8\right|$ $\gamma d_{b_4} = \left|\gamma bd_{10}\right|$

$\gamma d_{b_5} = \left|\gamma bd_{12}\right|$ $\gamma d_{b_6} = \left|\gamma bd_{14}\right|$ $\gamma d_{b_7} := \left|\gamma bd_{16}\right|$ $\gamma d_{b_8} := \left|\gamma bd_{17}\right|$

The following variable gives the mass of abrasive that strikes each target for a given orientation in any given minute of dispensing disc rotation:-

$$M_k := \frac{\Delta\gamma\, d_k}{360} \cdot M_{fr} \cdot 60$$

M_k is the value of the mass impacting each target per second allowing for the edge protector projection.

The calculation of the mean impact angle for any given target orientation is now performed.

$$\gamma m_l := \frac{\gamma d_{b_l} + \gamma d_{a_l}}{2}$$

Calculation of the Dispersion of the Particle Stream and It's Effect on the Targets Arranged at Various Orientations.

The following calculations are based upon a the experimental work carried out by D.R. McClusky in her Phd submitted at The University of Edinburgh 1992 [M10]. The model takes the form of some crude linear fits made to some of McClusky's data.

$$\Delta grad := 3.91484 \cdot 10^{-3} \cdot V_{res} \cdot \frac{sec}{m} + 0.075 \qquad \Delta grad = 0.1732$$

The above equations take the form of a linear fit to data representing the spread of the stream of particles emerging from a stationary nozzle and the increase in spread with the stream velocity. The result of this is that gradient selection based upon stream velocity is then used to to determine the dispersed depth of the stream at various distances from the edge of the dispensing disc. The distances considered are those to the edges of the targets determined in the sections above on the calculation of the range of likely particle impact angles.

$$r_{ba_k} := \left(\Delta grad \cdot x_{a_k} + R_t\right) \qquad r_{bb_k} := \left(\Delta grad \cdot x_{b_k} + R_t\right)$$

Graph of the Variation of the Spread of the Dispersing Particle Jet at the Edges of the Targets for the Given Target Orientations

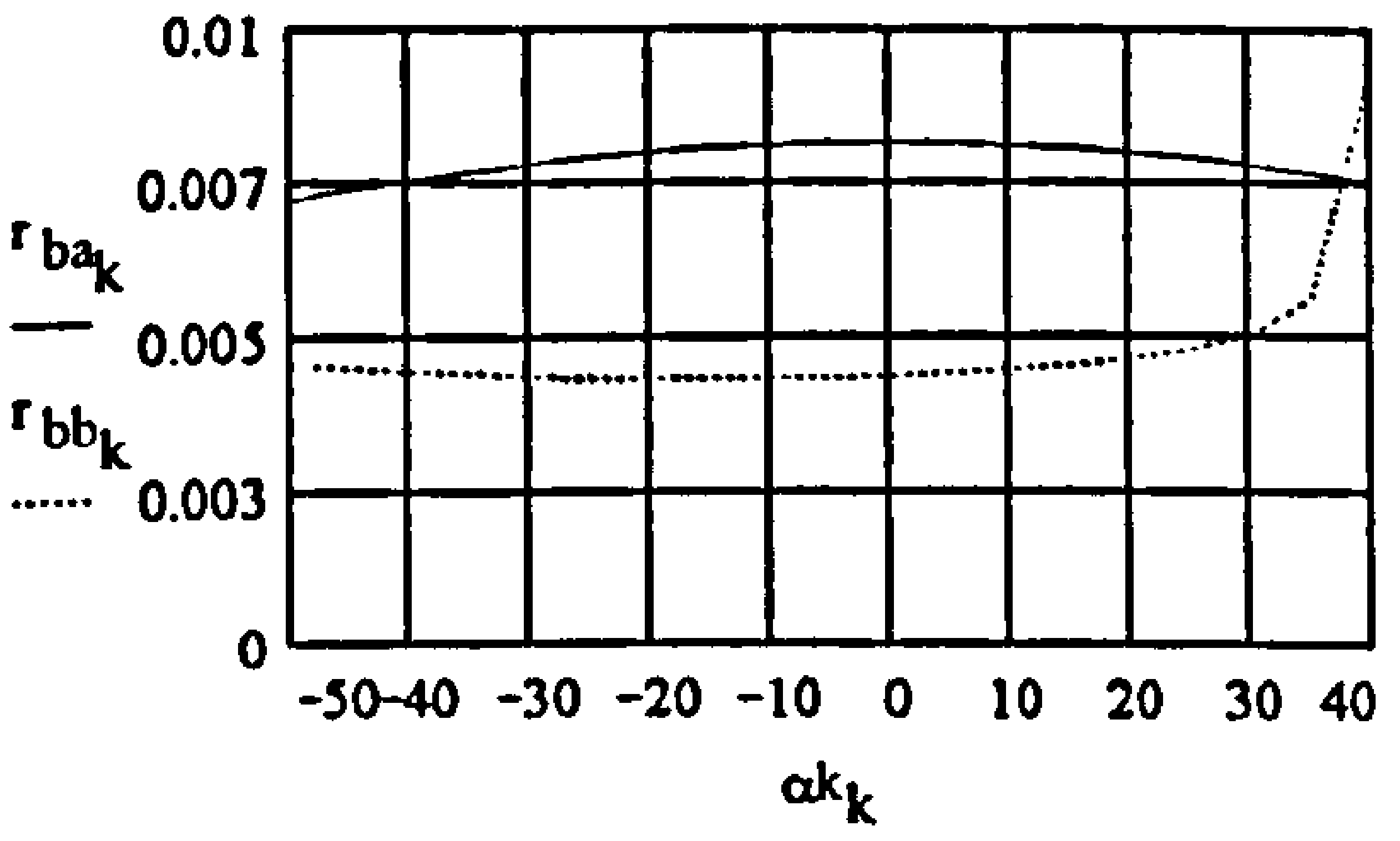

Erosion Centre Set Up.

Particle Velocity :-	$V_{air} = 25.3 \cdot m \cdot sec^{-1}$	
Suspension Density:-	$\rho_{ph} = 4 \cdot kg \cdot m^{-3}$	
Disc Rotational Velocity:-	$N_r = 1.605 \cdot 10^3$	(rpm).
Vibratory Feeder Potentiometer Set Point:-	$Vib_{sp} = 4.21$	
Abrasive Mass Flow Rate:-	$M_{fr} = 0.01868 \cdot kg \cdot sec^{-1}$	

Individual Target Information.

Please select the value of k which corresponds to the target holder orientation in which you are interested. A full set of impact conditions for a target at this angle will be presented along with information appertaining to the area of impact and the range of impact velocity vectors that should be expected over this area. **NB At the present values for -45, -35, -25, -15, -5, 5, 15, 25, 30 degrees are the only ones available**

$sk := 17$

Exit velocity from the dispensing disc:-

$V_{res} = 25.075 \cdot m \cdot sec^{-1}$ $\kappa = 38.0294 \cdot deg$

Distances to the edges and pivot of the target:-

pivot of target distance:- $x_d = 0.0225 \cdot m$

distance to edge A:- $x_{a_{sk}} = 0.0375 \cdot m$

distance to edge B:- $x_{b_{sk}} = 0.0215 \cdot m$

Angles of Impact at the Edges and the Target Pivot Point:-

angle of impact at the pivot point:- $\left|\gamma\_def_{sk}\right| = 11.587$

angle of impact at edge A:- $\left|\gamma ad_{sk}\right| = 7.14$

angle of impact at edge B:- $\left|\gamma bd_{sk}\right| = 8.4985$

mean impact angle:- $\left|\frac{\gamma ad_{sk} + \gamma bd_{sk}}{2}\right| = 7.8192$

The dimensional range of the dispersion of the particle jet at the target edges:-

Total range of particles at edge A:- $r_{ba_{sk}} = 0.0078 \cdot m$

Total range of particles at edge B:- $r_{bb_{sk}} = 0.005 \cdot m$

The calculation of the area of the target surface affected by erosion is as follows:-

The target width is:- $wid := a_{sk} + ab$ $wid = 0.0181 \cdot m$ NB The increase in dispersion is linear with an increase in distance from the nozzle.

The area is:- $Area := wid \cdot r_{bb_{sk}} + \left(r_{ba_{sk}} - r_{bb_{sk}}\right) \cdot wid$ $Area = 1.4109 \cdot 10^{-4} \cdot m^2$

The mass of particles striking this area is:-

Mass of Particles Striking this Area per second is:- $M_{sk} = 0.0042 \cdot kg \cdot sec^{-1}$

The particle mass flux at impact over the target is:-

Mean Particle Mass Flux Over the Target Area:- $MF_{tt} := \frac{M_{sk}}{Area}$ $MF_{tt} = 29.9826 \cdot kg \cdot m^{-2} \cdot sec^{-1}$

The distance between particles at impact on the target surface is:-

NB: THIS RESULT IS IN PARTICLE DIAMETERS.

Distance Between Particles for the Total Wear Scar Area:- $L := \left(\frac{M_p \cdot V_{res} \cdot Area}{M_{sk}}\right)^{\frac{1}{3}} \cdot \frac{1}{R_p}$ $L = 22.58$

Calculation of the instantaneous particle mass flux at the target:-

Calculation of the mass of abrasive particles striking the target per exposure of the target to each nozzle.

$M_{cy} := \frac{M_{sk}}{\frac{\omega}{2 \cdot \pi} \cdot T_{num}}$ $M_{cy} = 2.6357 \cdot 10^{-5} \cdot kg$

Calculation of the proportion of the perimeter occupied by the target face.

$lt := \frac{\Delta\gamma_{d_{sk}}}{360}$ $lt = 0.0038$

Calculation of the mean time of taken for the particle jet to sweep across the target surface.

$T_{cy} := \frac{lt \cdot 2 \cdot \pi}{\omega}$ $T_{cy} = 1.410675 \cdot 10^{-4} \cdot sec$

Calculation of the instantaneous particle mass flux on the target surface per cycle.

$MF_{inst} := \frac{M_{cy}}{Area \cdot T_{cy}}$ $MF_{inst} = 1.3242 \cdot 10^{3} \cdot kg \cdot m^{-2} \cdot sec^{-1}$

Mass Flux Calculations Based Upon Area of Particle Stream Striking the Target Surface:-

Calculation of the proportion of the perimeter occupied by the target face:-

$lt := \frac{\Delta\gamma_{d_{sk}}}{360} \cdot 2 \cdot \pi \cdot \left[L_t + \left(\frac{x_{a_{sk}} + x_{b_{sk}}}{2}\right)\right]$ $lt = 0.003556 \cdot m$

$W := \left[L_t + \left(\frac{x_{a_{sk}} + x_{b_{sk}}}{2}\right)\right] \cdot \sin\left(\frac{\Delta\gamma_{d_{sk}} \cdot \pi}{360}\right) \cdot 2$ $W = 0.003556 \cdot m$

The calculation of the area of the particle jet projected against the target surface is as follows:-

$Area_{pj} := W \cdot r_{bb_{sk}} + \left(r_{ba_{sk}} - r_{bb_{sk}}\right) \cdot W$ $Area_{pj} = 2.7686 \cdot 10^{-5} \cdot m^2$

Calculation of the instantaneous particle mass flux on the target surface per cycle.

$MF_{ipj} := \frac{M_{cy}}{Area_{pj} \cdot T_{cy}}$ $MF_{ipj} = 6.7485 \cdot 10^{3} \cdot kg \cdot m^{-2} \cdot sec^{-1}$

Mean Particle Mass Flux Over the Target Area:-

$MF_{ttpj} := \frac{M_{sk}}{Area_{pj}}$ $MF_{ttpj} = 152.7955 \cdot kg \cdot m^{-2} \cdot sec^{-1}$

Appendix 4C: Calibration of the Rotating Disc Accelerator Erosion Rig

4C.1 Introduction to the Calibration Methods

The rotating disc accelerator erosion test rig needed to be calibrated to ensure that the most important variables affecting the erosion damage were accurately controllable, and measurable within acceptable limits. With this tester three major variables needed to be checked. These were the accuracy and controllability of the mass flow rate of the abrasive into the tester using the vibratory feeder; the accuracy of the velocity vector calculated for the particles emerging from the rotating acceleration disc; and the amount by which the jet of particles had diverged by the time it reached the target surface. These three areas are dealt with in turn in the following three sections of this chapter.

4C.2 Calibration of the Vibratory Feeder

Calibration of the vibratory feeder was easily achieved. The potentiometer used to control the amplitude of the tray vibrations was varied throughout its full range of travel in ten increments. At each incremental position of the potentiometer a series of measurements were taken for the mass conveyed through the feeder in a given time. A graph of the results of these tests are shown in Figure 4C.1.

The data obtained from carrying out these tests on the vibratory feeder were included within the framework of the numerical model discussed in section 4.1.4. above and Appendix 4B, to enable the intensity of particle impacts in the region of the target surface to be calculated.

The actual mass flow rate of the abrasive into the erosion tester was measured using a load cell throughout the test programme. These measurements ensured that the feed rate from the vibratory feeder was within acceptable limits when compared to the calculated value using the method mentioned above.

4C.1 Graph of the variation of the mass flow rate with potentiometer set point position for the vibratory feeder

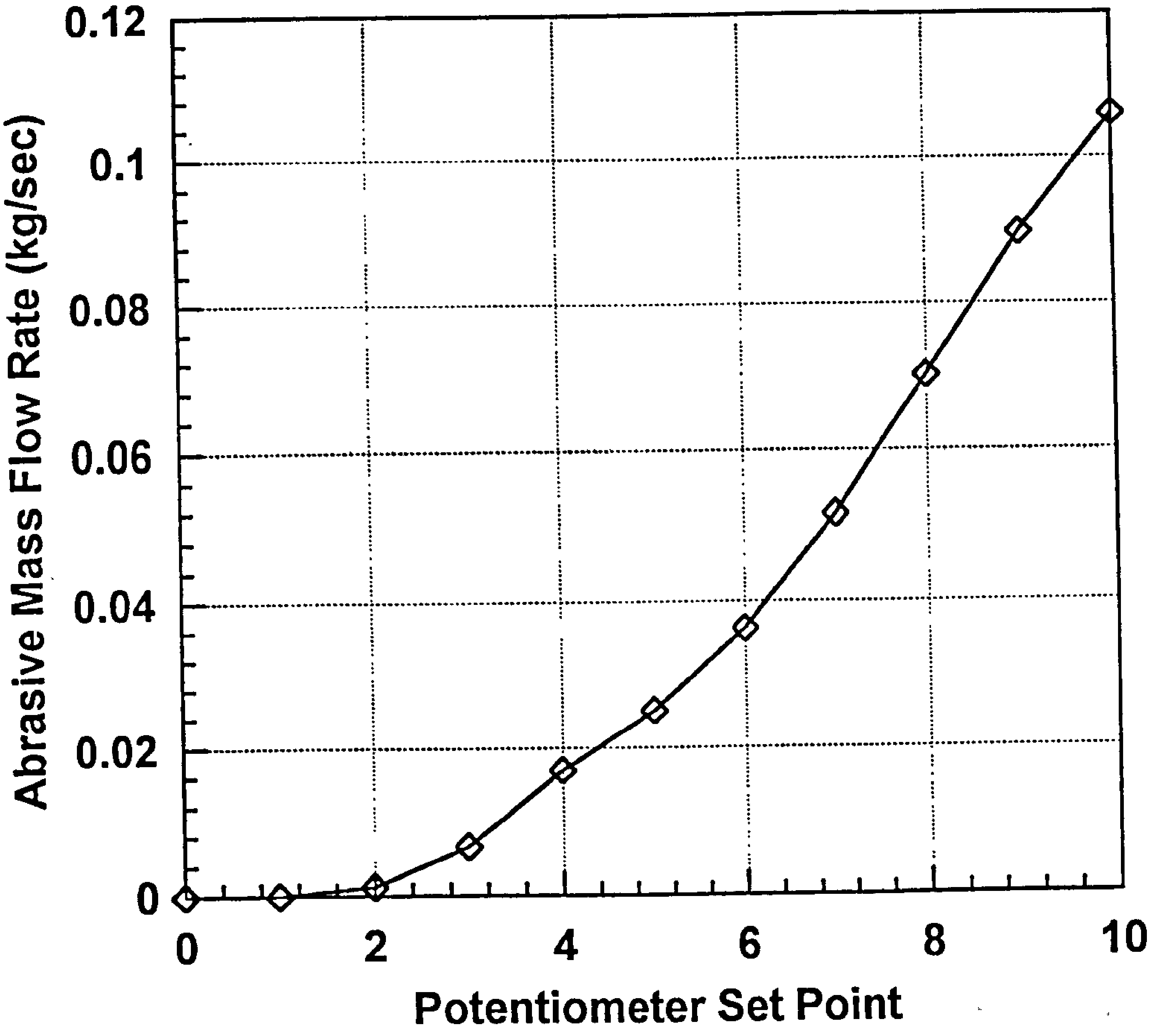

Maximum Error ±0.75% at Potentiometer Set Point of 10

4C.3 Calibration Tests to Confirm the Accuracy of the Particle Velocity Vector on Exit from the Rotating Disc

Currently, the best way to measure the particle velocity in erosion testers is that developed by Kosel and Anand [K10]. These researchers devised a non-intrusive optoelectronic velocity measurement device that has been used successfully by several other workers in the field of erosion studies, most notably Hutchings and co-workers [S9]. Unfortunately, a device of this type was not available for this project. The velocity vector was checked by using a static form of the Ruff and Ives slot and displaced wear scar method [R3] (see Figure 4C.2). The mean of the offset of the wear scar from the slot was derived from ten test measurements. The tangential velocity of the rotating disc was known, as was the geometry of the system at the time of these tests owing to the mechanical arrangement of the targets within the tester. Consequently, the only information missing was the direction of the particle travel.

This was found by using the distance between the positions of the slot and the wear scar. Once this information was available it was possible to work backwards to find the missing radial velocity component for the particles. This could then be used to calculate the magnitude and direction of the actual particle velocity. The tabulated results of this calibration work compared to the test facility set points derived from the model, are shown below in Table 4C.1.

Table 4C.1 Results for the Calibration Tests for the Particle Velocity Vector when Compared with Predictions from the Model

Erosion Condition. (Velocity; Particle Concentration).	**% Error in Impact Angle.** (between model and measured value) (- indicates model value less than actual value)	**% Error in Velocity.** (between model and measured value) (- indicates model value less than actual value)
15 m/s; 1 kg/m^3	-9.1	-4.3
25 m/s; 4 kg/m^3	-0.9	+6.7
35 m/s; 13 kg/m^3	+2.0	+6.0

The method employed in the calibration of the 'rotating disc accelerator' for the particle velocity vector was simplistic and crude. When it is considered that other researchers have previously found the Ruff and Ives method to be in error by up to 20% these results must be viewed as being quite good. The indication was that this erosion tester was capable of generating particle velocities within

4C.2 Schematic of the static form of the Ruff and Ives technique for measurement of the particle velocity vector

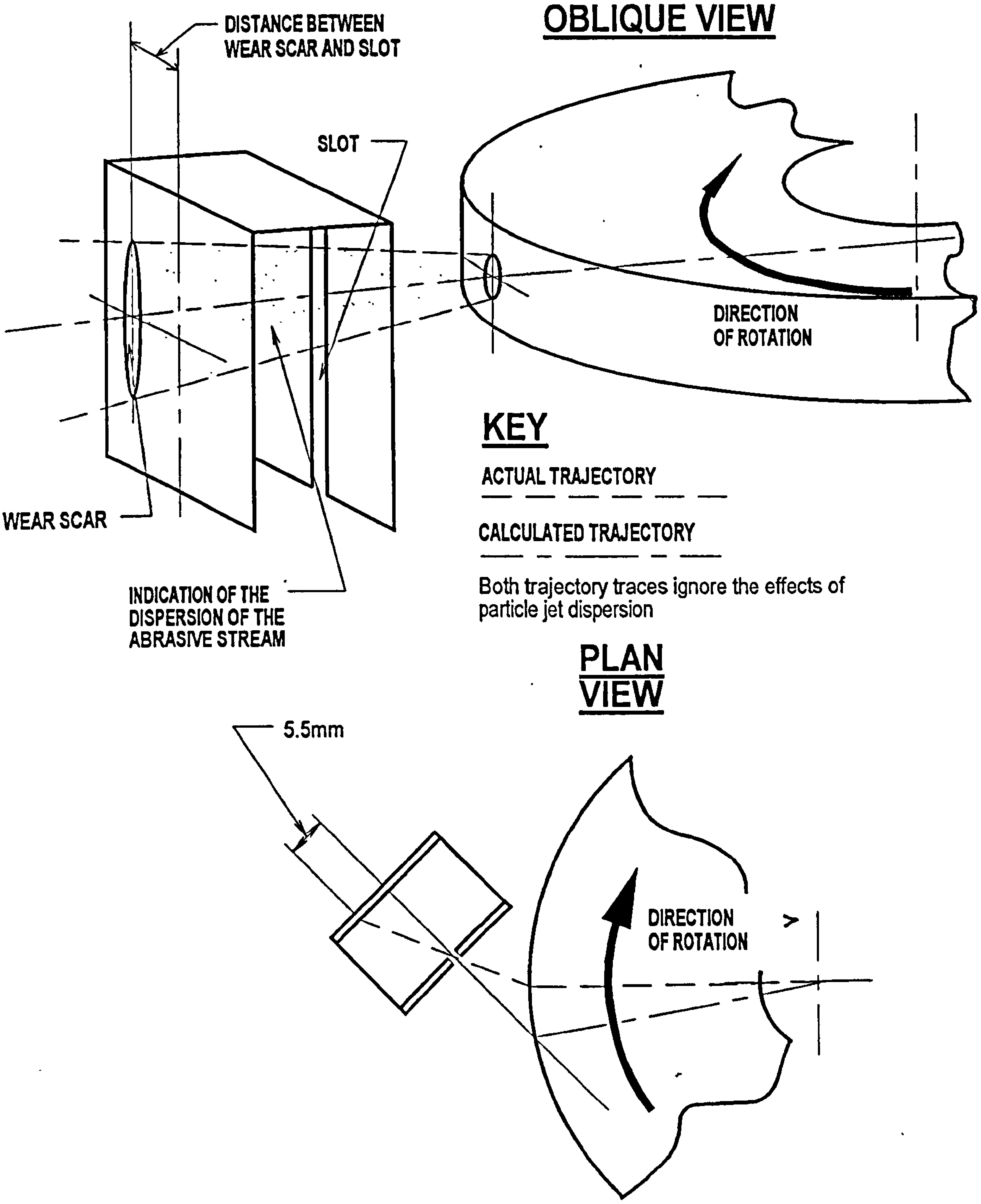

the range desired and with sufficient accuracy (see section 3.3.1). Obviously, it must be expected that the optoelectronic devices would give much more detailed information regarding the particle velocities generated in this erosion tester. However, it was felt that the method employed proved itself to be good enough considering the specifications for the experiment plan mentioned in Chapter 3 section 3.3.1.

4C.4 Calibration Tests for Assessing the Dispersion of the Particle Jet at the Target Surface

It was important to assess the amount by which the particle jet diverged as it travelled away from the rotating disc, since only in this way could the intensity of particle impacts on the target surface be found accurately. Assessment of the particle dispersion was made using a method proposed by Shipway and Hutchings [S11]. The surface of a polished mild steel target was covered by a thin layer of engineers marking blue (Kleenscribe Layout Dye, L.S. Starrett, CAT No. 1610-4, EDP No.53212). The targets were exposed to the abrasive stream at set conditions for a short period. Removal of the marking out dye occurred in the areas subject to particle impact. Manual measurement of the dimensions of the scar in the dye enabled an estimate of the dispersion of the abrasive jet across the surface of the target to be obtained. The results of this calibration work are set out in Table 4.2 overleaf.

Table 4C.2 Results of the Calibration Tests for Particle Jet Divergence when Compared with Values Predicted by the Model

Erosion Conditions (Velocity; Particle Concentration).	**% Error in Actual Dispersion from Empirical Calculation using Equation 4.1 section 4.2.3.5 Chapter 4.**			
	Edge Closest to Disc		Edge Furthest from Disc	
	30°	90°	30°	90°
15 m/s; 1 kg/m^3	-12	-13	+5	+0
25 m/s; 4 kg/m^3	+3	-11	+11	+1
35 m/s; 13 kg/m^3	-29	-8	-11	-11

Two factors must be considered when viewing these results. Firstly, because of the way in which measurements were taken, considerable inaccuracies occurred. Secondly, during the erosion process within this form of tester, debris has a chance of striking the target a second time after its initial impact. While the behaviour of these particles is thought to be such that they will not cause much further erosion because they will have expended a lot of their initial kinetic energy, they may still be able to remove the marking out blue from the target surface. This behaviour led to quite indistinct impact scar boundaries being seen and would hinder the taking of more accurate measurements. It must also be stated here that the data used for the generation of equation 4.1 section 4.2.3.5 Chapter 4 was for jet dispersion in a stream of particles emerging from a tube at 12.5 m/s into a following air stream travelling at 4 m/s, so extrapolation of this data to situations where the particle velocities reach 35 m/s is questionable. However, with the lack of any other data equation 4.1 must stand as the best available first approximation for the particle jet dispersion. Much further work could be carried out to study the effect of jet dispersion on the utilisation of test equipment and erosion behaviour. Work will also have to be carried out on trying to determine the actual particle distribution within the emerging jet and its variation with distance travelled from the nozzle of the acceleration tube. These facets of the operation of erosion testers in general has not been investigated in detail before. Therefore, considering these limitations and the need for further investigations the results given above seem tolerably accurate.

4C.5 Summary of the Calibration Work

The calibration work carried out on the rotating disc accelerator erosion tester indicated that the numerical model proposed in section 4.1.4. of Chapter 4 and Appendix 4B is a reasonably accurate representation of the particle dynamics within this test rig. Obviously, improvements can be made, especially in the area of estimating the dispersion of the jet of particles emerging from the rotating disc. However, considering the crude methods of carrying out the calibration tests, the results were quite encouraging. Errors in the estimation of the particle jet dispersion will affect the mass flux and by inference particle concentration in the region of the target surface. However, it must be remembered that considerable difficulties also occur in the measurement of detailed particle concentrations and velocities within pneumatic conveyor systems. Little information is available for the former of these variables. Considering these statements, and the fact that the results of the tests carried out on this device are to be employed in the prediction of wear in pneumatic conveyor bends, the errors indicated above were thought to be insignificant when compared to those expected in the experimental work to be undertaken on the pneumatic conveyor test facility.

Appendix 4D: The Method of Carrying Out Tests on the Rotating Disc Accelerator Erosion Rig

4D.1 The Test Method Employed for the Rotating Disc Accelerator Erosion Tester

The target specimens were prepared by removing any surface scale and finishing the surface suffering erosion with 240 grit abrasive paper where practicable. The effects of any spurious surface topography were therefore minimised. Prior to any measurements being taken the targets were thoroughly cleaned, by washing in isopropyl alcohol, and dried. Initial tests were undertaken to show when the rotating disc accelerator erosion tester was operating under steady state erosion conditions before results were taken.

The numerical model detailed in section 4.1.4 and Appendix 4B was used to find out the mass of abrasive that struck each target in a given time period. Accounting for the angle of orientation of the target to the flow of abrasive, the time required for an equal mass of abrasive to strike each target was found by the use of this model. The mass loss results were then converted to volume loss values. The time periods derived by the model were then used for interpolation purposes on the time history of the volume loss of each target specimen. This yielded a value for erosion damage in terms of volume loss for an identical mass of abrasive striking each target irrespective of the angle of particle impingement. Erosion performance of the target materials used were presented by simply dividing the volume of material removed from the target by the chosen fixed mass of abrasive striking the target surface. Details of the calculations that were carried out are given in Appendix 4F for a set of test results that were obtained as described later in the next paragraphs.

All tests were carried out on this tester using ten targets simultaneously.

1/ The rotating disc accelerator was set for the particle velocity and concentration required for the chosen impact conditions.

2/ The specimens were polished using a 240-grit abrasive paper. They were then thoroughly washed in neat isopropyl alcohol, then dried in hot air at a temperature of 30-50°C for 10 min and allowed to cool in ambient conditions for approximately 30 min. In the collaborative tests described in Appendix 4E the nitrile rubber specimens reacted with the isopropyl alcohol and were therefore cleaned in slightly soapy water and then dried.

3/ The weighing of the samples was carried out to an accuracy of 0.1 mg on an analytical balance.

4/ Ten samples were placed in the rotating disc accelerator erosion tester and exposed to the particle impact for a short period whose duration was derived from past experimental experience.

5/ Sections 2/, 3/ and 4/ above were repeated for a minimum of five exposures so that enough data were produced to yield a history of the mass loss with time for each target. The exposure times were selected based upon past experience with this form of erosion tester. Rig operation was carried out such that steady state erosion at all times without excessively deep wear scars occurring took place. In this way any effects due to wearing in of the surface being eroded and changes in the impingement angle due to the effects of the depth of the wear scar were minimised.

6/ The above process was then repeated for another ten target specimens.

Appendix 4E:

Comparisons Between the 'Rotating Disc Accelerator' Erosion Tester and the 'Gas Blast' Erosion Tester

4E.1 Introduction

The concept and use of the rotating disc accelerator erosion tester as used in this project is predominately a former Soviet block, Eastern European practice [G1,K6]. The preferred form of erosion tester in Western Europe has been the gas blast erosion tester [D3,A4]. In order to find out whether these erosion testers gave comparable results, a collaborative project between two institutions using these different forms of erosion tester was carried out. It was expected that significant and important differences in the results obtained from these testers would become apparent due to the different way in which particle acceleration was achieved within them.

The rotating disc accelerator erosion tester for these comparative trials was the one described in section 4.1.2 in Chapter 4 whilst the gas blast form of erosion tester was provided and operated by staff at The Department of Powder Science Technology (POSTEC) at The Telemark Technological Research and Development Centre (TEL-TEK), Porsgrunn, Norway. The method of testing for the 'rotating disc accelerator' was as detailed above. In the case of the gas blast erosion tester the researchers at POSTEC carrying out the work for this project generally followed the practice laid down in the German DIN standard [D3].

4E.2 A Brief Description of the Gas Blast Erosion Test Rig and Its Use

4E.2.1 A Brief Description of the Gas Blast Erosion Tester

The gas blast erosion rig that was used by POSTEC (shown in Figure 4E.1) utilised of a boron carbide nozzle 90 mm in length with an internal diameter of 3 mm. Acceleration of the abrasive by the gas stream was controlled by use of two valves. One valve controlled the dispersion of the abrasive within the injector housing to ensure that a homogeneous gas/particle mixture occurred. Control of the gas providing the motive power for the particles, 4E.1 Schematic view of the gas blast erosion tester used by POSTEC.

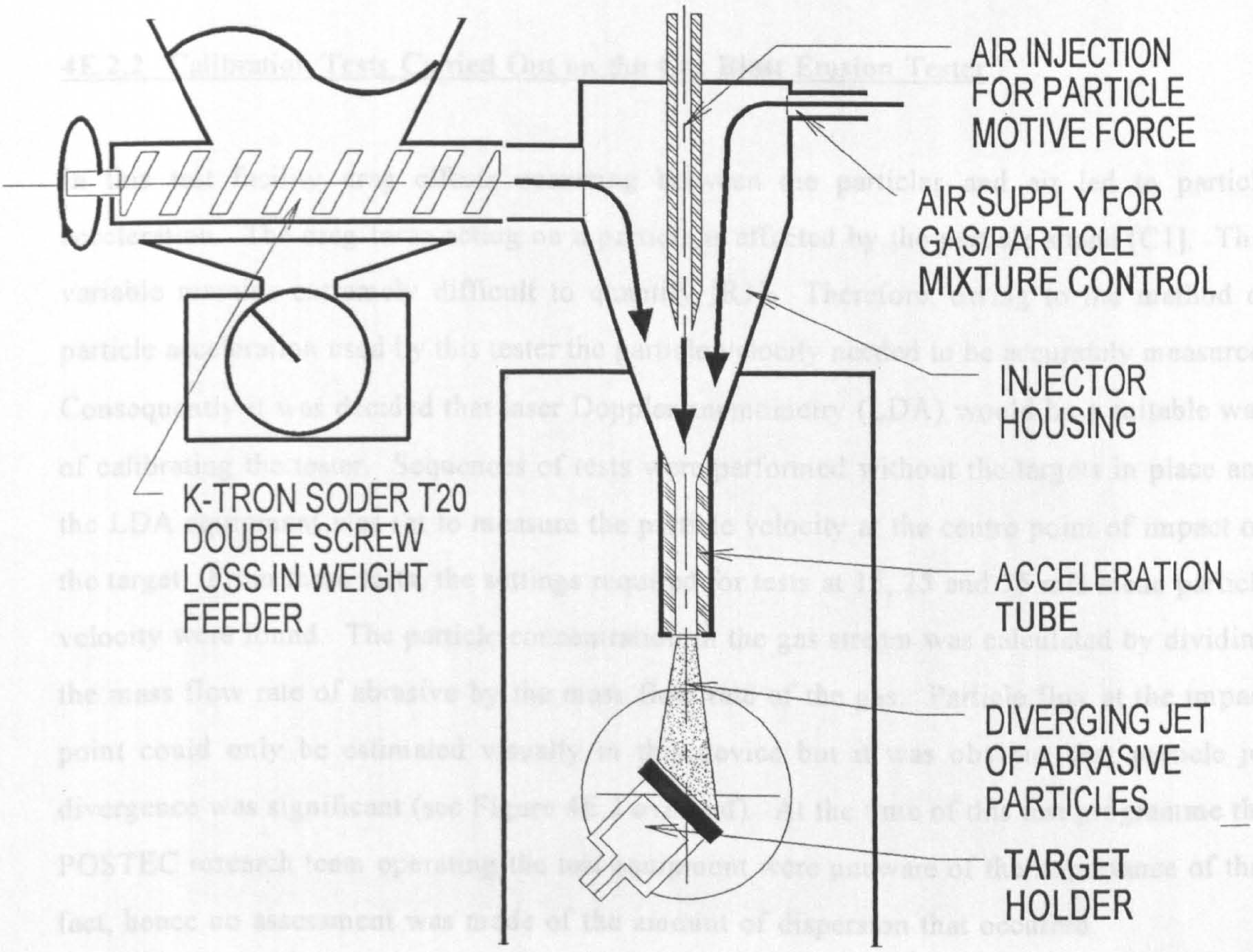

was achieved by using the other valve. A K-Tron Soder T20 double screw feeder mounted to form a loss in weight feeder fed the abrasive into the injector housing. The target holder consisted of a rotatable table to which the 25x25x4 mm specimens were attached by suction. Protection of the target edges was not deemed necessary. It was concluded by researchers at POSTEC that erosion of the test specimen occurred without a variation of the particle impingement angle across the target face, i.e. it was taken that particle impact angles were the same as the angle of orientation of the target. This has not always been shown to be the case [D1,C7].

4E.2.2 Calibration Tests Carried Out on the Gas Blast Erosion Tester

In this test facility drag effects occurring between the particles and air led to particle acceleration. The drag force acting on a particle is affected by the particle shape [C1]. This variable remains extremely difficult to quantify [R1]. Therefore, owing to the method of particle acceleration used by this tester the particle velocity needed to be accurately measured. Consequently it was decided that laser Doppler anemometry (LDA) would be a suitable way of calibrating the tester. Sequences of tests were performed without the targets in place and the LDA equipment was set to measure the particle velocity at the centre point of impact on the target. From these tests, the settings required for tests at 15, 25 and 35 m/s mean particle velocity were found. The particle concentration in the gas stream was calculated by dividing the mass flow rate of abrasive by the mass flow rate of the gas. Particle flux at the impact point could only be estimated visually in this device but it was obvious that particle jet divergence was significant (see Figure 4E.2 overleaf). At the time of this test programme the POSTEC research team operating the test equipment were unaware of the importance of this fact, hence no assessment was made of the amount of dispersion that occurred.

4E.2.3 Test Method Employed for the Gas Blast Erosion Tester

In the case of the gas blast erosion tester the erosion performance of the materials were found by simply dividing the volume of material removed from the target by the mass of abrasive striking the target surface, (i.e. in the same way as it was presented in the results obtained from the rotating disc accelerator erosion tester). For this form of erosion tester this was very easily achieved since all of the abrasive being fed through the tester was believed to strike the target surface.

4E.2 Photograph illustrating particle jet divergence in the gas blast erosion tester.

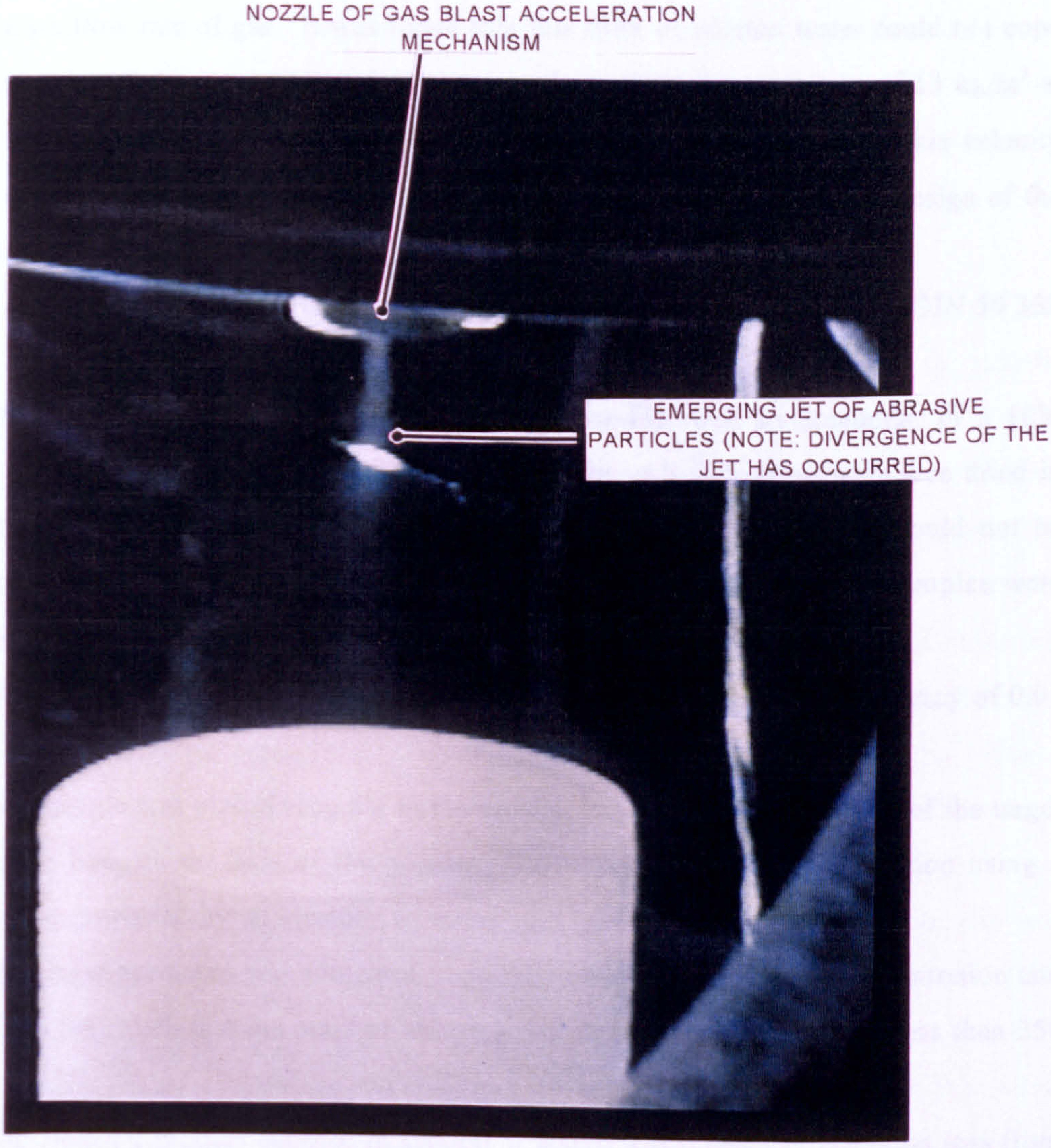

The method of carrying out tests on this device is laid out sequentially below.

1/ Following calibration of the test apparatus, the tester was set to produce the desired particle velocity and concentration. The particle concentration was theoretically calculated at the nozzle of the acceleration tube using figures based on the ratio of the mass flow rate of solids to mass flow rate of gas. It was found that this form of erosion tester could not cope with the quantity of abrasive necessary to simulate the particle concentration of 13 kg/m^3 at 35 m/s. The maximum concentration that could be achieved was 8 kg/m^3 at this velocity since the flow of abrasive through the nozzle was restricted by the mechanical design of the mixing chamber.

2/ Specimen polishing to a 1 μm finish was carried out in accordance with DIN 50 332 [D3].

3/ The specimen was cleaned first in soapy water followed by treatment in a 10% isopropyl alcohol solution in an ultrasonic bath for 2 min. All specimens were then dried in an oven for 120 min at approximately 40°C. The nitrile rubber specimens could not be cleaned in the alcohol mixture since they reacted with the mixture so these samples were cleaned by ultrasound but by using water instead.

4/ The sample was weighed on an analytical scale. The balance had an accuracy of 0.01 mg.

5/ The sample was placed securely in the erosion tester ensuring the centre of the target was vertically beneath the axis of the nozzle. The target was secured in position using a partial vacuum provided by an ejector.

6/ The target specimen was subjected to particle impact at the desired concentration and velocity for a time such that the mass of abrasive that struck the target was not less than 250 g.

7/ The cleaning process adopted in section 3/ above was repeated. The mass loss from the target was assessed using the balance mentioned above.

8/ This process was repeated for subsequent samples.

4E.3 Details of the Comparative Test Programme

4E.3.1 Erosion Test Conditions

It has been widely reported in previous research literature that the erosion damage suffered by a material depends predominantly on the velocity of the particle impact. Power law curve fitting exercises have taken place where the value of the exponent has been seen to vary from 2 to 4.5 [H1,M9]. Since the value of this exponent is so variable, scaling for the effect of velocity from test results obtained from carrying out high velocity experiments is inaccurate. Therefore, the only way in which values for erosion damage at the particle velocities seen in pneumatic conveyors can be assessed, is by replicating these velocities in the test equipment being used. The particle velocities selected were 15, 25 and 35 m/s; it was felt that these accurately represented a suitable range of particle velocities comparable with those seen in pneumatic conveyors.

Reports suggest that erosion damage in pneumatic conveyors is be dependent on the concentration of particles in the flowing suspension [M1]. With a decrease in particle concentration for a given conveying velocity, there is an increased occurrence of erosion damage per unit of abrasive striking the target [M1]. The fact that erosion damage is affected by particle concentration can be explained by the mechanism of 'shielding' proposed by Andrews and Horsfield [A2]. The mechanism of 'shielding' is based upon the observation that inter-particulate collisions between incoming and rebounding particles cause more dispersed transfer of impinging energy to the eroding surface. As a result of this the quantity of erosion damage per unit mass of abrasive that occurs is decreased. Consequently, the particle concentrations that were selected for this test programme were commensurate with those seen in low particle concentration conveying. Particle concentrations of 1, 4 and 13 kg/m^3 were selected. 13 kg/m^3 was selected because it was the highest particle concentration density that could be simulated in the 'rotating disc accelerator' erosion tester at a velocity of 35 m/s. This was a consequence of a restriction to abrasive flow that occurred within the acceleration mechanism caused by spacial restrictions in the mechanical design. Because of the calibration tests described in Appendix 4C it was felt that an estimate of the effects of these particle concentrations at the impact point on the target surface should be obtained.

Two impingement angles were used during this test programme; 30° & 90°. These angles were selected on the basis of the fact that the tests were designed to compare the erosion testers, not provide a full curve for the erosion damage of the materials plotted against impingement angle. These angles were selected by following procedures carried out by many other researchers in the past. Also, in theory these two angles should show the different mechanisms of wear clearly, certainly this was expected to be true in the case of metallic materials.

4E.3.2 Erosion Test Materials

The abrasive particulate material used in this test programme was the olivine sand described in section 3.5. and Appendix 3A. A series of five target materials were used in this test programme. These were a fused ceramic (HITEC 100 alumina), a cast ceramic (cast basalt, Abresist), a metal (EN3B mild steel), an ultra high molecular weight polyethylene (UHMW PE) polymer (Tivar 100) and an elastomer (nitrile rubber). Each material selected represented a general class of materials that is or could be used in pneumatic conveyor pipe construction. Table 4E.1 gives more information on these materials.

Table 4E.1 Erosion Target Material Description.

Material Type	Cast Ceramic	Fused Ceramic	Metal	Elastomer	Polymer
Material Description	Cast Basalt	Fused Alumina	Mild Steel	Rubber	UHMW PE
Trade Name	Abresist	Hitec 100	EN3B	Nitrile Rubber	Tivar 100
Supplier	Kingfisher Ind. Services, Washford East, Redditch, Birmingham, UK.	Morgan Matroc Ltd, Stourport-on-Severn, Worchestershire, UK.	Outlook Metal Stockholders Ltd., Banstead, Surrey, UK.	Arco Holman Nichols Ltd, Orpington, Kent, UK	PoliHi Solidur UK Ltd., Todmorden, Lancashire, UK.
Density (g/cm^3).	2.8	3.73	7.8	0.86	0.94
Hardness (Rockwell).	79C	82C	50C	3.35 N/mm^2 Vickers	64R
Constituents	SiO_2 - 46% Al_2O_3 - 15% Fe_2O_3 - 12% CaO - 11% MgO - 8% K_2O/Na_2O - 6% TiO_2 - 2%	Al_2O_3 - 97% + FILLERS	080A15 specification C - 0.16% Si - 0.09% S - 0.005% P - 0.01% Mn - 0.7%	Butadiene Acrylo-nitrile Co-polymer + FILLERS	Virgin Cross Linked Ultra High Molecular Weight Polyethylene.
Yield Strength (N/mm^2).	30 (in bending)	320 (in bending)	430 (ultimate tensile)	5 (ultimate tensile)	28 (ultimate tensile)

To minimise the effects of experimental errors due to variation in the test materials all the materials were obtained from sources in the UK. They were then divided between the two test laboratories at random.

4E.4 Comparative Test Programme Results

Results are presented in the following two tables for the erosion damage in terms of cm^3/g, i.e. volume loss per unit mass of abrasive striking the target surface. Table 4E.2 contains the data obtained from the gas blast erosion tester, while Table 4E.3 contains the data obtained from the rotating disc accelerator erosion tester.

Table 4E.2 Erosion Results Obtained from the Gas Blast Erosion Tester

Target Material	Mean Mass of Abrasive Striking Target (kg)	Suspension Density (kg/m^3	Impact Angle (Degrees)	Impact Velocity (m/s)	Mean Mass Loss (g/kg)
EN3B	0.40250	1	90	15	0.01102
	0.46900	1	30	15	0.01296
	0.58000	4	90	25	0.01938
	0.63400	4	30	25	0.04710
	0.46700	9	90	35	0.03178
	0.50900	9	30	35	0.06010
UHMW PE	0.37700	1	90	15	-0.00098
	0.68400	1	30	15	0.00346
	0.61100	4	90	25	-0.00022
	0.52400	4	30	25	0.01010
	0.50000	9	90	35	0.00051
	0.55100	9	30	35	0.01830
Abresist	0.39500	1	90	15	0.09589
	0.51200	1	30	15	0.03029
	0.56600	4	90	25	0.14253
	0.50200	4	30	25	0.07970
	0.47200	9	90	35	0.22020
	0.63500	9	30	35	0.08070
Alumina	0.72000	1	90	15	0.00052
	0.73700	1	30	15	0.00149
	0.83900	4	90	25	0.00323
	0.64000	4	30	25	0.00016
	0.77400	9	90	35	0.00015
	0.75900	9	30	35	0.00108
Nitrile Rubber	0.53300	1	90	15	0.00279
	0.59800	1	30	15	0.00913
	0.61500	4	90	25	0.00290
	0.54800	4	30	25	0.00845
	0.51700	9	90	35	0.01150
	0.51900	9	30	35	0.01601

Table 4E.3 Erosion Results Obtained from the Rotating Disc Accelerator Erosion Tester

Test Conditions	Impact Angle (degrees)	Target Material	Cumulative Erosion Damage (g)									
Cumulative Time (mins)			15	30	45	75	105	150	195	255	315	375
15 m/s 1 kg/m^3	90	Alumina	-0.0001	0.0000	0.0003	0.0008	0.0012	0.0017	0 0021	0.0030	0.0040	0.0049
		Abresist	0.0041	0.0094	0.0144	0.0223	0.0299	0.0406	0.0506	0.0681	0.0796	-
		EN3B	-0.0003	-0.0003	-0.0002	0.0004	0.0009	0.0019	0.0029	0.0051	0.0067	0.0087
		UHMW PE	-0.0001	-0.0001	-0.0002	-0.0002	-0.0001	-0.0001	-0.0004	-0.0004	-0.0002	-0.0001
		Nitrile Rubber	0.0003	0.0012	0.0022	0.0035	0.0039	0.0062	0.0088	0.0099	0.0117	0.0157
Cumulative Time (mins)			15	45	90	150	210	270	330	390	450	510
15 m/s 1 kg/m^3	30	Alumina	0.0000	0.0000	0.0003	0.0004	0.0008	0.0010	0.0012	0.0014	0.0017	0.0017
		Abresist	0.0020	0.0046	0.0073	0.0106	0.0136	0.0162	0.0188	0.0213	0.0241	0.0263
		EN3B	0.0002	0.0005	0.0014	0.0027	0.0040	0.0053	0.0068	0.0082	0.0097	0.0111
		UHMW PE	0.0002	0.0003	0.0004	0.0003	0.0006	0.0007	0.0007	0.0008	0.0012	0.0011
		Nitrile Rubber	0.0001	0.0020	0.0036	0.0058	0.0076	0.0100	0.0121	0.0144	0.0157	0.0174
Cumulative Time (mins)			10	15	25	35	45	70	90	135	180	225
25 m/s 4 kg/m^3	90	Alumina	0.0002	0.0004	0.0007	0.0013	0.0021	0.0037	0.0050	0.0095	0.0121	0.0132
		Abresist	0.0259	0 0375	0.0553	0.0761	0.0992	-	-	-	-	-
		EN3B	0.0009	0.0020	0.0037	0.0060	0.0088	0.0145	0.0178	0.0308	-	-
		UHMW PE	-0.0003	-0.0003	-0.0003	-0.0004	-0.0005	-0.0002	-0.0006	-0.0005	-0.0004	-0.0004
		Nitrile Rubber	-	-	-	-	-0.0001	-	0.0007	0.0025	0.0042	0.0050
Cumulative Time (mins)			15	30	45	75	105	135	150	195	240	285
25 m/s 4 kg/m^3	30	Alumina	-0.0002	-0.0002	0.0000	0.0004	0.0009	-	0.0016	0.0022	0.0031	0.0042
		Abresist	0.0048	0.0093	0.0144	0.0276	0.0379	-	0.0530	0.0709	-	-
		EN3B	0.0007	0.0021	0.0044	0.0110	0.0162	-	0.0247	0.0346	-	-
		UHMW PE	0.0002	-0.0001	0.0007	0.0011	0.0031	0.0046	0.0040	0.0058	0.0073	0.0091
		Nitrile Rubber	0.0024	-	0.0046	-	0.0146	0.0181	-	0.0212	0.0259	-
Cumulative time (mins)			1.5	2.5	3.5	5	6	7	8.5	9.5	10.5	-
35 m/s 13 kg/m^3	90	Alumina	0.0006	0.0021	0.0037	0.0057	0.0075	0.0095	0.0120	0.0139	0.0158	-
		Abresist	0.0664	0.1120	0.1508	-	-	-	-	-	-	-
		EN3B	0.0065	0.0128	0.0181	0.0262	0.0322	0.0377	-	-	-	-
		UHMW PE	-0.0005	-0.0006	-0.0006	-0.0006	-0.0004	-0.0004	-0.0002	-0.0001	0.0000	-
		Nitrile Rubber	0.0024	0.0029	0.0043	0.0083	0.0114	0.0133	0.0163	0.0197	0.0219	-
Cumulative time (mins)			1	2.5	3.5	4.5	5.5	6.5	7.5	8.5	10	-
35 m/s 13 kg/m^3	30	Alumina	-0.0004	-0.0002	-0.0001	0.0003	0.0005	0.0011	0.0013	0 0016	0.0021	-
		Abresist	0.0079	0.0171	0.0229	0.0288	0.0345	0.0409	0.0464	-	-	-
		EN3B	0 0037	0 0103	0.0143	0.0188	0.0231	0.0275	0.0321	-	-	-
		UHMW PE	0.0006	0.0021	0.0031	0.0039	0.0050	0.0061	0.0071	-	-	-
		Nitrile Rubber	0.0040	0.0071	0.0108	0.0152	0.0187	0.0223	0.0264	-	-	-

Each result for the cumulative erosion damage is the mean of readings taken from three test samples.

Figure 4E.3 shows the results obtained for the erosion damage caused at 90° while Figure 4E.4 shows the results for erosion damage at 30°. Both figures show the results obtained from both test facilities.

4E.5 Observations and Discussion

The test results show that the two test facilities provide similar results for the trends in the erosion damage between the materials that have been tested. Use of the cast basalt (Abresist), and the UHMW PE (Tivar 100), in impact erosive wear situations is unusual. Performance of the basalt material was poor in comparison to the other materials tested, at both angles of impingement. This, it was thought, was due to the porous, fragile nature of the samples obtained. The performance of the UHMW PE targets at normal impact were good. However, this performance changed for the worse as more oblique angles of impingement occurred. The data suggests that the ceramic materials follow the trends in behaviour expected of brittle

Figure 4E.3 Collaborative test programme results at normal particle impingement.

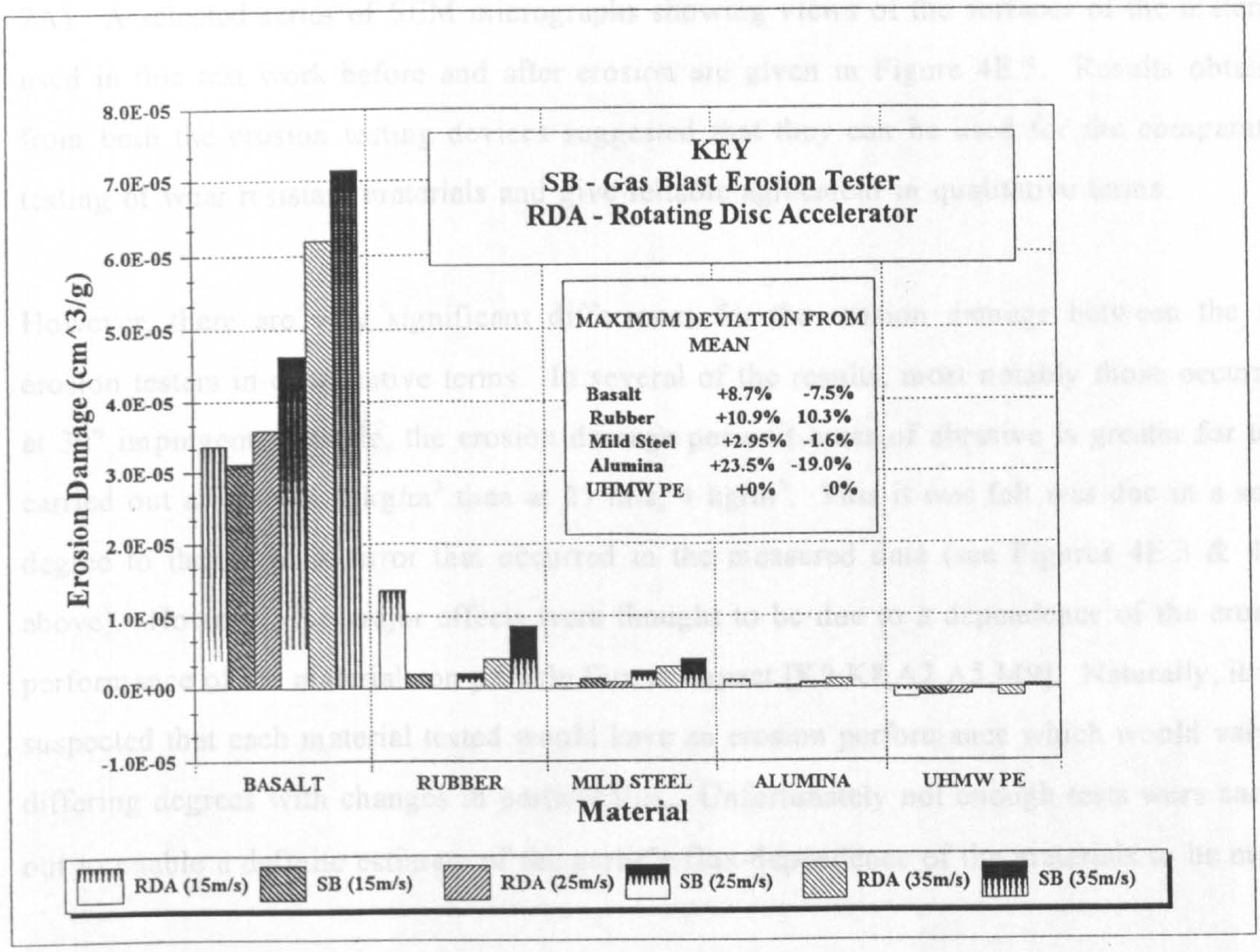

Figure 4E.4 Collaborative test programme results at 30° impingement angle.

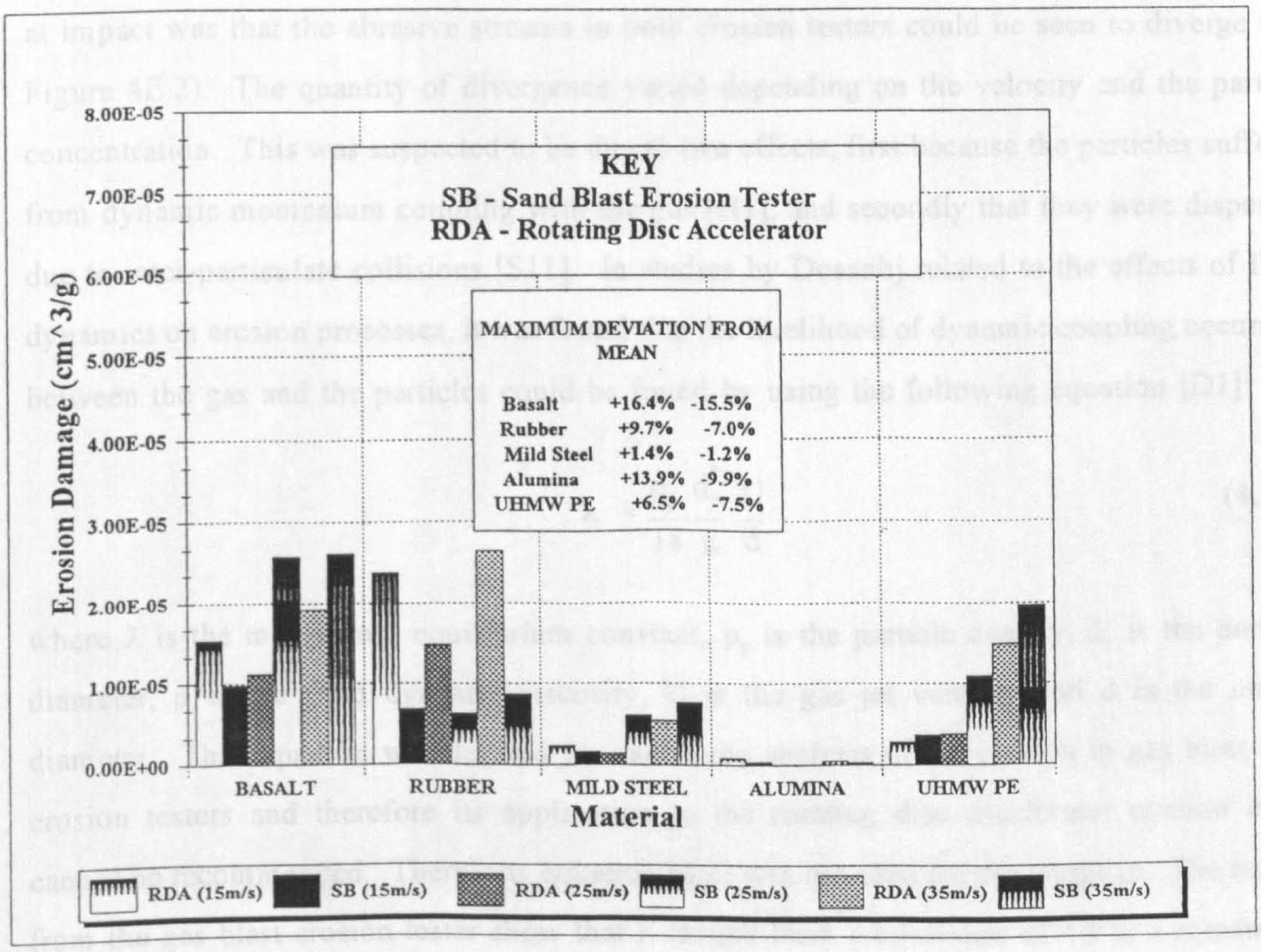

materials while the other materials show 'ductile' material trends [B11,B12] (see Appendix 2A). A selected series of SEM micrographs showing views of the surfaces of the materials used in this test work before and after erosion are given in Figure 4E.5. Results obtained from both the erosion testing devices suggested that they can be used for the comparative testing of wear resistant materials and give reliable agreement in qualitative terms.

However, there are very significant differences for the erosion damage between the two erosion testers in quantitative terms. In several of the results, most notably those occurring at 30° impingement angle, the erosion damage per unit mass of abrasive is greater for tests carried out at 15 m/s, 1 kg/m^3 than at 25 m/s, 4 kg/m^3. This it was felt was due in a small degree to the range of error that occurred in the measured data (see Figures 4E.3 & 4E.4 above). However, the major effects were thought to be due to a dependence of the erosion performance of the materials on particle flux at impact [K9,K8,A2,A5,M9]. Naturally, it was suspected that each material tested would have an erosion performance which would vary to differing degrees with changes in particle flux. Unfortunately not enough tests were carried out to enable a definite estimate of the particle-flux-dependence of the materials to be made.

The differences in the particle flux at impact would cause the energy imparted to the surface of the targets to vary considerably. The reason for the difficulty in assessing the particle flux at impact was that the abrasive streams in both erosion testers could be seen to diverge (see Figure 4E.2). The quantity of divergence varied depending on the velocity and the particle concentration. This was suspected to be due to two effects, first because the particles suffered from dynamic momentum coupling with the gas [H1], and secondly that they were dispersed due to inter-particulate collisions [S11]. In studies by Dosanhj related to the effects of fluid dynamics on erosion processes, it was found that the likelihood of dynamic coupling occurring between the gas and the particles could be found by using the following equation [D1]:

$$\lambda = \frac{\rho_p \, d_p^2}{18 \, \mu} \frac{U}{d} \qquad (4.1)$$

where λ is the momentum equilibrium constant, ρ_p is the particle density, d_p is the particle diameter, μ is the fluid dynamic viscosity, U is the gas jet velocity and d is the nozzle diameter. This equation was devised for use in the analysis of the erosion in gas blast type erosion testers and therefore its application to the rotating disc accelerator erosion tester cannot be recommended. Therefore, equation (4.1) was not used for this purpose. The results from the gas blast erosion tester show that λ ranged from a minimum of 4.8 to a maximum

4E.5 Micrographs illustrating some of the surfaces of the materials used in this test work before and after erosion.

STEEL - UNERODED

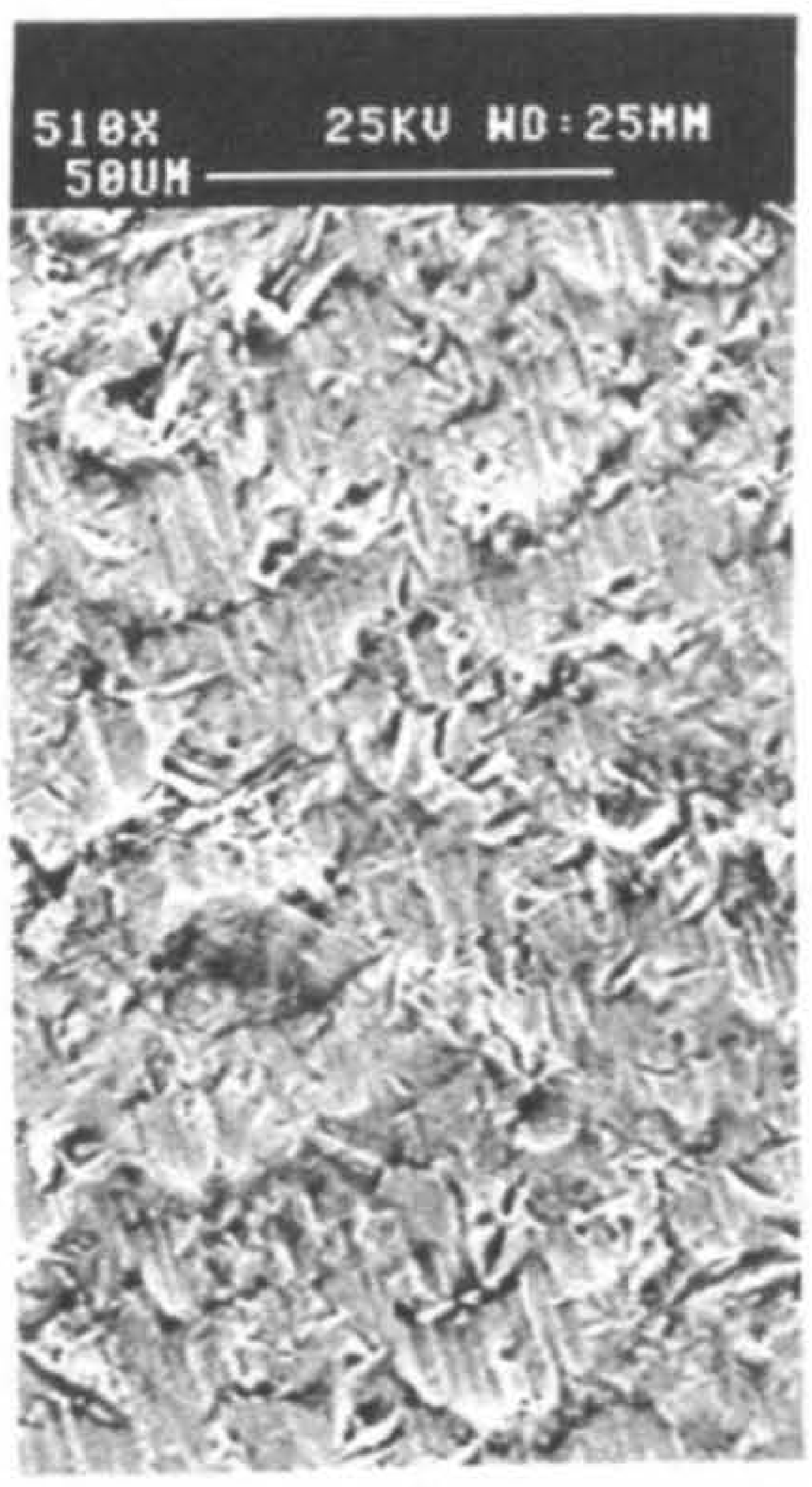

STEEL - 30°, 25.4 m/s & 4 kg/m^3

STEEL - 90°, 25.4 m/s & 4 kg/m^3

ALUMINA - UNERODED

ALUMINA - 30°, 25.4 m/s & 4 kg/m^3

ALUMINA - 90°, 25.4 m/s & 4 kg/m3

UHMW PE - UNERODED

UHMW PE - 30°, 25.4 m/s & 4 kg/m^3

UHMW PE - 90°, 25.4 m/s & 4 kg/m^3

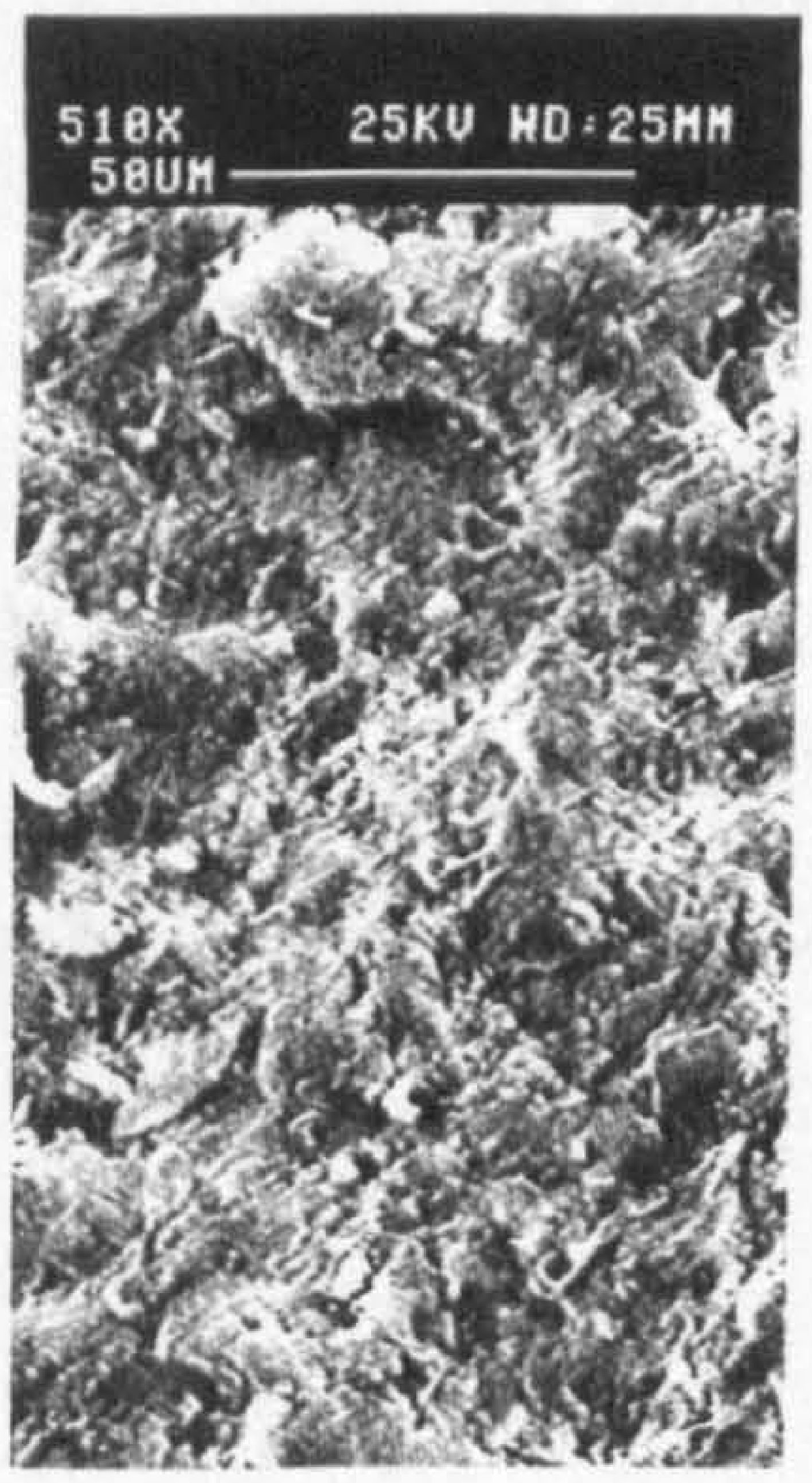

value of 124.6 for the conditions and particles used during the tests described in this work. It is stated by Dosanjh and Humphrey [D1] that if $\lambda > 10$ the particles are not affected by the gas flow around them to any degree. This was confirmed during the test work on the gas blast type erosion tester. In this rig none of the abrasive particles were seen to miss the targets completely, even during tests at 30° impact angle. Since an identical abrasive was used at similar velocities in the rotating disc accelerator it was felt that the behaviour of the particle stream would be similar.

It was concluded that the particle jet dispersion could only have been caused by inter-particulate collisions within the jet. McClusky [M10] showed the likely dispersion of particle jets being injected into gas flows, by carrying out particle image velocimetry measurement of the emerging abrasive jet from a nozzle placed concentrically in a pipe bore through which a gas was flowing. By deriving empirical equations from the experimental results presented in McClusky's work equation 4.1 section 4.2.3.5 Chapter 4 was generated. Table 4E.4 overleaf shows the results of using this equation. In subsequent examination of the erosion targets, the wear scar area profiles seen in both forms of erosion tester could be seen to be very close to those calculated using equation 4.1 section 4.2.3.5 Chapter 4. Further investigation into the divergence of the particle jet is obviously necessary for a thorough examination of the erosion phenomena to be undertaken.

It is therefore suggested that investigation of the following areas of the operation of erosion testers should be undertaken.

a) It was possible that the dispersion of the abrasive jet was not one that resulted in a homogeneous flow of particles; measurement of the concentration of the particles across the profile of the diverging jet at various distances needs to be carried out.

b) It was thought possible that the smaller particles could migrate away from the axis of the jet more than the larger particles. This suggested particle behaviour was a consequence of the ability of the small particles to be more significantly affected by the gas motion. This would lead to a variation in the flux of impinging kinetic energy across the erosion scar area, which in turn would lead to a distribution in the erosion damage caused.

Table 4E.4 The Results of Particle Flux and Inter-Particulate Distance Calculations.

Intended Velocity (m/s)	Intended Particle Concentration (kg/m^3)	Desired Mass Flux (kg/m^{2}s)	Mean Mass Flux (kg/m^{2}s) eqn. 4.2 section 4.2.3.5 Chapter 4		Divergence of Jet Radius at Impact (mm) eqn. 4.1 section 4.2.3.5 Chapter 4	Inter-particulate Distance (No. of Particle Diameters) eqn. 4.4 section 4.2.3.5 Chapter 4	
			At Nozzle	At Impact		At Nozzle	At Impact
FOR THE ROTATING DISC ACCELERATOR EROSION TESTER							
15	1	15.71	44.9	6.1	2.22	4.64	9.03
25	4	101.6	303.2	29.6	2.86	2.89	6.27
35	13	457.6	3298.1	241.9	3.50	1.45	3.47
FOR THE GAS BLAST EROSION TESTER							
15	1	15	9.4	1.0	3.21	13.99	29.14
25	4	100	94.3	7.3	4.09	7.70	18.06
35	8	280	282.9	16.2	4.97	5.97	15.50

c) To obtain a given velocity of impact between the abrasive particles and the target, the nozzle velocity of the gas flow needs to be varied. This results in a change in the particle flux at the impact surface. Consequently, expression of concentration in kg particles / kg gas may not be a satisfactory variable to use in the comparative evaluation of the two testers. During these tests the gas blast form of erosion tester has an air velocity at the exit from the nozzle approximately 2.7 times that of the particles. In the rotating disc accelerator the predictive model suggests that the gas accelerates, (due to the drag force acting upon the moving particles), and the gas velocity is therefore only 0.15 times the particle velocity at a maximum (see Appendix 4B). The motion of the gas in the two testers could therefore be quite different, and may cause the emerging jet of particles to diverge differently. This would depend again on the amount of momentum coupling between the particles and the gas.

Using the equation proposed by Shipway and Hutchings [S11] for the average distance between particles, (equation 4.4 section 4.2.3.5 Chapter 4 and Appendix 4B), an indication of the likelihood of inter-particulate collisions occurring can be surmised. Shipway and

Hutchings also suggested that particle streams could be seen to diverge once the mass flux of particles exceeded 1 kg/m^2s, for tests carried out at velocities of 30 and 45 m/s for two different size ranges of glass beads. It was concluded that if the distance between the particles was less than 10 mean particle diameters, particle collisions were likely to occur, whereas the opposite was the case for inter-particulate distances greater than 10 particle diameters.

The results of the particle flux analysis are shown in Table 4E.4 above. They show that the efforts made in the use of the rotating disc accelerator erosion tester to compensate for the divergence of the jet were not sufficiently effective to achieve a close comparison with the desired set point values selected. The results show, therefore, that in both testing facilities, the divergence of the abrasive jet was most likely to be caused by inter-particulate collisions at the exit from the accelerating nozzles. The particle mass flux at impact for the rotating disc accelerator was on average approximately 40% of that intended while with the gas blast type of erosion tester it was 7%. The much lower value for the gas blast rig was due to maintaining a similar distance between the nozzle exit and the impact point (22.5 mm) to that in the rotating disc accelerator rig. In future comparisons, achieving particle flux similarity at impact for the two testers, in conjunction with velocity similarity, should be the primary goal.

It can be seen from the results presented in Figures 4E.3 and 4E.4 above that the erosion performance of the materials used in this test programme are affected to different degrees by the particle flux at impact. When the particle flux at impact is reduced, the amount of erosion damage per unit mass of abrasive striking the target increases. This, it is suggested, can only be due to the effects of particle flux at impact and the dispersion of any incident energy by the occurrence of inter-particulate collisions as proposed by Andrews and Horsfield [A2].

There were small differences in the manner in which the targets were treated during the cleaning stage of the test procedure. The use of the ultrasonic cleaning device lead to an increase in the mass loss measurements obtained for the targets by a maximum of 5%. The differences in the method of cleaning the targets had a most significant effect in the comparison between the erosion results for the rubber material. In this case the same trends were indicated but a consistently greater magnitude of erosion was observed for the rotating disc accelerator erosion tester. However, it was felt that the effect of differences in the mass flux at the impact site was by far the overriding reason for the large differences seen in the results for the two testing facilities.

The wear scar depth could lead to the particles of abrasive striking the surface of the targets at angles different from those intended. This may have an effect on the progress of the erosion with time as described recently by Finnie *et al.* [F3]. It was therefore essential that the erosion measurements were taken when the erosion damage had reached steady state conditions, but before the depth of the wear scar became too great. This was less of a problem with the rotating disc accelerator than the gas blast erosion tester since the method of processing the experimental data for this machine relied upon the measurement of erosion over a range of exposure times. Consequently, any changes away from the steady state erosion conditions could be seen readily. Detailed experience in the operation of the gas blast erosion tester was required to ensure that this condition was met.

The operational envelope of the rotating disc accelerator erosion tester was not exceeded by the initial conditions that were required for this test programme. However, since the abrasive jet divergence was such that the particle mass flux over the impact area was significantly less than that originally wanted, the new mass flow rate of abrasive into the rig necessary to make good this deficit may choke the abrasive feed system on the rig as it was used in this programme. The problems of ensuring adequate feed of the abrasive into the gas blast erosion tester for this test programme exceeded the capability of the rig as it was from the outset. It is possible to bring the targets closer to the nozzle exit in this rig. This would lead to a reduction in the area of impact on the target surface and therefore an increase in the particle flux. Such a modification would aid in increasing the particle flux at impact.

If the particle mass flux at impact has an effect as great as that seen in the test results presented above, models for predicting erosion damage by particle impact that omit this variable [S3,E1] can never be accurate. The results presented above suggest that some materials have erosion damage resistances that are more dependent on particle mass flux than others. More work will need to be carried out to substantiate to what extent this is true.

Appendix 4F: Mild Steel Test Programme Results

4F.1 Introduction

This appendix contains information related to tests carried out on the mild steel samples using the rotating disc accelerator erosion tester.

This appendix consists of three parts:-

- First, tables of mass loss results obtained from testing mild steel samples in the rotating disc accelerator erosion tester are given. These are shown on pages 4F.2, for the results obtained at a particle impact velocity of 15 m/s; 4F.3, for results obtained at 25 m/s and 4F.4, for results obtained at 35 m/s.
- Secondly, a copy of the MathCad program that was used to process the mass loss measurements is given. The erosion rate determined by this program is described in terms of the volume loss per unit mass of abrasive striking the target surface.
- Finally, the final results for the erosion rate in graphs of the volume lost from the target per unit mass of abrasive material striking the target surface versus angle of particle impingement are given. Page 4F.10 contains the graphs pertaining to erosion results obtained at a particle impact velocity of 15 m/s; 4F.11 contains the graphs that are relevant to erosion at an impact velocity of 25 m/s, and finally, 4F.12, contains the graphs for erosion at 35 m/s.

Target Mass Loss for Samples Eroded at a Particle Velocity of 15 m/s

Suspension Density (kg/m^3):-	**1**
Particle Velocity (m/s):-	**15**

Particle Impingement Angle (degrees).	**Target Removal Time (mins)**								
	77.0	**180.9**	**140.8**	**204.5**	**332.0**	**587.0**	**834.3**	**1576.0**	**2565.0**
8.1	-	-	-	-	0.0029	0.0056	0.0085	0.0162	0.0259
8.1	-	-	-	-	0.0024	0.0052	0.0079	0.0150	0.0246
8.1	-	-	-	-	0.0027	0.0054	0.0081	0.0158	0.0254
13.6	-	-	0.0014	0.0025	0.0042	0.0080	0.0123	-	-
13.6	-	-	0.0013	0.0023	0.0040	0.0076	0.0115	-	-
13.6	-	-	0.0012	0.0021	0.0035	0.0066	0.0100	-	-
24.3	-	0.0010	0.0016	0.0030	0.0054	0.0110	-	-	-
24.3	-	0.0011	0.0018	0.0033	0.0057	0.0115	-	-	-
40.1	0.0008	0.0015	0.0023	0.0041	0.0077	-	-	-	-
61.2	0.0006	0.0013	0.0023	0.0042	0.0085	-	-	-	-

Suspension Density (kg/m^3):-	**4**
Particle Velocity (m/s):-	**15**

Particle Impingement Angle (degrees).	**Target Removal Time (mins)**								
	19.0	**27.0**	**35.0**	**51.0**	**83.0**	**147.0**	**208.8**	**394.0**	**641.0**
8.0	-	-	-	-	0.0023	0.0045	0.0067	0.0126	0.0204
8.0	-	-	-	-	0.0018	0.0041	0.0060	0.0119	0.0196
8.0	-	-	-	-	0.0021	0.0042	0.0062	0.0118	0.0192
13.5	-	-	0.0010	0.0015	0.0028	0.0057	0.0085	-	-
13.5	-	-	0.0011	0.0018	0.0030	0.0056	0.0081	-	-
13.5	-	-	0.0008	0.0015	0.0029	0.0057	0.0086	-	-
13.5	-	0.0010	0.0013	0.0022	0.0038	0.0075	-	-	-
24.2	-	0.0011	0.0015	0.0023	0.0041	0.0079	-	-	-
40.0	0.0004	0.0011	0.0017	0.0026	0.0049	-	-	-	-
61.1	-0.0002	0.0004	0.0011	0.0022	0.0044	-	-	-	-

Suspension Density (kg/m^3):-	**13**
Particle Velocity (m/s):-	**15**

Particle Impingement Angle (degrees).	**Target Removal Time (mins)**								
	5.0	**7.5**	**10.0**	**15.0**	**25.0**	**45.0**	**64.0**	**121.0**	**197.0**
7.9	-	-	-	-	0.0023	0.0046	0.0070	0.0129	0.0198
7.9	-	-	-	-	0.0019	0.0041	0.0061	0.0116	0.0178
7.9	-	-	-	-	0.0019	0.0038	0.0059	0.0110	0.0170
13.4	-	-	0.0007	0.0016	0.0027	0.0055	0.0082	-	-
13.4	-	-	0.0006	0.0013	0.0026	0.0052	0.0078	-	-
13.4	-	-	0.0009	0.0017	0.0032	0.0061	0.0089	-	-
24.1	-	0.0004	0.0009	0.0018	0.0035	0.0070	-	-	-
24.1	-	0.0008	0.0014	0.0023	0.0039	0.0074	-	-	-
40.0	0.0003	0.0006	0.0012	0.0023	0.0045	-	-	-	-
61.0	-0.0002	0.0003	0.0010	0.0020	0.0043	-	-	-	-

Target Mass Loss for Samples Eroded at a Particle Velocity of 25 m/s

Suspension Density (kg/m^	1
Particle Velocity (m/s):-	25

Particle Impingement	Target Removal Time (mins)								
Angle (degrees).	34.0	48.4	62.9	91.8	149.5	265.0	378.9	720.5	1176.0
7.9	-	-	-	-	0.0062	0.0118	0.0173	0.0351	0.0579
7.9	-	-	-	-	0.0067	0.0127	0.0185	0.0375	0.0642
7.9	-	-	-	-	0.0059	0.0112	0.0168	0.0344	0.0600
18.8	-	-	0.0051	0.0079	0.0138	0.0257	0.0378	-	-
18.8	-	-	0.0045	0.0071	0.0122	0.0226	0.0335	-	-
18.8	-	-	0.0037	0.0057	0.0098	0.0183	0.0268	-	-
24.1	-	0.0044	0.0061	0.0092	0.0159	0.0294	-	-	-
24.1	-	0.0046	0.0065	0.0098	0.0167	0.0309	-	-	-
40.0	0.0046	0.0073	0.0100	0.0154	0.0263	-	-	-	-
61.0	0.0054	0.0086	0.0119	0.0181	0.0314	-	-	-	-

Suspension Density (kg/m^	4
Particle Velocity (m/s):-	25

Particle Impingement	Target Removal Time (mins)								
Angle (degrees).	8.0	11.6	15.3	22.5	37.0	66.0	94.5	180.0	294.0
7.8	-	-	-	-	0.0069	0.0131	0.0189	0.0362	0.0562
7.8	-	-	-	-	0.0065	0.0120	0.0174	0.0334	0.0518
7.8	-	-	-	-	0.0058	0.0107	0.0156	0.0307	0.0481
18.8	-	-	0.0046	0.0073	0.0126	0.0228	0.0331	-	-
18.8	-	-	0.0043	0.0067	0.0112	0.0207	0.0301	-	-
18.8	-	-	0.0043	0.0069	0.0115	0.0211	0.0305	-	-
24.1	-	0.0041	0.0057	0.0085	0.0144	0.0264	-	-	-
24.1	-	0.0040	0.0058	0.0087	0.0150	0.0276	-	-	-
39.9	0.0037	0.0059	0.0079	0.0123	0.0210	-	-	-	-
61.0	0.0038	0.0062	0.0088	0.0138	0.0238	-	-	-	-

Suspension Density (kg/m^	13
Particle Velocity (m/s):-	25

Particle Impingement	Target Removal Time (mins)								
Angle (degrees).	2.0	3.1	4.3	6.5	11.0	20.0	28.8	55.0	90.0
7.8	-	-	-	-	0.0065	0.0115	0.0153	0.0278	0.0435
7.8	-	-	-	-	0.0066	0.0121	0.0165	0.0307	0.0487
7.8	-	-	-	-	0.0064	0.0118	0.0159	0.0294	0.0464
18.7	-	-	0.0044	0.0072	0.0116	0.0212	0.0290	-	-
18.7	-	-	0.0041	0.0066	0.0109	0.0199	0.0275	-	-
18.7	-	-	0.0044	0.0070	0.0113	0.0208	0.0284	-	-
24.0	-	0.0036	0.0053	0.0083	0.0134	0.0242	-	-	-
24.0	-	0.0032	0.0051	0.0082	0.0131	0.0241	-	-	-
39.9	0.0023	0.0044	0.0067	0.0107	0.0174	-	-	-	-
60.9	0.0018	0.0038	0.0063	0.0103	0.0170	-	-	-	-

Target Mass Loss for Samples Eroded at a Particle Velocity of 35 m/s

Suspension Density (kg/m^3):-	1
Particle Velocity (m/s):-	35

Particle Impingement Angle (degrees).	Target Removal Time (mins)								
	18.0	25.9	33.8	49.5	81.0	144.0	206.6	394.5	645.0
7.7	-	-	-	-	0.0232	0.0418	0.0614	0.1226	-
7.7	-	-	-	-	0.0251	0.0454	0.0661	0.1298	-
7.7	-	-	-	-	0.0370	0.0671	0.0891	-	-
13.2	-	-	0.0143	0.0222	0.0377	0.0675	0.1003	-	-
13.2	-	-	0.0132	0.0201	0.0339	0.0605	0.0886	-	-
13.2	-	-	0.0146	0.0224	0.0380	0.0183	0.0979	-	-
24.0	-	0.0157	0.0211	0.0324	0.0550	0.0294	-	-	-
24.0	-	0.0166	0.0226	0.0345	0.0587	0.0309	-	-	-
39.8	0.0158	0.0241	0.0323	0.0498	0.0850	-	-	-	-
60.9	0.0184	0.0277	0.0376	0.0584	0.1000	-	-	-	-

Suspension Density (kg/m^3):-	4
Particle Velocity (m/s):-	35

Particle Impingement Angle (degrees).	Target Removal Time (mins)								
	2.4	3.6	4.8	7.2	12.0	21.6	31.0	59.1	96.6
7.7	-	-	-	-	0.0096	0.0180	0.0256	0.0521	0.0864
7.7	-	-	-	-	0.0090	0.0167	0.0241	0.0479	0.0806
7.7	-	-	-	-	0.0099	0.0186	0.0256	0.0487	0.0826
18.6	-	-	0.0071	0.0113	0.0191	0.0348	0.0499	-	-
18.6	-	-	0.0071	0.0113	0.0191	0.0350	0.0500	-	-
18.6	-	-	0.0076	0.0122	0.0204	0.0378	0.0520	-	-
23.9	-	0.0062	0.0087	0.0136	0.0225	0.0412	-	-	-
23.9	-	0.0064	0.0088	0.0140	0.0233	0.0423	-	-	-
39.8	0.0059	0.0092	0.0125	0.0194	0.0325	-	-	-	-
60.8	0.0062	0.0099	0.0137	0.0215	0.0367	-	-	-	-

Suspension Density (kg/m^3):-	8
Particle Velocity (m/s):-	35

Particle Impingement Angle (degrees).	Target Removal Time (mins)								
	1.2	1.8	2.4	3.6	6.0	10.8	15.5	29.7	48.6
7.7	-	-	-	-	0.0101	0.0174	0.0245	0.0442	0.0725
7.7	-	-	-	-	0.0112	0.0189	0.0262	0.0472	0.0775
7.7	-	-	-	-	0.0100	0.0171	0.0242	0.0439	0.0722
18.6	-	-	0.0076	0.0114	0.0188	0.0320	0.0449	-	-
18.6	-	-	0.0077	0.0119	0.0198	0.0334	0.0469	-	-
18.6	-	-	0.0072	0.0114	0.0188	0.0330	0.0470	-	-
23.9	-	0.0070	0.0098	0.0151	0.0250	0.0434	-	-	-
23.9	-	0.0065	0.0093	0.0141	0.0236	0.0410	-	-	-
39.8	0.0051	0.0088	0.0124	0.0187	0.0312	-	-	-	-
60.8	0.0053	0.0094	0.0134	0.0204	0.0344	-	-	-	-

RESULTS FROM THE MAIN STEEL TEST PROGRAMME:- Results obtained from all tests at 25 m/s on BS43 Series C Mild Steel Pipe Segments with Renova Olivine Sand.

Density of Steel was taken to be:- $\rho_s := 7860 \cdot \frac{kg}{m^3}$

Fixed Mass of Striking Abrasive:- $FM := 0.70 \cdot kg$

Volume Loss Per Mass of Abrasive Striking Target:

Results at a Suspension Density Simulation of 4kg/m³.

$$R25\_4 := \begin{bmatrix} 8.0 & 11.6 & 15.3 & 22.5 & 37.0 & 66.0 & 94.5 & 180.0 & 294.0 \\ 0 & 0 & 0 & 0 & 0.0069 & 0.0131 & 0.0189 & 0.0362 & 0.0562 \\ 0 & 0 & 0 & 0 & 0.0065 & 0.0120 & 0.0174 & 0.0334 & 0.0518 \\ 0 & 0 & 0 & 0 & 0.0058 & 0.0107 & 0.0156 & 0.0307 & 0.0481 \\ 0 & 0 & 0.0046 & 0.0073 & 0.0126 & 0.0228 & 0.0331 & 0 & 0 \\ 0 & 0 & 0.0043 & 0.0067 & 0.0112 & 0.0207 & 0.0301 & 0 & 0 \\ 0 & 0 & 0.0043 & 0.0069 & 0.0115 & 0.0211 & 0.0305 & 0 & 0 \\ 0 & 0.0041 & 0.0057 & 0.0085 & 0.0144 & 0.0264 & 0 & 0 & 0 \\ 0 & 0.0040 & 0.0058 & 0.0087 & 0.0150 & 0.0276 & 0 & 0 & 0 \\ 0.0037 & 0.0059 & 0.0079 & 0.0123 & 0.0210 & 0 & 0 & 0 & 0 \\ 0.0038 & 0.0062 & 0.0088 & 0.0138 & 0.0238 & 0 & 0 & 0 & 0 \end{bmatrix} \qquad RT25\_4 := R25\_4^{T}$$

Conversion of Mass Loss Results to Volume Loss Values:-

$$R10_{25\_4} := \frac{RT25\_4^{\langle 1\rangle} + RT25\_4^{\langle 2\rangle} + RT25\_4^{\langle 3\rangle}}{3} \cdot 10^{-3} \cdot kg \qquad V10_{25\_4} := \frac{R10_{25\_4}}{\rho_s}$$

$$R20_{25\_4} := \frac{RT25\_4^{\langle 4\rangle} + RT25\_4^{\langle 5\rangle} + RT25\_4^{\langle 6\rangle}}{3} \cdot 10^{-3} \cdot kg \qquad V20_{25\_4} := \frac{R20_{25\_4}}{\rho_s}$$

$$R30_{25\_4} := \frac{RT25\_4^{\langle 7\rangle} + RT25\_4^{\langle 8\rangle}}{2} \cdot 10^{-3} \cdot kg \qquad V30_{25\_4} := \frac{R30_{25\_4}}{\rho_s}$$

$$R45_{25\_4} := RT25\_4^{\langle 9\rangle} \cdot 10^{-3} \cdot kg \qquad V45_{25\_4} := \frac{R45_{25\_4}}{\rho_s}$$

$$R65_{25\_4} := RT25\_4^{\langle 10\rangle} \cdot 10^{-3} \cdot kg \qquad V65_{25\_4} := \frac{R65_{25\_4}}{\rho_s}$$

Separation of the Time Matrix:-

$Tim := RT25\_4^{\langle 0\rangle} \cdot min$

Specification of the General Counter for Results:-

$Q := 0, 1 .. 4$

Manipulation of the Time and Volume Loss Results to Achieve a Match:-

For 10°:- $i := 4, 5 .. 8$ $\quad Vr10_{25\_4_{(i-4)}} := V10_{25\_4_i}$ $\quad T10_{25\_4_{(i-4)}} := Tim_i$ $\quad M10_{min} := 0.0031 \cdot \frac{kg}{min}$

For 20°:- $j := 2,3..6$ $Vr20_{25\_4_{(j-2)}} := V20_{25\_4_j}$ $T20_{25\_4_{(j-2)}} := Tim_j$ $M20_{min} := 0.0076\cdot\frac{kg}{min}$

For 30°:- $k := 1,2..5$ $Vr30_{25\_4_{(k-1)}} := V30_{25\_4_k}$ $T30_{25\_4_{(k-1)}} := Tim_k$ $M30_{min} := 0.0098\cdot\frac{kg}{min}$

For 45°:- $l := 0,1..4$ $Vr45_{25\_4_l} := V45_{25\_4_l}$ $T45_{25\_4_l} := Tim_l$ $M45_{min} := 0.0160\cdot\frac{kg}{min}$

For 65°:- $l := 0,1..4$ $Vr65_{25\_4_l} := V65_{25\_4_l}$ $T65_{25\_4_l} := Tim_l$ $M65_{min} := 0.0227\cdot\frac{kg}{min}$

Determination of the Erosion Rate in terms of Volume Loss per Mass of Abrasive Striking:-

For 10°:- $ER10_{25\_4} := \overrightarrow{\frac{Vr10_{25\_4}}{T10_{25\_4}\cdot M10_{min}}}$ For 45°:- $ER45_{25\_4} := \overrightarrow{\frac{Vr45_{25\_4}}{T45_{25\_4}\cdot M45_{min}}}$

For 20°:- $ER20_{25\_4} := \overrightarrow{\frac{Vr20_{25\_4}}{T20_{25\_4}\cdot M20_{min}}}$ For 65°:- $ER65_{25\_4} := \overrightarrow{\frac{Vr65_{25\_4}}{T65_{25\_4}\cdot M65_{min}}}$

For 30°:- $ER30_{25\_4} := \overrightarrow{\frac{Vr30_{25\_4}}{T30_{25\_4}\cdot M30_{min}}}$

Determination of the Time at which a Fixed Mass of Abrasive has Struck each Target:-

$Tsel10 := \frac{FM}{M10_{min}}$ $Tsel20 := \frac{FM}{M20_{min}}$ $Tsel30 := \frac{FM}{M30_{min}}$

$Tsel45 := \frac{FM}{M45_{min}}$ $Tsel65 := \frac{FM}{M65_{min}}$

$Tsel10 = 2.2581\cdot10^{2}\cdot min$ $Tsel30 = 71.4286\cdot min$ $Tsel65 = 30.8370\cdot min$

$Tsel20 = 92.1053\cdot min$ $Tsel45 = 43.7500\cdot min$

Formation of the Cubic Spline Fits to the Erosion Rate Data:-

$vxi := T10_{25\_4}$ $vyi := ER10_{25\_4}$ $vsi := lspline(vxi, vyi)$ $xi := 37\cdot min, 38\cdot min..294\cdot min$

$vxj := T20_{25\_4}$ $vyj := ER20_{25\_4}$ $vsj := lspline(vxj, vyj)$ $xj := 15\cdot min, 16\cdot min..95\cdot min$

$vxk := T30_{25\_4}$ $vyk := ER30_{25\_4}$ $vsk := lspline(vxk, vyk)$ $xk := 11\cdot min, 12\cdot min..66\cdot min$

$vxl := T45_{25\_4}$ $vyl := ER45_{25\_4}$ $vsl := lspline(vxl, vyl)$ $xl := 8\cdot min, 9\cdot min..37\cdot min$

$vxm := T65_{25\_4}$ $vym := ER65_{25\_4}$ $vsm := lspline(vxm, vym)$ $xm := 8\cdot min, 9\cdot min..37\cdot min$

Interpolation for Erosion Data Results for a Fixed Mass of Abrasive:-

$EDP10_{25\_4} := interp(vsi, vxi, vyi, Tsel10)$ $EDP10_{25\_4} = 7.5389\cdot\frac{mm^3}{kg}$

$EDP20_{25\_4} := interp(vsj, vxj, vyj, Tsel20)$ $EDP20_{25\_4} = 5.5304\cdot\frac{mm^3}{kg}$

$EDP30_{25\_4} := interp(vsk, vxk, vyk, Tsel30)$ $EDP30_{25\_4} = 5.3053\cdot\frac{mm^3}{kg}$

$EDP45_{25\_4} := interp(vsl, vxl, vyl, Tsel45)$ $EDP45_{25\_4} = 4.5243\cdot\frac{mm^3}{kg}$

$\mathrm{EDP65}_{25\_4} := \mathrm{interp}(\mathrm{vsm},\mathrm{vxm},\mathrm{vym},\mathrm{Tsel65})$ $\mathrm{EDP65}_{25\_4} = 3.5516 \cdot \frac{\mathrm{mm}^3}{\mathrm{kg}}$

Graphs of the Data in Various Formats:-

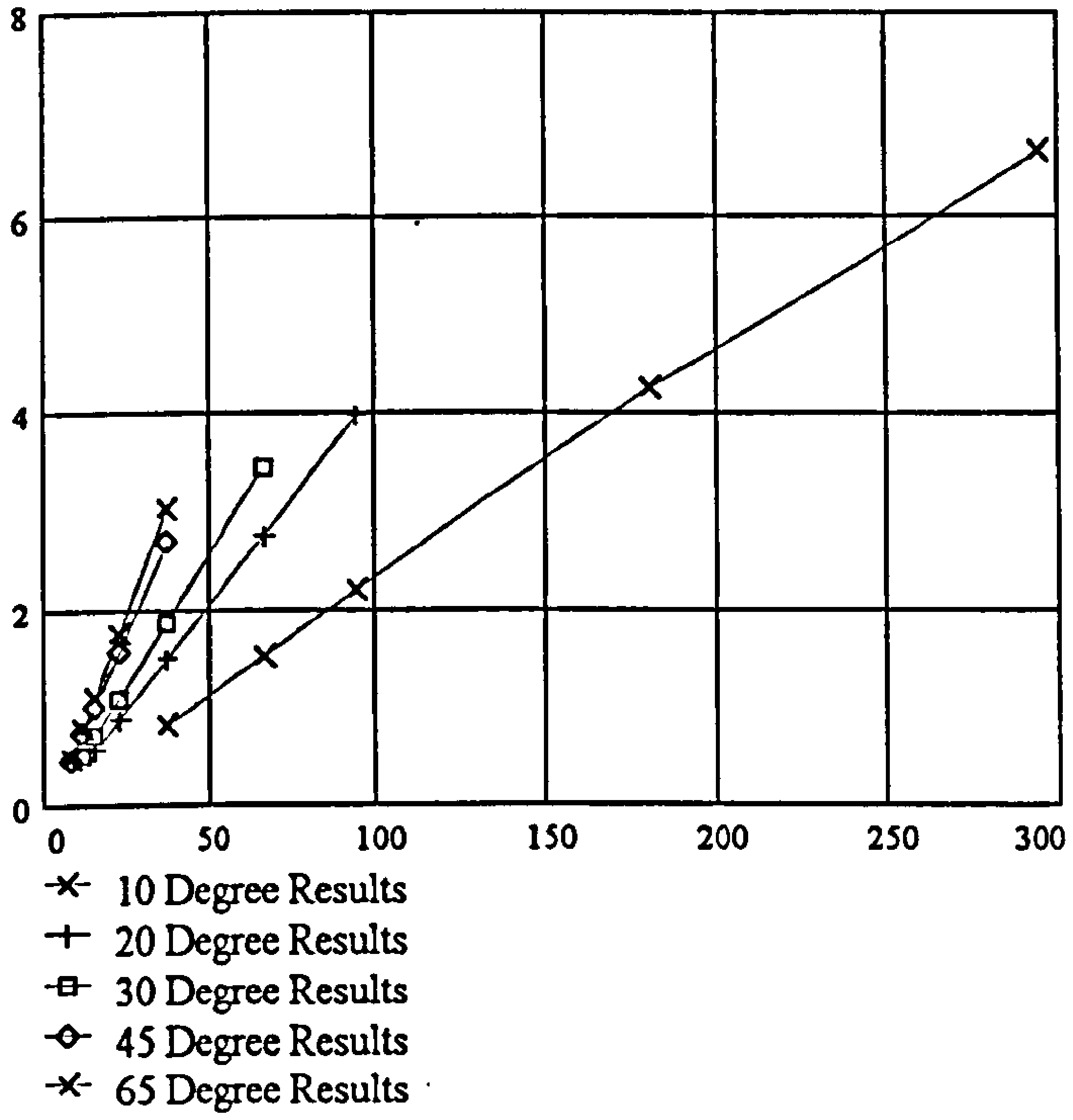

Graph of the Volume Loss Plotted Against Time (mm³ versus mins).

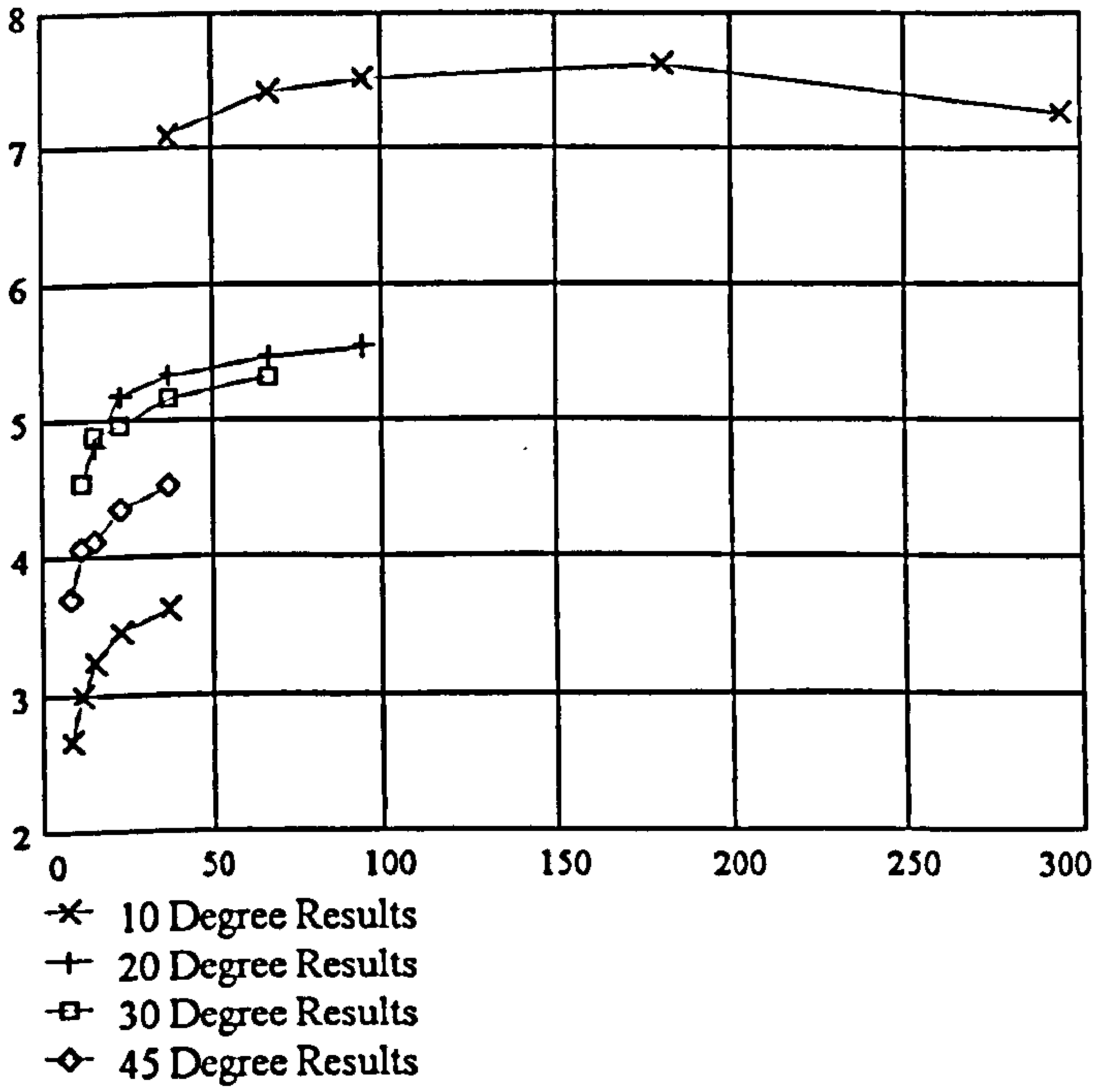

Graph of Erosion Rate Versus Time (mm³/kg versus min).

Sorting to Find a Maximum and Minimum Value for the Data Sets at the Low Angles:-

For 10°:-

$\mathrm{Ra10}_{25\_4} := \mathrm{augment}\left(\mathrm{RT25\_4}^{<1>},\mathrm{augment}\left(\mathrm{RT25\_4}^{<2>},\mathrm{RT25\_4}^{<3>}\right)\right)^{T}$

$Rb10_{25\_4} := \mathrm{csort}\left(Ra10_{25\_4}, 4\right)^{T}$ $Rmax10_{25\_4} := Rb10_{25\_4}{}^{<2>}$ $Rmin10_{25\_4} := Rb10_{25\_4}{}^{<0>}$

For 20°:-

$Ra20_{25\_4} := \mathrm{augment}\left(RT25\_4^{<4>}, \mathrm{augment}\left(RT25\_4^{<5>}, RT25\_4^{<6>}\right)\right)^{T}$

$Rb20_{25\_4} := \mathrm{csort}\left(Ra20_{25\_4}, 2\right)^{T}$ $Rmax20_{25\_4} := Rb20_{25\_4}{}^{<2>}$ $Rmin20_{25\_4} := Rb20_{25\_4}{}^{<0>}$

For 30°:-

$Ra20_{25\_4} := \left(\mathrm{augment}\left(RT25\_4^{<7>}, RT25\_4^{<8>}\right)\right)^{T}$

$Rb30_{25\_4} := \mathrm{csort}\left(Ra20_{25\_4}, 2\right)^{T}$ $Rmax30_{25\_4} := Rb30_{25\_4}{}^{<1>}$ $Rmin30_{25\_4} := Rb30_{25\_4}{}^{<0>}$

Conversion of Maximum and Minimum Mass Loss Results into Volume Loss Values:-

$$Vx10_{25\_4} := \frac{Rmax10_{25\_4} \cdot 10^{-3}}{\rho_s} \cdot kg \qquad Vm10_{25\_4} := \frac{Rmin10_{25\_4} \cdot 10^{-3}}{\rho_s} \cdot kg$$

$$Vx20_{25\_4} := \frac{Rmax20_{25\_4} \cdot 10^{-3}}{\rho_s} \cdot kg \qquad Vm20_{25\_4} := \frac{Rmin20_{25\_4} \cdot 10^{-3}}{\rho_s} \cdot kg$$

$$Vx30_{25\_4} := \frac{Rmax30_{25\_4} \cdot 10^{-3}}{\rho_s} \cdot kg \qquad Vm30_{25\_4} := \frac{Rmin30_{25\_4} \cdot 10^{-3}}{\rho_s} \cdot kg$$

Manipulation of the Maximum and Minimum Volume Loss Results to Achieve a Match With the other Data:-

$Vrx10_{25\_4_{(i-4)}} := Vx10_{25\_4_{i}}$ $Vrm10_{25\_4_{(i-4)}} := Vm10_{25\_4_{i}}$

$Vrx20_{25\_4_{(j-2)}} := Vx20_{25\_4_{j}}$ $Vrm20_{25\_4_{(j-2)}} := Vm20_{25\_4_{j}}$

$Vrx30_{25\_4_{(k-1)}} := Vx30_{25\_4_{k}}$ $Vrm30_{25\_4_{(k-1)}} := Vm30_{25\_4_{k}}$

Determination of the Erosion Rate for the Maximum and Minimum Volume Loss Results Obtained Above:-

$$ERx10_{25\_4} := \overrightarrow{\frac{Vrx10_{25\_4}}{T10_{25\_4} \cdot M10_{min}}} \qquad ERm10_{25\_4} := \overrightarrow{\frac{Vrm10_{25\_4}}{T10_{25\_4} \cdot M10_{min}}}$$

$$ERx20_{25\_4} := \overrightarrow{\frac{Vrx20_{25\_4}}{T20_{25\_4} \cdot M20_{min}}} \qquad ERm20_{25\_4} := \overrightarrow{\frac{Vrm20_{25\_4}}{T20_{25\_4} \cdot M20_{min}}}$$

$$ERx30_{25\_4} := \overrightarrow{\frac{Vrx30_{25\_4}}{T30_{25\_4} \cdot M30_{min}}} \qquad ERm30_{25\_4} := \overrightarrow{\frac{Vrm30_{25\_4}}{T30_{25\_4} \cdot M30_{min}}}$$

Formation of the Cubic Splines to Fit the Maximum and Minimum Erosion Rate Results:-

$vyix := ERx10_{25\_4}$ $vsix := \mathrm{lspline}(vxi, vyix)$ $vyim := ERm10_{25\_4}$ $vsim := \mathrm{lspline}(vxi, vyim)$

$vyjx := ERx20_{25\_4}$ $vsjx := \mathrm{lspline}(vxj, vyjx)$ $vyjm := ERm20_{25\_4}$ $vsjm := \mathrm{lspline}(vxj, vyjm)$

$vykx := ERx30_{25\_4}$ $vskx := \mathrm{lspline}(vxk, vykx)$ $vykm := ERm30_{25\_4}$ $vskm := \mathrm{lspline}(vxk, vykm)$

Interpolation of the Maximum and Minimum Erosion Rate Data For a Fixed Mass of Abrasive:-

$EDPx10_{25\_4} = \mathrm{interp}(vsix, vxi, vyix, Tsel10)$ $EDPx10_{25\_4} = 8.1564 \cdot \frac{mm^3}{kg}$

$EDPm10_{25\_4} := \mathrm{interp}(vsim, vxi, vyim, Tsel10)$ $EDPm10_{25\_4} = 6.9509 \cdot \frac{mm^3}{kg}$

$EDPx20_{25\_4} := \mathrm{interp}(vsjx, vxj, vyjx, Tsel20)$ $EDPx20_{25\_4} = 5.8560 \cdot \frac{mm^3}{kg}$

$EDPm20_{25\_4} := \mathrm{interp}(vsjm, vxj, vyjm, Tsel20)$ $EDPm20_{25\_4} = 5.3301 \cdot \frac{mm^3}{kg}$

$EDPx30_{25\_4} := \mathrm{interp}(vskx, vxk, vykx, Tsel30)$ $EDPx30_{25\_4} = 5.4144 \cdot \frac{mm^3}{kg}$

$EDPm30_{25\_4} := \mathrm{interp}(vskm, vxk, vykm, Tsel30)$ $EDPm30_{25\_4} = 5.1962 \cdot \frac{mm^3}{kg}$

Summary of Erosion Data Results:-

Erosion Rate Results With Full Range Information:-

$EDP10_{25\_4} = 7.5389 \cdot \frac{mm^3}{kg}$

$EDP20_{25\_4} = 5.5304 \cdot \frac{mm^3}{kg}$

$EDP30_{25\_4} = 5.3053 \cdot \frac{mm^3}{kg}$

$EDP45_{25\_4} = 4.5243 \cdot \frac{mm^3}{kg}$

$EDP65_{25\_4} = 3.5516 \cdot \frac{mm^3}{kg}$

$EDPx10_{25\_4} = 8.1564 \cdot \frac{mm^3}{kg}$

$EDPm10_{25\_4} = 6.9509 \cdot \frac{mm^3}{kg}$

$EDPx20_{25\_4} = 5.8560 \cdot \frac{mm^3}{kg}$

$EDPm20_{25\_4} = 5.3301 \cdot \frac{mm^3}{kg}$

$EDPx30_{25\_4} = 5.4144 \cdot \frac{mm^3}{kg}$

$EDPm30_{25\_4} = 5.1962 \cdot \frac{mm^3}{kg}$

Actual Impact Angle Results With Full Range Information:-

$$Ang_{mean} := \begin{bmatrix} 7.8315 \\ 18.7379 \\ 24.0585 \\ 39.9082 \\ 60.9532 \end{bmatrix}$$

$$Ang_{max} := \begin{bmatrix} 8.512 \\ 20.4068 \\ 26.2107 \\ 43.4197 \\ 65.9379 \end{bmatrix}$$

$$Ang_{min} := \begin{bmatrix} 7.151 \\ 17.069 \\ 21.9063 \\ 39.3966 \\ 55.9684 \end{bmatrix}$$

Graphs of Erosion Rate Versus Angle of Particle Impingement for an Impact Velocity of 15 m/s

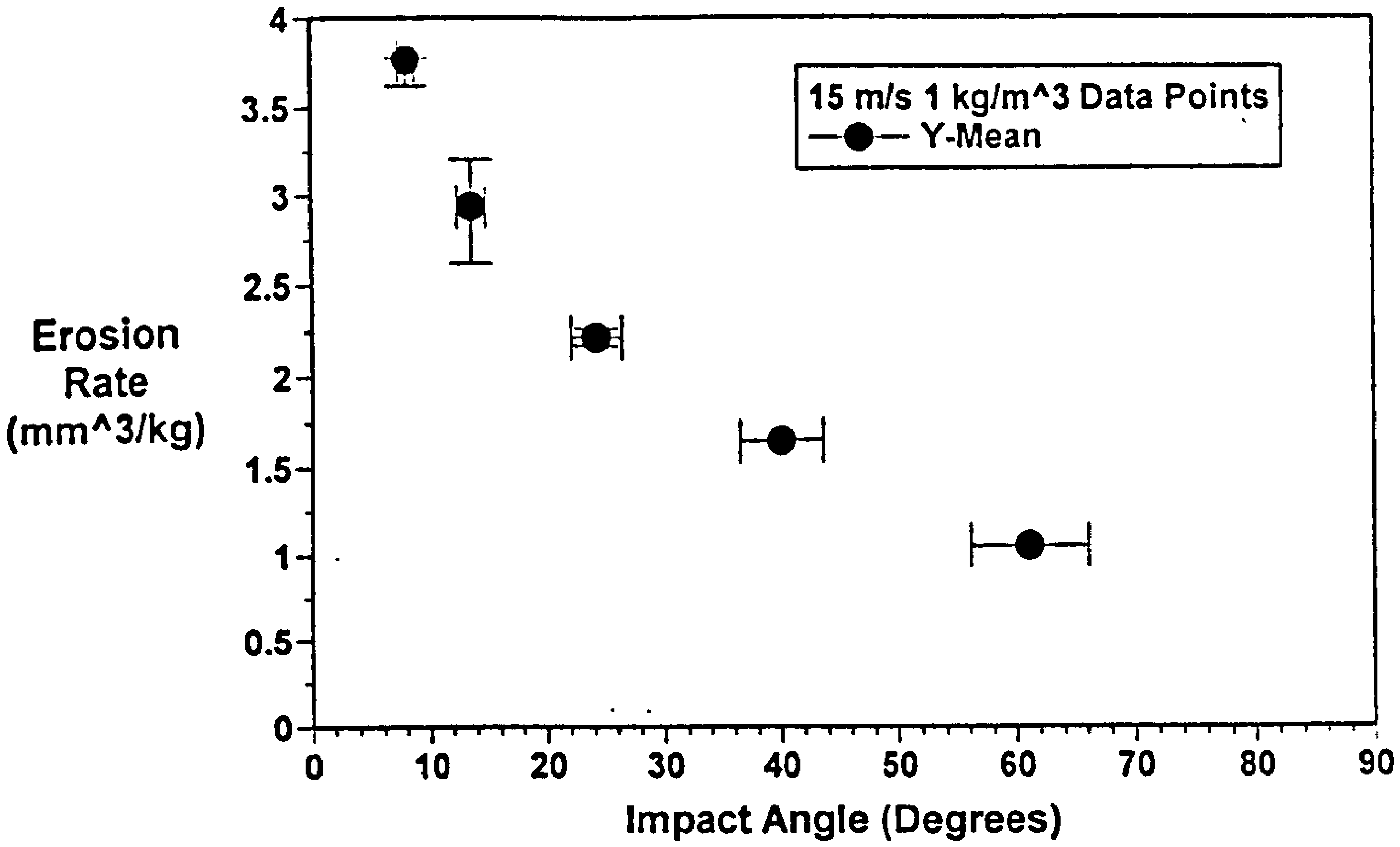

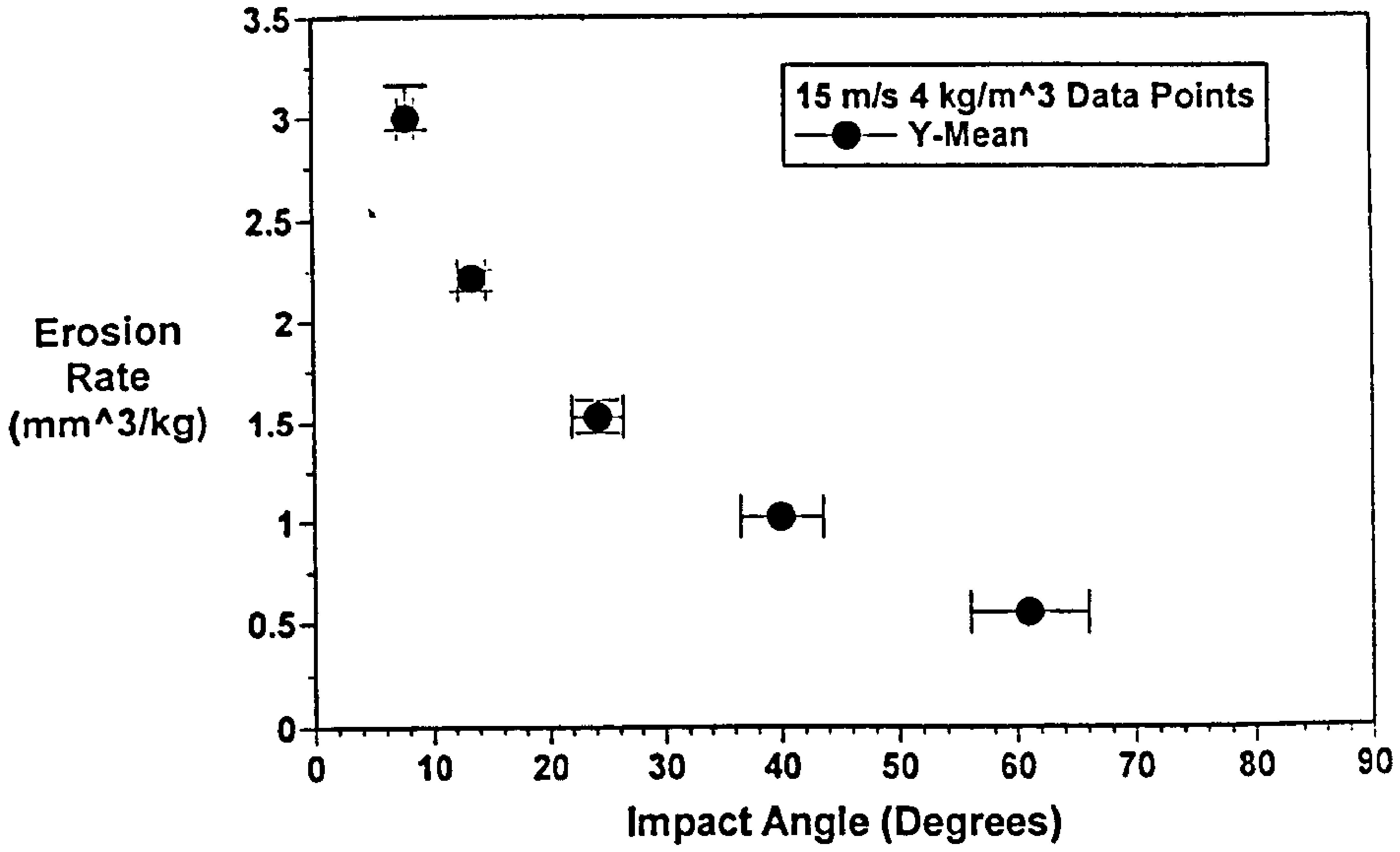

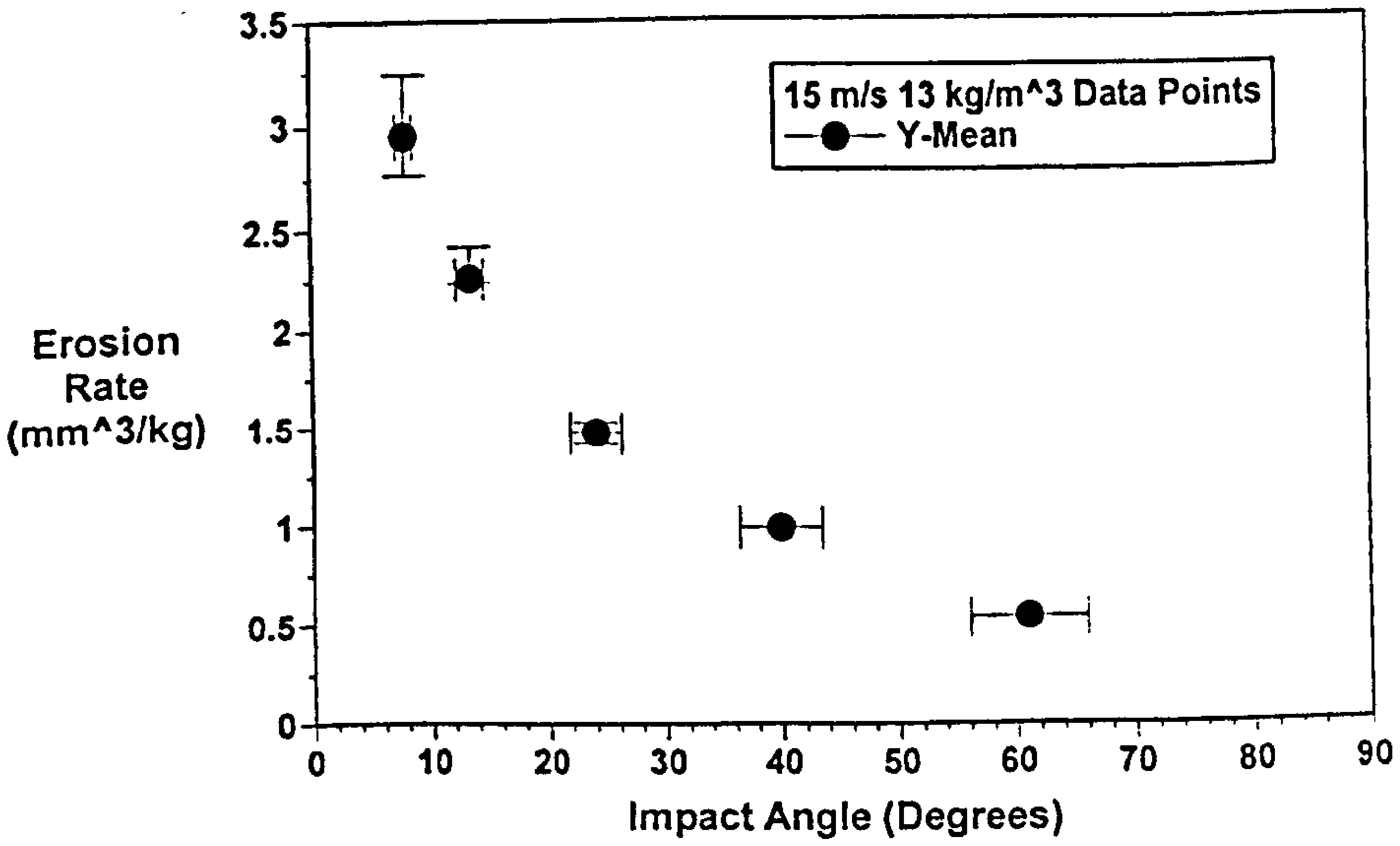

Graphs of Erosion Rate Versus Angle of Particle Impingement for an Impact Velocity of 25 m/s

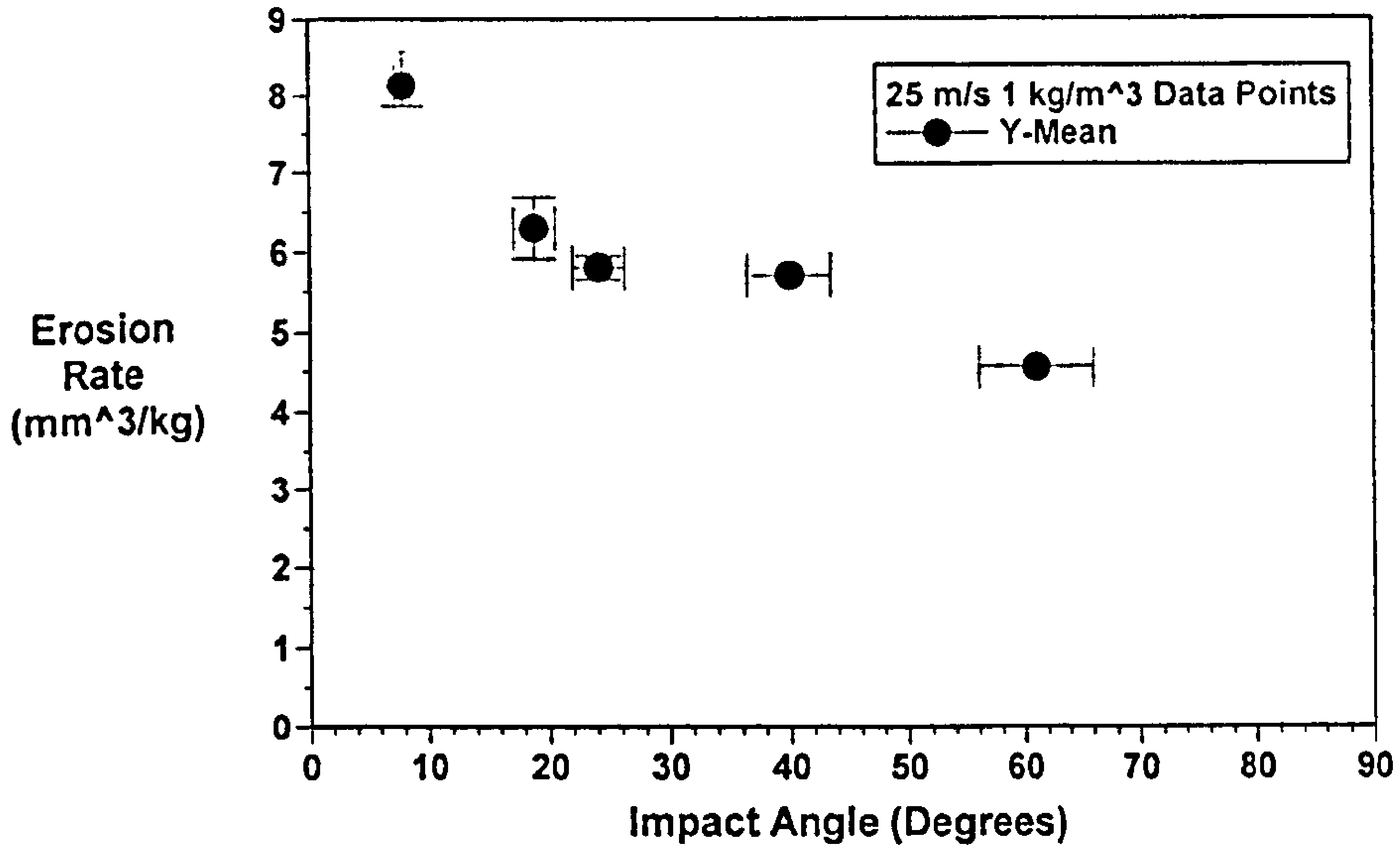

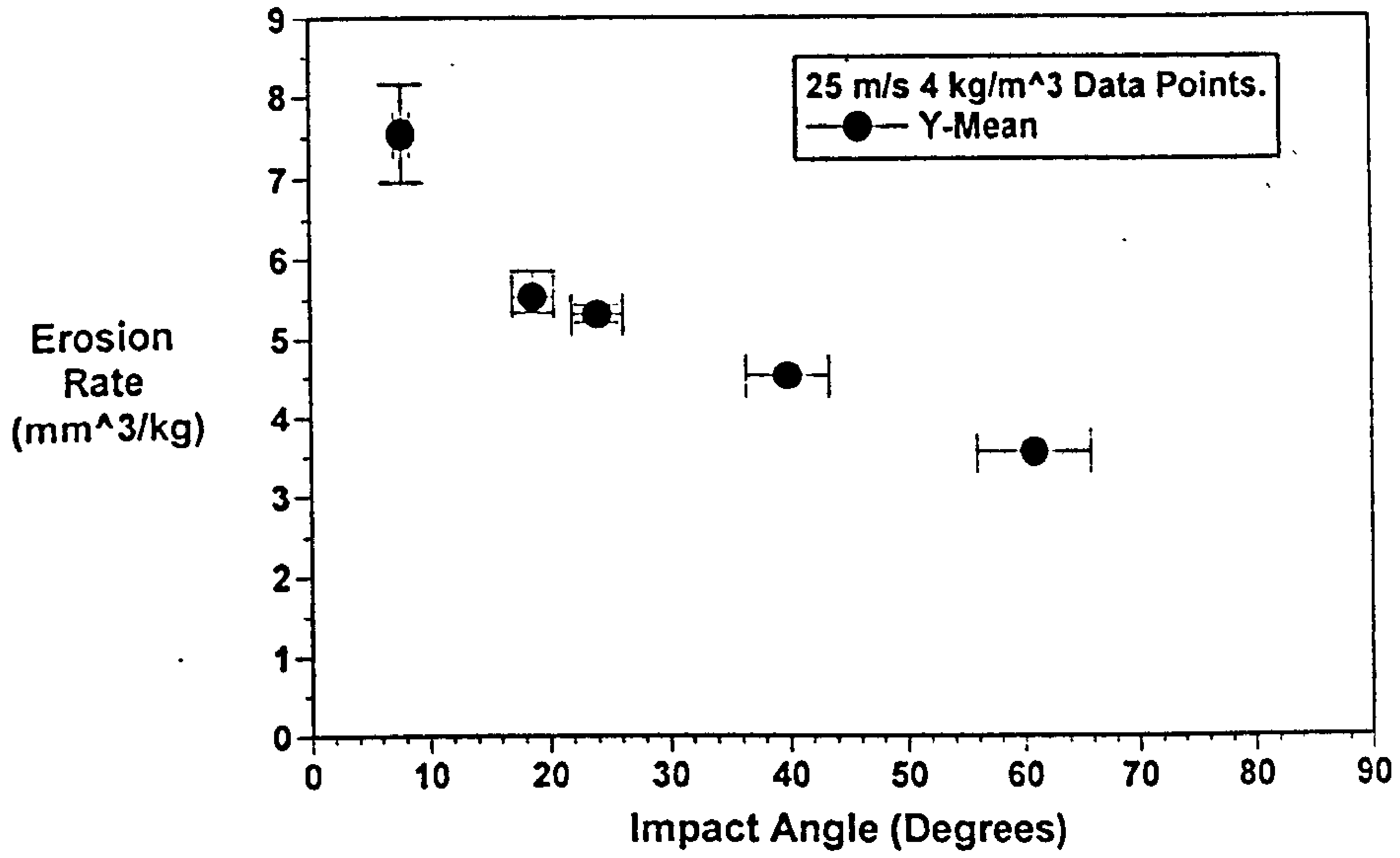

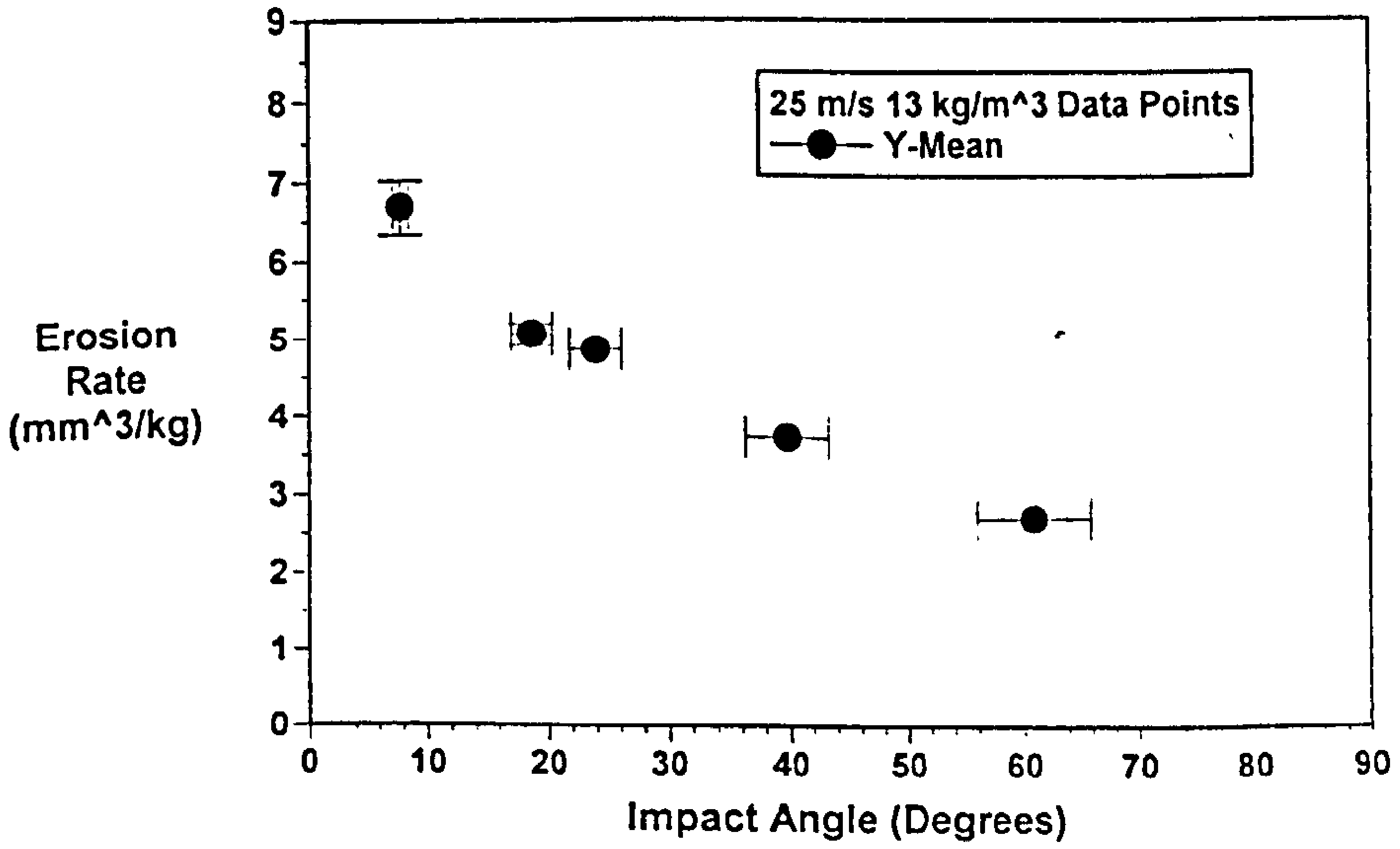

Graphs of Erosion Rate Versus Angle of Particle Impingement for an Impact Velocity of 35 m/s

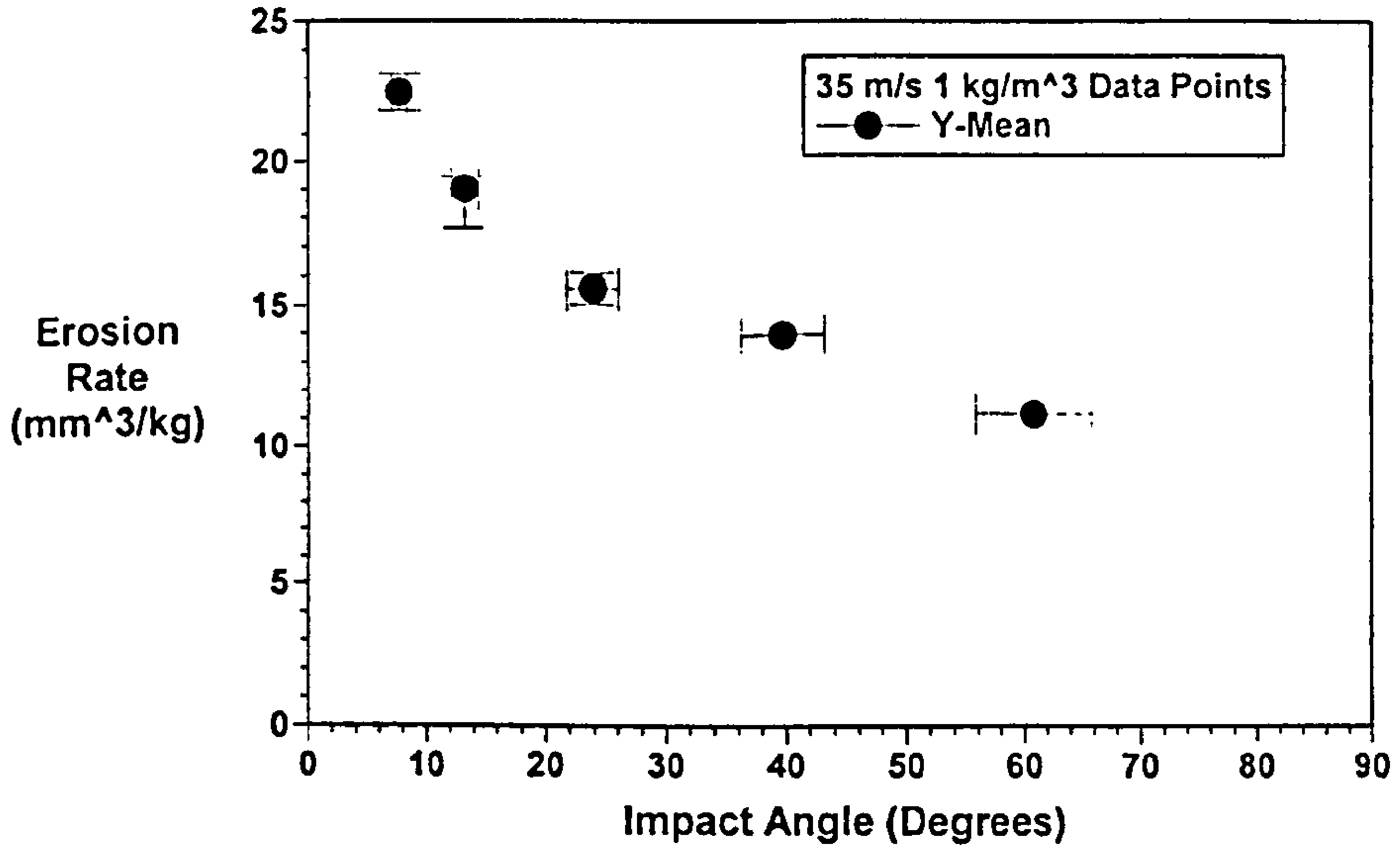

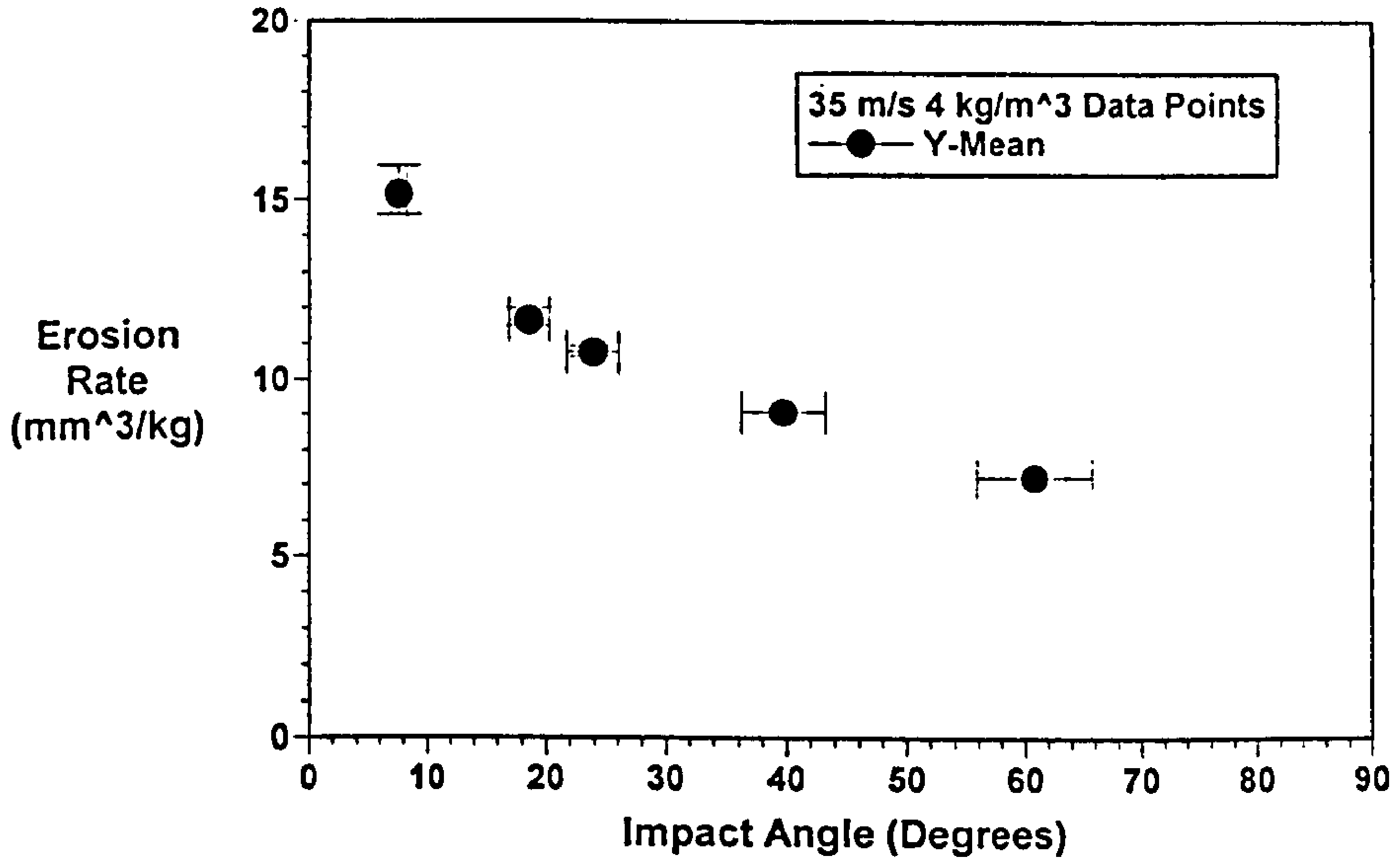

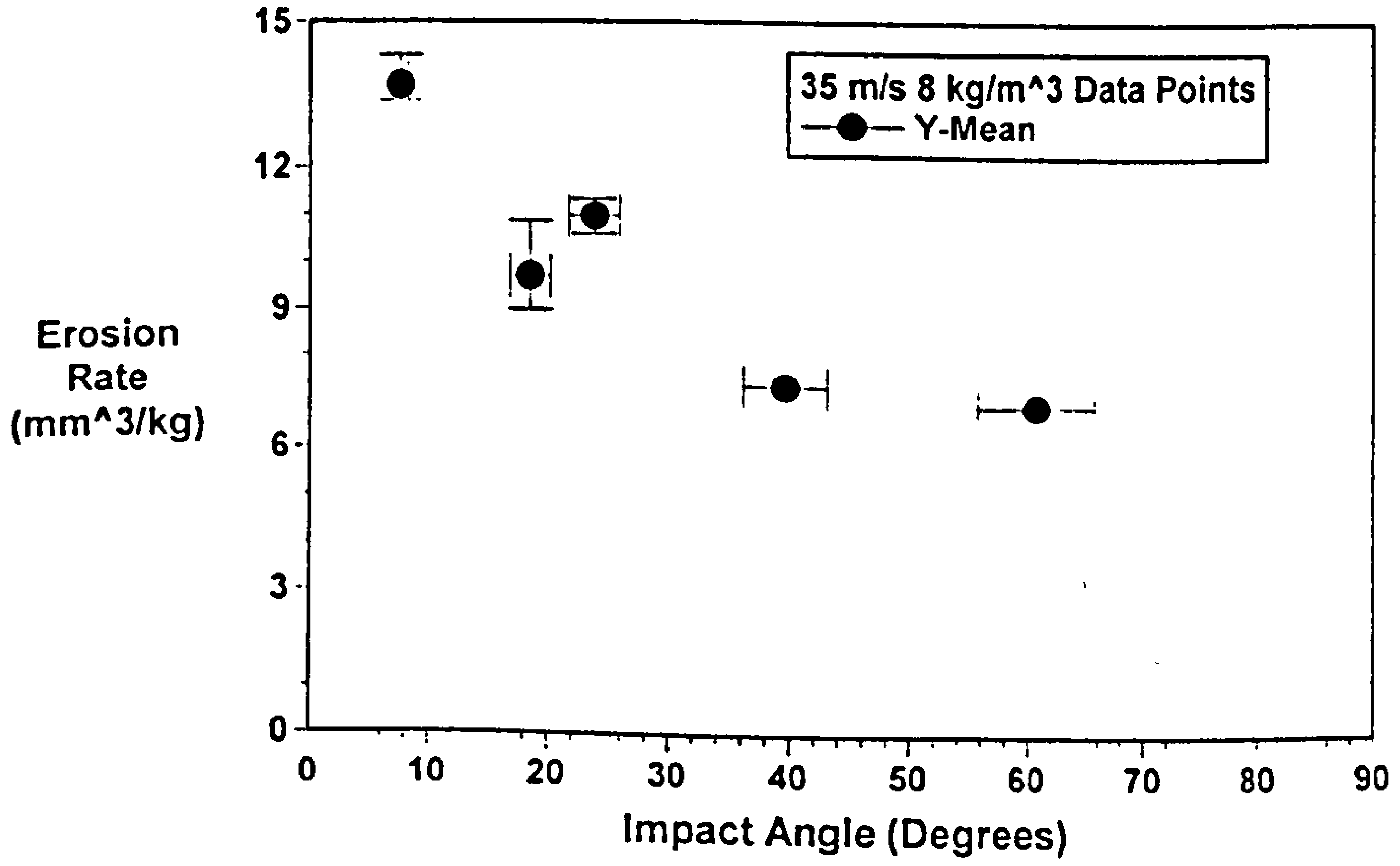

Appendix 4G: Modelling the Mild Steel Erosion Performance Using the Combined Finnie / Bitter Model.

4G.1 Introduction to the Combined Finnie / Bitter Erosion Model

The origins of this model began in 1958 when Finnie [F5] proposed a model for the erosion of ductile metals. The model was based on an analysis of a physical model of the mechanisms of kinetic energy exchange during the impact of a single solid particle where cutting was the predominant mechanism. This model did not allow for erosion damage to occur at an impact angle normal to the eroding target surface. This model was added to by Bitter in 1963 [B11,B12] who suggested that another mechanism, that of deformation wear, acted in conjunction with the cutting wear mechanism proposed by Finnie. This mechanism was described as the removal of surface material by a form of fatigue deformation wear. Bellman and Levy later found this form of mechanism to operate throughout the full range of impact angles [B16]. The resulting combined model can be used to predict the mean amount of material removed in one particle impact. It has been stated or implied by other researchers [B16,H11,R5] that single impacts do not always lead to the removal of material from the target surface; it is suggested that a roughening of the surface due to earlier particle impacts is required before material can be removed [B16]. However, the model that can be derived from the combination of the work carried out by Finnie and Bitter has been used successfully in the past to model steady state erosion damage, i.e. once enough impacts have occurred to begin a steady loss of material. The most recent use of a model of this form was by Sato *et al.* [S6] and Shimizu *et al.* [S5].

The following equations describe the combined model in detail. These equations were used in this project to fit curves to the experimental data obtained as described in section 4.3.3. above.

4G.2 The 'Cutting' Wear Model of Finnie

The original model proposed by Finnie [F5] was derived from solving the equations of motion for the tip of an abrasive particle striking a surface at an oblique angle. This analysis was confined to discussing particle / surface contacts at oblique angles in which the leading face of the particle was the only part of the particle in contact with the deforming surface; Finnie described this interaction as 'cutting in an idealised manner' [F5]. The equations of motion included the linear velocities in both the directions parallel and perpendicular to the eroding surface, and the velocity of rotation of the particle at contact. Using several simplifying suppositions, including fixing the ratio of the vertical and horizontal force components acting in the interaction as a constant, and that the surface material deformed at a constant value of plastic flow stress, enabled the equations to be reduced into a more easily solved form. The equations of motion were then solved. Following this the integral of the vertical depth of particle impression into the surface throughout the particle / surface interaction was used to find the volume of material removed from the surface.

For cutting wear, as proposed by Finnie and modified by Shimizu *et al.* [S5], the amount of wear occurring depended heavily on the angle of impingement of the particle:-

$$W_{c1} = \frac{\rho_t\, C\, M_p\, V_{res}^2}{P\, \varphi} \left[\sin(2\alpha) - \frac{2\left(1 + \frac{M_p\, r_p^2}{I_p}\right)}{K} \sin^2(\alpha) \right]$$

$$\text{for } \tan(\alpha) < \frac{K}{2\left(1 + \frac{M_p\, r_p^2}{I_p}\right)}$$

(4G.1)

$$W_{c2} = \frac{\rho_t\, C\, M_p\, V_{res}^2}{P\, \varphi} \left[\frac{K \cos^2(\alpha)}{2\left(1 + \frac{M_p\, r_p^2}{I_p}\right)} \right] \qquad \text{for } \tan(\alpha) > \frac{K}{2\left(1 + \frac{M_p\, r_p^2}{I_p}\right)} \quad ,$$

(4G.2)

$$\text{where} \quad P = \left[\frac{40}{\pi^4}\, \rho_p \left(\frac{1}{\frac{1 - q_p^2}{E_p} + \frac{1 - q_t^2}{E_t}} \right)^4 \right]^{1/5} \left(V_{res} \sin(\alpha) \right)^{2/5}$$

(4G.3)

and where ρ_t and ρ_p are the densities of the target and particle materials respectively; C is a model constant which has in the past been stated as being the proportion of particles that cut in an ideal manner, i.e. such that the leading face of the particle is the only part of the particle in contact with the surface during the particle / surface interaction; M_p is the mass of a particle of mean particle diameter; V_{res} is the particle impingement velocity; K is the ratio of the vertical to horizontal forces acting on the particle; P is a theoretically determined value of the normal stress found using Hertzian impact mechanics [T4]; α is the particle impingement angle; r_p is the mean particle radius;

I_p is the second moment of area of the particle; ψ is a constant for cutting wear = 2; E_t and E_p are the Young's modulus for the target and particle respectively; and q_t and q_p are the Poisson's ratio for the target and particle respectively. Figure 4G.1 illustrates the results that can be obtained from using Finnie cutting wear model alone.

4G.3 The 'Deformation' Wear Model of Bitter

Deformation wear can be modelled by using a model proposed by Bitter [B11,B12]. In this model the component of kinetic energy normal to the eroding surface imparted by the abrasive particle is used empirically to derive a value for the mass of material removed from the surface.

For the deformation wear as proposed by Bitter and utilised by Shimizu *et al.* [S5], the following equations apply:-

$$W_d = \frac{\frac{1}{2}\,\rho_p\,V_{res}\,M_p\left(V_{res}\,\sin(\alpha)\,-K'\right)^2}{\varepsilon} \tag{4G.4}$$

$$\text{where}\quad K' = \frac{\pi^2}{2\sqrt{10}}\left(1.59\;Y\right)^{2/5}\left(\frac{1}{\rho_p}\right)^{1/2}\left[\frac{1-q_p^2}{E_p}+\frac{1-q_t^2}{E_t}\right]^2$$

(4G.5)

and where Y is the yield stress of the target material; ε is the energy required to remove a unit volume of material from the target by deformation wear (deformation wear factor) and K' is a constant that is related to the material properties of both the particle and the surface suffering erosion; it describes the particle velocity threshold at which material removal by erosion just begins. Figure 4G.2 illustrates the type of results that can be obtained from using the Bitter deformation wear model alone.

4G.4 Use of the Combined Model

These equations were fitted to the data obtained from the tests described in section 4.3.3 in Chapter 4. This was achieved by multiplying the erosion rate, found in mm³/kg, by a fixed mass of abrasive and dividing by the mass of an individual particle of spherical shape and of mean particle diameter. Owing to the choice of impact angles made in the design of the test programme for the mild steel, it was necessary to fit an empirically derived curve to the data (as discussed in section

Figure 4G.1 Illustration of the results that can be obtained from the use of the Finnie cutting wear model alone.

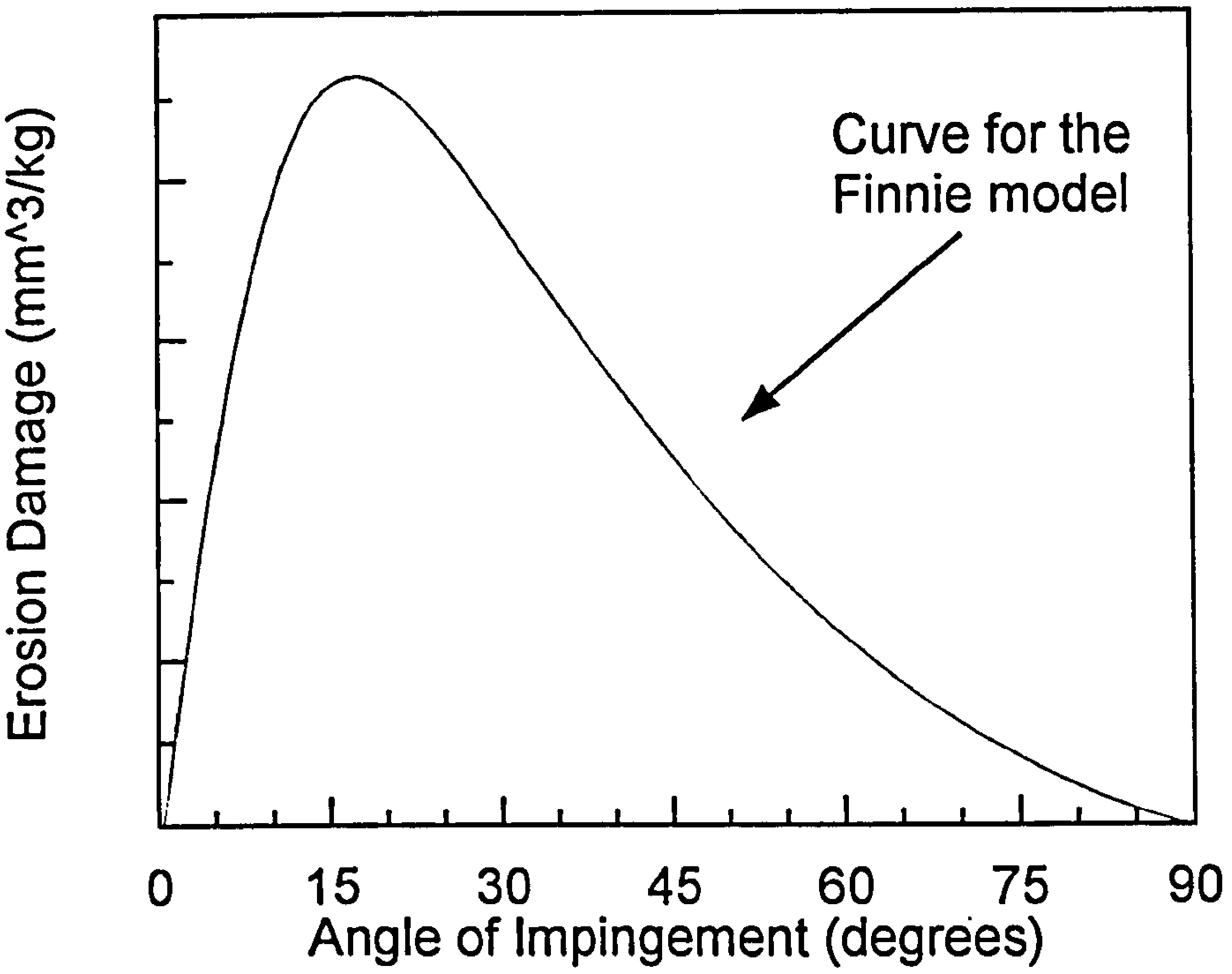

Figure 4G.2 Illustration of the results that can be obtained from the use of the Bitter deformation wear model alone.

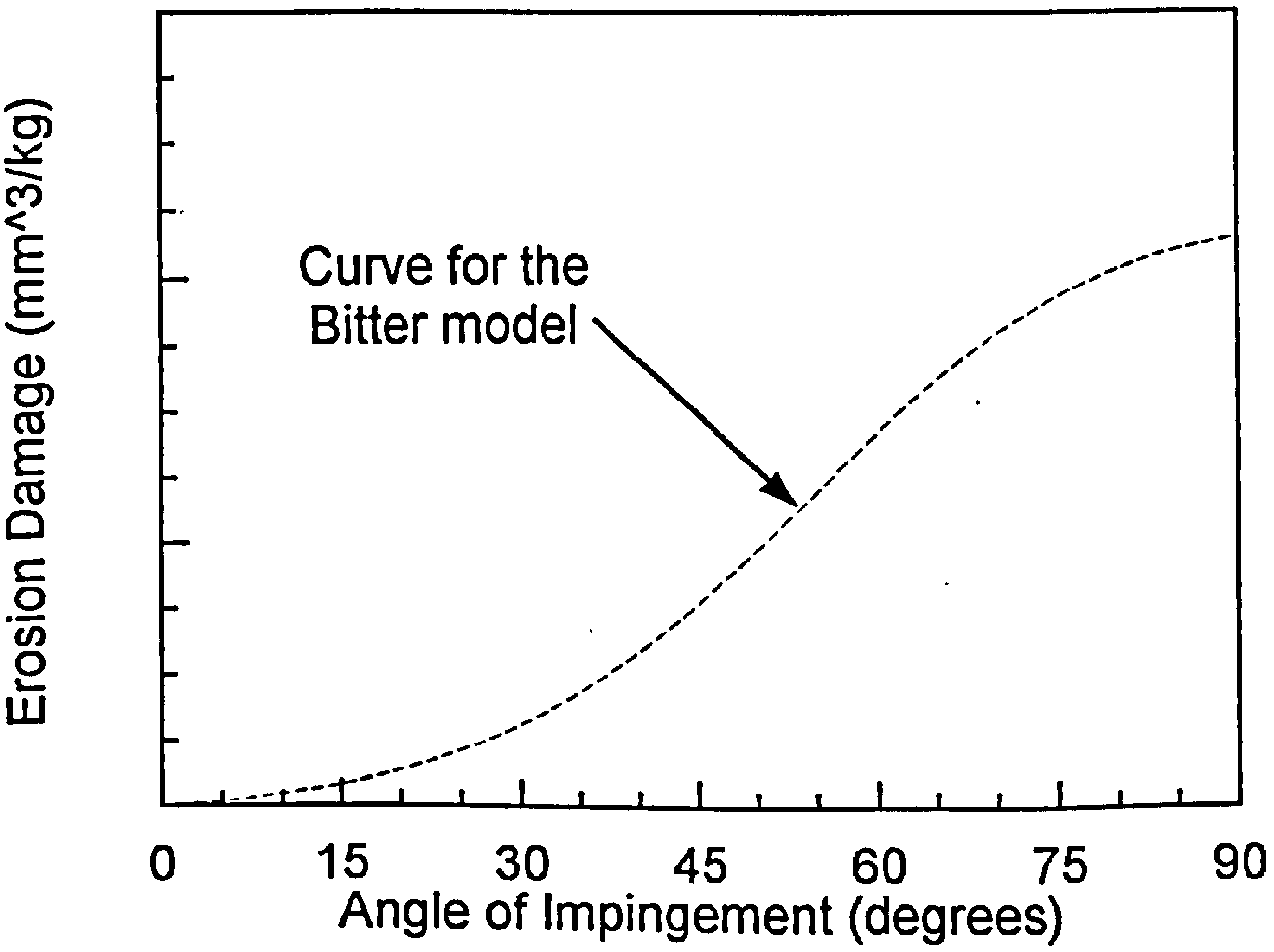

4.3.3 Chapter 4) to extrapolate the value of the erosion damage that would be expected to occur at an impact angle of 90°. Once this had been carried out, the value of the empirical constant in the Bitter model, ε, was easily found. Following this the values of the empirical constants for the Finnie cutting wear model, K & C, were adjusted until a fit with the erosion data, (obtained as described in section 4.3.3 Chapter 4), was obtained. Section 4G.7 at the end of this appendix gives details of the MathCad coded document used for the purposes of fitting this model to experimental data. Figure 4G.3 gives an indication of the parts that the Finnie and Bitter wear models make in ensuring the fit to experimental data is achieved.

4G.5 A Discussion Concerning the Empirical Constants Found for the Fitting of the Finnie / Bitter Erosion Model to the Steel Experimental Test Results

The table shown below, Table 4G.1, gives values for the three major empirical constants required in the Finnie / Bitter model, K, C and ε. Both ε and K are reasonably easy to understand; ε is the energy required to remove a unit volume of material from the target by the mechanism of deformation wear. Therefore, this is the empirical constant that can be altered to fit the experimental data so that the model gives a volume loss that compares favourably with that obtained experimentally at impact angles normal to the eroding surface. The value of ε will change with the properties of the target material.

K is the ratio of the vertical to the horizontal force components acting on the particle. Finnie [F5] assumed that the value of K was constant for any given possible impingement angle. In experimental tests carried out by Finnie, using force measurements made during dry grinding tests he found the mean value for this variable to be equivalent to 2. As can be seen in Table 4G.1 above this was not found to be the case during the fitting of this model to the mild steel test data. K has a significant effect on the position of the peak that is seen in the curve of erosion damage versus angle of impingement. For a maximum in this curve to occur at an angle of impingement of 15 - 17° the value of K must equal 2. However, in the data presented in Figure 4.5 section 4.3.3 Chapter 4 it can be seen that there is no apparent peak in this curve. The reasons for why this should be the case are discussed in the section 4.3.6 of Chapter 4.

The value of C is dependent on a collection of variables. In Finnie's original work [F5], C was described by the following equation:-

Figure 4G.3 The contribution made by the Finnie and Bitter wear models to the fit of the combined erosion model.

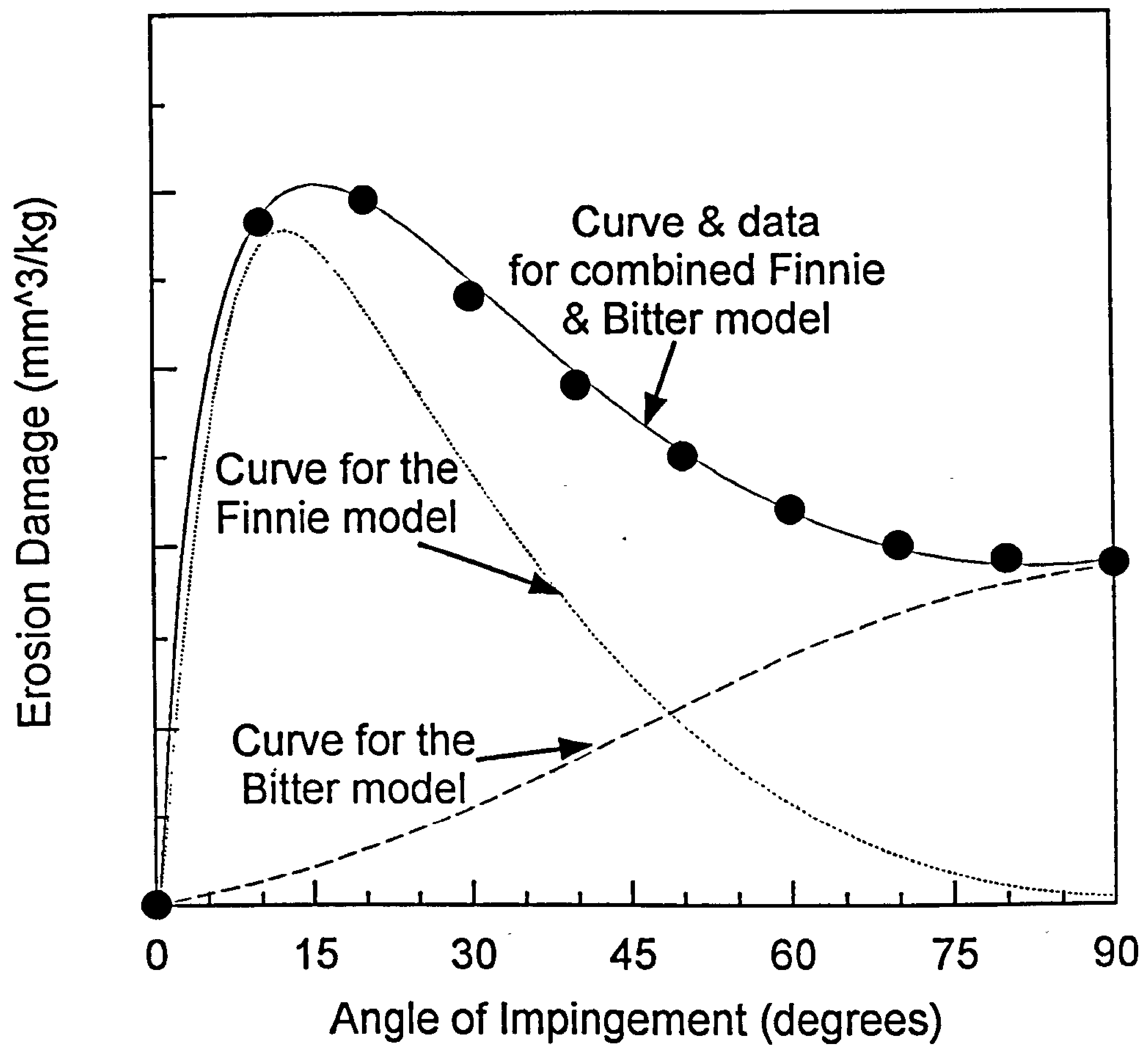

$$C = \frac{p\ \psi\ b\ K}{M_p} \qquad (4G.6)$$

where p was the horizontal component of the stress on the particle / target material contact face; ψ was the ratio of the length of contact between the particle and the target surface and the depth of the indentation and b was the width of the cutting face. The majority of these variables are functions of the shape of the particle and the material properties in a high strain rate indentation. Neither of these properties are well understood and they remain the subject of continuing research to this date.

Table 4G.1 The Values of the Empirical Constants Obtained by Fitting the Finnie / Bitter Erosion Model to Data Obtained by Experiment

Erosion Conditions (Velocity; Particle Concentration)	**K**	**C**	**ε (x 10^{10}) J/m^3**
15 m/s; 1 kg/m^3	1.25	0.48	5.065
15 m/s; 4 kg/m^3	1.125	0.35	9.870
15 m/s; 13 kg/m^3	1.125	0.365	10.220
mean values	1.167	0.398	8.385
25 m/s; 1 kg/m^3	1.385	0.475	3.087
25 m/s; 4 kg/m^3	1.25	0.495	4.009
25 m/s; 13 kg/m^3	1.225	0.45	5.216
mean values	1.287	0.473	4.104
35 m/s; 1 kg/m^3	1.65	0.65	2.529
35 m/s; 4 kg/m^3	1.35	0.5	3.873
35 m/s; 8 kg/m^3	1.3	0.5	4.286
mean values	1.43	0.55	3.563

From the results of the Finnie / Bitter model fitting work it can be seen that in general the values of K and C increase with an increase in the particle velocity. This was expected as the erosion damage increases with particle velocity. It is interesting to note that the increase in the value of K implies that the vertical force component acting on the particle increases more than the horizontal component with particle velocity. This is a consequence of the greater amount of material that the particle is moving whilst in contact with the target surface. This wedge of material will tend to force the particle away from the target surface. The reason for this is that the surface area of the leading edge of the particle in contact with the eroding surface will be greater, and, consequently, resistance to further indentation into the undisturbed surface in the path of the particle will be greater (see Figure 4G.4).

The value of C will be effected by changes in K. Also, it is likely that the value of p, the horizontal component of stress in the particle / target interaction will increase as the particle velocity increases. This is certainly true for the expressions for the dynamic pressure given in a work by Hutchings [H3]. The empirical value of the dynamic pressure is given in the following expression:-

$$P_e = \left[\frac{1280}{243\ \pi^4}\ \rho_p\ V_{res}^2 \left(\frac{1 - q_t^2}{\pi\ E_t} + \frac{1 - q_p^2}{\pi\ E_p} \right)^{-4} \right]^{1/5} \qquad (4G.7)$$

The value of b, the width of the cutting face, is likely to increase as the particle causes deeper indentations and causes larger lips of material to be displaced when higher velocity impacts occur. It is also highly unlikely that the value of ψ, the ratio of the cutting length in contact with the target surface to the depth of indentation will remain constant. The value of ε decreases with an increase in particle velocity. This is in keeping with the increase in erosion damage with particle velocity seen in the results. There are some trends in the variation of the empirical constants with particle concentration for any given particle velocity. In general terms the value of K increases and the value of ε decreases as the particle concentration increases. No particular trend can be seen for the variation of C with particle concentration. However, (in common with the majority of erosion models), according to the Finnie / Bitter model the particle concentration has no physical significance on the empirical constants being discussed. However, the interparticulate collisions and the subsequent variation in impact angles that may occur in the region of the eroding surface could lead to a shift in the mean values of K and ε. However, this is a far from satisfactory explanation and it cannot be substantiated.

4G.4 Schematic diagram of particle point cutting a target surface.

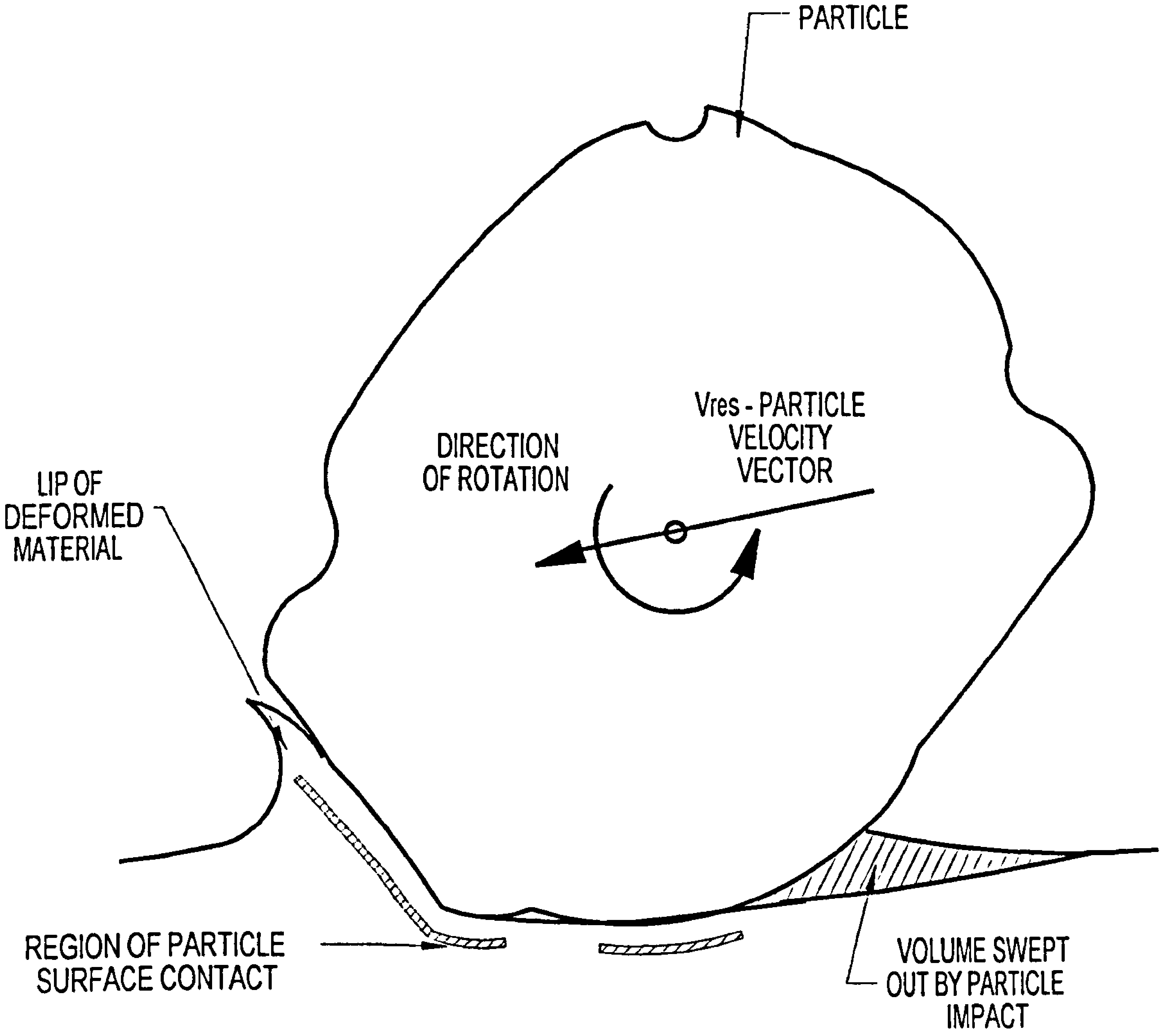

4G.6 Conclusions Relating to the Use of the Finnie / Bitter Erosion Model

The Finnie / Bitter combined erosion model proposed by Shimizu can be fitted successfully to the data obtained for the erosion of the structural mild steel considered in this project. However, some of the empirical variables which are used in this model cannot be constant if the curve fit is to be accurate. Most notably amongst these variables is the value of K, which is the ratio of the vertical force components acting on the particle tip over the horizontal force components at the same location. In Finnie's original work this is stated as being equal to 2; in this case the value is significantly less than this. Some interesting trends in the variation of these empirical terms was seen, however, it is very difficult to offer any definite reasoning for why this should be the case. This is especially true when it is considered that the modelling techniques adopted by Finnie and Bitter have been stated as being flawed by other researchers. These researchers have stated that erosion of ductile materials at velocities seen commonly in pneumatic conveyors requires multiple impacts, and therefore, a single particle is most unlikely to remove any material from the eroding surface. If this is the case then the model described by Finnie / Bitter, which is based on material being cut from a surface by an individual particle impact, can indeed be stated as being incorrect. However, in steady state erosion, i.e. erosion after a significant number of particle impacts, a mean amount of material removed from the surface can be found for each particle impact. The implications of this are that the Finnie / Bitter model can be used in the instance of finding this mean value of material volume removed per impact during steady state erosion. In this instance the model is used in a purely empirical manner.

4G.7 The Fitting of the Combined Finnie / Bitter Erosion Model to Experimentally Determined Erosion Data

The example of the MathCad listing shown in this section, contains all of the input data necessary to carry out to a successful conclusion, the calculations necessary for a situation where the particle velocity was 25 m/s and the suspension density was 4 g/m^3. The listing begins on the following page.

Erosion Model Used by Shimizu, Yagi, Yoshida and Yokomine: The model is based upon the combined efforts of Finnie and Bitter:

The information for this model has been obtained from papers by Shimizu *et al.* [S5] and Sato *et al.* [S6]. The model calculates the mean mass of material removed by impact of a single particle.

Input Variables:-

$r_p := 162\cdot10^{-6}\cdot\mathrm{m}$ $\rho_p := 3287\cdot\frac{\mathrm{kg}}{\mathrm{m}^3}$ $\rho_t := 7800\cdot\frac{\mathrm{kg}}{\mathrm{m}^3}$ $q_p := 0.22$ $q_t := 0.303$

$E_p = 7.13\cdot10^{10}\cdot\frac{\mathrm{newton}}{\mathrm{m}^2}$ $E_t := 2.1\cdot10^{11}\cdot\frac{\mathrm{newton}}{\mathrm{m}^2}$ $Y_t := 3.31\cdot10^{8}\cdot\frac{\mathrm{newton}}{\mathrm{m}^2}$

$U := 25\cdot\frac{\mathrm{m}}{\mathrm{sec}}$ $i := 1,2..18$ $\alpha_i := i\cdot5\cdot\frac{\pi}{180}$ $\psi := 2$

Model Constants (semi-empirical):-

$\varepsilon := 4.009109\cdot10^{10}\cdot\frac{\mathrm{joule}}{\mathrm{m}^3}$ $K := 1.25$ $C := 0.495$

NB The constants (semi-empirical) can be manipulated to ensure a fit to the actual erosion data.

Calculations pertaining to particle properties:-

$m_p := \frac{4}{3}\cdot\pi\cdot r_p^{\,3}\cdot\rho_p$ $m_p = 5.853739\cdot10^{-8}\cdot\mathrm{kg}$

$I_p := \frac{m_p\cdot r_p^{\,2}}{3}$ $I_p = 5.1209\cdot10^{-16}\cdot\mathrm{kg}\cdot\mathrm{m}^2$

$$K_s := \frac{\pi^2}{2\cdot\sqrt{10}}\cdot\left(1.59\cdot Y_t\right)^{\frac{5}{2}}\cdot\left(\frac{1}{\rho_p}\right)^{\frac{1}{2}}\cdot\left(\frac{1-q_p^{\,2}}{E_p}+\frac{1-q_t^{\,2}}{E_t}\right)^{2} \qquad K_s = 0.054008\cdot\mathrm{m}\cdot\mathrm{sec}^{-1}$$

Calculation of the angle of impingement at which maximum erosion damage occurs.

$$P_i := \left[\frac{40}{\pi}\cdot\rho_p\cdot\left[\frac{1}{\frac{1-q_p^{\,2}}{E_p}+\frac{1-q_t^{\,2}}{E_t}}\right]^{4}\right]^{\frac{1}{5}}\cdot\left(U\cdot\sin(\alpha_i)\right)^{\frac{2}{5}} \qquad P_c := \frac{K}{\left(1+\frac{m_p\cdot r_p^{\,2}}{I_p}\right)}$$

$\frac{\mathrm{atan}(P_c)}{\pi}\cdot180 = 17.354025$

NB. The angle of impingement at which the maximum rate of erosion will o is, according to Finnie [F7], P_c. The results indicated in this project show thi be incorrect.

Magnitude of Deformation Wear per Particle Impact as Proposed by Bitter [B11,B12].

$$W_{d_i} := \frac{0.5\cdot\rho_p\cdot m_p\cdot\left(U\cdot\sin(\alpha_i)-K_s\right)^2}{\varepsilon} \qquad W_{d_{18}} = 1.493333\cdot10^{-12}\cdot\mathrm{kg}$$

Magnitude of Cutting Wear per Particle Impact as Proposed by Finnie [F7].

$$A := \frac{K}{2\cdot\left(\frac{m_p\cdot r_p^{\,2}}{I_p}+1\right)} \qquad B_i := \tan(\alpha_i)$$

$$W_{c1_i} := \frac{\rho_t \cdot C \cdot m_p \cdot U^2}{P_i \cdot \psi} \cdot \left[\sin(2\cdot\alpha_i) - \frac{2\cdot\left(1+\frac{m_p \cdot r_p^{\,2}}{I_p}\right)}{K} \cdot \sin(\alpha_i)\cdot\sin(\alpha_i) \right]$$

$$W_{c2_i} := \frac{\rho_t \cdot C \cdot m_p \cdot U^2}{P_i \cdot \psi} \cdot \left[\frac{K\cdot\cos(\alpha_i)\cdot\cos(\alpha_i)}{2\cdot\left(1+\frac{m_p \cdot r_p^{\,2}}{I_p}\right)} \right]$$

$$W_{c_i} := \mathrm{if}\left(B_i \le A, W_{c1_i}, W_{c2_i}\right)$$

Total Erosion Damage is the Sum of the Deformation and Cutting Wear Components as follows:-

$$W_{t_i} := W_{d_i} + W_{c_i}$$

Fitting a Cubic Spline Curve Fit to the Calculated Data:-

$$ws1 := \mathrm{lspline}(\alpha, W_t) \qquad a := 5\cdot\frac{\pi}{180}, 10\cdot\frac{\pi}{180} .. 90\cdot\frac{\pi}{180}$$

Graph of the Shimizu (Finnie/Bitter) Erosion Model Results for the Wear of Pipe Segment Steel by Individual Olivine Sand Particles:-

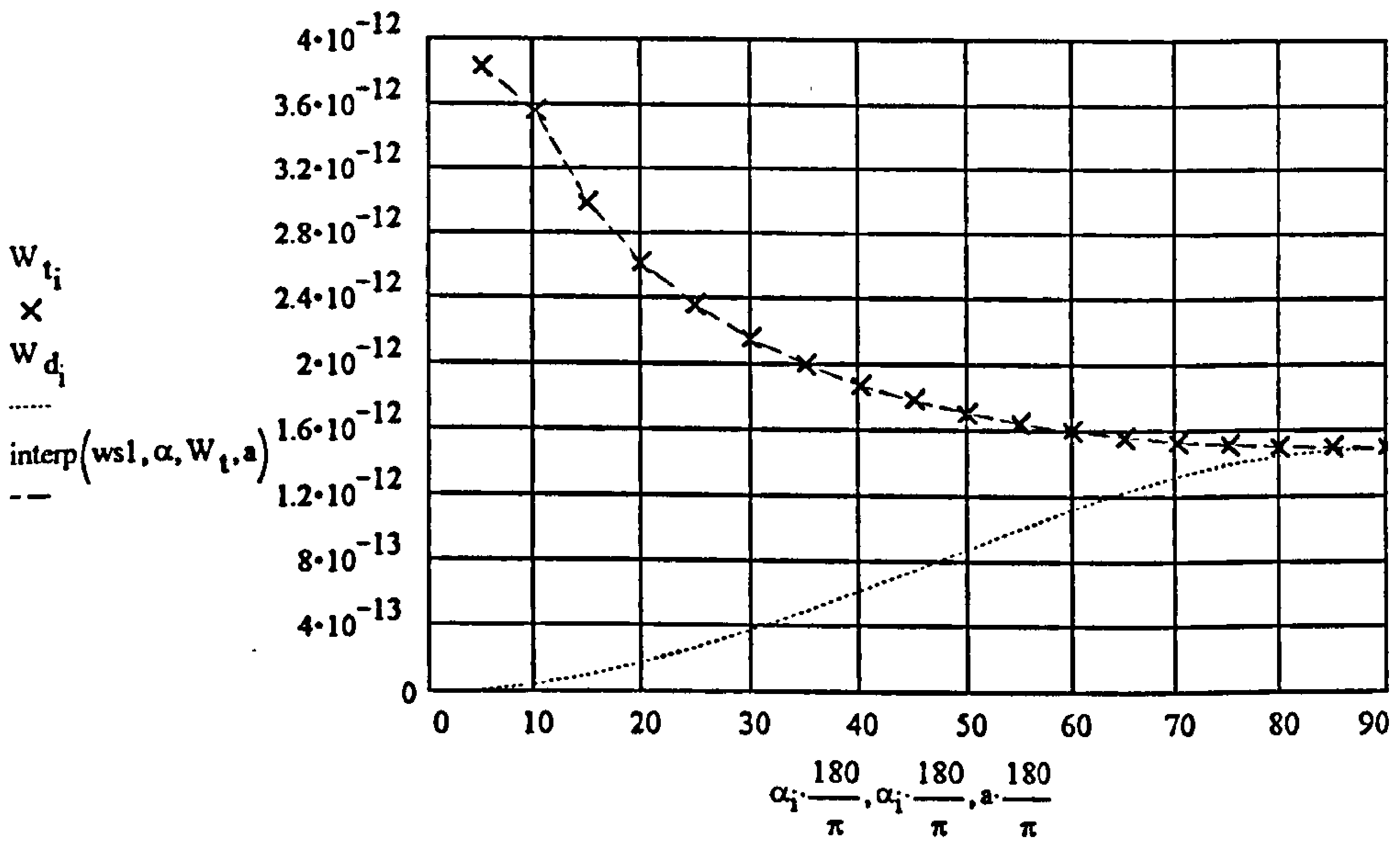

Comparison with Erosion Data Obtained From Test Work Carried out on the Rotating Disc Accelerator Erosion Tester:-

Input of Erosion and Rig Set Up Data:

$$E25\_4 := \begin{bmatrix} 7.8315 & 13.3604 & 0.0031 & 1.418\cdot10^{-4} & 7.5389 \\ 18.7379 & 11.5391 & 0.0076 & 1.6418\cdot10^{-4} & 5.5304 \\ 24.0585 & 11.1517 & 0.0098 & 1.6989\cdot10^{-4} & 5.5304 \\ 39.9082 & 10.5895 & 0.016 & 1.789\cdot10^{-4} & 4.5243 \\ 60.9532 & 10.5192 & 0.0227 & 1.801\cdot10^{-4} & 3.5516 \end{bmatrix}$$

$E25\_4a := E25\_4^{<0>}$ $E25\_4m := E25\_4^{<2>} \cdot kg$ $E25\_4e := \frac{E25\_4^{<4>}}{1 \cdot 10^{9}} \cdot \frac{m^3}{kg}$

$E25\_4mf := E25\_4^{<1>} \cdot \frac{kg}{m^2 \cdot sec}$ $E25\_4aa := E25\_4^{<3>} \cdot m^2$

Interpolation for the Mass Loss Caused by Each Individual Particle Impact According to the Above Model:-

$j := 0, 1 .. 4$

$$W_{tip_j} := interp\left[ws1, \alpha, W_t, \left(E25\_4a \cdot \frac{\pi}{180}\right)_j\right]$$

Mass Loss for 0.5kg of Abrasive Striking the Target Independent of Angle of Impact.

Experimental Calculated as per model

Mass Loss:- $MLe_j := E25\_4e_j \cdot \rho_t \cdot 0.5$ $MLc_j := W_{tip_j} \cdot \left(\frac{0.5}{m_p}\right)$

Curve Fit:- $E := MLe$

$cy_j := \ln\left(E_j\right)$ $cx_j := \ln\left(E25\_4a_j\right)$ Cubic Spline Fit:- $ws4 := lspline(E25\_4a, MLc)$

$slope(cx, cy) = -0.350913$

$intercept(cx, cy) = -9.690515$

$corr(cx, cy) = -0.984596$

$n25\_4 := slope(cx, cy)$ $n25\_4 = -0.350913$

$a25\_4 := e^{intercept(cx, cy)}$ $a25\_4 = 6.186751 \cdot 10^{-5}$

Graph of the Mass of the Target Removed by Impact of 0.5 kg of Abrasive Striking the Target Surface at 25 m/s at a Suspension Density of 4 kg/m³

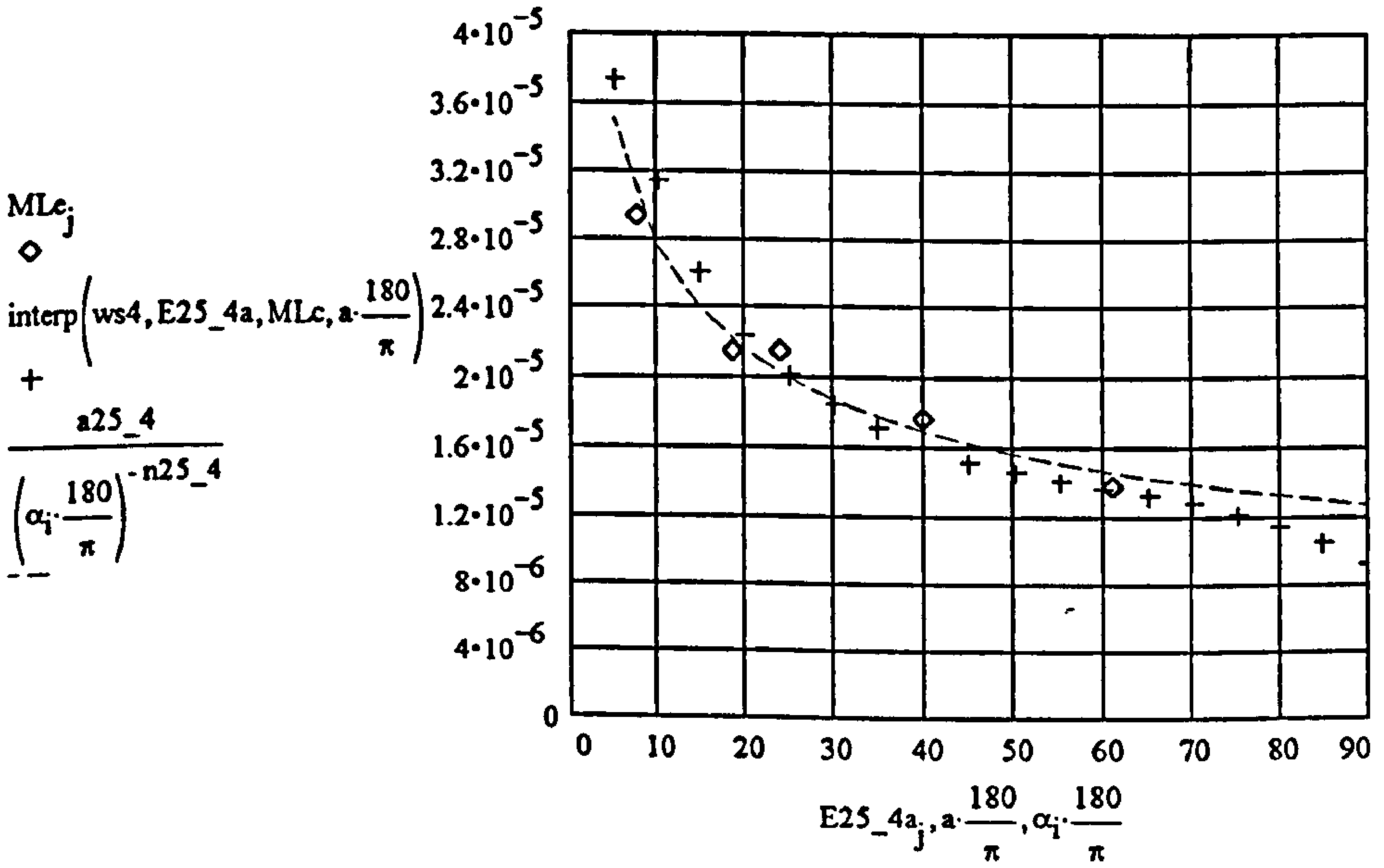

Calculation of the Improved Value of Epsilon:-

$m90 := \frac{a25\_4}{(90)^{-n25\_4}} \cdot \frac{m_p}{0.5}$ $\varepsilon n := \frac{0.5 \cdot \rho_p \cdot m_p \cdot \left(U \cdot \sin(0.5 \cdot \pi) - K_s\right)^2}{m90}$ $\varepsilon n = 4.009109 \cdot 10^{10} \cdot \frac{joule}{m^3}$

Calculation of the Energy Required to Remove a Unit Volme of Material by Deformation Wear.

$N_{pt} := 0.5 \cdot \frac{kg}{m_p}$ $I25\_4 := \frac{a25\_4}{(90)^{-n25\_4}} \cdot \frac{kg}{N_{pt}}$ $I25\_4 = 1.493333 \cdot 10^{-12} \cdot kg$

$$\varepsilon E := \frac{0.5 \cdot \rho_p \cdot m_p \cdot \left(U \cdot \sin\left(\frac{\pi}{2}\right) - K_s \right)^2}{I25\_4}$$

$\varepsilon E = 4.009109 \cdot 10^{10} \cdot \frac{joule}{m^3}$

Appendix 5A: The Design and Development of the Pneumatic Conveying Test Facility

5A.1 Introduction to the Design of the Pneumatic Conveying Test Facility

This appendix gives an indication of the layout of the pneumatic conveyor test facility used for this project. The conveyor was very similar in scale to devices commonly seen in industry, however, it was modified in some important areas to allow the measurement of the important variables discussed in Chapter 3. The description that follows is divided into several sections which relate to the main components of this test facility. These were:-

a) The pipeline geometry and the test bend,

b) The solid material handling system,

c) The air supply system,

d) The instrumentation system for pressure, velocity, mass of abrasive conveyed and temperature measurement,

e) The method of measuring the bend penetration,

f) The system for assessing the distribution of the particle concentration distribution across the pipe cross section.

A description of each of these systems will be given in turn. Figure 5A.1 is a schematic view of the test facility.

5A.2 The pipe geometry and the test bend

The size of the pipe line bore and length had to be similar to that which was seen in the use of such conveyors in industry. It was therefore decided that the pipe line should be of 2" nominal bore which was a reasonable size in comparison to those seen in the pipe work used in some solid fuel power stations to handle pulverised fuel ash. Puncture of the pipe work handling this material due to wear is a significant problem to the power generating companies, so this was thought to be a suitable application to use as an example of commercial practice. The overall length of the pipeline was not so critical as the length of pipe between each bend, since it was essential that the conveyed abrasive had a sufficient length of pipe prior to each bend to accelerate to its terminal velocity. To this end the simplest pipe line configuration was chosen. The pipe line was constructed on a square plan basis with 10m long sides.

Figure 5A.1 Overall schematic view of the test facility

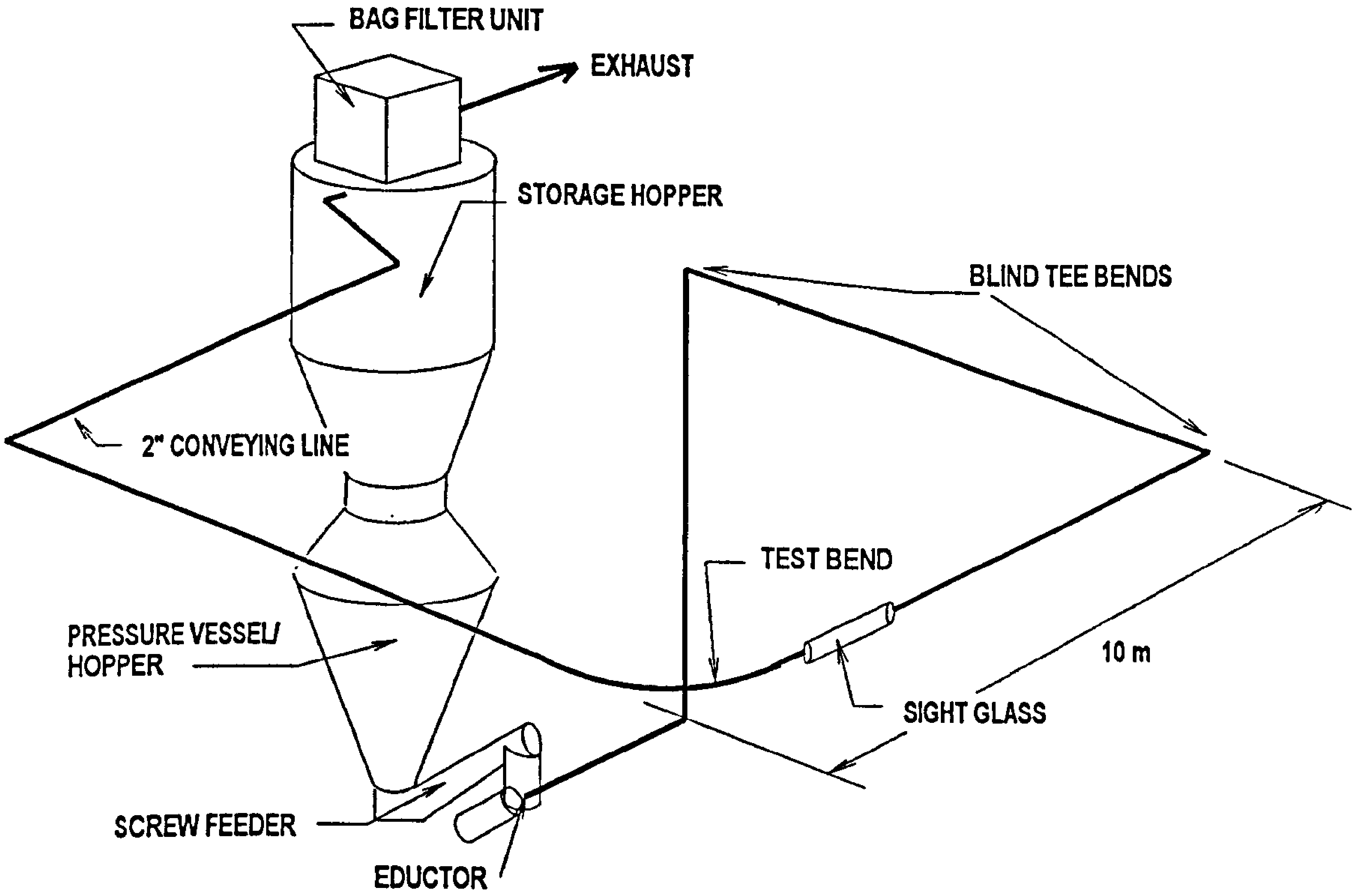

It was decided that enough data could be obtained by measuring the necessary variables on one test bend only (see Chapter 5 section 5.1). To this end all of the other bends within the system were of the blind-tee variety (see section 2.1.2 for a description of these bends and their features). In this way premature failure of these bends due to erosion damage was minimised. This enabled tests to be carried out on the actual test bend without having to worry about premature failure occurring in other parts of the test facility. A general schematic drawing of the layout of the conveying pipe line is given in Figure 5A.2.

The actual test bend itself was of a long radius, such as those which are commonly used in industry. Bends of this type are prone to severe erosive wear and therefore, would form the useful basis of a test programme to measure erosive damage in such components, without having extremely long test times. The test bend, made from 2" nominal bore pipe (internal diameter 53mm), had a radius of 750 mm to the pipe bore centre line, hence giving an R/d ratio of 14.15.

The majority of the pipe line components were secured together using screw-on unions of the type frequently used in gas pipe work. These have been found in the past to be quite convenient to use. All of the pipe components prior to and immediately after the test bend were secured together using flanges. The reason for the difference was that it was possible to align the pipe bores in these components more accurately when they were joined by flanges. This level alignment promoted flow free from perturbations caused by steps in the pipe bore disturbing the passage of particles. In the case of the unions the pipe outside diameters were aligned. However, the specification of the pipe used in the tests, indicated that there was a strong possibility that the inside and outside cross-sections of the pipe would not be concentric. The flanged method of joining the pipe components enabled problems due to bore misalignment to be minimised. This was achieved by using a plug which fitted the bores of the adjoining segments of pipe. The flanged ends were brought together and bolted together with the plug in place, then the flanges were drilled and pinned. The two aligned pipe segments were then separated and the plug was removed. When the pipe segments were connected again and pins were placed through the flanges, alignment of the bores was ensured.

5A.3 The Solid Material Feeding and Collecting System

The main purpose of the feeding arrangement was to ensure that the olivine sand could be fed into the pipe line against an upstream pressure of approximately 0.5 bar gauge. The feed rate of abrasive that was required was approximately 0.3 kg/s. However, the most important feature of the solid

Figure 5A.2 General schematic view of the pipe line

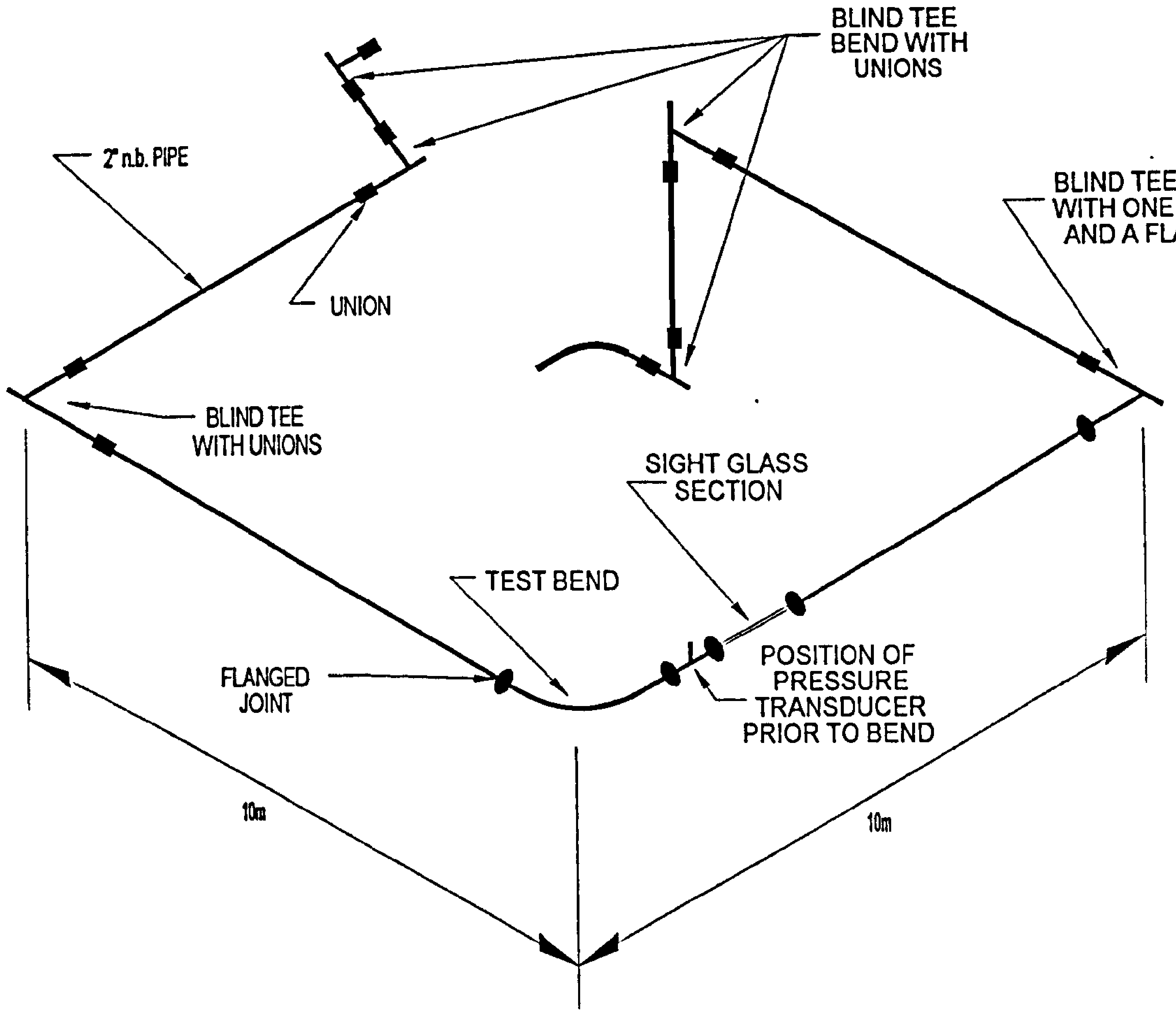

material handling system was that this system should provide as steady a feed of abrasive material into the pipeline as physically possible. In this way the conveying conditions causing erosion would be as constant as possible, hence leading to consistent erosion conditions in the test bend.

This part of the test facility was adapted from a blow tank feeding type test facility previously used and described by Selves [S15]. A brief description of the test facility will be given, and areas where modifications were made will be discussed in more detail.

Steady abrasive flow rates were achieved by modifying the system so that the material did not have to be fed into the pipeline by blow tank operation exclusively. The reason for this can be shown in previous work [B20], which indicated that the operation of a blow tank is prone to large start up and shut down transients. This behaviour is not acceptable in tests where the control of the particle velocity is of paramount importance, such as in erosion studies.

The system was modified by Selves [S15] so that the pressurised blow tank passed material through a screw feeder that was rotating at a constant velocity. This ensured that the feed rate of the abrasive material was steady. A venturi eductor was used to ease the problems that occurred with feeding material into a pipe line whose pressure was higher than atmospheric pressure. Figure 5A.3 illustrates the relative positions of these items. A brief description of the operation of the venturi form of feeder was given by Woodhead [W2]. The pressurisation of the blow tank was still found to be required in the operation of the test rig, because the back pressure generated in the pipe line was found to be sufficient to prevent the abrasive material from flowing into the screw feeder at an adequate rate. This problem was overcome by pressurising the blow tank to a maximum of 0.4 bar gauge. This was just enough to overcome the effects of back pressure from the pipeline, allowing the abrasive material to flow freely.

The collection of the abrasive material once it had been conveyed around the test loop was achieved by directing the end of the conveying line into a collecting hopper. The capacity of the hopper was 1.5 m^3 and it was mounted on three load cells to measure the mass of material conveyed during a known time period. This was placed above the blow tank feed system, to which it was connected by two butterfly valves. The first of these was attached to the hopper, and the second to the blow tank; these enabled the pressurisation of the blow tank to be carried out without pressurising the hopper. Therefore, the hopper did not have to be constructed as a pressure vessel. They also effectively separated the feeding operation from the collection operation as well as permitting the decoupling of the two vessels so that the load cells could provide accurate readings. The air used

Figure 5A.3 A schematic diagram illustrating the layout of the abrasive feeding equipment.

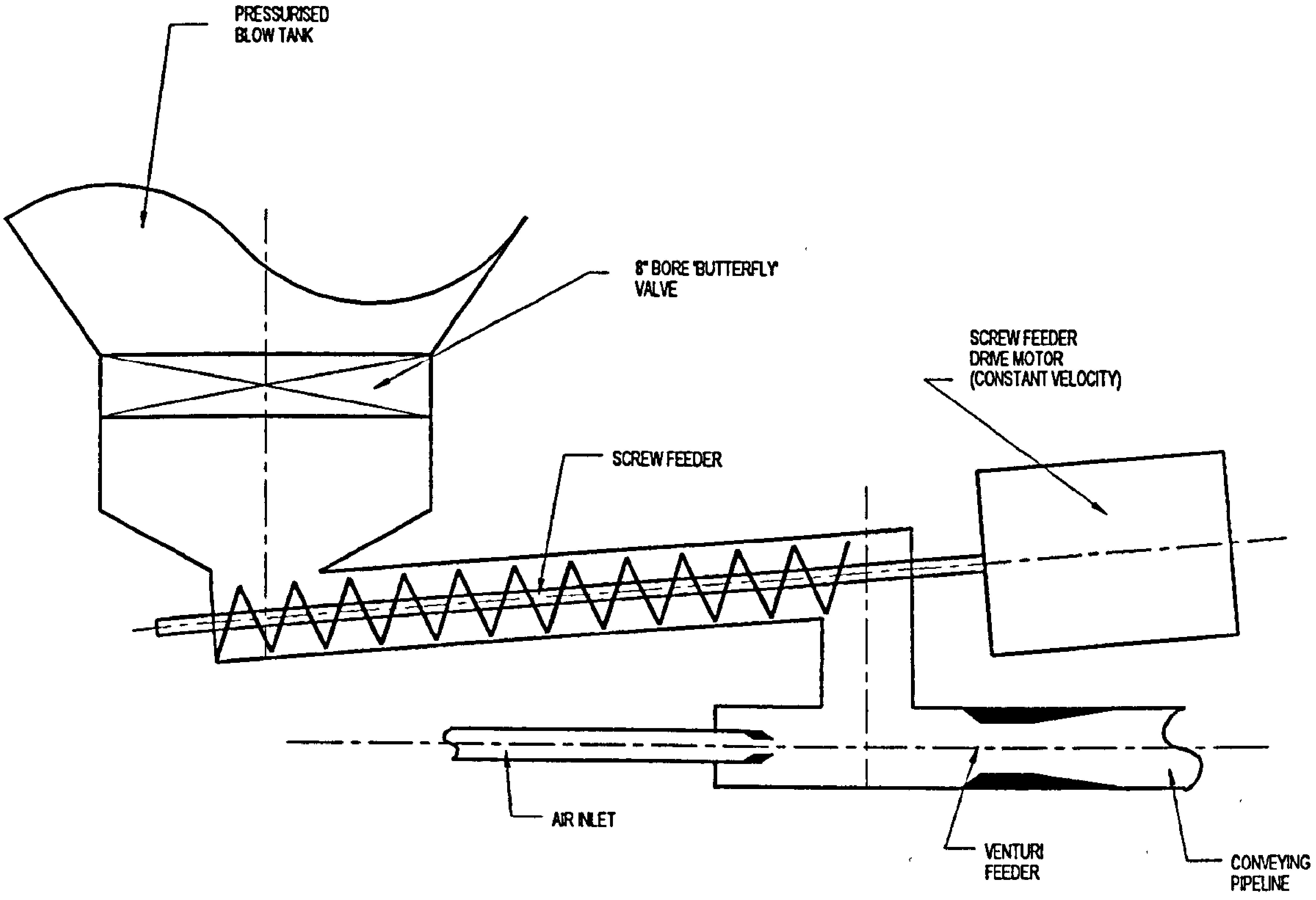

in the conveying process was separated from the conveyed abrasive using a dust filter made from woven fabric. Once the dust had been separated from the gas, the gas was vented outside the laboratory. The woven filter cloth was cleaned by mechanically shaking the filter at the end of each test run. In this way the efficiency of filtration was maintained.

A schematic view of the solid material handling system is shown in Figure 5A.4.

5A.4 The Air Supply System

The mass flow rate of the air entering the pipeline needed to be controlled to ±2% of the given set point value. This was achieved by using a choked flow nozzle to meter the flow of air. (Operation of the choked flow nozzles for this purpose is described in more detail by Bradley [B20]). The maximum air mass flow rate and pressure required were approximately 0.15m^3/s free air and 0.75 bar gauge respectively. The following relationship (obtained from work by Hitt [H22]) was used to enable the assessment of the effect of altering the upstream air pressure on the mass flow rate of the air fed into the conveying line.

$$\dot{m}_a = \frac{Q\,P}{T^{1/2}} \qquad where\ Q = 327\frac{1}{m\ sec\ K^{0.5}}. \qquad (5A.1)$$

The constant, Q, involved in this equation was derived empirically and confirmed by comparing the performance of the choked flow nozzle concerned against other nozzles of the same type. These had been calibrated against an orifice plate constructed and calibrated in accordance to BS1042 [B18]. P is the absolute pressure in bar, T is the temperature of the gas entering the nozzle in Kelvin and m is the mass flow rate of gas in g/s.

The main laboratory air supply was rated at 0.39 m^3/s free air at 6 bar gauge. This had to be reduced to a pressure of 4 bar gauge. This was achieved by using a standard 2" nominal bore regulator. The air was then passed through the choked flow nozzle to meter the gas mass flow rate and then passed through the venturi feeder to entrain the abrasive particles.

Pressurisation of the blow tank to overcome the back pressure of the pipeline was achieved by using the main laboratory air supply and passing air from it through a small regulator of 1/4" nominal bore. Since the main conveying air was derived from a metered source elsewhere, this air supply, adjusted to maintain an air pressure of 0.4 bar gauge in the blow tank, was purely necessary to overcome the

Figure 5A.4. A schematic diagram of the solid material handling system

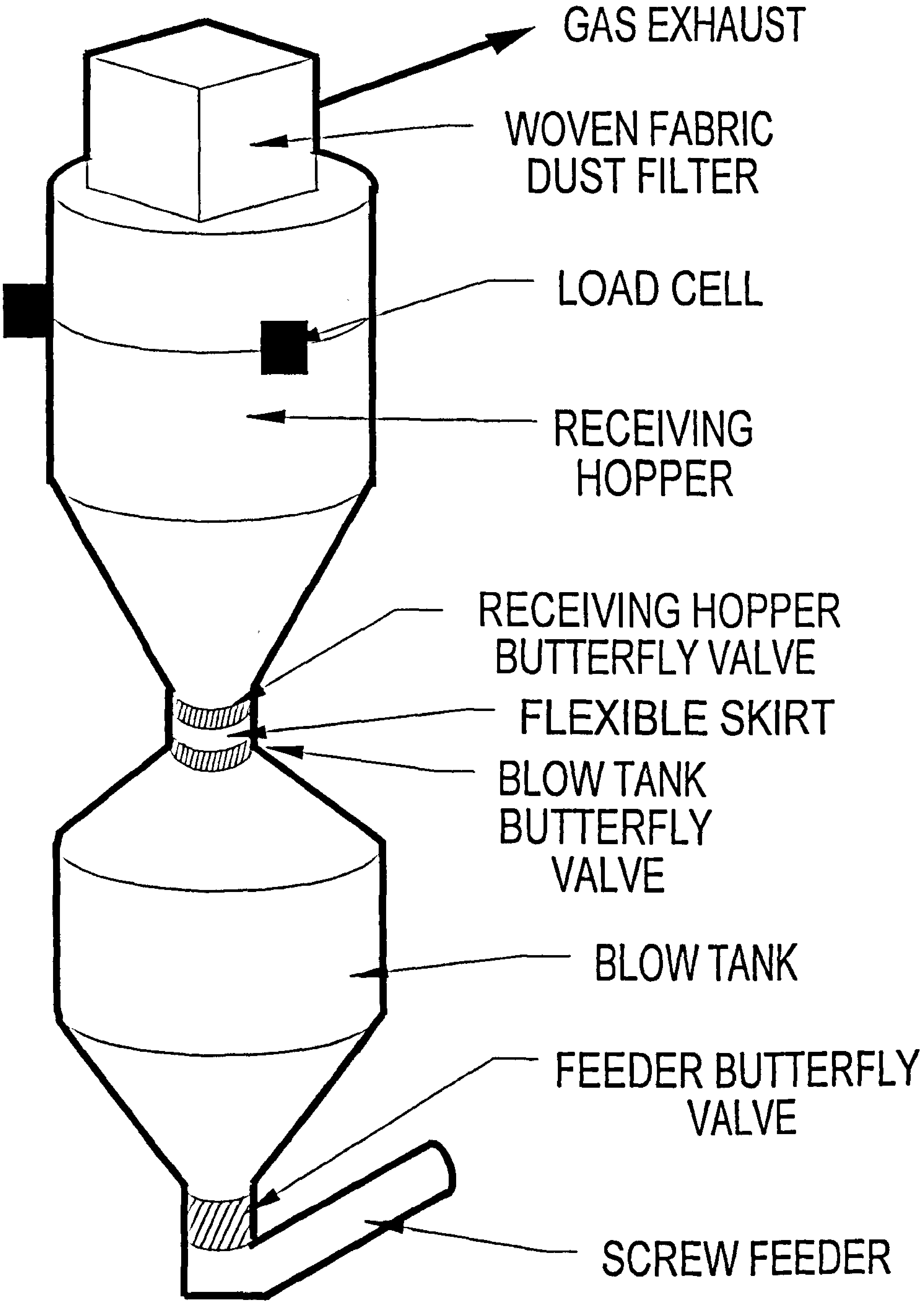

aforementioned back pressure. To account for the fact that air from the blow tank would permeate through the sand the actual air mass flow rate flowing through the pipe line was assessed. This was accomplished by using a thermocouple and pitot static tube mounted in the gas exhaust line emerging from the filtration system on top of the hopper. The data acquired from these instruments was compared to the expected mass flow rate of air passed through the choked flow nozzle. During the tests carried out for this project no evidence was found to suggest that blow tank pressurisation air passed into the conveying pipe line.

The interfacing of these air supplies with the abrasive feed system hardware is illustrated in Figure 5A.5.

5A.5 The Instrumentation System for Measurement of Pressure, Velocity, Mass of Abrasive Conveyed and Temperature

The main measurements that had to be taken during each conveying run were those necessary to find values for the local gas velocity and suspension density (mass flow rate of solids divided by the volume flow rate of air) at the entrance to the test bend. Values for these variables were derived by using measurements of the mass of abrasive material conveyed with time; the measurement of the local gas pressure just prior to the test bend; the pressure of the blow tank and the measurement of the temperature and velocity of the gas in the system exhaust. Each of these measurements will be discussed in turn.

Owing to the dynamic nature of the values to be measured a data collection system which interfaced to a personal computer (PC) was used. The data gathering system that was used was a commercially available system made by ELE Ltd. (model no. MM300) which was capable of simultaneously measuring 24 double ended signals or 48 single ended signals or a combination of these. This system contained a 12 bit analogue to digital converter. Control of this device was carried out by using an IBM compatible 486 PC which communicated with the data gathering system via an RS232 serial link. A full set of the calibration data used in the setting up of the ELE MM300 data collection system is given in Appendix 5B. Appendix 5B also includes a description of how the calculation of the values required for the assessment of the system conveying conditions during tests in their correct units of measure was carried out.

Figure 5A.5 Air supply interface schematic

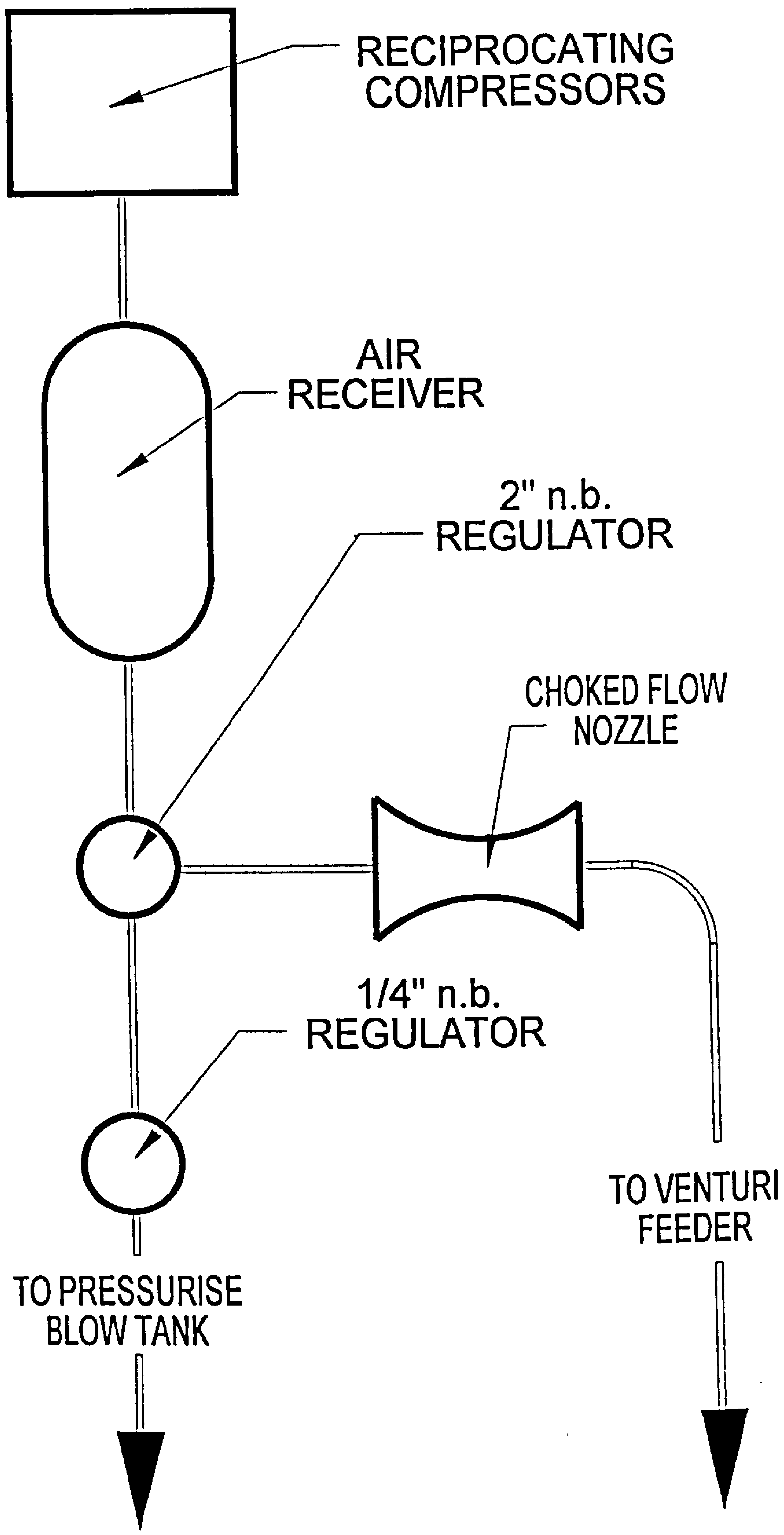

5A.5.1 Measurement of the Mass of Abrasive Material Conveyed with Time

The mass of abrasive conveyed was simply derived from measuring the weight of the receiving hopper and its contents at a series of time steps during the tests. This was achieved by using three interlinked load cells (Strainstall type 1865) capable of measuring up to 2500 kg capacity each. The stable DC voltage signal derived from these transducers was combined, amplified and fed to the data gathering interface. The load cell system was calibrated by applying a known load of 70 kg.

5A.5.2 Measurement of the Local Gas Pressure Just Prior to the Test Bend

The measurement of the local gas pressure at a point just prior to the test bend enabled an assessment of the particle velocity to be made. The method by which the velocity calculation was carried out was by using the equation of state for a perfect gas, and knowledge of the pipe bore dimensions as follows:-

$$c_{local} = \frac{\dot{m}\, R\, T}{p_{local}\, A} \qquad (5A.2)$$

where c_{local} is the local air velocity, and, by inference, the local particle velocity (assuming slip between the two phases to be negligible); $\dot{m}$ is the mass flow rate of gas in the system pipe line (this can be found from either equation 5.1 or subsequent measurements; see section 5A.5.4; both were used in the results analysis); R is the gas constant for air (287 J/kg K); T is the local temperature of the surroundings, which for these purposes this was taken to be 293°K; p_{local} is the local gas pressure measured just prior to the test bend and A is the cross-sectional area of the pipe bore.

The measurement of p_{local} was carried out by using a Druck PDCR810 pressure transducer capable of measuring up to 1 bar gauge. The output from this device was passed into the data gathering facility as described earlier.

5A.5.3 The Pressure in the Blow Tank

The blow tank pressure was measured using a pressure transducer similar to that used for measuring the air pressure just prior to the test bend. The reason for measuring this pressure was that the stability of the conveying conditions in the conveyor could be assessed from the stability in the readings obtained for the pressure in this vessel. It also served another purpose; that of indicating if a blockage had occurred in the abrasive feed mechanism. If the blow tank pressure rose suddenly it could be surmised that a blockage had occurred and corrective action could then rapidly be taken.

5A.5.4 The Measurement of the Temperature and Velocity of the Air in the Exhaust System

The air used to pressurise the blow tank came directly from the main laboratory air supply without being passed through the choked flow nozzle. As a consequence of this the total mass of air supplied into the system pipe line was unknown. The reason for this was that it was possible for the air pressurising the blow tank to seep through the abrasive material remaining in the blow tank and enter the conveying line with the particles. However, the amount of air entering the pipe line via this route was expected to be small. Finding the value of the air mass flow rate in the gas exhaust duct alleviated this problem since all of the air entering the line left through the exhaust duct. To obtain a value of the air mass flow rate in the exhaust duct it was necessary to measure the air velocity and temperature. These measurements would consequently enable an estimate to be made of the overall mass flow rate of air through the conveying pipe line.

Exhaust air temperature was measured by utilising a thermocouple integrated circuit (National Semiconductors LM35 Three Terminal Integrated Circuit) mounted in the wall of the exhaust duct. A pitot static tube was used to measure the air velocity. The pitot static tube was mounted so that the probe tip was facing into the oncoming air stream on the pipe bore centre line (see Figure 5A.6). The installation of the pitot static tube was carried out in accordance with directions given in BS1042 [B18], including being placed approximately 5 m away from the beginning of the gas exhaust duct, so that the air flow regime in the duct would be fully developed and stable. The two pressure lines from the pitot static tube, one measuring the static pressure and the other the dynamic pressure, were taken to two small reservoirs to damp any large pressure fluctuations. The pressures in these reservoirs were measured using a differential pressure transducer (Furness Controls Ltd., FCO44) prior to a signal being passed to the data collection system.

The measurements taken by these two transducers were used to derive the value for the total mass flow rate of air in the pneumatic conveyor pipe line by using the following equation [B18]:-

$$\dot{m} = \frac{P\,v\,A}{RT} \qquad where \qquad v = 1.414\sqrt{\frac{\Delta p_{corr}}{C\,\rho_a}} \qquad (5A.3)$$

where P is taken to be atmospheric pressure; A is the cross-sectional area of the pipe at the point of transducer attachment; R is the gas constant for air (287 J/kg K); T is the temperature of the gas at this point in K; Δp_{corr} is the pressure differential measured by the pitot static tube which has been corrected for local gas temperatures by using the equation of state for a perfect gas; ρ_a is the local gas density; $\dot{m}$ is the air mass flow rate and C is a constant that is supplied by the maker of the pitot

Figure 5A.6 Pitot static tube and thermocouple arrangement

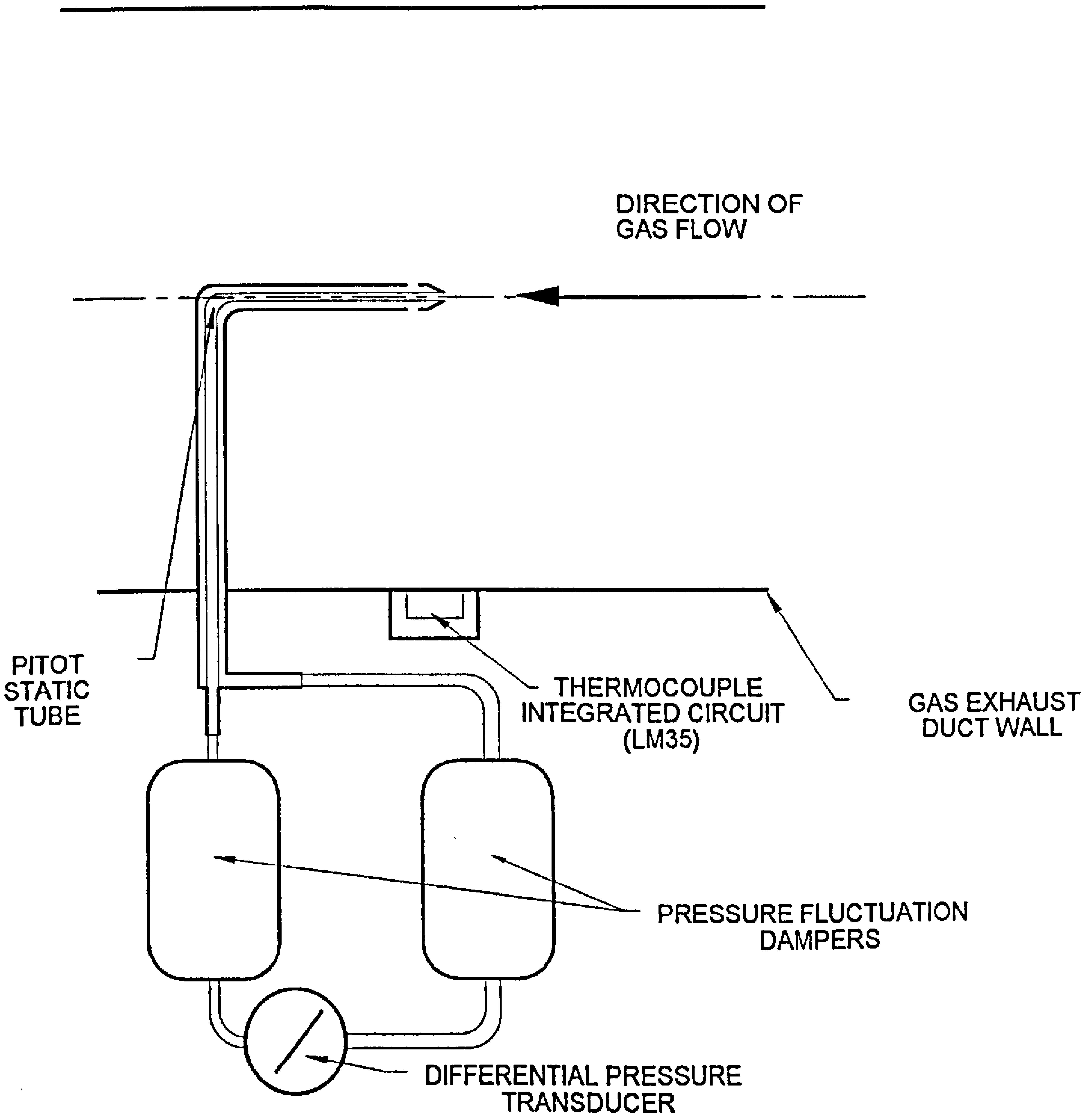

static tube for calibration purposes. This calculation was undertaken automatically by the software controlling the gathering of data as the data arrived. By use of these measurements it was discovered that the air mass flow rate contribution made by the unregulated air entering the pipe line from blow tank pressurisation was minimal. However, to be sure of the results the local air velocities entering the test bend were calculated using the pitot static tube and thermocouple readings.

5A.6 The Method of Measuring the Bend Penetration

The bend penetration was measured manually after a fixed mass of abrasive material had been conveyed. This was achieved by using an ultrasonic thickness transducer. This device was manufactured by Inspection Instruments (Kawatetsu Keiryoki Nishinomiya, Japan) Model TI-5. It was capable of measuring thicknesses between 1 and 99.9 mm and its resolution was 0.1 mm. The probe head of this device was 12 mm in diameter. Accurate and repeated positioning of the probe on the same point for each measurement location were complicated because of the curved nature of the external pipe bend surface. Another major difficulty of using a system such as this, was that of correctly positioning the measurement locations. This was achieved by testing a bend of identical dimensions to destruction and then opening the bend up to see where the major wear locations were. Trajectory modelling was also used to try and predict the initial impact locations. This method is discussed in more depth in section 5.4 of Chapter 5. The problem of measuring the wall thickness accurately and repeatedly was overcome in the following way:- (i) flats were filed on to the outside surface of the pipe bend at locations where severe wear was found to occur; (ii) washers of 12 mm internal diameter were welded on to these flats; Then accurate and repeatable placement of the transducer probe could be achieved. Figure 5A.7 illustrates these measurement locations clearly. The final test bend had a total of 45 measurement locations. These were placed in groups of five around the bend radius starting at 15° and ending at 35° in 2.5° steps. In each group the five locations were positioned equally at 30° and 60° either side of the bend centre line on the extrados. Figure 5A.8 illustrates this. Each and every measurement location was given a unique identification mark prior to testing being undertaken.

5A.7 The System for Measurement of the Particle Concentration Distribution

The assessment of the distribution of particle concentration across the pipe bore was carried out using an optical technique. The method that was employed was that of light obscuration.

Figure 5A.7 Ultrasonic thickness measurement probe location arrangements.

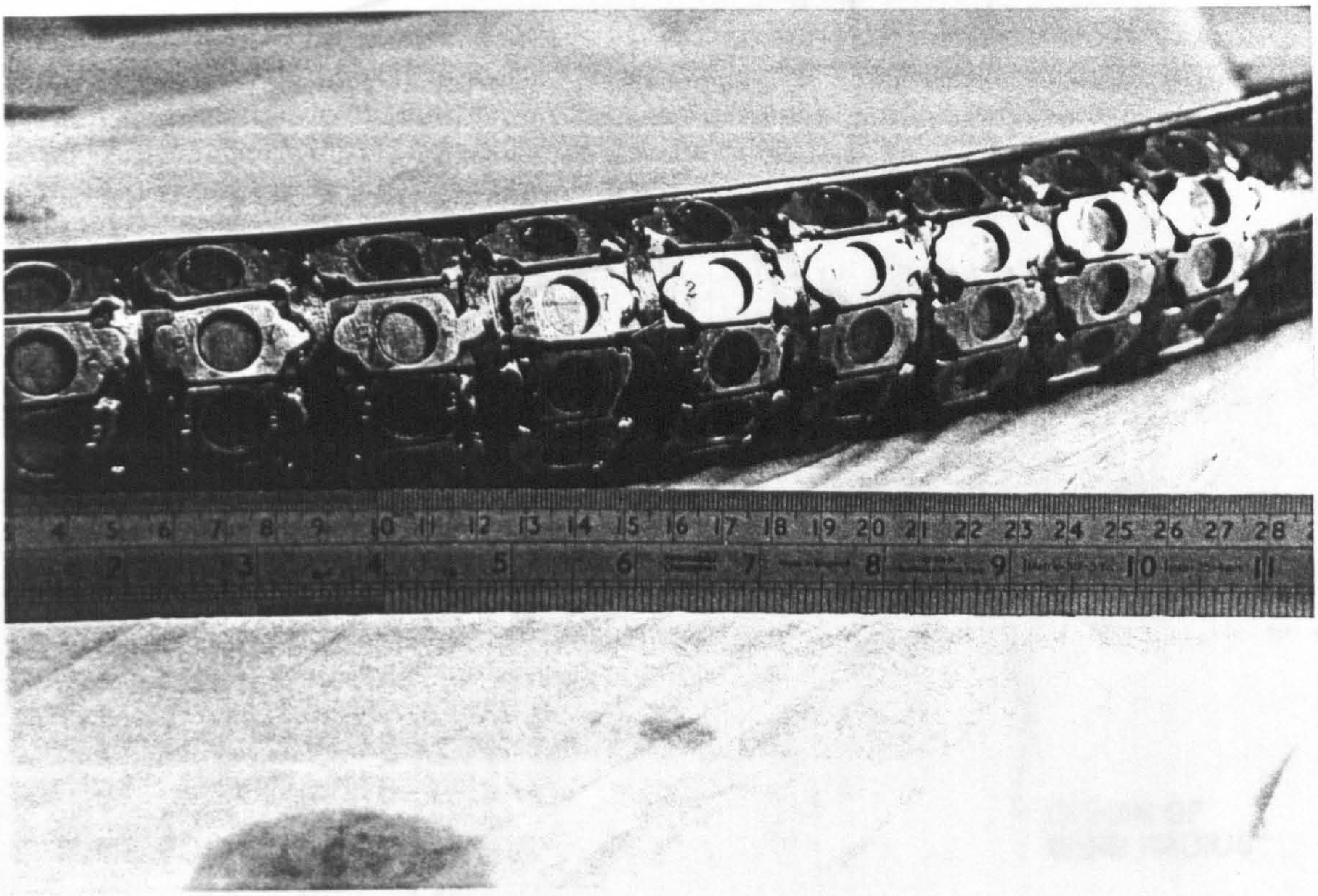

Figure 5A.8 Penetration measurement location coordinate system and orientation.

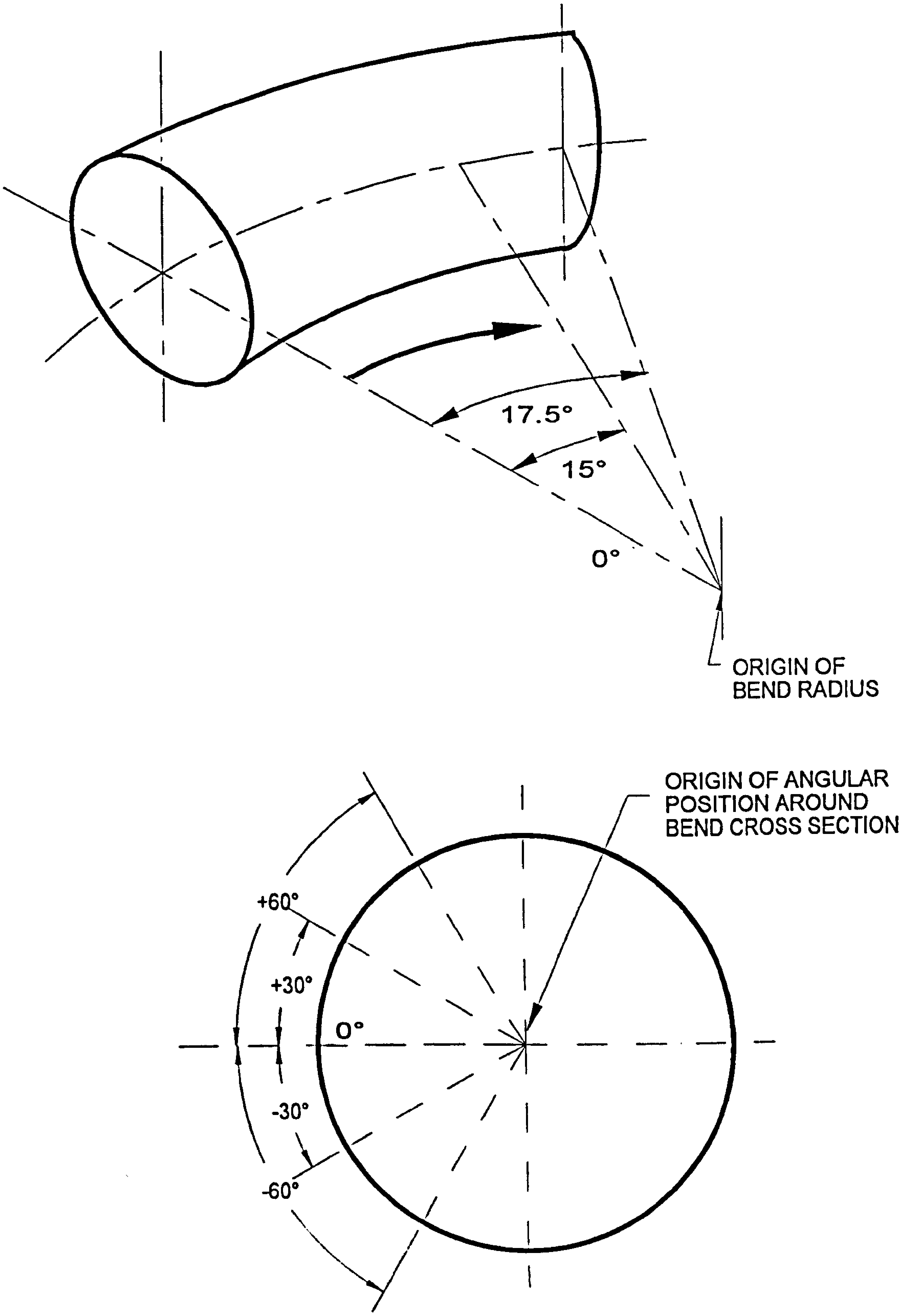

A 2mW HeNe laser was used to provide a narrow beam of light which was projected through a glass section of tubing placed just prior to the test bend during conveying. The light that passed through the stream of particles was caught on a specially selected photodiode (type BWP21) (see Figure 5A.9). This photodiode was selected because it was not sensitive to ambient light conditions, but tailored to use in operations where the wavelengths of the light involved were similar to those of the laser used. Focusing the laser beam, by using standard lenses, was required because the amount of obscuration that would occur at the photodiode was dependent on the spread of the light beam. The greater the width of the laser beam, the greater the amount of particles that would be required to give an adequate amount of obscuration for measurement. Ideally the number of particles obscuring the laser beam should be no more than one. If this were the case, the assessment of the particle concentration would be as accurate as possible. Therefore, a small beam width was required since the particle concentration could be more accurately assessed if this were the case. In the case of the conveying trials carried out with the olivine sand particles used in this project, it was expected that the mean number of particles passing through the laser beam at any one time would be less than one. However, there was always the possibility that one particle may pass through the laser beam in the shadow of another. As a consequence of this, the data obtained from this device could not be related directly to a number based particle concentration distribution. Further description of this device is given by Selves [S15].

The photodiode that was used in this test equipment was used in a photovoltaic mode. This mode of operation ensures that any measurements of the output of the photodiode are as accurate as possible [H12]. The linearity of the photodiode was checked prior to use for the purposes described above. This is described in more detail in Appendix 5B.

Data was taken from the photodiode by amplifying the DC signal produced by the incident light using an AD524 instrumentation amplifier and passing this to the data acquisition system. The position of the laser beam in relation to the glass tube section was adjusted manually using an M16 screw thread to gauge the distance moved by the beam. This enabled the laser beam to be moved across the glass section in 2 mm steps. Each time the movement of the beam had been completed a stable 5V DC signal was passed into the data acquisition system for a fixed period of time to ensure that the readings from the photodiode were correctly selected from the continuous readings taken. The 5V DC signal was switched off prior to moving the laser to the next measurement position. This procedure was continued until a complete traverse across the pipe had taken place.

Figure 5A.9 Photograph and schematic drawing of the device for assessment of the particle concentration distribution.

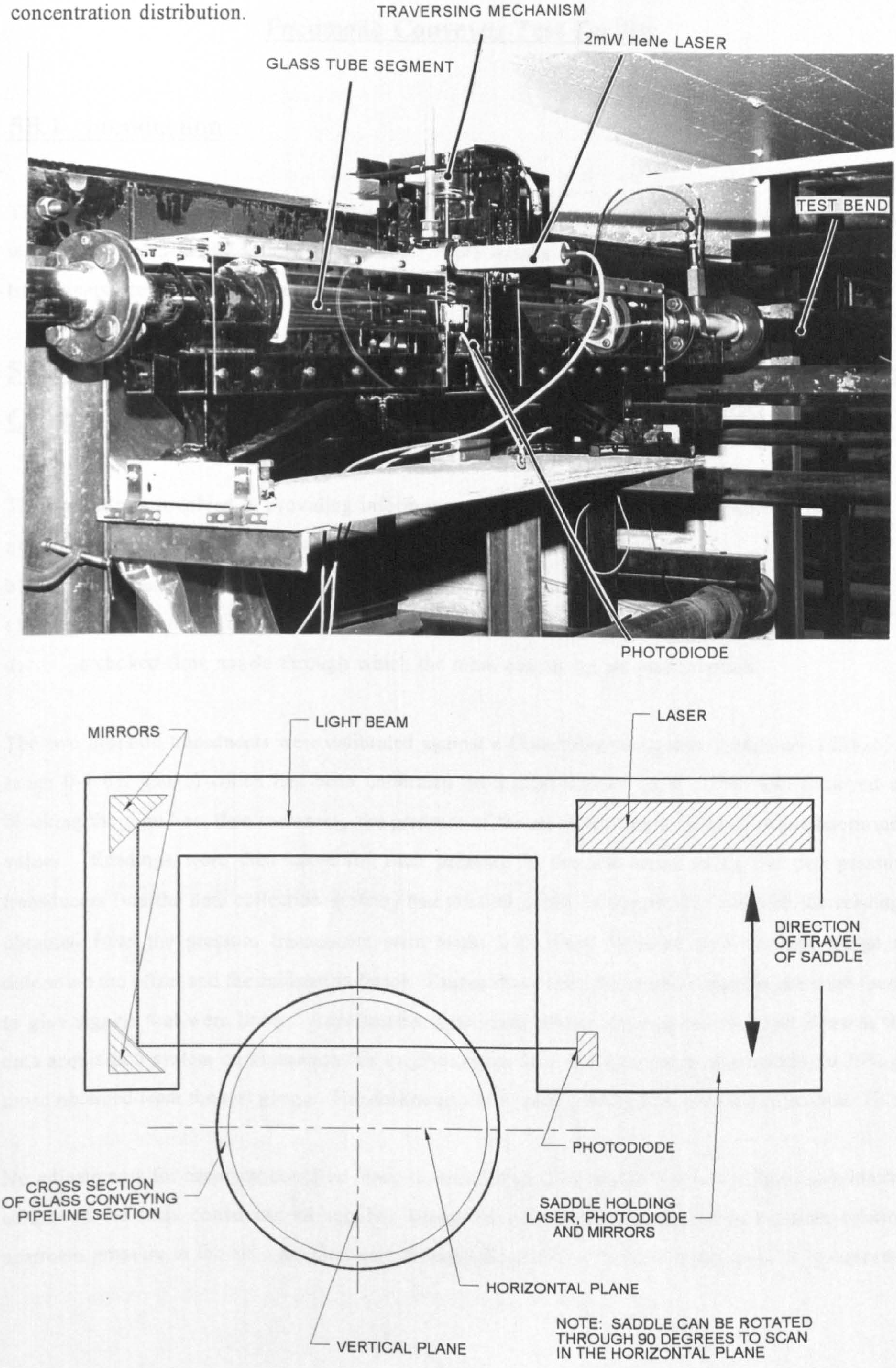

Appendix 5B: Calibration of the Instrumentation Used on the Pneumatic Conveyor Test Facility

5B.1 Introduction

The calibration of the transducers used in the instrumentation on the pneumatic conveyor test facility will be discussed in the following sections. More details regarding the number and type of the transducers used on this rig are given in Appendix 5A.

5B.2 Calibration of the Transducers Used to Determine the Conveying Conditions

The transducers involved in providing information regarding the conveying conditions, include:-

a) a pressure transducer just before the test bend;
b) a pressure transducer on the blow tank;
c) a temperature measurement transducer and pitot static tube on the gas exhaust duct, and
d) a choked flow nozzle through which the main conveying air was supplied.

The two pressure transducers were calibrated against a Budenberg test gauge (gauge no. 12582650: range 0-4 bar gauge) which had been calibrated on a dead weight tester. This was achieved by blocking the pipe line, then increasing the pressure of the air in the line to a series of predetermined values. Readings were then taken for each pressure in the test series using the two pressure transducers (via the data collection system) and the test gauge. Comparisons between the readings obtained from the pressure transducers were made with those obtained from the test gauge to determine the offset and the calibration factor. During these tests the pressure transducers were found to give signals that were linear. Adjustments were made where necessary to the algorithms in the data acquisition system configuration file to give output from the transducers that within ±0.75% of those obtained from the test gauge. The data acquisition configuration file is shown in section 5B.5.

No adjustments for accuracy could be made to the choked flow nozzle that was used to provide the control of the main conveying air supply. Numerical constants were used in an equation relating upstream pressure to the air mass flow rate through the nozzle. These were determined by carrying out comparative tests between the nozzle and an orifice plate constructed and instrumented to BS1042 [B18], this work being carried out by Hitt [H22].

The pitot-static tube installation included a differential pressure transducer that was used to measure the difference in pressures found in two small reservoirs positioned at the end of the pitot static tube pressure connections. (The reason the small reservoirs were used was to damp out any perturbations occurring in the output signal, which, in turn led to greater accuracy in the readings obtained). The signal generated from this transducer was processed using equation 5A.3 Appendix 5A, and calibrated against a range of gas flow rates provided by the choked flow nozzle mentioned above. Again, adjustments to the data acquisition system configuration file were made to ensure that the readings obtained from the two flow registering devices were as similar as possible over the range of operation expected. Fortunately, it was also found that the pitot static tube differential pressure output varied in a consistent manner with the square of the flow rate being considered.

The temperature transducer selected was capable of giving a linear temperature measurement over the range in which the tests were being carried out. The calibration of the transducer was checked against a digital hand held temperature measurement device. Alterations to the data acquisition system configuration file were made to ensure that the readings obtained from the two measurement devices were equal.

The load cells that weighed the contents of the receiving hopper were calibrated by weighing a person and getting them to climb on to the top of the hopper.

5B.3 Calibration of the Equipment Used to Measure the Penetration Suffered by the Test Bend

The penetration of the test bend was measured using an ultrasonic thickness transducer as described in Appendix 5A. Since the measurements were carried out manually and not logged on a computer, only one adjustment was made for calibration purposes. This was done by measuring the thickness of a specially machined piece of steel of a known dimension. The thickness of this test sample was compared to the digital reading given by the tester. Adjustment was made to the ultrasonic tester, by using a potentiometer, which adjusted for the speed of sound in the material being measured. This altered the reading given by the tester. Adjustments continued until the reading on the thickness tester compared to within ± 0.1 mm of the stated sample dimension.

5B.4 Calibration of the Particle Concentration Distribution Assessment Equipment

Since these measurements were quite unusual in their scope, no formal calibration was carried out as such. The only test that was undertaken was that of checking for the linearity of the variation of the signal obtained from the photodiode with light obscuration. This was achieved by using a neutral density filter, (which contained ten graduations of opacity from totally clear to complete obscuration arranged in a linear manner with distance across the filter). The results obtained from these linearity tests are shown in Figure 5B.1. Relating the readings taken using this device directly to the particle number concentration is not possible for the following two reasons; First the sampling rate of the data acquisition system was not fast enough to distinguish between the obscuration caused by individual particles. Secondly, it is possible that a situation where two particles pass through the light beam simultaneously may occur. In this case the light will be obscured by one of the particles only and the passage of the second particle will remain undetected. It is possible to estimate the probability of this occurring. In conclusion, the device used in this project can only be used to obtain a time averaged mean obscuration caused by the passage of the particles.

Despite the fact that no calibraton of the photodiode output to the number density of particles could be carried out, it was still necessary to use the computer based data acquisition system to automatically read the values of the voltage signal derived from the photodiode. To achieve this another configuration file was used to set up the data acquisition equipment to carry out these tests. The configuration file is shown in section 5B.6 below.

5B.5 The Data Acquisition Configuration File for Conveying Condition Measurement

The configuration file used to give the output signals obtained from the transducers in terms of actual engineering measurement units, and specify the hardware set up for the acquisition process, is given on the following pages.

Figure 5B.1 Graph illustrating the linearity of the photodiode output with light obscuration.

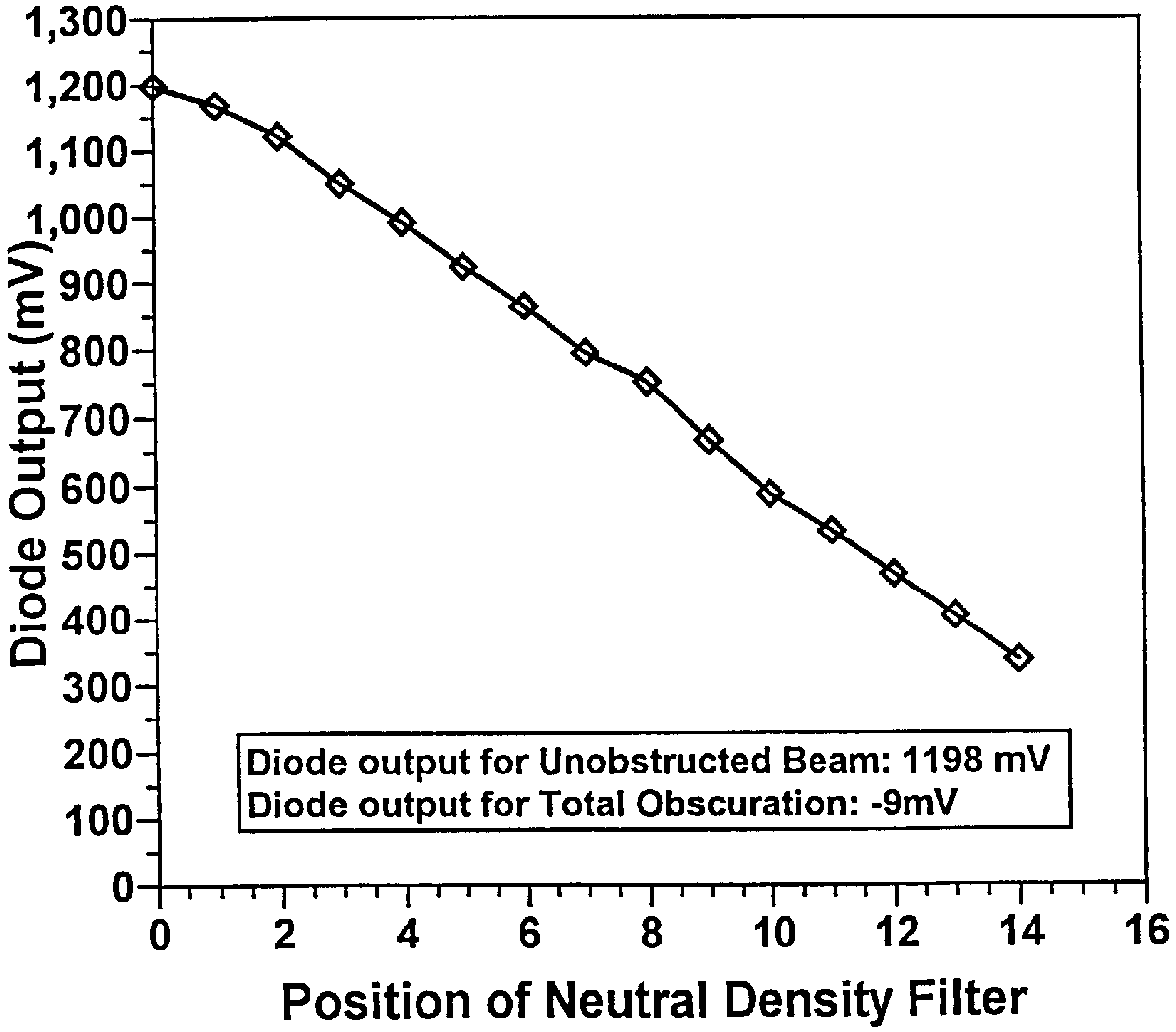

```
**** Hard Copy of D I A L O G Configuration Parameters ****

Interface type : RS-232 COM 2

Scan rate :  1  Hertz

Task automatically started on start

Channels Defined
----------------

No. Type                 Name      Units     Format     A0         A1        G  AF

  0 Digital              Time      Secs      ######     0          1         0  NN
  2 Relative Low         RH Prod   kg        ####.#     0          1.577825  0  NY
  4 Absolute DC          Man press Bar       ###.###    -.66776    .0144173  1  NY
  5 Relative Low         RH PST              ###.###    0          1         1  NY
 16 Absolute DC          BT Press  mbar      ######.#   2          .3344617  2  NY
 21 Absolute DC          TB press  mbar      ######.#   7          .4920283  2  NY
 55 Absolute DC          RH Temp   Kelvin    ###.#      273        .04561    1  NY

Logging Parameters
------------------

Logging Task Type : Intervals

Task No. :  1

Channels : 0 2 4 5 55 21 16

No. Readings :  500

Rates     Unit        1st Rd.      Final Rd.
 1         5           1            500
 2         0           0            0
 3         0           0            0
 4         0           0            0
 5         0           0            0
 6         0           0            0
 7         0           0            0
 8         0           0            0

Averaging Parameters:-
     No. of samples to average      : 6
     Scan interval between samples  : 1

No. Type                 Name      Units     Format     k1         k2        c1  c2

  1 k1.(SQR(c1))+k2      RH AMFR   g/s       ####.###   1.916483   -1.522     4   0
  2 k2.(c1.c2)+k1        AMFR COR  g/s       ####.###   0          .003464    8   5
  3 k1.(SQR(c1))+k2      RH Vel    m/s       ##.###     .1310789   -.15       4   0
  4 k2.(c1/c2)+k1        AMFR ACT  g/s       ###.#####  0          4175.73   10   5
  5 k2.(c1/c2)+k1        Vel TB    m/s       ###.###    0          37465.6   11  13
  6 k1+(k2.c1)           TB Press  N/m^2     ######.#   101396.2   101.396    6   0
```

5B.6 The Data Acquisition Configuration File for Photodiode Output Measurement

The configuration file used to acquire the output signal obtained from the photodiode in data bits, and specify the hardware set up for this acquisition process, is given on the following page.

```
**** Hard Copy of D I A L O G Configuration Parameters ****

Interface type : RS-232 COM 1

Scan rate :  1  Hertz

Task automatically started on start

Channels Defined
----------------

No. Type                 Name      Units     Format     A0       A1       G  AF

  0 Digital              Time      Secs      ######     0        1        0  NN
 22 Relative Low         Diode     Bits      ######.#   0        5        0  NY
 23 Absolute DC          position            ######.#   0        1        0  NN

Logging Parameters
------------------

Logging Task Type : Intervals

Task No. :  1

Channels : 0 22 23

No. Readings :  3000

Rates    Unit       1st Rd.     Final Rd.
 1        3          1           3000
 2        0          0           0
 3        0          0           0
 4        0          0           0
 5        0          0           0
 6        0          0           0
 7        0          0           0
 8        0          0           0

Averaging Parameters:-
     No. of samples to average     : 1
     Scan interval between samples : 6


Template Columns
----------------

No. Type                 Name      Units     Format     k1       k2       c1   c2
```

Appendix 5C: Method of Carrying Out Tests on the Pneumatic Conveyor Test Facility

5C.1 Introduction

The tests carried out on the pneumatic conveyor test facility can be separated into three phases. These are 1) The main conveying trials, 2) measurement of the bend penetration, and 3) assessment of the particle concentration distribution. Effectively 1) and 2) are related and they will be discussed jointly. However, the assessment of the particle concentration distribution formed a completely different set of tests, and consequently will be discussed separately.

5C.2 Method of Carrying Out Conveying Characteristic and Bend Penetration Measurements

Since the measurement of the progression of penetration with time under fixed conveying conditions was required, a series of detailed measurements of the bend wall thickness had to be undertaken. Tests of this type for 45 measurement locations (see Appendix 5A section 5A.6) took considerable time. It was therefore necessary to stop the conveying cycle periodically to undertake the necessary measurements. Owing to the careful design and operational procedure adopted for the test facility, the start up and shut down transients normally seen in pneumatic conveyor operations were minimised. Hence, the effects of such transients on the erosion process by frequent stopping and starting of the conveyor were not seen. Figure 5C.1 illustrates the performance of the pneumatic conveying system throughtout a test run well.

Test cycles consisted of the following operations:-

a) The butterfly valve on the base of the blow tank was shut.

b) Two butterfly valves fitted between the hopper and blow tank were opened to allow charging of the blow tank to occur. The charge of abrasive material was always greater than 250 kg so that the abrasive material would not run out during a conveying run. When charging had finished, the two butterfly valves were shut. The ball valve on the pressure release vent for the blow tank was also shut.

c) The computer based data acquisition system was activated.

d) The air supply to the conveying line was switched on and allowed to reach a steady state condition, (this normally took approximately 30 to 45 seconds).

Figure 5C.1 Graph illustrating the variation of the raw data taken during a pneumatic conveying test with time.

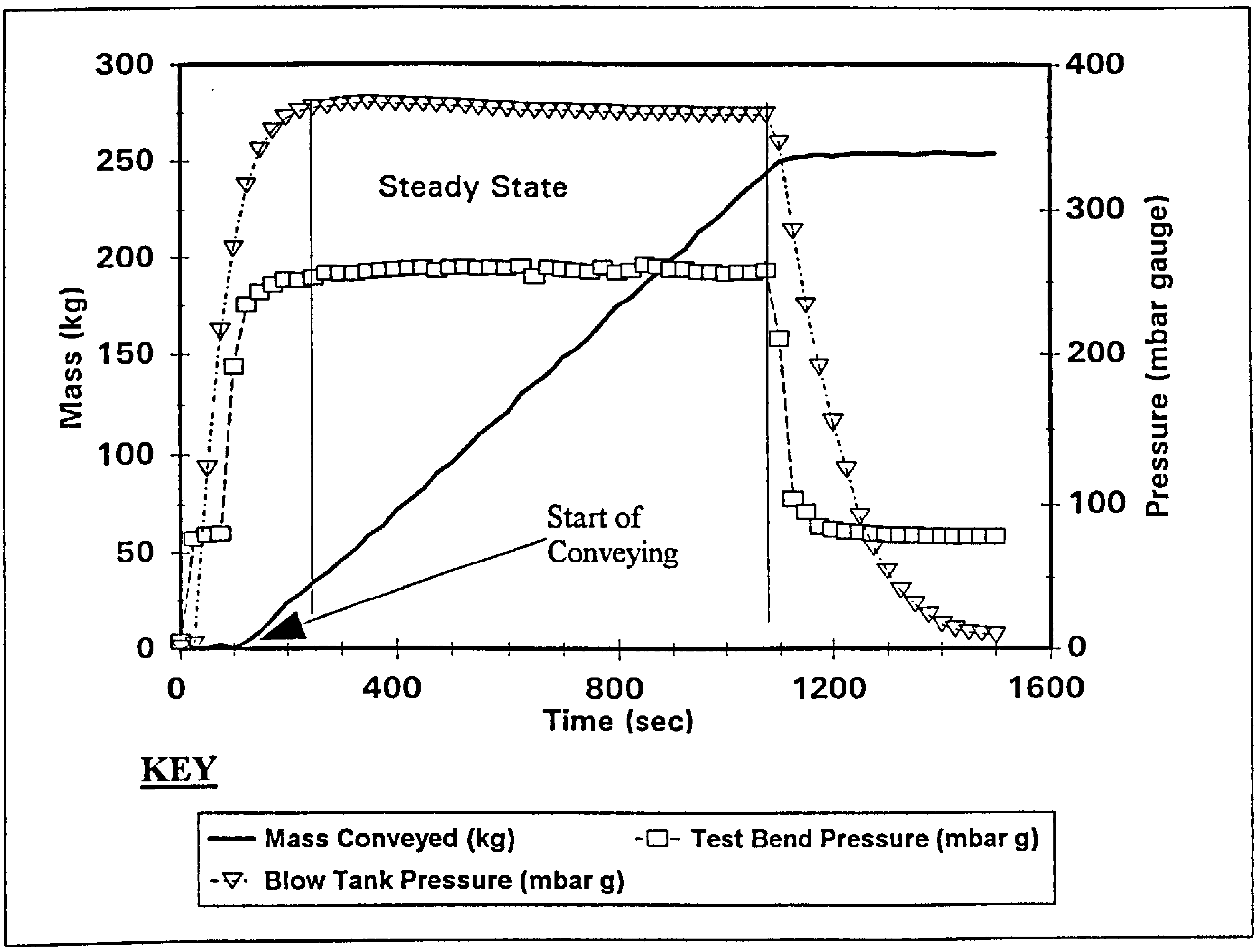

e) The screw feeder was switched on and allowed to reach its steady rotational speed, (again 30 to 45 seconds was allowed for this to occur).

f) Pressurising the blow tank was undertaken, and the pressure was allowed to increase to a value of 230 mbar gauge, (this value was selected since it was found, during preliminary trials on the pneumatic conveyor test rig, that the conveying cycle was free from perturbations in conveying velocity and mass flow rate of abrasive if the blow tank pressure was at this level prior to the start of conveying). Once this pressure was reached the valve on the bottom of the blow tank was opened and the abrasive material was allowed to flow into the screw feeder.

g) A continuous check was made on the pressure levels and other measurements during the test run by using the computer based data acquisition system.

h) Once the mass of material conveyed into the receiving hopper had reached 245 kg, the valve on the bottom of the blow tank was shut and the application of pressurising air to the blow tank was stopped. The abrasive material remaining in the conveying line was conveyed to the receiving hopper. Once the rate of material entering the hopper had reduced to zero, the conveying line air supply and the screw feeder were switched off.

i) Measurement of the test bend wall thickness at the previously mentioned measurement locations was carried out using the ultrasonic thickness tester described in Appendix 5A.

j) The data for the conveying run obtained by the data acquisition system from the various transducers involved was saved on a computer. The readings taken from the ultrasonic thickness transducer were kept in hand written records.

k) Once all the necessary data had been saved the above procedure was repeated. This was continued until the test bend punctured.

5C.3 Method of Carrying out the Assessment of the Distribution of Particle Concentration Using the Laser Obscuration Technique

Assessment of the particle concentration distribution by light obscuration required the use of the data acquisition equipment normally used to assess the conveying characteristics of each test. However, the experience gained using the test facility indicated that once the relevant valve and control settings had been set, the repeatability of the test conditions were reasonably good. Repeatability in conveying velocity to within ±1%, and suspension density to within ±3%, was judged to be good enough to permit the data acquisition equipment to be released from the task of measurement of the major conveying variables involved, to particle concentration distribution assessment. The method of carrying out the tests necessary to assess the particle concentration distribution is described below.

a) Without the conveying system being switched on, a series of calibration readings were taken for the measurement of the obscuration suffered by the laser beam, at a series of positions during a traverse of the glass section of the pipe. These operations follow the pattern as described in sections i) to vi) given below:-
    i) Data acquisition of the DC voltage signal from the photodiode amplifier was initiated. This was a continuous measurement sequence (see Appendix 5B section 5B.6 for the data acquisition system configuration file for these tests).
    ii) The position of the laser beam in relation to the glass section of the pipe bore was changed to new sample locations in a series of 2 mm steps across the glass section of the pipe. This was accomplished by using a 2 mm pitch leadscrew.
    iii) A stable 5V DC signal was passed to the data acquisition system on another channel. This was maintained for approximately twenty seconds to ensure that a reasonable sample of data readings for light obscuration were obtained.
    iv) The 5V DC signal was switched off, and the position of the beam was moved another 2 mm step across the glass section of pipe as described above.
    v) The 5V DC signal was switched on again.
    vi) This process was repeated until the entire traverse of the glass pipe section was completed.

    Three of these calibration tests were carried out before each and every test run was started.

b) Measurement of the amount of light obscuration occurring during a conveying test was then undertaken. The points a), b), d)-h) from section 5C.2 described above were used as before to initiate a conveying run. A series of measurements were made for light obscuration with distance travelled across the pipe bore during each test run, as described in section a) i) through vi) above.

c) This sequence of events, including the matching calibration tests, was repeated three times in the vertical scan orientation and three more times in the horizontal orientation.

d) At the end of each traverse of the laser beam the data was extracted from the data acquisition system and saved on a computer.

Appendix 5D: Data Collected During the Main Pneumatic Conveying Trials

5D.1 Introduction

Data illustrative of that collected from carrying out tests on the pneumatic conveyor test facility for the primary conveying characteristics are presented in this appendix. An example of the raw data obtained during a test run is also given, along with a table of the final conveying characteristics for each of the twenty two conveying tests carried out. Also presented in this appendix is a complete set of the bend wall penetration measurement results.

5D.2 The Variation with Time of the Raw Data Derived During a Pneumatic Conveying Test

Figure 5D.1 shows a graph of the variation of the blow tank air pressure, the mass of abrasive conveyed and the pressure just prior to the test bend against time. It must be emphasised that the mass of abrasive conveyed with time is steadily increasing and the two pressure readings do not deviate much with time. These facts indicate that a steady state conveying regime is occurring.

5D.3 The Pneumatic Conveying Characteristics

Table 5D.1, shown below, gives the mean values for the air velocity just prior to the test bend, mass flow rate of the abrasive, suspension density (mass flow rate of solids divided by volume flow rate of air) and the solids loading ratio (ratio of the mass flow rate of solids to the mass flow rate of gas) for each one of the twenty two pneumatic conveying tests.

Figure 5D.1 Graph illustrating the variation of raw data taken during a pneumatic conveyor test with time.

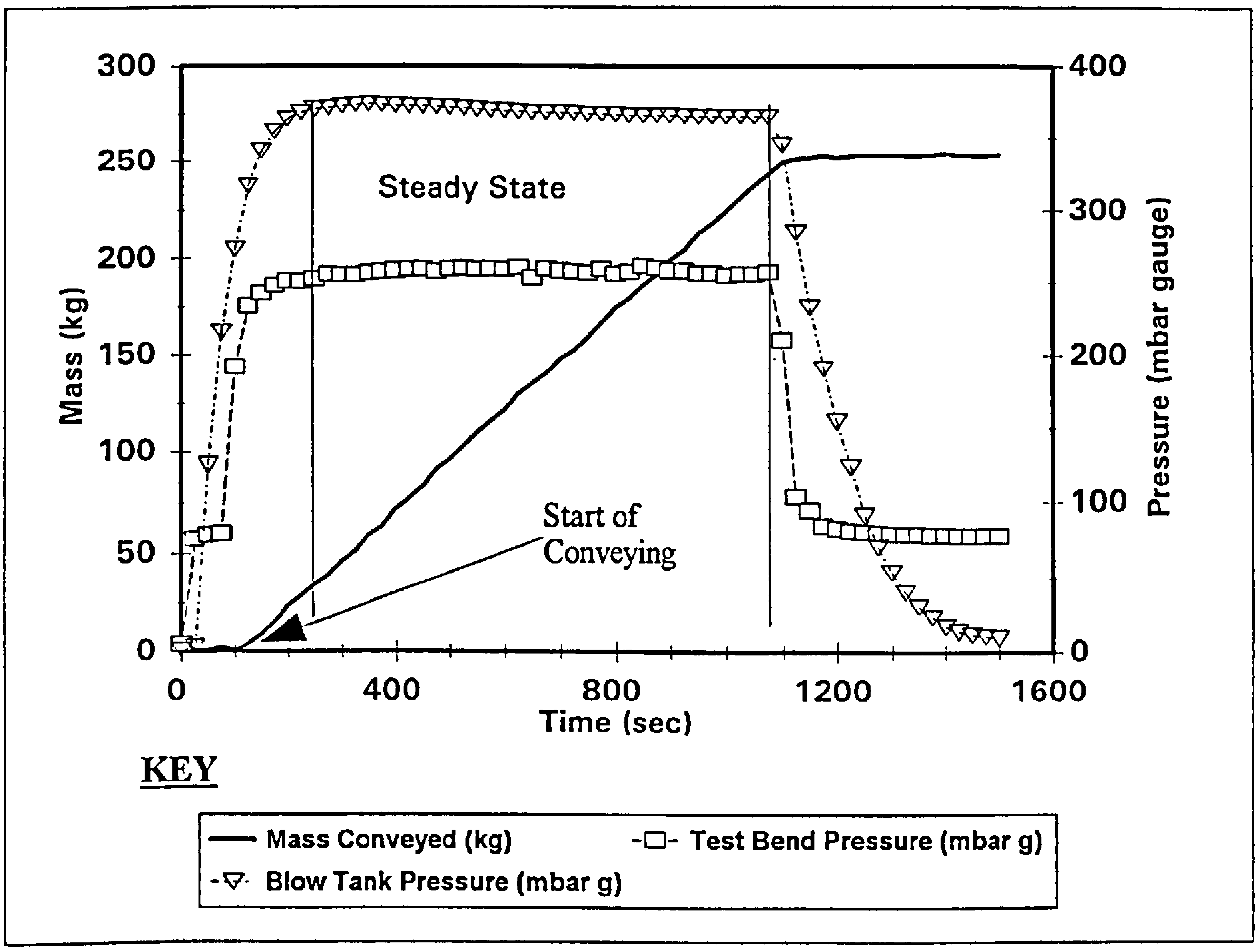

Table 5D.1 Values for the Conveying Characteristics Obtained for the Tests Carried out on the Pneumatic Conveyor

Test Number	Mass Flow Rate of Abrasive (g/s)	Local Air Velocity (m/s)	Suspension Density (kg/m^3)	Solids Loading Ratio (kg/kg)
1	236.6	25.50	3.503	2.920
2	240.6	25.47	3.552	2.960
3	247.0	25.51	3.610	3.009
4	252.4	25.70	3.523	2.936
5	256.1	25.70	3.523	2.936
6	256.4	25.49	3.265	2.720
7	257.5	25.48	3.418	2.849
8	259.6	25.64	3.550	2.959
9	260.8	25.37	3.582	2.985
10	261.1	25.15	3.644	3.036
11	261.1	25.83	3.605	3.004
12	261.1	25.69	3.637	3.030
13	261.5	25.71	3.618	3.015
14	261.7	25.61	3.657	3.048
15	262.2	25.70	3.347	2.789
16	264.2	25.69	3.200	2.666
17	265.9	25.74	3.453	2.877
18	265.9	25.58	3.474	2.895
19	267.6	25.61	3.560	2.967
20	267.7	25.49	3.538	2.948
21	268.8	25.60	3.543	2.953
22	269.9	25.46	3.601	3.000

5D.5 Pneumatic Conveyor Bend Wall Thickness Measurements

Table 5D.2 shown on the following page gives the full series of bend wall thickness measurements that were taken using the ultrasonic thickness measurement transducer. Readings were taken for the penetration of the bend wall in 45 locations for every 250 kg of abrasive material conveyed.

Table 5D 2 Bend Penetration Data

Position	Initial Thicknes	Test Number 1	2	3	4	5	6	7	8	9	10	11	12	13	14	15	16	17	18	19	20	21	22	Micrometer Reading (mm	Penetration Depth (mm)
1	2.2	2.2	2.2	2.2	2.2	2.2	2.2	2.1	2.1	2.1	2.1	2.1	2.1	2.1	2.1	2.1	2.1	2.1	2.1	2.1	2.1	2.1	2.1	2.032	0.168
2	2.4	2.3	2.3	2.2	2.1	2.1	2.0	2.0	2.0	1.9	1.9	1.8	1.8	1.8	1.7	1.7	1.6	1.6	1.6	1.6	1.5	1.5	1.5	1.511	0.889
3	2.3	2.1	2.2	2.0	2.0	1.8	1.7	1.7	1.7	1.6	1.5	1.5	1.4	1.3	1.3	1.2	1.1	1.0	1.0	1.0	0.9	0.9	0.9	0.927	1.373
4	2.4	2.2	2.2	2.1	2.0	2.0	1.9	1.8	1.8	1.8	1.7	1.7	1.6	1.4	1.5	1.5	1.4	1.4	1.3	1.2	1.1	0.9	0.8	0.838	1.562
5	2.5	2.5	2.5	2.5	2.5	2.5	2.5	2.5	2.5	2.5	2.5	2.5	2.4	2.4	2.5	2.5	2.5	2.5	2.5	2.5	2.5	2.5	2.4	2.388	0.100
6	2.1	2.1	2.1	2.1	2.1	2.1	2.1	2.1	2.1	2.1	2.1	2.1	2.1	2.1	2.1	2.1	2.1	2.1	2.1	2.1	2.1	2.1	2.1	2.083	0.000
7	2.2	2.2	2.2	2.1	2.0	1.9	1.9	1.8	1.8	1.8	1.8	1.7	1.6	1.6	1.6	1.5	1.6	1.5	1.6	1.6	1.6	1.5	1.4	1.372	0.828
8	2.5	2.5	2.5	2.4	2.3	2.1	2.1	2.0	2.0	1.9	1.8	1.7	1.6	1.6	1.4	1.4	1.3	1.2	1.2	1.1	1.0	0.9	0.8	0.826	1.674
9	2.4	2.2	2.1	1.9	1.8	1.6	1.7	1.6	1.6	1.6	1.6	1.5	1.5	1.4	1.4	1.4	1.3	1.2	1.1	1.2	1.1	1.1	1.1	1.181	1.219
10	2.5	2.2	2.3	2.3	2.3	2.2	2.1	2.1	2.1	2.2	2.2	2.2	2.2	2.2	2.2	2.2	2.2	2.2	2.2	2.2	2.2	2.2	2.2	2.172	0.300
11	2.5	2.4	2.4	2.4	2.4	2.4	2.4	2.4	2.4	2.4	2.4	2.4	2.4	2.4	2.4	2.4	2.4	2.4	2.4	2.4	2.4	2.4	2.3	2.286	0.214
12	2.5	2.4	2.4	2.4	2.3	2.2	2.3	2.2	2.2	2.2	2.1	2.1	2.1	2.1	2.1	2.1	2.1	2.0	2.0	2.0	2.0	2.0	2.0	1.981	0.519
13	2.7	2.6	2.4	2.3	2.2	2.1	2.0	1.9	2.0	1.9	2.0	1.8	1.9	1.9	1.8	1.5	1.3	1.4	1.4	1.5	1.4	1.4	1.3	1.354	1.346
14	2.6	2.554	2.6	2.4	2.4	2.3	2.3	2.3	2.3	2.3	2.4	2.4	2.4	2.2	2.2	2.2	2.2	2.2	2.2	2.2	2.2	2.2	2.2	2.154	0.400
15	2.7	2.7	2.6	2.6	2.5	2.4	2.4	2.4	2.4	2.5	2.4	2.4	2.4	2.3	2.4	2.5	2.5	2.5	2.4	2.5	2.5	2.5	2.4	2.393	0.307
16	2.4	2.4	2.4	2.5	2.4	2.4	2.4	2.4	2.4	2.4	2.4	2.4	2.4	2.4	2.4	2.4	2.4	2.4	2.4	2.5	2.4	2.5	2.4	2.393	0.000
17	2.4	2.4	2.4	2.4	2.3	2.3	2.3	2.3	2.2	2.2	2.2	2.2	2.2	2.2	2.2	2.2	2.2	2.2	2.2	2.1	2.2	2.1	2.2	2.169	0.231
18	2.4	2.4	2.3	2.0	1.9	1.9	1.9	1.9	1.9	1.9	1.8	1.8	1.8	1.8	1.8	1.8	1.8	1.8	1.7	1.8	1.8	1.8	1.8	1.854	0.546
19	2.6	2.6	2.4	2.4	2.4	2.4	2.4	2.4	2.4	2.4	2.3	2.3	2.3	2.3	2.2	2.3	2.3	2.3	2.3	2.2	2.3	2.3	2.2	2.169	0.431
20	2.5	2.6	2.4	2.3	2.3	2.3	2.3	2.2	2.2	2.3	2.3	2.3	2.3	2.2	2.2	2.2	2.2	2.3	2.2	2.3	2.3	2.3	2.2	2.243	0.257
21	2.2	2.2	2.2	2.2	2.2	2.2	2.2	2.2	2.2	2.1	2.2	2.1	2.2	2.2	2.1	2.1	2.1	2.2	2.2	2.2	2.1	2.1	2.1	2.070	0.130
22	2.2	2.1	2.1	2.1	2.1	2.1	2.1	2.0	2.0	2.0	1.9	1.9	2.0	1.9	2.0	1.9	1.9	1.9	1.9	1.9	1.9	2.0	1.9	1.895	0.305
23	2.4	2.3	2.2	2.1	2.1	2.0	1.9	1.8	1.9	1.9	1.9	1.9	1.8	1.9	1.9	1.8	1.8	1.8	1.8	1.8	1.8	1.7	1.8	1.847	0.553
24	2.3	2.1	2.1	2.1	2.1	2.0	2.1	2.0	2.0	2.1	2.1	2.0	2.1	2.1	2.0	2.0	2.0	2.0	2.0	2.0	2.0	2.0	2.1	2.093	0.200
25	2.5	2.6	2.4	2.3	2.4	2.2	2.3	2.2	2.3	2.3	2.3	2.3	2.3	2.3	2.2	2.2	2.2	2.2	2.2	2.3	2.2	2.2	2.3	2.319	0.181
26	2.2	2.2	2.2	2.2	2.2	2.2	2.2	2.1	2.1	2.2	2.1	2.1	2.1	2.1	2.1	2.0	2.0	2.0	2.0	2.1	2.0	2.0	1.9	1.999	0.201
27	2.3	2.3	2.3	2.3	2.3	2.3	2.2	2.2	2.2	2.3	2.3	2.2	1.8	2.2	2.2	2.2	2.2	2.2	2.1	2.0	2.1	2.1	2.1	2.063	0.237
28	2.5	2.6	2.6	2.5	2.5	2.5	2.5	2.5	2.5	2.5	2.5	2.5	2.4	2.4	2.4	2.4	2.4	2.3	2.3	2.3	2.3	2.3	2.2	2.245	0.255
29	2.5	2.8	2.4	2.3	2.3	2.2	2.3	2.3	2.2	2.3	2.3	2.3	2.3	2.2	2.2	2.1	2.2	2.2	2.2	2.2	2.2	2.2	2.3	2.311	0.189
30	2.5	2.5	2.3	2.3	2.3	2.2	2.3	2.2	2.2	2.3	2.2	2.1	2.2	2.2	2.2	2.2	2.2	2.2	2.2	2.2	2.2	2.2	2.3	2.311	0.189
31	2.3	2.4	2.4	2.4	2.4	2.4	2.4	2.4	2.4	2.4	2.4	2.4	2.3	2.3	2.3	2.2	2.2	2.2	2.2	2.2	2.2	2.2	2.1	2.090	0.255
32	2.1	2.1	2.1	2.0	2.0	1.9	1.9	1.8	1.9	1.9	1.9	1.8	1.7	1.7	1.7	1.7	1.7	1.7	1.7	1.7	1.6	1.7	1.6	1.610	0.490
33	2.3	2.3	2.3	2.3	2.3	2.2	2.2	2.2	2.2	2.1	2.2	2.2	2.2	2.2	2.2	2.1	2.2	2.2	2.2	2.1	2.2	2.2	2.2	2.200	0.100
34	2.4	2.3	2.3	2.3	2.1	2.1	2.1	2.0	2.0	2.0	2.0	2.0	2.0	2.0	2.0	1.9	2.0	2.0	2.0	2.0	2.0	2.0	2.1	2.063	0.300
35	2.4	2.4	2.3	2.2	2.3	2.2	2.2	2.2	2.2	2.2	2.2	2.2	2.2	2.1	2.2	2.2	2.2	2.2	2.1	2.2	2.2	2.2	2.1	2.116	0.284
36	2.3	2.3	2.3	2.3	2.2	2.2	2.3	2.3	2.2	2.3	2.3	2.2	2.1	2.2	2.1	2.1	2.2	2.1	2.1	2.1	2.1	2.1	2.1	2.118	0.182
37	2.1	1.9	1.9	2.0	2.0	1.9	1.8	1.8	1.8	1.7	1.6	1.5	1.7	1.7	1.7	1.8	1.7	1.7	1.7	1.7	1.7	1.8	1.8	1.793	0.307
38	2.3	2.3	2.2	2.3	2.3	2.2	2.3	2.2	2.2	2.2	2.2	2.1	2.1	2.1	2.1	2.2	2.0	2.0	2.0	2.0	2.1	2.0	2.1	2.085	0.215
39	2.3	2.3	2.3	2.3	2.2	2.2	2.2	2.2	2.2	2.2	2.2	2.2	2.2	2.2	2.2	2.2	2.1	2.1	2.1	2.1	2.1	2.2	2.2	2.154	0.146
40	2.2	2.2	2.0	2.1	2.0	2.2	1.9	1.9	1.9	1.9	1.9	1.9	2.2	1.9	1.9	1.9	1.9	1.9	1.9	1.9	1.9	1.9	2.0	2.004	0.200
41	2.5	2.5	2.5	2.4	2.5	2.5	2.4	2.4	2.5	2.5	2.5	2.3	2.5	2.5	2.5	2.5	2.5	2.5	2.5	2.5	2.5	2.5	2.5	2.489	0.000
42	2.6	2.6	2.5	2.4	2.3	2.2	2.1	2.0	2.1	2.0	1.9	2.0	1.9	1.9	2.1	1.9	1.9	1.9	1.9	1.9	1.9	1.9	1.9	1.880	0.700
43	2.3	2.3	2.3	2.3	2.2	2.2	2.1	2.1	2.3	2.2	2.2	2.1	2.1	2.2	2.2	2.1	2.1	2.0	2.1	2.0	2.1	2.1	2.1	2.149	0.200
44	2.6	2.6	2.5	2.5	2.6	2.5	2.5	2.5	2.5	2.6	2.5	2.5	2.5	2.5	2.5	2.4	2.4	2.4	2.4	2.5	2.5	2.5	2.4	2.487	0.100
45	2.3	2.3	2.4	2.3	2.3	2.3	2.3	2.3	2.3	2.4	2.3	2.3	2.3	2.4	2.3	2.3	2.3	2.3	2.3	2.3	2.3	2.3	2.3	2.278	0.022

Appendix 5E: Data Manipulation for the Particle Distribution Assessment Results

5E.1 Introduction

This appendix contains all the relevant information concerning the manipulation of the results obtained from the particle distribution assessment device.

5E.2 Processing the Raw Data to Give Curves of Light Obscuration in both the Vertical and Horizontal Planes

Values of the output from the photodiode being struck by the laser was acquired for a range of measurement locations, and stored by the data acquisition system. Since the raw data could not be related to the particle number distribution directly, owing to the fact that the data acquistion system could not acquire the data fast enough to distinguish between individual particles, the data was stored in data bit format. Three calibration trials, designed to measure the non-conveying obscuration of the laser were carried out for each test run. These calibration trials also accounted for the diffraction of the laser beam as a result of passing across glass / air boundaries. The mean of the values obtained from the three calibration scans was obtained.

The calibration data set was used effectively as a series of zero points for each measurement location in the scan; This took account of flaws in the glass surfaces, attached dust particles and diffraction caused by the passage of the laser through the glass / air boundaries, and led to a shift in the value for the free unobstructed laser beam data bit reading at each measurement location. Total obscuration of the laser led to a fixed maximum value of the photodiode output. The scaling of the data obtained during a conveying run for each measurement location, needed to be such that a common maximum and minimum scale was used between all the measurement positions. (Calibration trials proved that the photodiode output was nominally linear with degrees of obscuration (see appendix 5B)). Scaling factors were derived for each measurement position to account for the effects of the change in the zero value. These factors considered the change in the magnitude between the actual zero position, i.e. without particles being conveyed, and the value of total light obscuration. The sensitivity of measurements was also adjusted as a consequence of the use of these factors, by accounting for a change in the slope between these values. The scaling factors were then calculated using the following equation:-

$$SF = \left(\frac{T}{T - C} \right) \tag{5E.1}$$

where SF is the scaling factor; T is the value in data bits obtained from the photodiode when total obscuration occurs, and C is the value obtained from the photodiode during the calibration tests for each measurement location. The data value obtained for each measurement position whilst conveying is in progress is multiplied by this scaling factor. Once this has been calculated, the scaled data value is divided by the chord length to give the final scaled data reading of light obscuration for a fixed sample volume. Normalisation is carried out to tidy the data up.

Three calibration tests were carried out for each scan undertaken during conveying. Four scans in both the vertical and horizontal directions were carried out. The mean value of the four data sets was determined and normalised for each orientation of scan. Figures 5E.1 and 5E.2 illustrate the data that resulted from this treatment. A more thorough discussion of these results and the implications that arise from them is given in sections 5.3.3 & 5.3.4 of Chapter 5.

5E.3 Manipulation of the Normalised Scan Information to Produce a Three-Dimensional Surface Plot of Particle Density Distribution

A surface plot of the particle distribution within the pipe bore was felt to be necessary for further development of an improved pipe bend erosion model. To this end, the data sets obtained from tests carried out in the vertical and horizontal scan orientations, were utilised to generate a three dimensional surface plot of the particle density distribution within the pipe segment being examined. Strictly, this is not permissible since the data values obtained were not measures of the particle concentration at a point, but of those along a chord length across the pipe bore. However, since no other means of assessing the particle distribution was available for this project, the following method was the only possible way in which a three dimensional plot of the particle distribution could be derived.

It must be reiterated that during a horizontal scan the laser was mounted so that its beam was in the vertical plane, whilst for a vertical scan the laser beam was in the horizontal plane.

From the test results it was observed that the horizontal scan was symmetrical about the pipe bore centre line. It was presumed that this was true for any given horizontal plane taken through the pipe bore. The horizontal scan data set was adjusted for dimension to fit a range of chords positioned

Figure 5E.1 Normalised Obscuration Scan Results in the Horizontal Direction Plotted against Distance Across the Pipe Bore

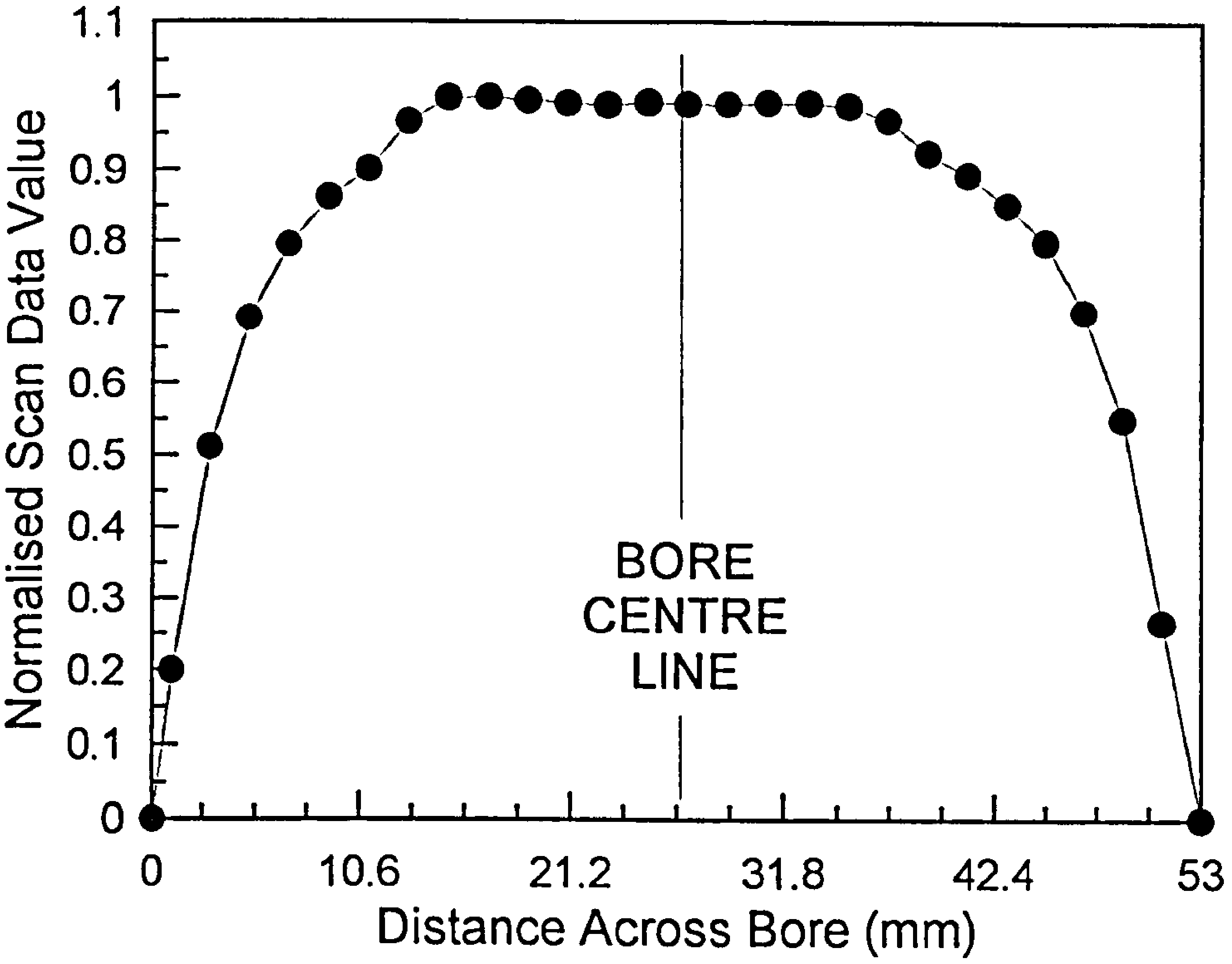

Figure 5E.2 Normalised Obscuration Scan Results in the Vertical Direction Plotted against Distance Across the Pipe Bore

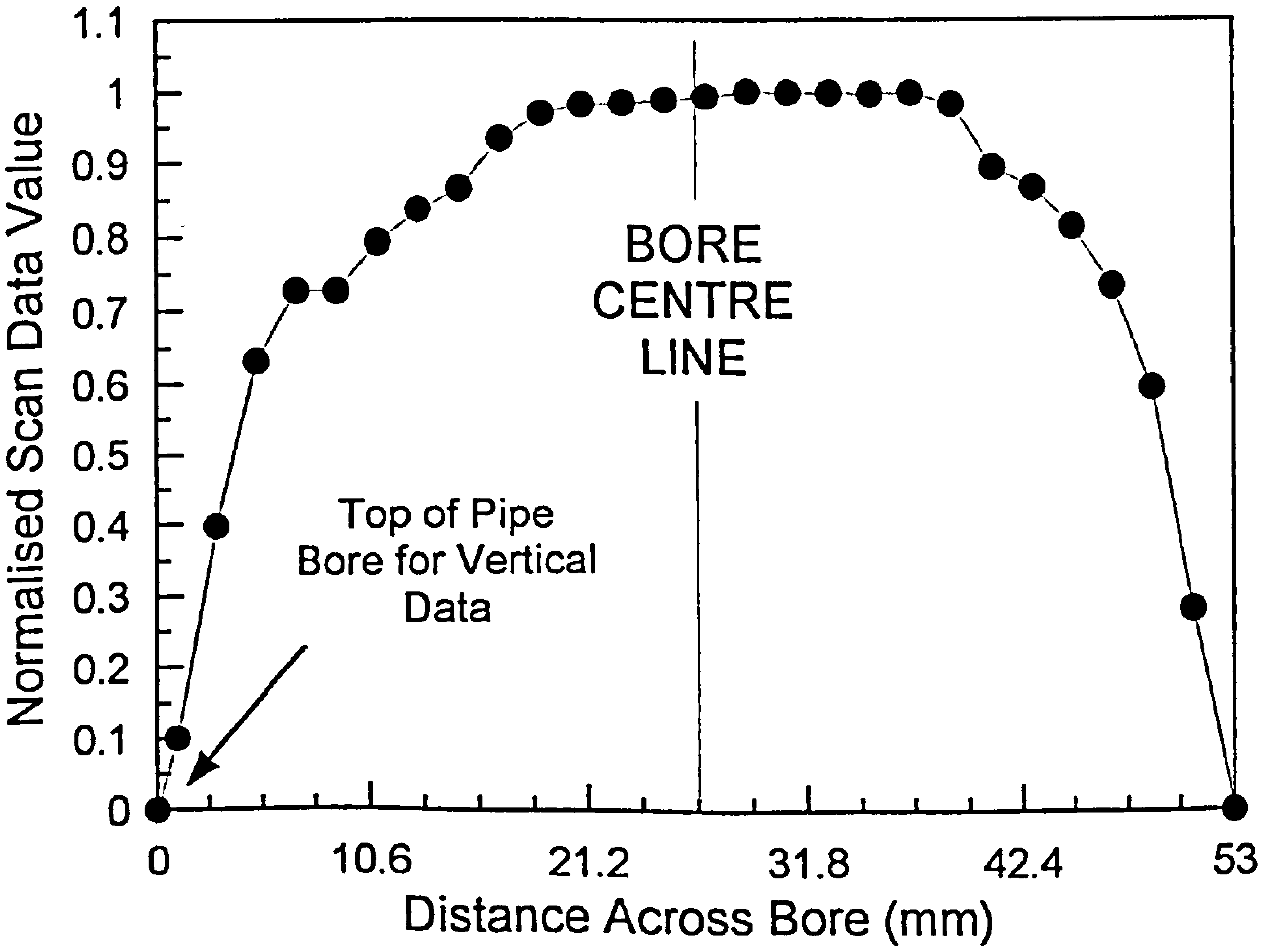

across the pipe bore cross section at the measurement locations used in the vertical scans. Each fitted horizontal data set was then multiplied by the ordinate of the vertical scan data set at this measurement location. This process was repeated for each and every measurement location in the vertical plane.

If a point is taken on one of the combined vertical / horizontal scan data sets, it will represent an estimate of the probability of a certain degree of light obscuration occurring in the pipe bore at the chosen point.

The data sets produced in this way were formed into volumes by taking the width of each scaled data set to be 2 mm. Summation (in a similar manner to that used in the midordinate rule) of all of these volumes followed. This gave an approximate value of the total volume under the surface so formed which was equivalent to the percentage probability of a certain degree of light obscuration occurring for the area of pipe bore. Probability of light obscuration was related to the presence of the particles; therefore, it was decided to equate the probability dimension in the volume to the mean value of the particle concentration density (suspension density) obtained from the pneumatic conveying trials. As a consequence of this, the value of an ordinate of the three dimensional surface at any position within the pipe bore would yield an estimated value of particle concentration density in kg/m^3 at this locality. Note it was not possible to modify the volume to equate to any variable which was based upon time since the measurement technique and the values obtained were time invariant. The ordinate values at a series of predetermined positions within the pipe bore were found. These were used in the Yeung particle trajectory model described in section 5.4.2 of Chapter 5 and Appendix 5F. This work will be discussed further in Chapter 6. MathCad programs and data files to carry out these manipulations are given in the next eight pages.

Analysis of the Particle Distribution Measurements Made Using a Laser Obscuration Technique.

The purpose of this programme is to analyse the results obtained by using a laser obscuration technique to measure particle density distribution. The data that is read into this document is the result of averaging the data taken from a series of repeated test runs. This programme uses this data to generate a three dimensional surface plot of particle concentration density across the pipe bore.

INPUT DATA

$$IN = \begin{bmatrix} 0 & 0 & 0 \\ 1 & 0.1 & 0.2 \\ 3 & 0.39719 & 0.51250 \\ 5 & 0.63209 & 0.69235 \\ 7 & 0.72902 & 0.79583 \\ 9 & 0.79387 & 0.86233 \\ 11 & 0.83711 & 0.90181 \\ 13 & 0.86522 & 0.96643 \\ 15 & 0.93500 & 0.99871 \\ 17 & 0.97031 & 1.00000 \\ 19 & 0.98236 & 0.99591 \\ 21 & 0.98460 & 0.99226 \\ 23 & 0.98841 & 0.98893 \\ 25 & 0.99305 & 0.99272 \\ 27 & 1.00000 & 0.98975 \\ 29 & 0.99890 & 0.98955 \\ 31 & 0.99837 & 0.99202 \\ 33 & 0.99745 & 0.99189 \\ 35 & 0.99937 & 0.98773 \\ 37 & 0.98363 & 0.96880 \\ 39 & 0.92976 & 0.92412 \\ 41 & 0.89478 & 0.89446 \\ 43 & 0.86551 & 0.85319 \\ 45 & 0.81156 & 0.80099 \\ 47 & 0.73059 & 0.70262 \\ 49 & 0.59214 & 0.55150 \\ 51 & 0.27999 & 0.26918 \\ 53 & 0 & 0 \end{bmatrix}$$

$$Dist := IN^{\langle 0 \rangle} \cdot 10^{-3}$$

$$Vert_{norm} := IN^{\langle 1 \rangle}$$

$$Horiz_{norm} := IN^{\langle 2 \rangle}$$

Counter specification.

$$N := rows(IN)$$

$$N = 28$$

$$i := 0, 1 .. N - 1$$

Calculation of the Sample Volume / Chord Length of the Laser in the Pipe Bore.

$r = 26.5 \cdot 10^{-3}$ $\quad C_i := 2 \cdot \sqrt{Dist_i \cdot (r \cdot 2 - Dist_i)}$

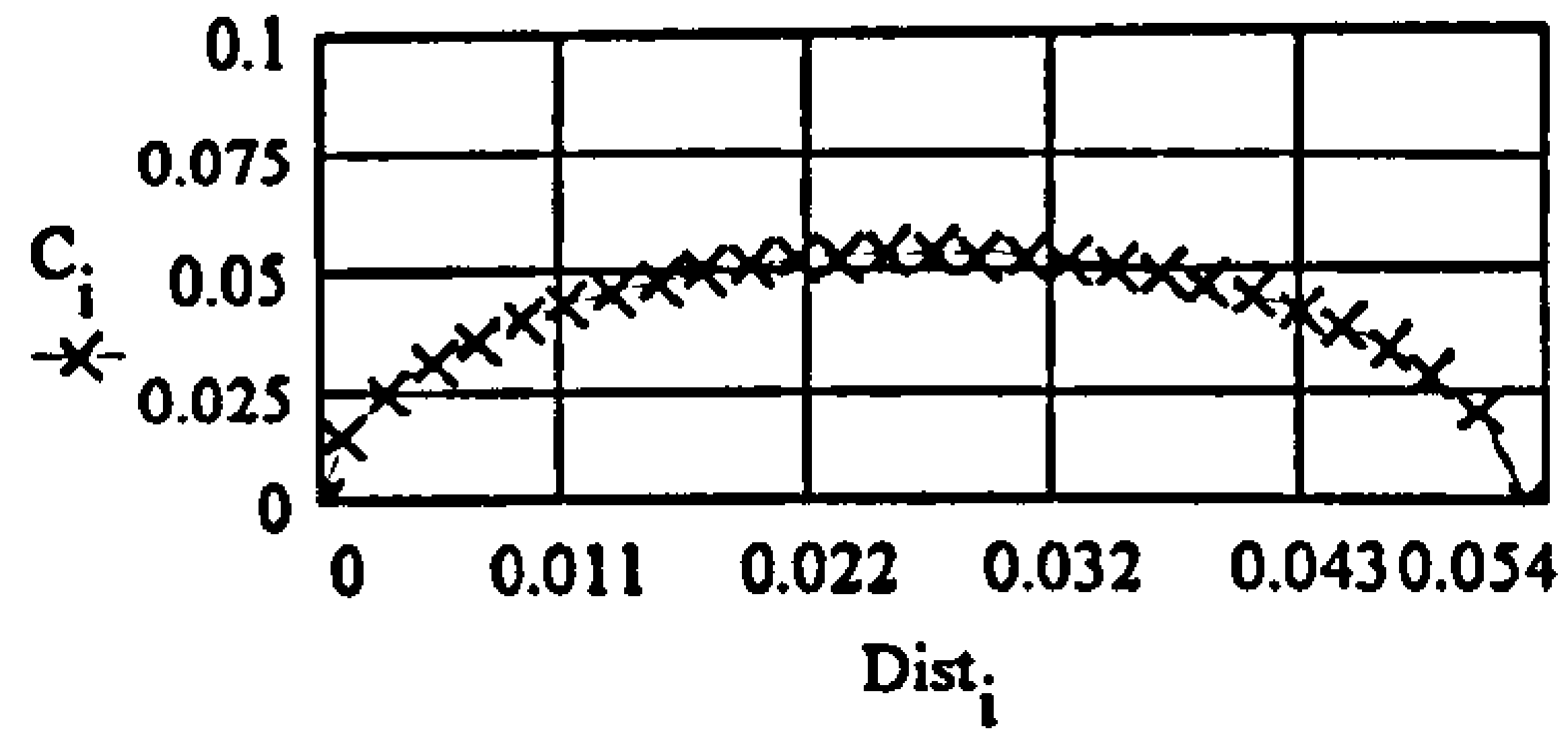

Graph of the Normalised Horizontal and Vertical Concentration Data Sets.

Combined Graph of Normalised Data Sets.

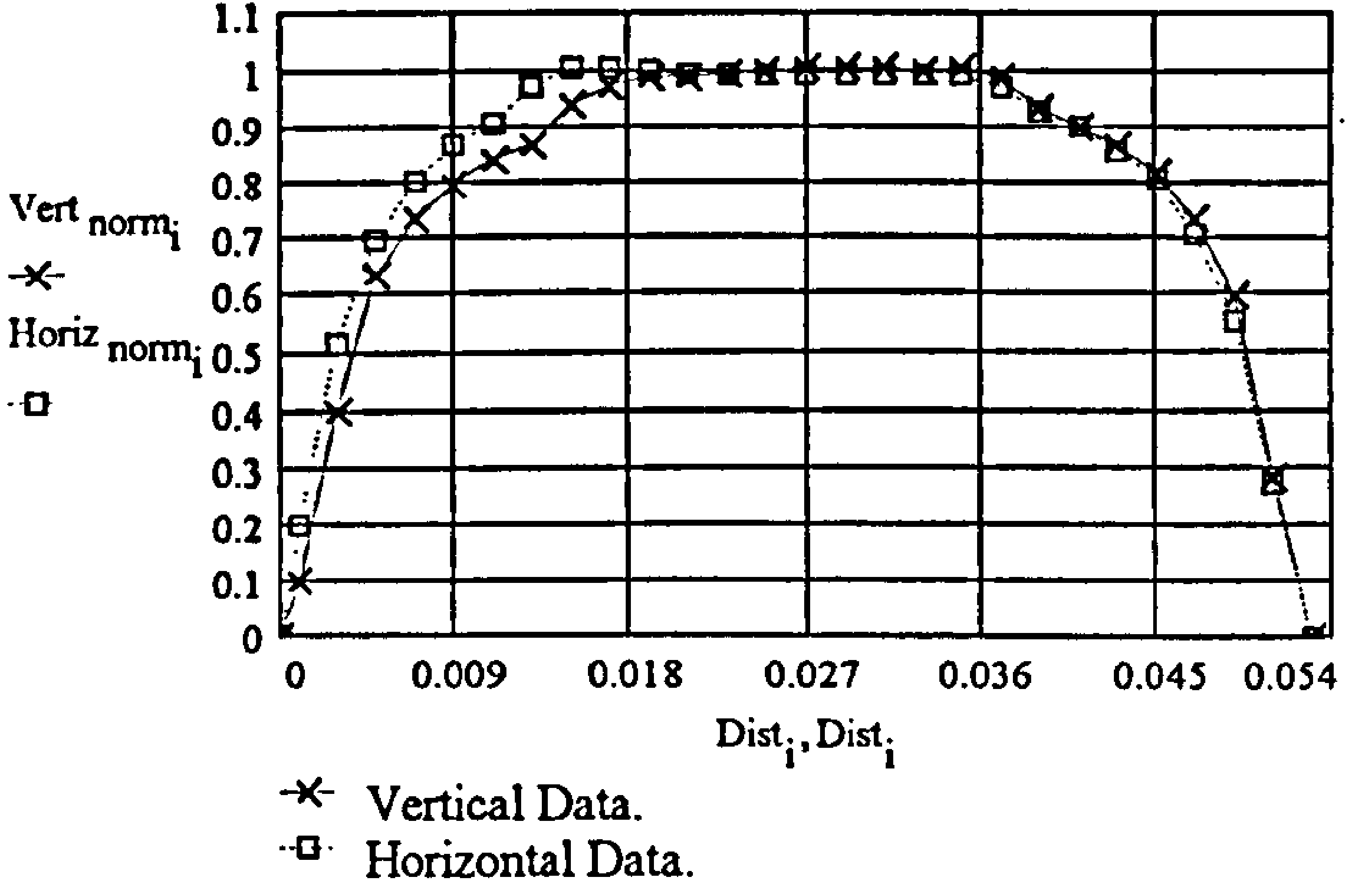

NB:- At distance zero the vertical position is at the bottom of the glass tube for vertical scans and on the inside surface of the conveying line circuit for horizontal scans.

Modifying the Data Preparatory to Creating A Three Dimensional Data File:

The data obtained from the horizontal scans is scaled to fit the chord length that occurs at the various measurement locations in the vertical plane. The corresponding values of the vertical ordinates are then used to scale the horizontal data sets found in this way.

$k := 0, 1 .. 13$

Number of data points across the pipe bore on this horizontal slice.

$$Sd_i := \mathrm{if}\left(C_i \cdot 10^3 - \mathrm{floor}\left(C_i \cdot 10^3\right) < 0.5, \mathrm{floor}\left(C_i \cdot 10^3\right), \mathrm{ceil}\left(C_i \cdot 10^3\right)\right)$$

The start point from the origin in the x direction for each of the horizontal planes is calculated.

$$SP_i := \mathrm{if}\left[\frac{\left(53 - C_i \cdot 10^3\right)}{2} - \mathrm{floor}\left[\frac{\left(53 - C_i \cdot 10^3\right)}{2}\right] < 0.5, \mathrm{floor}\left[\frac{\left(53 - C_i \cdot 10^3\right)}{2}\right], \mathrm{ceil}\left[\frac{\left(53 - C_i \cdot 10^3\right)}{2}\right]\right]$$

DESCRIPTION OF THE PARTICLE DENSITY DISTRIBUTION FOR EACH HORIZONTAL SEGMENT:

Top/Bottom -1 horizontal segment:

$D1 := Dist\cdot\frac{C_1}{53\cdot10^{-3}}$ $C_1 = 0.014$

$R1 := lspline(D1, Horiz_{norm})$

$T1 := 0, 1 .. Sd_1$

$P1_{T1} := interp(R1, D1, Horiz_{norm}, T1\cdot10^{-3})$

Top/Bottom -2 horizontal segment:

$D2 := Dist\cdot\frac{C_2}{53\cdot10^{-3}}$ $C_2 = 0.024$

$R2 := lspline(D2, Horiz_{norm})$

$T2 := 0, 1 .. Sd_2$

$P2_{T2} := interp(R2, D2, Horiz_{norm}, T2\cdot10^{-3})$

Top/Bottom -3 horizontal segment:

$D3 := Dist\cdot\frac{C_3}{53\cdot10^{-3}}$ $C_3 = 0.031$

$R3 := lspline(D3, Horiz_{norm})$

$T3 := 0, 1 .. Sd_3$

$P3_{T3} := interp(R3, D3, Horiz_{norm}, T3\cdot10^{-3})$

Top/Bottom -4 horizontal segment:

$D4 := Dist\cdot\frac{C_4}{53\cdot10^{-3}}$ $C_4 = 0.036$

$R4 := lspline(D4, Horiz_{norm})$

$T4 := 0, 1 .. Sd_4$

$P4_{T4} := interp(R4, D4, Horiz_{norm}, T4\cdot10^{-3})$

Top/Bottom -5 horizontal segment:

$D5 := Dist\cdot\frac{C_5}{53\cdot10^{-3}}$ $C_5 = 0.04$

$R5 := lspline(D5, Horiz_{norm})$

$T5 := 0, 1 .. Sd_5$

$P5_{T5} := interp(R5, D5, Horiz_{norm}, T5\cdot10^{-3})$

Top/Bottom -6 horizontal segment:

$D6 := Dist\cdot\frac{C_6}{53\cdot10^{-3}}$ $C_6 = 0.043$

$R6 := lspline(D6, Horiz_{norm})$

$T6 := 0, 1 .. Sd_6$

$P6_{T6} := interp(R6, D6, Horiz_{norm}, T6\cdot10^{-3})$

Top/Bottom -7 horizontal segment:

$D7 := Dist\cdot\frac{C_7}{53\cdot10^{-3}}$ $C_7 = 0.046$

$R7 := lspline(D7, Horiz_{norm})$

$T7 := 0, 1 .. Sd_7$

$P7_{T7} := interp(R7, D7, Horiz_{norm}, T7\cdot10^{-3})$

Top/Bottom -8 horizontal segment:

$D8 := Dist\cdot\frac{C_8}{53\cdot10^{-3}}$ $C_8 = 0.048$

$R8 := lspline(D8, Horiz_{norm})$

$T8 := 0, 1 .. Sd_8$

$P8_{T8} := interp(R8, D8, Horiz_{norm}, T8\cdot10^{-3})$

Top/Bottom -9 horizontal segment:

$D9 := Dist\cdot\frac{C_9}{53\cdot10^{-3}}$ $C_9 = 0.049$

$R9 := lspline(D9, Horiz_{norm})$

$T9 := 0, 1 .. Sd_9$

$P9_{T9} := interp(R9, D9, Horiz_{norm}, T9\cdot10^{-3})$

Top/Bottom -10 horizontal segment:

$D10 := Dist\cdot\frac{C_{10}}{53\cdot10^{-3}}$ $C_{10} = 0.051$

$R10 := lspline(D10, Horiz_{norm})$

$T10 := 0, 1 .. Sd_{10}$

$P10_{T10} := interp(R10, D10, Horiz_{norm}, T10\cdot10^{-3})$

Top/Bottom -11 horizontal segment:

$D11 := Dist\cdot\frac{C_{11}}{53\cdot10^{-3}}$ $C_{11} = 0.052$

$R11 := lspline(D11, Horiz_{norm})$

$T11 := 0, 1 .. Sd_{11}$

$P11_{T11} := interp(R11, D11, Horiz_{norm}, T11\cdot10^{-3})$

Top/Bottom -12 horizontal segment:

$D12 := Dist\cdot\frac{C_{12}}{53\cdot10^{-3}}$ $C_{12} = 0.053$

$R12 := lspline(D12, Horiz_{norm})$

$T12 := 0, 1 .. Sd_{12}$

$P12_{T12} := interp(R12, D12, Horiz_{norm}, T12\cdot10^{-3})$

Top/Bottom -13 horizontal segment:

$D13 := \mathrm{Dist}\cdot\frac{C_{13}}{53\cdot 10^{-3}}$ $C_{13} = 0.053$

$R13 := \mathrm{lspline}(D13, \mathrm{Horiz}_{\mathrm{norm}})$

$T13 := 0, 1 .. Sd_{13}$

$P13_{T13} := \mathrm{interp}(R13, D13, \mathrm{Horiz}_{\mathrm{norm}}, T13\cdot 10^{-3})$

Top/Bottom -14 horizontal segment:

$D14 := \mathrm{Dist}\cdot\frac{C_{14}}{53\cdot 10^{-3}}$ $C_{14} = 0.053$

$R14 := \mathrm{lspline}(D14, \mathrm{Horiz}_{\mathrm{norm}})$

$T14 := 0, 1 .. Sd_{14}$

$P14_{T14} := \mathrm{interp}(R14, D14, \mathrm{Horiz}_{\mathrm{norm}}, T14\cdot 10^{-3})$

Each of the vertical scan readings is multiplied by the corresponding horizontal layers. Because the pipe is symmetrical about two axes it is possible to use the above thirteen sets of data twice over once for each of the two hemispheres (upper and lower) that have been considered.

$SP =$

	0
0	27
1	19
2	14
3	11
4	9
5	7
6	5
7	4
8	3
9	2
10	1
11	1
12	0
13	0
14	0
15	0

$P11\cdot \mathrm{Vert}_{\mathrm{norm}_{11}} =$

	0
0	0
1	0.201
2	0.375
3	0.512
4	0.614
5	0.689
6	0.745
7	0.79
8	0.827
9	0.853
10	0.871
11	0.895
12	0.928
13	0.959
14	0.977
15	0.985

Finding the Volume of the Horizontal Layers

$G := Sd_2$ $\quad Scad := P2\cdot \mathrm{Vert}_{\mathrm{norm}_{26}}$

$i := 0, 1 .. G$ $\quad R_i := i\cdot 10^{-3}$ $\quad \max(R) = 0.024$

Graph for this horizontal segment

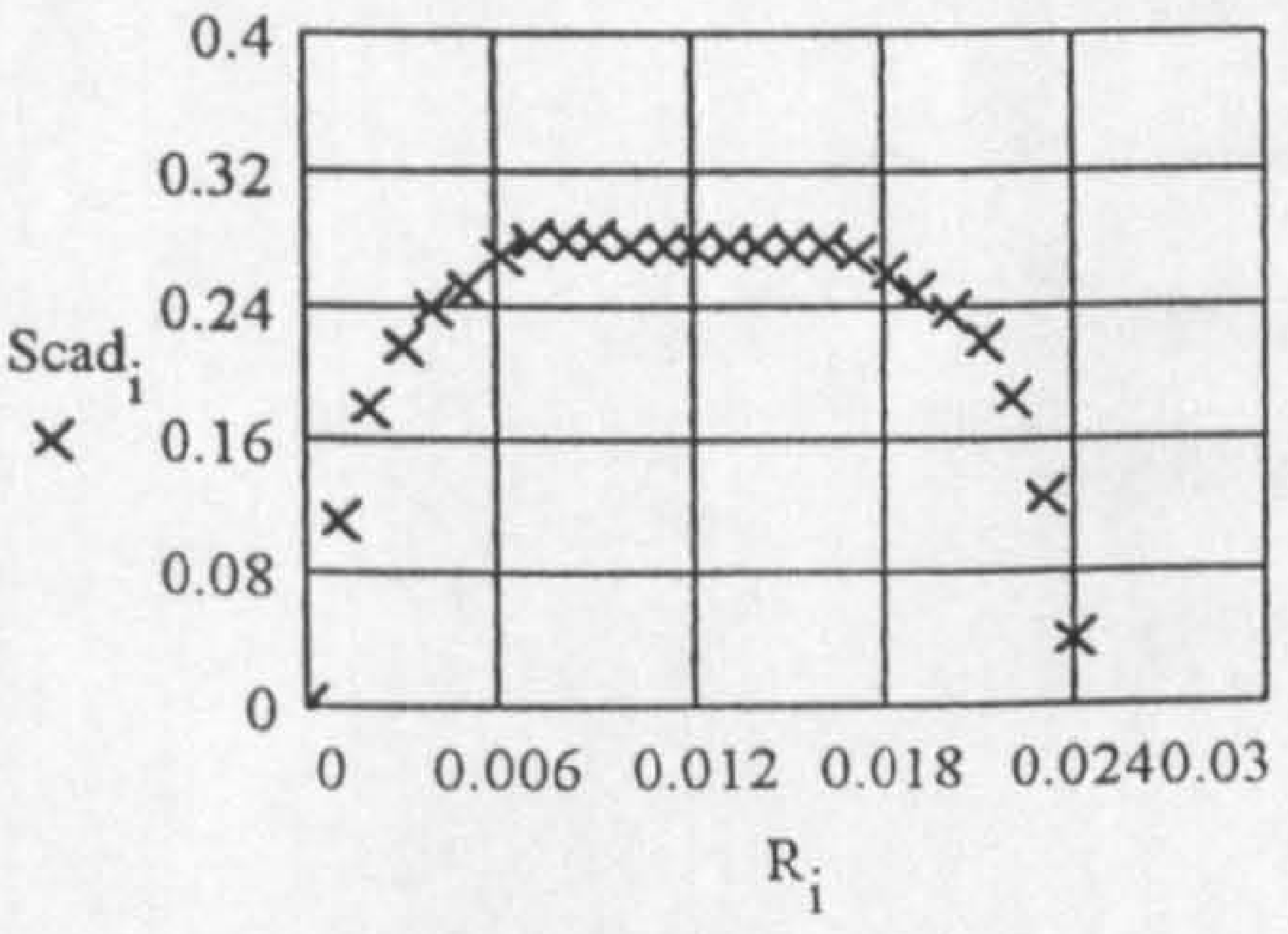

$M := \mathrm{rows}(Scad)$

Cubic spine fit to find the volume of a 2 mm wide strip through distribution on this level.

$VS1 := \mathrm{lspline}(R, Scad)$

$x := 0, 0.5\cdot 10^{-3} .. G\cdot 10^{-3}$

$j := 0 .. (G - 2)$

$h_j := \mathrm{if}\left[j<(M-1), R_{(j+1)} - R_j, 0\right]$

$A3_j := \frac{1}{6\cdot h_j}\cdot\left[VS1_{(j+1)} - VS1_j\right]$ $\quad C3_j := \frac{1}{h_j}\cdot\left[Scad_{(j+1)} - Scad_j\right] - \frac{1}{6}\cdot h_j\cdot\left[VS1_{(j+1)} + 2\cdot VS1_j\right]$

$B3_j := \frac{1}{2}\cdot VS1_j$ $\quad D3_j := Scad_j$

$$A_{slab} := \sum_{j} \int_{R_j}^{R_{(j+1)}} \left[A3_j\cdot(x-R_j)^3 + \left[B3_j\cdot(x-R_j)^2 + \left[C3_j\cdot(x-R_j) + D3_j\right]\right]\right] dx \qquad A_{slab} = 0.005554$$

The area under the cubic spline fitted curve is determined using these equations which were derived from Etter, [E4].

Volume of the slice of the distribution for this 2 mm wide horizontal slice is.

$Vol_a := 0.002\cdot A_{slab}$

$Vol_a = 1.111\cdot 10^{-5}$ Cubic units of volume.

$$Vol_m := \begin{bmatrix} 2.274\cdot 10^{-6} \\ 1.576\cdot 10^{-5} \\ 3.211\cdot 10^{-5} \\ 4.297\cdot 10^{-5} \\ 5.194\cdot 10^{-5} \\ 5.913\cdot 10^{-5} \\ 6.493\cdot 10^{-5} \\ 7.344\cdot 10^{-5} \\ 7.876\cdot 10^{-5} \\ 8.214\cdot 10^{-5} \\ 8.397\cdot 10^{-5} \\ 8.547\cdot 10^{-5} \\ 8.642\cdot 10^{-5} \\ 8.713\cdot 10^{-5} \\ 8.693\cdot 10^{-5} \\ 8.633\cdot 10^{-5} \\ 8.506\cdot 10^{-5} \\ 8.356\cdot 10^{-5} \\ 7.984\cdot 10^{-5} \\ 7.303\cdot 10^{-5} \\ 6.715\cdot 10^{-5} \\ 6.113\cdot 10^{-5} \\ 5.31\cdot 10^{-5} \\ 4.307\cdot 10^{-5} \\ 3.008\cdot 10^{-5} \\ 1.111\cdot 10^{-5} \end{bmatrix}$$

<u>The Total Volume Under the Data Surface is as follows:-</u>

$Tot := \sum Vol_m \qquad Tot = 0.001607 \qquad \sum\left(\frac{Vol_m}{Tot}\right) = 1$

Determination of the Scaling Factor so that the vertical measurements are displayed as values in kg/m³:-

$Scal := \frac{3.5}{Tot}\cdot\pi\cdot 0.0265^2 \qquad Scal = 4.806$

NB: Numerator is the mean suspension density in kg/m^3.

The only values which need to be scaled are the values of the vertical distribution $Vert_{norm}$ in order to construct the surface representing the particle density distribution.

```
0.000, 0.000, 0.000, 0.000, 0.000, 0.000, 0.000, 0.000, 0.000, 0.000, 0.000, 0.958, 0.956, 0.961, 0.961, 0.962, 0.968, 0.000, 0.000, 0.000, 0.000, 0.000, 0.000, 0.000, 0.000, 0.000, 0.000,
0.000, 0.000, 0.000, 0.000, 0.000, 0.000, 0.000, 0.000, 0.995, 1.825, 1.800, 2.449, 2.448, 2.463, 2.463, 2.463, 2.474, 1.823, 1.857, 1.009, 0.000, 0.000, 0.000, 0.000, 0.000, 0.000, 0.000,
0.000, 0.000, 0.000, 0.000, 0.000, 0.000, 1.756, 1.829, 2.506, 2.978, 2.952, 3.302, 3.306, 3.327, 3.327, 3.326, 3.335, 2.991, 3.030, 2.541, 1.819, 0.990, 0.000, 0.000, 0.000, 0.000, 0.000,
0.000, 0.000, 0.000, 0.000, 0.996, 1.781, 2.778, 2.932, 3.332, 3.601, 3.581, 3.792, 3.800, 3.825, 3.825, 3.822, 3.830, 3.627, 3.663, 3.378, 2.915, 2.438, 1.841, 0.000, 0.000, 0.000, 0.000,
0.000, 0.000, 0.000, 0.000, 2.349, 2.767, 3.304, 3.510, 3.804, 3.988, 3.973, 4.104, 4.117, 4.114, 4.114, 4.141, 4.146, 4.025, 4.057, 3.856, 3.491, 3.183, 2.861, 1.832, 0.000, 0.000, 0.000,
0.000, 0.000, 0.000, 1.776, 2.980, 3.266, 3.611, 3.862, 4.080, 4.196, 4.188, 4.296, 4.306, 4.334, 4.334, 4.331, 4.339, 4.243, 4.269, 4.136, 3.840, 3.604, 3.377, 2.780, 1.779, 0.000, 0.000,
0.000, 0.000, 1.702, 2.611, 3.315, 3.535, 3.828, 4.064, 4.318, 4.491, 4.461, 4.605, 4.615, 4.644, 4.644, 4.642, 4.652, 4.520, 4.568, 4.378, 4.041, 3.825, 3.655, 3.250, 2.617, 1.594, 0.000,
0.000, 0.761, 2.397, 3.009, 3.560, 3.802, 4.105, 4.380, 4.602, 4.700, 4.696, 4.747, 4.767, 4.799, 4.799, 4.795, 4.795, 4.757, 4.781, 4.665, 4.355, 4.128, 3.931, 3.485, 3.016, 2.246, 0.536,
0.000, 1.477, 2.691, 3.248, 3.800, 4.012, 4.163, 4.497, 4.669, 4.724, 4.737, 4.748, 4.772, 4.805, 4.805, 4.800, 4.796, 4.799, 4.806, 4.733, 4.472, 4.297, 4.148, 3.801, 3.255, 2.521, 1.041,
0.000, 1.713, 2.985, 3.993, 3.812, 4.021, 4.144, 4.486, 4.651, 4.703, 4.718, 4.729, 4.752, 4.786, 4.786, 4.780, 4.777, 4.779, 4.785, 4.715, 4.461, 4.296, 4.157, 3.905, 3.501, 2.796, 1.207,
0.389, 1.908, 3.037, 3.498, 3.793, 4.001, 4.126, 4.467, 4.633, 4.686, 4.700, 4.711, 4.735, 4.768, 4.768, 4.763, 4.758, 4.762, 4.767, 4.697, 4.442, 4.277, 4.137, 3.887, 3.505, 2.845, 1.345,
0.479, 1.899, 3.017, 3.479, 3.773, 3.980, 4.113, 4.446, 4.612, 4.668, 4.680, 4.698, 4.719, 4.752, 4.752, 4.747, 4.746, 4.741, 4.749, 4.675, 4.421, 4.256, 4.116, 3.867, 3.486, 2.826, 1.339,
0.476, 1.890, 3.009, 3.468, 3.787, 3.992, 4.127, 4.457, 4.627, 4.686, 4.694, 4.715, 4.737, 4.771, 4.771, 4.765, 4.763, 4.755, 4.768, 4.690, 4.432, 4.265, 4.127, 3.864, 3.475, 2.819, 1.332,
0.476, 1.888, 3.005, 3.470, 3.773, 3.981, 4.112, 4.450, 4.617, 4.672, 4.687, 4.700, 4.723, 4.756, 4.756, 4.751, 4.747, 4.748, 4.752, 4.680, 4.425, 4.258, 4.116, 3.863, 3.478, 2.815, 1.331,
0.468, 1.894, 3.013, 3.469, 3.783, 3.984, 4.121, 4.446, 4.614, 4.672, 4.680, 4.702, 4.722, 4.755, 4.755, 4.750, 4.749, 4.742, 4.753, 4.677, 4.421, 4.255, 4.119, 3.861, 3.476, 2.822, 1.335,
0.398, 1.856, 3.008, 3.476, 3.783, 3.992, 4.125, 4.458, 4.626, 4.684, 4.692, 4.713, 4.739, 4.767, 4.767, 4.762, 4.760, 4.753, 4.765, 4.689, 4.433, 4.267, 4.127, 3.870, 3.484, 2.817, 1.308,
0.099, 1.704, 2.902, 3.453, 3.747, 3.980, 4.109, 4.455, 4.624, 4.681, 4.694, 4.710, 4.733, 4.767, 4.767, 4.761, 4.757, 4.755, 4.762, 4.688, 4.430, 4.262, 4.115, 3.857, 3.461, 2.719, 1.201,
0.000, 1.495, 2.714, 3.283, 3.556, 3.898, 4.013, 4.427, 4.598, 4.653, 4.678, 4.685, 4.712, 4.746, 4.746, 4.740, 4.732, 4.739, 4.734, 4.661, 4.402, 4.221, 4.030, 3.756, 3.291, 2.543, 1.054,
0.000, 0.865, 2.485, 3.112, 3.394, 3.686, 3.806, 4.282, 4.470, 4.521, 4.600, 4.571, 4.618, 4.655, 4.655, 4.695, 4.617, 4.660, 4.600, 4.532, 4.258, 4.035, 3.811, 3.546, 3.119, 2.328, 0.610,
0.000, 0.000, 1.969, 2.883, 3.175, 3.528, 3.653, 4.085, 4.260, 4.314, 4.387, 4.360, 4.404, 4.440, 4.440, 4.430, 4.404, 4.444, 4.389, 4.318, 4.062, 3.868, 3.647, 3.361, 2.890, 1.844, 0.000,
0.000, 0.000, 0.679, 2.410, 2.764, 3.302, 3.438, 3.915, 4.103, 4.161, 4.240, 4.218, 4.263, 4.298, 4.298, 4.288, 4.261, 4.296, 4.233, 4.159, 3.893, 3.669, 3.414, 3.081, 2.415, 0.636, 0.000,
0.000, 0.000, 0.000, 1.358, 1.981, 2.860, 3.040, 3.686, 3.883, 3.946, 4.044, 4.014, 4.064, 4.099, 4.099, 4.088, 4.054, 4.096, 4.014, 3.937, 3.666, 3.389, 2.957, 2.516, 1.361, 0.000, 0.000,
0.000, 0.000, 0.000, 0.000, 0.529, 2.067, 2.378, 3.253, 3.514, 3.601, 3.793, 3.729, 3.809, 3.848, 3.848, 3.832, 3.766, 3.843, 3.664, 3.562, 3.234, 2.858, 2.137, 1.281, 0.000, 0.000, 0.000,
0.000, 0.000, 0.000, 0.000, 0.000, 0.641, 1.039, 2.556, 2.918, 3.039, 3.318, 3.224, 3.333, 3.374, 3.374, 3.352, 3.256, 3.361, 3.091, 2.958, 2.542, 1.821, 0.663, 0.000, 0.000, 0.000, 0.000,
0.000, 0.000, 0.000, 0.000, 0.000, 0.000, 0.000, 1.171, 1.713, 1.946, 2.573, 2.368, 2.589, 2.646, 2.646, 2.604, 2.392, 2.606, 1.980, 1.736, 1.165, 0.392, 0.000, 0.000, 0.000, 0.000, 0.000,
0.000, 0.000, 0.000, 0.000, 0.000, 0.000, 0.000, 0.000, 0.307, 0.532, 1.196, 0.973, 1.227, 1.287, 1.287, 1.235, 0.982, 1.211, 0.541, 0.312, 0.000, 0.000, 0.000, 0.000, 0.000, 0.000, 0.000,
0.000, 0.000, 0.000, 0.000, 0.000, 0.000, 0.000, 0.000, 0.000, 0.000, 0.000, 0.000, 0.000, 0.000, 0.000, 0.000, 0.000, 0.000, 0.000, 0.000, 0.000, 0.000, 0.000, 0.000, 0.000, 0.000, 0.000,
```

Reading in the Data for the 3-D Suspension Density Distribution.

M := READPRN(input)

Plotting 3-D Suspension Density Distribution in Contour and Surface Formats

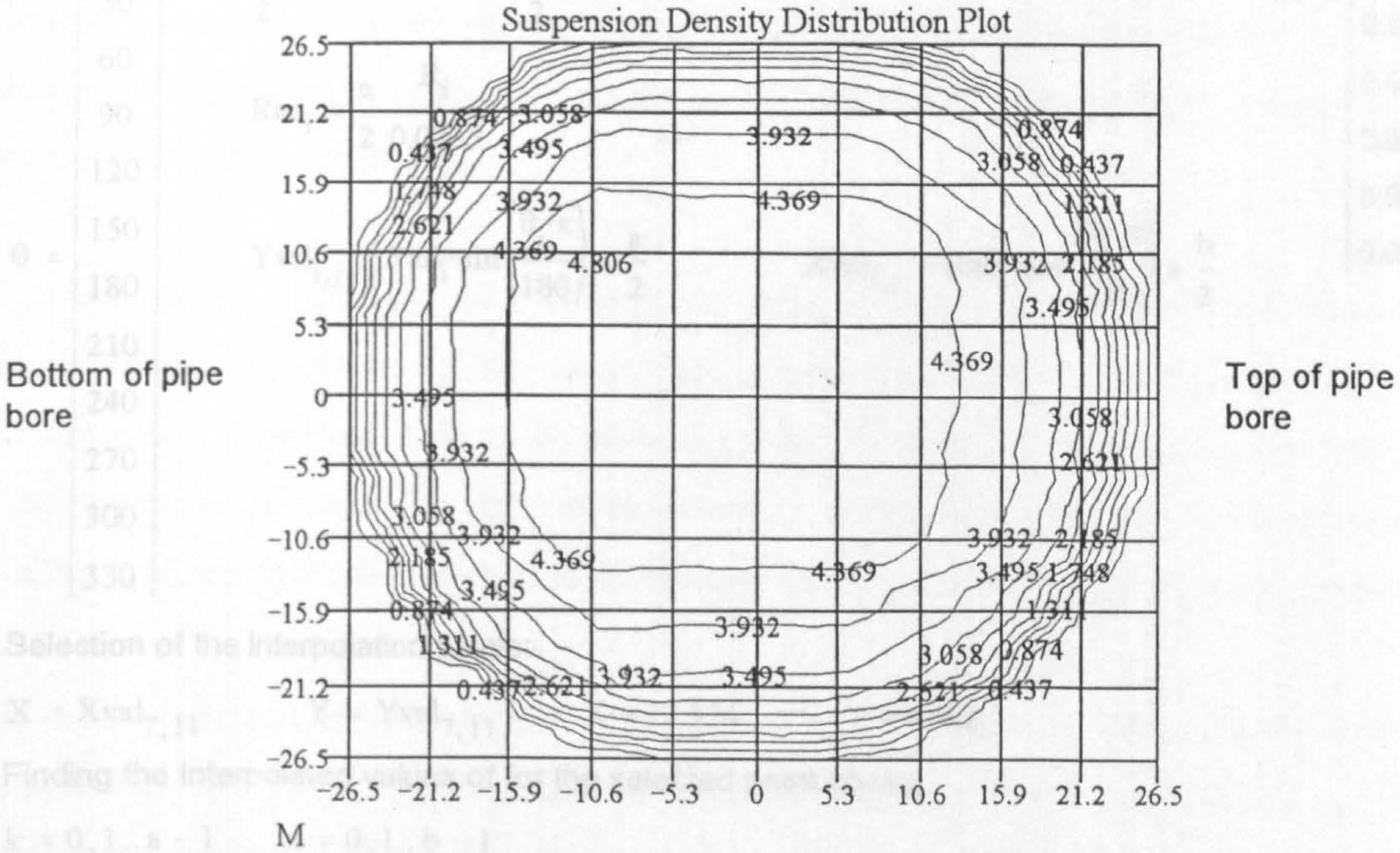

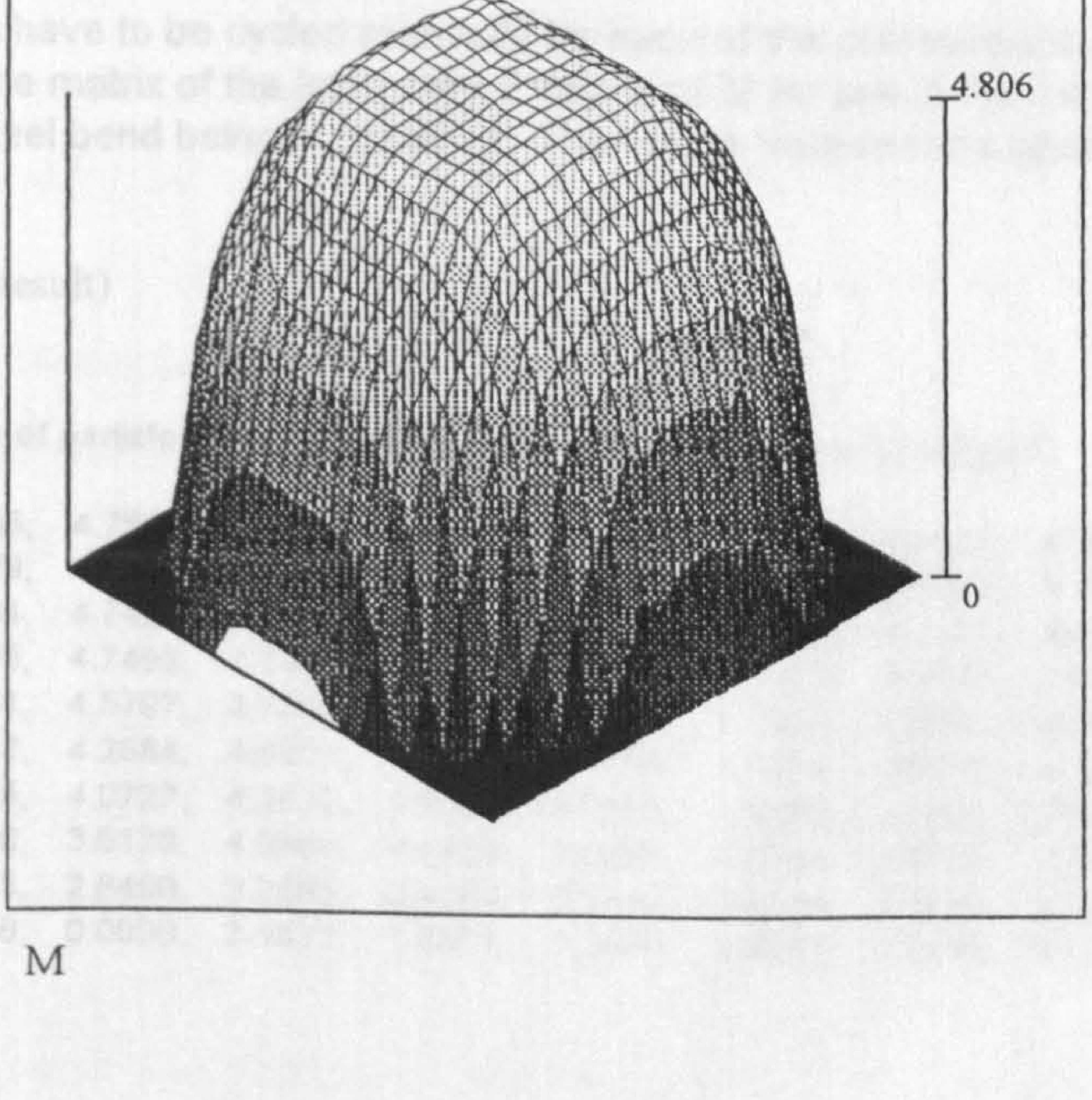

An Attempt at Two Dimensional Interpolation.

Finding the values of the interpolation points:

$a := \mathrm{cols}(M)$ $\quad b := \mathrm{rows}(M)$ $\quad i := 0,1..9$

$a = 27$ $\quad b = 27$ $\quad j := 0,1..11$

$\frac{a}{2} = 13.5$ $\quad \frac{b}{2} = 13.5$

$$R := \begin{bmatrix} 0.0001 \\ 0.0029 \\ 0.0058 \\ 0.0087 \\ 0.0116 \\ 0.0142 \\ 0.0171 \\ 0.0200 \\ 0.0229 \\ 0.0261 \end{bmatrix}$$

$$\mathrm{Rad}_i := \frac{a}{2}\cdot\frac{R_i}{0.0265}$$

$$\theta := \begin{bmatrix} 0 \\ 30 \\ 60 \\ 90 \\ 120 \\ 150 \\ 180 \\ 210 \\ 240 \\ 270 \\ 300 \\ 330 \end{bmatrix}$$

$$\mathrm{Yval}_{i,j} := \mathrm{Rad}_i\cdot\sin\left(\frac{\theta_j\cdot\pi}{180}\right) + \frac{a}{2} \qquad \mathrm{Xval}_{i,j} := \mathrm{Rad}_i\cdot\cos\left(\frac{\theta_j\cdot\pi}{180}\right) + \frac{b}{2}$$

Selection of the interpolation points:-

$X := \mathrm{Xval}_{7,11}$ $\quad Y := \mathrm{Yval}_{7,11}$ $\quad X = 22.324$ $\quad Y = 8.406$

Finding the Interpolated values of for the selected point above.

$k := 0,1..a-1$ $\quad n := 0,1..b-1$

$S_k := k$

$C_n := \mathrm{interp}\left(\mathrm{cspline}\left(S, M^{<n>}\right), S, M^{<n>}, X\right)$

$\mathrm{Ixy} := \mathrm{interp}(\mathrm{cspline}(S,C), S, C, Y)$

$\mathrm{Ixy} = 3.38069$

These calculations have to be cycled manually for each of the corresponding values of Xval and Yval to construct the matrix of the interpolated values of M for use in the Yeung model of the trajectory and wear of the mild steel bend being considered. The values selected are given below:-

$\mathrm{Res} := \mathrm{READPRN}(\mathrm{result})$

Matrix of selected values of particle concentration density (suspension density) in kg/m^3.

```
4.7557, 4.7556, 4.7555, 4.7555, 4.7555, 4.7556, 4.7556, 4.7557, 4.7557, 4.7557, 4.7558, 4.7557,
4.7696, 4.7629, 4.7529, 4.7475, 4.7562, 4.7685, 4.7747, 4.7643, 4.7354, 4.7194, 4.7332, 4.7598,
4.7651, 4.7599, 4.7594, 4.7427, 4.7625, 4.7468, 4.7586, 4.7195, 4.7137, 4.6895, 4.7114, 4.7330,
4.6624, 4.7140, 4.7595, 4.7493, 4.7467, 4.7656, 4.7883, 4.7225, 4.6796, 4.6705, 4.6925, 4.6653,
4.3949, 4.5024, 4.7341, 4.5797, 4.7315, 4.7890, 4.8149, 4.7350, 4.6460, 4.5678, 4.6469, 4.4551,
4.1573, 4.3282, 4.4542, 4.2884, 4.5054, 4.7838, 4.7108, 4.7202, 4.5306, 4.1921, 4.4879, 4.2703,
3.7660, 4.0138, 4.0545, 4.0727, 4.2872, 4.5534, 4.2833, 4.4786, 4.1322, 3.9498, 3.8221, 3.9503,
2.9275, 3.4631, 3.6300, 3.6128, 4.0966, 4.1453, 3.9358, 4.0768, 3.9734, 3.5710, 3.5116, 3.3807,
1.0334, 2.1680, 3.0485, 2.6450, 3.3991, 3.4630, 3.2232, 3.4116, 3.3549, 2.8686, 2.9292, 2.2061,
0.0000, 0.0000, 0.4596, 0.0000, 2.1871, 1.6871, 1.3479, 1.8097, 2.3339, 0.7562, 0.4963, 0 0000,
```

5E.3 Use of the Normalised Scan Data Obtained in the Vertical Plane to Produce a Skewed Air Velocity Distribution

From previous literature it became evident that the presence of the particles would have a significant effect on the air velocity distribution in the pipe bore. Experimental evidence suggests that as the number of particles in any given part of the flowing suspension increases, there will be a corresponding reduction in the air velocity [L2,K1,T2] and a corresponding increase in velocity in other regions of the pipe bore.

The data derived from the laser obscuration tests in this work, indicate that there is a greater concentration of particles in the lower half of the pipe bore. Consequently, the air velocity distribution is therefore likely to be skewed so that its peak occurs in the upper half of the pipe. Since no means of measuring the local air velocities occurring in the pipe line during conveying was available, efforts to model the skewed air velocity distribution using existing information were made.

Previous work carried out on the experimental measurement of gas velocity distributions in conjunction with particle concentration distribution measurements is very limited in extent, and is sometimes conflicting [T2,K1]. However, the results presented by Tsuji *et al.* [T2] indicate that taking the relationship between particle concentration distribution and gas velocity to be inversely proportional is a reasonable first approximation for this relationship.

The flat peak in the profile of laser obscuration data obtained for the vertical scan with the laser in the horizontal plane enabled the fitting of a straight line to this peak to be carried out. This line was mirrored in a vertical plane taken through the apex of the laser obscuration curve. Therefore, formation of a biasing factor, (based upon the assertion that the distribution of the superficial air velocity in the vertical plane through the pipe bore was inversely proportional to the particle concentration distribution), which was used to give the peak in the superficial air velocity in the upper half of the pipe bore was then easily achieved. An expression originally derived by Prandtl for the profile of a turbulent air velocity distribution in a pipe [P2], was used and normalised. Since both data sets were then effectively non-dimensional it was possible to add the biasing factor to the curve predicted by Prandtl. This produced a skewed superficial air velocity distribution with the peak in the upper half of the pipe bore.

The area under this curve was then found and it was normalised so that the mean ordinate value was equivalent to 1. Using manual interpolation features within MathCad, it was possible to determine the contours of normalised air velocity distribution within the pipe bore, providing it was assumed that the air velocity was symmetrical in any given horizontal plane.

The air velocity values at a series of predetermined positions within the pipe bore were found. These will be used in the Yeung particle trajectory model described in section 5.4.2 of Chapter 5 and Appendix 5F This will be explained in Chapter 6. MathCad programs to carry out the manipulations described in this section are given in the next eight pages.

Use of the Vertical Particle Density Distribution Data to Skew the Prandtl Model of Air Velocity Distribution

Because of the skewed nature of the particle distribution in the vertical plane it is expected that the corresponding air velocity profile will be skewed. This behaviour has been noted in work carried out by several researchers who have measured the air velocity profile [L2,K1,T2].

Input of Normalised Vertical Scan Data

$$N_{vert} := \begin{bmatrix} 3 & 0.27999 \\ 5 & 0.59214 \\ 7 & 0.73059 \\ 9 & 0.81156 \\ 11 & 0.86551 \\ 13 & 0.89478 \\ 15 & 0.92976 \\ 17 & 0.98363 \\ 19 & 0.99937 \\ 21 & 0.99745 \\ 23 & 0.99837 \\ 25 & 0.99890 \\ 27 & 1.00000 \\ 29 & 0.99305 \\ 31 & 0.98841 \\ 33 & 0.98460 \\ 35 & 0.98236 \\ 37 & 0.97031 \\ 39 & 0.93500 \\ 41 & 0.86522 \\ 43 & 0.83711 \\ 45 & 0.79387 \\ 47 & 0.72902 \\ 49 & 0.63209 \\ 51 & 0.39719 \end{bmatrix}$$

$Dist := N_{vert}^{\langle 1 \rangle}$ $\quad$ $Vert_{scan} := N_{vert}^{\langle 2 \rangle}$

Counter Specification:-

$N := rows\left(N_{vert}\right)$ $\quad$ $N = 25$

$i := 1, 2 .. N$

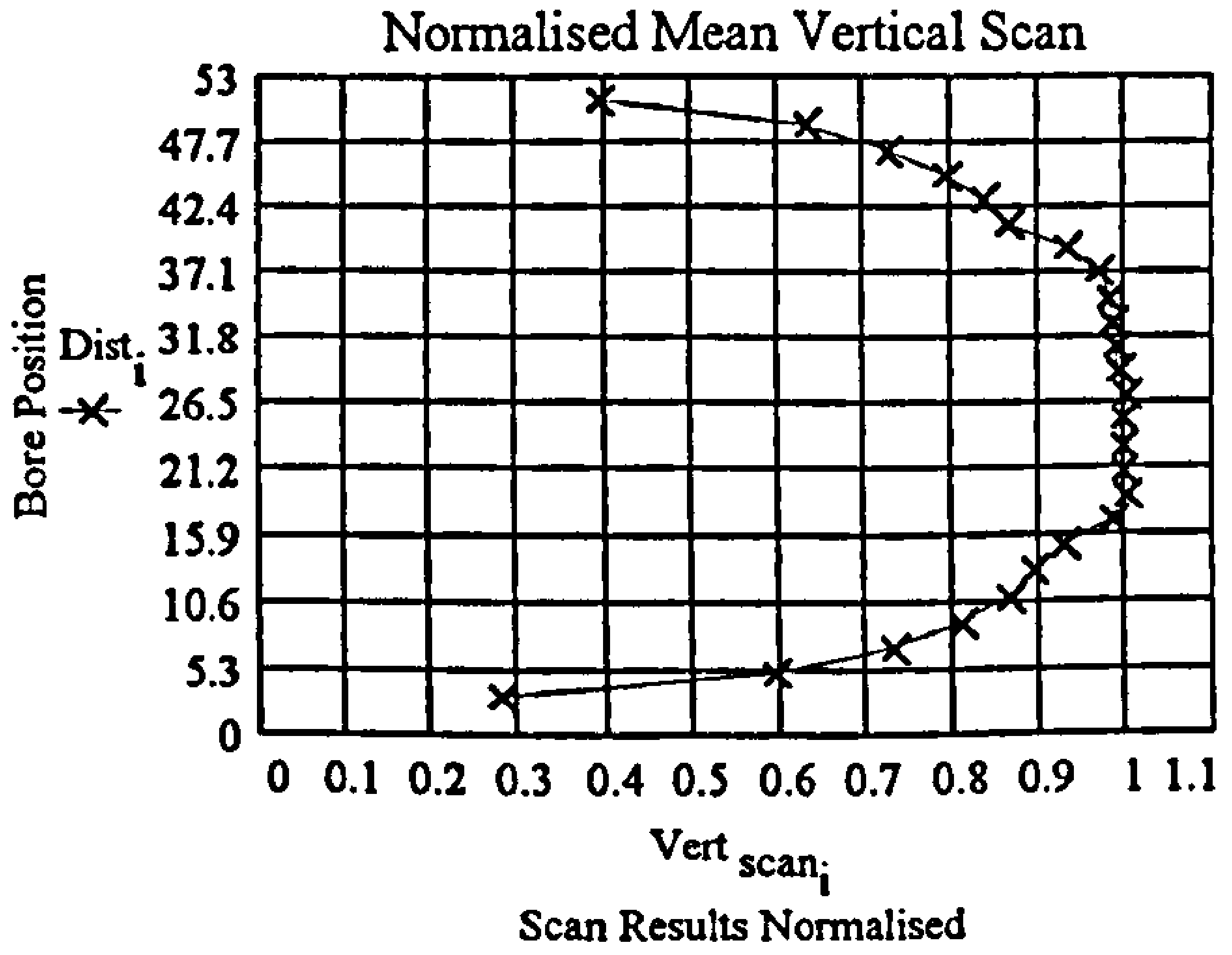

By inspection the slope of the leading edge of the particle distribution density data can be calculated by extracting the data obtained from the graph above where the flat peak of the curve begins. The change in directions of the curve occur mainly at i=13 and i=18.

Submatrix Extraction:- $\quad$ $S_{peak} := submatrix\left(N_{vert}, 13, 18, 1, 2\right)$

$M := rows\left(S_{peak}\right)$ $\quad$ $M = 6$ $\quad$ $\left(S_{peak}^{\langle 1 \rangle}\right)_1 = 27$

$j := 1, 2 .. M$

$$\mathrm{Dist}_{sub} := S_{peak}^{\langle 1\rangle} - \left(S_{peak}^{\langle 1\rangle}\right)_1$$

$$\mathrm{Data}_{peak} := S_{peak}^{\langle 2\rangle} - 1$$

Slope and Intercept of the Relected Line:

$$SL_{orig} := \mathrm{slope}\left(\mathrm{Data}_{peak}, \mathrm{Dist}_{sub}\right) \qquad SL_{orig} = -360.263$$

$$INT_{orig} := \mathrm{intercept}\left(\mathrm{Data}_{peak}, \mathrm{Dist}_{sub}\right) \qquad INT_{orig} = 0.12$$

$$x := -1, -0.995 .. 1$$

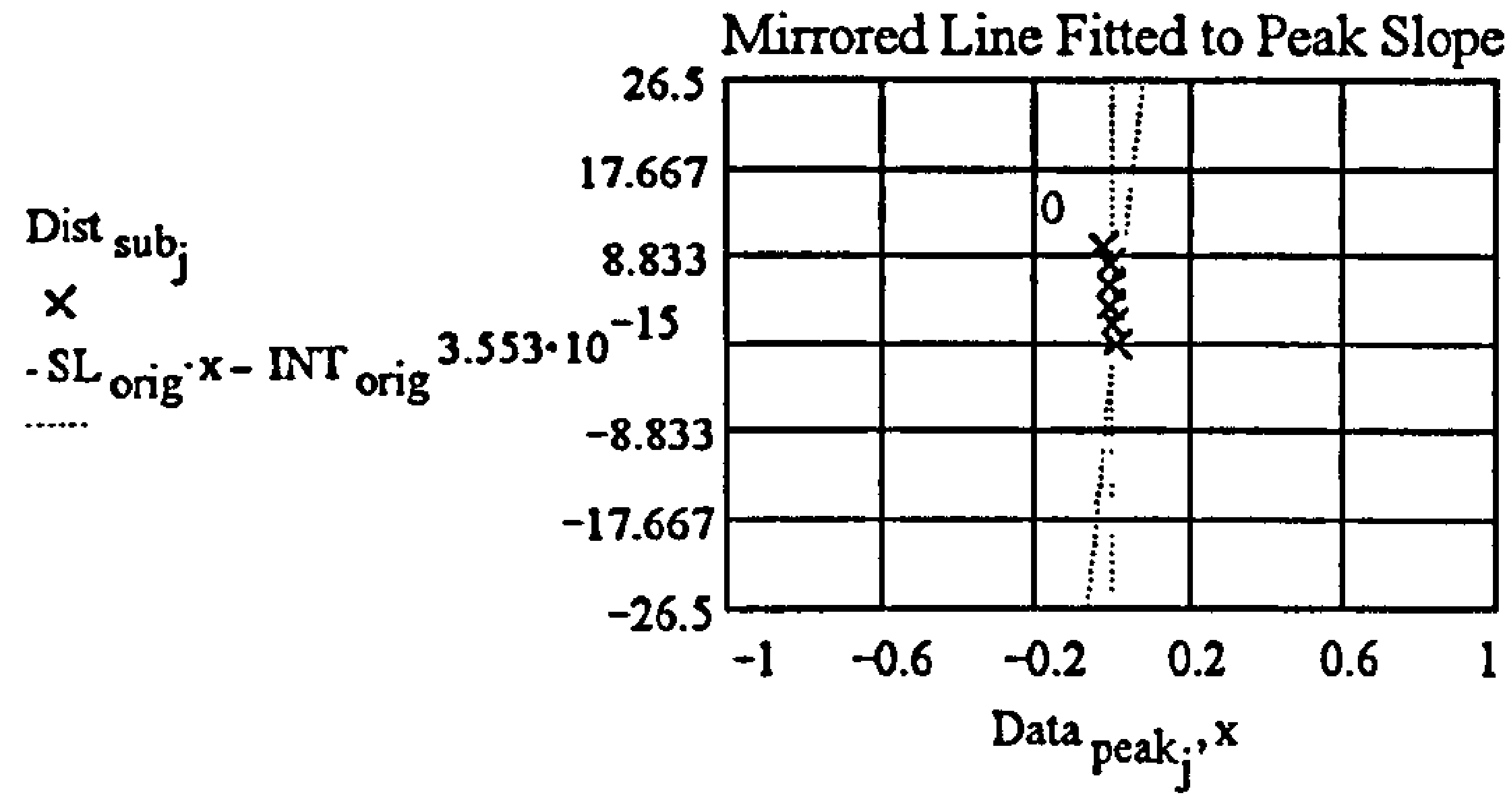

The modified slope and intercept for the reflected best fit line through the data that forms the peak of the particle distribution density curve is used to modifiy the Prandtl Curve [P2].

Equation of Reflected Line: $y = -SL_{orig}x - INT_{orig}$

The value of x for a known y so that the x dimension when the value of y = 26.5 units, i.e. at the pipe wall boundaries, can be found.

$$\mathrm{Mlt1}_{wall} := \frac{32 + INT_{orig}}{-SL_{orig}} \qquad \mathrm{Mlt1}_{wall} = 0.08916 \qquad \mathrm{Mlt2}_{wall} := \frac{21 + INT_{orig}}{-SL_{orig}} \qquad \mathrm{Mlt2}_{wall} = 0.05862$$

Construction of the Prandtl Air Velocity Distribution:-

$$k := 1 .. 53 \qquad \mathrm{Rad}_k := k \cdot 0.5 \qquad R_{final} := 26.5$$

$$V_k := 5.52 \cdot \log\left(\frac{\mathrm{Rad}_k}{1.59 \cdot 10^{-5}}\right) + 5.5 \qquad U1_k := \frac{V_k}{\max(V)} \qquad U2 := \mathrm{reverse}(\mathrm{sort}(U1))$$

Modification of the Prandtl air velocity distribution by using the skewing factors determined from the vertical particle density distribution profile in the previous section will be given on the next page.

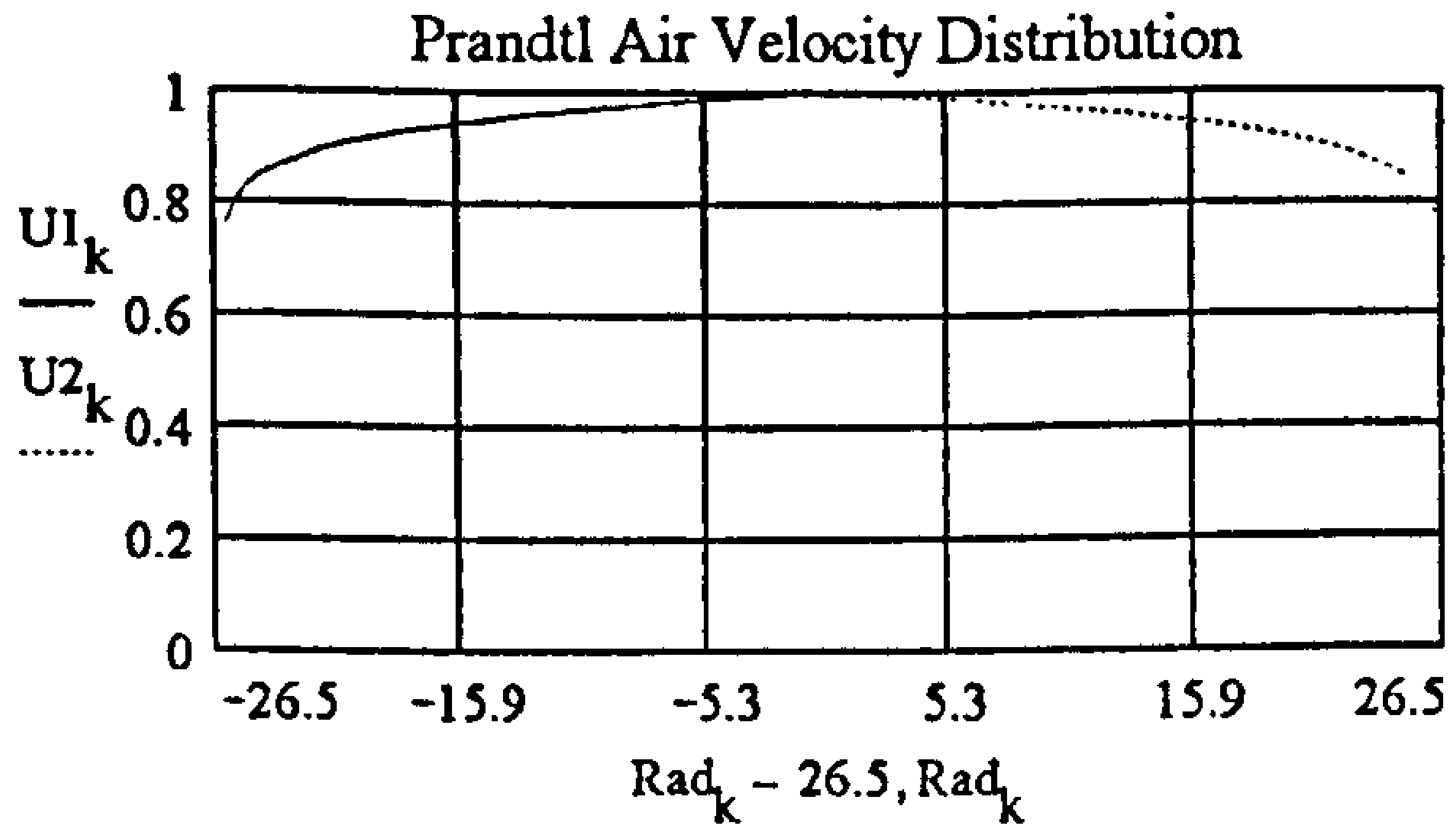

Skewing the Prandtl Air Velocity Profile

$l := 1,2..42$ $\quad$ $Rad1_l := l \cdot 0.5 - 27$ $\qquad$ $m := 1,2..63$ $\quad$ $Rad2_m := m \cdot 0.5 - 6$

$VX1 := \text{submatrix}(U1,1,42,1,1)$ $\qquad$ $VXadd1 := \text{submatrix}(U1,43,53,1,1)$

$VXadd2 := \text{submatrix}(U2,2,53,1,1)$

$VX2 := \text{stack}(VXadd1,VXadd2)$

$$Mlt1_l := \frac{Rad1_l + INT_{orig}}{-SL_{orig}} \qquad Mlt2_m := \frac{Rad2_m + INT_{orig}}{-SL_{orig}}$$

$WX1 := VX1 + Mlt1$ $\qquad$ $WX2 := VX2 + Mlt2$

$\max(WX1) = 0.969683$ $\qquad$ $\max(WX2) = 1.000244$

$$VSkew1 := \frac{WX1}{\max(WX2)} \qquad VSkew2 := \frac{WX2}{\max(WX2)}$$

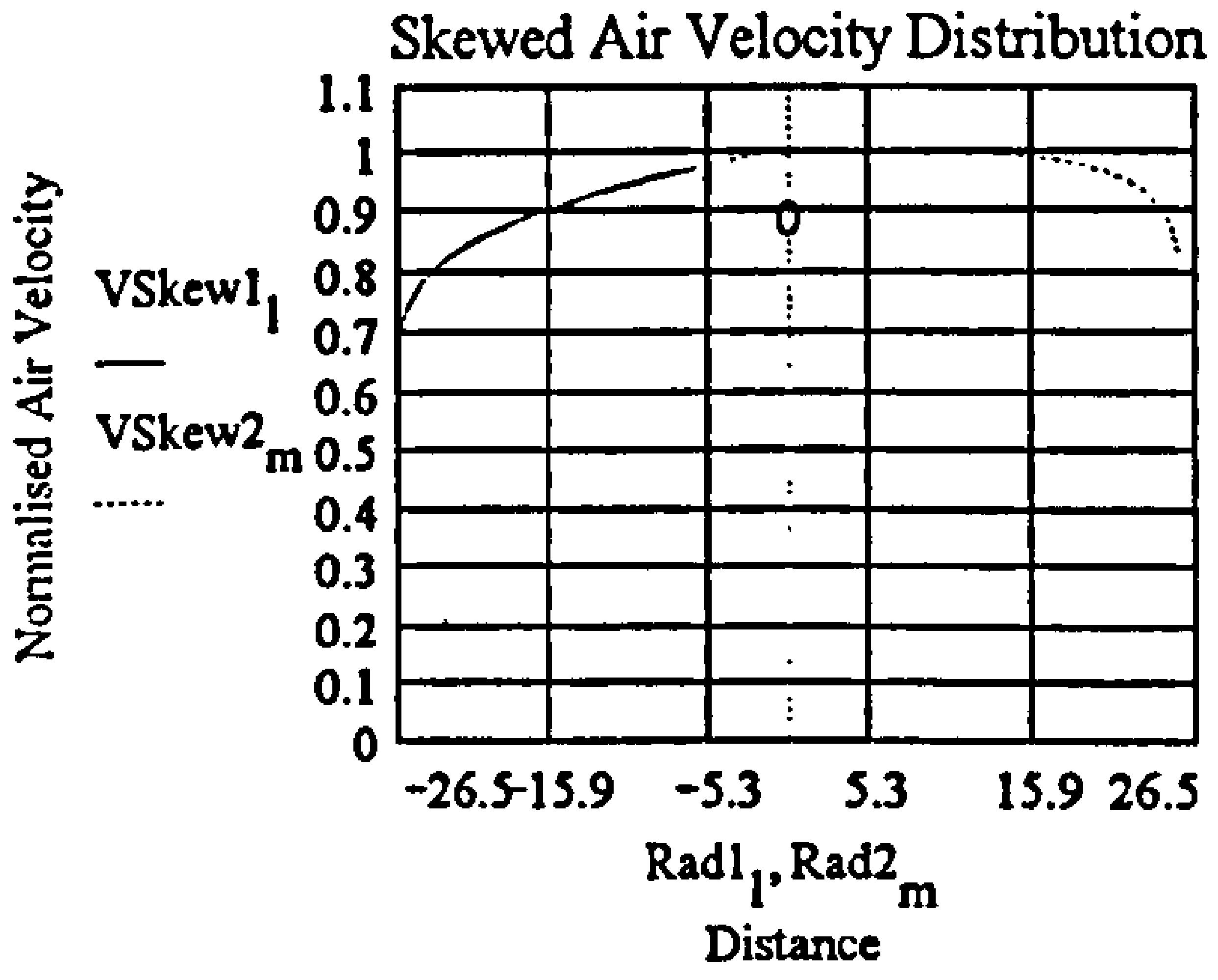

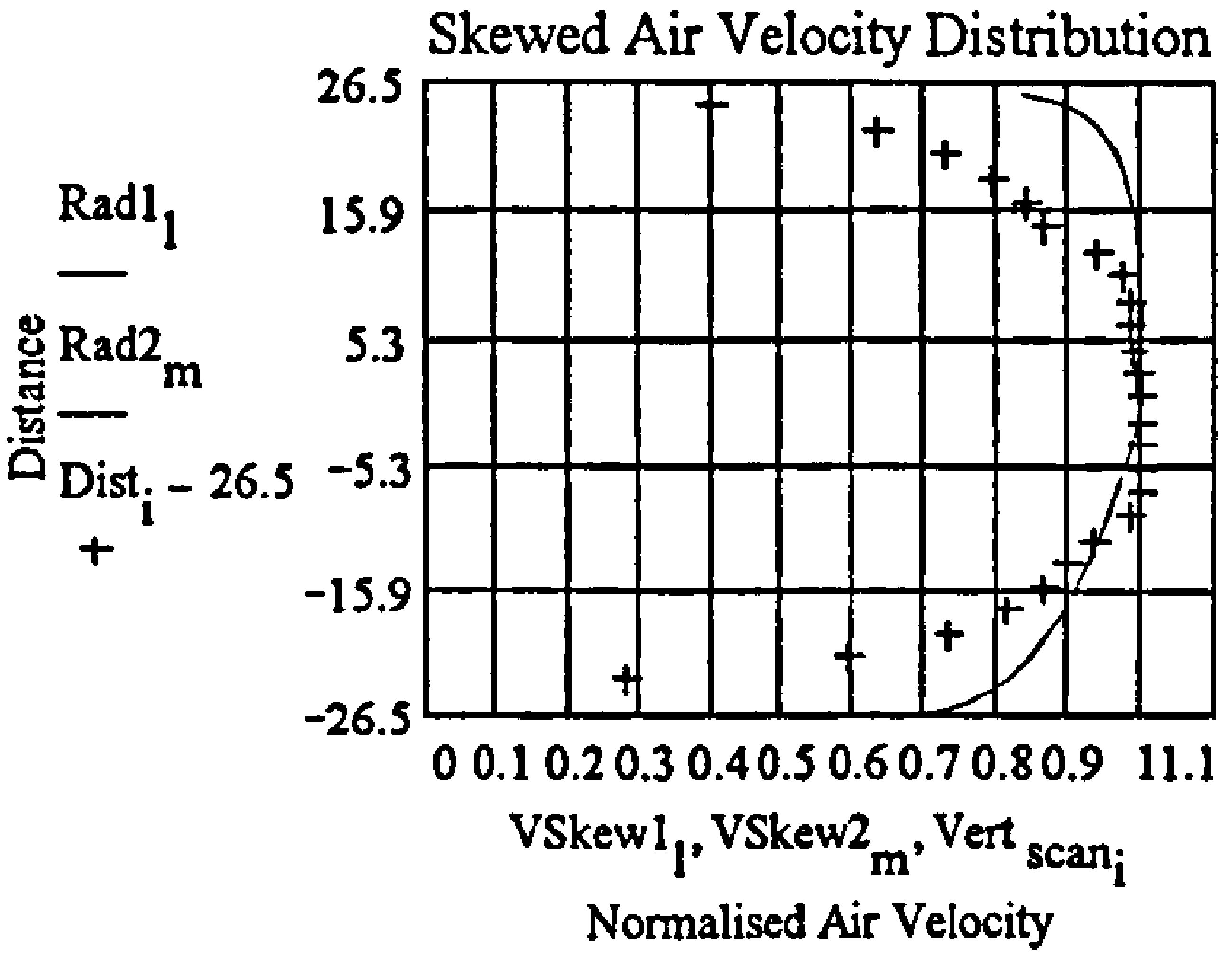

An effort to ensure that the mean air velocity is equivalent to the value extractred from tests carried out on the pneumatic conveyor test facility is presented next. The mean value of the ordinates for the normalised air velocity is calculated and the scaling factor to ensure that the mean ordinate value is equal to 1 is found.

Total Number of Ordinates:- $Tot := \text{rows}(VSkew1) + \text{rows}(VSkew2)$ $\quad$ $Tot = 105$

Sum of all Ordinates:- $Sum := \sum VSkew1 + \sum VSkew2$ $\quad$ $Sum = 98.837$

Mean Ordinate Value:- $Mean := \frac{Sum}{Tot}$ $\quad$ $Mean = 0.941$

Scaling Factor:- $SF := \frac{1}{Mean}$ $\quad$ $SF = 1.062$

Corrected Ordinate Information:- $AV1 := VSkew1 \cdot SF$ $\quad$ $AV2 := VSkew2 \cdot SF$

Graph on the following page illustrates the correctly scaled air velocity ordinates and the particle density distribution for comparison.

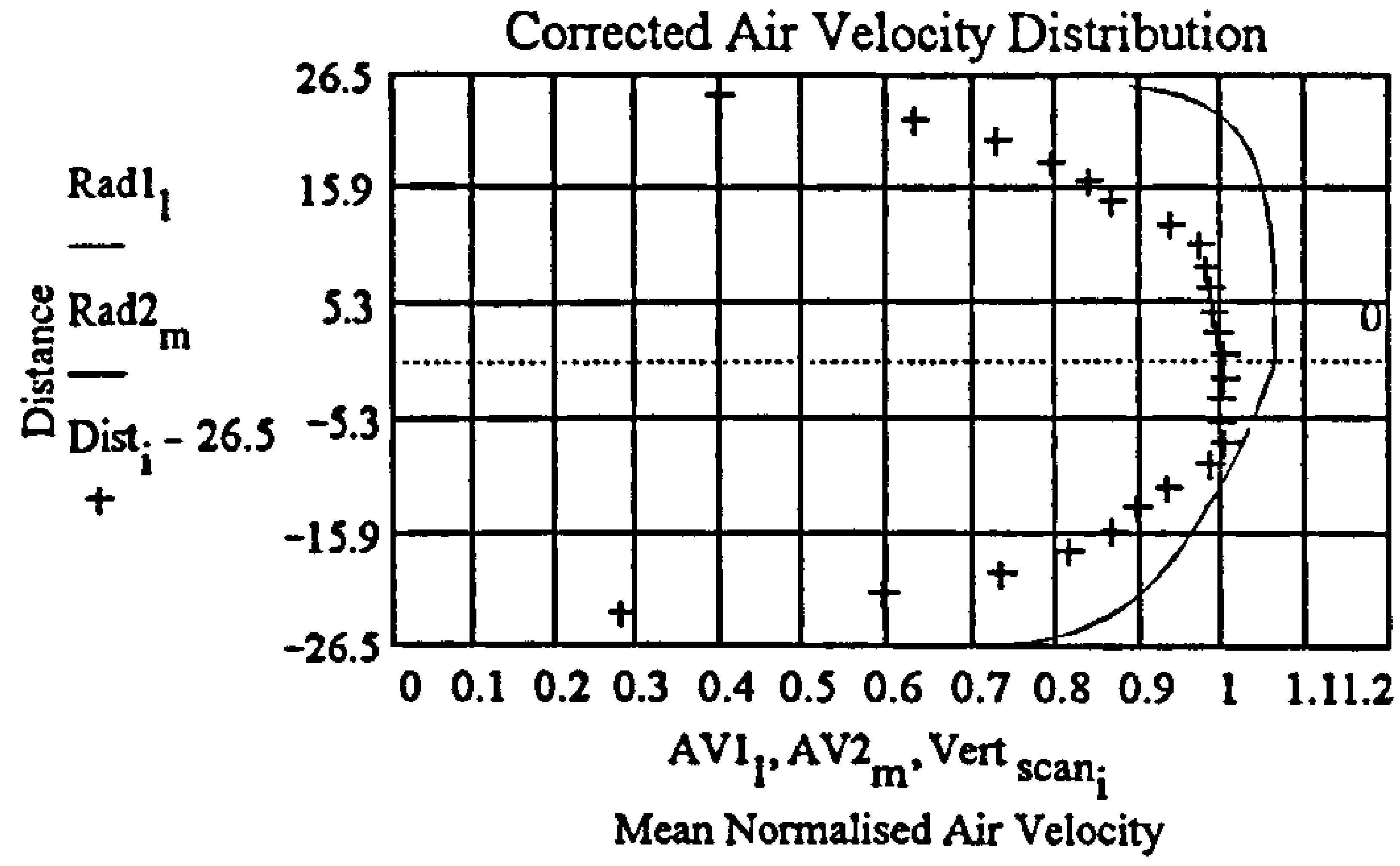

The location of contour centres for the air velocity distribution for the skewed data needs to be found so that a polar contour plot can be made that matches that already derived for the particle distribution density (see Figure 5.8). Cubic splines will be fitted to the data to aid in this process.

$$SPoints := \begin{bmatrix} -26.1 \\ -22.9 \\ -20.0 \\ -17.1 \\ -14.2 \\ -11.6 \\ -8.7 \\ -5.8 \\ -2.9 \\ 0 \\ 2.9 \\ 5.8 \\ 8.7 \\ 11.6 \\ 14.2 \\ 17.1 \\ 20.0 \\ 22.9 \\ 26.1 \end{bmatrix}$$

$ii := 1, 2 .. 19$

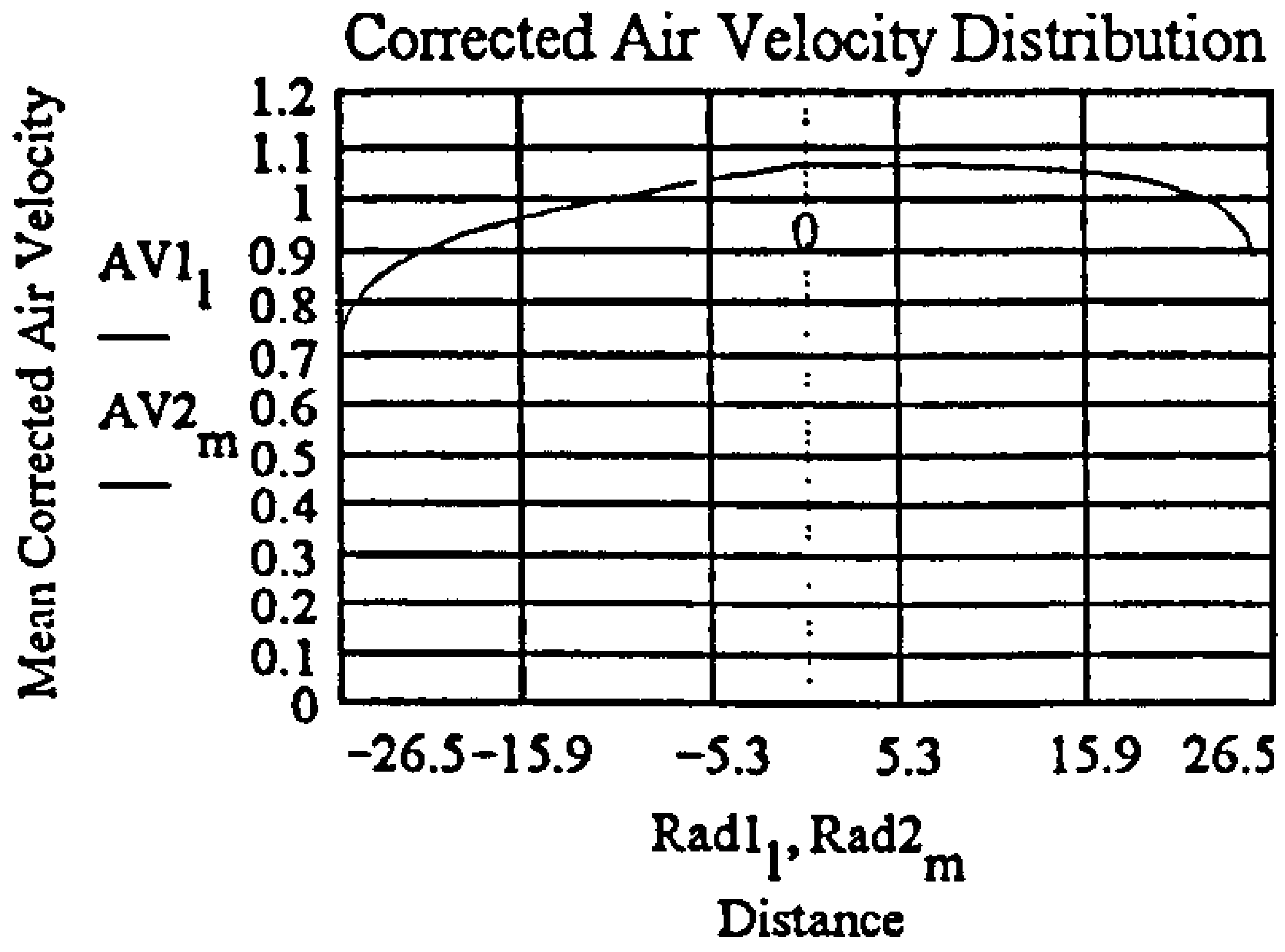

$Pt1_{ii} := \mathrm{if}(SPoints_{ii} > -5.5, 0, \mathrm{linterp}(Rad1, AV1, SPoints_{ii}))$

$Pt2_{ii} := \mathrm{if}(SPoints_{ii} < -5.5, 0, \mathrm{linterp}(Rad2, AV2, SPoints_{ii}))$

$Profile := Pt1 + Pt2$

$vs1 := \mathrm{lspline}(SPoints, Profile) \qquad x := -26.5, -26 .. 26.5$

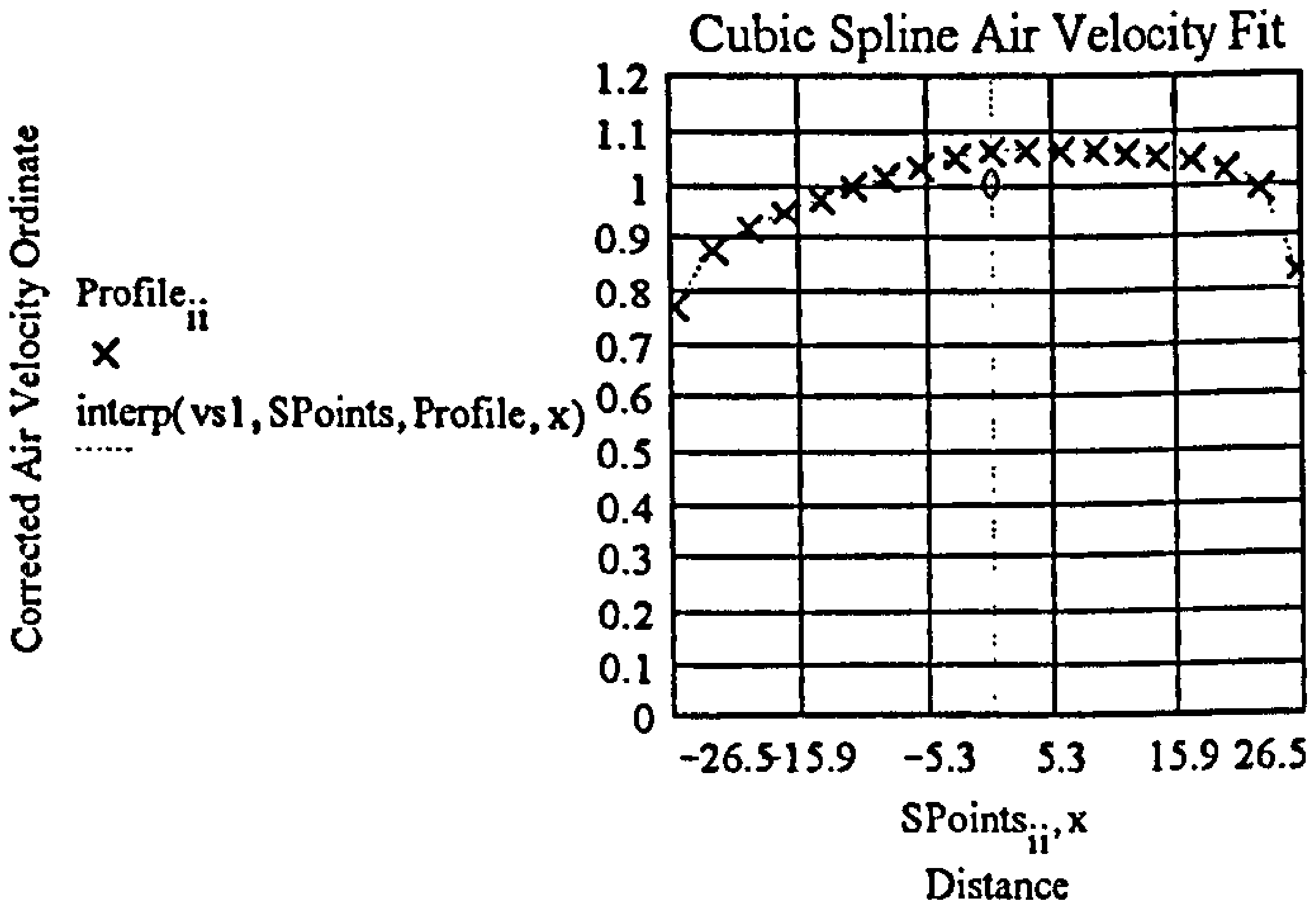

The crosshairs facility available in MathCad was used to find the bore coordinates when the air velocity ordinates crossed certain prescribed levels. This data will be used to form the contours of mean corrected air velocity required for polar contour plot generation. Data generated via this route is presented in the following matrix of values:-

$$C := \begin{bmatrix} 0.8 & -25.2 & 26.4 \\ 0.825 & -24.6 & 26.2 \\ 0.85 & -24.1 & 25.7 \\ 0.875 & -23 & 25.2 \\ 0.9 & -21.9 & 24.9 \\ 0.925 & -19.8 & 24.6 \\ 0.95 & -17.1 & 24.1 \\ 0.975 & -14.2 & 23.8 \\ 1.0 & -10.5 & 22.4 \\ 1.025 & -7.3 & 20.8 \\ 1.05 & -3.52 & 16.5 \end{bmatrix}$$

$b := C^{\langle 3 \rangle}$ $a := C^{\langle 2 \rangle}$ $\mathrm{ConVal} := C^{\langle 1 \rangle}$

$ij := 1,2..11$

Finding the centre position of each circular contour from the bore axis:-

$$\mathrm{ConCent}_{ij} := \frac{b_{ij} + a_{ij}}{2}$$

Finding the radius of the individual contour lines from their centres:-

$$\mathrm{ConRad}_{ij} := \frac{b_{ij} - a_{ij}}{2}$$

Finding the equations of the contour coordinates:-

$x = r \cdot \cos(\theta)$ $y = r \cdot \sin(\theta)$ Equation of Circle:- $x^2 - (y - \mathrm{ConCent})^2 = r^2$

$\mathrm{Num} := 50$ $\theta := 0, \left(2 \cdot \frac{\pi}{\mathrm{Num}}\right) .. 2 \cdot \pi$

$\mathrm{Slope30} := 0.5573502692$

$\mathrm{Slope60} := 1.732050808$

$XX_{ij} := \mathrm{ConRad}_{ij} \cdot \cos(\theta)$ $YY_{ij} := \mathrm{ConRad}_{ij} \cdot \sin(\theta) - \mathrm{ConCent}_{ij}$

$ik := 1,2..14$

$\mathrm{RAD}_{ik} := ik \cdot 5 - 35$

$Yl_{ik} := 0$

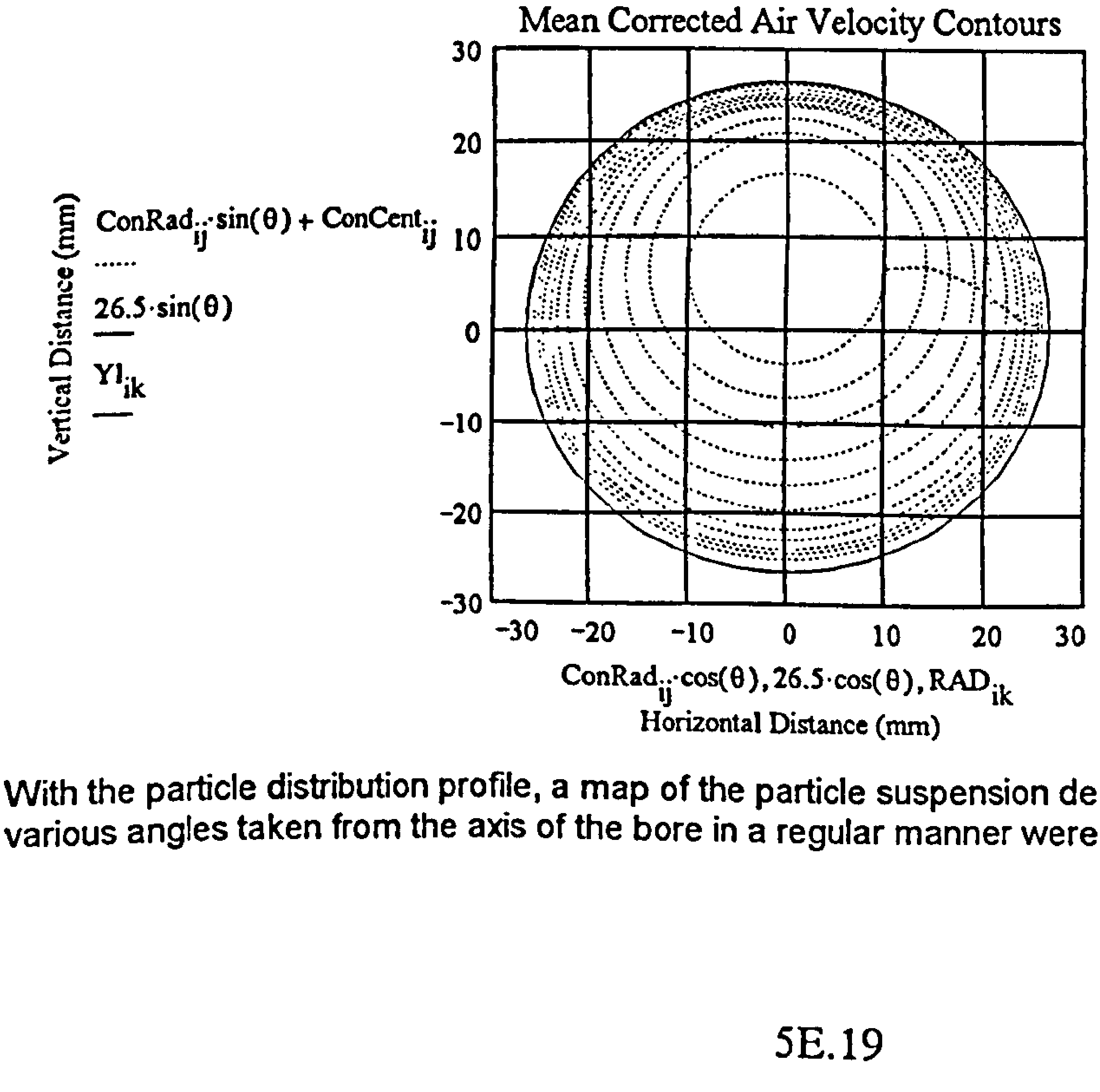

With the particle distribution profile, a map of the particle suspension density for a range of radii at various angles taken from the axis of the bore in a regular manner were extracted (see Figure 5.8).

The corresponding positions for the air velocity distribution need to be found and values extracted for the same positions. This was achieved by positioning a line on the contour plot shown above that corresponds to the necessary radial position for which readings are required. The air velocity distribution along this line was found using the cross hairs method in MathCad, and a cubic spline curve fit was undertaken. Data values were found by interpolation from the resulting curve fit for the necessary radial positions.

Data Obtained for a Line Placed at 30 Degrees to the Bore Axis Position:-

$$DF30 := \begin{bmatrix} -23.2 & 0 \\ -22.3 & 0.8 \\ -21.9 & 0.825 \\ -21.4 & 0.85 \\ -20.5 & 0.875 \\ -19.6 & 0.9 \\ -18.3 & 0.925 \\ -16.2 & 0.95 \\ -14.0 & 0.975 \\ -11.1 & 1.0 \\ -8.12 & 1.025 \\ -4.51 & 1.05 \\ 9.92 & 1.05 \\ 14.0 & 1.025 \\ 16.2 & 1.0 \\ 18.3 & 0.975 \\ 19.4 & 0.95 \\ 20.5 & 0.925 \\ 21.0 & 0.9 \\ 21.4 & 0.875 \\ 22.1 & 0.85 \\ 22.6 & 0.825 \\ 22.8 & 0.80 \\ 23.2 & 0 \end{bmatrix}$$

$AirVel30 := DF30^{\langle 2 \rangle}$

$$Rad30 := \frac{DF30^{\langle 1 \rangle}}{\cos(Ang30)}$$

$im := 1,2..rows(DF30)$

$$R := \begin{bmatrix} -26.1 \\ -22.9 \\ -20.0 \\ -17.1 \\ -14.2 \\ -11.6 \\ -8.7 \\ -5.8 \\ -2.9 \\ 0 \\ 2.9 \\ 5.8 \\ 8.7 \\ 11.6 \\ 14.2 \\ 17.1 \\ 20.0 \\ 22.9 \\ 26.1 \end{bmatrix}$$

$$Ang30 := \frac{\pi}{6}$$

$il := 1,2..19$

Fitting Cubic Spline Curves to this Data:-

$vs30 := lspline(Rad30, AirVel30)$

$x30 := -27, -26.5..27$

Interpolating for the desired radial positions:-

$Pt30_{il} := interp\left(vs30, Rad30, AirVel30, R_{il}\right)$

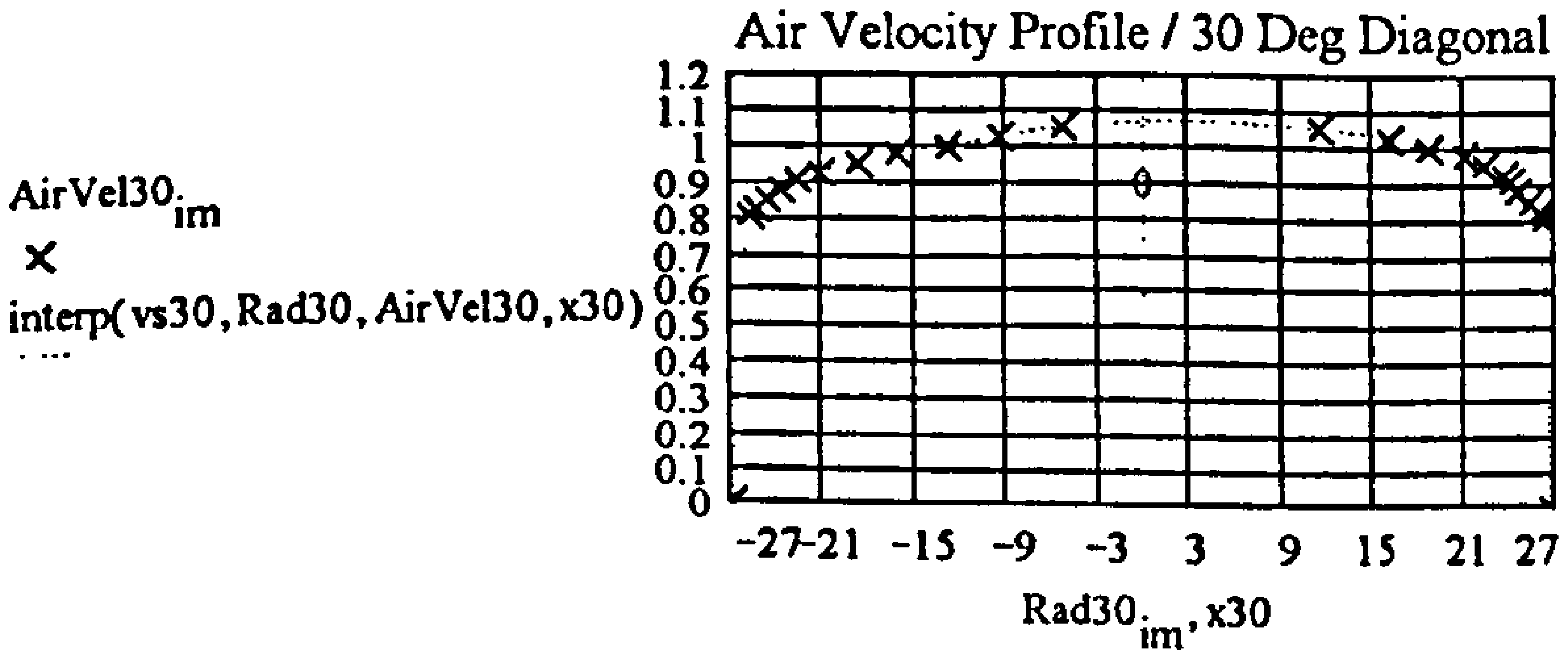

Data Obtained for a Line Placed at 60 Degrees to the Bore Axis Position:-

$$DF60 := \begin{bmatrix} -13.1 & 0 \\ -12.6 & 0.8 \\ -12.2 & 0.825 \\ -12.0 & 0.85 \\ -11.5 & 0.875 \\ -11.1 & 0.9 \\ -9.92 & 0.925 \\ -8.80 & 0.95 \\ -7.22 & 0.975 \\ -5.60 & 1.0 \\ -4.06 & 1.025 \\ -2.03 & 1.05 \\ 7.44 & 1.05 \\ 9.70 & 1.025 \\ 10.6 & 1.0 \\ 11.5 & 0.975 \\ 11.7 & 0.95 \\ 12.2 & 0.925 \\ 12.4 & 0.9 \\ 12.9 & 0.875 \\ 13.1 & 0.85 \\ 13.2 & 0.825 \\ 13.25 & 0.80 \\ 13.3 & 0 \end{bmatrix}$$

$AirVel60 := DF60^{<2>}$

$Ang60 := \frac{\pi}{3}$

$Rad60 := \frac{DF60^{<1>}}{\cos(Ang60)}$

$im := 1, 2 .. rows(DF60)$

Fitting Cubic Spline Curves to this Data:-

$vs60 := lspline(Rad60, AirVel60)$

$x60 := -27, -26.5 .. 27$

Interpolating for the desired radial positions:-

$Pt60_{il} := interp\left(vs60, Rad60, AirVel60, R_{il}\right)$

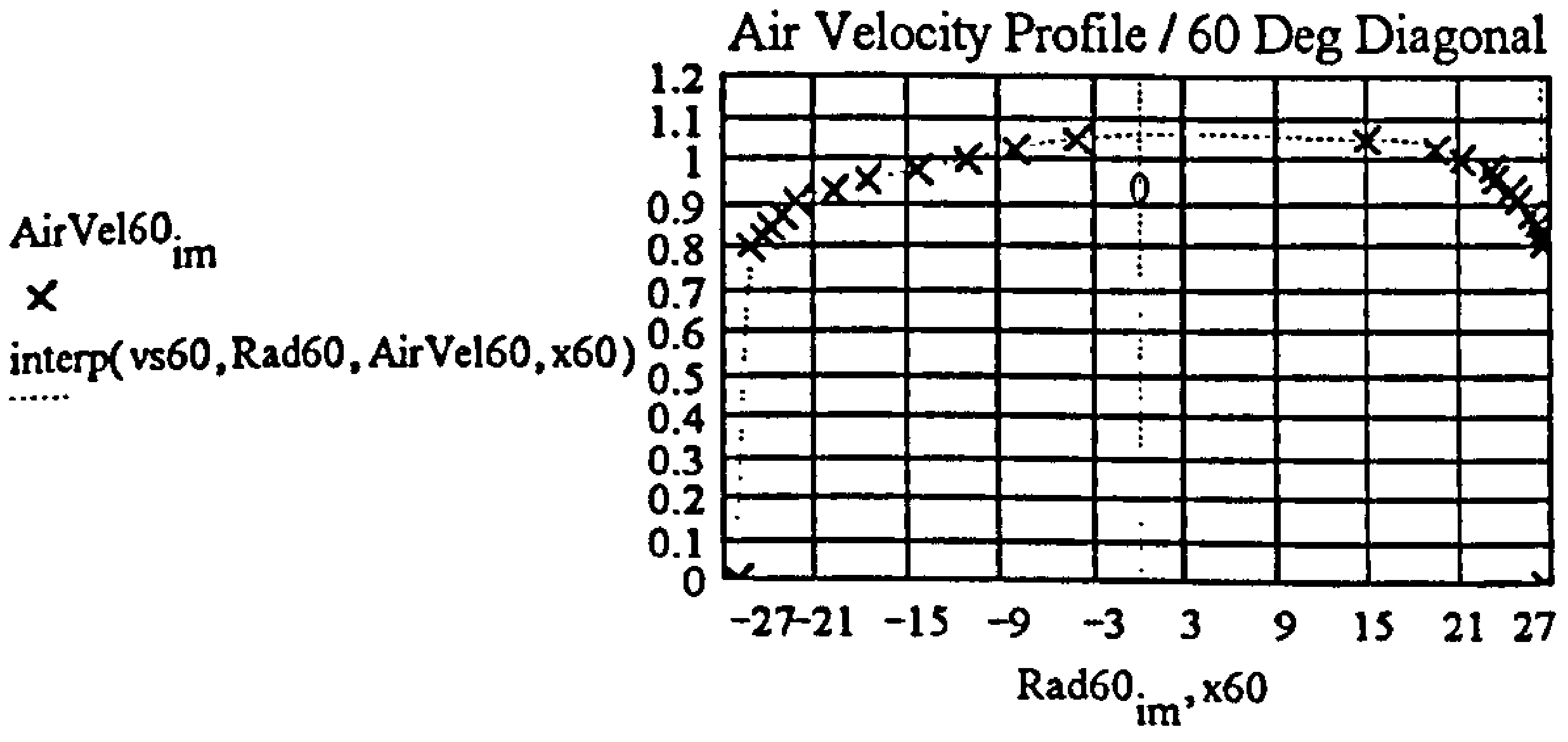

The remaining two sets of angular positioned data are at 0 and 90 degrees to the bore axis. This data can be found simply by using the crosshairs capability; no scaling is necessary.

(see overleaf)

Data Obtained for a Line Placed at 90 Degrees to the Bore Axis Position:-

$$DF90 = \begin{bmatrix} -26.5 & 0 \\ -25.2 & 0.8 \\ -24.5 & 0.825 \\ -24.0 & 0.85 \\ -23.0 & 0.875 \\ -21.8 & 0.9 \\ -19.7 & 0.925 \\ -17.0 & 0.95 \\ -14.2 & 0.975 \\ -10.6 & 1.0 \\ -7.2 & 1.025 \\ -3.6 & 1.05 \\ 16.6 & 1.05 \\ 20.9 & 1.025 \\ 22.3 & 1.0 \\ 23.8 & 0.975 \\ 24.0 & 0.95 \\ 24.5 & 0.925 \\ 25.0 & 0.9 \\ 25.2 & 0.875 \\ 25.7 & 0.85 \\ 26.2 & 0.825 \\ 26.475 & 0.80 \\ 26.5 & 0 \end{bmatrix}$$

$AirVel90 := DF90^{<2>}$

$Rad90 := DF90^{<1>}$

$im := 1,2..rows(DF90)$

Fitting Cubic Spline Curves to this Data:-

$vs90 := lspline(Rad90, AirVel90)$

$x90 := -27, -26.5 .. 27$

Interpolating for the desired radial positions:-

$Pt90_{il} := interp\left(vs90, Rad90, AirVel90, R_{il}\right)$

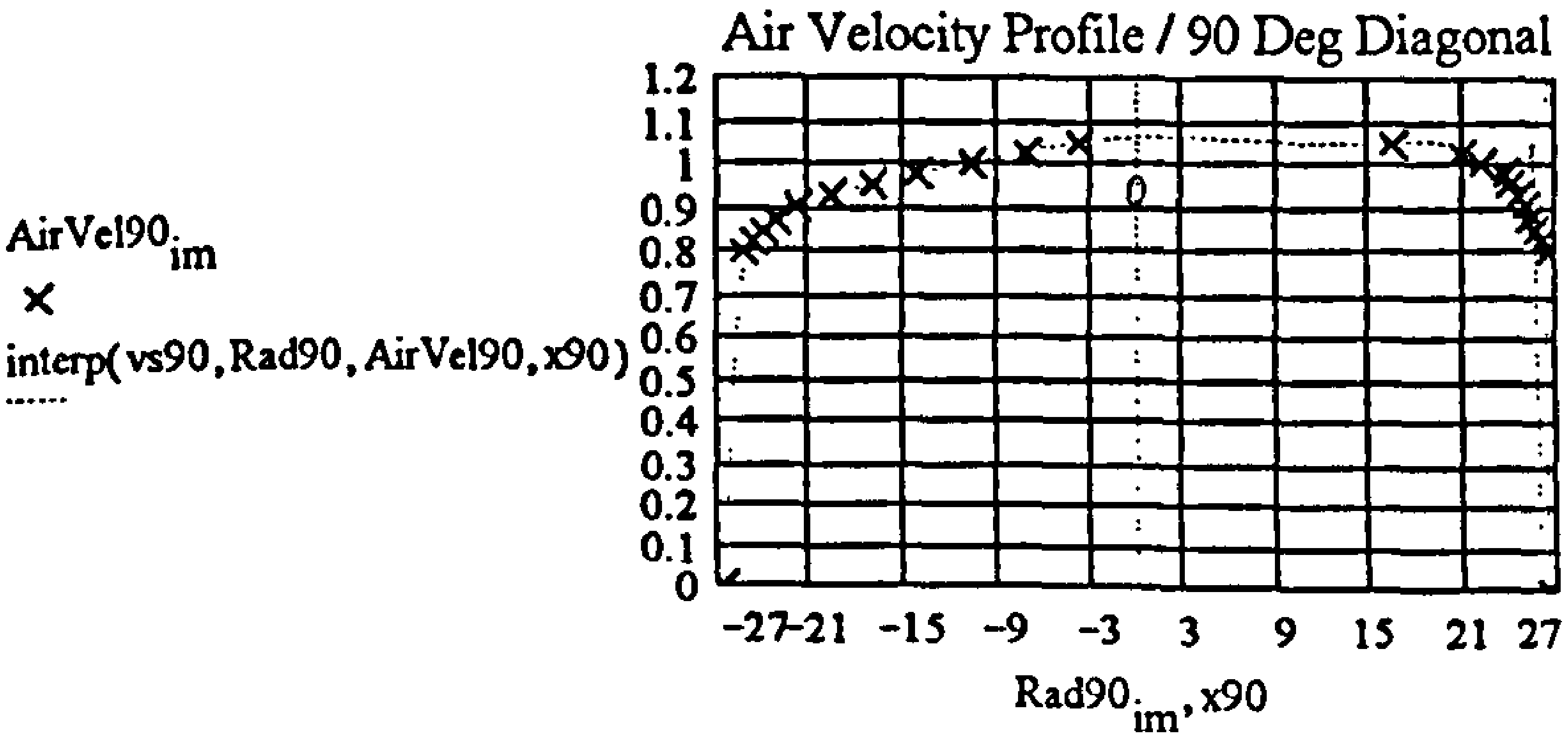

Data Obtained for a Line Placed at 0 Degrees to the Bore Axis Position:-

$$DF0 := \begin{bmatrix} -26.5 & 0 \\ -25.7 & 0.8 \\ -25.5 & 0.825 \\ -24.8 & 0.85 \\ -23.9 & 0.875 \\ -23.2 & 0.9 \\ -22.1 & 0.925 \\ -20.3 & 0.95 \\ -18.5 & 0.975 \\ -15.3 & 1.0 \\ -12.4 & 1.025 \\ -7.67 & 1.05 \\ 7.67 & 1.05 \\ 12.4 & 1.025 \\ 15.3 & 1.0 \\ 18.5 & 0.975 \\ 20.3 & 0.95 \\ 22.1 & 0.925 \\ 23.2 & 0.9 \\ 23.9 & 0.875 \\ 24.8 & 0.85 \\ 25.5 & 0.825 \\ 25.7 & 0.80 \\ 26.5 & 0 \end{bmatrix}$$

$AirVel0 := DF0^{<2>}$

$Rad0 := DF0^{<1>}$

$im := 1,2..rows(DF0)$

Fitting Cubic Spline Curves to this Data:-

$vs0 := lspline(Rad0, AirVel0)$

$x0 := -27, -26.5..27$

Interpolating for the desired radial positions:-

$Pt0_{il} := interp\left(vs0, Rad0, AirVel0, R_{il}\right)$

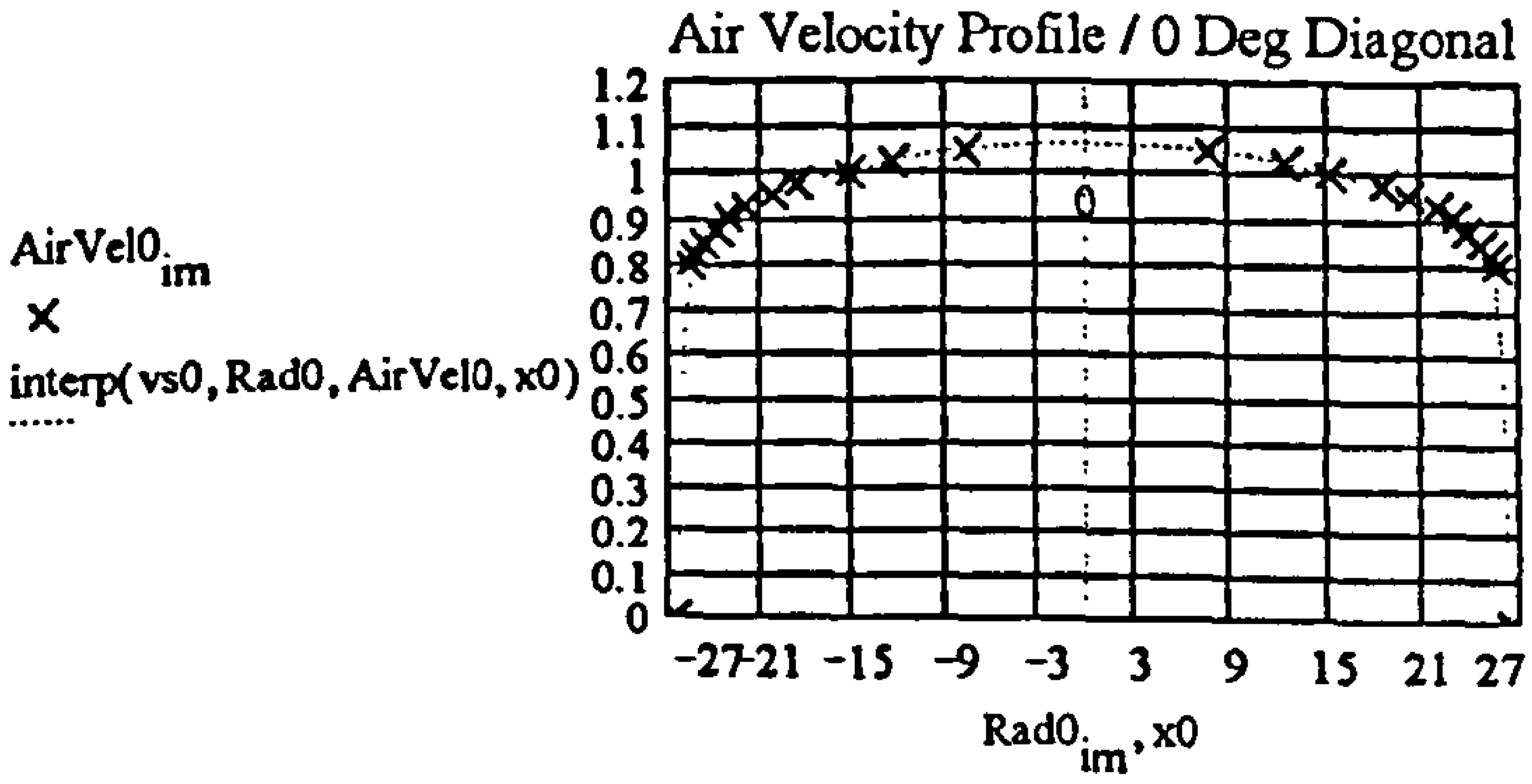

These data sets were then multiplied by the mean value of the air velocity at the entrance to the test bend measured during the pneumatic conveying trials. This results in Figure 5.9.

Appendix 5F: Modelling the Particle Trajectories Within the Test Bend

5F.1 Introduction to the Particle Trajectory Modelling

Traditionally there are two ways to model the particle trajectories within a pipe bend. These involve two different model formulations. The first of these is a finite differencing code based on Eulerian principles. This method aims to describe the bulk mixture of particles and gas in continuum mechanics terms, and plots its behaviour at the interfaces or boundaries of the problem geometry. Modelling of this type does not make it possible to consider the trajectory of an individual particle within the flow. This can only be achieved by using the second model formulation. The second method is known as the Lagrangian method. In this form of model individual particle trajectories are considered in detail. It is possible to link the two different forms of modelling technique and gain the best of both these modelling techniques at the cost of much longer computing times [O1]. With the linked modelling structure it is possible to model the effects that the particles have on the gas phase as well as the other way around. This is of great importance in modelling situations where there is a relatively high concentration of particles. However, in the case where the particle concentration is low the basic Lagrangian formulation can be used on its own by ignoring the effect of the particles on the gaseous phase. A linked Eulerian / Lagrangian finite differencing model and a basic Lagrangian formulated model were used in the estimation of the particle trajectories and the primary impact locations within the test bend used in this project. The combined Eulerian / Lagrangian model was also used to give an indication of the position of the secondary impact locations within the bend.

The first trajectory model that was used was that devised for estimatring the particle trajectories in a radiused bend containing gas-solid particle flows reported by Yeung [Y1]. The second was a commercial trajectory modelling software package called GENTRA which forms part of the industry standard PHOENICS computational fluid mechanics (CFD) programme [R6].

Both of these models will be considered in turn and comparison between the results obtained from them will be undertaken where applicable.

5F.2 Introduction to the Yeung Trajectory Model

The model presented by Yeung [Y1] was the first, and is the most basic particle trajectory model that is available at present.

The form of modelling used is that of finite differencing with one-way coupling between the particles and the gas, so that the effects of the solid phase upon the gas are neglected. The use of this type of model required the time period over which modelling was taking place to be split into many small steps. A set of calculations was performed at the end of each time increment, and the results obtained from each set of calculations were used as the initial conditions for the next iteration of the same set of calculations.

This appendix is divided into four main sections. These are as follows:-

i) Calculation of the particle trajectory within the radiused bend.

ii) Calculations of the location of particle impact, the angle of impingement and impact velocity.

iii) Brief conclusions concerning the use of this model.

iv) Listing of the completed Yeung model coded in MathCad syntax.

5F.2.1 Calculation of the Particle Trajectory within the Radiused Bend Using the Yeung Model

As mentioned earlier (in section 5F.1), the Yeung model was of the Lagrangian one way coupling form which considerably eased the difficulty in modelling the particle trajectory. A variety of other simplifications were made by Yeung [Y1] to reduce the complexity of the model to the barest minimum. These were as follows:-

a) The particle concentration was taken to be so small that the effects of inter-particulate collisions could be neglected.

b) The particle concentration was small enough that the particles were assumed to have a negligible effect on the gas surrounding them. Hence the model became one of one-way coupling between the gas and the particles, where the gas motion significantly affected the particles but the converse was ignored.

c) All of the hydrodynamic forces acting on the particles other than the drag force were taken to be so much smaller as to permit their omission from the model formulation (see Figure 2.1 for indication of the forces that may act on a particle).

d) Stokes' law was used to model the drag force acting on the particles.

e) At the entrance to the pipe bend the gas solid mixture was assumed to enter with a uniform velocity where the particles were in dynamic equilibrium with the gas. The particle distribution was also taken to be homogenous over the pipe bore.

As a consequence of these simplifications Yeung considerably reduced the complexity of the model.

The coordinate system shown in Figure 5F.1 was adopted for use in this model.

The use of the simplifying decisions made by Yeung as described above, led to a situation where the effects of the hydrodynamic forces acting on the particle within the bend could be reduced to one expression. Yeung [Y1] derived this expression, by grouping all of the terms that were not based on velocity components or positions into one term. This was called the momentum equilibration.

$$\tau_m = \frac{2}{9}\,\frac{\sigma^2\,\rho_p}{\mu_f} \qquad \text{(5F.1)}$$

where τ_m is the momentum equilibration; σ is the mean particle diameter (taking the particle to be spherical); ρ_p is the particle density and μ_f is the gas viscosity. This expression was used in the following equations for the resolved acceleration terms in each of the principle coordinate directions (see Figure 5F.1). These equations were derived from applying Newton's second law to the motion of an individual particle. They are shown below after further manipulation had been carried out.

$$\frac{\delta u_p}{\delta t} = \frac{w_p^2 \cos(\psi)}{R + r\cos(\psi)} + \frac{v_p^2}{r} - \frac{u_p}{\tau_m}$$

$$\frac{\delta v_p}{\delta t} = \frac{w_p^2 \sin(\psi)}{R + r\cos(\psi)} + \frac{u_p\,v_p}{r} - \frac{v_p}{\tau_m}$$

$$\frac{\delta w_p}{\delta t} = \frac{u_p\,w_p \cos(\psi)}{R + r\cos(\psi)} + \frac{v_p\,w_p \sin(\psi)}{R + r\cos(\psi)} + \frac{W - w_p}{\tau_m}$$

(5F.2)

where u_p is the particle velocity in the r direction (bore radius coordinate) (see Figure 5F.1); t is the time increment; w_p is the particle velocity in the direction parallel to the axis of the bore of the pipe bend, ϕ (see Figure 5F.1); R is the radius of the pipe bend based on the pipe bore axis; v_p is the linear particle velocity in the in-bore angular direction, ψ; W is the initial particle velocity at entrance to the pipe bend and τ_m is the momentum equilibration as defined by Yeung [Y1] and given above.

Figure 5F.1 Toroidal coordinate system used in the Yeung model.

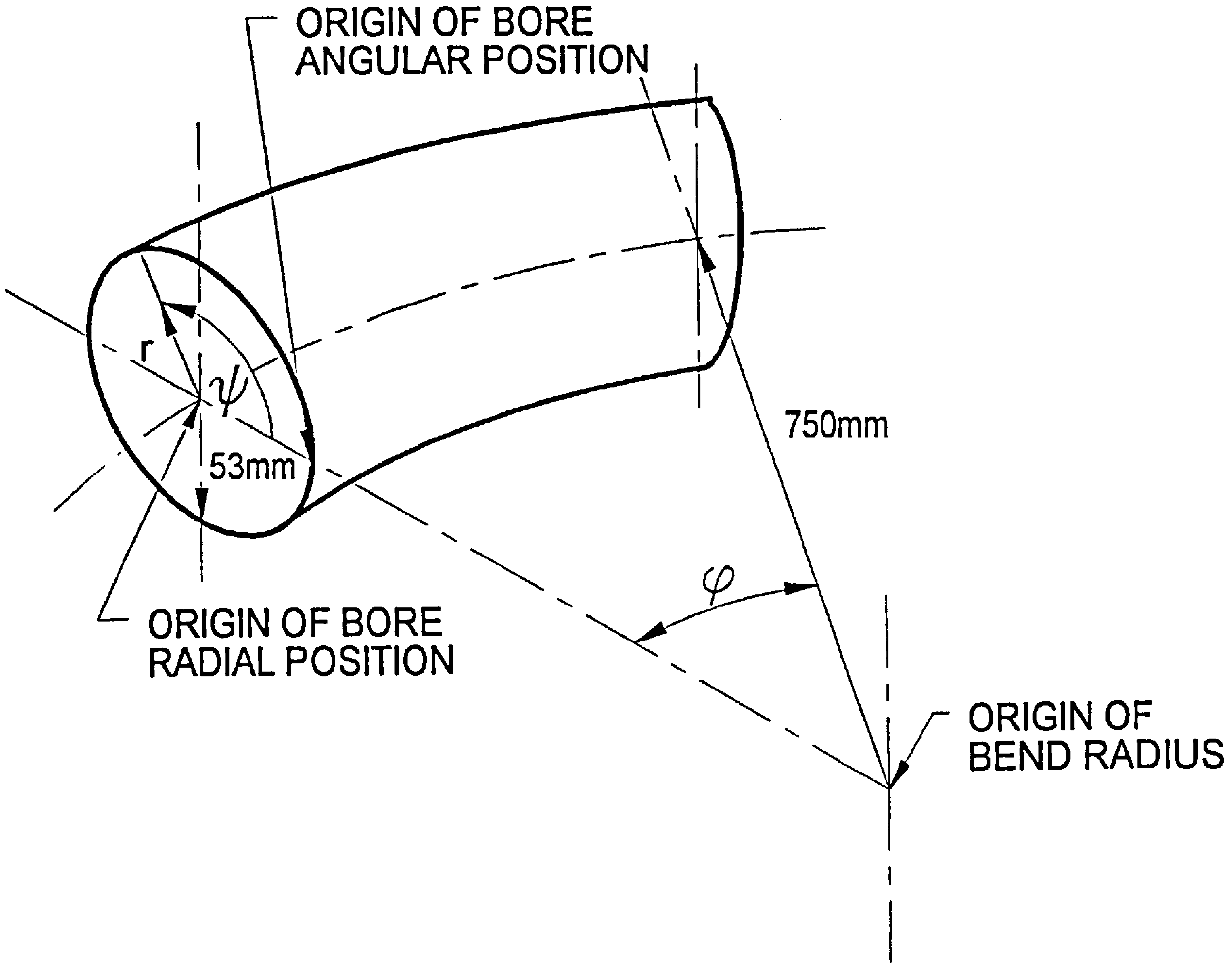

The velocities were derived from the accelerations given in equation 5F.2 above, by using the basic velocity acceleration relationship expression shown below,

$$v = u + \Delta t \; a \qquad (5F.3)$$

where v is the new velocity value; u is the initial velocity value; Δt is the time step increment and a is the value of the acceleration in the same direction as v and u. Obviously this applies to any of the three coordinates used in this analysis.

The resulting locations of a particle in the toroidal coordinate system at any time are determined using the following expressions:-

$$r = u_p \, \Delta t$$

$$\psi = \frac{v_p \, \Delta t}{r} \qquad (5F.4)$$

$$\phi = \frac{w_p \, \Delta t}{R + r \cos(\psi)}$$

where r, ϕ and ψ are as shown in Figure 5F.1 and the remaining variables are as described above. The expressions used for finding values of the new velocities given in equation 5F.3 above were used to find the position of the particle within the pipe bore in terms of the toroidal coordinates at the end of each time step.

The initial conditions for the analysis that were required were a value of W which was taken to be the mean superficial gas velocity (which, for the purposes of this work, was taken to be equivalent to the particle velocity) at the entrance to the test bend; also values of the initial start radius and angle within the pipe bore, i.e. a value of r and ψ, were required.

5F.2.2 Calculation of the Location of Particle Impact, the Angle of Impingement and the Impact Velocity

The calculations were terminated when either the particle struck the wall of the pipe bend or exited the bend without striking the internal bend wall. Logic operators within MathCad were used to find the stage in the calculations when either of these conditions occurred. At this point the calculations were stopped and the relevant data was extracted. The impact locations within the pipe bend were easily obtained by taking the last calculated values of the particle coordinates, r, ϕ and ψ. The angle of impingement and impact velocity of the particle on the internal bend surface were derived as shown in the following equations.

The surface of a toroidal geometry can be described by the following expressions:-

$$\begin{aligned} r \text{ component } - \; e_r &= (R + r\cos(\psi)) \cos(\phi) \\ \psi \text{ component } - \; e_\psi &= (R + \cos(\psi)) \sin(\phi) \\ \phi \text{ component } - \; e_\phi &= r \sin(\psi) \end{aligned} \qquad \text{(5F.5)}$$

where the variables have the same meanings as those described above. The magnitude of the particle velocity impact vector was obtained from the component velocities as follows:-

$$Q = \begin{vmatrix} u_{fin} \\ v_{fin} \\ w_{fin} \end{vmatrix} \qquad \text{(5F.6)}$$

where the subscript 'fin' refers to the final values of r, ϕ and ψ. The angle of impingement was determined via the calculation of the normal to the pipe surface, S, at the point of impact. This was found in the following manner:-

$$n = \nabla S = e_r$$

$$\text{where} \qquad \text{(5F.7)}$$

$$\nabla \equiv \frac{\partial}{\partial r} e_r + \frac{1}{r} \frac{\partial}{\partial \psi} e_\psi + \frac{1}{(R + r\cos(\psi))} \frac{\partial}{\partial \phi} e_\phi$$

where e_r, e_ψ and e_ϕ are as given in equation 5F.5 and S represents the surface of the pipe bore. Hence the normal vector, n, could be determined as:-

$$n = \begin{bmatrix} \cos(\psi_{fin}) \cos(\phi_{fin}) \\ -\sin(\psi_{fin}) \sin(\psi_{fin}) \\ 0 \end{bmatrix} \qquad \text{(5F.8)}$$

The impact angle, α, was determined as follows:-

$$\alpha = \sin^{-1} \left(\frac{Q \cdot n}{|Q| \cdot |n|} \right) \qquad \text{(5F.9)}$$

The model presented above was run ninety six times with a different start position each time for the particle entrance to the pipe bend. Results of this work are included in the following two figures

(Figure 5F.2 and 5F.3). This was achieved by using the 'dynamic data exchange' facilities available with the Windows versions of the QuattroPro and Mathcad computer software packages.

Figure 5F.2 Impact velocities plotted against initial start positions for the Yeung model.

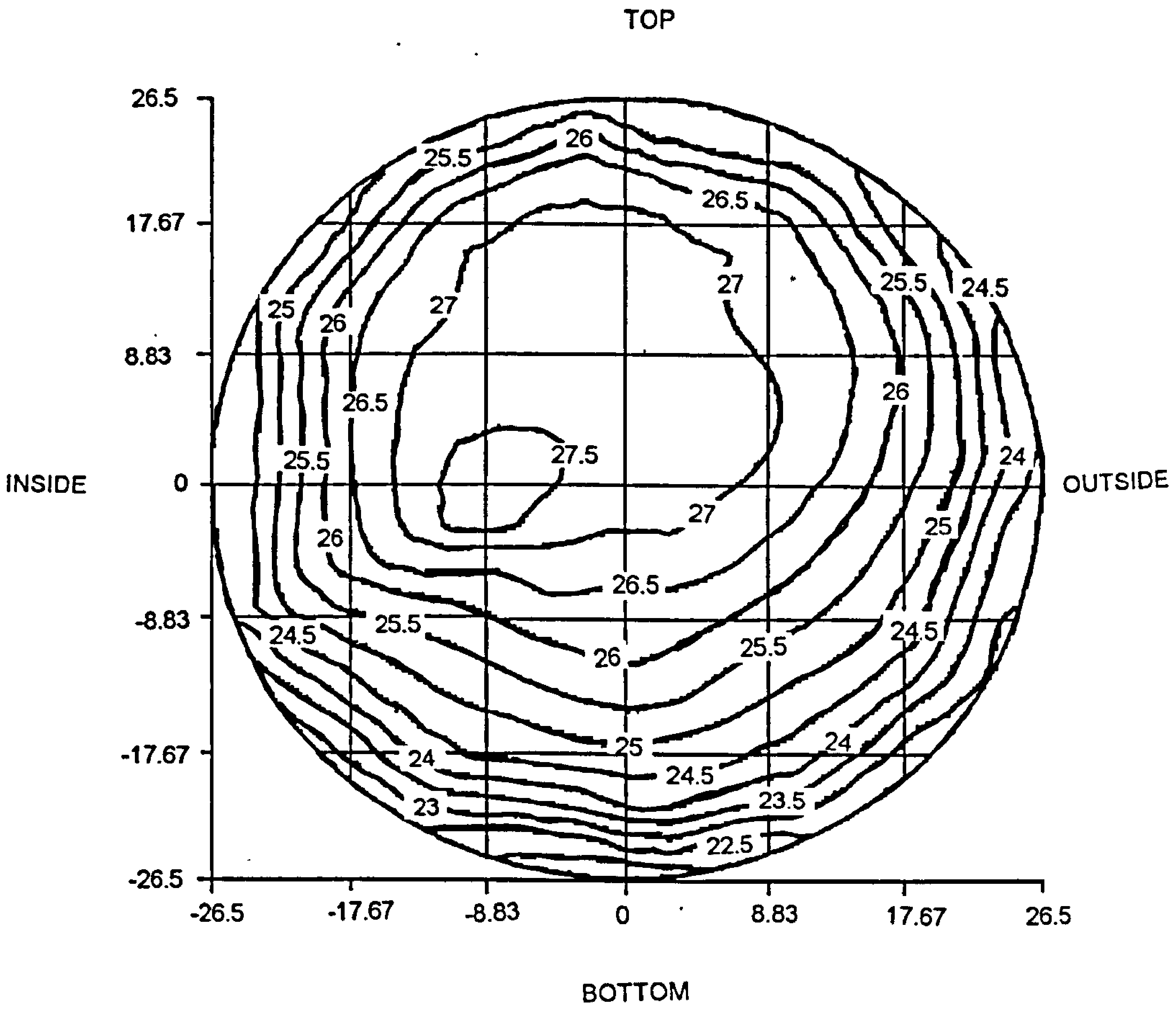

Figure 5F.3 Impingement angles plotted against initial start positions for the Yeung model.

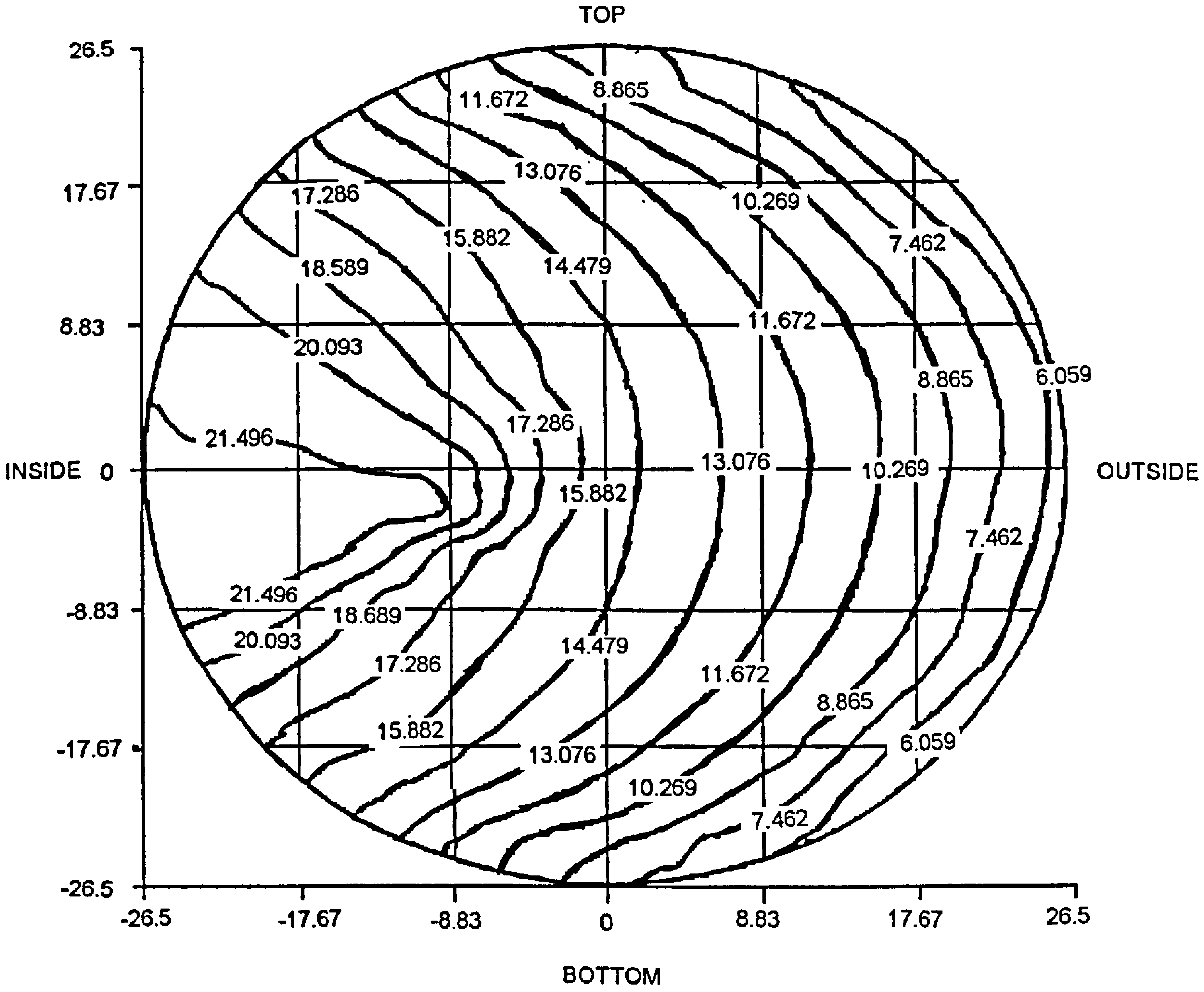

5F.2.3 Listing of the Completed Yeung Model Coded in MathCad Syntax

The MathCad listing of the Yeung particle trajectory model constructed as described above is given on the next three pages.

Modelling Particle Dynamics in a Bend Using a Model Proposed by Yeung.

$W := 25\cdot\frac{m}{sec}$ $rs := 0.0147$ $pss := 3.45$ $R := 0.75\cdot m$

$\rho_p := 3287.2\cdot\frac{kg}{m^3}$ $\sigma := 161.9\cdot 10^{-6}\cdot m$ $\mu_t := 1.82\cdot 10^{-5}\cdot\frac{kg}{m\cdot sec}$

Where ρ_p is the particle density, σ is the particle diameter, μ_t is the fluid viscosity.

$\tau_m := \frac{2}{9}\cdot\frac{\sigma^2\cdot\rho_p}{\mu_t}$ $\tau_m = 1.052049\cdot sec$ This expression is known as the momentum relaxation time.

$\Delta t := 0.0001\cdot sec$ This is the value for the time increment used in this analysis.

$i := 0 .. 1000$ This is the number of iterative passes that will be made.

Definition of the system initial conditions now follows: The system of equations will take the form of a series of nine simultaneous equations with nine unknowns.

$$\begin{bmatrix} au_0 \\ av_0 \\ aw_0 \\ u_0 \\ v_0 \\ w_0 \\ r_0 \\ \psi_0 \\ \phi_0 \end{bmatrix} := \begin{bmatrix} 0\cdot\frac{m}{sec^2} \\ 0\cdot\frac{m}{sec^2} \\ 0\cdot\frac{m}{sec^2} \\ 0\cdot\frac{m}{sec} \\ 0\cdot\frac{m}{sec} \\ W \\ rs\cdot m \\ pss\cdot rad \\ 0\cdot rad \end{bmatrix}$$

Where au,av & aw are the acclerations in each of the three toroidal dimensions being used in this analysis. u,v & w are the velocities in each of these dimensions and the remaining three terms at the bottom of this matrix equation are the positions. All of these variables apply to the position and state of the particle in the toroidal coordinate system.

The matrix equation detailing the equations of motion of a particle in the toroidal coordinate system is shown on the following page.

$$\begin{bmatrix} au_{(i+1)} \\ av_{(i+1)} \\ aw_{(i+1)} \\ u_{(i+1)} \\ v_{(i+1)} \\ w_{(i+1)} \\ r_{(i+1)} \\ \psi_{(i+1)} \\ \phi_{(i+1)} \end{bmatrix} := \begin{bmatrix} \dfrac{(w_i)^2\cdot\cos(\psi_i)}{R + r_i\cdot\cos(\psi_i)} + \dfrac{(v_i)^2}{r_i} - \dfrac{u_i}{(\tau_m)} \\ \dfrac{-(w_i)^2\cdot\sin(\psi_i)}{R + r_i\cdot\cos(\psi_i)} - \dfrac{u_i\cdot v_i}{r_i} - \dfrac{v_i}{\tau_m} \\ \dfrac{-u_i\cdot w_i\cdot\cos(\psi_i)}{R + r_i\cdot\cos(\psi_i)} + \dfrac{v_i\cdot w_i\cdot\sin(\psi_i)}{R + r_i\cdot\cos(\psi_i)} + \dfrac{W - w_i}{\tau_m} \\ u_i + au_i\cdot\Delta t \\ v_i + av_i\cdot\Delta t \\ w_i + aw_i\cdot\Delta t \\ \mathrm{if}\left(r_i \le 0.0005\cdot m, -0.0005\cdot m, \mathrm{until}\left(0.0254\cdot m - r_i, u_i\cdot\Delta t + r_i\right)\right) \\ \dfrac{v_i\cdot\Delta t}{r_i} + \psi_i \\ \mathrm{until}\left(\dfrac{\pi}{2} - \phi_i, \dfrac{w_i\cdot\Delta t}{R + r_i\cdot\cos(\psi_i)} + \phi_i\right) \end{bmatrix}$$

The values of the variables where the particle collision occurs are extracted.

$N1 := \mathrm{last}(r) - 1 \qquad N1 = 91$

Initial starting values for the iterative calculations are:

$rs = 0.0147 \qquad pss = 197.670439\cdot deg \qquad \phi_0 = 0\cdot deg$

The values of the variables for position at the point where collision with the wall occurs are:

$r_{N1} = 0.024895\cdot m \qquad \psi_{N1} = 364.744\cdot deg \qquad \phi_{N1} = 17.185296\cdot deg$

$psn1 := \psi_{N1} \qquad phn1 := \phi_{N1}$

$psn1 = 364.744182\cdot deg \quad phn1 = 17.185296\cdot deg$

The variables phn1 & psn1 are utilised in DDE transfer with QPRO.

The values of the velocity components at the collision location are extracted:

$u_{N1} = 9.566742\cdot m\cdot sec^{-1} \qquad v_{N1} = 0.570761\cdot m\cdot sec^{-1} \qquad w_{N1} = 23.770631\cdot m\cdot sec^{-1}$

<u>PLOTTING THE RESULTANT PARTICLE TRAJECTORY THROUGH THE PIPE BEND.</u>

$j := 0..N1 \qquad \phi d_j := \dfrac{\phi_j\cdot 360}{2\cdot\pi} \qquad \psi d_j := \dfrac{\psi_j\cdot 360}{2\cdot\pi}$

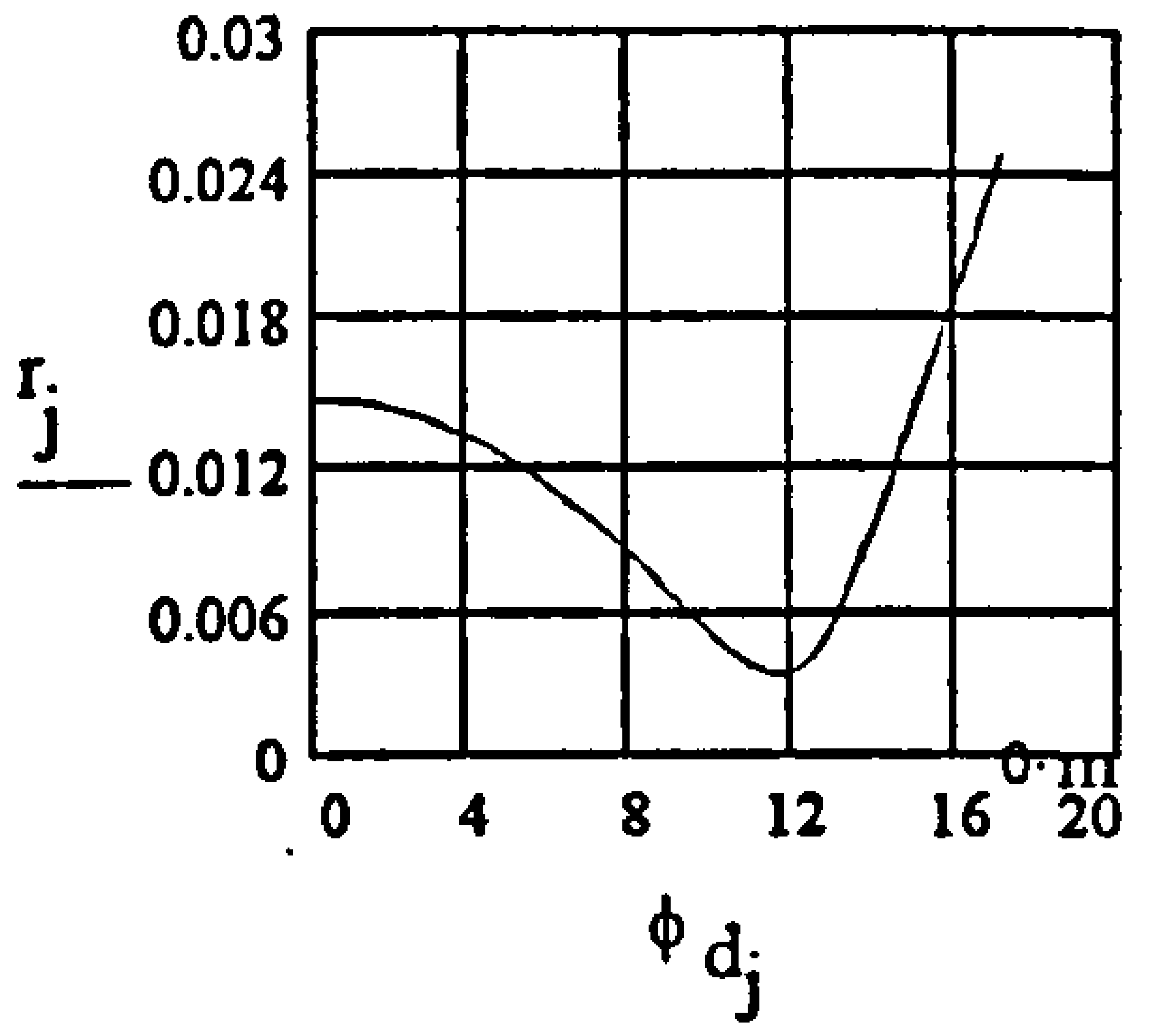

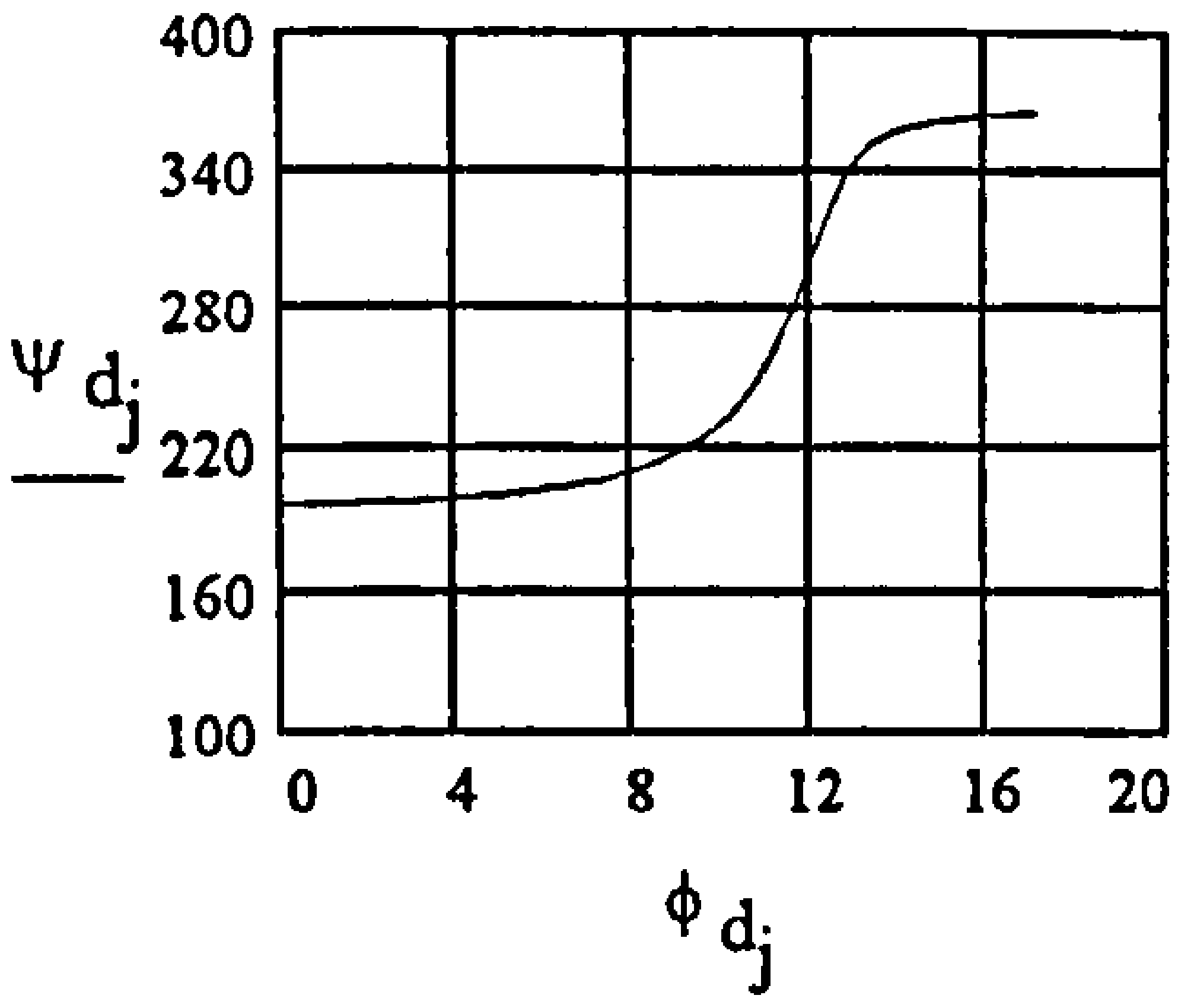

The impact angle and velocity are determined: The normal vector to the pipe wall is determined and the 'DOT' product is taken of this with the velocity vector to produce the angle of impact. The magnitude of the velocity vector is given by resolving the components of the velocity vectors at the point of impact.

$$Q := \begin{bmatrix} u_{N1} \\ v_{N1} \\ w_{N1} \end{bmatrix} \qquad Q = \begin{pmatrix} 9.566742 \\ 0.570761 \\ 23.770631 \end{pmatrix} \cdot m \cdot sec^{-1} \qquad Qr := |Q| \quad Qr = 25.629889 \cdot m \cdot sec^{-1}$$

The variable Qr is used in DDE transfer to QPRO.

The normal vector n was determined using the grad operator from Yeung's work on the coordinates of the parametric surface plot example shown in the MathCad handbook and the MathCad symbolic solver.

$$n := \begin{bmatrix} \cos(\psi_{N1}) \cdot \cos(\phi_{N1}) \\ -\sin(\psi_{N1}) \cdot \sin(\phi_{N1}) \\ 0 \end{bmatrix} \quad n = \begin{pmatrix} 0.952081 \\ -0.024437 \\ 0 \end{pmatrix}$$

The impact angle is then determined as follows:-

$$\alpha_{imp} := \operatorname{asin}\left(\frac{Q \cdot n}{|Q| \cdot |n|}\right) \qquad aimp := \alpha_{imp} \qquad aimp = 21.874251 \cdot deg$$

The variable aimp is used for DDE transfer to QPRO.

5F.2.4 Conclusions and Comments Relating to the Yeung Model

The model discussed above was run ninety-six times, with different start positions each time for the particle at the entrance to the pipe bend. The results of this work are illustrated in the Figures 5F.2 and 5F.3 shown above. This was achieved by using the 'dynamic data exchange' facilities available with the Windows versions of the QuattroPro and MathCad computer software packages. It is interesting to note that the particle velocity did not deviate from the initial air velocity by more that 0.5% for the range of particle sizes and densities measured in this project (see Appendix 3A). Likewise it was found that the particle trajectories could be described as being straight line trajectories, with impact locations of different sized particles with the same start locations being within ±1.5% of each other. Only when olivine sand particles of approximately 40µm diameter were considered, did significant changes in the particle velocity or the position of the primary impact location occur with this model.

A problem that did occur with the modelling of the particle trajectories using Yeung's model was that of numerical instability occurring in the solution of the finite differencing equations. This was due to the fact that the model grid used, effectively had a cell with a volume of zero at the origin of the coordinate system, i.e. at the pipe bore axis. In more advanced programs such as that explained in the next section, the calculation of the finite differencing equations occur based upon a spacial grid pattern that comprises the volume of the flow channel being considered [P3,P4]. One important way of ensuring numerical stability is by ensuring that the elements that form the grid all have volumes greater than zero. These advances have occurred since the paper by Yeung has been published. The method of overcoming this has been to position the origin of the grid system outside the flow channel volume being considered and using a cartesian coordinate system to define the model geometry. Modifying the coordinate system within the Yeung model is possible (with difficulty), but it was felt that it was easier to use pre-written commercial programs that already had these features built into them.

It was quite easy to fit any form of erosion model or data to the end of this programme to give values for penetration rate of the material at the primary impact location. This method was one of the ways in which the erosion models derived from the 'rotating disc accelerator' erosion tester were used to see if a link could be obtained between the results derived from the two test facilities. Modelling of this sort is described in more detail in Chapter 6. However, as argued earlier in this Chapter, penetration occurs at the second impact location rather than the primary location. Consequently, whilst modelling of the wear in the primary impact location would be instructive in assessing the validity of the erosion modelling technique using the Yeung idea as a basis, it cannot be used to determine the life of a pipe bend unless the position of at least the second impact within the bend is modelled.

It would be possible to develop this model further so that the secondary impact details and locations could be found. To do this, a reliable impact model that modelled the rebound trajectory will be required. Values for the coefficient of restitution and dynamic contact friction coefficient in particle / wall contacts would be needed. Values for these variables are not easy to find and consequently, more detailed experimental work would be required for their assessment. However, only in this way could the Yeung model be developed and used to model the actual wear life of a bend in a pneumatic conveyor.

Sato *et al.* have suggested that the effect of hydrodynamic forces acting on the particle have a significant effect on the particle trajectories within the pipe bore [S6]. Most important of these forces is the Magnus force which relies on particle rotation effects. These effects are completely ignored in this model. To account for these effects a substantial gas flow model is required and the whole model tends towards the combined Eulerian / Lagrangian models discussed by Oesterle and Petitjean [O1].

There are more significant problems that limit the usefulness of this model. The model does not account for inter-particulate collisions or changes in the contours of the internal surfaces of the bend with increased amounts of erosion damage, however, this was found to be common to all of the modelling techniques available at the time of writing this thesis.

5F.3 Modelling the Particle Trajectories using the GENTRA Routine of the Commercial PHOENICS CFD Package [P5]

PHOENICS is a well recognised commercial computational fluid dynamics programme. It has a small subset called GENTRA (General Particle Tracking Program) which is capable of modelling the trajectories of particles within the two phase flow situation being considered. The PHOENICS package and sub-programs form the basis of an extremely large and complex program. It is not the intention of the author to explain, in detail, the way in which this program works but to explain the most important areas which relate to this work. Should further information be required readers would be well advised to study the references applicable to this program [R6,M12].

The purposes of using this program were first, to verify the results obtained by using the particle trajectory model proposed by Yeung [Y1] which is described in section 5F.2 of this Appendix, and second, to obtain an indication of the probable particle trajectories that may occur after the particles strike the bend wall for the first time, and from there, to model possible second impact locations.

5F.3.1 Overview of the GENTRA / PHOENICS Model

The GENTRA PHOENICS subset works in conjunction with the main PHOENICS code. This code uses a form of the well known κ-ε turbulence model [S6,Y2] to model the behaviour of the gaseous phase using Eulerian principles which were briefly described in section 5F.1 (where κ is the kinetic energy of turbulent eddies within a calculation cell and ε is the dissipation rate of the energy of the turbulent eddies within the same cell; both these variables are empirically used to model the turbulence of the flow of the gas in the model). The solid particle phase is modelled as discrete items in the gas flow where the particles are allowed to affect the gas as well as permitting the gas to affect the motion of the particles. The GENTRA code can account for momentum and heat and mass transfer between the particles and the gas, however, it does have some limitations. These limitations, as stated by CHAM, the UK suppliers of the PHOENICS software, are as follows...

> 'the effects of particle dispersion by turbulence, the effects of turbulence on interphase transport rates and the effects of the particles on the turbulence itself are not considered. The particles are assumed to interact only with the mean gas motion and therefore, they follow deterministic trajectories. ...' [M12].

Other limitations include the fact that collisions between particles are not considered and that the volume fraction of the solid phase in the mixed two phase flow is assumed to be negligibly small.

5F.3.2 The Mathematical Basis of the GENTRA Particle Tracking Model

The particle motion is modelled in GENTRA by using Newtons second law to balance the motion of the particle to the forces acting upon it. This results in the well known equation for the motion of a particle in a cartesian field. This equation accounts for the effects of particle inertia, drag and gravitational effects.

$$m_p a = F \qquad \text{where} \qquad F = C_D \frac{1}{2} \rho c^2 + m_p g$$

$$\therefore m_p \frac{d\bar{v}}{dt} = C_D \rho (\bar{u} - \bar{v}) |\bar{u} - \bar{v}| \frac{A_d}{2} + m_p g \qquad \textbf{(5F.10)}$$

where m_p is the particle mass; c is the differential velocity between the gas local to the particle and the particle; v is the particle velocity vector; t is the time variable; C_D is the drag coefficient which is further described in equation 5F.11; ρ is the gas density; u is the gas velocity vector; A_d is the profile area of the particle and g is the gravitational force vector. The equation that follows is that for the drag coefficient (this was based upon empirical curve fitting to physical data obtained from experiments carried out by Schiller and Nauman in 1933 [C1,M12]).

$$C_D = \left[\frac{24}{Re}\right] (1 + 0.15 \, Re^{0.687})$$

$$\text{where} \qquad Re = \rho \frac{|\bar{u} - \bar{v}| \, d}{\mu} \qquad \textbf{(5F.11)}$$

where d is the particle diameter; μ is the viscosity of the gas and Re is the Reynolds number for the particle based upon the velocity between the gas surrounding the particle and the particle itself. This equation was solved for v, the new particle velocity [M12], as...

$$v = u - (u - v_o) \exp\left[\frac{-\Delta t}{\tau}\right] - g \tau \left[1 - \exp\left[\frac{-\Delta t}{\tau}\right]\right]$$

$$\text{where} \qquad \tau = \frac{\rho_p d^2}{18 \mu f}$$

(5F.12)

where τ is the mean time taken for a particle to respond to changes in the direction of the flow of the gas; ρ_p is the particle density; v_o is the initial velocity and $f = C_D Re/24$.

The way in which the particle effects on the gas are accounted for is by using the principle of what is known as a momentum sink. These are basically calculations of the amount of momentum loss suffered by the gas in dragging the particles through each calculation cell volume. The calculation of the momentum sink accounts for the possibility of multiple particle trajectories passing through the cell provided that the conditions regarding particle space volume and number volume are adhered to.

5F.3.3 Results Obtained for the GENTRA / PHOENICS Analysis [P5]

Results of the analysis using the expressions given above are given in the following figures; Figure 5F.4 and Figure 5F.5 illustrate the positions of the primary and secondary impact locations respectively. As can be seen from these illustrations, the scar formed by the secondary impact site is focused to the plane containing the pipe bore axis more than that seen for the primary impact location. However, the secondary impact locations are more widely distributed around the bend radius. Evidence that the GENTRA model has predicted particles crossing across the plane of the bore axis can be seen. The plane of the bore axis is expected to be a region of frequent interparticulate collisions, however, due to the spread of the secondary impact locations around the bend the intensity of these collisions can only be surmised from these results. Without the capability of modelling interparticulate collisions the modelling of the particle behaviour in the region of secondary impacts using GENTRA cannot be made any more accurate than is shown. It was found that the particle velocity prior to primary impact did not deviate much from the initial gas velocity used in these models, or indeed of the local gas velocity calculated following measurement of the local gas pressure in the conveying line in the experimental work. This result is the same as that found from using the Yeung trajectory model.

5F.3.4. Conclusions and Comments on the GENTRA / PHOENICS Model

It can be seen from the above equations that the hydrodynamic force that pertains to the rotation of the particle, i.e. the Magnus force, and the force caused by fluid shear in the region of the particle, i.e. the Saffman force, as well as any basic lift forces are neglected when the unmodified GENTRA code is used. A more complete equation of motion can be seen in the work by Sato *et al.* [S6] which includes these missing terms. However, it is concluded in Sato's work that it is not just the absence of these terms which cause serious inaccuracies in the predictive capabilities of models of this sort. When modelling erosion where accurate estimates of the number and location of impacts are required, it is probable that an irregular rebound model similar to that proposed by Tsuji *et al.* [T5] will be essential in improving the accuracy of the modelling process. Only when the irregular shape of the particles and their rotation is considered will it be possible to accurately model the number of particle impacts, their positions and frequency of collision. Once these factors are accounted for in a model, it will then be possible to predict the magnitude of the erosion damage suffered by the pipe wall and give results that compare more favourably to those achieved in experiments. Since the GENTRA code omits the rotational and fluid shear effects and possibilities of having irregularly shaped

Figure 5F.4 The primary impact locations as found using PHOENICS [P5].

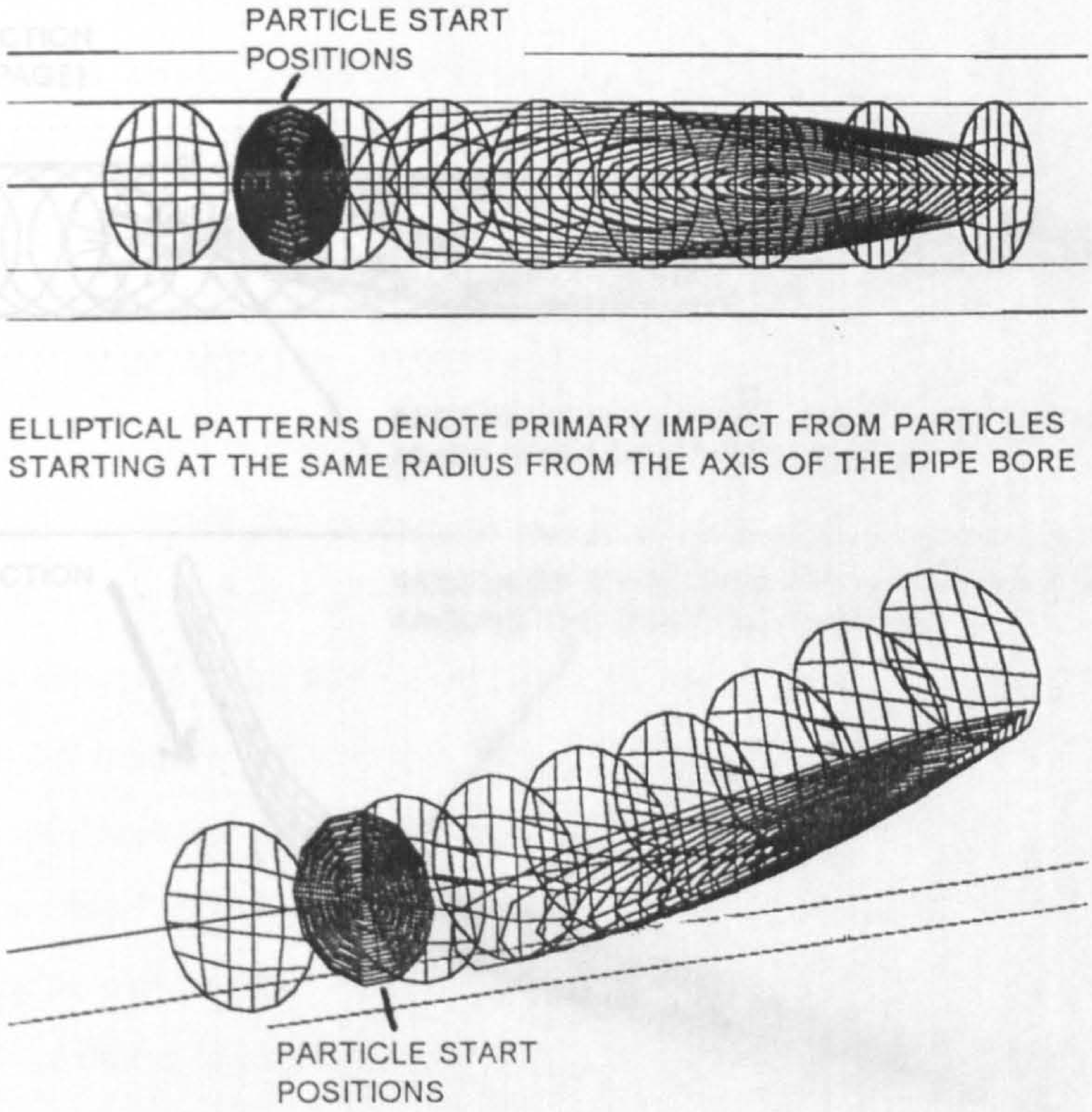

ELLIPTICAL PATTERNS DENOTE PRIMARY IMPACT FROM PARTICLES STARTING AT THE SAME RADIUS FROM THE AXIS OF THE PIPE BORE

Figure 5F.5 The secondary impact locations as found by using PHOENICS [P5].

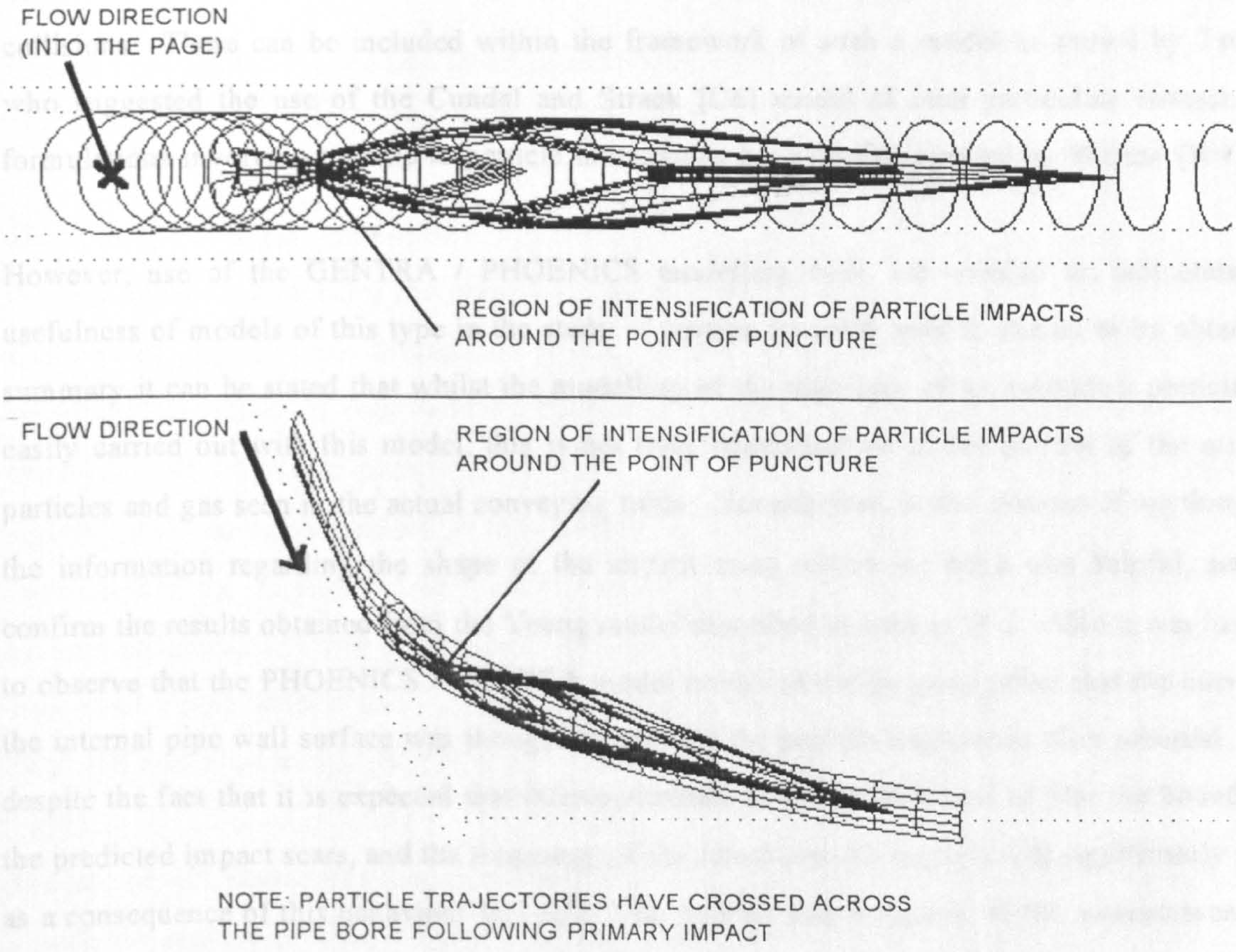

particles, accurate modelling of erosion behaviour in such two phase flows is unlikely. Considerable modification of the GENTRA code would be required to account for these terms and work to do this was felt to be beyond the scope of this project.

As stated above the GENTRA code has no means of assessing the effects of inter-particulate collisions. These can be included within the framework of such a model as shown by Tsuji [T6], who suggested the use of the Cundal and Strack [C6] model of inter-particulate contact. Other formulations involving particle to particle interactions have been suggested by Walton [W4].

However, use of the GENTRA / PHOENICS modelling code has enabled an indication of the usefulness of models of this type in the study of erosion by solid particle impact to be obtained. In summary it can be stated that whilst the modelling of the trajectory of an individual particle can be easily carried out with this model, this is not truly representative of the motion of the mixture of particles and gas seen in the actual conveying trials. Nevertheless, in the absence of anything better, the information regarding the shape of the impact scars within the bend was helpful, serving to confirm the results obtained from the Yeung model described in section 5F.2. Also it was instructive to observe that the PHOENICS / GENTRA model predicted the focusing effect that the curvature of the internal pipe wall surface was thought to have on the particle trajectories after rebound. This is despite the fact that it is expected that inter-particulate collisions will tend to blur the boundaries of the predicted impact scars, and the frequency of the actual particle impacts will significantly increase as a consequence of this behaviour [A2,A5]. The number and frequency of the measurements taken for the pipe wall thickness were not accurate enough or large enough in number to give a definite indication of whether the PHOENICS model had given a reasonable indication of the shape of the wear scars or not in either quantitative or qualitative terms. Certainly, as erosion damage of the internal pipe wall surfaces increase, the trajectories of the particles after rebound will change significantly, and therefore the expected successive particle impact locations will change greatly. Since the PHOENICS code cannot at present model changing boundaries, the change in the focus caused by the erosion damage of the pipe wall surfaces cannot be investigated using this programme. Improving the PHOENICS code to account for this is also beyond the scope of this project.

5F.4 Conclusions and Discussion Regarding the Particle Trajectory Modelling

The particle trajectory modelling that has been carried out has assisted in the construction of the descriptive model described in Chapter 5 section 5.3.4.

Results obtained for the position of the primary impacts in the test bend predicted by both the Yeung model [Y1] and the PHOENICS modelling are in close agreement.

The Yeung model and the use of PHOENICS are attempts to obtain detailed information regarding the individual trajectories of the particles in the pipe bore. However, in most pneumatic conveying applications the particle concentrations are quite high and interparticulate collisions become significant, especially in regions where erosion is prevalent. In this case the use of these modelling techniques are limited in accuracy. Unless a model which deals with interparticulate collisions is incorporated into the framework of these programs, this will remain the case. It was also noted that the change in the internal surface profiles also has an effect on the erosion of the pipe wall surfaces as time progresses. These effects have not been accounted for in any model of the solid particle erosion of a pipe bend to date. If significant improvements in bend erosion modelling are to occur they will also need to be considered.

The use of the Yeung model is discussed further in Chapter 6 where attempts are described to use it with the erosion models derived from tests carried out on the 'rotating disc accelerator' erosion tester to predict the puncture of the test bend.

Appendix 5G: Predicting the Bend Puncture Location Using an Optical Analogy

5G.1 Introduction to the Curve of Aberration Puncture Location Model

This appendix briefly describes the way in which the curve of aberration for a cylindrical mirror can be used to predict, empirically, the location of the puncture point in a radiused bend. The model that has been derived to do this contains two major parts. First, the curve of aberration for a cylindrical mirror is derived. Secondly, the apex of this curve is used in a linear trajectory model (similar to that of a ray trace) to locate the puncture point.

5G.2 Brief Description of the Way in Which the Geometry of the Curve of Aberration for a Cylindrical Mirror is Derived

It is the geometry of the internal surface of the pipe bore, that is, in this case, taken to be the shape of a cylindrical mirror, that determines the shape of the curve of aberration. The method of generating this curve involves predicting the angle of reflection of a series of parallel straight lines that are projected against the concave surface. Where a reflected line crosses the path of its neighbouring reflected line this location marks a point on the curve of aberration. This process is repeated for a series of parallel lines (see Figure 5G.1). The position of the apex of the curve of aberration on the plane containing the centre line of the bore is noted.

5G.3 Prediction of the Puncture Location in a Radiused Bend

The apex of the curve of aberration is a key geometric property of the pipe bore geometry. Ray tracing techniques are used to find the position of the first impact in the bend geometry of a particle having a starting location extreme intrados of the pipe bore at the entrance to the bend. Construction of the normal where this first ray intercepts the bend extrados is carried out. The distance of the apex of the curve of aberration from the bend wall is used to find a start position for a second ray (see Figure 5G.2). Intercept of the second ray with the bend extrados is compared with the experimentally derived puncture point obtained from the pneumatic conveying test work.

Figure 5G.1 Geometry and construction of the curve of aberration for a cylindrical mirror in the pipe bore.

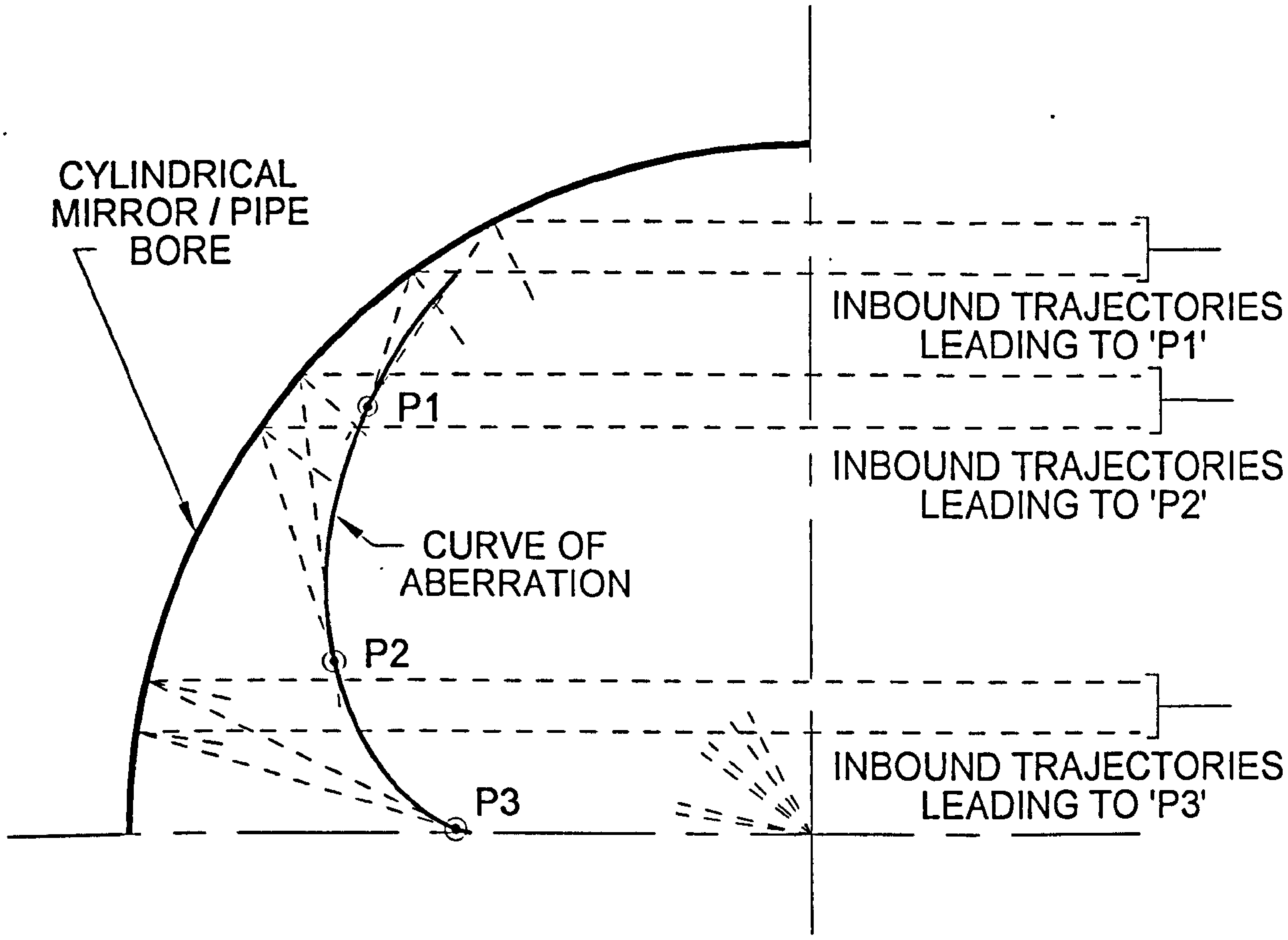

Figure 5G.2 Particle trajectory / ray trace used to predict the puncture location in the pipe bend.

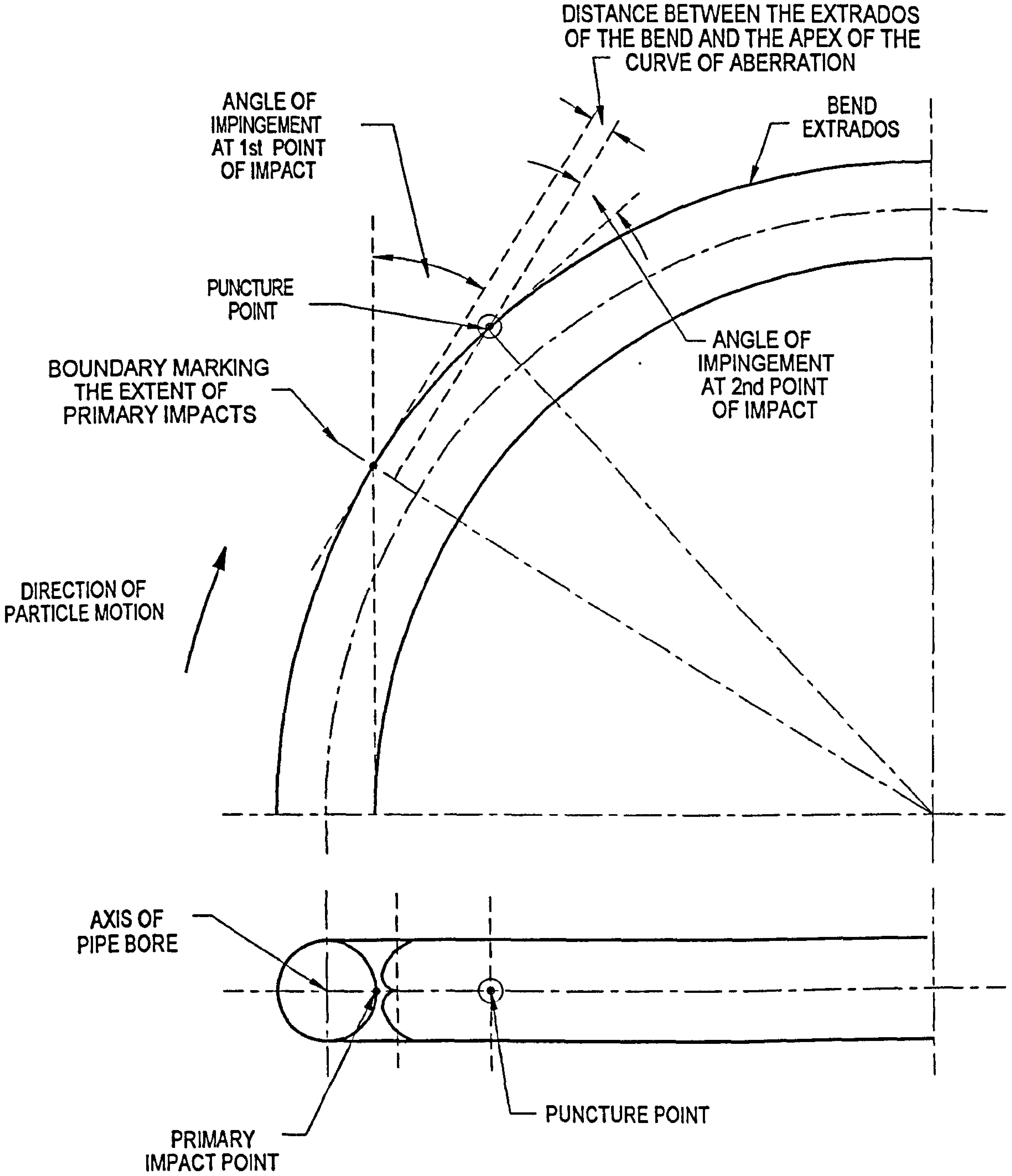

5G.4 Conclusions

Further details regarding the use of this model for predicting the puncture location in the test bend are given in Chapter 5 section 5.4.4.

5G.5 MathCad Programme Describing the Curve of Aberration Trajectory Model

The four pages at the end of this appendix contain a complete listing of the MathCad document used for programming this model.

Modelling of the Curve of Aberration for a Cylindrical Mirror

This model consists of a two parts; a) the construction of the curve of aberration for a cylindrical mirror and b) derivation of an expression that relates the apex of this curve to the location of the mean second impact position of the particles against the pipe wall. The curve of aberration is constructed using ray tracing principles. Intercepts between neighbouring rebound traces from the concave surface are used to define points on the curve of aberration. Similar ray tracing operations are used to find the mean second impact location of a particle trajectory.

Specification of the Input Variables:

Pipe bore radius:- $R := 26.5$ (Working in millimeters).

X incremental distance specification:- $\delta := \frac{R}{40}$ $i := 1, 2 .. 39$

Calculation of the Interception Points Between the Vertical Planes and The Circle:

$y_i = \sqrt{R^2 - (\delta \cdot i)^2}$ y is the value of the vertical distance of the intercept above the axis of the origin.

Calculation of the Equation of the Tangent and Normal to the Circle at these Points:

$\sqrt{R^2 - x^2}$ by differentiation, yields $\frac{-1}{\sqrt{R^2 - x^2}} \cdot x$ this differential enables the slope of the tangent to be assessed.

Substitution of the values of x & R to find the slope of the tangent.

$$m_{tan_i} = \frac{-1}{\sqrt{R^2 - (i \cdot \delta)^2}} \cdot (i \cdot \delta)$$

The slope of the normal is the reciprocal of the slope of the tangent.

$$m_{norm_i} = \frac{-1}{m_{tan_i}}$$

The equation of the slopes of the tangent and normal to the circle at the selected points are now defined. The intercepts with the y axis for the tangent is the only term that is now required since the intercept of any normal to a tangent of a circle will pass throught the centre of the circle.

$$int_{tan_i} := -m_{tan_i} \cdot i \cdot \delta + y_i$$

Calculation of the Angle θ i.e. the Angle Between the Normal and Vertical Line

$\theta_i = \operatorname{atan}\left(\frac{i \cdot \delta}{y_i}\right)$ The angle of the rebound trajectory from the vertical inbound line is twice this angle.

Calculation of the Position Where the Rebound Trajectory Crosses the X-axis.

$$x_{ab_i} = \left| y_i \cdot \tan(2 \cdot \theta_i) \right|$$

Calculation of the Position of the Intercept of the Y-axis and the Rebound Trajectory

$$\mathrm{ytraj}_{\mathrm{int}_i} := \mathrm{if}\left[2\cdot\theta_i<\frac{\pi}{2},\frac{x_{\mathrm{ab}_i}-i\cdot\delta}{\left|\tan\left(2\cdot\theta_i\right)\right|},\left(i\cdot\delta+x_{\mathrm{ab}_i}\right)\cdot\tan\left(2\cdot\theta_i-\frac{\pi}{2}\right)\right]$$

The Slope of the Rebound Trajectrory is Calculated as follows:-

$$\mathrm{mtraj}_i := \mathrm{if}\left(2\cdot\theta_i<\frac{\pi}{2},\frac{y_i}{x_{\mathrm{ab}_i}},\frac{\mathrm{ytraj}_{\mathrm{int}_i}}{i\cdot\delta+x_{\mathrm{ab}_i}}\cdot -1\right)$$

To find the Intercept Between Neighbouring Rebound Trajectories

These points will lie on the curve of aberration for the cylindrical mirror being considered.

$j := 2,3..39$

$$X_{\mathrm{cacm}_j} := \frac{\mathrm{ytraj}_{\mathrm{int}_j}-\mathrm{ytraj}_{\mathrm{int}_{j-1}}}{\mathrm{mtraj}_{j-1}-\mathrm{mtraj}_j} \qquad Y_{\mathrm{cacm}_j} := \mathrm{mtraj}_j\cdot X_{\mathrm{cacm}_j}+\mathrm{ytraj}_{\mathrm{int}_j} \qquad \mathrm{xx} := 0,0.5..26.5$$

Fitting a Cubic Spine curve (with cubic ends) to the points found for the Caustic Curve:-

The most important figure that is required is the intercept on the y axis for the caustic curve.
This can be found by either using the cubic spline curve fitting routines or the multiple curve fit routines.
The cubic spline method will be used here.

Cubic Spline Fit:-

$k := 1,2..38$ $\qquad X_c := \mathrm{submatrix}\left(X_{\mathrm{cacm}},2,39,1,1\right)$ $\qquad Y_c := \mathrm{submatrix}\left(Y_{\mathrm{cacm}},2,39,1,1\right)$

$\mathrm{vs1} := \mathrm{cspline}\left(X_c,Y_c\right)$ $\qquad \mathrm{xx} := 0,0.25..26.5$

$Y_{\mathrm{int}} := \mathrm{interp}\left(\mathrm{vs1},X_c,Y_c,0\right)$ $\qquad Y_{\mathrm{int}} = 13.264$

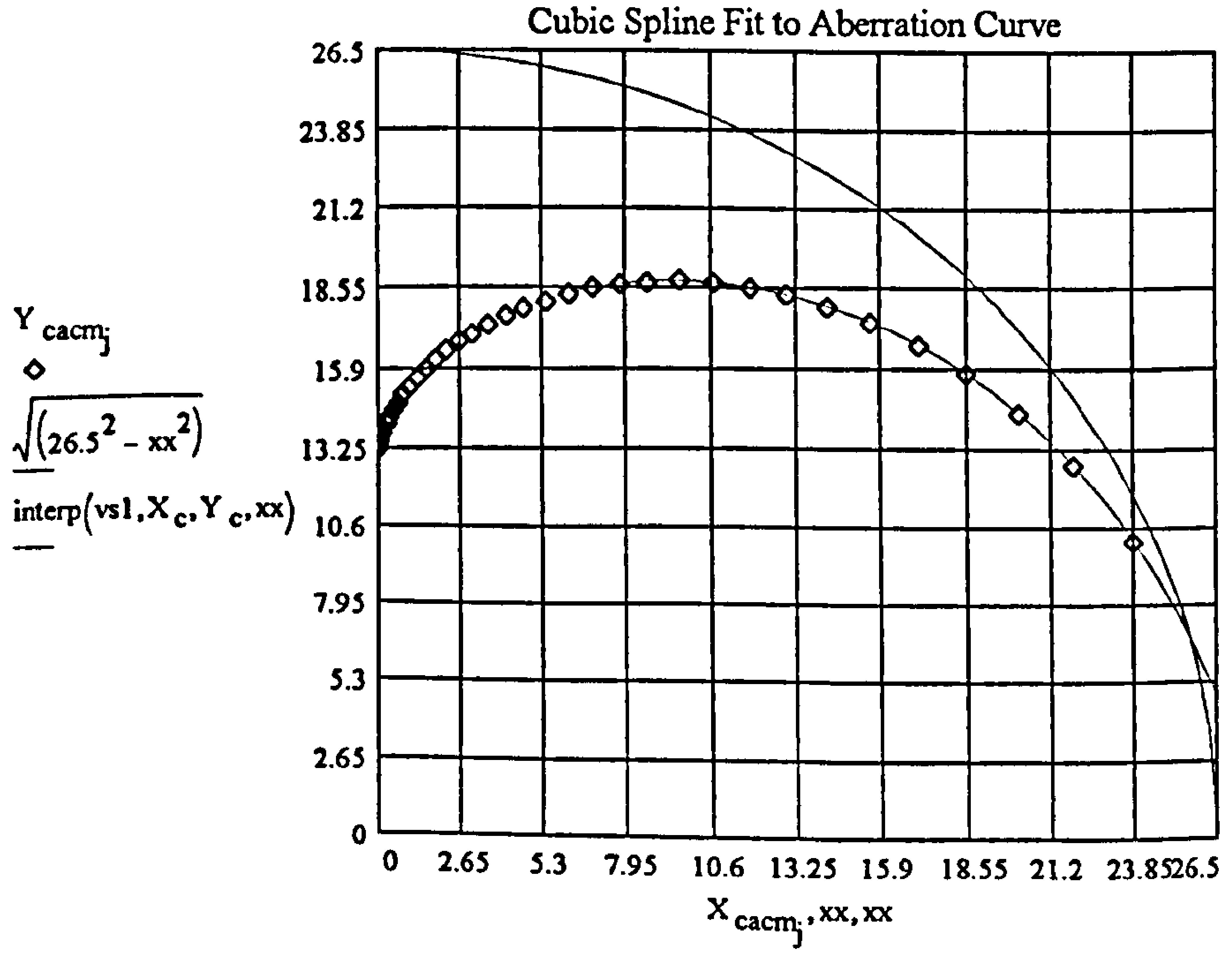

The apex of the cubic spline and the y axis occurs at:- $y_{st} := Y_{int}$

This is the value of the suggested start position for the trajectory that will be used to find the location of the puncture point in the bend.

Using the Apex of the Curve of Aberration to Determine the Position of the Puncture Point in the Region of Secondary Impacts.

Selection of In Bore Start Position: $y_{st} = 13.264$

$y_{v} := 723.5$

Calculation of the Primary Impact Location Based on the Particle Start Position Being Positioned at the Bend Intrados:-

$x_{pl} := \sqrt{776.5^2 - y_v^{\,2}}$ $\quad x_{pl} = 281.957$ $\quad PI_{pt} := \mathrm{acos}\left(\frac{y_v}{776.5}\right)$ $\quad PI_{pt} = 21.292 \cdot \mathrm{deg}$

Calculation of the Particle Trajectory After Primary Impact:-

$\sqrt{R^2 - x^2}$ by differentiation, yields $\frac{-1}{\sqrt{R^2 - x^2}} \cdot x$ This differential enables the slope of the tangent to be assessed.

$\mathrm{stan}_{pl} = \frac{-1}{\sqrt{776.5^2 - x_{pl}^{\,2}}} \cdot x_{pl}$ $\quad \mathrm{stan}_{pl} = -0.389713$ The slope and intercept of the tangent along with the impact angle on the pipe wall are calculated here.

$\mathrm{inttan}_{pl} := y_v - \mathrm{stan}_{pl} \cdot x_{pl}$ $\quad \mathrm{inttan}_{pl} = 833.383$

$\phi 1 = \mathrm{atan}\left(\frac{\mathrm{inttan}_{pl} - y_v}{x_{pl}}\right)$ $\quad \phi 1 = 21.292 \cdot \mathrm{deg}$

Calculation of the Equation Governing the Particle Trajectory After Primary Impact:-

$x_{new} := (776.5 - y_{st}) \cdot \cos\left(\frac{\pi}{2} - \phi 1\right)$ $\quad x_{new} = 277.141$

$y_{new} := (776.5 - y_{st}) \cdot \sin\left(\frac{\pi}{2} - \phi 1\right)$ $\quad y_{new} = 711.141$

$\mathrm{stan2} := \frac{x_{new} \cdot -1}{y_{new}}$ $\quad \mathrm{stan2} = -0.38971$

$\mathrm{inttan}_{p2} := \tan(\phi 1) \cdot x_{new} + y_{new}$ $\quad \mathrm{inttan}_{p2} = 819.147$

Finding the Intercept Between the Second Trajectory Line and the Outer Radius of the Circle in Cartesian Location Coordinates

$y_{p2} = \mathrm{stan2} \cdot x_{p2} + \mathrm{inttan}_{p2}$

$x_{p2}^{\,2} + y_{p2}^{\,2} = 776.5^2$ The solution of these two equations that gives the greatest value of x is used as shown below:

by substitution, yields

$x_{p2}^{\,2} + \left(\mathrm{stan2} \cdot x_{p2} + \mathrm{inttan}_{p2}\right)^2 = 602952.25$

has solutions:-

$$\begin{bmatrix} \frac{.5}{\left(1.+stan2^2\right)}\cdot\left[-2.\cdot stan2\cdot inttan_{p2}+\sqrt{\left(-4.\cdot inttan_{p2}^2\right)+2411809.+2411809.\cdot stan2^2}\right] \\ \frac{.5}{\left(1.+stan2^2\right)}\cdot\left(-2.\cdot stan2\cdot inttan_{p2}-1.\cdot\sqrt{-4.\cdot inttan_{p2}^2+2411809.+2411809.\cdot stan2^2}\right) \end{bmatrix}=\begin{pmatrix}410.297\\143.985\end{pmatrix}$$

$$x_{p2}:=\frac{.5}{\left(1.+stan2^2\right)}\cdot\left[-2.\cdot stan2\cdot inttan_{p2}+\sqrt{\left(-4.\cdot inttan_{p2}^2\right)+2411809.+2411809.\cdot stan2^2}\right]$$

$x_{p2}=410.297$

$y_{p2}:=\sqrt{776.5^2-x_{p2}^2}$ $\quad y_{p2}=659.249$

Comparison Between the Actual and Predicted Puncture Locations in Cartesian Coordinates:-

Experimental Impact Location		Predicted Impact Location
$x_{pun}:=776.5\cdot\sin\left(\frac{28.5\cdot\pi}{180}\right)$	$x_{pun}=370.514$	$x_{p2}=410.297$
$y_{pun}:=776.5\cdot\cos\left(\frac{28.5\cdot\pi}{180}\right)$	$y_{pun}=682.401$	$y_{p2}=659.249$
Puncture occurred 28.5° around the bend radius.		$Pun_{pt}:=\mathrm{acos}\left(\frac{y_{p2}}{776.5}\right)$
		$Pun_{pt}=31.897\cdot deg$

Calculation of the Angle of Impact at the Secondary Impact Location

$stan_{p3}:=\frac{-1}{\sqrt{776.5^2-x_{p2}^2}}\cdot x_{p2}$ $\quad stan_{p3}=-0.62237$

The slope and intercept of the tangent along with the impact angle on the pipe wall are calculated here.

$inttan_{p3}:=y_{p2}-stan_{p3}\cdot x_{p2}$ $\quad inttan_{p3}=914.605$

$\phi 2:=\mathrm{atan}\left(\frac{inttan_{p3}-y_{p2}}{x_{p2}}\right)-\phi 1$ $\quad \phi 2=10.605\cdot deg$

$xx:=0,10..780$

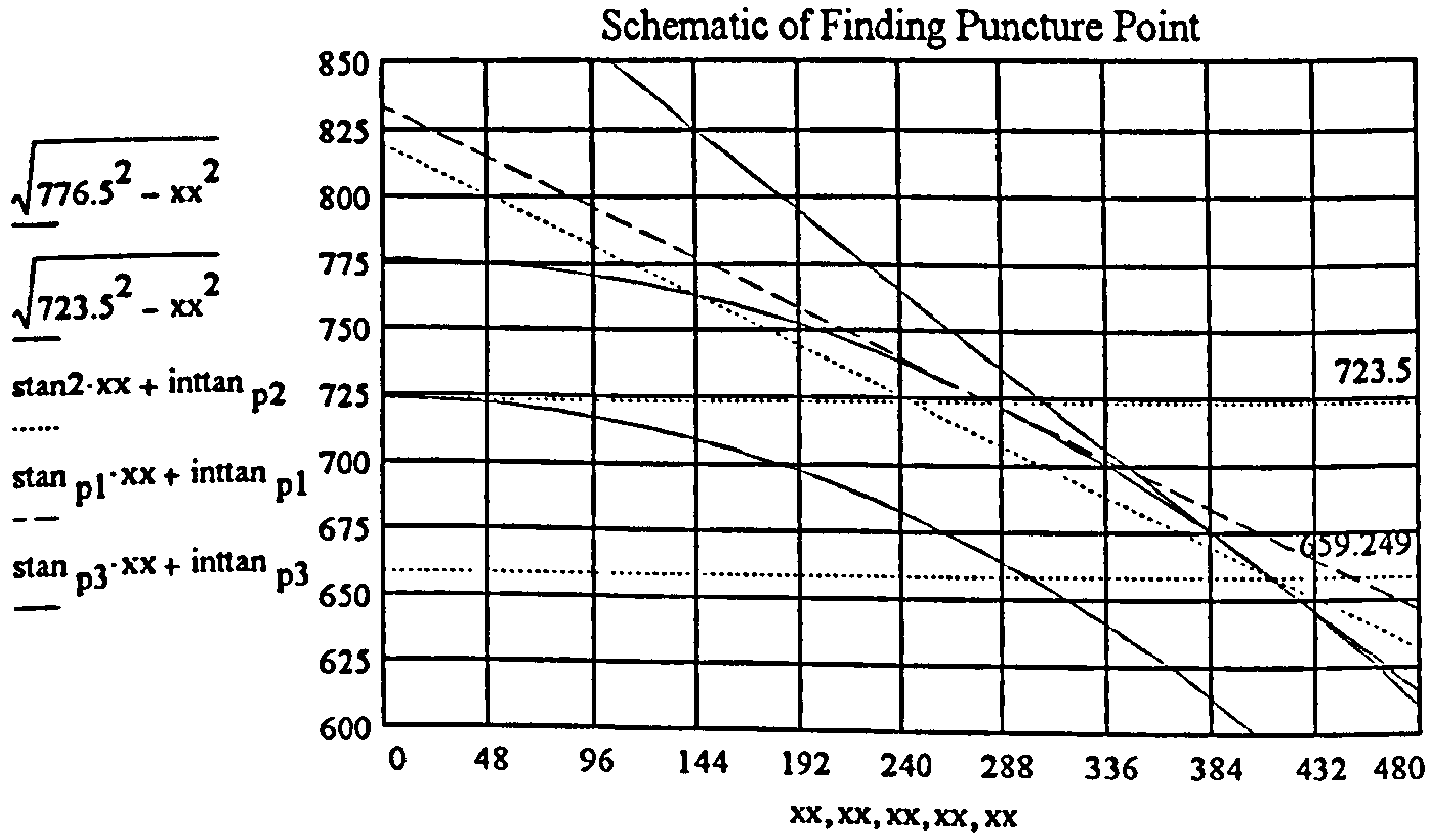

Appendix 6A: The Bikbaev Model [B8] for Predicting Wear in Pneumatic Conveyor Bends

6A.1 Introduction to Bikbaev Model

The model for the erosive wear and penetration of radiused pneumatic conveyor bends proposed by Bikbaev *et al.* [B8] was derived as a consequence of carrying out a large number of tests on a pneumatic conveyor test facility. Bikbaev *et al.* used bends of 50 mm bore with several radii up to 360 mm. The particle velocity used in the tests carried out by these works was 22.3 m/s and several particle concentrations up to a maximum of 2.33 kg of abrasive material / kg of air were used. Test bends were made from mild steel and the abrasive was a quartz sand of 295μm mean particle diameter and a particle density of 2600 kg/m^3.

Results obtained from these tests enabled Bikbaev to fit empirical models for the wear rate (expressed in terms of mm/hr) as a function of particle concentration, the wear rate at any point on the surface of the radiused bend in mm/hr, and finally the position of maximum wear. The expressions so obtained were based on the geometry of the bend, the conveying velocity and the particle concentration.

The expression for the wear rate in terms of the particle concentration is as follows:-

$$I_G = \frac{0.45}{\left(R_{av} + \frac{d}{2} \right)^{0.35}} e^{0.36\,\mu} \qquad \text{(6A.1)}$$

where R_{av} is the bend radius in millimetres; d is the pipe bore diameter in millimetres; μ is the particle concentration in terms of mass of abrasive conveyed divided by the mass of air moving it, and I_G is the wear rate in mm/hr.

The expression derived for the prediction of the wear rate at any point on the surface of the radiused bend is as shown on the following page:-

$$I = V_M^n \, l^b \, e^{0.36\,\mu - cl} \, \frac{0.011}{\left(R_{av} + \frac{d}{2} \right)^{0.72}}$$

where

$$n = \frac{3.1}{\left(R_{av} + \frac{d}{2} \right)^{0.15}} \qquad l = 0.017 \left(R_{av} + \frac{d}{2} \right) \alpha \qquad \textbf{(6A.2)}$$

$$b = \frac{3.32}{\left(R_{av} + \frac{d}{2} \right)^{0.096}} \qquad c = \frac{16.87}{\left(R_{av} + \frac{d}{2} \right)^{0.46}}$$

where V_M is the particle velocity in m/s; α is the angle around the bend radius; n, l, b and c are empirical constants as defined above, and I is the wear rate at any point around the bend radius. All of the other terms have been defined for the previous expression.

Finally, the expression for the prediction of the point of maximum wear around the bend radius is:-

$$\alpha_m = \frac{67.4}{\left(\frac{R_{av}}{d} \right)^{0.57}} \qquad \textbf{(6A.3)}$$

where α_m is the angle around the bend radius at which maximum wear occurs and all of the variables in this expression have been defined for the previous expressions.

6A.2 Listing of a MathCad Programme for the Bikbaev Model

The following page contains the listing of a MathCad programme which uses the aforementioned expressions to determine the wear rate as a function of particle concentration, the variation of the wear rate around the bend radius and the position of around the bend radius at which maximum wear occurs.

MathCad Listing for the Bikbaev Model [B8].

Input Variables:-

$R_{av} := 0.75$ $d := 0.053$ $V_M := 25.6$ $\mu := 3.048$ $i := 0,1..18$ $\alpha_i := i \cdot 5$

Calculation of the Empirical Constants:-

$$n := \frac{3.1}{\left(R_{av} + \frac{d}{2}\right)^{0.15}} \qquad n = 3.22 \qquad l_i := 0.017 \cdot \left(R_{av} + \frac{d}{2}\right) \cdot \alpha_i$$

$$b := \frac{3.32}{\left(R_{av} + \frac{d}{2}\right)^{0.096}} \qquad b = 3.402 \qquad c := \frac{16.87}{\left(R_{av} + \frac{d}{2}\right)^{0.46}} \qquad c = 18.952$$

Wear Rate mm/hr as a Function of Distance Around Bend Radius Travelled:-

$$I_i := V_M^{\,n} \cdot \left(l_i\right)^b \cdot e^{\left(0.36 \cdot \mu - c \cdot l_i\right)} \cdot \frac{0.011}{\left(R_{av} + \frac{d}{2}\right)^{0.72}} \qquad vs := \mathrm{lspline}(\alpha, I) \qquad \alpha x := 0,1..90$$

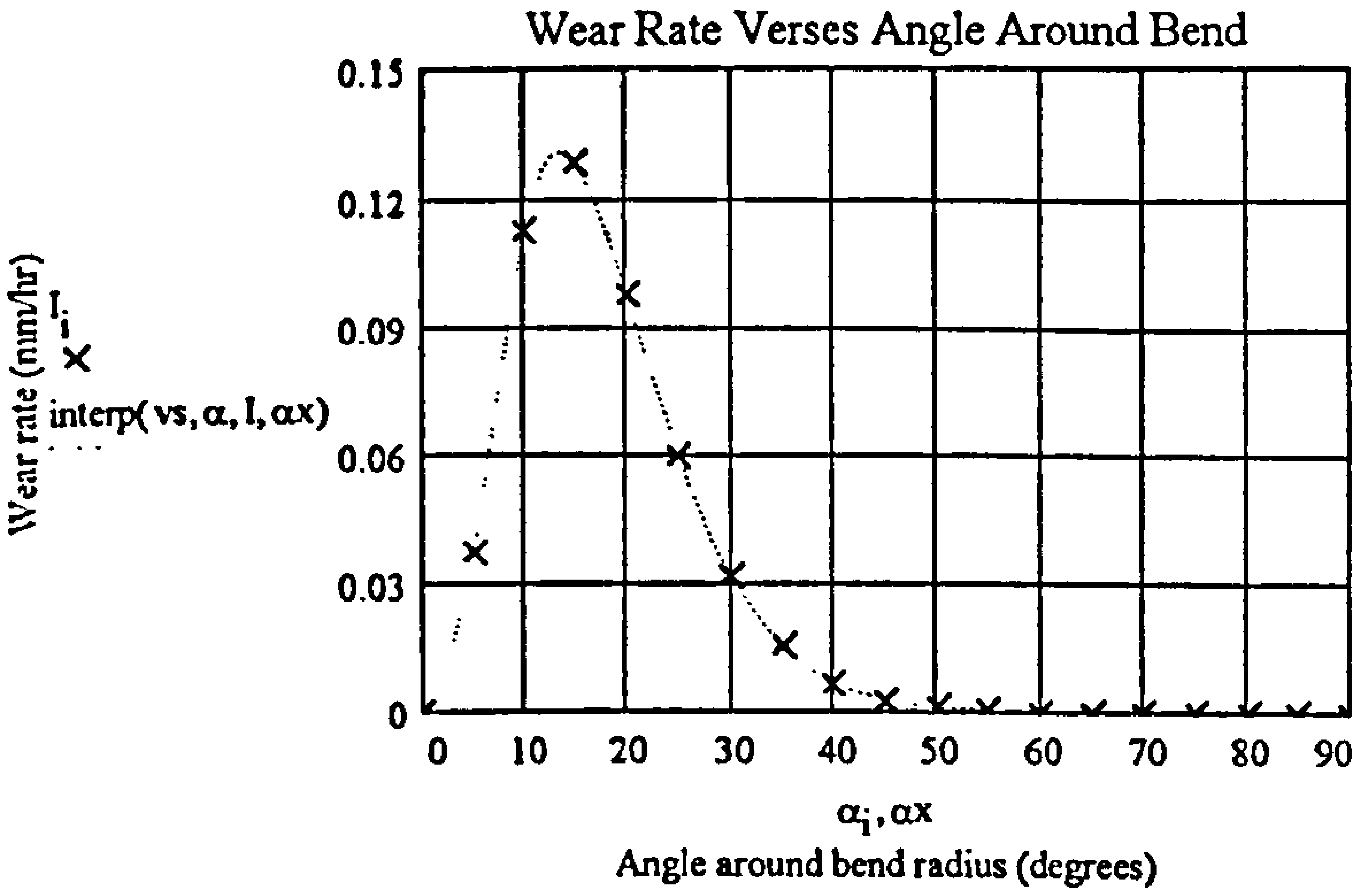

Angle at which Maximum Erosion Rate Occurs:-

$$\alpha_1 := \frac{67.4}{\left(\frac{R_{av}}{d}\right)^{0.57}} \qquad \alpha_1 = 14.884 \quad \text{degrees}$$

Wear Rate as a Function of Particle Concentration:-

$$I_G := \frac{0.45}{\left(R_{av} + \frac{d}{2}\right)^{0.35}} \cdot e^{0.36 \cdot \mu} \qquad I_G = 1.473 \quad \text{mm/hr}$$

6A.3 Results Obtained from the Bikbaev Model

When the actual wear rate of the bend wall (see Chapter 5 section 5.3.2 and Appendix 5D) is compared with the results obtained from the use of the expressions derived by Bikbaev *et al.* [B8], the expressions of Bikbaev are found to overestimate the mean wear rate by 3.55 times. Also the model predicts puncture to occur in the region of primary impact. In tests puncture occurred in the region of secondary impacts (see Chapter 5 section 5.3).

It is believed that the effects of three main areas of fundamental difference between the tests carried out by Bikbaev *et al.* [B8] and those described in Chapter 5 are the cause of these discrepancies. The first major difference is that the expressions of Bikbaev *et al.* were derived from results obtained from wear observed in bends whose maximum radius of curvature was 360 mm; approximately half that of the bends used in this test work. There was also a difference in the properties of the materials used in the tests carried out by Bikbaev; the material being conveyed was different from that used during this project, and there was also a possibility that the type of mild steel used was different from that used in this work. Finally, the concentrations of particles used in the tests carried out for this project were greater than those used by Bikbaev *et al.* These three facts could combine to give the differences stated above.

Appendix 6B: The Combined Yeung Trajectory and Erosion Model for Predicting Penetration in the Region of Primary Particle Impact

6B.1 Introduction to Model for Predicting Wall Penetration in the Primary Impact Location

The model described in this appendix consists of the combination of the Finnie / Bitter erosion model [S6] described in Appendix 4G, the power law erosion model described in Chapter 4 section 4.3.4, (both of these models were fitted to the results obtained from the rotating disc accelerator erosion tester), and the Yeung particle trajectory model [Y1] which has been discussed in detail in Appendix 5F. No repeat of the details regarding the derivation of each of these models will be given in this Appendix.

This combined model was used for ninety six different start positions of the particles within the pipe bore (see Figure 6B.1). Results for the erosive penetration at the point of impact for each of these start positions were generated from a MathCad coded programme which used both the Finnie / Bitter erosion model and the power law erosion model. The time required to use the combined model coded in MathCad in an iterative manner was considerably reduced by using the 'dynamic data exchange' facility contained within MathCad to read data input values from, and write values for results back to, a Quattro Pro spreadsheet.

6B.2 Comments Regarding the Trajectory Model Proposed by Yeung [Y1]

This model is based upon the Yeung trajectory model [Y1] which is discussed in detail in Appendix 5F. To reiterate, the input required by this model consists of values for the particle velocity (taken to be the superficial air velocity in this work), the start position of the particle within the pipe bore and details of the particle size and density.

As discussed in section 5.3.3 of Chapter 5, because the particle concentration distribution is skewed in the pipe bore the values of the superficial air velocity within the pipe bore will also be skewed. Owing to a lack of the necessary equipment, the distribution of the superficial air velocity in the pipe bore was estimated by using the particle concentration density profile obtained from the laser

Figure 6B.1 Positions selected for the start of the particle trajectories in the Yeung model.

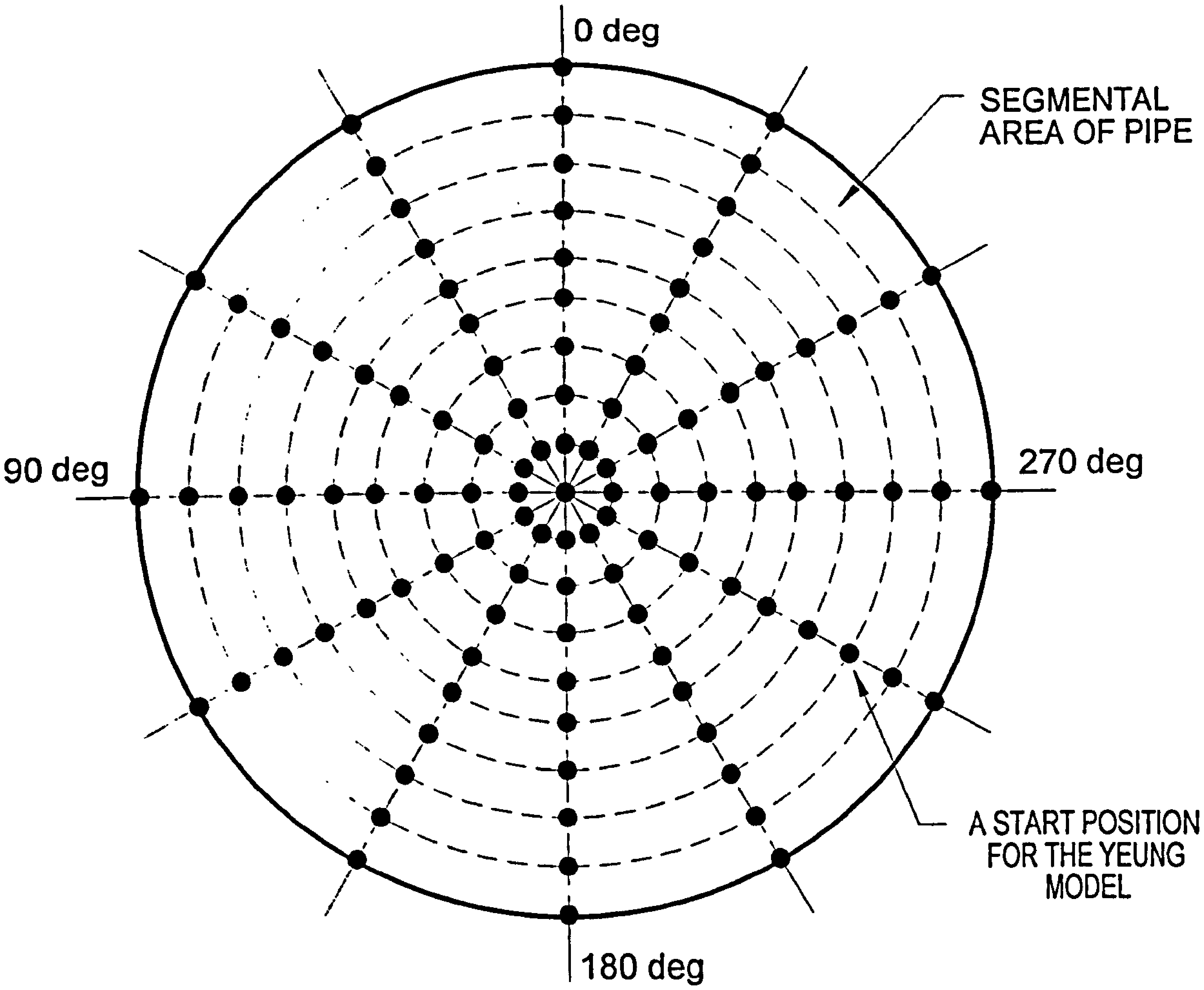

obscuration work. The method by which this was achieved is discussed in detail in Appendix 5E. For each start location of the particle trajectories used in the Yeung model, a value of the superficial air velocity was extracted from the distribution generated following manipulation of the data resulting from the particle concentration density distribution assessment. Each of these values for the superficial air velocity was taken to be the particle velocity for input into the Yeung model.

6B.3 Comments Relating the Erosion Models that were Used

The particle trajectory model based upon the work carried out by Yeung [Y1] was used to provide input information for the erosion models used in the combined model. Values for the location of the particle impact against the pipe wall, the impact velocity and the angle of particle impingement were derived from the trajectory model. However, yet more input data was required by the erosion models. This included values for the particle concentration at the entrance to the test bend. Values of the local particle concentration density for each of the selected particle start locations was extracted from the distribution of such values obtained from the laser obscuration work carried out as described in Chapter 5 section 5.3.3 and Appendix 5E.

Each of the erosion models yielded a value for the erosion rate of a localised area of the pipe wall in terms of mm^3/kg.

Figure 6B.1 also illustrates the areas into which the pipe bore was split to permit an analysis of the erosion on a localised area of the pipe wall to be calculated. The use of these areas permitted this value of erosion rate to be reduced into terms of millimetres of penetration for the amount of abrasive material conveyed during the erosion trials in the pneumatic conveyor (see Figure 6B.2 which offers an explanation of how this was carried out). The area of the pipe wall affected by particles flowing down the arbitrarily selected flow channel was calculated. Also the mass of abrasive particles flowing down the flow channel during the pneumatic conveying tests was found. After the values of the area struck by particles, and the mass of abrasive striking this area were calculated, the penetration of the bend wall was calculated using the following expression:-

$$P_p = \frac{V_{loss}}{A_{strk}} \cos\left(\frac{\pi}{2} - \alpha_{imp} \right) \qquad (6B.1)$$

where V_{loss} is the volume loss determined by multiplying the mass of abrasive striking the area of the pipe wall at the end of the flow tube by the erosion rate predicted using the power law model

Figure 6B.2 The arbitrary flow channel used in the determination of the predicted value of the bend wall penetration.

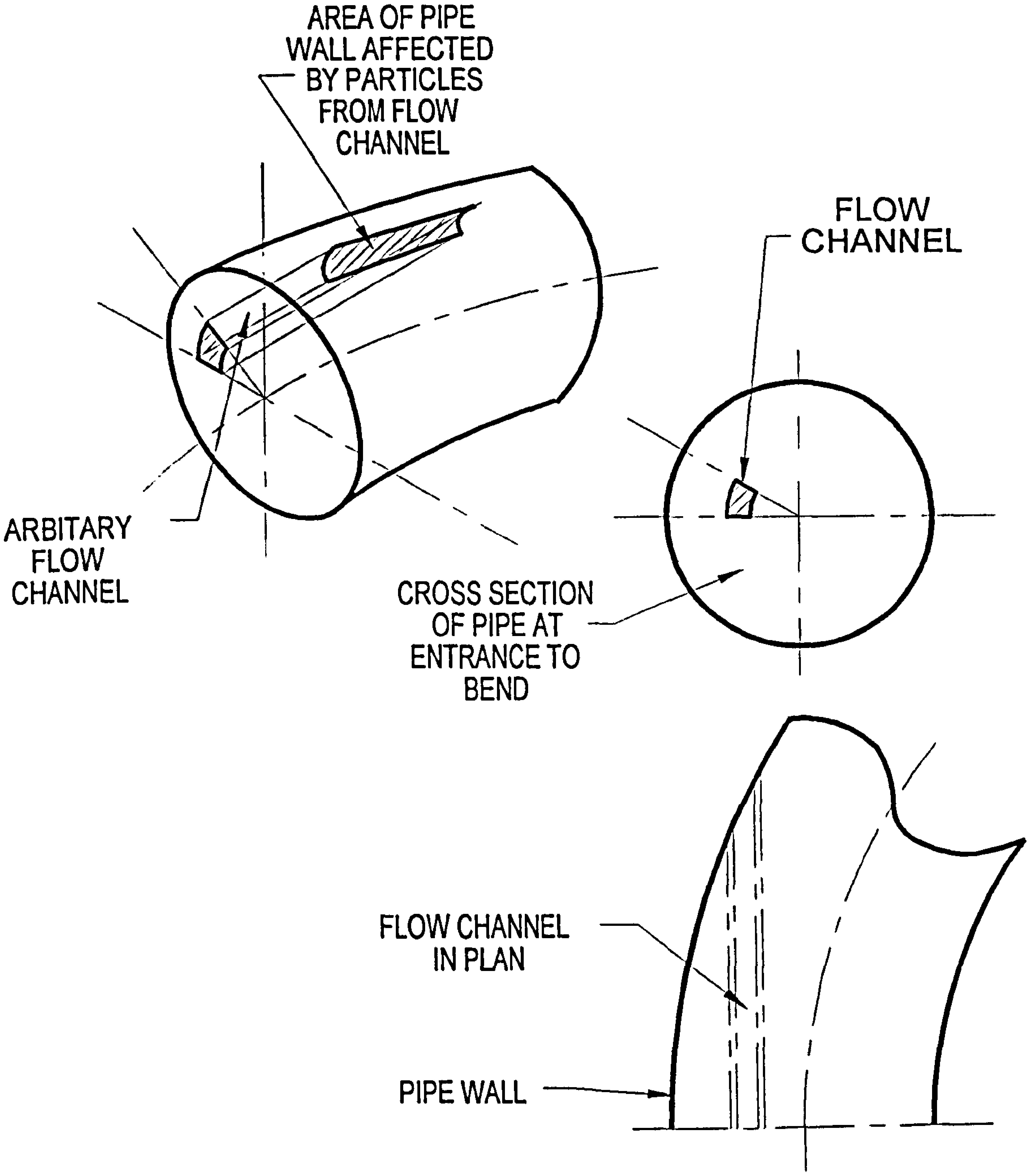

described in section 4.3.4 Chapter 4; A_{strk} is the area of the pipe wall struck by the particles at the end of the arbitrary flow channel; α_{imp} is the angle of impingement at the puncture point as found from the model used to predict the location of the puncture point in the bend, and P_p is the penetration at the puncture point. (The factor $\pi/2$ arises from the geometry of the particle impact).

6B.4 The Combined Trajectory / Erosion Model Programme Listings

The combined trajectory / erosion model consisted of two separate programme elements. The first of these was the Quattro Pro spreadsheet and 'dynamic data exchange' macro. This contained all of the input data required by the combined model, as well as, following the use of the 'dynamic data exchange' macro, all of the results for impact location and penetration for each of the erosion models after 5475 kg of abrasive (the total amount of abrasive used in the pneumatic conveying trials) had passed through the bend. The second part of the programme was the MathCad coded programme for the particle trajectory and both erosion models.

Control of the two programme elements was carried out by the Quattro Pro 'dynamic data exchange' macro. This macro opened the MathCad programme remotely, entered each of the necessary input variable values listed in the Quattro Pro spreadsheet for each particle start location and returned the results for the penetration and impact location in the bend from the MathCad programme to the Quattro Pro spreadsheet. As stated before this was repeated ninety six times for each of the particle start locations.

The following two pages contain examples of the Quattro Pro spreadsheet input data and corresponding results, and the Quattro Pro 'dynamic data exchange' macro. Following this, on seven pages, the MathCad programme is presented.

DDE Communication with MathCad App 6b.MCD Programme

Calculations for 500 kg of sand being conveyed For comparison with actual read values Mean particle size used

Channel 1

Radial Pos rs (mm)	Angular Pos pss (rad)	Angular Pos pss (deg)	Air Vel. Ws (m/s)	Part Conc. rhos (kg/m^3)	Impact Position psn1 (deg)	phn1 (deg)	Impact Vector Qr (m/sec)	aimp (deg)	Wear Rate (m). PenFB	PenAJB	Corrected psn1 (deg)
0.004	0.087267	5.0	27.157	4.7712	0.55	13.99	27.19	13.75	5.44E-05	7.10E-05	0.55
0.0075	0.087267	5.0	26.942	4.7305	1.28	12.85	26.97	12.62	4.62E-05	5.83E-05	1.28
0.0094	0.087267	5.0	26.768	4.5990	1.63	12.35	26.80	12.12	4.15E-05	5.17E-05	1.63
0.01175	0.087267	5.0	26.460	4.3700	2.13	11.41	26.49	11.18	3.38E-05	4.10E-05	2.13
0.0147	0.087267	5.0	25.848	4.1073	2.73	10.17	25.87	9.95	2.52E-05	2.90E-05	2.73
0.017	0.087267	5.0	25.395	3.8021	3.16	9.23	25.41	9.01	1.93E-05	2.13E-05	3.16
0.0201	0.087267	5.0	24.504	2.9322	3.77	7.62	24.52	7.41	9.88E-06	1.05E-05	3.77
0.023	0.087267	5.0	23.310	1.0410	4.33	5.69	23.32	5.50	1.67E-06	1.82E-06	4.33
0.004	0.5236	30.0	27.287	4.7659	3.00	14.26	27.32	14.02	5.68E-05	7.47E-05	3.00
0.0075	0.5236	30.0	27.153	4.7403	7.20	13.16	27.19	12.87	4.87E-05	6.20E-05	7.20
0.0094	0.5236	30.0	27.035	4.6760	9.53	12.49	27.07	12.15	4.34E-05	5.41E-05	9.53
0.01175	0.5236	30.0	26.856	4.4906	12.18	11.79	26.88	11.39	3.72E-05	4.52E-05	12.18
0.0147	0.5236	30.0	26.524	4.2899	15.69	10.65	26.55	10.15	2.90E-05	3.36E-05	15.69
0.017	0.5236	30.0	26.030	4.0282	18.38	9.67	26.05	9.10	2.21E-05	2.44E-05	18.38
0.0201	0.5236	30.0	25.308	3.4386	22.36	7.89	25.32	7.24	1.21E-05	1.25E-05	22.36
0.023	0.5236	30.0	24.074	2.0964	25.64	6.07	24.09	5.41	3.52E-06	3.94E-06	25.64
0.004	1.0472	60.0	27.211	4.7364	4.71	14.63	27.25	14.46	5.91E-05	7.85E-05	4.71
0.0075	1.0472	60.0	27.115	4.7552	11.92	13.97	27.16	13.60	5.31E-05	6.90E-05	11.92
0.0094	1.0472	60.0	27.042	4.7619	15.91	13.53	27.08	13.00	4.92E-05	6.28E-05	15.91
0.01175	1.0472	60.0	26.955	4.7271	21.01	12.88	26.99	12.12	4.34E-05	5.39E-05	21.01
0.0147	1.0472	60.0	26.882	4.3814	27.85	11.85	26.91	10.73	3.32E-05	3.95E-05	27.85
0.017	1.0472	60.0	26.807	4.0688	33.02	11.02	26.84	9.61	2.61E-05	2.96E-05	33.02
0.0201	1.0472	60.0	25.922	3.6147	40.65	9.50	25.94	7.72	1.51E-05	1.58E-05	40.65
0.023	1.0472	60.0	24.960	3.0179	48.47	7.48	24.98	5.48	5.75E-06	6.19E-06	48.47
0.004	1.65806	95.0	27.368	4.7461	3.71	15.14	27.43	15.23	6.49E-05	8.81E-05	3.71
0.0075	1.65806	95.0	27.409	4.7481	11.98	15.17	27.47	14.99	6.36E-05	8.58E-05	11.98
0.0094	1.65806	95.0	27.375	4.7468	16.94	14.97	27.44	14.54	6.04E-05	8.06E-05	16.94
0.01175	1.65806	95.0	27.285	4.5699	22.45	14.92	27.35	14.17	5.54E-05	7.36E-05	22.45
0.0147	1.65806	95.0	27.104	4.2648	30.74	14.44	27.16	13.12	4.50E-05	5.86E-05	30.74
0.017	1.65806	95.0	26.919	4.0942	36.72	14.16	26.97	12.39	3.87E-05	4.97E-05	36.72
0.0201	1.65806	95.0	26.541	3.6080	47.25	13.20	26.58	10.66	2.62E-05	3.20E-05	47.25
0.023	1.65806	95.0	25.023	2.6376	58.47	11.92	25.05	8.80	1.24E-05	1.42E-05	58.47
0.004	2.0944	120.0	27.211	4.7601	0.51	15.28	27.30	15.86	6.83E-05	9.42E-05	0.51
0.0075	2.0944	120.0	27.115	4.7483	7.95	15.85	27.22	16.17	6.95E-05	9.67E-05	7.95
0.0094	2.0944	120.0	27.042	4.7485	12.06	16.02	27.14	16.16	6.90E-05	9.58E-05	12.06
0.01175	2.0944	120.0	26.955	4.7265	16.64	16.38	27.06	16.26	6.87E-05	9.58E-05	16.64
0.0147	2.0944	120.0	26.882	4.4507	23.00	16.57	26.99	16.02	6.28E-05	8.78E-05	23.00
0.017	2.0944	120.0	26.807	4.2921	28.63	16.55	26.91	15.57	5.76E-05	8.00E-05	28.63
0.0201	2.0944	120.0	25.922	4.0842	35.78	16.62	26.01	15.05	4.76E-05	6.55E-05	35.78
0.023	2.0944	120.0	24.960	3.3687	43.78	16.42	25.04	14.20	3.25E-05	4.48E-05	43.78
0.004	2.618	150.0	27.287	4.7632	-11.57	14.53	27.60	17.74	8.14E-05	1.18E-04	-11.57
0.0075	2.618	150.0	27.153	4.7564	-3.50	15.90	27.44	18.36	8.43E-05	1.24E-04	-3.50
0.0094	2.618	150.0	27.035	4.7708	-0.58	16.46	27.32	18.68	8.58E-05	1.27E-04	-0.58
0.01175	2.618	150.0	26.856	4.7904	2.55	17.17	27.14	19.15	8.77E-05	1.32E-04	2.55
0.0147	2.618	150.0	26.524	4.7628	6.55	17.78	26.81	19.48	8.65E-05	1.31E-04	6.55
0.017	2.618	150.0	26.030	4.5656	9.67	18.25	26.31	19.71	8.03E-05	1.23E-04	9.67
0.0201	2.618	150.0	25.308	4.1311	13.62	18.92	25.57	20.04	6.91E-05	1.08E-04	13.62
0.023	2.618	150.0	24.074	3.4292	17.55	19.47	24.31	20.22	5.09E-05	8.16E-05	17.55
0.004	3.45	197.7	27.114	4.7604	429.40	11.54	29.18	21.96	1.09E-04	1.74E-04	-69.40
0.0075	3.45	197.7	26.846	4.7505	383.57	14.37	27.87	22.22	1.08E-04	1.73E-04	-23.57
0.0094	3.45	197.7	26.625	4.7546	376.15	15.26	27.50	21.99	1.04E-04	1.66E-04	-16.15
0.01175	3.45	197.7	26.239	4.7665	370.43	16.24	27.01	22.00	1.00E-04	1.60E-04	-10.43
0.0147	3.45	197.7	25.611	4.6962	365.58	17.40	26.29	22.30	9.44E-05	1.52E-04	-5.58
0.017	3.45	197.7	25.183	4.3547	362.68	18.07	25.82	22.50	8.48E-05	1.39E-04	-2.68
0.0201	3.45	197.7	24.275	3.9416	359.07	18.91	24.84	22.73	7.07E-05	1.18E-04	-0.93
0.023	3.45	197.7	23.302	3.2010	355.89	19.59	23.81	22.90	5.21E-05	8.90E-05	-4.11
0.004	3.6652	210.0	27.012	4.7510	371.23	14.58	27.31	17.73	7.90E-05	1.14E-04	-11.23
0.0075	3.6652	210.0	26.559	4.7187	363.13	15.93	26.83	18.31	7.87E-05	1.16E-04	-3.13
0.0094	3.6652	210.0	26.236	4.7246	360.19	16.56	26.50	18.67	7.84E-05	1.16E-04	-0.19
0.01175	3.6652	210.0	25.797	4.7359	356.76	17.08	26.06	18.93	7.67E-05	1.14E-04	-3.24
0.0147	3.6652	210.0	25.261	4.6970	353.04	17.88	25.51	19.44	7.48E-05	1.13E-04	-6.96
0.017	3.6652	210.0	24.759	4.4910	349.85	18.29	25.01	19.61	6.88E-05	1.05E-04	-10.15
0.0201	3.6652	210.0	23.969	4.0636	346.07	18.99	24.20	20.00	5.87E-05	9.15E-05	-13.93
0.023	3.6652	210.0	22.796	3.3768	341.95	19.47	23.01	20.10	4.31E-05	6.86E-05	-18.05
0.004	4.189	240.0	26.887	4.7253	359.39	15.30	26.98	15.87	6.57E-05	9.07E-05	-0.61
0.0075	4.189	240.0	26.357	4.6903	351.76	15.80	26.45	16.10	6.33E-05	8.79E-05	-8.24
0.0094	4.189	240.0	25.982	4.6751	348.02	16.17	26.08	16.28	6.19E-05	8.62E-05	-11.98
0.01175	4.189	240.0	25.484	4.6427	342.66	16.26	25.58	16.08	5.73E-05	7.94E-05	-17.34
0.0147	4.189	240.0	24.916	4.4765	336.30	16.48	25.00	15.87	5.11E-05	7.06E-05	-23.70
0.017	4.189	240.0	24.483	4.1408	331.20	16.58	24.57	15.59	4.39E-05	6.08E-05	-28.80
0.0201	4.189	240.0	23.650	3.9656	322.85	16.42	23.72	14.74	3.52E-05	4.79E-05	-37.15
0.023	4.189	240.0	22.400	3.3180	315.08	16.27	22.46	13.98	2.35E-05	3.19E-05	-44.92
0.004	4.79966	275.0	26.683	4.7069	355.47	14.96	26.73	14.93	5.84E-05	7.87E-05	-4.53
0.0075	4.79966	275.0	26.238	4.6775	346.98	14.72	26.29	14.41	5.26E-05	6.98E-05	-13.02
0.0094	4.79966	275.0	26.062	4.6622	342.57	14.62	26.11	14.11	4.98E-05	6.56E-05	-17.43
0.01175	4.79966	275.0	25.768	4.5600	336.62	14.27	25.81	13.43	4.37E-05	5.66E-05	-23.38
0.0147	4.79966	275.0	25.024	4.1326	328.73	13.69	25.06	12.33	3.21E-05	4.07E-05	-31.27
0.017	4.79966	275.0	24.410	3.9695	321.80	13.01	24.44	11.17	2.49E-05	3.03E-05	-38.20
0.0201	4.79966	275.0	23.614	3.5664	312.04	11.90	23.64	9.42	1.60E-05	1.80E-05	-47.96
0.023	4.79966	275.0	21.417	2.8733	300.77	10.18	21.43	7.21	6.48E-06	6.70E-06	-59.23
0.004	5.236	300.0	26.887	4.7248	355.11	14.46	26.93	14.29	5.58E-05	7.39E-05	-4.89
0.0075	5.236	300.0	26.357	4.6972	348.04	13.97	26.40	13.60	4.87E-05	6.33E-05	-11.96
0.0094	5.236	300.0	25.982	4.6888	343.73	13.39	26.02	12.85	4.29E-05	5.45E-05	-16.27
0.01175	5.236	300.0	25.484	4.6417	339.09	12.94	25.52	12.19	3.71E-05	4.62E-05	-20.91
0.0147	5.236	300.0	24.916	4.4079	332.32	11.91	24.94	10.81	2.78E-05	3.28E-05	-27.68
0.017	5.236	300.0	24.483	3.8400	326.85	10.98	24.51	9.59	1.94E-05	2.19E-05	-33.15
0.0201	5.236	300.0	23.650	3.4937	319.55	9.55	23.67	7.80	1.17E-05	1.22E-05	-40.45
0.023	5.236	300.0	22.400	2.9105	311.33	7.38	22.41	5.41	4.06E-06	4.34E-06	-48.67
0.004	5.76	330.0	27.012	4.7556	356.92	14.12	27.05	13.88	5.44E-05	7.12E-05	-3.08
0.0075	5.76	330.0	26.559	4.7062	352.89	13.26	26.59	12.97	4.62E-05	5.90E-05	-7.11
0.0094	5.76	330.0	26.236	4.6270	350.48	12.51	26.26	12.18	3.99E-05	4.97E-05	-9.52
0.01175	5.76	330.0	25.797	4.4419	347.71	11.71	25.82	11.32	3.28E-05	3.97E-05	-12.29
0.0147	5.76	330.0	25.261	4.2310	344.12	10.52	25.28	10.03	2.47E-05	2.84E-05	-15.88
0.017	5.76	330.0	24.759	3.9652	341.47	9.57	24.78	9.01	1.88E-05	2.05E-05	-18.53
0.0201	5.76	330.0	23.969	3.3564	337.85	8.01	23.98	7.37	1.06E-05	1.09E-05	-22.15
0.023	5.76	330.0	22.796	2.1380	334.19	5.92	22.81	5.27	2.93E-06	3.27E-06	-25.81

Average Values	183.2306	14.0342	26.2306	14.2593	4.93E-05	6.91E-05	-1.66

Max Values	429.4048	19.5852	29.1790	22.8982	1.09E-04	1.74E-04	58.47
Min Values	-11.5667	5.6875	21.4342	5.2715	1.67E-06	1.82E-06	-69.40
Std Deviation	168.3482	3.2512	1.4207	4.5248	2.58E-05	4.19E-05	23.56

Impact Position		Impact Vector		Wear Rate (m).		Corrected
psn1 (deg)	phn1 (deg)	Qr (m/sec)	aimp (deg)	PenFB	PenAJB	psn1 (deg)

DDE Transfer/Reponse Macro between MathCad and QuattroPr

```
{EXEC "D:\WINAPPS\WINMCAD\MCAD.EXE",1}
{INITIATE MCAD,APP_6B.MCD,A B4}
{POKE A.B4,rs,A:A8}
{POKE A.B4,pss,A:B8}
{POKE A:B4,Ws,A.D8}
{POKE A.B4,rhos,A.E8}
{REQUEST A:B4,psn1,A:F8}
{REQUEST A.B4,phn1,A.G8}
{REQUEST A:B4,Qr,A.H8}
{REQUEST A:B4,aimp,A:I8}
{REQUEST A:B4,PenFB,A:J8}
{REQUEST A:B4,PenAJB,A:K8}
{POKE A:B4,rs,A:A9}
{POKE A:B4,pss,A:B9}
{POKE A.B4,Ws,A:D9}
{POKE A.B4,rhos,A:E9}
{REQUEST A:B4,psn1,A:F9}
{REQUEST A:B4,phn1,A:G9}
{REQUEST A.B4,Qr,A H9}
{REQUEST A.B4,aimp,A:I9}
{REQUEST A.B4,PenFB,A.J9}
{REQUEST A.B4,PenAJB,A K9}
{POKE A:B4,rs,A:A10}
{POKE A.B4,pss,A.B10}
{POKE A.B4,Ws,A·D10}
{POKE A.B4,rhos,A E10}
{REQUEST A:B4,psn1,A.F10}
{REQUEST A.B4,phn1,A.G10}
{REQUEST A.B4,Qr,A.H10}
{REQUEST A.B4,aimp,A:I10}
{REQUEST A·B4,PenFB,A.J10}
{REQUEST A.B4,PenAJB,A K10}
{POKE A:B4,rs,A:A11}
{POKE A:B4,pss,A.B11}
{POKE A.B4,Ws,A·D11}
{POKE A:B4,rhos,A.E11}
{REQUEST A:B4,psn1,A.F11}
{REQUEST A.B4,phn1,A·G11}
{REQUEST A.B4,Qr,A H11}
{REQUEST A:B4,aimp,A I11}
{REQUEST A B4,PenFB,A.J11}
{REQUEST A B4,PenAJB,A K11}
{POKE A B4,rs,A.A12}
{POKE A B4,pss,A:B12}
{POKE A:B4,Ws,A.D12}
{POKE A.B4,rhos,A E12}
{REQUEST A.B4,psn1,A F12}
{REQUEST A.B4,phn1,A G12}
{REQUEST A.B4,Qr,A H12}
{REQUEST A.B4,aimp,A.I12}
{REQUEST A.B4,PenFB,A.J12}
{REQUEST A B4,PenAJB,A K12}
{POKE A.B4,rs,A.A13}
{POKE A.B4,pss,A.B13}
{POKE A.B4,Ws,A.D13}
{POKE A.B4,rhos,A E13}
{REQUEST A.B4,psn1,A.F13}
{REQUEST A.B4,phn1,A G13}
{REQUEST A:B4,Qr,A·H13}
{REQUEST A:B4,aimp,A.I13}
{REQUEST A.B4,PenFB,A.J13}
{REQUEST A.B4,PenAJB,A K13}
{POKE A.B4,rs,A:A14}
{POKE A:B4,pss,A.B14}
{POKE A:B4,Ws,A:D14}
{POKE A.B4,rhos,A.E14}
{REQUEST A.B4,psn1,A·F14}
{REQUEST A.B4,phn1,A·G14}
{REQUEST A.B4,Qr,A.H14}
{REQUEST A.B4,aimp,A.I14}
{REQUEST A.B4,PenFB,A.J14}
{REQUEST A B4,PenAJB,A:K14}
{POKE A B4,rs,A:A15}
{POKE A:B4,pss,A.B15}
{POKE A.B4,Ws,A.D15}
{POKE A:B4,rhos,A:E15}
{REQUEST A:B4,psn1,A.F15}
{REQUEST A:B4,phn1,A.G15}
{REQUEST A.B4,Qr,A.H15}
{REQUEST A.B4,aimp,A I15}
{REQUEST A.B4,PenFB,A.J15}
{REQUEST A B4,PenAJB,A K15}
```

Modelling the Erosive Penetration of a Pneumatic Conveyor Bend at the Primary Impact Position

The particle velocity and the particle concentration density at the particle start position are specified:-

$Ws := 25.5$ $\qquad$ $rhos := 2.138$

The start position of the particle at the entrance to the bend is specified:-

$rs := 0.01175$ $\qquad$ $pss := 5.76$

The bend radius is:-

$R := 0.75 \cdot m$

$\rho_p := 3287.2 \cdot \frac{kg}{m^3}$ $\qquad$ Where ρ_p is the particle density.

$\sigma := 161.9 \cdot 10^{-6} \cdot m$ $\qquad$ σ is the particle diameter.

$\mu_t := 1.82 \cdot 10^{-5} \cdot \frac{kg}{m \cdot sec}$ $\qquad$ μ_t is the fluid viscosity.

$\tau_m := \frac{2}{9} \cdot \frac{\sigma^2 \cdot \rho_p}{\mu_t}$ $\qquad$ This expression is known as the momentum relaxation time.

$\tau_m = 1.052049 \cdot sec$

$\Delta t := 0.0001 \cdot sec$ $\qquad$ This is the value for the time increment used in this analysis.

$i := 0 .. 1000$ $\qquad$ This is the number of iterative passes that will be made.

Definition of the system initial conditions now follows: The system of equations will take the form of a series of nine simultaneous equations with nine unknowns.

$$\begin{bmatrix} au_0 \\ av_0 \\ aw_0 \\ u_0 \\ v_0 \\ w_0 \\ r_0 \\ \Psi_0 \\ \phi_0 \end{bmatrix} := \begin{bmatrix} 0 \cdot \frac{m}{sec^2} \\ 0 \cdot \frac{m}{sec^2} \\ 0 \cdot \frac{m}{sec^2} \\ 0 \cdot \frac{m}{sec} \\ 0 \cdot \frac{m}{sec} \\ Ws \cdot \frac{m}{sec} \\ rs \cdot m \\ pss \cdot rad \\ 0 \cdot rad \end{bmatrix}$$

Where au,av & aw are the acclerations in each of the three toroidal dimensions being used in this analysis. u,v & w are the velocities in each of these dimensions and the remaining three terms at the bottom of this matrix equation are the positions.

The matrix equation detailing the equations of motion of a particle in the toroidal coordinate system is shown on the following page.

$$\begin{bmatrix} au_{(i+1)} \\ av_{(i+1)} \\ aw_{(i+1)} \\ u_{(i+1)} \\ v_{(i+1)} \\ w_{(i+1)} \\ r_{(i+1)} \\ \psi_{(i+1)} \\ \phi_{(i+1)} \end{bmatrix} := \begin{bmatrix} \dfrac{(w_i)^2\cdot\cos(\psi_i)}{R + r_i\cdot\cos(\psi_i)} + \dfrac{(v_i)^2}{r_i} - \dfrac{u_i}{(\tau_m)} \\ \dfrac{-(w_i)^2\cdot\sin(\psi_i)}{R + r_i\cdot\cos(\psi_i)} - \dfrac{u_i\cdot v_i}{r_i} - \dfrac{v_i}{\tau_m} \\ \dfrac{-u_i\cdot w_i\cdot\cos(\psi_i)}{R + r_i\cdot\cos(\psi_i)} + \dfrac{v_i\cdot w_i\cdot\sin(\psi_i)}{R + r_i\cdot\cos(\psi_i)} + \dfrac{Ws\cdot\frac{m}{sec} - w_i}{\tau_m} \\ u_i + au_i\cdot\Delta t \\ v_i + av_i\cdot\Delta t \\ w_i + aw_i\cdot\Delta t \\ \mathrm{if}\left(r_i \le 0.0005\cdot m, -0.0005\cdot m, \mathrm{until}\left(0.0265\cdot m - r_i, u_i\cdot\Delta t + r_i\right)\right) \\ \dfrac{v_i\cdot\Delta t}{r_i} + \psi_i \\ \mathrm{until}\left(\dfrac{\pi}{2} - \phi_i, \dfrac{w_i\cdot\Delta t}{R + r_i\cdot\cos(\psi_i)} + \phi_i\right) \end{bmatrix}$$

The values of the variables where the particle collision occurs are extracted.

$N1 := \mathrm{last}(r) - 1$ $\quad N1 = 62$

Initial starting values for the iterative calculations are:

$rs = 0.01175$ $\quad pss = 330.02369\cdot deg$ $\quad \phi_0 = 0\cdot deg$

The values of the variables for position at the point where collision with the wall occurs are:

$r_{N1} = 0.026293\cdot m$ $\quad \psi_{N1} = 347.778\cdot deg$ $\quad \phi_{N1} = 11.767833\cdot deg$

$psn1 := \psi_{N1}$ $\quad phn1 := \phi_{N1}$

$psn1 = 347.778217\cdot deg$ $\quad phn1 = 11.767833\cdot deg$

The variables phn1 & psn1 are utilised in DDE transfer with QuattroPro.

The values of the velocity components at the collision location are extracted:

$u_{N1} = 4.985968\cdot m\cdot sec^{-1}$ $\quad v_{N1} = 1.155722\cdot m\cdot sec^{-1}$ $\quad w_{N1} = 25.006914\cdot m\cdot sec^{-1}$

The impact angle and velocity are determined: The normal vector to the pipe wall is determined and the 'DOT' product is taken of this with the velocity vector to produce the angle of impact. The magnitude of the velocity vector is given by resolving the components of the velocity vector at the point of impact.

$$Q := \begin{bmatrix} u_{N1} \\ v_{N1} \\ w_{N1} \end{bmatrix} \qquad Q = \begin{pmatrix} 4.985968 \\ 1.155722 \\ 25.006914 \end{pmatrix}\cdot m\cdot sec^{-1} \qquad Qr := |Q| \qquad Qr = 25.525307\cdot m\cdot sec^{-1}$$

The variable Qr is used in DDE transfer to QPRO.

The normal vector n was determined using the grad operator from Yeung's work on the coordinates of the parametric surface plot example shown in the MathCad handbook and the MathCad symbolic solver.

$$n := \begin{pmatrix} \cos(\psi_{N1})\cdot\cos(\phi_{N1}) \\ -\sin(\psi_{N1})\cdot\sin(\phi_{N1}) \\ 0 \end{pmatrix} \qquad n = \begin{pmatrix} 0.956794 \\ 0.043175 \\ 0 \end{pmatrix}$$

The impact angle is then determined as follows:-

$$\alpha_{imp} := \operatorname{asin}\left(\frac{Q\cdot n}{|Q|\cdot|n|}\right) \qquad aimp := \alpha_{imp} \qquad aimp = 11.371913\cdot deg$$

The variable aimp is used for DDE transfer to QPRO.

Calculation of the Total Conveying Time:-

The total mass of abrasive material conveyed before bend failure occurred was:-

$$M_t := 250\cdot kg \qquad MFR_t := 0.25935\cdot\frac{kg}{sec}$$

The particle concentration and air velocity / particle velocity of the abrasive striking this surface is dependent upon the three dimensional map of the particle concentration density within the pipe bore before the conveying bend as determined from the laser obscuration work described in Chapter 5 section 5.3.3 & Appendix 5E. The three dimensional map can be used to interpolate a value for the mass flow rate for a any given point within the pipe bore as selected by the values provided from the associated Quattro Pro file which describes the input information to this file. Similar interpolations can be obtained from the three dimensional air velocity plot found by skewing the Prandtl air velocity distribution as discussed in section 5.3.3 & Appendix 5E as well.
The total conveying time is found:-

$$Tct := \frac{M_t}{MFR_t} \qquad Tct = 963.948332\cdot sec$$

The Approximate Areas of Each of the 96 Segments of the Pipe Bore are Determined:-

$$k := 0, 1 .. 6$$

$$RadPos := \begin{bmatrix} 0.0040 \\ 0.0075 \\ 0.0094 \\ 0.01175 \\ 0.0147 \\ 0.0170 \\ 0.0201 \\ 0.0230 \end{bmatrix}$$

The area of any given segment depends upon its position within the pipe bore. Owing to the way in which the positions of the trajectory start positions were chosen and the geometry of the pipe, the area of each segment was found by dividing successive annular rings within the pipe bore into 12, the number of segments per annular ring. This means that the the segments closer to the walls of the pipe will have a larger area than those at the centre of the pipe.

Radius of the Annular Rings:-

$$g_k := RadPos_k + \frac{RadPos_{k+1} - RadPos_k}{2}$$

Area of the Segments in the Annular Rings:-

$$A1 := \frac{\pi\cdot(g_0)^2}{12} \qquad A2 := \frac{\pi\cdot\left[(g_1)^2 - (g_0)^2\right]}{12} \qquad A3 := \frac{\pi\cdot\left[(g_2)^2 - (g_1)^2\right]}{12}$$

$$A4 := \frac{\pi\cdot\left[(g_3)^2 - (g_2)^2\right]}{12} \qquad A5 := \frac{\pi\cdot\left[(g_4)^2 - (g_3)^2\right]}{12} \qquad A6 := \frac{\pi\cdot\left[(g_5)^2 - (g_4)^2\right]}{12}$$

$$A7 := \frac{\pi\cdot\left[(g_6)^2 - (g_5)^2\right]}{12} \qquad A8 := \frac{\pi\cdot\left[(0.0265)^2 - (g_6)^2\right]}{12}$$

Selection of the Correct Segment Area for any given Radius:-

$$As := \mathrm{if}\left[rs \le g_0, A1, \mathrm{if}\left[(rs \le g_1), A2, \mathrm{if}\left[(rs \le g_2), A3, \mathrm{if}\left[(rs \le g_3), A4, \mathrm{if}\left[(rs \le g_4), A5, \mathrm{if}\left[(rs \le g_5), A6, \mathrm{if}(rs \le g_6, A7, A8)\right]\right]\right]\right.\right.\right.$$

$$As \cdot m^2 = 1.651169 \cdot 10^{-5} \cdot m^2$$

Use of the Combined Finnie/Bitter Erosion Model to Predict the Erosive Penetration of the Test Bend.

The model being used was extracted from a recent paper by Sato [S6].

Input Variables:-

$r_p := \sigma \qquad r_p = 1.619 \cdot 10^{-4} \cdot m \qquad \rho_p := 3287 \cdot \frac{kg}{m^3} \qquad \rho_t := 7800 \cdot \frac{kg}{m^3} \qquad q_p := 0.22 \qquad q_t := 0.303$

$E_p := 7.13 \cdot 10^{10} \cdot \frac{newton}{m^2} \qquad E_t := 2.1 \cdot 10^{11} \cdot \frac{newton}{m^2} \qquad Y_t := 3.31 \cdot 10^{8} \cdot \frac{newton}{m^2}$

$U := Ws \cdot \frac{m}{sec} \qquad U = 25.5 \cdot m \cdot sec^{-1} \qquad i := 1, 2 .. 18 \qquad \alpha_i := i \cdot 5 \cdot \frac{\pi}{180} \qquad \psi := 2$

Model Constants (semi-empirical):-

$\varepsilon := 4.009109 \cdot 10^{10} \cdot \frac{joule}{m^3} \qquad K := 1.25 \qquad C := 0.495$

NB The constants (semi-empirical) were manipulated to ensure a fit to the actual erosion data.

Calculations appertaining to particle properties:-

$m_p := \frac{4}{3} \cdot \pi \cdot r_p^{\,3} \cdot \rho_p \qquad m_p = 5.842905 \cdot 10^{-8} \cdot kg$

$I_p := \frac{m_p \cdot r_p^{\,2}}{3} \qquad I_p = 5.105065 \cdot 10^{-16} \cdot kg \cdot m^2$

$$K_s := \frac{\pi^2}{2 \cdot \sqrt{10}} \cdot \left(1.59 \cdot Y_t\right)^{\frac{5}{2}} \cdot \left(\frac{1}{\rho_p}\right)^{\frac{1}{2}} \cdot \left(\frac{1 - q_p^{\,2}}{E_p} + \frac{1 - q_t^{\,2}}{E_t}\right)^2 \qquad K_s = 0.054008 \cdot m \cdot sec^{-1}$$

$$P_i := \left[\frac{40}{\pi^4} \cdot \rho_p \cdot \left[\frac{1}{\frac{1 - q_p^{\,2}}{E_p} + \frac{1 - q_t^{\,2}}{E_t}}\right]^4\right]^{\frac{1}{5}} \cdot \left(U \cdot \sin(\alpha_i)\right)^{\frac{2}{5}}$$

Magnitude of Deformation Wear as Proposed by Bitter [B11,B12].

$$W_{d_i} := \frac{0.5 \cdot \rho_p \cdot m_p \cdot \left(U \cdot \sin(\alpha_i) - K_s\right)^2}{\varepsilon} \qquad W_{d_{18}} = 1.55092 \cdot 10^{-12} \cdot kg$$

Magnitude of Cutting Wear as Proposed by Finnie [F7].

$$A := \frac{K}{2 \cdot \left(\frac{m_p \cdot r_p^{\,2}}{I_p} + 1\right)} \qquad B_i := \tan(\alpha_i)$$

$$W_{c1_i} := \frac{\rho_t \cdot C \cdot m_p \cdot U^2}{P_i \cdot \psi} \cdot \left[\sin(2 \cdot \alpha_i) - \frac{2 \cdot \left(1 + \frac{m_p \cdot r_p^{\,2}}{I_p}\right)}{K} \cdot \sin(\alpha_i) \cdot \sin(\alpha_i) \right]$$

$$W_{c2_i} := \frac{\rho_t \cdot C \cdot m_p \cdot U^2}{P_i \cdot \psi} \cdot \left[\frac{K \cdot \cos(\alpha_i) \cdot \cos(\alpha_i)}{2 \cdot \left(1 + \frac{m_p \cdot r_p^{\,2}}{I_p}\right)} \right]$$

$$W_{c_i} := \mathrm{if}\left(B_i \le A, W_{c1_i}, W_{c2_i}\right)$$

Total Erosion Damage is the Sum of the Deformation and Cutting Wear Components as follows:-

$$W_{t_i} := W_{d_i} + W_{c_i}$$

Fitting a cubic spline to this data so that more accurate data interpolation can be made for the calculated impact angle. (The calculated figure ERate is the mass lost due to each particle impact).

$\mathrm{ERate1} := \mathrm{interp}\left(\mathrm{lspline}\left(\alpha, W_t\right), \alpha, W_t, \alpha_{imp}\right)$ $\mathrm{ERate1} = 3.438612 \cdot 10^{-12} \cdot \mathrm{kg}$

The actual mass of abrasive striking the small segment of the pipe wall being considered is now calculated.

$\mathrm{Mstrk} := \mathrm{rhos} \cdot \frac{\mathrm{kg}}{\mathrm{m}^3} \cdot \mathrm{Ws} \cdot \frac{\mathrm{m}}{\mathrm{sec}} \cdot \mathrm{As} \cdot \mathrm{m}^2 \cdot \mathrm{Tct}$ $\mathrm{Mstrk} = 0.867747 \cdot \mathrm{kg}$

The number of particles striking the segmental surface being considered is:-

$N_{hit} := \frac{\mathrm{Mstrk}}{m_p}$ $N_{hit} = 1.485129 \cdot 10^{7}$

The mass of material removed from the segmental surface area is as follows:-

$M1_{loss} := N_{hit} \cdot \mathrm{ERate1}$ $M1_{loss} = 5.106783 \cdot 10^{-5} \cdot \mathrm{kg}$

This is converted into a volume loss as follows:-

$V1_{loss} := \frac{M1_{loss}}{\rho_t}$ $V1_{loss} = 6.547158 \cdot 10^{-9} \cdot \mathrm{m}^3$

The area affected by the elemental flow stream being considered is:-

$A_{strk} := \mathrm{As} \cdot \frac{1}{\cos\left(\frac{\pi}{2} - \alpha_{imp}\right)} \cdot \mathrm{m}^2$ $A_{strk} = 8.374053 \cdot 10^{-5} \cdot \mathrm{m}^2$

The penetration damage caused to this elemental area is:-

$\mathrm{Pen1} := \frac{V1_{loss}}{A_{strk}} \cdot \cos\left(\frac{\pi}{2} - \alpha_{imp}\right)$ $\mathrm{PenFB} := \mathrm{Pen1}$ $\mathrm{PenFB} = 1.541604 \cdot 10^{-5} \cdot \mathrm{m}$

The variable PenFB is used for DDE transfer to QPRO.

Use of the Power Law Erosion Model Derived from the Erosion Tests to Predict the Erosive Penetration of the Test Bend.

The model being used was derived as shown in Chapter 4 section 4.3.4 and reference [B1].

Mean Distance Between Particles:-

$D := \frac{69.599}{(rhos)^{0.286511}}$ $D = 55.982484$

Calculation of the Power Law Exponent n:-

$c_n := 0.00988 \cdot D + 1.239$ $c_n = 1.792107$

Reading in Raw Data for m_n and Extracting an Interpolated Reading for this Variable:-

$mndat := \begin{pmatrix} 1 & 0.0143 \\ 4 & 0.02399 \\ 13 & 0.0238 \end{pmatrix}$

$rx := mndat^{<0>}$ $mnv := mndat^{<1>}$

$vsmn := lspline(rx, mnv)$ $rv := 0, 0.1 .. 13$ $l := 0, 1 .. 3$

$m_n := interp(vsmn, rx, mnv, rhos)$

$m_n = 0.018372$

Finding a Value for n:-

$n := m_n \cdot aimp + c_n$ $n = 1.795753$

Calculation of the Power Law Constant a:-

$c_a := 0.0007983 \cdot -1 \cdot D + 0.0751$ $c_a = 0.030409$

Reading in Raw Data for m_a and Extracting an Interpolated Reading for this Variable:-

$madat := \begin{pmatrix} 1 & 0.0605 \cdot -1 \\ 4 & 0.0935 \cdot -1 \\ 13 & 0.0955 \cdot -1 \end{pmatrix}$

$rx := madat^{<0>}$ $mav := madat^{<1>}$

$vsma := lspline(rx, mav)$ $rv := 0, 0.1 .. 13$ $l := 0, 1 .. 2$

$m_a := interp(vsma, rx, mav, rhos)$

$m_a = -0.074331$

Finding a Value for a:-

$a := c_a \cdot e^{m_a \cdot aimp}$ $a = 0.029964$

Finding a Value for the Erosion Rate Using the Power Law Model:-

$ERate3 := a \cdot Ws^n$ $ERate3 \cdot 10^{-9} \cdot \frac{m^3}{kg} = 1.005534 \cdot 10^{-8} \cdot kg^{-1} \cdot m^3$

The erosion rate has units of mm³/kg of abrasive striking the wall surface.

The actual mass of abrasive striking the small segment of the pipe wall being considered is now calculated.

$Mstrk := rhos \cdot \frac{kg}{m^3} \cdot Ws \cdot \frac{m}{sec} \cdot As \cdot m^2 \cdot Tct$ $Mstrk = 0.867747 \cdot kg$

The volume loss is as follows:-

$V3_{loss} := ERate3 \cdot 10^{-9} \cdot \frac{m^3}{kg} \cdot Mstrk$ $\qquad V3_{loss} = 8.725492 \cdot 10^{-9} \cdot m^3$

The area affected by the elemental flow stream being considered is:-

$A_{strk} := As \cdot \frac{1}{\cos\left(\frac{\pi}{2} - \alpha_{imp}\right)} \cdot m^2$ $\qquad A_{strk} = 8.374053 \cdot 10^{-5} \cdot m^2$

The penetration damage caused to this elemental area is:-

$Pen3 := \frac{V3_{loss}}{A_{strk}} \cdot \cos\left(\frac{\pi}{2} - \alpha_{imp}\right)$ $\qquad PenAJB := Pen3 \quad PenAJB = 2.054518 \cdot 10^{-5} \cdot m$

The variable PenAJB is used for DDE transfer to QPRO.

6B.5 The Results Obtained from the Combined Model

The results obtained from this combined model are shown in the following two figures. Figure 6B.3 illustrates the penetration results obtained from the power law erosion model plotted in the form of a surface plot with the two axes in the horizontal plane being the radial position within the pipe bore and angle around the pipe bend radius. Figure 6B.4 contains a similar surface plot but of the penetration results obtained from the combined Finnie / Bitter erosion model.

A comparison of these results and a discussion regarding the differences seen between the results obtained from the two erosion models is carried out in Chapter 6 section 6.3.

Figure 6B.3 Prediction of the erosion damage in the primary impact area made by using the Yeung trajectory model (see Appendix 5F) in conjunction with the Finnie / Bitter erosion model (see Appendix 4G); the data points included on this graph show some of the results obtained from the experiments described in Chapter 5. (Please note that the corrugations in the fitted surface were caused by the fitting routine in the graph plotting program that was used).

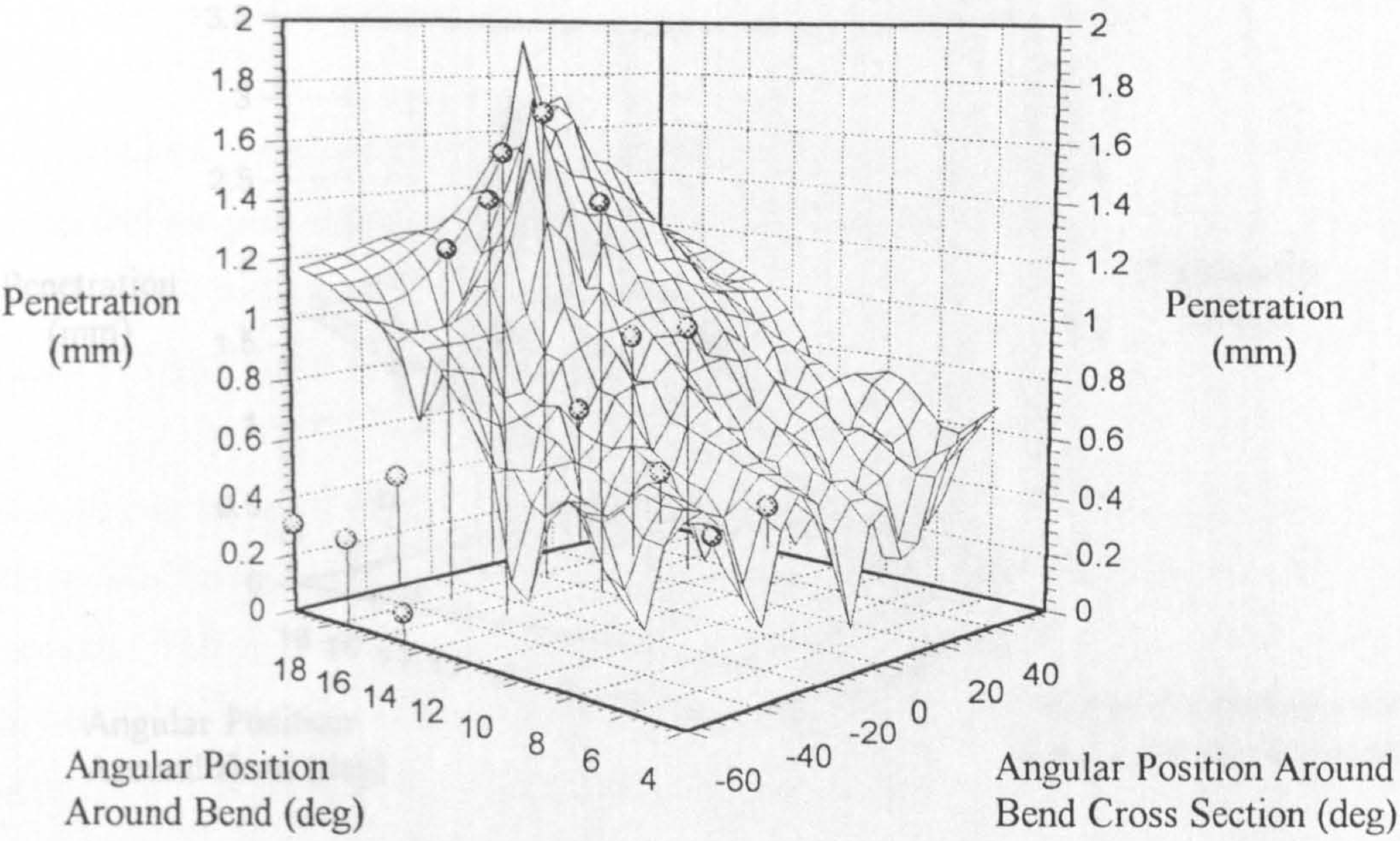

Figure 6B.4 Prediction of the erosion damage in the primary impact area made by using the Yeung trajectory model (see Appendix 5F) in conjunction with the power law erosion model (see Chapter 4 section 4.3.4); the data points included on this graph show some of the results obtained from the experiments described in Chapter 5. (Please note that the corrugations in the fitted surface were caused by the fitting routine in the graph plotting program that was used).

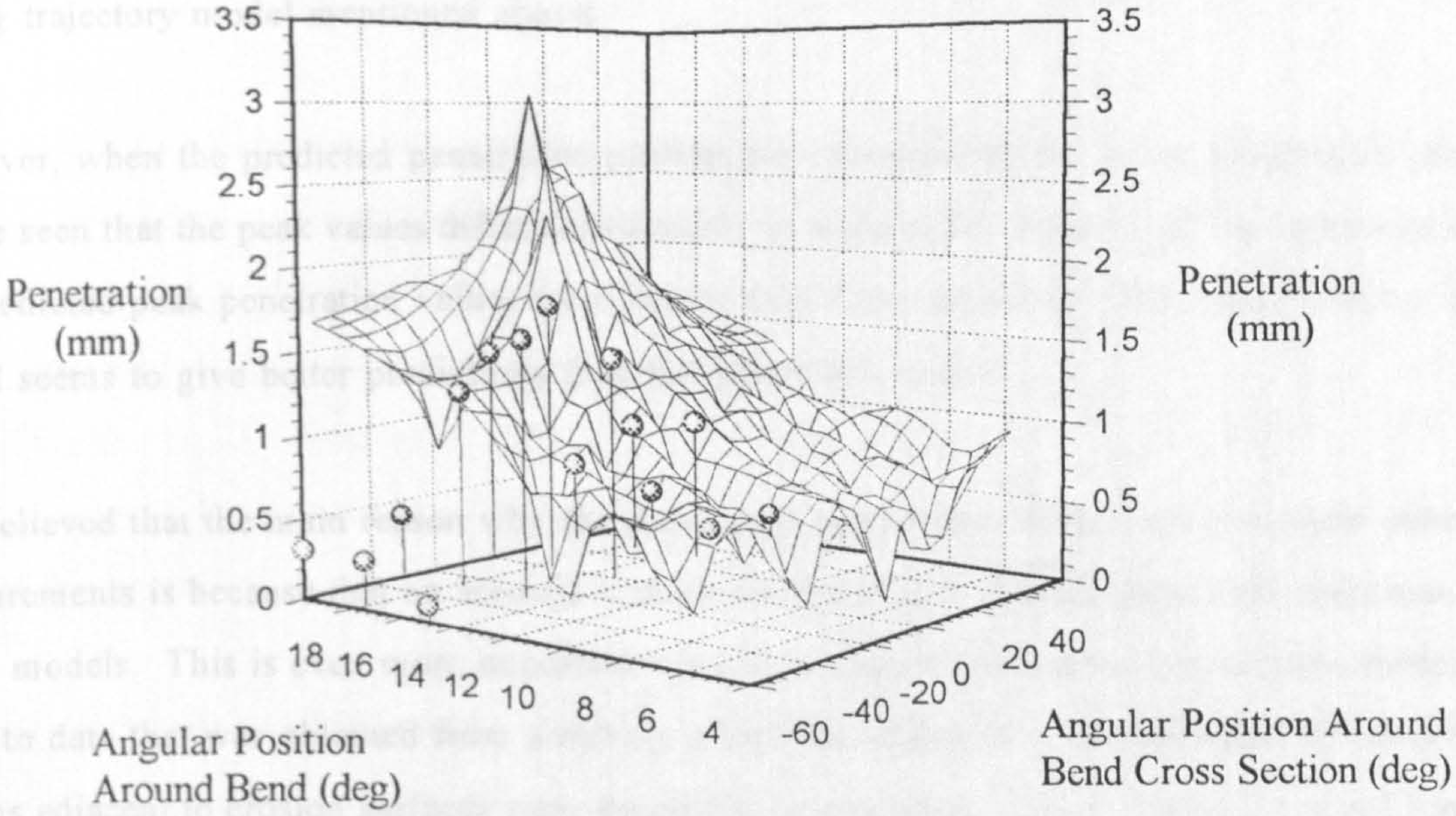

6B.6 Discussion Regarding the Results Obtained from the Combined Yeung Trajectory and Erosion Model

In comparison to the actual measurements of bend wall penetration obtained from the pneumatic conveying test work, it is interesting to note that the greatest amount of penetration of the bend wall in the primary impact area occurs at between 16° and 18° around the sweep of the bend from its entrance. This is very close to that calculated using either of the erosion models combined with the Yeung trajectory model mentioned above.

However, when the predicted penetration profiles are compared to the actual penetration profile, it can be seen that the peak values differ considerably in magnitude. For both of the combined models the predicted peak penetration values were higher than those measured. The Finnie / Bitter erosion model seems to give better predictions than the power law model.

It is believed that the main reason why the penetration predictions differ from the actual penetration measurements is because that no account is made for the effects of inter-particulate collisions in any of the models. This is even more important when it is considered that the two erosion models were fitted to data that was obtained from a test rig where the effects of inter-particulate collisions in the regions adjacent to erosion surfaces were negligible (see sections 4.3.6.3.2 and 4.3.6.4 in Chapter 4). Considering that the area of greatest penetration in the region of primary impacts tends to be furthest from the particle entrance into the bend, the proportion of particles rebounding from the bend surface will increase as the point of greatest penetration is approached (see Figure 6.3). Therefore the rebounding particles will tend to prevent the incoming particles, i.e. those that have not struck the bend wall as yet, from having an unobstructed approach to the eroding surface. It is possible that the incoming particles may strike rebounding particles. This will lead to a lessening of the intensity of particle impacts per unit area in the primary impact area, and a small reduction in the mean kinetic energy of the particles striking the bend wall. In turn, this will reduce the amount of erosion that occurs in the areas of primary particle impact, but will increase the intensity of particle impacts per unit area in the region of secondary impacts. As a consequence of this, the results predicted by the power law model and the Yeung model may be more representative of the actual behaviour of the particles in the bend, excluding inter-particulate collision effects.

Appendix 6C: Bend Puncture Predicted Using the Model Based Upon the Curve of Aberration for a Cylindrical Mirror

6C.1 Introduction to the Bend Puncture Model

The model derived for predicting the puncture of the bend in the pneumatic conveyor consists of three parts. These are as follows:-

a) Predicting the location of the puncture point and the angle of impact of a particle at this point.

b) Predicting the amount of wear that occurs at the puncture point using a model for the erosion derived from the tests carried out on the rotating disc accelerator.

c) Using the model based on the curve of aberration for a cylindrical mirror to evaluate the effect of particle accumulation caused by the internal shape of the bend; a correction factor for the erosive wear caused by the accumulation of particles against the bend wall in the region of the puncture point is derived.

Each of the points will be dealt with in turn.

This appendix will conclude with a listing of the MathCad programme that describes the various features of this model.

6C.2 Predicting the Location of the Point of Bend Puncture

The method by which the curve of aberration for a cylindrical mirror was constructed, and used to predict the location of the puncture point in the pneumatic conveyor bend, has been thoroughly described in Appendix 5G and section 5.4 in Chapter 5. Readers are directed to these sections for further information. The method used to predict the puncture point also enables an estimate to be made for the angle of impingement of a particle striking at the puncture point.

6C.3 Predicting the Erosive Penetration at the Puncture Point

Erosive damage in the region of the puncture point was predicted using the power law erosion model derived from the results obtained from the tests carried out on the rotating disc accelerator erosion tester as described in section 4.3.4 Chapter 4. The reader is directed to that part of the thesis for a detailed explanation of this model.

Values for the following variables were required as input into this model:-

1. The particle velocity (in this work this was taken to be the same as the mean superficial air velocity measured during the pneumatic conveying tests see Table 5.1 section 5.3.1 Chapter 5), therefore, the value of the particle velocity was taken to be 25.6 m/s.
2. The particle concentration density or suspension density (the mean value for this variable determined during the pneumatic conveying trials was used: see Table 5.1 section 5.3.1 Chapter 5), therefore, the value of the particle concentration density was taken to be 3.5 kg/m^3.
3. The angle of impingement of the particles against the pipe wall at the point of puncture. (As part of the method used to predict the point of puncture in the pneumatic conveyor bend, an estimate of the angle of particle impingement against the bend wall was found). For the test bend geometry used in this work the angle of impingement at the puncture point was estimated to be approximately 10°.

As will be seen later on in section 6C.5 of this Appendix the rate of wear at the puncture point was found using the model described in section 4.3.4 of Chapter 4 to be 9.54 mm^3/kg. An arbitrary sized flow channel within the pipe bore was used to find the degree of penetration of the bend wall over a small area affected by the flow of particles in the pipe bore. By this means, the erosion rate found by using the model described in section 4.3.4 was reduced into terms of millimeters of penetration for the amount of abrasive material conveyed during the erosion trials in the pneumatic conveyor (see Figure 6C.1 which offers an explanation of how this was carried out). The area of the pipe wall affected by particles flowing down the arbitrarily sized flow channel was calculated. Also the mass of abrasive particles flowing down the flow channel during the pneumatic conveying tests was found. After the values of the area struck by particles, and the mass of abrasive striking this area were calculated the penetration of the bend wall was calculated using the following expression:-

$$P_p = \frac{V_{loss}}{A_{strk}} \cos\left(\frac{\pi}{2} - \phi 2 \right) \qquad \text{(6C.1)}$$

where V_{loss} is the volume loss determined by multiplying the mass of abrasive striking the area of the pipe wall at the end of the flow tube by the erosion rate predicted using the power law model

Figure 6C.1 The arbitrary flow channel used in the determination of the predicted value of the bend wall penetration.

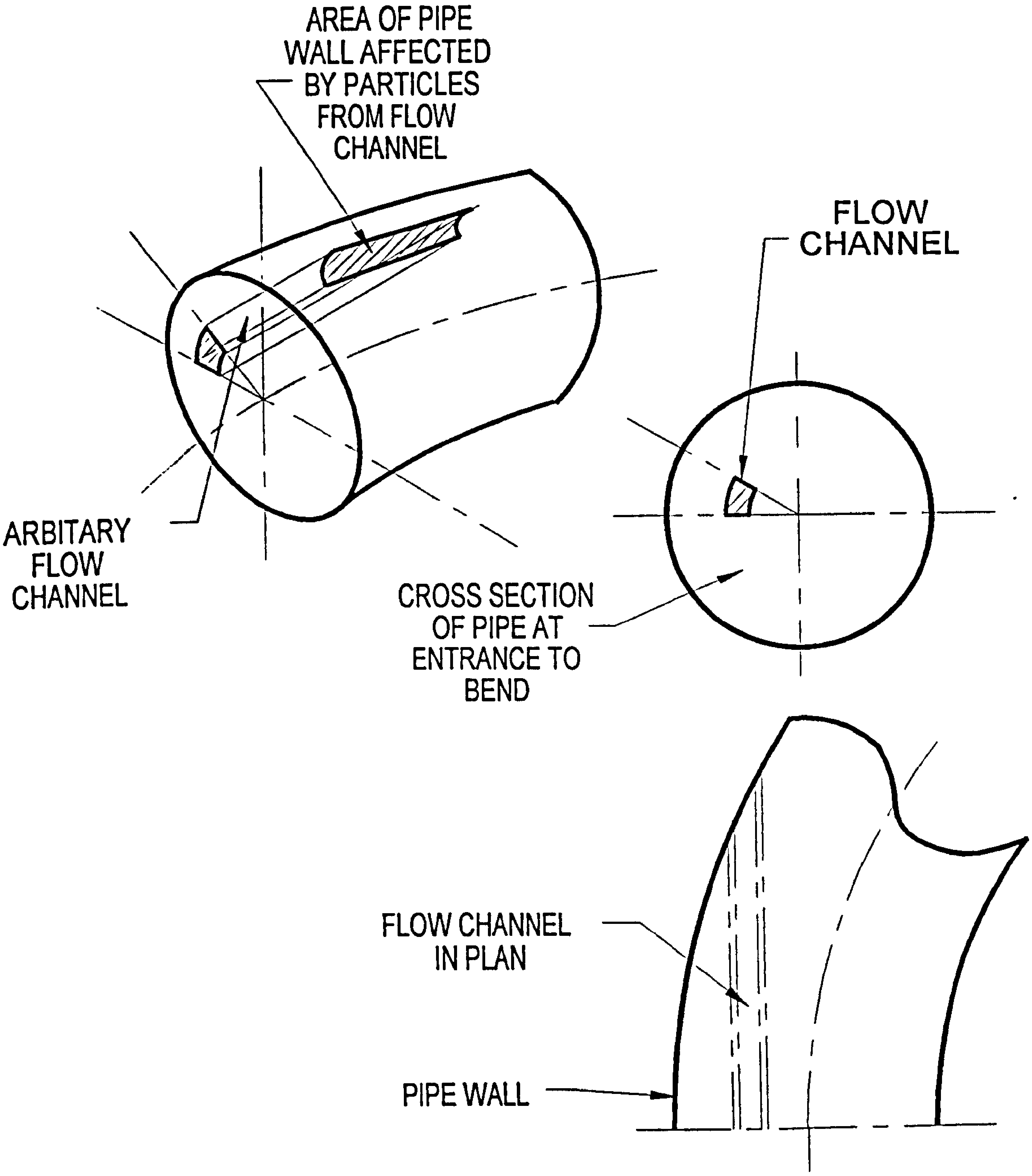

described in section 4.3.4 Chapter 4; A_{strk} is the area of the pipe wall struck by the particles at the end of the arbitrary flow channel; $\phi 2$ is the angle of impingement at the puncture point as found from the model used to predict the location of the puncture point in the bend; P_p is the penetration at the puncture point, and the term $\cos(\pi/2 - \phi 2)$ accounts for the effect of the angle of impingement of the particles.

Use of this model results in a prediction that the amount of wall penetration that occurs at the puncture point after the passage of 5475 kg of olivine sand is 0.61 mm (where 5475 kg is the amount of sand conveyed in the experiments before puncture occurred). This is only 25.6% of the actual amount of penetration that was found to occur.

6C.4 Correcting for the Particle Accumulation Against the Bend Wall in the Region of the Pipe Bore Close to the Puncture Point

It has been observed during tests carried out by other researchers that particles tend to concentrate against the extrados of a bend in a pneumatic conveyor [M4,B9,S4,J3]. This concentration will lead to an increase in the intensity of particle impacts against the pipe wall in the region of puncture, and therefore, to an increase in the amount of erosion damage caused. This statement can be justified only if the particles retain enough kinetic energy following their first contact with the pipe wall to cause damage at the secondary impact / puncture point (this can be justified because the majority of particles strike the bend wall with low angles of impingement and the loss of kinetic energy that occurs is small); and that the increase in the intensity of particle-wall collisions is great enough to overcome the dispersive effects of any inter-particulate collisions (this is justified by referring to the work of Andrews *et al.* and Anand *et al.* [A2,A5] who both suggest that much higher particle concentrations are required before inter-particulate collisions beome a significnat factor). An in depth discussion that suggests that these two points can be satisfied is given in Chapter 6 section 6.4.2.

An empirical factor based upon the area contained beneath the curve of aberration for a cylindrical mirror fitted to a quadrant of the pipe bore, and the area of the quadrant of the pipe bore itself, was used (see Figure 6C.2). The expression used to derive this factor is as shown below:-

$$F_c \propto \frac{\pi R_p^2}{2\left(A_{\text{quadrant}} - A_{\text{aberration}}\right)} \qquad (6C.2)$$

Where F_c is a factor that is related to the increase in the intensity of particle impacts; R_p is the radius of the pipe bore; $A_{quadrant}$ is the area of the quadrant of the pipe bore being considered and $A_{aberration}$ is the area under the curve of aberration for a cylindrical concave mirror fitted in the same quadrant.

For the bend tested in this project, equation 6C.2 predicts that the factor will have a value of 4.33. The ratio of the predicted erosive penetration at the puncture point to the actual erosive penetration is 3.91. These two values are not dissimilar, being within 10.8% of each other.

Figure 6C.2 Illustration of the areas being considered for the determination of the factor, F_c.

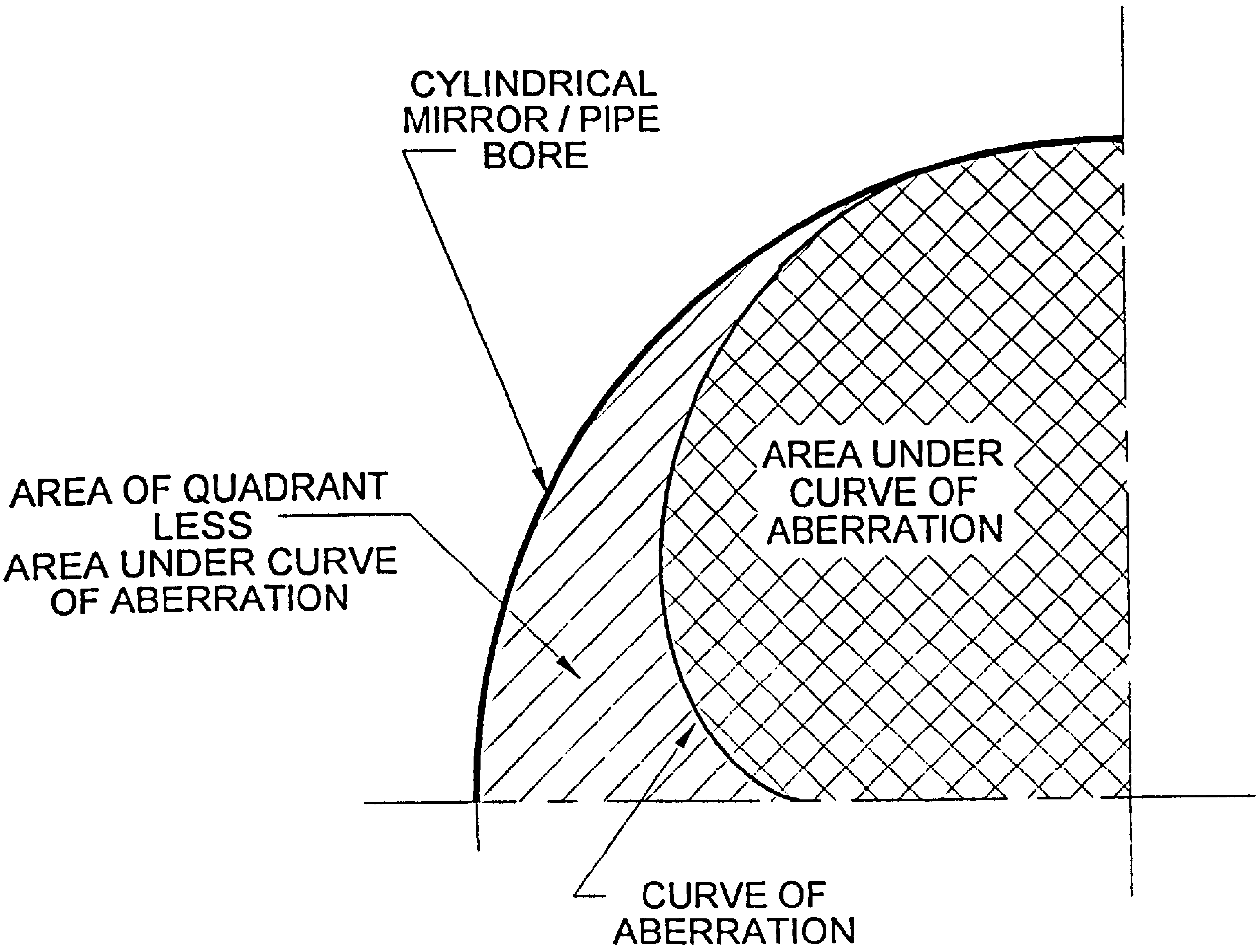

6C.5 MathCad Listing of the Model for the Prediction of the Position and Penetration of the Test Bend Based Upon the Curve of Aberration

The following seven pages of this Appendix contain the MathCad listing for the model of bend puncture based upon the curve of aberration for a cylindrical mirror.

The Model for Predicting Bend Life Based Upon the Curve of Aberration for a Cylindrical Mirror

This model consists of a four parts; a) the construction of the curve of aberration for a cylindrical mirror, b) derivation of an expression that relates the apex of this curve to the location of the mean second impact position of the particles against the pipe wall, c) determining the rate of erosion damage using the power law erosion model derived in Chapter 4 section 4.3.4, and d) determining the accumulation and inter-particulate effect coefficient by using the areas under the curve of aberration for a cylindircal mirror fitted to the pipe bore geometry.

Specification of the Input Variables:

Pipe bore radius:- $R := 26.5$ (Working in millimeters).

X incremental distance specification:- $\delta := \frac{R}{40}$ $i := 1,2..39$

Calculation of the Interception Points Between the Vertical Planes and The Circle:

$y_i := \sqrt{R^2 - (\delta \cdot i)^2}$ y is the value of the vertical distance of the intercept above the axis of the origin.

Calculation of the Equation of the Tangent and Normal to the Circle at these Points:

$\sqrt{R^2 - x^2}$ by differentiation, yields $\frac{-1}{\sqrt{R^2 - x^2}} \cdot x$ this differential enables the slope of the tangent to be assessed.

Substitution of the values of x & R to find the slope of the tangent.

$$m_{tan_i} := \frac{-1}{\sqrt{R^2 - (i\,\delta)^2}} \cdot (i \cdot \delta)$$

The slope of the normal is the reciprocal of the slope of the tangent.

$$m_{norm_i} := \frac{-1}{m_{tan_i}}$$

The equation of the slopes of the tangent and normal to the circle at the selected points are now defined. The intercepts with the y axis for the tangent is the only term that is now required since the intercept of any normal to a tangent of a circle will pass through the centre of the circle.

$$int_{tan_i} := -m_{tan_i} \cdot i \cdot \delta + y_i$$

Calculation of the Angle θ i.e. the Angle Between the Normal and Vertical Line

$\theta_i := \operatorname{atan}\left(\frac{i \cdot \delta}{y_i}\right)$ The angle of the rebound trajectory from the vertical inbound line is twice this angle.

Calculation of the Position Where the Rebound Trajectory Crosses the X-axis.

$$x_{ab_i} := \left| y_i \cdot \tan(2 \cdot \theta_i) \right|$$

Calculation of the Position of the Intercept of the Y-axis and the Rebound Trajectory

$$ytraj_{int_i} := \mathrm{if}\left[2\cdot\theta_i < \frac{\pi}{2}, \frac{x_{ab_i} - i\cdot\delta}{\left|\tan\left(2\cdot\theta_i\right)\right|}, \left(i\cdot\delta + x_{ab_i}\right)\cdot\tan\left(2\cdot\theta_i - \frac{\pi}{2}\right)\right]$$

The Slope of the Rebound Trajectrory is Calculated as follows:-

$$mtraj_i := \mathrm{if}\left(2\cdot\theta_i < \frac{\pi}{2}, \frac{y_i}{x_{ab_i}}, \frac{ytraj_{int_i}}{i\cdot\delta + x_{ab_i}}\cdot -1\right)$$

To find the Intercept Between Neighbouring Rebound Trajectories

These points will lie on the curve of aberration for the cylindrical mirror being considered.

$j := 2,3..39$

$$X_{cacm_j} := \frac{ytraj_{int_j} - ytraj_{int_{j-1}}}{mtraj_{j-1} - mtraj_j} \qquad Y_{cacm_j} := mtraj_j\cdot X_{cacm_j} + ytraj_{int_j} \qquad xx := 0,0.5..26.5$$

Fitting a Cubic Spine curve (with cubic ends) to the points found for the Curve of Aberration:-

The most important figure that is required is the intercept on the y axis for the curve of aberration. This can be found by either using the cubic spline curve fitting routines or the multiple curve fit routines. The cubic spline method will be used here.

Cubic Spline Fit:-

$k := 1,2..38 \qquad X_c := \mathrm{submatrix}\left(X_{cacm},2,39,1,1\right) \qquad Y_c := \mathrm{submatrix}\left(Y_{cacm},2,39,1,1\right)$

$vs1 := \mathrm{cspline}\left(X_c, Y_c\right) \qquad xx := 0,0.25..26.5$

$Y_{int} := \mathrm{interp}\left(vs1, X_c, Y_c, 0\right) \qquad Y_{int} = 13.264$

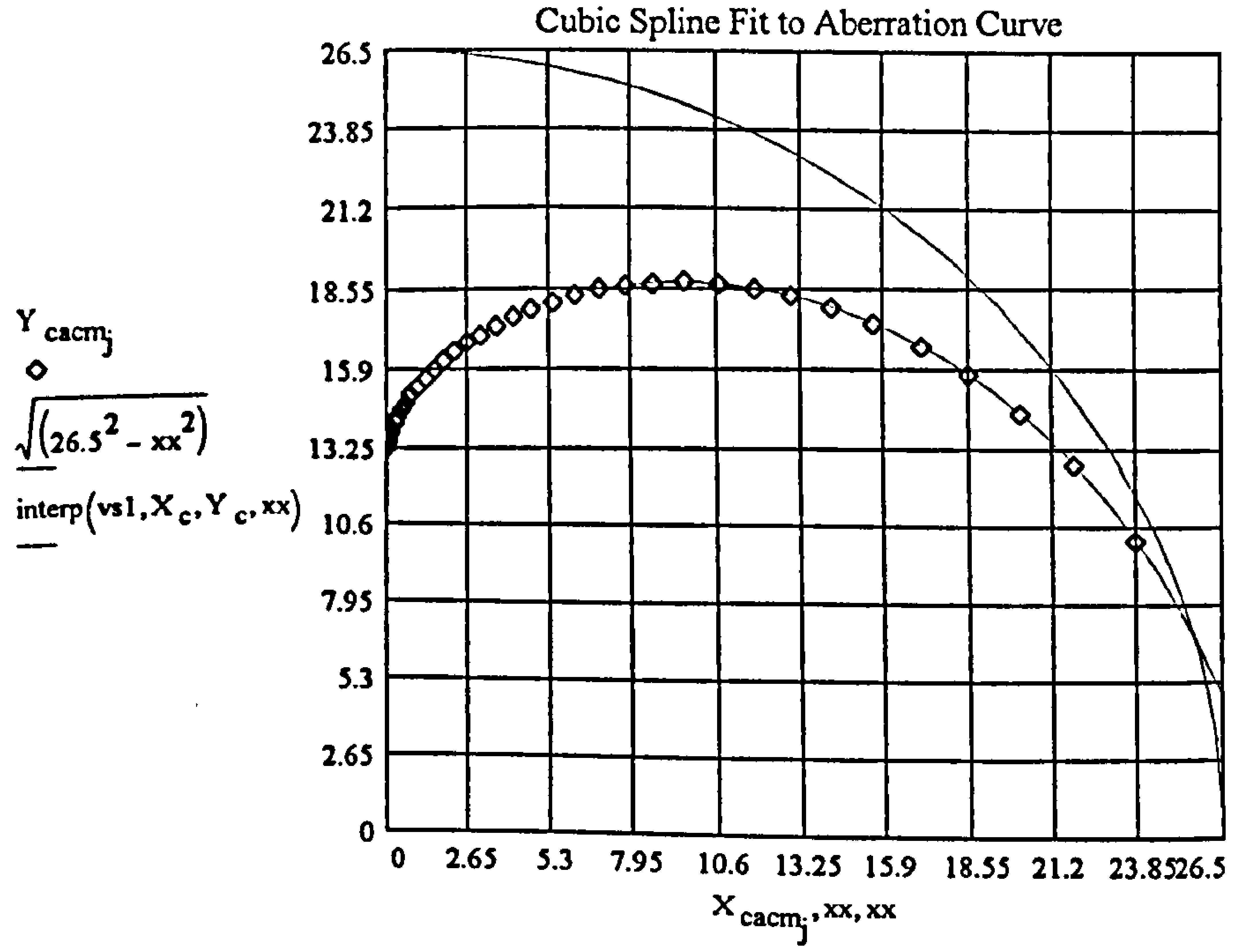

The apex of the cubic spline and the y axis occurs at:- $y_{st} = Y_{int}$

This is the value of the suggested start position for the trajectory that will be used to find the location of the puncture point in the bend.

__Using the Apex of the Curve of Aberration to Determine the Position of the Puncture Point in the Region of Secondary Impacts.__

Selection of In Bore Start Position: $y_{st} = 13.264$

$y_v = 723.5$

__Calculation of the Primary Impact Location Based on the Particle Start Position Being Positioned at the Bend Intrados:-__

$x_{pl} := \sqrt{776.5^2 - y_v^2}$ $x_{pl} = 281.957$ $PI_{pt} := \mathrm{acos}\left(\frac{y_v}{776.5}\right)$ $PI_{pt} = 21.292 \cdot \mathrm{deg}$

__Calculation of the Particle Trajectory After Primary Impact:-__

$\sqrt{R^2 - x^2}$ by differentiation, yields $\frac{-1}{\sqrt{R^2 - x^2}} \cdot x$ This differential enables the slope of the tangent to be assessed.

$stan_{pl} := \frac{-1}{\sqrt{776.5^2 - x_{pl}^2}} \cdot x_{pl}$ $stan_{pl} = -0.389713$ The slope and intercept of the tangent along with the impact angle on the pipe wall are calculated here.

$inttan_{pl} := y_v - stan_{pl} \cdot x_{pl}$ $inttan_{pl} = 833.383$

$\phi 1 := \mathrm{atan}\left(\frac{inttan_{pl} - y_v}{x_{pl}}\right)$ $\phi 1 = 21.292 \cdot \mathrm{deg}$

__Calculation of the Equation Governing the Particle Trajectory After Primary Impact:-__

$x_{new} := (776.5 - y_{st}) \cdot \cos\left(\frac{\pi}{2} - \phi 1\right)$ $x_{new} = 277.141$

$y_{new} := (776.5 - y_{st}) \cdot \sin\left(\frac{\pi}{2} - \phi 1\right)$ $y_{new} = 711.141$

$stan2 := \frac{x_{new} \cdot -1}{y_{new}}$ $stan2 = -0.38971$

$inttan_{p2} := \tan(\phi 1) \cdot x_{new} + y_{new}$ $inttan_{p2} = 819.147$

__Finding the Intercept Between the Second Trajectory Line and the Outer Radius of the Circle in Cartesian Location Coordinates__

$y_{p2} = stan2 \cdot x_{p2} + inttan_{p2}$

$x_{p2}^2 + y_{p2}^2 = 776.5^2$ The solution of these two equations that gives the greatest value of x is used as shown below:

by substitution, yields

$x_{p2}^2 + (stan2 \cdot x_{p2} + inttan_{p2})^2 = 602952.25$

has solutions:-

$$\begin{bmatrix} \frac{.5}{\left(1.+\mathrm{stan2}^2\right)}\cdot\left[-2.\cdot\mathrm{stan2}\cdot\mathrm{inttan}_{p2}+\sqrt{\left(-4.\cdot\mathrm{inttan}_{p2}{}^2\right)+2411809.+2411809.\cdot\mathrm{stan2}^2}\right] \\ \frac{.5}{\left(1.+\mathrm{stan2}^2\right)}\cdot\left(-2.\cdot\mathrm{stan2}\cdot\mathrm{inttan}_{p2}-1.\cdot\sqrt{-4.\cdot\mathrm{inttan}_{p2}{}^2+2411809.+2411809.\cdot\mathrm{stan2}^2}\right) \end{bmatrix}=\begin{pmatrix}410.297\\143.985\end{pmatrix}$$

$$x_{p2}:=\frac{.5}{\left(1.+\mathrm{stan2}^2\right)}\cdot\left[-2.\cdot\mathrm{stan2}\cdot\mathrm{inttan}_{p2}+\sqrt{\left(-4.\cdot\mathrm{inttan}_{p2}{}^2\right)+2411809.+2411809.\cdot\mathrm{stan2}^2}\right]$$

$x_{p2}=410.297$

$y_{p2}:=\sqrt{776.5^2-x_{p2}{}^2}$ $\quad y_{p2}=659.249$

Comparison Between the Actual and Predicted Puncture Locations in Cartesian Coordinates:-

Experimental Impact Location		Predicted Impact Location
$x_{pun}:=776.5\cdot\sin\left(\frac{28.5\cdot\pi}{180}\right)$	$x_{pun}=370.514$	$x_{p2}=410.297$
$y_{pun}:=776.5\cdot\cos\left(\frac{28.5\cdot\pi}{180}\right)$	$y_{pun}=682.401$	$y_{p2}=659.249$
Puncture occurred 28.5° around the bend radius.		$\mathrm{Pun}_{pt}:=\mathrm{acos}\left(\frac{y_{p2}}{776.5}\right)$
		$\mathrm{Pun}_{pt}=31.897\cdot\mathrm{deg}$

Calculation of the Angle of Impact at the Secondary Impact Location

$\mathrm{stan}_{p3}:=\frac{-1}{\sqrt{776.5^2-x_{p2}{}^2}}\cdot x_{p2}$ $\quad \mathrm{stan}_{p3}=-0.62237$

The slope and intercept of the tangent along with the impact angle on the pipe wall are calculated here.

$\mathrm{inttan}_{p3}:=y_{p2}-\mathrm{stan}_{p3}\cdot x_{p2}$ $\quad \mathrm{inttan}_{p3}=914.605$

$\phi2:=\mathrm{atan}\left(\frac{\mathrm{inttan}_{p3}-y_{p2}}{x_{p2}}\right)-\phi1$ $\quad \phi2=10.605\cdot\mathrm{deg}$

$xx:=0,10..780$

Calculation of the Erosion Damage at Each Impact Model Found for this Simulation:-

Interpolated values for the particle velocity and concentration at the start position determined above are as follows:-

$V_{st}:=25.6$ $\quad \rho_{con}:=3.5$

Calculation of the Total Conveying Time:-

The total mass of abrasive material conveyed before bend failure occurred was:-

$M_t:=5475\cdot\mathrm{kg}$ $\quad \mathrm{MFR}_t:=0.25935\cdot\frac{\mathrm{kg}}{\mathrm{sec}}$

The total conveying time is found:-

$\mathrm{Tct}:=\frac{M_t}{\mathrm{MFR}_t}$ $\quad \mathrm{Tct}=2.111\cdot10^4\cdot\mathrm{sec}$

Selection of an Arbitary Segment Area:-

$As := \pi \cdot 0.005^2$ $\qquad As \cdot m^2 = 7.854 \cdot 10^{-5} \cdot m^2$

Use of the Power Law Erosion Model Derived from the Erosion Tests to Predict the Penetration of the Test Bend at the Secondary Impact Site.

The model being used was derived in section 4.3.4 Chapter 4 from experimental results.

Mean Distance Between Particles:-

$$D := \frac{69.599}{\left(\rho_{con}\right)^{0.286511}} \qquad D = 48.61$$

Calculation of the Power Law Exponent n:-

$c_n := 0.00988 \cdot D + 1.239$ $\qquad c_n = 1.719$

Reading in Raw Data for m_n and Extracting an Interpolated Reading for this Variable:-

$$mndat := \begin{pmatrix} 1 & 0.0143 \\ 4 & 0.02399 \\ 13 & 0.0238 \end{pmatrix}$$

$rx := mndat^{<1>}$ $\qquad mnv := mndat^{<2>}$

$vsmn := lspline(rx, mnv)$ $\qquad rv := 0, 0.1 .. 13$

$m_n := interp\left(vsmn, rx, mnv, \rho_{con}\right)$

$m_n = 0.023$

Finding a Value for n:-

$n := m_n \cdot \phi 2 + c_n$ $\qquad n = 1.72346$

Calculation of the Power Law Constant a:-

$c_a := 0.0007983 \cdot -1 \cdot D + 0.0751$ $\qquad c_a = 0.036$

Reading in Raw Data for m_a and Extracting an Interpolated Reading for this Variable:-

$$madat := \begin{pmatrix} 1 & 0.0605 \cdot -1 \\ 4 & 0.0935 \cdot -1 \\ 13 & 0.0955 \cdot -1 \end{pmatrix}$$

$rx := madat^{<1>}$ $\qquad mav := madat^{<2>}$

$vsma := lspline(rx, mav)$ $\qquad rv := 0, 0.1 .. 13$

$m_a := interp\left(vsma, rx, mav, \rho_{con}\right)$

$m_a = -0.089$

Finding a Value for a:-

$a := c_a \cdot e^{m_a \cdot \phi 2}$ $\qquad a = 0.0357$

Finding a Value for the Erosion Rate Using the Power Law Model:-

$ERate := a \cdot V_{st}^{\,n}$ $\qquad ERate \cdot 10^{-9} \cdot \frac{m^3}{kg} = 9.544 \cdot 10^{-9} \cdot kg^{-1} \cdot m^3$

The erosion rate has units of mm^3/kg of abrasive striking the wall surface.

The actual mass of abrasive striking the small segment of the pipe wall being considered is now calculated.

$$\mathrm{Mstrk} = \rho_{con}\cdot\frac{kg}{m^3}\cdot V_{st}\cdot\frac{m}{sec}\cdot As\cdot m^2\cdot Tct \qquad \mathrm{Mstrk} = 148.558\cdot kg$$

The volume loss is as follows:-

$$V_{loss} := ERate\cdot 10^{-9}\cdot\frac{m^3}{kg}\cdot Mstrk \qquad V_{loss} = 1.418\cdot 10^{-6}\ \cdot m^3$$

The area affected by the elemental flow stream being considered is:-

$$A_{strk} := As\cdot\frac{1}{\cos\left(\frac{\pi}{2} - \phi 2\right)}\cdot m^2 \qquad A_{strk} = 4.267\cdot 10^{-4}\ \cdot m^2$$

The penetration damage caused to this elemental area is:-

$$P_p := \frac{V_{loss}}{A_{strk}}\cdot\cos\left(\frac{\pi}{2} - \phi 2\right) \qquad P_p = 6.11483\cdot 10^{-4}\ \cdot m$$

Comparisons Between the Actual and Predicted Values of Bend Wall Penetration at the Puncture Location

The secondary impact location on the bend wall, whose initial thickness was 2.39 mm, was punctured.

$$W_{th} := 2.39\cdot 10^{-3}\cdot m$$

There main reason why the predicted amount of penetrative erosion damage in the secondary impact area is considerably different from that which actually occurred is that the number of particle impacts occurring on any given area of the pipe wall increases due to the particle accumulation caused by the effects of the internal shape of the pipe bend wall. Attempts to estimate the effects of these variables will be made during in the following sections of this document.

$$\frac{W_{th}}{P_p} = 3.909$$

Calculation of the Area Under the Cubic Spline Fit to the Curve of Aberration of a Cylindrical Mirror

NB: The coefficents contained in vs1 are the second derivatives of the curves taken at the position of each of the data points; these values are directly comparable with the slope of the cubic line at these points. The cspline function assumes the cubic spline has cubic line segments at each end of the data set.

$$x := 0, 0.5 .. 26.5 \qquad N := \mathrm{rows}(vs1) \qquad N = 38$$

$$ij := 1 .. N - 1 \qquad h_{ij} := \mathrm{if}\left(ij<N, y_{ij+1} - y_{ij}, 0\right)$$

The cubic spline fit referred to is simply a method by which a large series of cubic curves are fitted between each pair of data points. The coefficients of each of these curves is determined in the section below following equations laid out by Etter in reference [E4].

$$A1_{ij} = \frac{1}{6\cdot h_{ij}}\cdot\left[vs1_{(ij+1)} - vs1_{ij}\right] \qquad C1_{ij} := \frac{1}{h_{ij}}\cdot\left[Y_{c_{(ij+1)}} - Y_{c_{ij}}\right] - \frac{1}{6}\cdot h_{ij}\cdot\left[vs1_{(ij+1)} + 2\cdot vs1_{ij}\right]$$

$$B1_{ij} = \frac{1}{2}\cdot vs1_{ij} \qquad D1_{ij} := Y_{c_{ij}}$$

The area under the fitted cubic spline curve that forms the cubic spline curve is as follows:-

$$\sum_{ij}\int_{y_{ij}}^{y_{(ij+1)}}\left[A1_{ij}\cdot\left(x-y_{ij}\right)^{3}+\left[B1_{ij}\cdot\left(x-y_{ij}\right)^{2}+\left[C1_{ij}\cdot\left(x-y_{ij}\right)+D1_{ij}\right]\right]\right]dx=-296.80477$$

The difference between this area and that in each quadrant of the pipe bore is as follows:-

$$A_{dif}:=\frac{\pi\cdot 26.5^{2}}{4}+\sum_{ij}\int_{y_{ij}}^{y_{(ij+1)}}\left[A1_{ij}\cdot\left(x-y_{ij}\right)^{3}+\left[B1_{ij}\cdot\left(x-y_{ij}\right)^{2}+\left[C1_{ij}\cdot\left(x-y_{ij}\right)+D1_{ij}\right]\right]\right]dx$$

$$A_{dif}=254.741$$

The particles become concentrated into half of the pipe bore by the time the puncture point is reached hence half the ratio.

$$F_{c}:=\frac{\pi\cdot 26.5^{2}}{2\cdot A_{dif}}$$

$$F_{c}=4.33025$$

$$\frac{F_{c}\cdot P_{p}}{W_{th}}=1.108$$

6C.6 Conclusions

The result of using this model is very encouraging. Owing to the ease of use and its simplicity, once corroboration of its use has been obtained, the model should prove to be an effective technique for estimating the location of the puncture point, the rate of wall penetration and the local concentration of particles in long radius bends in pneumatic conveyors.

Since the model described above has a good physical basis, a discussion regarding the further development of this model is contained in Chapter 7.

PUBLICATIONS

powder handling & processing Volume 5, No. 2, June 1993

Wear in Pneumatic Conveying Pipelines

A Review of Past and Present Work

A.J. Burnett, U.K.

Wear of the components of a pneumatic conveying system is one of the major reasons why such systems suffer unplanned maintenance. This would not be a problem if the wear lives of the components could be predicted with reasonable accuracy. However, our knowledge is not advanced enough at present.

The problem of wear in such systems is a very complex one in which several phenomena have important parts to play, with the process being affected by properties of the surface, the particles and the flow as well as the system geometry. This paper includes a review and comparison of the research based on experimental work carried out on both industrial and bench sized equipment that has taken place. It is concluded that none of the mathematical models so far derived have been general enough to be used for all possible situations. Details of an experimental wear rig where the centrifugal effect is used to project particles at a series of targets being developed at The Wolfson Centre for Bulk Solids Handling Technology, University of Greenwich will be presented. This device has the advantage that a large number of specimens can be tested under identical conditions, simultaneously. A discussion of the intended work plan for this research will then be presented in conjunction with details of possible future developments for this project.

1. Introduction

A considerable amount of work has been dedicated to the investigation of wear in industrial plant subjected to erosive damage by particulate impact. In order to prolong plant life, various wear resistant materials are commonly used in components which suffer from the worst erosive damage. These materials must be selected carefully because those which are most erosion resistant under some circumstances are not necessarily the most resistant under others.

Pneumatic conveyors are widely used in industry. Through the nature of their operation they are susceptible to extreme amounts of erosive damage in certain places. The components of pneumatic conveyors which can suffer severely from erosion are the pipeline bends, where particle-pipe wall interactions are at their greatest. Fig. 1 shown below showed damage that can be typically found in the bends of such conveyors.

Fig. 1: Examples of eroded pneumatic conveyor bends showing considerable penetrative damage and weight loss. (Ref. *J.S. Mason*, Phd Thesis, Liverpool Polytechnic, 1972)

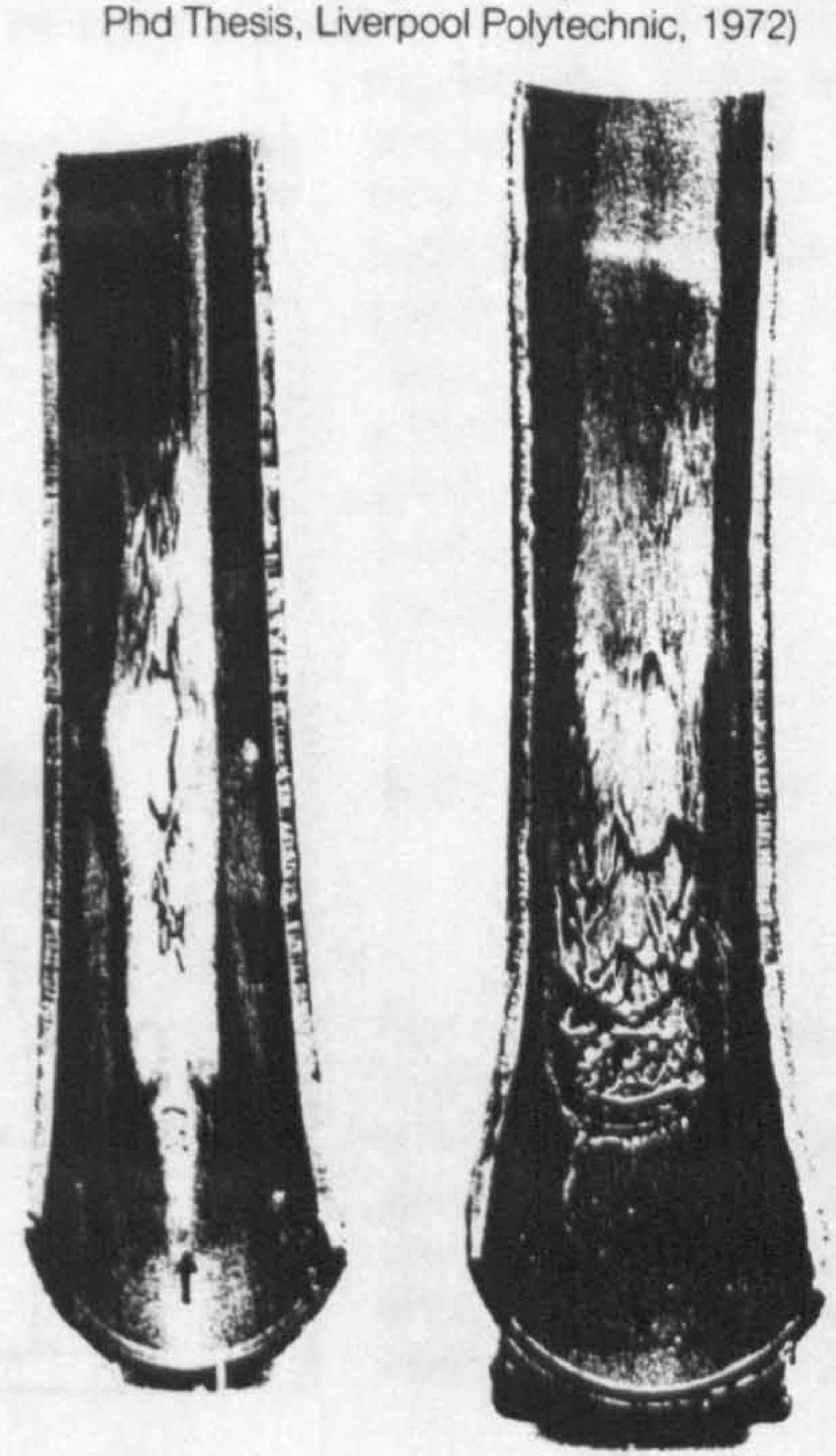

One way in which the problem of predicting the wear life may be addressed is to build a pneumatic conveying pilot rig and conduct trials to determine the bend wear, however this is expensive and time consuming. To alleviate these drawbacks a suitable bench sized test facility from which information concerning erosion in pneumatic conveyors can be determined is desirable.

This paper includes a review of the current state of knowledge on erosive wear in general terms. In addressing the problems mentioned earlier a short description of the objectives for a new research programme being undertaken at The Wolfson Centre at The University of Greenwich is presented.

2. The Nature of the Problem

2.1 The Problem of Two Phase Turbulent Flow

The details of single phase turbulent flow have only recently been modelled with any degree of accuracy. The models give rise to very complex systems of equations which require the full power of modern micro-processors for their solution [1,2]. It is therefore to be expected that the modelling of the interaction between the particles and the gas will also require the solution of a complex set of equations. The introduction of particles into a flowing gas stream will induce turbulence, which together with inter-particulate collisions, will randomise the particle dispersion in the conveying line [3]. The particles will be affected to varying degrees by the fluid motion depending on the distributions of size and shape amongst them [4,5]. Effects of this type are seen when the particle size drops below a threshold of approximately 100 µm diameter. In this instance the momentum of the particles is not great enough to overcome the

A.J. Burnett, The Wolfson Centre for Bulk Solids Handling Technology, The University of Greenwich, London, SE 18 6PF, U.K.
Tel.: +44 81 316 86 46; Fax: +44 81 316 86 47
Details about the author on page 196
If contacting direct, please refer to **php 2/93** as source of information.

forces inflicted on the particles by the motion of the air. To further complicate matters there is a considerable problem with the modelling of particle rebound and the subsequent 'shielding' of the eroding surface that occurs [6]. ('Shielding' is the term used to describe·the manner in which incoming particles are prevented from causing the maximum possible damage to the eroding surface by collisions with the rebounding particles). Another area in which very little progress has been made is the understanding of the effect of the change in component profile with erosive damage, and the effect this has on the flow regime and erosion patterns within the pipe bend. However, this problem is inextricably linked with the erosion behaviour itself. Fig. 2 is illustrative of the kind of flow regime that may occur after severe erosive damage has occurred. However it must be noted that the conveying velocity used in the testing of this bend is not representative of those commonly seen in pneumatic conveyors, where velocities are usually significantly lower.

Numerous approximate methods for determining the impact location, the particle velocity, the angle of attack and the particle flux on the surface, have been derived. To make these models more easily soluble and to simplify their development, many significant variables have been eliminated. Examples of these models are provided by Yeung [7], Hoadley et al [8], Benchaita [9] and Dosanjh and Humphrey [10].

2.2 The Problems of Determining Particle Properties and Their Effects

Coupled with the complexity of turbulent two phase flow as mentioned in section 2.1 is the nature of the eroding material itself. Conflicting evidence of the effects of particle properties has been reported. Erosion tests specifically designed to investigate the effects of particle properties such as shape and size have been carried out [11,12,13,14], however they have proved to be inconclusive. The major difficulty with assessing the propensity of the particles to cause erosive damage is the fact that particle size and shape are difficult to quantify. The work of Svarovsky [15] shows the methods by which shape and size are commonly measured. However, the shape of a particle remains one of the most difficult variables to quantify. Except for results obtained by use of bulk solids which show the extremes of particle shape such as the spherical shape of glass ballotini for quantitative erosion rates, very little information is available. Major changes in the erosion rate with changes in the particle shape for mild steel have been reported by Cousens et al [14]. It has been found that the hardness of the particle is of very little use in determining particles erosive capability. For example, Head et al. [16] reported that fluorite caused more erosive damage than alumina, which is considerably harder, under certain conditions. From the findings of Cousens and Head it is clear that further work in this area is required.

In a bulk solid material it is common to find many constituents. Each constituent of the bulk material will show a different propensity to cause erosive damage. This confuses the understanding with which engineers view the erosion problem in their plant. The problems associated with the ability of the various constituents of a bulk material to cause erosive damage is of major importance to the coal processing industry, and a large amount of work has been carried out on determining the erosive capability of coal [17,18]. This problem is also common with the handling of wheat grain as well as other bulk solid materials.

Fig. 2: A schematic of a particle flow pattern that is possible in a pneumatic conveyor bend. (v = 85 m/s, SLR = 2.6) [Ref. *J.S. Mason*, Phd Thesis, Liverpool Polytechnic, 1972]

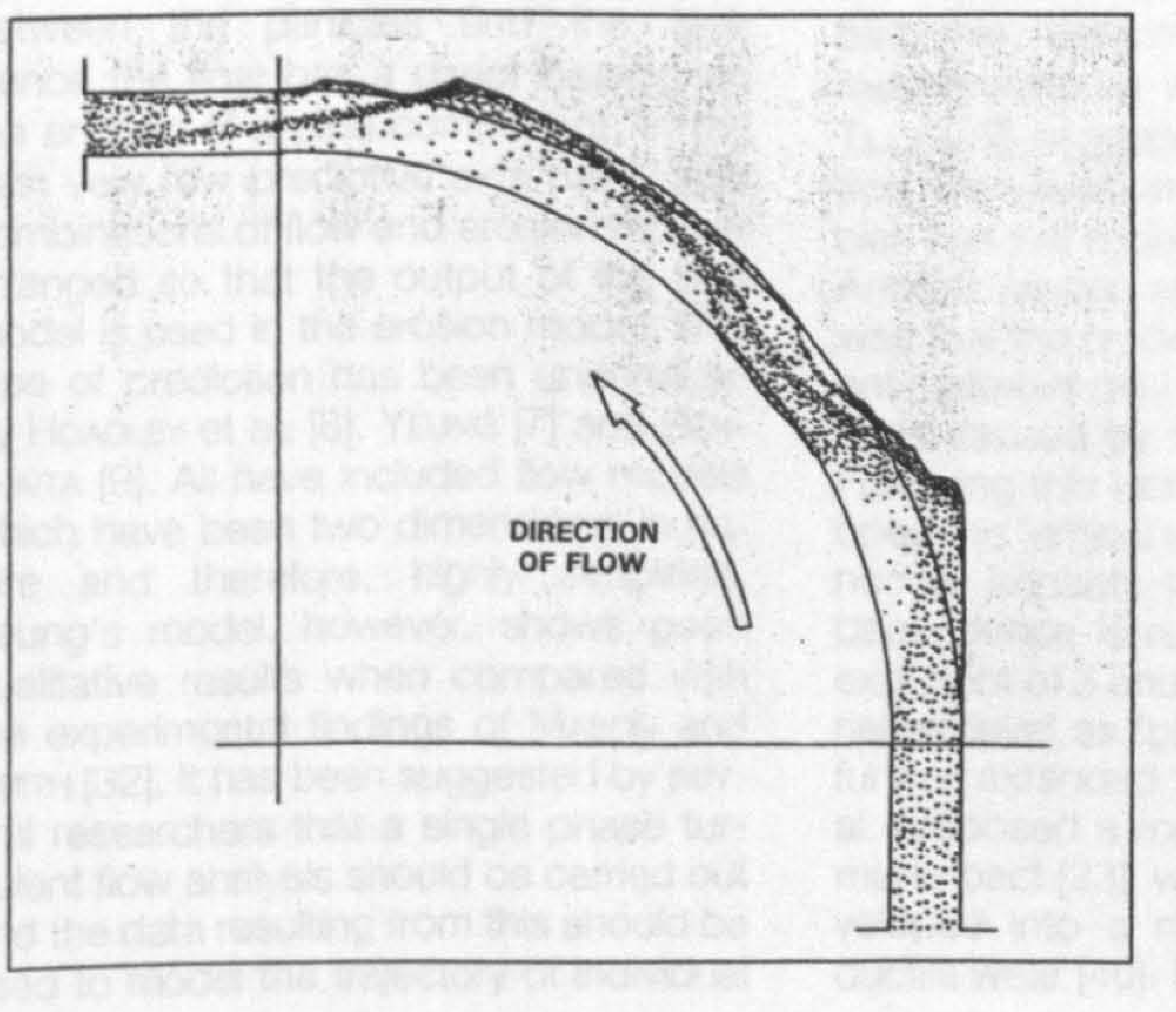

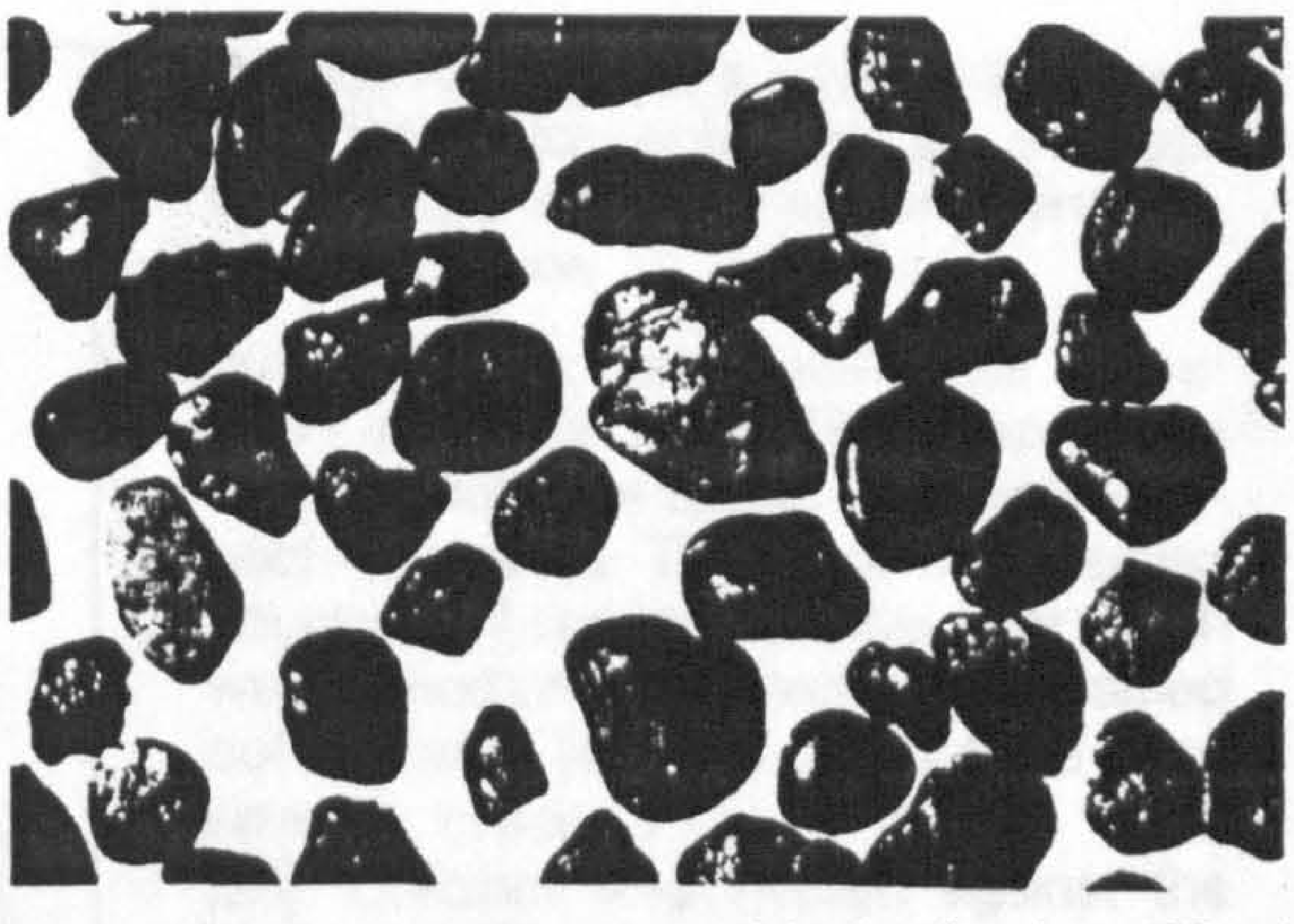

Fig. 3: Magnified view of ilmenite particles (median size = 195 µm) to illustrate the likely variation of size and shape within a typical bulk solid material

2.3 The Effects of Wall Material Properties

Numerous wear resistant material types are used in industry to alleviate the problems of wear caused by both abrasive and erosive particulate interaction. Each material has a different micro-structure and hence a different behaviour when subjected to particulate attack. It is now widely recognised that the velocity of impact, the angle of attack, the geometry of the system, and wall and particle properties will all affect the erosion resistance of the material. The diagram below (Fig. 4) shows the erosion curves for a ductile material and a brittle material [19,20]. These curves are from the work of two specific researchers but they are typical of those seen for materials which behave in either a brittle or ductile manner. However, the detailed erosion behaviour of materials tends to be very complex.

Several factors must be taken into account before the material behaviour can be assessed. The impact of a single particle is a high speed event, and as a consequence the material is subject to high strain rate effects [21]. Experimental corroboration of this fact is given by Buttle et al. [22]. As a consequence theoretical models which incorporate the results of quasi-static material property data are flawed. It can be shown that in high strain rate testing of some materials their properties can vary quite substantially [23].

In the case of the erosion of ductile materials, particulate impact will cause a large amount of plastic deformation. In turn a temperature rise in the material will occur. The effects of this temperature rise will further alter the micro-structure of the material.

The mechanisms by which this occurs are still a matter of debate, although some progress has been made recently by Sundararajan et al. [12,24], Cousens et al. [25] and Hutchings et al. [26]. It is also probable that some form of micromachining mechanism is also active although evidence for the various mechanisms which are occurring during erosion are still the subject of investigation [27].

For brittle materials, less work has been carried out when compared to the volume of research on the erosion of ductile materials. 'Brittle' is a term which is applicable to a wide range of diverse materials

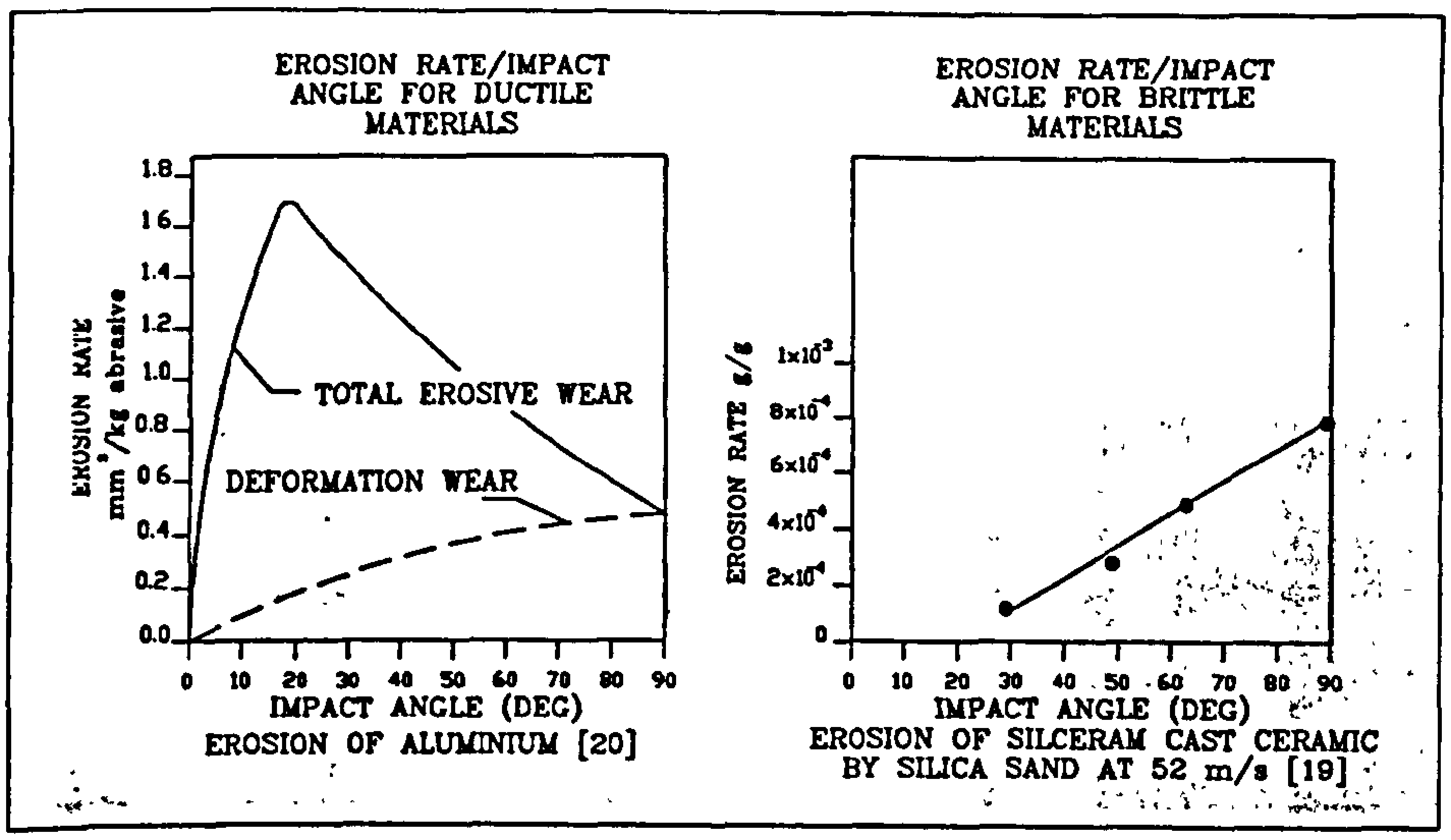

Fig. 4: Examples of the erosion behaviour of materials when subjected to particulate impact at varying angles of attack

incorporating cast ceramics such as basalt and fused materials such as alumina. The micro-structural details of these materials are quite different and it is highly probable that the mechanisms by which material is removed may vary with different micro-structures [17,19,28].

In comparison to the quantity of work carried out on metallic and ceramic materials the information on elastomeric and polymeric material erosion resistance is small. Natural rubber and polyurethane materials have been investigated by Arnold et al. [29] and Li et al. [30], whilst the determination of the particle impact erosion resistance of polymers has been carried out by Walley et al. [31]. The properties which effect the erosive damage of these materials is still open to debate.

3. Modelling Approaches That Have Been Used in the Past

The flow regime within the pipeline will dictate the locations of the impact between the particles and the wall. Hence the flow has a direct bearing on the erosion of a pipe component. In the past very few predictive aids have used combinations of flow and erosion models arranged so that the output of the flow model is used in the erosion model. This type of prediction has been undertaken by Hoadley et al. [8], Yeung [7] and Benchaita [9]. All have included flow models which have been two dimensional in nature and therefore, highly simplified. Yeung's model, however, shows good qualitative results when compared with the experimental findings of Mason and Smith [32]. It has been suggested by several researchers that a single phase turbulent flow analysis should be carried out and the data resulting from this should be used to model the trajectory of individual particles [4,5]. There is a problem, however, with models of this sort: the solids to air loading ratio on a mass basis must be less than 1 since inter-particulate collision effects have not yet been incorporated into a model of this sort. The only model which in any way accounts for inter-particulate collisions, the effects of 'shielding' by rebounding particles and greater solids loading ratios is the Monte-Carlo analysis work of Kitron et al. [3].

Several models for predicting the amount of erosive wear have been proposed. The early models of Finnie [33] and Bitter [20,34] predicted that erosion would occur by a micro-machining mechanism. The kinetic energy of the particles at impact was used as the driving energy for the erosion, and the models predicted a square law relationship between erosion rate and impact velocity.

However, several other researchers such as Tilly [35], Mills and Mason [36] and Ruff and Weiderhorn [37] to name a few have shown that instead of the erosion rate being proportional to the incident velocity squared, it is related to a higher exponent of the velocity. In an effort to explain this, researchers suggested several mechanisms by which this could occur: Tilly [38] suggested particle fragmentation. However, the degradation of particles has still received very little attention. Another reason stated by Hutchings [21] was that the properties of the wear resistant materials may vary with the high strain rates caused by the particulate impacts. Following this work Hutchings [39] developed the 'critical strain erosion model' for normal impacts where the erosion rate dependence is related to velocity by an exponent of 3 and is dependent on material removal as 'platelets'. The work was further extended when Sundararajan et al. proposed a model for erosion at normal impact [23], which has now been developed into a more general model of ductile wear [40]. Both of Sundararajan's models incorporate a material behaviour equation which accounts for the high strain rates and temperatures encountered in erosion.

For predicting the erosive wear of ceramic materials Finnie [33] proposed a model which was based on Hertzian impact mechanics. The empirically derived equations of ceramic erosive wear which were based on experimental work carried out by Evans [41] and others have been severely criticised by Aghajanian et al. [28]. Criticism was levelled against the proposed models because they were too specific and did not take account of the micro-structure of the ceramics. These, however, are the only models which are available at present. The main difficulty with ceramics is that of accounting for micro-structural variations in their lattice. In some, hard particles are embedded in a glassy matrix in which case it is the glass phase which is usually eroded away. At present no predictive aids for the erosion of elastomers and polymers exist.

It is clear that in a pneumatic conveyor, it is the depth of penetration into a bend by erosive damage which is the important consideration in relation to bend life. In the work of Mills and Mason [36] it was deduced experimentally that the velocity exponent for penetration effects was of the order of 3.5 to 4.5 for mild steel bends in a pilot scale rig. This cannot be explained solely by the models of wear in ductile materials currently in existence. However, the work carried out by Humphrey [4] has pointed out that there is a possibility that the further increments of the velocity exponent can be explained by flow effects rather than those attributed to other variables.

Modelling of the effects of particle fragmentation and particle shielding have received very little attention. The possibility that the pattern of erosion damage may alter the flow behaviour of the suspension, and hence alter the quantity of erosive wear occurring, has hardly been addressed at all. These omissions, coupled with the ongoing problems of producing models for the erosive wear of materials and the understanding of turbulent flow, (two phase or otherwise) account for the limited choice of predictive aids being available in this area. It can be concluded therefore that there is considerable opportunity for the development of new predictive models in this field.

4. Methods of Erosion Testing

The testing of the erosion resistance of a material can be carried out by several methods. Considerable use has been made of bench sized test rigs in the past on which accelerated tests have been carried out, whilst several researchers have carried out work on industrial scale rigs. It has, so far, not been possible to reconcile the results from a bench scale rig to tests carried out on an industrial scale pneumatic conveyor [8, 42].

4.1 Bench Sized Erosion Testing Rigs

Several forms of bench sized test rig have been developed in the past. The first form of rig that will be discussed is the 'air blast' type which was used by Finnie [43] and numerous other workers since. This type of rig has been the subject of an ASTM Standard (Designation: G 76-83 (Re-approved 1989)). Care has to be taken with the design and installation of this rig to ensure that the acceleration length provided is sufficient for the particles to reach their terminal velocities. This rig is also likely to suffer from problems if the average particle size falls within the range of that which is affected substantially by the gas motion [4]. One of the major difficulties, therefore, is that of controlling the particle velocity for a distributed range of particle sizes and ensuring a consistent angle of attack. Another disadvantage is that only one test can be carried out at any one time, hence a considerable length of time will be required to carry out a large number of tests. There is also a possibility that repeatability errors in taking the data may occur.

Another commonly used form of erosion rig is that first used by Goodwin et al. [44]. It consists of a rotating arm which has a target specimen fitted on either end and particulate abrasive is dropped into the path of the arm as it rotates. The rig operates in a vacuum. The rotational velocity of the arm is controlled accurately and this ensures a consistent impact velocity. The rig was first developed to carry out research into the erosive wear of turbine blades at high speed conditions. This rig probably has the greatest control over particle velocity and angle of attack. The number of targets usually seen in this form of rig is two.

Yet another form of rig adopted is that used by Söderberg et al. [45]. This rig takes the form of a spinning disc, onto the centre of which particulate abrasive is dropped. The centrifugal effects are then used to accelerate the particles to the desired velocity whereupon they leave the disc and strike a series of targets which are arranged around it. Up to twenty different targets can be tested simultaneously under identical conditions of velocity and solids loading but at varying angles of attack. As with the 'air blast' type rig the size and mass of each particle will dictate the velocity at which it travels. However, this loss of accuracy can be minimised if care is taken in the measurement of the distribution of the size of the particles used. The major advantage is that a large number of tests can be carried out under identical conditions. The disadvantages are that of determining the mass of material which has struck each target and determining the velocity and angle of attack that the particles have when they strike the targets. It is also probable that the effects of gas motion on the trajectories of particles may cause adverse results for the measurement of the particle velocities.

The other form of rig which has been used extensively to investigate the mechanisms behind single particle removal of material is the 'gas gun'. The shape and size of particle used is limited to unrealistically large sizes and regular shapes. This is not the major problem however; it is now widely recognised that in the majority of erosive wear situations that multiple impacts are required before material removal occurs [25, 39]. None-the-less this rig has been used effectively by Hutchings [46] and Walley et al. [31] for determining material behaviour under impact conditions.

4.2 Industrial Scale Test Facility Use

A large proportion of the industrially scaled pneumatic conveyor erosion testing has been carried out at Thames Polytechnic in London by Mills and Mason [36]. The rigs constructed were of pilot size proportions (50 to 100 mm nominal bore pipelines) designed to simulate industrial conditions. The major difficulty with carrying out work with this form of equipment is that of trying to control the numerous variables involved. The financial costs and costs in terms of time are large but the results tend, however, to be representative of actual erosion patterns seen in pneumatic conveyors.

Several research programs have been carried out on industrial plant units. Most notable amongst these is that of Hoadley and Johnson [8], Johnson et al. [42] and Snowshill [47].

5. Research in Progress at the University of Greenwich

A research programme into the erosion of pneumatic conveying pipeline bends is being undertaken at The Wolfson Centre for Bulk Solids Handling Technology, The University of Greenwich at the present time. The main thrust of this research program is to aid industry by producing an easily workable method by which the wear life of pneumatic conveyor bends can be predicted with a sufficient degree of accuracy. In order to carry out this work a considerable quantity of experimental results are required. To do this two rigs are being developed. The first rig is of the 'centrifugal effect' (see section 4.1) type which will be used to produce the majority of the data necessary. The second will be an industrial scale pneumatic conveying rig. Fig. 5 shows a view of the 'Centrifugal Effect' type erosion testing rig constructed at The Wolfson Centre, whilst Fig. 6 is a schematic illustration of the pneumatic conveyor test facility being used in the research programme.

Both rigs will be suitably instrumented to ensure reasonably accurate measurement of the variables of importance. One of the major goals of this work is to link the erosion test results obtained on the

Fig. 5: View of the partially complete 'Centrifugal Effect' type rig currently under construction at The Wolfson Centre, The University of Greenwich

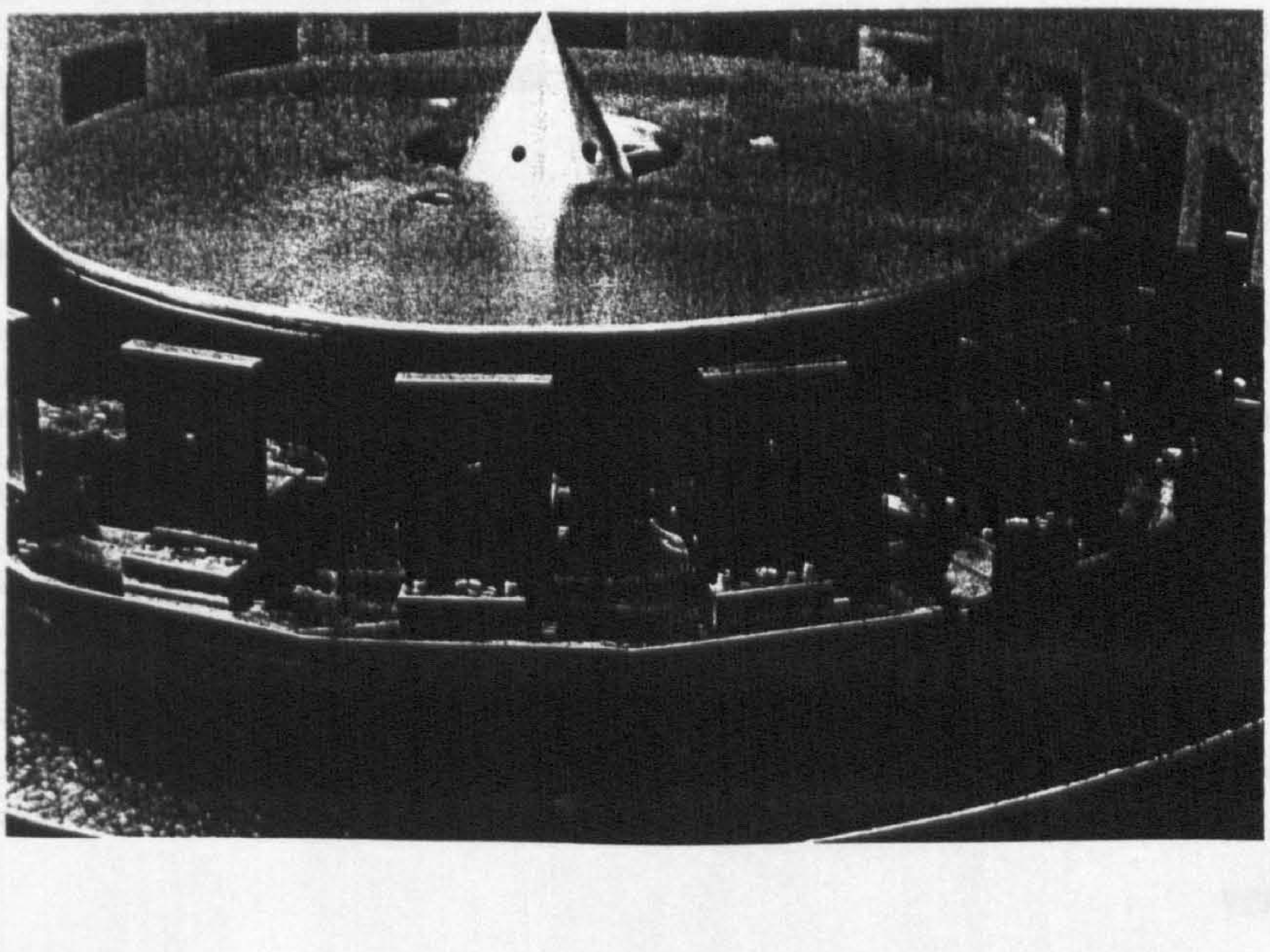

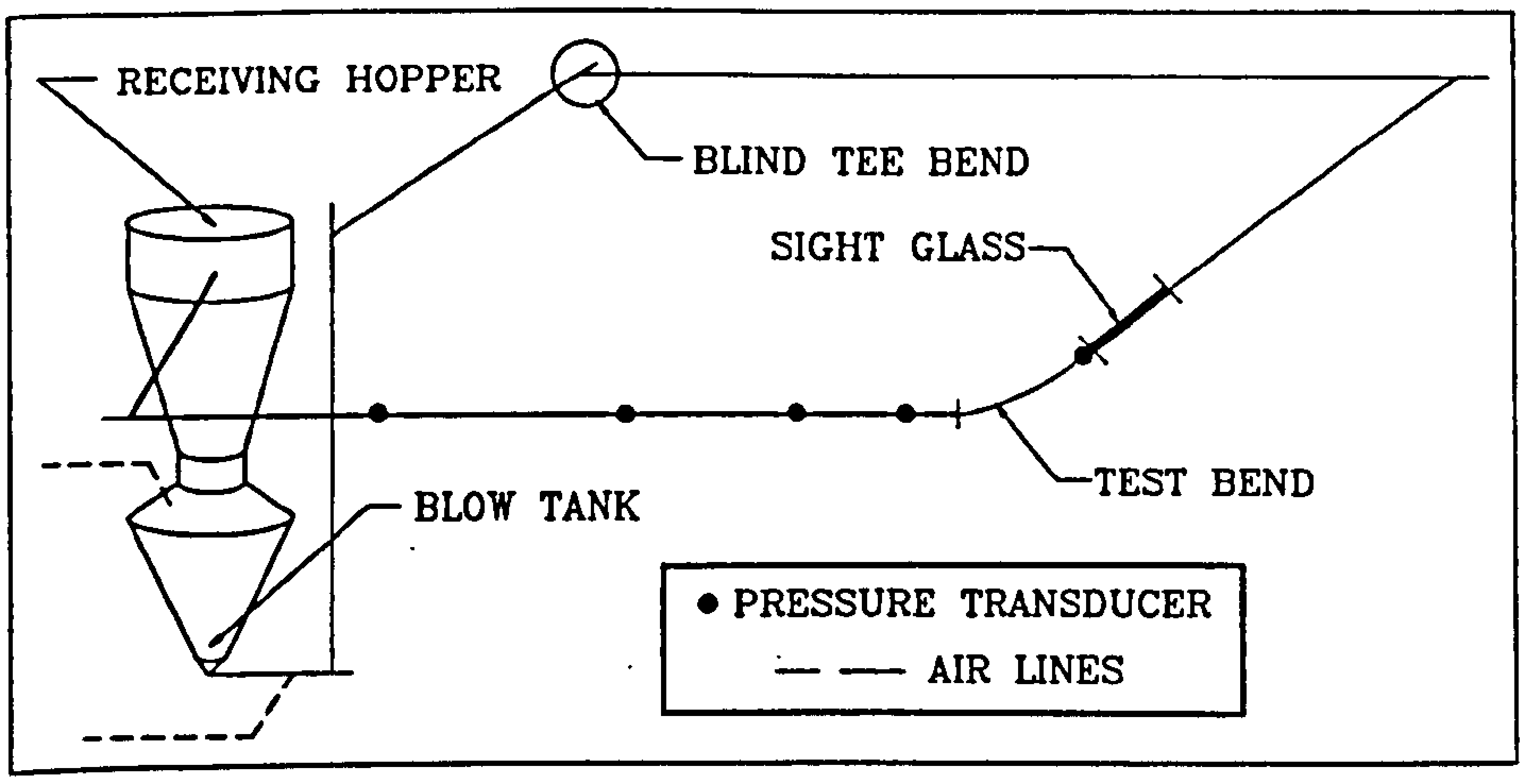

Fig. 6: Schematic of the Pneumatic Conveyor Test Rig in Use at The Wolfson Centre, The University of Greenwich.

'centrifugal effect' rig to those obtained from the pneumatic conveying system. If and when this is achieved it should be possible to predict the rate of erosion in new pneumatic conveyor system designs without having to resort to the building of a pilot sized rig. As a result it is anticipated that both time and money will be more effectively used.

It is expected that the achievement of the goal of obtaining the link between the pneumatic conveyor rig and the 'Centripetal Effect' type erosion tester will prove to be difficult. The main reason for this is that the particle velocity and the localised particle concentrations in a gas solid flow remain very difficult to quantify. In an attempt to overcome this problem it is intended that the 'on-line' measurement of these variables be undertaken using photographic and/or optical obscuration measurement techniques. Only when the behaviour of these variables has been measured will the linking of the results from the two rigs be possible.

In order to ensure the relevance of this work to industrial plant designers it is intended to test a selection of materials which are representative of the those commonly used for manufacturing wear resistant bends for use in pneumatic conveying applications. For this reason the following range of materials will be tested: mild steel, a cast basalt, a fused alumina, synthetic rubber and a polymer. Each one of these materials is representative of a class of materials that are used in erosive situations. It is evident from past work that the difference in the erosion resistance offered by a material of a different class is more important than the erosion resistance of materials in the same class [45], so consequently it is the decision as to which class of material that is to be used which is most important for the design engineer; a point well made by *Johnson et al.* [48]. In order to ensure a broad spectrum of erosion tests are carried out it is intended to use various abrasive bulk solids; for example, olivine sand, alumina and ilmenite. A range of different size distributions will be used to investigate the effects of particle size on erosion. Also, the abrasives above each have a different quasi-static particle hardness and therefore material strength, and so the effects of these properties on erosion will be established.

Obviously the effects of pipeline geometry on the flow of the gas-solid mixture will have a marked effect on the erosion behaviour of the pipeline components. As a consequence it is anticipated that investigations using bends of various geometries will be carried out and quantitative data regarding the two phase flow regimes that occur will be obtained.

Along-side this work a comparative study of the predictive power of the current erosion models will be carried out. Further studies will be made of the mechanisms by which material is removed. From the data collected it is hoped it will be possible to suggest further improvements in the predictive models currently available. Investigations into the variation of specific erosion rate with change in abrasive bulk solid, solids concentration and velocity will also be undertaken in both rigs to further broaden current knowledge of the erosion process in industrial pneumatic conveyors.

Acknowledgement

The author would like to thank The Science and Engineering Research Council (of Great Britain) and The Wolfson Centre for Bulk Solids Handling Technology at The University of Greenwich for giving me the opportunity for carrying out this work, as well as Prof. A.R. Reed and Dr. M.S.A. Bradley for their guidance.

N.B.: This paper was originally presented in a shortened form in the Symposium on Attrition and Wear, Utrecht, 12-14 October 1992.

References

[1] Lai, Y.G., R.M.C. So, M. Anwer and B.C. Hwang: Proc. Inst. Mech. Engrs., 1991, Vol. 205, No. C 4, 231-244.

[2] Tsuji, Y., N.Y. Shen, and Y. Morikawa: Advanced Powder Technology, Vol. 2, No. 1, 63-81.

[3] Kitron, A., T. Elperin and A. Tamir: Journal of Thermo-Physics, Vol. 3, No. 2, 1982, 112-122.

[4] Humphrey, J.A.C.: Int. Jour. of Heat and Fluid Flow, Vol. 11, No.3, Sept 1990, 170-195.

[5] Laitone, J.A.: Wear (1979), 239-246.

[6] Andrews, D.R. and N. Horsfield: J. Phys. D: Applied Physics, 16 (1983), 525-538.

[7] Yeung, W.S.: Wear (1979), 91-106.

[8] Hoadley, D., and T.D. Johnson: Proc. 7th Int. Conf. on Erosion by Solid and Liquid Impact, (1987), Paper 76, Cambridge, U.K.

[9] Benchaita, M.T.: STLE Transactions, Vol. 31, No. 1, 133-140, (1988).

[10] Dosanjh, S. and J.A.C. Humphrey: Wear, 102, (1985), 309-330.

[11] Bahadur, S. and R. Badruddin: Wear, 138 (1990), 189-208.

[12] Sundararajan, G.: Wear, 149 (1991), 129-153.

[13] Jennings, W.H., W.J. Head and C.R. Manning: Wear, 40 (1976), 93-112.

[14] Cousens, A.K. and I.M. Hutchings: Proc. 6th Int. Conf. on Erosion by Liquid and Solid Impact, (1983), paper 41, Cambridge, U.K.

[15] Svarovsky, L.: Solid and Liquid Separation, 2nd Ed., Butterworths, UK.

[16] Head, W.J., L.D. Lineback and C.R. Manning: Wear, 23 (1973), 291-298.

[17] Dimond, C.R.: Proc. of Solidex'84, Exhibition & Conference, Paper A5, Harrogate, U.K.

[18] Raask, E.: Erosive Wear in Coal Utilisation Plants; Hemisphere Publication Corporation, (1988)

[19] Sparks, A.J. and I.M. Hutchings: Wear, 149, (1991), 99-110.

[20] Bitter, J.G.A.: Wear, 6 (1963), 169-190.

[21] Hutchings, I.M.: Journal of Physics D: Applied Physics, Vol. 10 (1977), L 179-L 184.

[22] Buttle, D.J. and C.B. Scruby: Wear, 137 (1990), 63-90.

[23] Campbell, J.D.: Materials Science and Engineering, 12 (1973), 3-21.

[24] Sundararajan, G. and P.G. Shewmon: Wear, 84 (1983), 237-258.

[25] Cousens, A.K. and L.M. Hutchings: Wear, 88 (1983), 335 - 348.

[26] Hutchings, I.M. and A.V. Levy: Wear, 131 (1989), 105-121.

[27] Hammarsten, Å., S. Söderberg and S. Hogmark: Proc. Int. Conf. on Wear of Materials, (1983), ASME, 373-381.

[28] Aghajanian, M.K., E. Breval, J.S. Jennings and N.H. MacMillan: Materials Science and Engineering, 91 (1987), 257-264.

[29] Arnold, J.C. and L.M. Hutchings: Wear of Materials, (1989), Vol. 1, 99-107.

[30] Li, J. and L.M. Hutchings: Wear of Materials, (1989), Vol. 1, 109-114.

[31] Walley, S.M., J.E. Field, I.M. Scullion, F.P.M Heukensfeldt Jansen and D. Bell: Proc. 7th Int. Conf. on Erosion by Liquid and Solid Impact, (1987), Paper 58, Cambridge, U.K.

[32] Mason, J.S. and B.V. Smith: Powder Technology, Vol. 6 (1972) 323-335.

[33] Finnie, I.: Wear, 3 (1960), 87-103.

[34] Bitter, J.G.A.: Wear, Vol. 6 (1963), 5-21.

[35] Tilly, G.P.: Erosion Caused by Impact of Solid Particles; Treatise on Materials Science and Technology, Vol. 13, edited by C. Preece, 1979.

[36] Mills, D. and J.S. Mason: The Influence of Velocity on the Erosive Wear of Pipe Bends in Pneumatic Conveying Systems; Proc. Int. Conf. on Powder and Bulk Solids Handling and Processing, Philadelphia, Pennsylvania, 1979.

[37] Ruff, A.W. and S.M. Wiederhorn: Erosion by Solid Particle Impact; Treatise on Materials Science and Technology, Vol. 16, edited by C. Preece, 1979.

[38] Tilly, G.P.: Wear, Vol. 23 (1973), 87-96.

[39] Hutchings, I.M.: Wear, Vol. 70 (1981), 269-281.

[40] Sundararajan, G.: Wear, Vol. 149 (1991), 111-127.

[41] Evans, A.G.: Impact Damage Mechanics: Solid Particles; Treatise on Materials Science and Technology, Vol. 16, edited by C. Preece, (1979).

[42] Johnson, T.D., N.B.J. Low, M.T. Parry and D.J. Wall: Proc. 7th Int. Conf. on Erosion by Liquid and Solid Impact, Cambridge, U.K., (1987), Paper 74.

[43] Finnie, I.: Soc. Exptl. Stress Analysis, Spring Meeting, 1959, Washington, D.C.

[44] J.E. Goodwin, Miss W. Sage and G.P. Tilly: Proc. of the Inst. of Mech. Eng., (1969-70), Vol. 1984, Part 1, 279-292.

[45] Söderberg, S., S. Hogmark, U. Engmant and H. Swahn: Tribology International, Dec 1981, 333-343.

[46] Hutchings, I.M., R.E. Winter and J.E. Field: Proc. Royal Society (London), Vol. A348 (1976), 379-392.

[47] Snowshill, W.L.: Wear Experience in CERL Riffles; CEGB, RD/L/N/261/75, March 1976.

[48] Johnson, T.D., N.B.J. Low, M.T. Parry and D.J. Wall: Proc. ERPI Coal Pulverised Symposium, Nov. 13-15, 1985, Denver, CO, USA.

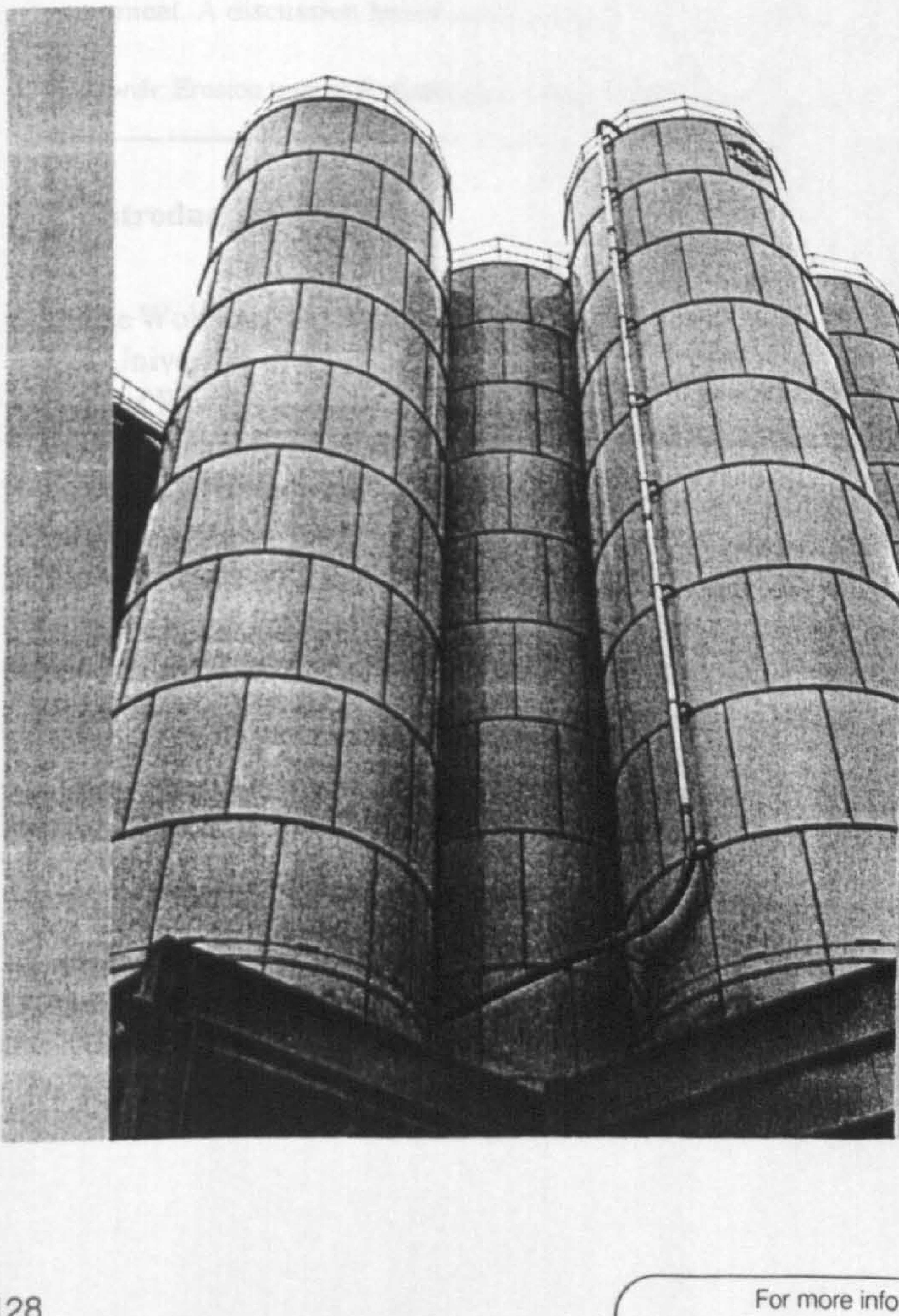

ELSEVIER

Wear 186–187 (1995) 168–178

WEAR

Comparisons between "sand blast" and "centripetal effect accelerator" type erosion testers

A.J. Burnett [a], S.R. De Silva [b], A.R. Reed [a]

[a] *The Wolfson Centre for Bulk Solids Handling Technology, The University of Greenwich, Wellington St., Woolwich, London SE18 6PF, UK*
[b] *Telemark Technological Research and Development Centre, Department of Powder Science Technology (POSTEC), Kjölnes Ring, N-3914 Porsgrunn, Norway*

Abstract

There are two major types of erosion testing devices that are used throughout the world for quantifying particle impact erosion against a solid surface. The first of these uses pressurised air to accelerate abrasive particles through a nozzle so that they impinge upon a target specimen. The second adopts a rotating disc to accelerate abrasive particles using the centripetal effect so that they impinge upon a series of targets arranged around the periphery of the disc.

This paper reports the findings of a collaborative project that was designed to compare the performance and results obtained from a rig of each of the two types mentioned above. The sand blast type rig was provided by The Department of Powder Science Technology (POSTEC) at The Telemark Technological Research and Development Centre (TEL-TEK), Porsgrunn, Norway while the centripetal effect accelerator was provided by The Wolfson Centre for Bulk Solids Handling Technology, University of Greenwich, London, UK. The test programme included tests against a wide range of materials that are commonly used in pneumatic handling facilities. (Pneumatic handling is a means of conveying and transporting powders and granular solid materials in bulk in industrial process plant, through pipelines using a gas as the carrier medium.) Olivine sand was used as the abrasive and it was projected against the test specimens at velocities and concentrations commensurate with those seen in pneumatic conveyors. In all instances the materials used in the test programme were taken from the same batch so that scatter of experimental results due to specimen variation was minimised. The paper contains a series of recommendations for erosion testing equipment. A discussion based on the results and their applicability to the prediction of wear in pneumatic conveyors concludes the paper.

Keywords: Erosion testers; Particle impact; Sand blast erosion tester; Centripetal effect accelerator erosion tester

1. Introduction

The Wolfson Centre for Bulk Solids Handling Technology, The University of Greenwich, London, UK and The Department of Powder Science Technology (POSTEC) at The Telemark Technological Research and Development Centre, Porsgrunn, Norway have a strong history of research into the behaviour and performance of pneumatic conveying systems. Owing to their mode of operation pneumatic conveying systems are sometimes prone to severe damage caused by solid particle impact erosion. Traditional methods of carrying out research into erosive wear in pneumatic conveying systems are by building a pilot plant and carrying out tests under controlled conditions [1]. However, the accurate control of all the system variables is extremely difficult in such a plant. The Wolfson Centre for Bulk Solids Handling Technology has therefore embarked on a long term research programme into the investigation of erosion damage within pneumatic conveyors. A smaller bench scale erosion testing device was developed to try to eliminate some variable control problems that occur in carrying out tests on pneumatic conveyors. This device would also allow detailed investigation into the erosion performance of various materials. Attempts to find a correlation between the results obtained from the erosion tester selected and the results of carefully controlled tests carried out on a pneumatic conveyor would then be carried out. Burnett [2] has proposed an outline test programme of this nature.

The form of erosion tester selected was a centripetal accelerator type of erosion tester originally proposed by Kleis [3] and modified and used by Söderberg et al. [4]. This erosion testing device allows up to twenty targets to be tested under identical conditions simultaneously. It was felt that this advantage of the centripetal accelerator would enable a large amount of erosion data to be collected in as short a time as possible. The centripetal accelerator erosion tester is the subject of GOST 23.201-78 [5]; this is a national standard of the former Soviet Union. From 1955, eastern European

0043-1648/95/$09.50 © 1995 Elsevier Science S.A. All rights reserved
SSDI 0043-1648(95)07143-1

nations and the countries of the former Soviet Union have extensively used this form of erosion tester. A rotating disc is used in this form of rig to induce forces on the particles that cause them to accelerate to the required velocity.

The other major type of erosion tester that is widely used is that known as the sand blast or gas blast type. Equipment of this type is the subject of national standards ASTM G76-89 [6] and DIN 50 332 [7]. This form of erosion tester has proved to be popular in most of the western European nations and the USA since the early 1960s. The sand blast erosion tester utilises a pressurised gas to accelerate particles of abrasive through a nozzle.

It was decided that a collaborative test programme with an institution that uses a sand blast type of tester should be carried out to enable a thorough appraisal of the performance of the two erosion testers to be undertaken. There were two reasons for this. First, derivation of most of the erosion data that is available in western Europe has occurred by tests carried out on sand blast type testers. Secondly, the two instruments use quite different methods for particle acceleration. The Department of Powder Science Technology (POSTEC) at TEL-TEK, Porsgrunn, Norway was the institution that provided the use of the sand blast testing instrument.

It was felt that the collaborative test programme could accomplish two goals as it went on. First, it would enable the test equipment to be thoroughly investigated for the suitability of two phase flow simulation and its similarities with conditions in pneumatic conveyors. Second, experiments could be carried out to investigate the performance, under controlled particle impact conditions, of a wide range of materials used in the construction of pneumatic conveyor components. The results of this test programme would lead to recommendations for further research into the behaviour of these testing devices. Also, some idea of the particle impact erosion behaviour of a range of materials under conditions seen in pneumatic conveyors could be obtained. This paper describes the results of this test programme.

2. Description of the test programme

2.1. Erosion test conditions

It is unusual for properly designed pneumatic conveyors to operate such that the particle velocities are higher than 45 m s^{-1}. It has been widely reported in previous research literature that the erosion damage suffered by a material depends predominantly on the velocity of the particle impact. Power law curve fitting exercises have taken place where the value of the exponent can vary from 2 to 4.5 [8,9]. Since the value of this exponent is so variable, scaling for the effect of velocity from test results obtained from carrying out high velocity experiments is inaccurate. Therefore, the only way in which values for erosion damage at these comparatively low particle velocities can be assessed is by replicating these velocities in the test equipment being used. The particle velocities selected were 15, 25 and 35 m s^{-1}; it was felt that these accurately represented a suitable range of particle velocities compatible with those seen in pneumatic conveyors.

Reports suggest that erosion damage in pneumatic conveyors must be dependent on the concentration of particles in the flowing suspension [10]. Consequently, when the particle concentration decreases and the conveying velocity increases there is an increased occurrence of erosion damage. The fact that erosion damage is affected by particle concentration can be explained by the mechanism of "shielding" proposed by Andrews and Horsfield [11]. The mechanism of "shielding" is based upon the observation that interparticulate collisions cause more dispersed transfer of impinging energy to the eroding surface and as a result the quantity of erosion damage that occurs is decreased. Consequently, the particle concentrations that were selected for this test programme were commensurate with those seen in low particle concentration conveying. Therefore, the particle concentrations of 1, 4 and 13 kg m^{-3} were selected. Because of these tests it was felt that an estimate of the effects of these particle concentrations at the impact point on the target surface could be obtained.

It was felt that a sequence of three tests each at 30° and 90° would prove to be sufficient. It was not the intention to fully characterize the performance of the erosion behaviour of the test materials but to examine the performance of the test equipment.

2.2. Erosion test materials

The Wolfson Centre for Bulk Solids Handling Technology supplied all the materials used in the test programme from sources in the UK. Duplicate sets of materials were forwarded to POSTEC in Norway for their use during this test programme. In this way any errors due to material variation in the experimental results could be minimised.

2.2.1. Erodent material

The erodent that was selected for this test work was a relatively fine, olivine sand. This material was marketed under the name "Renova Fine" by Hepworth Minerals and Chemicals Ltd., Staffordshire, UK. This material was selected since it has no free silica content and is therefore safe for handling under current UK safety regulations. It also shares many properties in common with conventional silica sand, i.e. being angular and inert. The mean particle diameter was 323.8 μm. The range of the size distribution showed that 10% of the sample was below 213 μm and 90% was below 455 μm in diameter. The particle density was 3.28 g cm^{-3} on average. It was found that an indication of the sphericity could be obtained by comparing photographs of the olivine sand particles with outlines shown in the Rittenhouse sphericity scale. The sphericity index, obtained by this means, was approximately 0.75 [12]. This abrasive consisted of 50% MgO, 42% SiO_2, 7% Fe_2O_3 with the remainder being made up from traces of metallic oxides.

Table 1
Erosion target material description

Material type	Cast ceramic	Fused ceramic	Metal	Elastomer	Polymer
Material description	Cast basalt	Fused alumina	Mild steel	Rubber	UHMW PE
Trade name	Abresist	Hitec 100	EN3B	Nitrile rubber	Tivar 100
Supplier	Kingfisher Ind. Services, Washford East, Redditch, Birmingham, UK	Morgan Matroc Ltd, Stourport-on-Severn, Worchestershire, UK	Outlook Metal Stockholders Ltd., Banstead, Surrey, UK	Arco Holman Nichols Ltd, Orpington, Kent, UK	PoliHi Solidur UK Ltd., Todmorden, Lancashire, UK
Density (g cm^{-3})	2.8	3.73	7.8	0.86	0.94
Hardness (Rockwell)	79C	82C	50C	–	64R
Constituents	SiO_2 46% Al_2O_3 15% Fe_2O_3 12% CaO 11% MgO 8% K_2O/Na_2O 6% TiO_2 2%	Al_2O_3 97% + fillers	080A15 specification C 0.16% Si 0.09% S 0.005% P 0.01% Mn 0.7%	Butadiene acrylo-nitrile co-polymer + fillers	Virgin cross-linked ultrahigh molecular weight polyethylene
Yield strength (N mm^{-2}).	30 (in bending)	320 (in bending)	430 (ultimate tensile)	–	28 (ultimate tensile)

2.2.2. *Erosion target materials*

Five erosion target materials were selected. Each material selected represented a general class of materials that could be or is used in pneumatic conveyor pipe construction. Table 1 gives information regarding these materials.

2.2.3. *Erosion rigs*

2.2.3.1. *The sand blast erosion test facility*

The sand blast erosion rig that was used by POSTEC, TEL-TEK, Norway consisted of a boron carbide nozzle 90 mm in length with an internal diameter of 3 mm. The acceleration of the abrasive was achieved by use of two air flow rate control valves. One valve controlled the dispersion of the abrasive within the injector housing to ensure that a homogeneous gas/particle mixture occurred. Control of the gas, necessary for the motive power for the particles, was provided by the other valve. A K-Tron Soder T20 double screw feeder mounted to form a loss in weight feeder fed the abrasive into the injector housing. The target holder consisted of a rotatable table to which the 25×25×4 mm specimens were attached by suction. Protection of the target edges was not necessary. Therefore, erosion of the test specimen occurred at one angle of impingement only. Fig. 1 shows the layout of this test facility.

2.2.3.2. *The centripetal accelerator test facility*

The centripetal accelerator erosion test facility that was used by The Wolfson Centre for Bulk Solids Handling Technology consisted of a balanced disc whose velocity of rotation could be varied continuously and fixed at any given value. The disc was 0.12 m in radius and contained six radial channels made from a high quality alumina ceramic. These were 2.6 mm in internal diameter and 6.1 mm in external diameter. A mechanical arrangement ensured even splitting of the abrasive flow into the six acceleration tubes. Abrasive particles were fed into the rotating disc system by a vibratory feeder of a type developed by Barnes [13]. This feeder permitted the selection of a given constant feed rate of abrasive. This was achieved by use of amplitude feedback control to ensure that the amplitude of tray vibration was kept constant despite variations in the load on the feeder tray. Tests involving the use of several target specimens at once can be carried out with this form of erosion tester; ten targets were utilised per test in this instance. The ten target holders were equally spaced around a ring running concentrically with the acceleration disc. Each target holder could be angled independently to the flow in 5° increments for angles of orientation from 5° to 90° to the trajectory of the particles. Each target was mounted in a vertical plane. Protection was given to both the leading and trailing edges of the target to prevent erosion taking place at unwanted angles of impingement (see Fig. 2). The erosion tester used by The Wolfson Centre for Bulk Solids Handling Technology was based on the tester developed by Söderberg et al. [4]. This tester was a variant of the ZUK-3M developed by Kleis at the Tallinn Technical University, Estonia in 1967 [14]. The ZUK-3M is the subject of the GOST 23.201-78 national standard.

2.3. *Calibration of test equipment*

2.3.1. *Calibration tests carried out on the sand blast erosion tester*

In this test facility drag effects occurring between the particles and air led indirectly to particle acceleration. The drag force acting on a particle is due to the particle shape [15]. This variable remains extremely difficult to quantify [12]. Therefore, owing to the method of particle acceleration used by this tester the particle velocity needed to be accurately assessed. Consequently it was decided that laser Doppler anemometry (LDA) would be a suitable way of calibrating the tester. Sequences of tests were performed without the

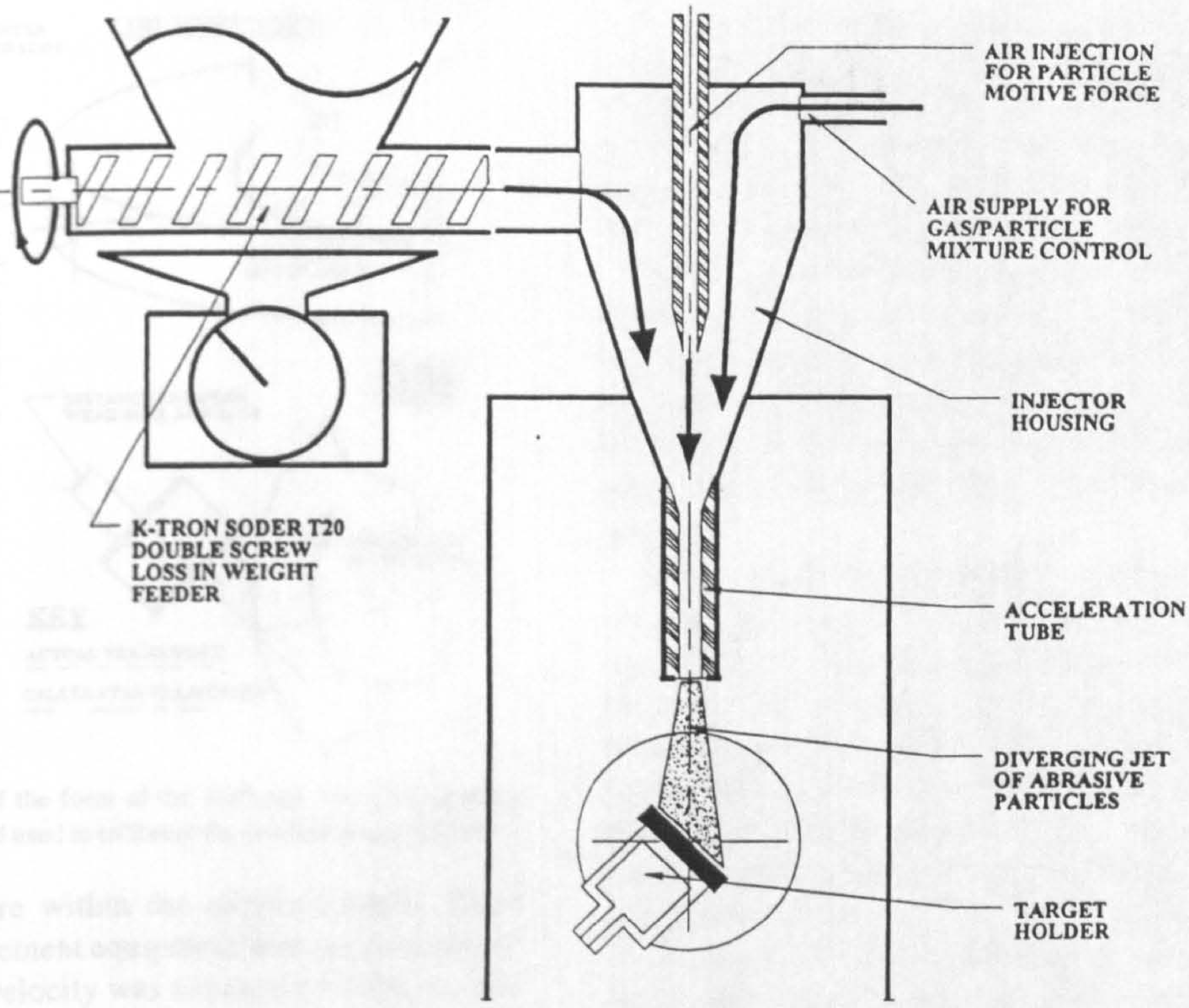

Fig. 1. Schematic diagram of the sand blast type erosion tester.

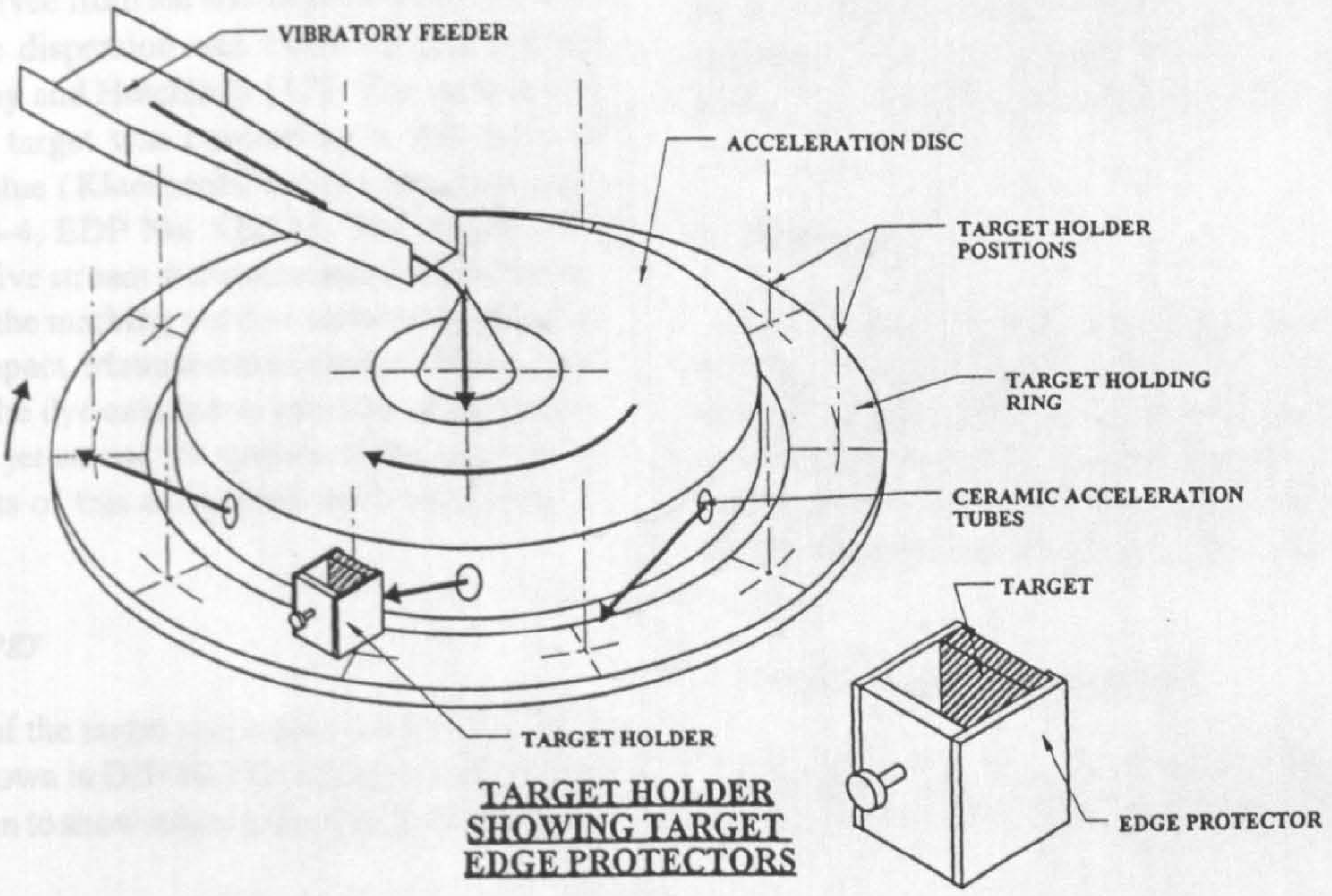

Fig. 2. Schematic diagram of the centripetal accelerator type erosion tester.

targets in place and the LDA equipment was set to measure the particle velocity at the centre point of impact on the target. Therefore, derivation of the settings required for tests at 15, 25 and 35 m s^{-1} mean particle velocity were found. The particle concentration in the gas stream was calculated by dividing the mass flow rate of abrasive by the mass flow rate of the gas. Particle flux at the impact point could only be estimated visually in this device.

2.3.2. *Calibration tests carried out on the centripetal accelerator erosion tester*

The method of acceleration of the particles used in this form of erosion tester relies primarily upon the particle mass. The mean particle mass is found by use of information regarding size distribution and particle density; these variables are measurable. The centripetal accelerator erosion tester was checked to ensure that the particle velocity and the spread of

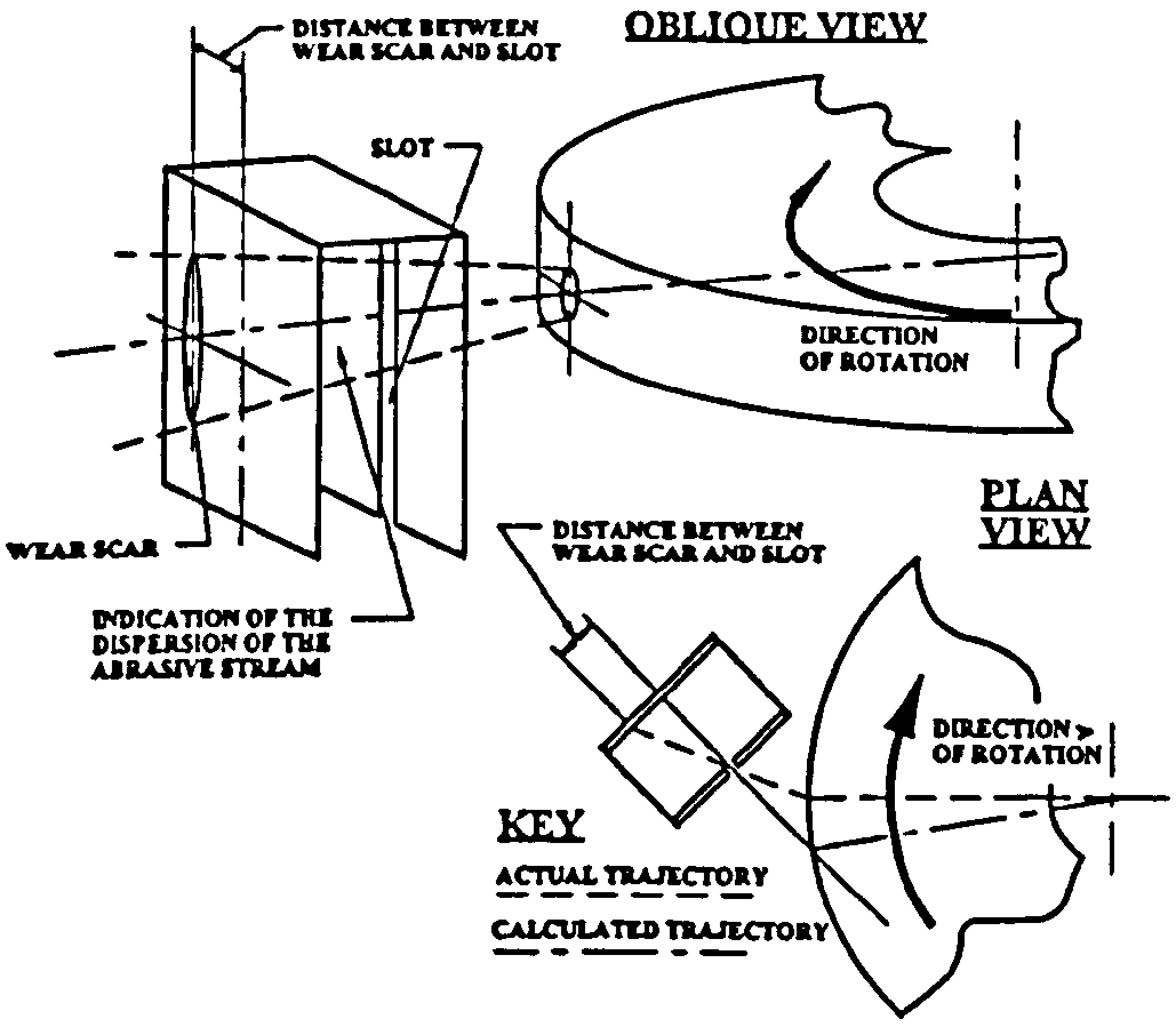

Fig. 3. Schematic diagram of the form of the Ruff and Ives [16] particle velocity measurement method used to calibrate the centripetal erosion tester.

particles at impact were within the required limits. Since optical velocity measurement equipment was not available at the time of testing the velocity was checked by using a static form of the Ruff and Ives slot and displaced wear scar method [16] (see Fig. 3). The mean of the offset of the wear scar from the slot was derived from ten test measurements. Assessment of the particle dispersion was made using a method proposed by Shipway and Hutchings [17]. The surface of a polished mild steel target was covered by a thin layer of engineers marking blue (Kleenscribe Layout Dye, L.S. Starrett, CAT No. 1610-4, EDP No. 53212). The targets were exposed to the abrasive stream at the set conditions for a short period. Removal of the marking out dye occurred in the areas subject to particle impact. Manual measurement of the dimensions of the scar in the dye enabled an estimate of the dispersion of the abrasive jet across the surface of the target to be obtained. The results of this calibration work are set out in Table 2.

2.4. Test methodology

The preparation of the target specimens was carried out to the guidelines laid down in DIN 50 332 where possible. Initial tests were undertaken to show when both of the erosion testers were operating under steady state erosion conditions before results were taken. Minimization of the effects of any spurious surface topography effects was therefore achieved. Prior to any measurements being taken the targets were thoroughly cleaned and dried. Full details of the experimental procedure for both of the erosion testers are given in Appendix A.

In the case of both erosion testers the erosion performance of the materials was presented in terms of $cm^3\ g^{-1}$ by simply dividing the volume of material removed from the target by the mass of abrasive striking the target surface. For the sand blast erosion tester this was very easily achieved since all of the abrasive being fed through the tester struck the target surface.

However, in the centripetal accelerator erosion tester this was not the case. The reason for this was that not all the abrasive particles struck the surface of each target or indeed the sum of all the target surfaces. It was obvious that a target at an oblique angle to the flow of abrasive could not be struck by as much abrasive as one that was placed perpendicular to the flow. A numerical model [18] was used to find out the mass of abrasive that struck each target. Depending on the angle of orientation of the target to the flow of abrasive, the time required for an equal mass of abrasive to strike each target was found by the use of this model. The mass loss results were converted to volume loss values. The periods derived by the model were then used for interpolation purposes on the time history of the volume loss of each target specimen. Then this yielded a value for erosion damage in $cm^3\ g^{-1}$ for an identical mass of abrasive striking each target.

3. Test results

Results are presented in the following two graphs for the erosion damage in terms of $cm^3\ g^{-1}$, i.e. volume loss per mass of abrasive striking the target surface. Fig. 4 shows the results obtained for the erosion damage caused at 90° while Fig. 5 shows the results for erosion damage at 30°. Both figures show the results obtained from both test facilities.

4. Observations and discussion

The test results show that the two test facilities provide similar comparative results for the trends in the erosion dam-

Table 2
Centripetal erosion tester calibration results

Erosion condition	Percentage error in impact angle	Percentage error in velocity	Percentage error in dispersion from theoretical calculations using Eq. (3)			
			Edge closest to disc		Edge furthest from edge	
			30°	90°	30°	90°
$15\ m\ s^{-1}$, $1\ kg\ m^{-3}$	−9.05	−4.34	−12.0	−12.9	+5.1	+0.1
$25\ m\ s^{-1}$, $4\ kg\ m^{-3}$	−0.86	+6.70	+2.9	−10.7	+10.8	+0.9
$35\ m\ s^{-1}$, $13\ kg\ m^{-3}$	+2.03	+6.00	−28.6	−7.9	−11.4	−11.0

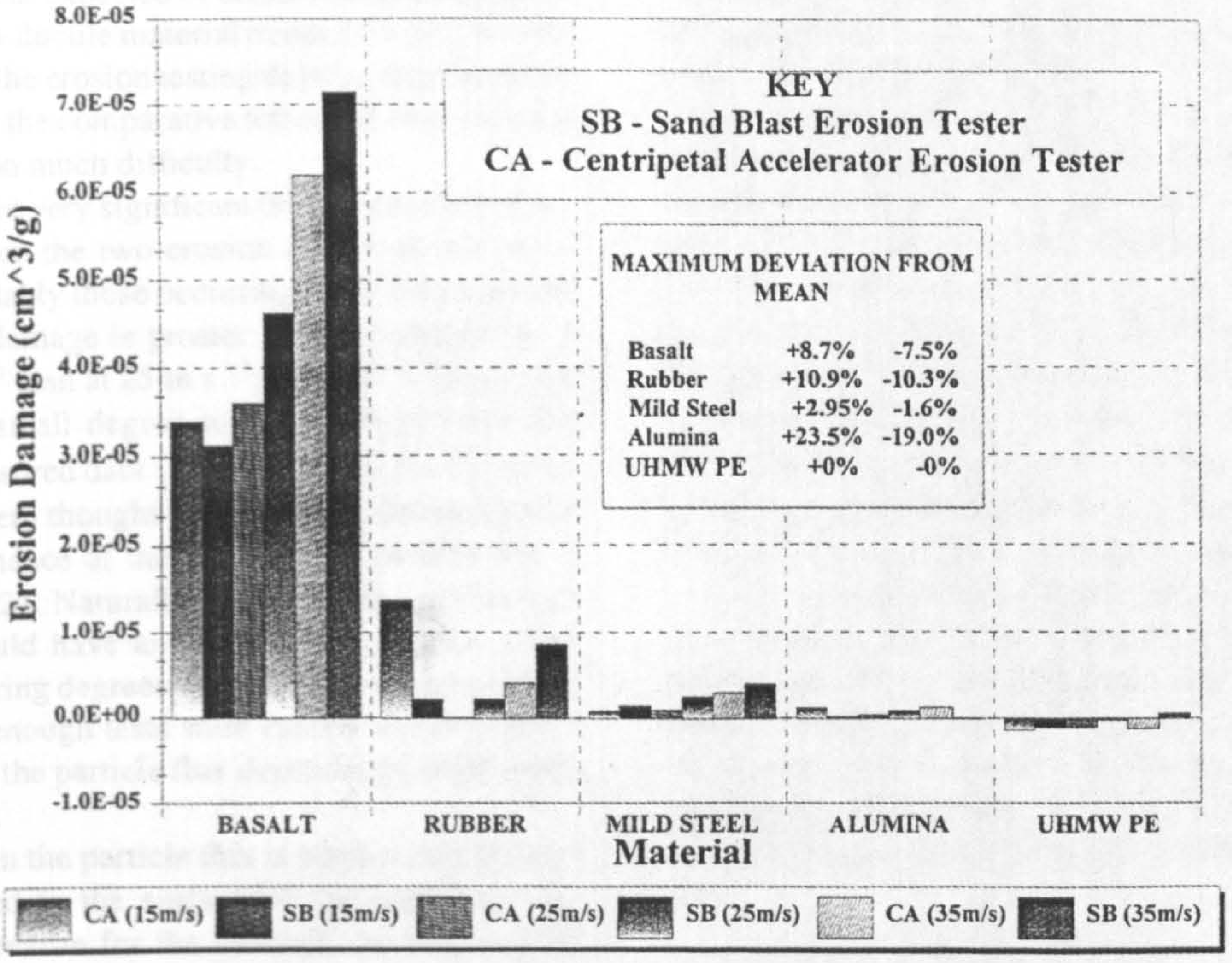

Fig. 4. Erosion damage at an impact angle normal to the target surface.

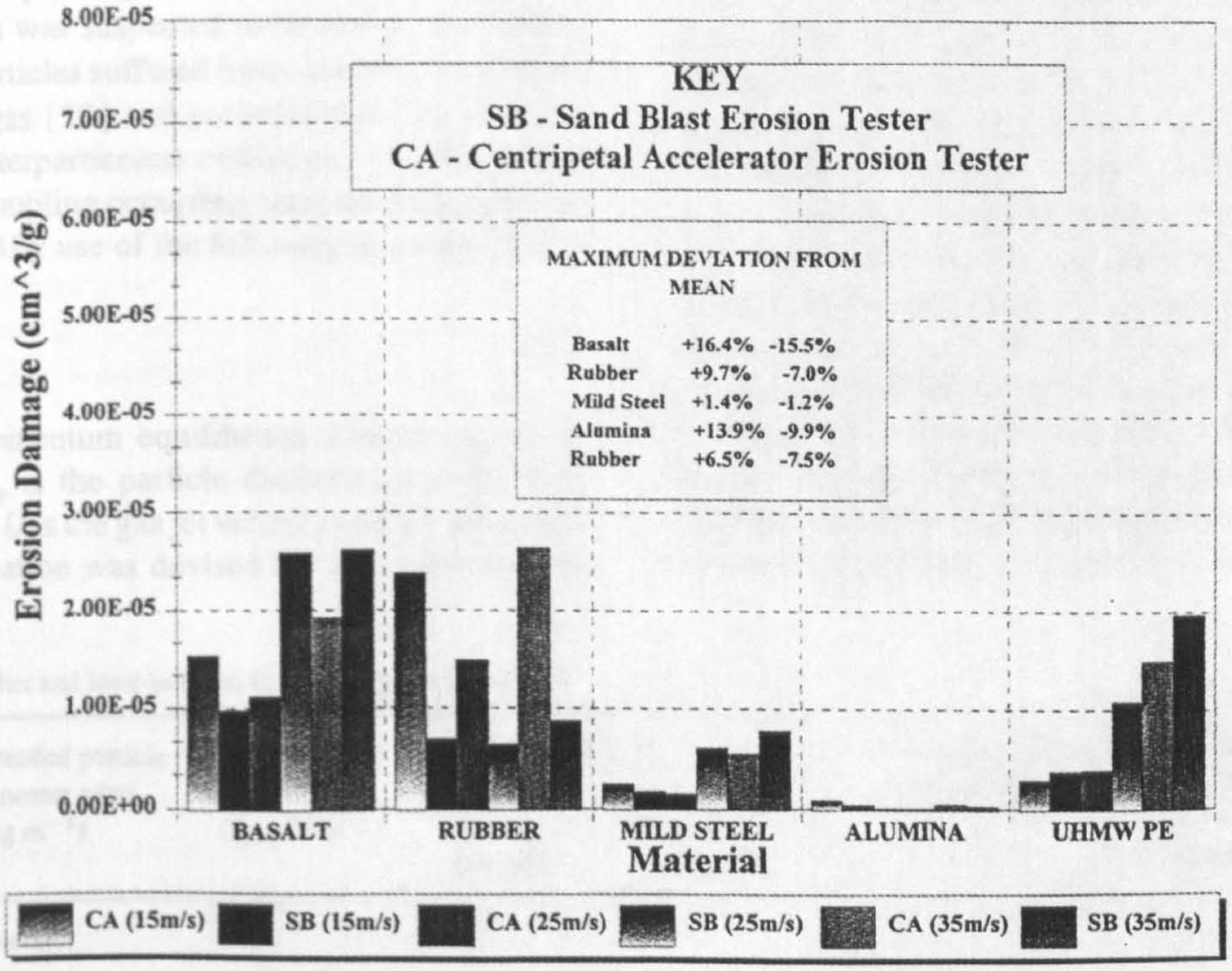

Fig. 5. Erosion damage at an impact angle of 30° to the target surface.

age between the materials that have been tested. Use of the cast basalt, (Abresist) and the UHMW PE, (Tivar 100) in impact erosive wear situations are unusual. Performance of the basalt material was poor in comparison to the other materials tested at both angles of impingement. This, it was thought, was due to the porous, fragile nature of the samples obtained. The performance of the UHMW PE targets at normal impact were good. However, this performance changed for the worse as more oblique angles of impingement occurred. The data suggests that the ceramic materials follow the trends in behaviour expected of brittle materials while the other materials show ductile material trends [19,20]. Results obtained from both the erosion testing devices suggested that they can be used for the comparative testing of wear resistant materials without too much difficulty.

However, there are very significant differences for the erosion damage between the two erosion testers. In several of the results, most notably those occurring at 30° impingement angle, the erosion damage is greater for tests carried out at 15 m s^{-1}, 1 kg m^{-3} than at 25 m s^{-1}, 4 kg m^{-3}. This it was felt was due in a small degree to the range of error that occurred in the measured data (see Figs. 4 and 5). However, the major effects were thought to be due to a dependence of the erosion performance of the materials on particle flux at impact [11,17,21,22]. Naturally, it was suspected that each material tested would have an erosion performance which would vary to differing degrees with changes in particle flux. Unfortunately not enough tests were carried out to enable a definite estimate of the particle flux dependence of the materials to be assessed.

The differences in the particle flux at impact would cause the energy imparted to the surface of the targets to vary considerably. The reason for the difficulty in assessing the particle flux at impact was that the abrasive streams in both erosion testers could be seen to diverge. The quantity of divergence varied depending on the velocity and the particle concentration. This was suspected to be due to two effects, first because the particles suffered from dynamic momentum coupling with the gas [23] and secondly that they were dispersed owing to interparticulate collisions [17]. The likelihood of dynamic coupling occurring between the gas and the particles was found by use of the following equation [23]:

$$\lambda=\frac{\rho_p d_p^2}{18\mu}\frac{U}{d} \qquad (1)$$

where λ is the momentum equilibrium constant, ρ_p is the particle density, d_p is the particle diameter, μ is the fluid dynamic viscosity, U is the gas jet velocity and d is the nozzle diameter. This equation was devised for use in the analysis of the erosion of sand blast type erosion testers and therefore its application to the centripetal accelerator erosion tester cannot be recommended. The results from the sand blast erosion tester show that λ for the lowest velocity/particle concentration/size fraction in the abrasive was 4.8 and the maximum value was 124.6. It is stated by Dosanjh and Humphrey [23] that if $\lambda > 10$ the particles are not affected by the gas flow around them to any degree. This was confirmed during the test work on the sand blast type erosion tester. In this rig none of the abrasive particles were seen to follow the air stream lines and miss the targets completely, even during tests at 30° impact angle. Since an identical abrasive was used at similar velocities in the centripetal accelerator it was felt that the behaviour of the particle stream would be similar.

It was concluded that the particle jet dispersion could only have been caused by interparticulate collisions within the jet. McClusky [24] showed the likely dispersion of particle jets being injected into gas flows by carrying out particle image velocimetry measurement of the emerging abrasive jet. Extrapolating from data presented in this work by carrying out elementary curve fitting has yielded the following equation:

$$R_j=(3.92\times10^{-3}V+0.075)x_d+r \qquad (2)$$

where R_j is the radius of the jet, V is the average particle velocity, x_d is the distance from the nozzle to the target and r is the radius of the nozzle. This equation was utilised as an estimate since the test data on which it was derived was found as part of some tests carried out at 12.5 m s^{-1} and a particle concentration of 4 kg m^{-3} only. The data for jet dispersion at 25 and 35 m s^{-1} with the accompanying suggested particle concentrations was not available at the time of testing. Table 3 shows the results of using this equation. In subsequent examination of the erosion targets, the wear scar area profiles seen in both forms of erosion tester could be seen to be very close to those calculated using Eq. (2). Further investigation into the divergence of the particle jet is obviously necessary for a thorough examination of the erosion phenomena to be undertaken. It is therefore suggested that investi-

Table 3
The results of particle flux and inter-particulate distance calculations

Intended velocity (m s^{-1})	Intended particle concentration (kg m^{-3})	Desired mass flux (kg m^{-2} s^{-1})	Mean mass flux (kg m^{-2} s^{-1})		Divergence of jet radius at impact (mm)	Inter-particulate distance (no. of particle diameters)	
			At nozzle	At impact		At nozzle	At impact
For the centripetal accelerator							
15	1	15.71	44.9	6.1	2.22	4.64	9.03
25	4	101.6	303.2	29.6	2.86	2.89	6.27
35	13	457.6	3298.1	241.9	3.50	1.45	3.47
For the sand blast erosion tester							
15	1	15	9.4	1.0	3.21	13.99	29.14
25	4	100	94.3	7.3	4.09	7.70	18.06
35	8	280	282.9	16.2	4.97	5.97	15.50

gation of the following areas of the operation of erosion testers should be undertaken.

(a) It was possible that the dispersion of the abrasive jet was not one that resulted in a homogeneous flow of particles; measurement of the concentration of the particles across the profile of the diverging jet at various distances needs to be carried out.

(b) It was thought possible that at the lower particle velocities, the smaller particles could migrate away from the axis of the jet more than the larger particles. This suggested particle behaviour being a consequence of the ability of the small particles to be more significantly affected by the gas motion. This would lead to a variation in the flux of impinging kinetic energy across the erosion scar area, which in turn would lead to a change in the erosion damage caused.

(c) To obtain a given velocity of impact between the abrasive particles and the target, the nozzle velocity of the gas flow needs to be varied. This results in a change in the particle flux at the impact surface. Consequently, expression of concentration in kg kg^{-1} gas may not be a satisfactory variable to use in the comparative evaluation of the two testers. During these tests the sand blast form of erosion tester has an air velocity at the exit from the nozzle approximately 2.7 times that of the particles. In the centripetal accelerator the gas accelerates owing to the drag force acting upon the moving particles and the gas velocity is therefore only 0.15 times the particle velocity. The motion of the gas in the two testers could therefore be quite different, and may cause the emerging jet of particles to diverge differently. This would depend again on the amount of momentum coupling between the particles and the gas.

Using the equation proposed by Shipway and Hutchings [17] for the average distance between particles,

$$L=\left(\frac{mV\pi r^2}{Q_o}\right)^{1/3} \tag{3}$$

where L is the average distance between particles, m is the average mass of a particle, V is the mean particle velocity, r is the nozzle radius and Q_o is the particle mass flow rate. An indication of the likelihood of interparticulate collisions occurring can therefore be surmised from this equation. Shipway and Hutchings also suggested that particle streams could be seen to diverge once the mass flux of particles exceeded 1 kg m^{-2} s^{-1}. Shipway and Hutchings conclude that if the distance between the particles was less than 10 mean particle diameters, particle collisions are likely to occur.

The results of the particle flux analysis are shown in Table 3. They show that the efforts made in the use of the centripetal accelerator erosion tester to compensate for the divergence of the jet were not sufficiently effective to achieve a favourable comparison with the desired set point values selected. The results show, therefore, that in both testing facilities, the divergence of the abrasive jet was most likely to be caused by interparticulate collisions at the exit from the accelerating nozzles. The particle mass flux at impact for the centripetal accelerator was on average approximately 40% of that intended while with the sand blast type of erosion tester it was 7%. The much lower value for the sand blast rig was due to maintaining a similar distance between the nozzle exit and the impact point (22.5 mm) to that in the centripetal rig. In future comparisons, achieving particle flux similarity at impact for the two testers should be the primary goal.

It can therefore be seen from the results presented in Figs. 4 and 5 above that the erosion performance of the materials used in this test programme are affected to different degrees by the particle flux at impact. When the particle flux at impact is reduced, the amount of erosion damage per unit mass of abrasive striking the target increases. This, it is suggested, can only be due to the effects of particle flux at impact and the dispersion of any incident energy by the occurrence of interparticulate collisions as proposed by Andrews and Horsfield [11].

There were small differences in the manner in which the targets were treated during the cleaning stage of the test procedure. The use of the ultrasonic cleaning device led to an increase in the mass loss measurements obtained for the targets by a maximum of 5%. The differences in the method of cleaning the targets had a most significant effect in the comparison between the erosion results for the rubber material. In this case the same trends were indicated but a consistently greater magnitude of erosion was observed for the centripetal accelerator erosion tester. However, it was felt that the effect of differences in the mass flux at the impact site was by far the overriding reason for the large differences seen in the results for the two testing facilities.

The wear scar depth could lead to the particles of abrasive striking the surface of the targets at angles different from those intended. This may have an effect on the progress of the erosion with time as described recently by Finnie et al. [25]. It was therefore essential that the erosion measurements were taken when the erosion damage had reached steady state conditions but before the depth of the wear scar became too great. This was less of a problem with the centripetal accelerator than the sand blast erosion tester since the method of processing the experimental data for this machine relied upon the measurement of erosion over a range of exposure times. Consequently, any changes away from the steady state erosion conditions could be readily seen. Detailed experience in the operation of the sand blast erosion tester was required to ensure that this condition be met.

The operational envelope of the centripetal erosion tester was not exceeded by the initial conditions that were required for this test programme. However, since the abrasive jet divergence was such that the particle mass flux over the impact area was significantly less than that originally wanted, the new mass flow rate of abrasive into the rig necessary to make good this deficit may choke the abrasive feed system on the rig as it is now. The problems of ensuring adequate feed of the abrasive into the sand blast erosion tester for this test programme exceeded the capability of the rig as it was in this area from the outset. It was possible to bring the targets closer to the nozzle exit in this rig. This would lead to a reduction in the area of impact on the target surface and therefore an increase in the particle flux. This modification will aid in increasing the particle flux at impact. However, it may be necessary to increase the mass flow rate of abrasive through this tester to further compensate for the particle jet divergence.

If the particle mass flux at impact has an effect as great as that seen in the test results presented above, all the current theories for predicting erosion damage by particle impact. [26,27] will need to be altered to account for this variable. The comparisons of results presented above suggest that the results in erosion damage between the two erosion testers for the different materials involved is not constant. This would suggest that some materials will have erosion damage resistance that is more dependant on particle mass flux than others.

5. Conclusions and recommendations

5.1. Recommendations

Before the results obtained from using either of these two forms of erosion tester can be used for the prediction of erosion in industrial equipment, a detailed series of calibration tests should be carried out. These tests should include checks on the range of particle velocities emerging from the acceleration mechanism, the range of jet dispersion and the concentration of the particles within the particle jet. Once the calibration has taken place the test conditions can be definitively stated.

To simulate the mass flux seen in industrial situations the two erosion testers should be examined to see if the maximum particle mass flux at impact on the target in the tester is sufficient. In the examination of pneumatic conveyors only the lower particle concentration conveying regimes can be analysed. However these regimes are the ones in which erosion damage reaches a maximum. An alternative erosion testing device should be developed if the testing apparatus cannot simulate the necessary particle fluxes at impact.

5.2. Conclusions

Both of the erosion testing devices utilised in this work can provide a means for the comparative wear testing of various materials under a range of velocity and particle concentration conditions. There are several advantages and disadvantages to the use of each of these forms of erosion tester; they are displayed in Table 4.

Significant differences in the erosion data obtained were found when results from the two testing facilities were compared. Analyses were carried out to examine the conditions of the jets emerging from the respective acceleration mechanisms of the two rigs concerned. These suggested that in the centripetal accelerator erosion tester, the divergence of the particle jet had been accounted for while in the sand blast erosion tester it was not. Consequently, the mass particle flux at impact varied considerably between the two erosion testers and from the desired concentrations suggested as the set points for the test programmes. This is concluded to be the most likely reason for the variation in the test results obtained from the two rigs when they were compared.

The results provided in this document suggest that both the erosion testing devices show similar results for the general ranking of materials in terms of erosion resistance. However, no comparison between the values for impact erosion behaviour of the materials could be made. This was due to the problems caused by particle jet dispersion. The results do suggest the possibility that the materials have an erosion resistance that depends on particle flux at impact. Unfortunately there are not enough results from this test programme to quantify this effect to any degree.

It was concluded using ideas presented by other authors [17,23,24] that the main cause of the particle jet dispersion was due to interparticulate collisions in the jet at the nozzle of the various acceleration mechanisms. Momentum coupling

Table 4
A comparison of the advantages and disadvantages of both forms of erosion tester

Erosion tester type	Advantages	Disadvantages
Sand blast erosion tester	— short test duration — simple results analysis	— difficulty in assessing when steady state conditions occur (prior experience is often required) — difficulty in assessing particle velocity — high probability of adverse gas/particle interactions occurring — limited particle concentration simulation capability
Centripetal accelerator erosion tester	— ten targets tested simultaneously (problems due to experimental error are minimised) — velocity determination is simple — reasonable range of particle concentration simulation — particle/gas interaction is minimal — steady state erosion conditions are easily assessed due to the test method that was adopted	— difficulty in assessing the mass of abrasive that strikes each target — test duration is long due to the necessity of finding the erosion time history of each target

between the particles and the gas did not affect the erosion behaviour of the materials greatly.

As a result of these findings it has been decided jointly by the two organisations involved that this programme of work will be modified and continued in the future. This work will aid in the more accurate assessment of the effects of particle jet dispersion on erosion performance of materials, and to assess more accurately the performance of these popular forms of erosion testing device.

Acknowledgements

The author wishes to thank Mr. G.J. Liaklev, an M.Sc. student of POSTEC, TEL-TEK, and Mr. P.T. Moore, an exchange student from Loughborough University of Technology, Loughborough, UK, spending his industrial placement at TEL-TEK for carrying out the experimental work in Norway. Thanks are also extended to Dr. M.S.A. Bradley and the technical staff of The Wolfson Centre for Bulk Solids Handling Technology, The University of Greenwich, London, UK for their guidance and assistance during the progress of this work. Morgan Matroc Ltd, Stourport-on-Severn, Worchestershire, UK, and PoliHi Solidur UK Ltd., Todmorden, Lancashire, UK are thanked for their generous donations of materials for the test work.

Appendix A. Test methodology

A.1. Test methodology for the sand blast erosion tester

The method of carrying out tests on this device is laid out sequentially below.

(1) Following calibration of the test apparatus, the tester was set to produce the desired particle velocity and concentration. The particle concentration was theoretically calculated at the nozzle of the acceleration tube using figures based on the ratio of the mass flow rate of solids to mass flow rate of gas. It was found that this form of erosion tester could not cope with the quantity of abrasive necessary to simulate the particle concentration of 13 kg m^{-3} at 35 m s^{-1}. The maximum concentration that could be achieved was 8 kg m^{-3}.

(2) Specimen polishing to a 1 μm finish was carried out wherever possible.

(3) The specimen was cleaned first in soapy water followed by treatment in a 10% isopropyl alcohol solution in an ultrasonic bath for 2 min. All specimens were then dried in an oven for 120 min at approximately 40 °C. The nitrile rubber specimens could not be cleaned in the alcohol mixture since they reacted with the mixture.

(4) The sample was weighed on an analytical scale. The balance had an accuracy of 0.01 mg.

(5) The sample was placed securely in the erosion tester ensuring the centre of the target is vertically beneath the axis of the nozzle. The target was secured in position using a vacuum provided by an "eductor".

(6) The target specimen was subjected to particle impact at the desired concentration and velocity for a time such that the mass of abrasive that struck the target was not less than 250 g.

(7) The cleaning process adopted in item (3) above was repeated. The mass loss of the target was assessed using the balance mentioned above.

(8) This process was repeated for subsequent samples.

A.2. Test methodology for the centripetal accelerator erosion tester

The method of carrying out the tests on this device is laid out sequentially below. All tests carried out on this tester involved ten targets simultaneously.

(1) The centripetal accelerator is set for the required velocity and particle concentration required for impact conditions. It was realised that the jet of abrasive emerging from the nozzles of the acceleration tubes diverged. Efforts were made to account for this in the setting up of the test rig. This was achieved by calculating the particle concentration using an estimated spread of the particle jet at the impact site for the area of impingement.

(2) The specimens were polished using a 400-grit abrasive paper. In this way it was possible to achieve a 1 μm roughness finish. The specimens were then thoroughly washed in neat isopropyl alcohol. They were then hot air dried at a temperature of 30–50 °C for 10 min and allowed to cool in ambient conditions for approximately 30 min. The nitrile rubber specimens reacted with the isopropyl alcohol and were therefore cleaned in soapy water.

(3) An accuracy of 0.1 mg on an analytical balance was achieved during the weighing of the samples.

(4) Ten samples were placed in the centripetal erosion tester and exposed to the particle impact for a short period whose duration was derived from past experimental experience.

(5) Processes (2), (3) and (4) above were repeated for a minimum of seven exposures so that enough data were found for a history of the mass loss with time for each target to be obtained.

(6) The above process was then repeated for another ten target specimens.

References

[1] D. Mills, J.S. Mason and K.N. Tong, The role of penetrative wear in the erosion of pipe bends, in J.E. Field and N.S. Corney (eds.), *Proc. 6th Int. Conf. on Erosion by Liquid and Solid Impact, Cavendish Laboratory, Cambridge, UK, 1983*, paper 58.

[2] A.J. Burnett, Wear in pneumatic conveying pipelines; a review of past and present work, *Powder Handling Process.*, *5* (2) (1993) 123–128.

[3] I.R. Kleis, A test rig for the investigation of wear in a loose abrasive, *Trans. of the Tallinn Polytech. Inst.*, *152* (1958) 1–18 (in Russian).

[4] S. Söderberg, S. Hogmark, U. Engman and H. Swahn, Erosion classification of materials using a centrifugal erosion tester, *Tribol. Int.*, *14* (6) (1981) 333–343.

[5] GOST 23.201-78 (in Russian).

[6] ASTM G76-89, *Standard Practice for Conducting Erosion Tests by Solid Particle Impingement using Gas Jets*, ASTM, Philadelphia, 1992.

[7] DIN 50 332, *Strahlverschleißprüfung*, DIN, Berlin, 1984 (in German).

[8] J.A.C. Humphrey, Fundamentals of fluid motion in erosion by solid particle impact, *Int. J. Heat and Fluid Flow*, *11* (3) 1990 170–195.

[9] D. Mills and J.S. Mason, The influence of velocity on the erosive wear of pipe bends in pneumatic conveying systems, *Proc. Int. Conf. on Powder and Bulk Solids Handling and Processing, Philadelphia, PA, 1979*, Industrial and Scientific Conference Management, Chicago, IL, 1979, 300–314.

[10] D. Mills, Erosive wear problems in industry with particular reference to process plant, power stations and bulk solids handling systems, *SOLIDEX 86, The Solids Handling Exhibition, Harrogate, June, 1986*, conference course notes.

[11] D.R. Andrews and N. Horsfield, Particle collisions in the vicinity of an eroding surface, *J. Phys. D: Appl. Phys.*, *16* (1983) 525–538.

[12] E. Raask, *Erosive Wear in Coal Utilisation Plants*, Hemisphere, New York, 1988, p. 14

[13] R.N. Barnes, Resonant vibratory feeders, *Proc. 4th IEAust. Int. Conf. on Bulk Solids Materials Handling and Transportation and 7th IFPS Int. Symp. on Freight Pipelines, Wollongong, Australia, July 1992*, The Institution of Engineers, Australia, Barton, ACT, 1992, pp. 321–326.

[14] I.R. Kleis, H.H. Uuemois, L.A. Uksti and T.A. Pappel, Centrifugal accelerators for erosion research and standard wear testing, in K.C. Ludema, W.A. Glaeser, S.K. Rhee (eds.), *Proc. Int. Conf. on Wear of Materials, Dearborn, MI, April, 1979*, ASME, New York, 1979, pp. 212–218.

[15] R. Clift, J.R. Grace and M.E. Weber, *Bubbles, Drops and Particles*, Academic Press, London, 1978.

[16] A.M. Ruff and L.K. Ives, Measurement of solid particle velocity in erosive wear, *Wear*, *35* (1975) 195–199.

[17] P.H. Shipway and I.M. Hutchings, A method for optimising the particle flux in erosion testing with a gas blast apparatus, *Wear*, *174* (1994) 169–175.

[18] A.J. Burnett, The particle dynamics within centripetal accelerator erosion testers, in preparation.

[19] J.G.A. Bitter, A study of erosion phenomena, part I, *Wear*, *6* (1963) 5–21.

[20] J.G.A. Bitter, A study of erosion phenomena, part II, *Wear*, *6* (1963) 169–190.

[21] P.R. Krishnamoorthy, S. Seetharamu and P. Sampathkumara, Influence of the mass flux and impact angle of the abrasive on the erosion resistance of materials used in pulverised fuel bends and other components in thermal power station, *Wear*, *165* (1993) 151–157.

[22] S.R. De Silva, Prevention and reduction of attrition and wear, *Proc. Symp. Attrition and Wear in Powder Technology, Utrecht, The Netherlands, 12–14, October, 1992*, pp. 303–340.

[23] S. Dosanjh and J.A.C. Humphrey, The influence of turbulence on erosion by a particle laden fluid jet, *Wear*, *103* (1985) 309–330.

[24] D.R. McClusky, An optical investigation of air–particle flows, *Ph.D. Thesis*, The University of Edinburgh, Edinburgh, Scotland, UK.

[25] I. Finnie, G.R. Stevick and J.R. Ridgely, The influence of impingement angle on the erosion of ductile metals by angular abrasive particles, *Wear*, *152* (1992) 91–98.

[26] G. Sundararajan, A comprehensive model for the solids particle erosion of ductile materials, *Wear*, *149* (1991) 111–127.

[27] R.R.R. Ellermaa, Erosion prediction of pure metals and carbon steels, *Wear*, *162–164* (1993) 1114–1122.

5th International Conference on
Bulk Materials Storage, Handling and Transportation.
Newcastle, 10 - 12 July 1995.

An Investigation of the Low Velocity / Low Concentration Solid Particle Erosion of a Structural Mild Steel Using a Centripetal Erosion Tester.

A.J. BURNETT[1], M.S. BINGLEY[2], M.S.A. BRADLEY[1]

[1] The Wolfson Centre for Bulk Solids Handling Technology, The University of Greenwich, Wellington St, Woolwich, London, SE18 6PF, UK. (Phone +44 181 331 8646: Fax +44 181 331 8647).
[2] The School of Engineering, The University of Greenwich, Wellington St., Woolwich, London, SE18 6PF, UK. (Phone +44 181 331 8636: Fax +44 181 331 8605).

Summary

Mild steel is the material that is most commonly used in the construction of pneumatic conveyor pipelines. Consequently, the resistance of mild steels to erosion damage by solid particle impingement is of considerable interest to designers of such equipment. This paper describes an investigation into erosion of one mild steel.

A centripetal erosion tester developed at The Wolfson Centre for Bulk Solids Handling Technology, The University of Greenwich, London, UK was used to investigate the erosion resistance of this material. This device uses a high speed rotating disc to accelerate the particles to the necessary velocity so that they strike a series of target specimens. A series of conditions was specified which were closely comparable to those seen in pneumatic conveyor operation in industry.

The test results obtained displayed no peak in the graphs of erosion rate verses angle of impingement. It was concluded that this was due to the manner in which the test data was manipulated for analysis purposes. A power law model was fitted to the erosion data. Some useful trends were discovered in the test data and they are presented in this paper.

1. INTRODUCTION

Mild steel pipeline components are widely utilised in pneumatic conveyor installations in a diverse set of industrial situations because they are readily available and cheap in price. However, due to the mechanisms of gas and solid particle flow that occur in a pneumatic conveyor, collisions between the solid particles and the pipe wall are inevitable. These collisions occur with a much greater frequency at the pipe bends where a radical change in the direction of flow takes place. Erosive wear due to these collisions can become a serious problem where hard abrasive materials are being conveyed at the velocities used in the normal operation of pneumatic conveyors (1).

An investigation of the erosive wear performance of a basic mild steel was carried out at The Wolfson Centre for Bulk Solids Handling Technology, The University of Greenwich. Tests were carried out on a centripetal accelerator type erosion tester (2,3) (see Figure 1). This form of tester allows tests to be carried out on a range of samples at various angles simultaneously, under identical conditions of particle velocity and particle concentration. The abrasive particles were projected at the mild steel at a range of velocities and concentrations commensurate with those conditions used in phase pneumatic conveying. Lean phase pneumatic conveying being where the particles are suspended in the gas as the mixture flows along. The results obtained from this test work and the implications that may be inferred for the future prediction of erosive wear in pneumatic conveyor components is discussed in this paper.

2. DESCRIPTION OF THE TEST PROGRAMME

2.1 Test Conditions

Test conditions were selected so that they fell within the range of particle velocities and concentrations that are normally used in pneumatic conveyor operation. Three particle velocities were chosen, 15, 25 and 35 m/s. For each of these velocities tests were carried out at three suspension densities (particle concentrations) of 1, 4 and 13 kg/m^3. These particle concentrations are similar to those that are seen in typical low suspension density pneumatic conveying. Efforts were made to ensure that these particle concentrations were achieved at the sample surface instead of at the exit of the particle acceleration mechanism. This was achieved by carrying out calibration tests (4). Only in tests at 35 m/s and 13 kg/m^3 did problems occur. It was found that there was a hardware restriction to the amount of abrasive material that could be fed through the erosion tester under these conditions. Consequently, the maximum particle concentration that could be achieved at 35 m/s was 8 kg/m^3.

The angles of sample orientation to the flow of abrasive material were fixed as follows, 8°, 15°, 24°, 40° & 61°. These angles were selected since the angles of impingement that occur in pneumatic conveyor bends having a long radius (bend radius equals 14 pipe diameters or greater) tend to be in the range 5° to 30° (5). Three samples were tested at the 8° and 15° impingement angles, two samples at 24° and one at each of the remaining angles. The increase in the number of samples tested at the lower impingement angles was necessary since scatter in the experimental results at these angles was greater during calibration tests. Calibration tests confirmed the accuracy of the angular placement of the samples (4).

2.2 Test Materials

The abrasive material that was used throughout the test programme was fine olivine sand. This material was obtained from Hepworth Minerals and Chemicals Ltd., Staffordshire, UK as Renova Fine. This material contains no free silica and is therefore safe for mechanical handling according to current UK safety regulations. The material is generally angular and inert and shares many properties in common with silica sand. The mean particle diameter was 323.8 µm with 10% of the sand being below 213 µm in diameter and 90% being below 455 µm in diameter. The particle density and hardness were measured to be 3.28 g/cm^3 and Moh 6.5-7 respectively. This material mainly consisted of $(Mg,Fe)_2\ SiO_4$.

The mild steel that was selected for the test programme was cut from mild steel pipe of the type that would be used in the construction of pneumatic conveyor pipe work. The steel was made according to BS4360 Grade 43C / BS EN10210 Parts 1 & 2. The steel had the following constituents:- Carbon 0.21% (±0.03%), Silicon 0.5% (+0.05%-0%), Manganese 1.3% (±0.1%), Phosphorus 0.05% (±0.01%) and Sulphur 0.05% (±0.01%). This steel was supplied in the hot rolled condition but included the effects of rolling into tube form and induction welding along the seam. The samples from the pipe segment were machined to give one flat surface and cleaned using 240 grit abrasive paper to give a uniform surface finish. Samples were not taken from areas next to the welded seam. The samples were orientated so that the grain structure was aligned with the direction of particle motion as would be the case in the actual pipes.

3. TEST EQUIPMENT

The centripetal accelerator erosion tester that was used by The Wolfson Centre for Bulk Solids Handling Technology consisted of a balanced disc 0.12 m in radius that contained six 2.6 mm internal diameter alumina ceramic tubes. The velocity of rotation of the disc could be varied and fixed at any given value. The abrasive particles were guided into the six alumina tubes by mechanical means so that the split between the tubes was without bias. Control of the feed of the abrasive into the disc was achieved by use of a vibratory feeder of a design proposed by Barnes (6). This feeder permitted a constant feed rate of abrasive to be selected. Ten samples of mild steel were tested simultaneously. The targets were held in specially designed holders arranged equally spaced around the periphery of the acceleration disc. The target holders could be angled independently to the flow in 5° increments of angle from 5° to 90° to the trajectory of the particles. These holders ensured that the leading and trailing edges of the targets were protected. Protection of this form prevented impingement occurring at unwanted angles of impact. A schematic of the erosion tester is shown in Figure 1. The design of the centripetal accelerator erosion tester in use at The Wolfson Centre for Bulk Solids Handling Technology was based upon the tester developed by Söderberg et al. (3). This was in turn a variant of the ZUK-3M developed by Kleis at the Tallinn Technical University in 1967 (2). The ZUK-3M is the subject of the GOST 23.201-78 Soviet national standard.

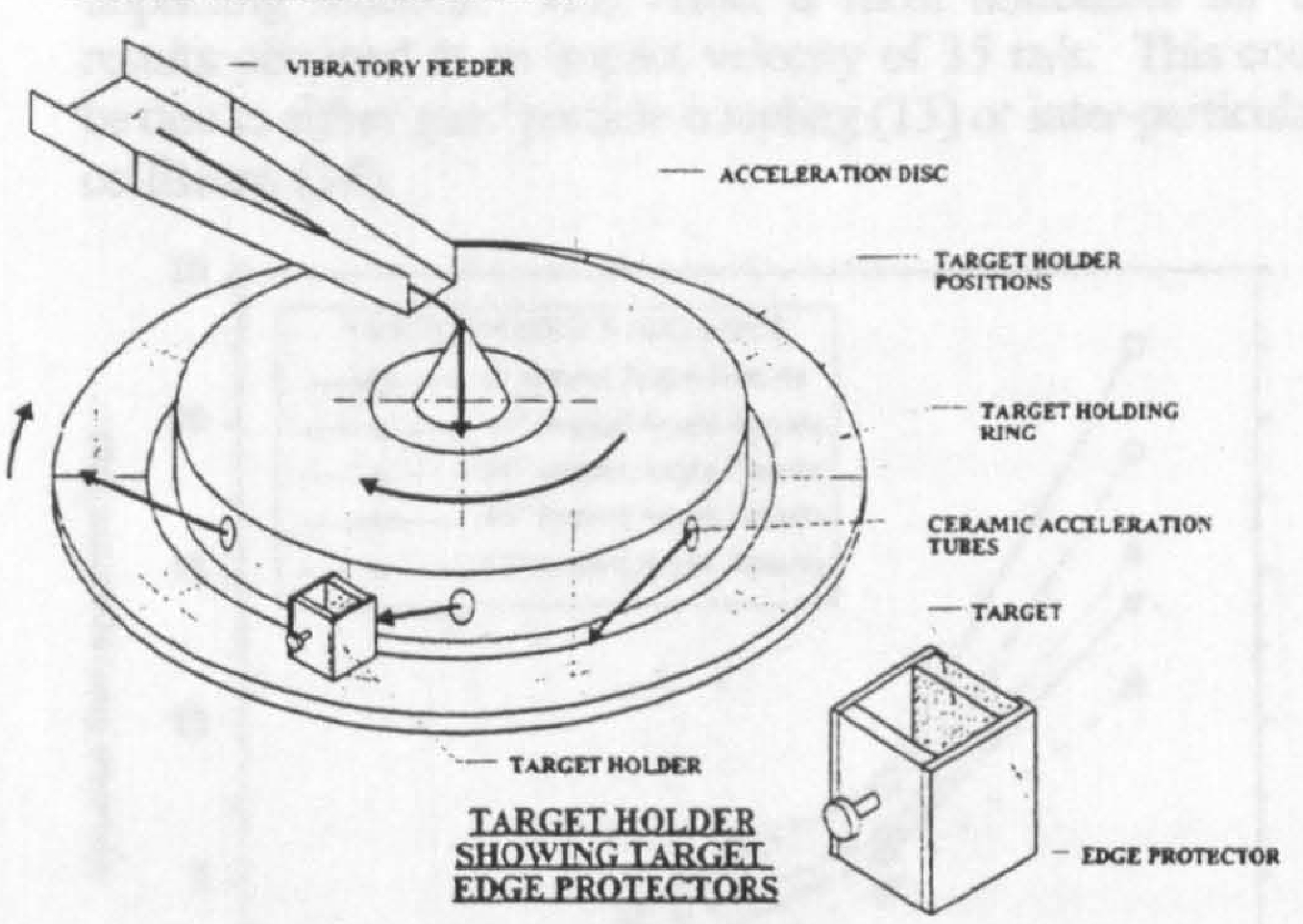

Figure 1: Schematic View of the Centripetal Accelerator Erosion Tester.

4. TEST METHOD

The tests were organised so each test consisted of ten samples at each combination of particle velocity and concentration. These targets were arranged so that the five angles of impingement were set sequentially in the rig, i.e. the three targets at 8° were placed in target holders 1 to 3 and so on. This arrangement was adopted for all of the tests. A target at 8° to the flow of abrasive particles will be struck by fewer particles than a target arranged at 90°. Assessment of the mass of abrasive material striking each target was required. A numerical model of the dynamics of the particles within the rig was used for this purpose (7). A series of five exposure times for each target angle was assumed. Obviously longer exposure times were required for the targets arranged at the more oblique angles so that they could be struck by the mass of abrasive.

The mass lost by each target at each of these predetermined exposure times was measured following careful cleaning of the targets using isopropyl alcohol. The fixed mass of abrasive was typically 700 grammes. The time required for each target to be struck by this mass of abrasive was calculated. These 'equal mass' exposure times were used on a graph of mass loss versus time to interpolate for the mass loss caused by the fixed mass of abrasive particles striking the target surface. The results of this method of carrying out the tests and analysing them has lead to the results that are shown later in this paper.

5. TEST RESULTS

Figure 2 shown overleaf is a micrograph of the eroded surface of one sample used in this test programme. Orientation of this target was at approximately 25°. The surface of the sample shows typical features seen throughout previous research in this area that have been described as been illustrative of the classical form of 'ductile erosive wear' (8,9).

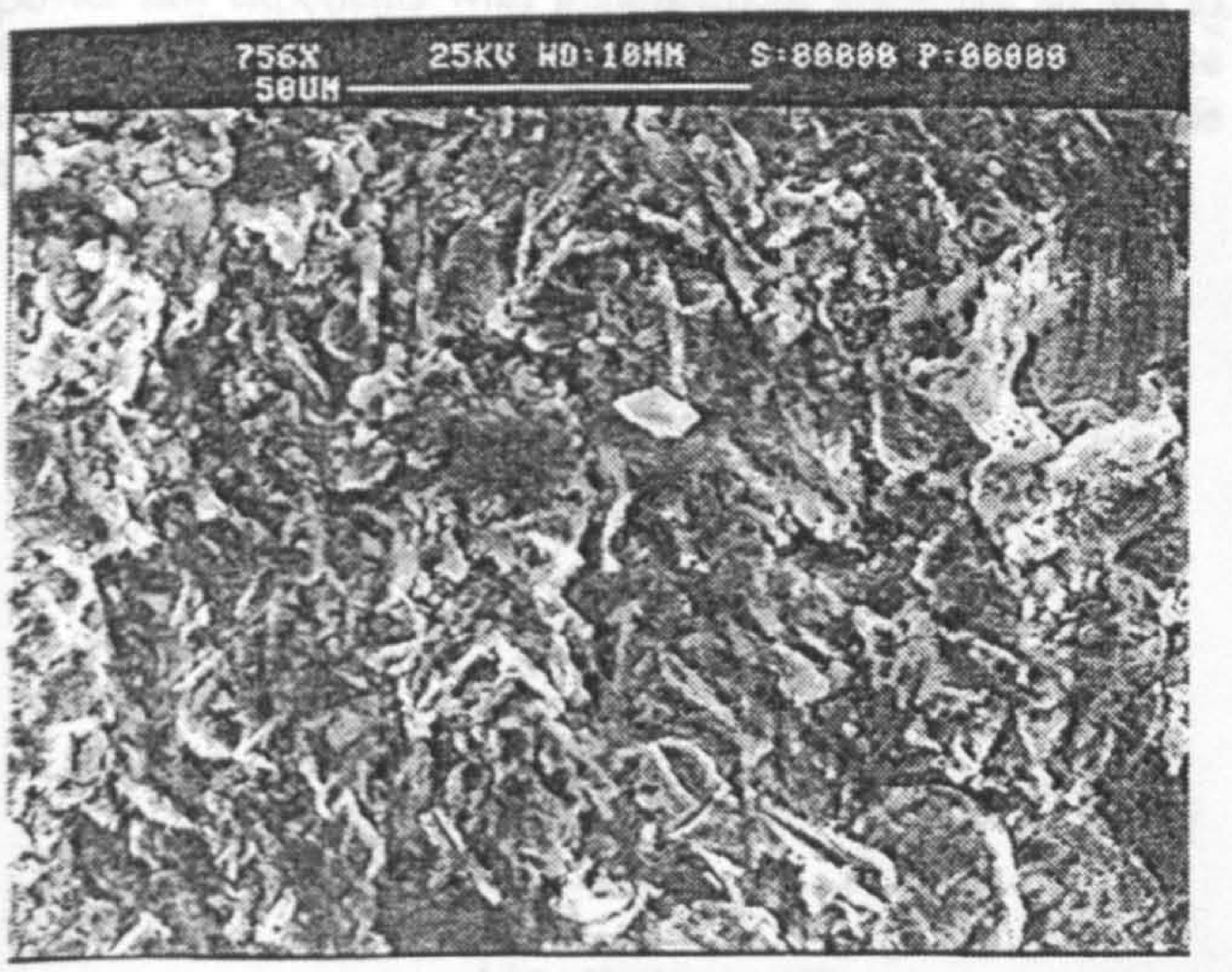

Figure 2: Photo-micrograph of the eroded mild steel surface after impact at 25° impingement angle by multiple abrasive particles.

Figure 3 illustrates the nine curves obtained from the test work for the erosion of the mild steel under the conditions mentioned in Section 2.1 above. The curves are plotted against axes of volume loss per mass of abrasive striking the sample surface verses angle of impingement.

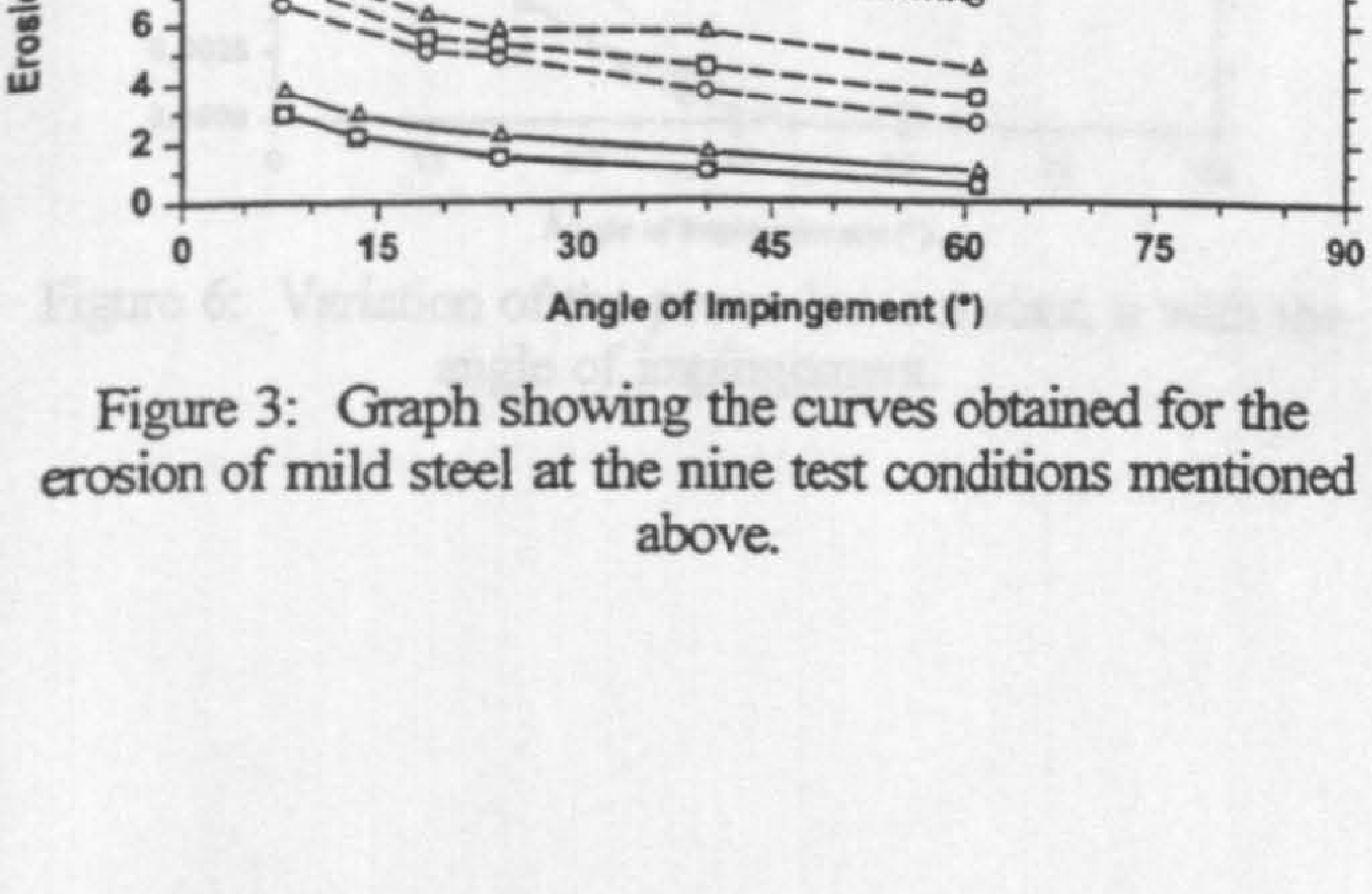

Figure 3: Graph showing the curves obtained for the erosion of mild steel at the nine test conditions mentioned above.

These curves show several interesting trends. The most important of these trends is that the authors of previously published work have always shown a maximum in the erosion data that has occurred at an impingement angle of between 20° and 30°. In the test work reported in this paper this behaviour was not observed. The volume loss tends to increase exponentially as a zero degree angle of impingement is approached. This is different from previously reported results (10,11). Secondly, there are three broad groupings of results that are dependent on the impact velocity. This echoes the well-reported fact that the primary variable effecting the amount of erosion damage is particle impact velocity (12). This dependency is better illustrated in Figure 4 shown below for one group of results obtained for a particle concentration of 1 kg/m³. Figure 3 suggests that as the particle concentration increases the erosion damage per unit mass impacting reduces. This effect is most noticeable for the results obtained at an impact velocity of 35 m/s. This could be due to either gas / particle coupling (13) or inter-particulate collisions (14).

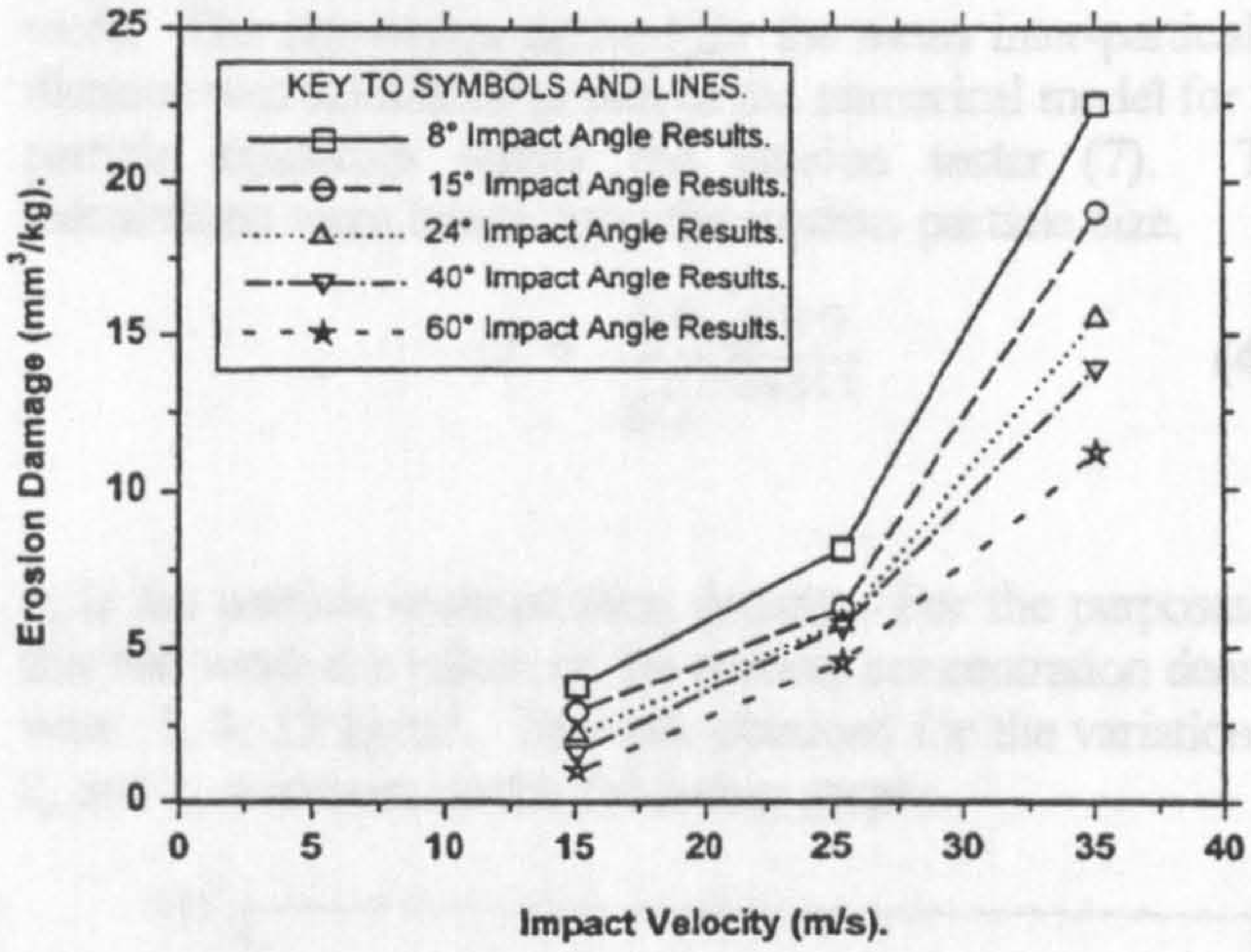

Figure 4: Erosion damage for mild steel at a particle concentration of 1 kg/m³ plotted against particle velocity.

Two other graphs illustrating families of curves similar to that shown in Figure 4 were created for particle concentrations of 4 and 13 kg/m³, however, for the sake of brevity these have been omitted from this paper.

6. DEVELOPMENT OF A NUMERICAL MODEL FOR THE EROSION OF MILD STEEL

In the past the models of erosion phenomena were obtained by fitting power law curves to the results obtained from test work. The same method was adopted in this work. Obviously, the numerical model should contain reference to the dominant variables in the system. These are particle impact velocity, impingement angle and particle concentration. Attempts to quantify any dependence of this form of erosion on material properties for either the abrasive or sample material cannot be made since only one of each of these materials was used.

The power law model took the following form: -

$$E = a\ V_p^n \qquad (1)$$

Where both a and n are found empirically, V_p is the particle impact velocity and E is the erosion rate in terms of volume loss per unit mass of abrasive striking.

Figure 4, above, suggests that if a series of power law curves is fitted to the erosion data the impingement angle affects the slope and intercept of these curves. This method was also used on the data obtained at the other two particle concentrations. Once the power law curves of the above form were fitted to the experimental data, an investigation of the variation of the power law exponents and constants with impingement angle was carried out. The variations of the power law exponents with impingement angle are shown to follow approximately linear trends (Figure 5). It should be noticed that as the velocity and particle concentration increase the data scatter increases.

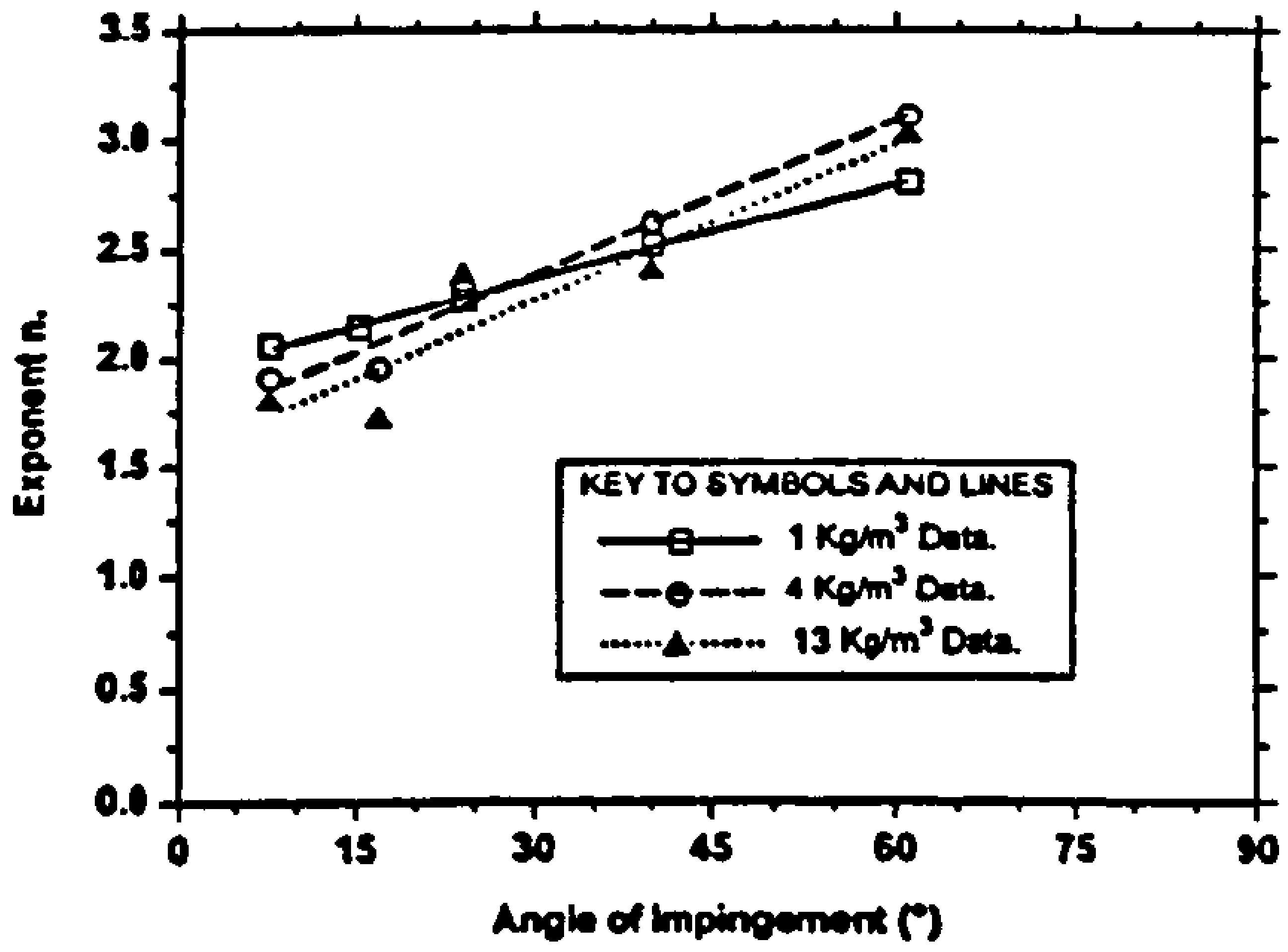

Figure 5: Variation of the power law exponent plotted against angle of impingement.

The power law constants, a for the three series of particle concentration data are shown to vary exponentially with the impingement angle (Figure 6). However, there is a significant amount of scatter in the data for the variation of 'a' especially as the particle concentration increases.

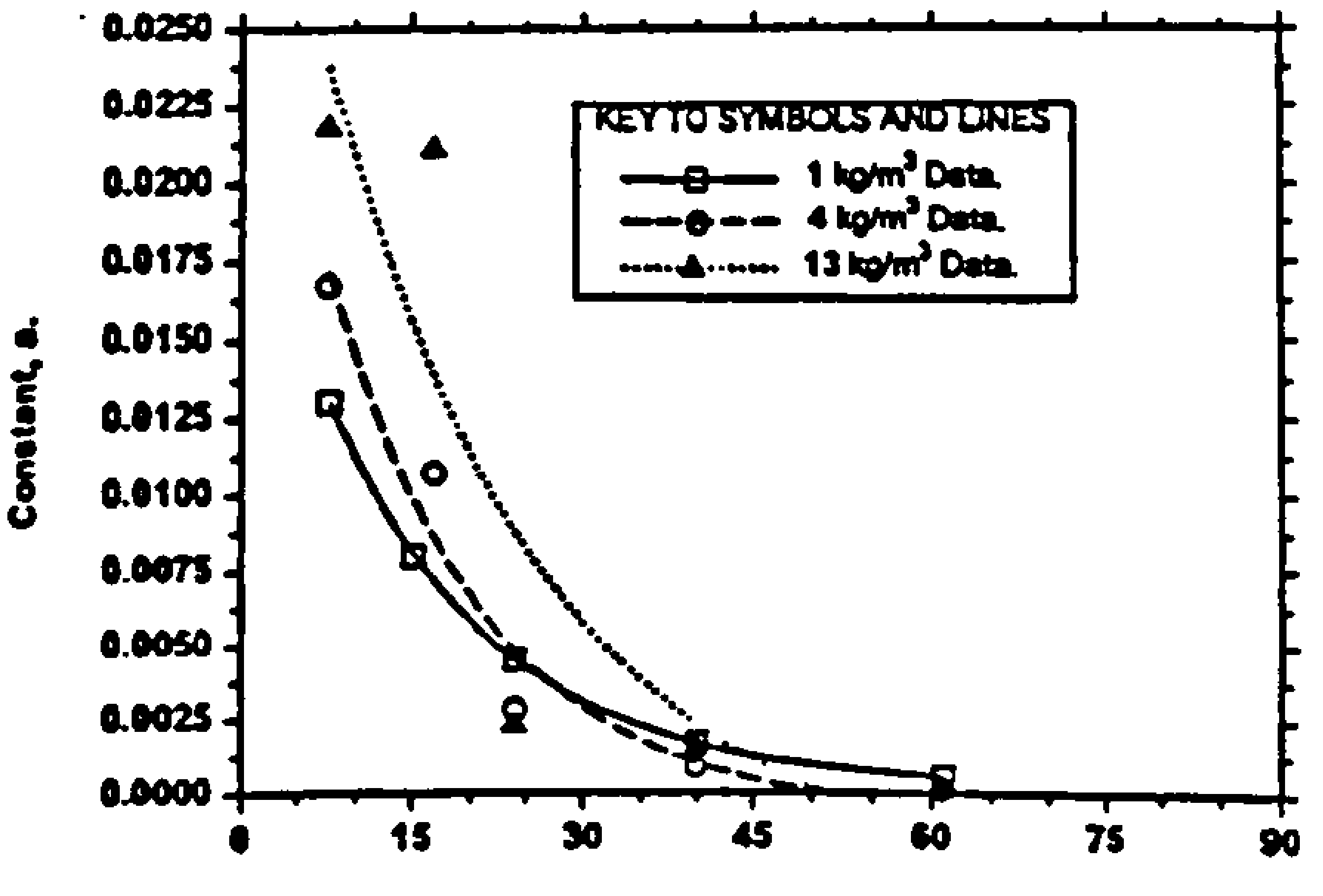

Figure 6: Variation of the power law constant, a with the angle of impingement.

Linear equations for both the power law exponent and constant can be fitted to the above graphs. These are as follows:

For the power law exponents, n:

$$n = m_n\ \alpha + c_n \qquad (2)$$

For the power law constants, a:

$$a = c_a\ e^{m_a\ \alpha} \qquad (3)$$

Where m_n, c_n, m_a and c_a are numerical curve fit constants and α is the angle of impingement.

Further investigation of the numerical curve fit constants has led to findings that both c_n and c_a vary linearly with particle concentration. As far as particle concentration is concerned the mean distance between the particles can be calculated and related to the particle concentration density which is the manner in which the concentration is described for this test work. The expression derived for the mean inter-particulate distance was calculated as part of the numerical model for the particle dynamics within the erosion tester (7). The calculations were based upon the median particle size.

$$D = \frac{69.599}{\rho_s^{0.286511}} \qquad (4)$$

ρ_s is the particle concentration density. For the purposes of this test work the values of the particle concentration density were 1, 4, 13 kg/m³. The data obtained for the variation of c_n and c_a is shown on the following graphs.

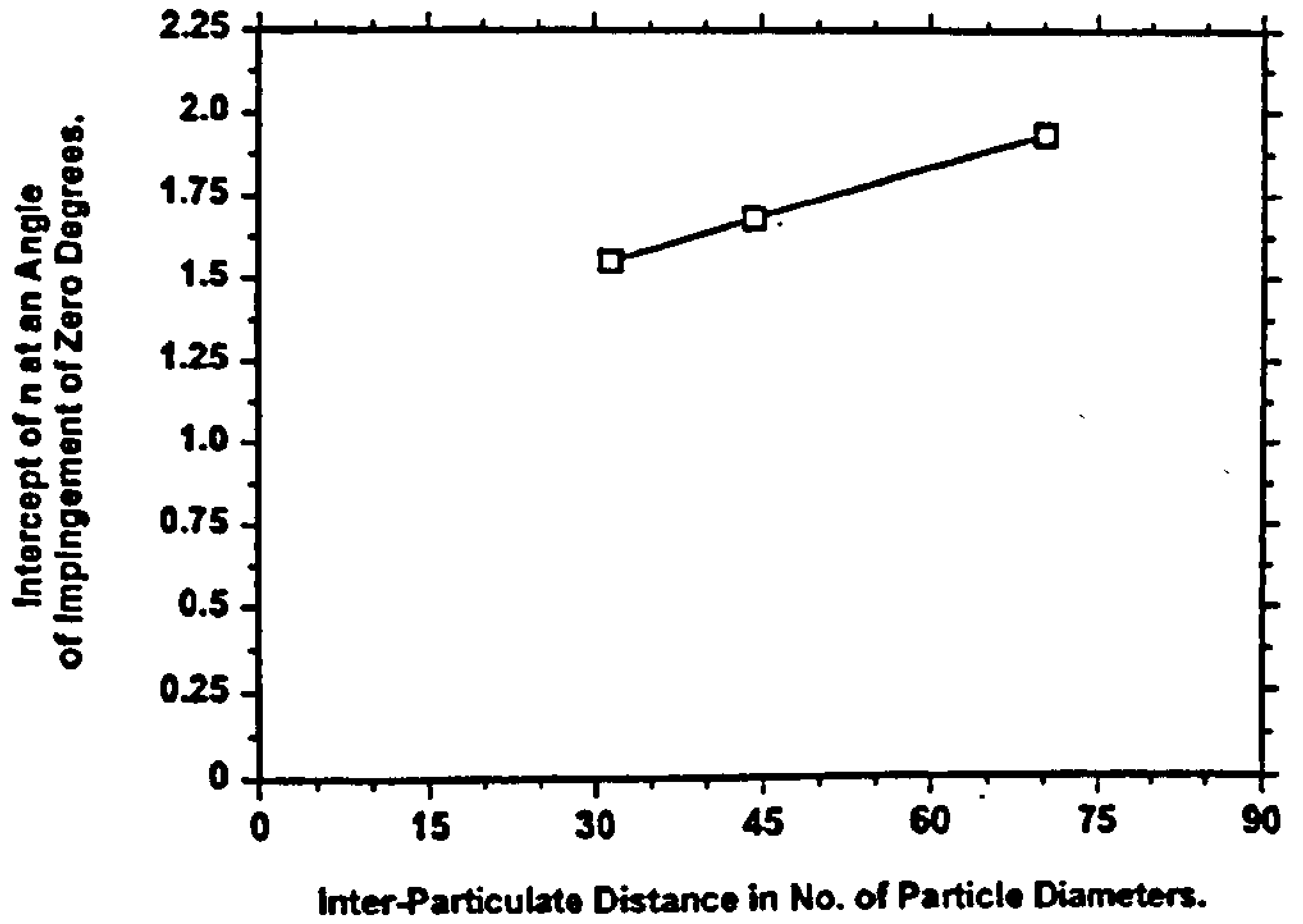

Figure 7: Variation of the intercept of the power law exponent, n, with inter-particulate distance.

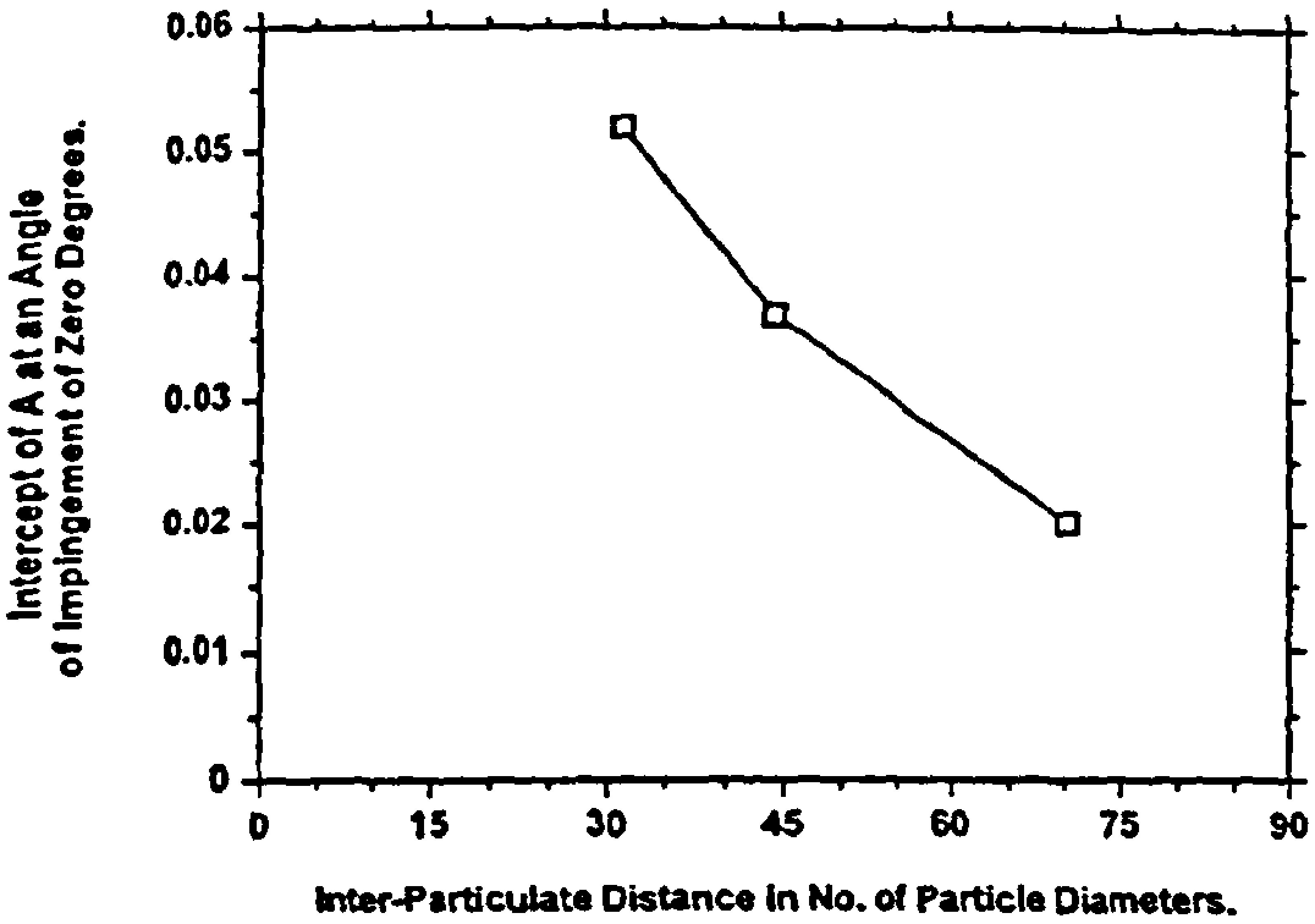

Figure 8: Variation of the intercept of the power law constant, a, with inter-particulate distance.

The linear equations fitted to the data obtained for the variation of c_n and c_a with inter-particulate distance, D, are as follows:-

For the intercept for the power law exponent, n;

$$c_n = 0.00988\ D + 1.239 \qquad (5)$$

For the intercept for the power law constant, a;

$$c_a = -7.983E\text{-}4\ D + 0.0751 \qquad (6)$$

In both cases trying to fit curves to the variation of the slopes of the curves fitted to the power law constant and exponents proved to be very unreliable. The main reason for this was that there are only three data points for each constant. However, there was a consistent trend between the values of m_n and m_a. Actual values of these slopes are shown in the following table.

Particle Concentration Density (kg/m³)	m_n	m_a
1	0.0143	-0.0605
4	0.02399	-0.0935
13	0.0238	-0.0955

In both instances the above values seem to suggest that there have been step changes in the values of these variables between a particle concentration density of 1 and 4 kg/m³. However, there are not enough data to be definitive about the cause of this behaviour.

All of the numerical curve fit constants used in the above equations will be dependent on a combination of the properties of the abrasive or sample materials.

7. DISCUSSION

Several unusual and novel features of erosion behaviour have arisen because of this test work. The most fundamental of these is the fact that the erosion damage does not seem to reduce as the impingement angle approaches zero degrees. This is different from previously reported data as mentioned earlier. There are two main reasons why this may be the case. First, previous erosion tests may have been carried out using similar times of exposure to the stream of abrasive materials. This is a different approach from that used in the derivation of the results presented in this paper. The graphical presentation of the results of some calculations for the time required for a fixed mass of abrasive to strike a target made for the centripetal accelerator erosion tester is shown below.

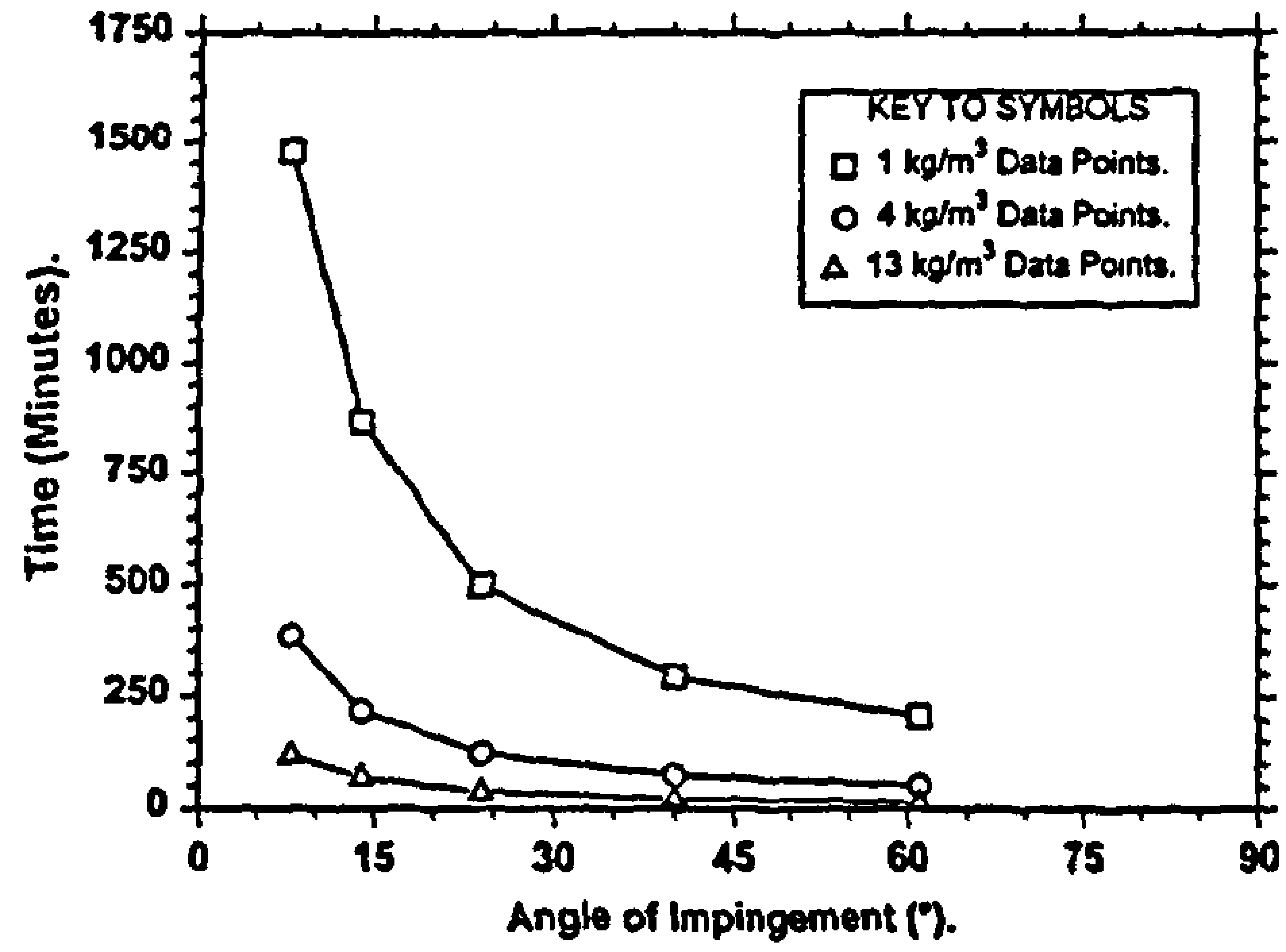

Figure 9: Graph of time taken for a fixed mass of abrasive of 500g to strike targets at a range of orientations.

The graph shows that as the target angle is reduced it takes a longer time for the same mass of abrasive to strike the target, in comparison to those targets orientated to give the higher impingement angles. This leads to the situation where a target orientated at a small angle of impingement to the particle trajectory will not be struck by a sufficient quantity of abrasive to ensure that steady state erosion is occurring. Obviously this is a problem that could be argued to be particular to the centripetal accelerator form of erosion tester. However, in a centripetal accelerator form of erosion tester the gas velocity induced in the acceleration of the particles is considerably smaller than the gas velocity found in the accelerating mechanism of a gas blast type erosion tester. The dynamic coupling between the particles and gas in a gas blast type erosion tester is therefore likely to be greater than in the centripetal accelerator form of rig (4). In testing in a gas blast type tester with small, low momentum particles there is an increased possibility that some particles will fail to strike the eroding surface. It is more likely, however, that they will strike at an impact angle different from that which was intended (13). It is therefore possible that the mass of abrasive striking a sample in such a tester is smaller than the mass of abrasive projected at it. Therefore the erosion damage expressed in terms of mm³/kg will be incorrect since the mass of abrasive striking the surface of the target will be in error.

Another reason the results are so different could be attributed to particle jet divergence that is a feature of the form of particle acceleration mechanism (13). As the sample orientation alters towards the lower impingement angles the area of the sample submitted to erosion damage will increase. Therefore, there will be a decrease in the intensity of particle impact in the area undergoing erosion. This will alter any effects due to inter-particulate collision that may have been occurring at higher impingement angles. Either of these two, or a combination of these two factors, may be the cause of these unexpected phenomena. Because of these findings it must be concluded that it is important that the manner in which the test results were obtained must be clearly stated. This fact is argued clearly in earlier work (3).

There are some very important implications to note because of these findings. The first of these are that although the erosion that occurs at very low impingement angles is the most severe per unit mass of abrasive striking the target, it takes much longer for the mass of abrasive causing the erosion to strike the surface at this angle. It is therefore quite conceivable that the angle of impingement where erosion damage first becomes apparent in a pneumatic conveyor bend will be approximately 20° to 35°. This is because the mass of abrasive striking at this impact angle will be greater when taken in comparison with that which occurs at lower impingement angles (Figure 7). Consequently, the product of the erosion damage per unit mass of abrasive and the mass flow rate per unit surface area is greatest at this angle.

From the curve fitting exercises that have been carried out it seems that the impingement angle dictates to a large degree the size of the power law exponent that can be fitted to the erosion versus impact velocity data. This statement is also applicable to the variation of the power law constant. In Humphrey's paper (13) it is said that the power law exponent should vary between 2.3 and 2.7 for a ductile metal. However, no mention was made of the fact that the impingement angle had such an important effect on the erosion damage power law exponent. Modification to the exponent could be made, according to Humphrey, by adding an extra factor, m. This factor accounts for the fact that the coupling between the gas and particles may cause the particles to strike the target at angles different from those originally intended. Calculations have concluded that the olivine sand particles used in the tests described in this paper will suffer very little from these coupling effects due to their comparatively large mass (4). The minimum exponent value occurs at the boundary of zero degree impingement angle and has a value of approximately 1.55 for tests carried out at a particle concentration density of 13 kg/m^3. We suggest the reason the value of the exponent was significantly less than 2 was due to the effects of inter-particulate distance or more generally particle concentration. The number density of particles near the eroding surface will affect the efficiency with which the particles cause erosion. It is proposed that the erosion damage could perhaps be modelled in the following manner: -

$$E = a\,V_p^{(2\ n\ m)} \tag{7}$$

Where E is the erosion damage in mm^3/kg; V_p is the particle velocity in m/s; a & n are numerical constants that vary with the angle of impingement and the inter-particulate distance as described earlier in this paper, and m is a constant that depends upon the level of coupling between the gas and particles. Obviously many tests would have to be carried out to establish whether this is a viable method of modelling erosion.

8. CONCLUSIONS

It has been confirmed that the particle impact velocity is the variable that erosion damage is most dependent upon. A series of power law curves can be fitted to data for erosion that has occurred at a range of angles of impingement. Apparently the variations of the exponents and constants of multiplication for these power laws vary in definite ways with inter-particulate distance and angle of impingement. We think a general particle impact velocity based power law model can be used to predict damage by erosive wear. However, a considerable amount of further experimental work needs to be carried out to establish whether this method is valid or not.

In the prediction of erosion damage within pneumatic conveyor components, long radius mild steel conveying bends will suffer from particle collisions at low impingement angles. The erosion caused at these angles is a maximum but it will take a significantly longer time for a significant mass of abrasive to strike the wall at this angle. Consequently, the failure of the pipe bend in the area where particle impact is occurring at these low impact angles will be delayed. Failure occurs where the particle impact angle is higher (approximately 30°) simply due to that fact that significantly more abrasive material will strike in this area, and cause greater erosion damage than at smaller angles of impingement in any fixed unit of time.

Two sure ways of increasing the life of any given pneumatic conveyor component are by either reducing the particle velocity or increasing the particle concentration of the flowing suspension; The velocity effect is by far the most effective method when taken in isolation.

9. ACKNOWLEDGEMENTS

The authors would like to thank The Science and Engineering Research Council of the United Kingdom (now the EPSRC) for funding this research project. We would also like to thank all the members of staff and technical support staff of The Wolfson Centre for Bulk Solids Handling Technology and The School of Engineering at The University of Greenwich, London, UK.

10. REFERENCES

1. MILLS D., MASON J.S., 'The influence of velocity on the erosive wear of pipe bends in pneumatic conveying

systems', Proceedings of the Technical Program of the Int'l Powder and Bulk Solids Handling and Processing Conf., Philadelphia, Pennsylvania, May 15-17, 1979, 300-314.

2. KLEIS I.R., UUEMOIS H.H., UKSTI L.A., PAPPEL T.A., 'Centrifugal accelerators for erosion research and standard wear testing', The Int'l Conf. on Wear of Materials, Dearborn, Michigan, April 16-18, 1979, 212-218.

3. SÖDERBERG S., HOGMARK S., ENGMAN U., SWAHN H., 'Erosion classification of materials using a centrifugal erosion tester', Tribology Int'l, December, 1981, 333-343.

4. BURNETT A.J., DE SILVA S.R., REED A.R., 'Comparisons between 'sand blast' and 'centripetal effect accelerator' type erosion testers', Proceedings of the 8th Int'l Conf. on Erosion by Liquid and Solid Impact, Cambridge, UK, 4-8 September 1994, to be published in a special edition of Wear, July, 1995.

5. YEUNG W.S., 'Erosion in a curved pipe', Wear, 55 (1979), 91-106.

6. BARNES R.N.,'Resonant Vibratory Feeders', Int'l Conf. on Bulk Materials Handling and Transportation, Symposium on Freight Pipelines, Wollongong, Australia, 6-8 July 1992, 321-326.

7. BURNETT A.J. 'Particle dynamics within centripetal accelerator erosion testers', in preparation.

8. HUTCHINGS I.M., LEVY A.V., 'Thermal effects in the erosion of ductile metals', Wear, 131 (1989), 105-121.

9. RUFF A.W., WEIDERHORN S.M., 'Erosion by solid particle impact', Treatise on Materials Science and Technology, Vol. 16, ed. C. Preece, 69-126.

10. ELLERMAA R.R.R., 'Erosion prediction of pure metals and carbon steels', Wear, 162-164 (1993), 1114-1122.

11. KRISHNAMOORTHY P.R., SEETHARAMU S., SAMPATHKUMARAN P., 'Influence of the mass flux and impact angle of the abrasive on the erosion resistance of materials used in pulverised fuel bends and other components in thermal power stations', Wear, 165 (1993), 151-157.

12. FINNIE I., 'Erosion of surfaces by solid particles', Wear, 3 (1960), 87-103.

13. HUMPHREY J.A.C., 'Fundamentals of fluid motion in erosion by solid particle impact', Int. J. of Heat and Fluid Flow, Vol. 11, No. 3, September 1990, 170-195.

14. ANDREWS D.R., HORSFIELD N., 'Particle collisions in the vicinity of an eroding surface', J. Phys. D: Appl. Phys., 16, (1983), 525-538.